Spring 2020

Synthesis and Characterization of Biomimetic Model Systems for the Study of Diiron Hydrogenase and Porphyrin Enzymes

Brian Francis Patenaude
University of New Hampshire, Durham

SYNTHESIS AND CHARACTERIZATION OF BIOMIMETIC MODEL SYSTEMS FOR THE STUDY OF DIIRON HYDROGENASE AND PORPHYRIN ENZYMES

BY

BRIAN F PATENAUDE

B.S. Physics & B.S. Mathematics, University of New Hampshire, 2009

DISSERTATION

Submitted to the University of New Hampshire

In Partial Fulfillment of

the Requirements for the Degree of

Doctor of Philosophy

In

Chemistry

May 2020

This dissertation has been examined and approved in partial fulfillment of the requirements for the degree of Doctor of Philosophy in Chemistry by:

Dissertation Director, Samuel Pazicni, Assistant Professor of Chemistry, University of Wisconsin - Madison

Roy P. Planalp, Associate Professor of Chemistry

Christopher F. Bauer, Professor of Chemistry

Glen P. Miller, Professor of Chemistry and Materials Science, Chair of Chemistry Department

Karsten Pohl, Professor of Physics and Material Science, Chair of Physics & Astronomy Department

On April 1st, 2020

DEDICATION

To my wife, Adina, who is my pillar of strength and to my daughter, Ariana, who has fought through a difficult start in life and makes me prouder every day.

ACKNOWLEDGEMENTS

I would like to thank my advisor, Samuel Pazicni, for his continued support and understanding as I grew as a chemist. You made my graduate career exciting and enjoyable as you allowed me a great degree of independence in my research which made the research projects feel much more personal. In addition, you were an excellent and patient mentor with a wealth of knowledge to share.

I would like to thank Prof. Rudi Seitz for his supportive advice as I transitioned from a continuing education student without an actual degree in chemistry to a full graduate student. Without meeting with you I may not have started my path as a graduate student in chemistry.

I would like to thank Prof. Erik Berda for his continued support during the porphyrin project. Whether discussing polymer synthesis and characterization, martial arts, or life in general, conversations with you tended to refocus me and send me in the right direction.

I would like to thank my past and current committee members, Profs. Marc Boudreau, Christine Caputo, Gonghu Li, Christopher Bauer, Glen Miller, Roy Planalp, and Karsten Pohl for your guidance and continued support. It was greatly helpful to have a group of professors in which I felt comfortable consulting with, without fear of judgement due to my own lack of knowledge or perspective. You all helped hone my approach to problem solving and aided my growth as a scientist.

I would like to thank Dr. Pat Wilkinson for her continual help with spectroscopy and instrumentation. Your mentoring and hard work are greatly appreciated. Without your guidance and training I would not have been able to finish my projects.

I would like to thank everyone in the chemistry office and stockroom; Cindi, Peg, Laura, and Kristin thank you for keeping the department running smoothly and advocating for the students. You were always there when the graduate students were in need.

Thank you to all my friends in the department; Carter, Charlie, Ethan, Hannah, Jon, Liz, M.J., Stacie, and Zane your support and camaraderie made graduate school a great and fulfilling experience. And to the previous Pazicni group members; Christian, David, Kyle, Matt, Sarah, Drew, Madison, Cole, and Graham thank you for being great coworkers. May you all have success in all your future endeavors.

Lastly, if it wasn't for the support of my friends and family, I would not have the chance to pursue my love of science. To my wife, thank your continued patience through this time and for keeping me sane. To my daughter Ariana thank you for giving me a new perspective on life. To my parents thank you for imbuing me with a love for science and logic and the work ethic to never give up.

TABLE OF CONTENTS

LIST OF SCHEMES

LIST OF FIGURES

LIST OF TABLES

ABSTRACT

SYNTHESIS AND CHARACTERIZATION OF BIOMIMETIC MODEL SYSTEMS FOR THE STUDY OF DIIRON HYDROGENASE AND PORPHYRIN ENZYMES

By

Brian F. Patenaude

University of New Hampshire, May 2020

The branch of biomimetic chemistry aims to imitate natural reactions and enzymatic processes in order to advance many other areas of chemistry, including inorganic and organic catalysis as well as materials science. To study the mechanisms of enzyme activity and the effect of secondary coordination sphere interactions, the synthesis and characterization of two artificial metallo-enzymes were pursued.

In order to further understand the mechanism of [FeFe]-hydrogenase and the effect of secondary coordination sphere interactions within the protein binding pocket, the synthesis of an optimized biotin-avidin [FeFe] artificial enzyme was pursued. This dissertation describes the synthesis and characterization of the small molecule components explored for the insertion of an azadithiolato bridged [FeFe] cluster into avidin or streptavidin in order to generate a novel biotin-avidin [FeFe] hydrogenase. While further research is required in order to obtain the desired aza-bridged [FeFe] cluster compatible with insertion into avidin, the insight obtained through the attempted synthesis herein may aid others in their synthesis of [FeFe]-hydrogenase model complexes.

In order to study heme enzymes, a suite of zinc porphyrin-cored random coil polymers and polymeric nanoparticles with varying degrees of potential hydrogen bonding character and steric bulk were synthesized to study secondary coordination sphere interactions. Cyanide binding studies intended to probe for hydrogen bonding environments generated by the polymer scaffold resulted in the catalytic reaction of cyanide with the solvent N,N-dimethylformamide. The reaction of cyanide with N,N-dimethylformamide in the presence of the biomimetic polymers was monitored via UV-Vis spectroscopy. The spectroscopic data lead to the determination that the collapsed topology of the polymeric nanoparticles led to higher catalytic activity than that of the random coil polymers with the fastest reactions rates occurring with polymeric nanoparticles with a greater number of potential hydrogen bond donors and larger steric bulk.

Chapter I. Introduction to Artificial Enzymes

A Brief History of Artificial Enzymes

In 1926, Urease became the first enzyme to be successfully crystallized and determined to be a protein, winning James Sumner the Nobel Prize for Chemistry in 1946. Prior to Sumner's discovery that enzymes were proteins, enzymes were suspected to be low molecular weight catalysts which in solution would bind to proteins.[1]

The first reported attempt to replicate enzyme activity via a macromolecular model was reported by Katchalski and coworkers. In their 1960 publication, Katchalski et al. sought to elucidate the roll of histidine and serine in the active site of chymotrypsin, an enzyme which hydrolyzes esters, via a set of histidine containing synthetic polypeptides.[2] Unfortunately, all Histidine containing polymers tested presented less than 1/1000 of the activity of the natural chymotrypsin enzyme and less than a third of the activity of imidazole for the hydrolysis of p-nitrophenyl acetate.[2]

Several years later, inclusion compounds of cyclodextrin joined the ranks of the first macromolecular compounds to mimic the activity of enzymes. In 1965, Friedrich Cramer et al. reported two model reactions for the mechanism of enzymes including the catalysis of decarboxylation of carboxylic acids and the fission of pyrophosphate by cyclodextrin.[3,4] Cramer found that cyclodextrins bound particular substrates in such a way that cyclodextrin could act as a proton acceptor and donor simultaneously much like the expected function of an enzyme. [3,4]

Though earlier groups sought to emulate the catalytic action found in natural enzymes, the term "Artificial enzyme" wasn't coined until 1970 by Breslow and Overman referring to the incorporation of a metal catalytic group into a hydrophobic binding cavity. In the first study of an

"Artificial enzyme", cyclohexaamylose, a toroidal polysaccharide, functionalized with an Ni(II) pyridine-carboxaldoxime catalyst was utilized to catalyze the hydrolysis of a non-ligand substrate, p-nitrophenyl acetate.[5] The cyclohexaamylose acted as a binding pocket for the p-nitrophenyl acetate increasing the reaction rate by a factor of four in comparison to the free Ni(II) pyridine-carboxaldoxime catalyst.[5] Breslow and Overman's nickel functionalized cyclohexaamylose was the first example of an artificial metallo-enzyme.

Despite several attempts to prepare synthetic polymers with similar catalytic activity to native enzymes particularly chymotrypsin,[2,6–10] it wasn't until 1971 that Klotz et al. reported the first polymer to have catalytic activity comparable with the native enzyme being modelled.[11] In the report by Klotz et al., a series of polyethyleneimine polymers alkylated with dodecyl and methylene imidazole substituents were able to catalyze the hydrolysis of nitrophenyl esters with one third the activity of the chymotrypsin enzyme and more than 100 times the activity of the small molecule imidazole.[11]

As the field of artificial enzymes and nature inspired synthesis was expanding, the term "biomimetic chemistry" was first introduced in 1972 by Ronald Breslow. Biomimetic chemistry became the branch of chemistry which aims to imitate natural reactions and enzymatic processes to improve the reactivity and more importantly the selectivity of reactions.[12,13] At the time, this growing field of chemistry was also referenced to as "enzyme-mimetic chemistry".[13]

In 1978, Wilson and Whitesides reported the first conversion of a catalytically non-active protein into a fully functional artificial enzyme catalyst. In Wilson and Whitesides' report, the inclusion of N,N-bis(2-diphenylphosphinoethyl)biotinamide rhodium norbornadiene triflate into the barrel protein avidin lead to the enantioselective hydrogenation of α-acetamidoacrylic acid. Attempting hydrogenation of α-acetamidoacrylic acid with the N,N-bis(2-

diphenylphosphinoethyl)biotinamide in the presence of avidin precomplexed with biotin resulted in the loss of enantioselectivity. Thus, synthesizing the first biotin-avidin artificial enzyme and giving evidence to the importance of secondary coordination sphere interactions.

In the same year, 1978, the general method for the technique of site-directed mutagenesis was published by Hutchison et al, eventually earning the principle investigator Michael Smith the Nobel Prize in Chemistry in 1993.[14] Site-directed mutagenesis would later become key in the systematic exploration of natural enzyme mechanisms and the optimization of several artificial enzymes generated from protein substrates. [15–17]

In 1986, Pollack, Jeffrey and Schultz reported a new form of artificial enzymes, catalytic antibodies. Pollack et al. exploited the geometry of hydrogen bonding in the phosphorylcholine ester binding site of immunoglobin MOPC167 to place p-nitrophenyl N-trimethylammonioethyl carbonate chloride into a geometry similar to the expected transition state for its hydrolysis, resulting in the lowering the free energy of activation and eventual hydrolysis of the carbonate.[18] While the new catalytic antibody was selected for enzyme activity rather than synthesized Pollack et al. described a methodology in which further research into the chemical derivation of binding sites may generate novel catalysts.[18,19] Following a similar selection methodology to that of Pollack et al., artificial enzymes prepared from RNA and DNA , RNAzyme and DNAzyme, were eventually reported in 1994 and 1996, respectively.[20–22]

In 2004, the term “Nanozyme” was coined by Manea et al. in reference to the use of a functionalized nanoparticle as a model complex for enzymatic processes. In the publication by Manea et al., as a model of a RNase enzyme, gold nanoparticles were functionalized with Cu^{II} or Zn^{II} bound azacrown-thiols to yield nano catalysts for cleavage of the phosphate bond of phosphodiesters.[23]

While providing a brief snapshot of the history of artificial enzymes and the strategies used to mimic natural enzymes, the field of biomimetic chemistry is ever growing. Currently, "artificial enzyme" has been mentioned over 200 times a year and "biomimetic chemistry" have been mentioned over 1500 times a year in the scientific literature for the last five years (figure 1). With such an active research community it will be interesting to see how the biomimetic chemistry field progresses in the future.

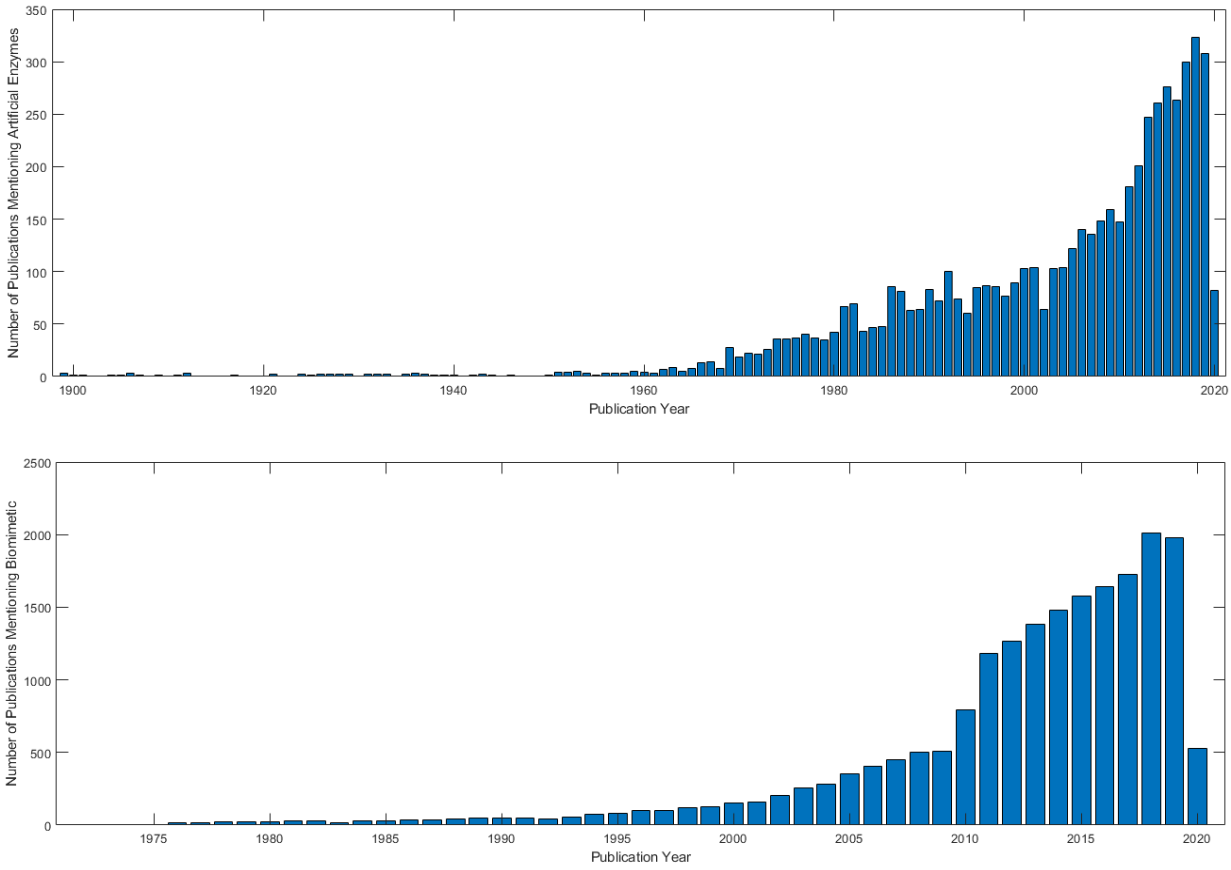

Figure 1: Bar graphs of the number of publications mentioning "Artificial Enzymes" (Top) and "Biomimetic" (Bottom) per year. Sample analysis of publications exported from Scifinder on March 17th, 2020.

Introduction Biotin-Avidin Artificial Enzymes

Avidin, a homo-tetrameric glycosylated calycin protein, is well known for its high binding affinity for the small molecule biotin, $K_d = 10^{-15}$ M (figure 2).[24–26] Avidin was first isolated from egg whites by Eakin et al. in 1941 while investigating the cause of dermatitis in animals fed dried eggs.[27] There are 14 specific amino acids responsible for the high binding affinity for biotin. The carbonyl of urea is bound by Tyr33, Ser16, and Asn12, the protons of the urea hydrogen bond with Thr35 and Asn12 and the hydrogen bonds with Ala39, Thr40, and Ser75 (figure 2). Further, van der Waals interactions with the aliphatic regions of the substrates can be achieved through the Thr38, Trp70, Phe72, Thr77, Trp97, Trp110, and Asn118 residues. [24,26]

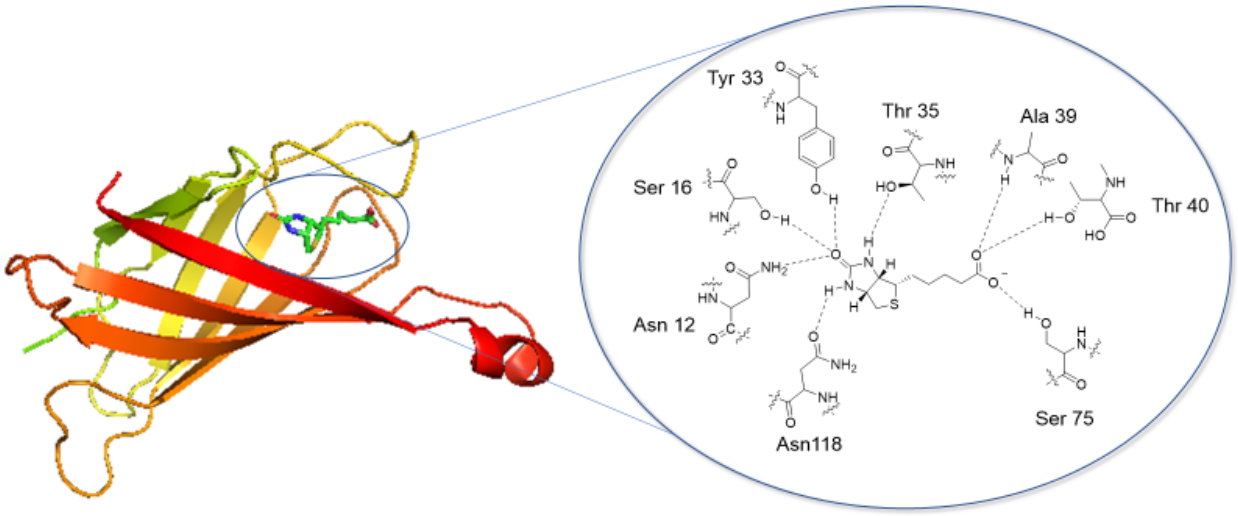

Figure 2: Structure of Avidin monomer unit with biotin bound PDB 2AVI (left)[28]*, biotin hydrogen bonding environment (right)*[26] *Protein structure plotted with PyMOL.* [29]

Avidin's high binding affinity for biotin and the ease of chemical modification of biotin's carboxylic group via amide coupling reactions has led to a variety of affinity technologies. These technologies include but are not limited to affinity chromatography, localization, immunoassays, labeling, gene probes, pre-targeting of tumors for radio-labeling, and most relevant to this report artificial metallo-enzymes.[30–38]

The first report of a biotin-Avidin metallo-enzyme was that of avidin bound N,N-bis(2-diphenylphosphinoethyl)biotinamide rhodium norbornadiene triflate (1·RhNBD^{+}Tf^{-}) synthesized by Wilson and Whitesides in 1978.[39] In the study (1·RhNBD^{+}Tf^{-}) was shown to be a moderately active hydrogenation catalyst of its own merit with no enantioselectivity in the reduction of α-acetamidoacrylic acid. In the presence of avidin, (1·RhNBD^{+}Tf^{-}) was shown to have a marked increase in activity with a ~ 40 % S enantiomeric excess (ee). In the presence of avidin pre complexed with biotin, the enantioselectivity of (1·RhNBD^{+}Tf^{-}) ⊂Avidin was lost. [39] (In artificial enzyme literature, ⊂ symbolizes the inclusion of the cofactor into the specified protein.)

Replication of Wilson and Whitesides' hydrogenation experiment by Collot et al., resulted in a 37 % S ee for the hydrogenation of α-acetamidoacrylic acid with (1·RhNBD^{+}Tf^{-}) ⊂Avidin. Further screening of the hydrogenation of α-acetamidoacrylic acid varying the host protein, buffer, and ligand by Collot et al. resulted in a 7 % S ee with (1·RhNBD^{+}Tf^{-}) ⊂ neutravidin, 92% R ee with (1·RhNBD^{+}Tf^{-}) ⊂Streptavidin, and a 96 % R ee with (1·RhNBD^{+}Tf^{-}) ⊂StreptavidinS122G. The results of the screening show a wide degree of variation in enantioselectivity based the secondary coordination sphere interactions provided by the protein environment.[35]

Further screening by Klein et al. of the hydrogenation of α-acetamidoacrylic acid and a-acetamidocinnamic acid against 360 different artificial enzymes generated by the combination of 20 host proteins produced through saturated mutagenesis of streptavidin at position 112 and 18 biotin-rhodium complexes, resulted in the selective isolation of either the R and S reduction products in high ee and % conversion. Based on the screening it was found that enantioselectivity was predominantly controlled by the chemical optimization of the biotin-rhodium complexes while the genetic optimization through saturation mutagenesis allowed for fine tuning of the secondary coordination sphere interactions leading to increased reactivity.[40]

The synthesis of biotin-avidin artificial enzymes is a continually growing field of research. Since the initial hydrogenation experiments of Wilson and Whitesides, the use of biotin-avidin enzymes has expanded to a wide variety of applications from transfer hydrogenation to olefin metathesis (Table 1). Most recently, the Thomas Ward group has been expanding the use of biotin-avidin systems into multiple enzyme systems to study cascade reactions involving artificial enzymes.[38] It was the intent of the artificial diiron hydrogenase project to expand upon the growing list of biotin-avidin applications, it will be interesting to see how the field grows from here on out.

Table 1: Select applications of biotin-avidin artificial enzymes (P,P = various diphosphine ligands, N,N = various diamine ligands, NHC = N-Heterocyclic Carbene)

Reaction Type	Substrate	Metal	Ligand	host	ref
Hydrogenation	Alkene	Rh	P,P	Avidin	[35,39]
		Rh	P,P	neutravidin	[35]
		Rh	P,P	Streptavidin	[35,40]
Transfer hydrogenation	Ketone	Ru	N,N	Avidin	[41]
		Ru, Rh, Ir	N,N	Streptavidin	[36,41]
	Imine	Ir	(Cp*) (N,N)	Streptavidin	[42–44]
		Ir	(Cp*)(phen$(OH)_2$)	Streptavidin	[45]
Allylic alkylation	Allyl	Pd	P,P	Avidin	[46]
		Pd	P,P	Streptavidin	[46]
Sulfoxidation	Sulfide	Mn	Salen	Streptavidin	[47]
Alcohol oxidation	Alcohol	Ru	(Cp)(N,N)	Avidin	[48]
		Ru, Rh, Ir	(Cp*)(N,N),(Cp)(N,N)	Streptavidin	[48]
Olefin metathesis	Alkene	Ru	NHC	Avidin	[49]
		Ru	NHC	Streptavidin	[49]

Introduction to Polymeric Enzyme Models

The field of biomimetic polymer systems have grown to encompass a large variety of applications including but not limited to biomimetic super hydrophobic surfaces, biomimetic cellular structures, nano-reactors, drug-delivery, and artificial enymes.[50–56] Of interest to the research of this dissertation are polymer systems which specifically model natural enzymes. In this section, select examples in the progress to enzymes and enzymatic activity will be presented.

Katchalski et al. were the first to report an attempt at replicating the activity of an enzyme via a synthetic polymer model. In their 1960 publication, Katchalski et al. probed the effects of histidine and serine in the active site of chymotrypsin during the hydrolysis of esters via a set of histidine containing synthetic polypeptides.[2] Unfortunately, all Histidine containing polymers presented less than 1/1000 of the activity of the chymotrypsin enzyme and less than one third the activity of imidazole for the hydrolysis of p-nitrophenyl acetate.[2]

It wasn't until several years later that Klotz et al. reported the first polymer to successfully mimic the enzyme activity. In the reports by Klotz et al., a series of polyethyleneimine polymers were tested as catalysts for the hydrolysis of nitrophenyl esters, resulting in catalytic activity comparable to a third of the native chymotrypsin enzyme and ~ 1000 times greater than the histidine polypeptide predecessor.[11] In addition, regeneration of the imidazole-dodecyl-polyethyleneimine catalyst was observed making reported polymer a true catalyst or synzyme.[11]

As the polyethyleneimine polymer synthesized by Klotz et al. was not functionalized with any functional groups which mimic the serine associated with the active site of the natural chymotrypsin enzyme, Kiefer and coworkers proposed the comparison of the polymer to a more representative natural enzyme, Arylsulfatase.[57] In their 1972 publication, Kiefer et al. found that polyethyleneimine-imidazole-dodecyl polymers were capable of catalyzing the hydrolysis of

sulfates 10^9 times increase in efficiency compared to free imidazole and an 100 fold increase in catalytic activity compared to type IIA arylsulfatase from kangaroo liver.[57] Making polyethyleneimine-imidazole-dodecyl polymers the first polymeric enzyme model to exceed the catalytic activity of the natural enzyme it was modelling.

Advances in single chain polymeric nanoparticles (SCNPs) have allowed for a greater variety of artificial enzymes targets. Recently in 2013, Sanchez-Sanchez and coworkers of the Pomposo group expanded the application of single chain polymers to incorporate reversible enzyme like vitamin binding.[58] In the study, a methyl methacrylate – (2-acetoacetoxy)ethyl methacrylate copolymer was synthesized via reversible addition-fragmentation chain-transfer (RAFT) polymerization.[58] The randomly dispersed β-ketoester functional groups acted as Michael donors upon addition of Michael acceptor cross-linkers caused the single chain polymer to collapse into a nanoparticles resembling disordered multidomain proteins.[58] Testing of the potential drug delivery application of these nanoparticles resulted in the controlled delivery of a 41% percent vitamin B_9 loading over the course of 6 hours in water.[58]

In the same year Perez-Baena and coworkers of the Pomposo group, reported the synthesis of a new set of SCNPs with inherent reductase and polymerase enzymatic properties. The SCNPs were synthesized by the post polymerization modification of benzyl methacrylate/glycidyl methacrylate co polymer via a tris(pentafluorophenyl)borane catalyzed intramolecular cross-linking.[59] The resulting SCNPs were able to reduce α-diketones to 1,2-diols with turnover frequencies up to 5595 h^{-1} and were able to polymerize tetrahydrofuran at room temperature in the presence of glycidyl phenyl ether.[59]

In 2015, through the combination of single chain polymer nanoparticle and thiol-ene click chemistry Tooley and coworkers reported the first SCNP-based model for metalloenzymes bearing

a single active site.[60] The reported polymers included a series of styrene/methyl methacrylate/9-antrhacynlmethyl methacrylate copolymers and poly(Methyl N-isopropylacrylamide) polymers which had been coupled to either (μ-allylazadithiolato)diiron(I) hexacarbonyl or (μ-propargylazadithiolato)diiron(I) hexacarbonyl through a thiol-ene click reaction followed by photoinduced dimerization of the anthracene units to generate a series of SCNP model complex es of the [FeFe]-hydrogenase enzyme.[60] While the formation of the artificial hydrogenases were characterized by size exclusion chromatography and infrared spectroscopy the enzymatic activity of these compounds were not reported.

In 2016, Rodriguez et al. reported the synthesis of the first collapsible heme-centered star polymer to act as models for heme enzymes.[61] In Rodriguez and coworker's report, porphyrin cored methyl methacrylate/9-anthracenylmethyl methacrylate copolymers were synthesized via RAFT polymerization and iron was complexed by the addition of iron bromide and collapsed into nanoparticles via photodimerization of the anthracene units.[61] The Iron-porphyrin cored star polymers were then screened for ligand-binding reactivity against ligands known to bind heme enzymes, resulting in the determination that the resulting porphyrin cored polymer nanoparticles had displayed similar ligand binding reactivity as that of natural heme enzymes.

It was the goal of the second project of this dissertation to expand upon the work of Rodriguez et al. by probing the secondary coordination sphere interactions present at the porphyrin core due to the polymer scaffold.

Chapter II. Artificial Diiron Hydrogenase Enzyme

Introduction

Hydrogenases are a class of metalloenzymes which reversibly catalyze the redox reaction of dihydrogen to protons and electrons (equation 1).[62–66]

$$H_2 \rightleftharpoons 2H^+ + 2e^- \qquad (1)$$

In nature, various bacteria, archaea and some eukarya use the reducing power of hydrogen oxidation to fuel their metabolism (Table 2) or as "electron sinks" when the reverse reaction is favorable.[67–70] The earliest report of the isolation of an organism capable of using the oxidation of hydrogen by molecular oxygen as a source of energy was that of B. pantotrophus (Hydrogenomonas pantotropha) published by Kaserer in 1906.[71] The term hydrogenase was coined by Stephenson and Stickland for the enzymes responsible the activation of molecular hydrogen in 1931.[72] Currently there are several subclasses of hydrogenases based on the composition of their catalytic centers including [NiFe], [NiFeSe],[FeFe], and [Fe-only] hydrogenases.[62–65,73–77]

Table 2: Utilization of H_2 by hydrogenase enzyme containing microorganisms under anerobic conditions [63,78]

Electron Acceptor	Reaction	Genus or Species
Sulfate, SO_4^{2-}	$4\,H_2 + SO_4^{2-} \rightarrow S^{2-} + 4\,H_2O$	Desulfovibrio
Carbon dioxide, CO_2	$4\,H_2 + CO_2 \rightarrow CH_4 + 2\,H_2O$	Methanobacterium
Carbon dioxide, CO_2	$4\,H_2 + 2\,CO_2 \rightarrow CH_3COOH + 2\,H_2O$	Acetobacterium
Sulfur, S^0	$H_2 + S^0 \rightarrow H_2S$	Campylobacter
Nitrate, NO_3^-	$5\,H_2 + 2\,NO_3^- + H^+ \rightarrow N_2 + 6\,H_2O$	Paracoccus denitrificans
Fumarate	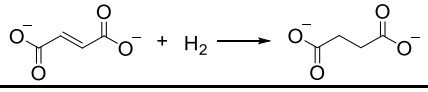	Vibrio Succinogenes

Due to the recent developments of the H_2 fuel economy to combat pollution and global warming,[79–81] [FeFe]-hydrogenases have become a main focal point for hydrogen evolution reaction (HER) research.[82–88] [FeFe]-Hydrogenases (figure 3) are a sub-class of the natural

catalytic enzymes found in a variety of anaerobic bacteria such as clostridiums and desulfovibrionales as well as eukaryotes such as piromyces and spirotricheas.[89] [FeFe]-Hydrogenase are known for their efficient catalysis of hydrogen reduction with measured turn over numbers ranging from 641 to 8200 μmol $H_2 \cdot min^{-1} \cdot mg^{-1}$ with turn over frequencies extrapolated up to ~21000 s^{-1}(Table 3).[62,90–92]

Table 3: Comparison of turn over frequency (TOF) and turnover number (TON) of select hydrogenase enzymes and biomimetic complexes

Complex	Technique	H_2 TOF (s^{-1})	TON (μmol $H_2 \cdot min^{-1} \cdot mg^{-1}$)	ref
Desulfovibrio desulfuricans ATCC 7757	methyl viologen reduction assay	-	8200	90
CaHydA	Electrochemical STM gold electrode	~1000 (extrapolated to ~21000)	-	93
CpI	methyl viologen reduction assay	-	1087 ± 146	91
Wild-type HydA1	methyl viologen reduction assay	-	641 ± 88	91
HydA1-1a	Gas chromatography	442 ± 50	-	94
HydA1-1b	Gas chromatography	207 ± 40	-	94
HydA1-2a	Gas chromatography	0.76 ± 0.25	-	94
HydA1-2b	Gas chromatography	0.13 ± 0.02	-	94
HydA1-3a	Gas chromatography	6.1 ± 1.1	-	94
HydA1-3b	Gas chromatography	0.19 ± 0.02	-	94
$[HFe_2(adt^{NH})(CO)_2(dppv)_2]^+$, $[t\text{-}H1NH]^+$	Electrochemical	5000	-	95
$[HFe_2(adt^{NH}H)(CO)_2(dppv)_2]^{2+}$, $[t\text{-}H1NH2]^{2+}$	Electrochemical	58000	-	95
$[Fe_2(adt^{NH})(\mu\text{-}H)(CO)_2(dppv)^{2+}$, $[\mu\text{-}H1NH]^+$	Electrochemical	20	-	95
$[HFe_2(pdt)(CO)2(dppv)2]^+$, $[t\text{-}H2]$	Electrochemical	5	-	95
$[Fe_2(pdt)(\mu\text{-}H)(CO)2(dppv)2]^+$, $[\mu\text{-}H2]^+$	Electrochemical	3	-	95

[FeFe]-Hydrogenases feature several motifs which enhance enzyme activity, including a binuclear active site, iron-sulfide clusters dispersed through the protein structure acting as an electron relay (figure 3), and a hydrophobic gas channel running from the protein surface to the distal iron of the binuclear active site.[62,96] The binuclear active which is covalently bound to the

protein substrate though a cysteine residue site consists of a diiron cluster with a bridging dithiolate, two CN^-, and three CO ligands (figure 3).[62] The structure of the diiron active site was relatively unknown until the first crystal structures of Clostridium pasteurianum and D. desulfuricans ATCC 7757 were solved by Peters et al. in 1998 and Nicolet et al. in 1999 respectively.[96,97] Initially, the bridging dithiolato ligand was modeled as 1,3-propanedithiolate. In 2001, Nicolet et al. rejected their original assessment of 1,3-propanedithiolate as the bridging ligand and proposed that azadithiolato was the actual bridging ligand based on stereochemical and mechanistic considerations (figure 3).[98]

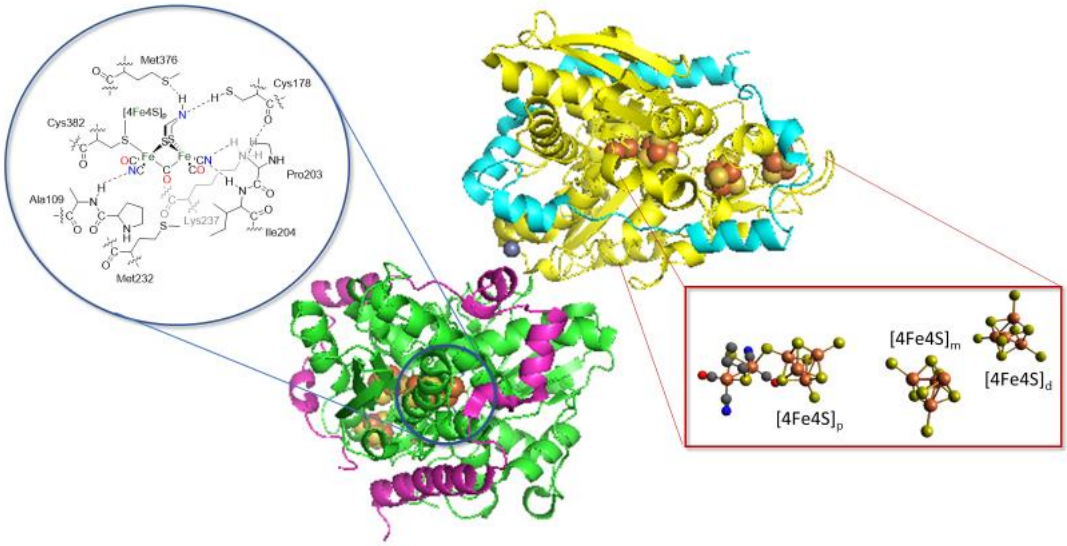

Figure 3: Hydrogenase enzyme from Desulfovibrio Desulfuricans (PDB 1HFE)[96] *(Center), [FeFe]-hydrogenase active site (left circle), and the electron transfer chain made up of iron-sulfur clusters (Right square). Protein structure plotted with PyMol*[29]*. Active site drawn with residue interactions based on 1HFE structure with replacement of μ-propanedithiolate ligand with μ-azadithiolate ligand predicted by Nicolet et al.*[62,98] *The electron transfer chain plotted with Avogadro based on 1HFE structure.*[62,99]

Evidence confirming the presence of an azadithiolate bridging ligand in native [FeFe]-hydrogenases was presented by Berggren et al. in 2013. In the studies conducted by Berggren et al., three synthetic mimics of the binuclear active site with varying dithiolate ligands were

transferred to apo-hydrogenase through a bacterial thermotogamaritima HydF intermediary. Of the prepared synthetic enzymes only those containing the azadithiolato ligand achieved hydrogen reduction activity comparable with that of the native C. reinhardtii hydrogenase enzyme CrHydA1, confirming the presence of an azadithiolate bridging ligand in the native enzyme.[100]

Insertion of model complexes into the apo-enzyme prior to artificial maturation was further explored by Siebel et al.[94] In their study, 15 different diiron complexes of varying ligation were transferred to apo-hydrogenase through a bacterial thermotogamaritima HydF intermediary prior to maturation. Changes in electronics lead to a moderate changes in activity, for example maturation of CrHydA1 with (μ-azadithiolato)diiron pentacarbonyl monocyano $[Fe_2(adt)(CO)_5(CN)]^-$ versus (μ-azadithiolato)diiron tetracarbonyl dicyano $[Fe_2(adt)(CO)_4(CN)_2]^{2-}$ lead to a ~2.25 fold decrease in TOF for hydrogen reduction. The greatest change in activity was observed due the change in bridging dithiolate ligand. Modification of the active center by replacing the azadithiolate with 1,3-propanedthiolate lead to a ~600 fold decrease in TOF for hydrogen reduction.[94]

In order study the mechanism hydrogen reduction exhibited by [FeFe] species, various small molecule and macromolecular diiron hydrogenase mimics have been synthesized. Of these model complexes few have achieved the catalytic activity comparable with that of the native enzyme.[101–107] An exception to the trend in low reactivities outside a protein substrate was that of the azadithiolate bridged $[Fe_2(adtNH_2)(CO)_2(dppv)_2]$ complex which was reported by Carroll et al. to have a turn over frequency of 58000 s^{-1} using bulk electrolysis against ferrocene in acetonitrile with trifluoroacetic acid as a sacrificial proton donor.[95] Under similar conditions the 1,3-propanedithiolate bridged $[Fe_2(pdt)(CO)_2(dppv)_2]$ was reported to have a turn over frequency of 5 s^{-1} in the presence of $HBF_4 \cdot Et_2O$ as a sacrificial proton donor.[95] Which continues the trend in which

the azadithiolate bridging ligand is key to the high activity for hydrogen reduction of [FeFe]-hydrogenases.

In order to study the effects of macromolecular environments on the catalysis of hydrogenase mimics coupling of diiron hydrogenase model complexes to polypeptides and non-native proteins have been previously explored.[108,109] While artificial hydrogenases generated by coupling biomimetic model complexes to polypeptides were unable to replicate the activity of the native enzymes,[108] the synthesis of an artificial hydrogenase enzyme using nitrobindin as a non-native protein environment reported by Onoda and coworkers offered promising results.[109] When coupled with $[Ru(bpy)3]^{2+}$ as a photosensitizer the nitrobindin artificial hydrogenase was found to have a TON of ~130 and a TOF of 2.3/min for hydrogen reduction which is comparative to the TOF of other alkyl bridged systems (Table 3).[109] As the nitrobindin artificial hydrogenase reported by Onoda et al, lacked the azadithiolate bridging ligand required for efficient catalysis of the hydrogen evolution reaction, it is expected the incorporation of an azadithiolato bridged diiron cluster into an non-native protein may increases proton reduction efficiency.

The research reported herein encompassed the attempted synthesis and characterization of an artificial [FeFe]-hydrogenase system by incorporating an azadithiolato ligated diiron cluster into a non-native protein via exploitation of the strong interaction of the small molecule biotin and the protein streptavidin (Figure 4).[110] The biotin-avidin system proposed for this research was designed to take advantage of streptavidin solubility in aqueous media and the ease of biotin tagging to address the issues of water solubility and size limitations of the binding site, as well as allow for systematic electronic and stearic tuning of the catalytic iron cluster via ligand substitution. Upon optimization of the biotinylated-diiron cluster it was expected that further

secondary coordination spheres interactions could be optimized through site-directed mutagenesis allowing for a fully optimized hydrogen evolution reaction catalyst.

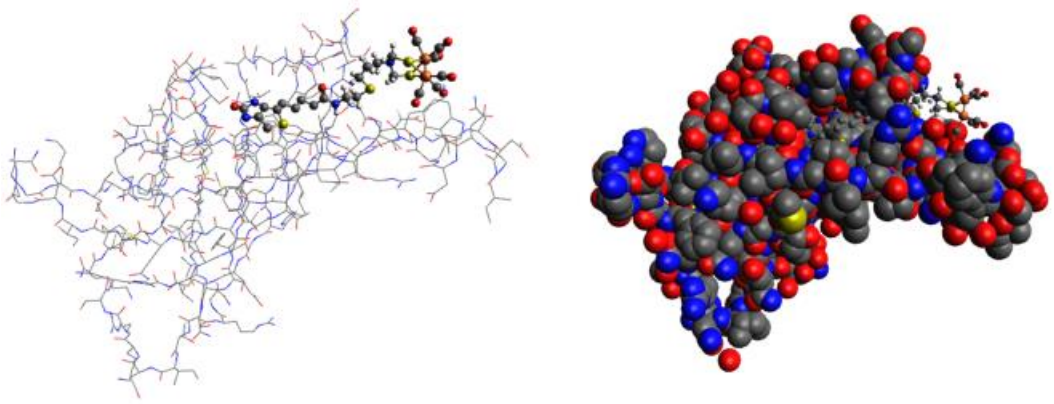

Figure 4: Cartoon of the proposed biotin-avidin artificial hydrogenase Avidin protein environment wire model (left) and Van der Waals spheres model (right) with Biotinylated-diiron cluster in ball and stick view. Cartoon generated with Avogadro molecule editor software [99] *with crystal structure of biotin bound avidin (PDB 2AVI)* [28] *set as fixed atoms and biotinylated diiron cluster geometry optimized using the universal force field (UFF) in the Avogadro software.*

Results and Discussion

In order to achieve an optimized artificial hydrogenase enzyme, synthetic routes which allowed for a set 3^3-factorial experimental design (Figure 5) comparing linker length, pKa of bridging ligand, and ligand field strength were sought (Scheme 1). It was theorized that the [(μ-S_2)$Fe_2(CO)_6$] cluster could be adjusted such that it sits just within the binding pocket of avidin allowing for moderate interaction with water as well as access to photosensitizers when in a photocatalytic application, while still allowing for steric and electronic tuning via ligand substitution.

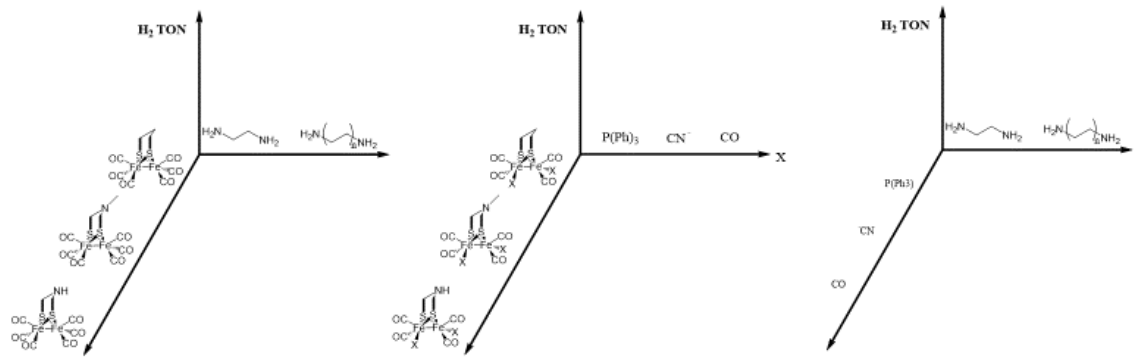

Figure 5: Proposed 3^3 factorial experiment comparing the effects of linker length, bridging ligand, ligand field strength for the elucidation of optimal biotinylated diiron cluster parameters for hydrogen evolution

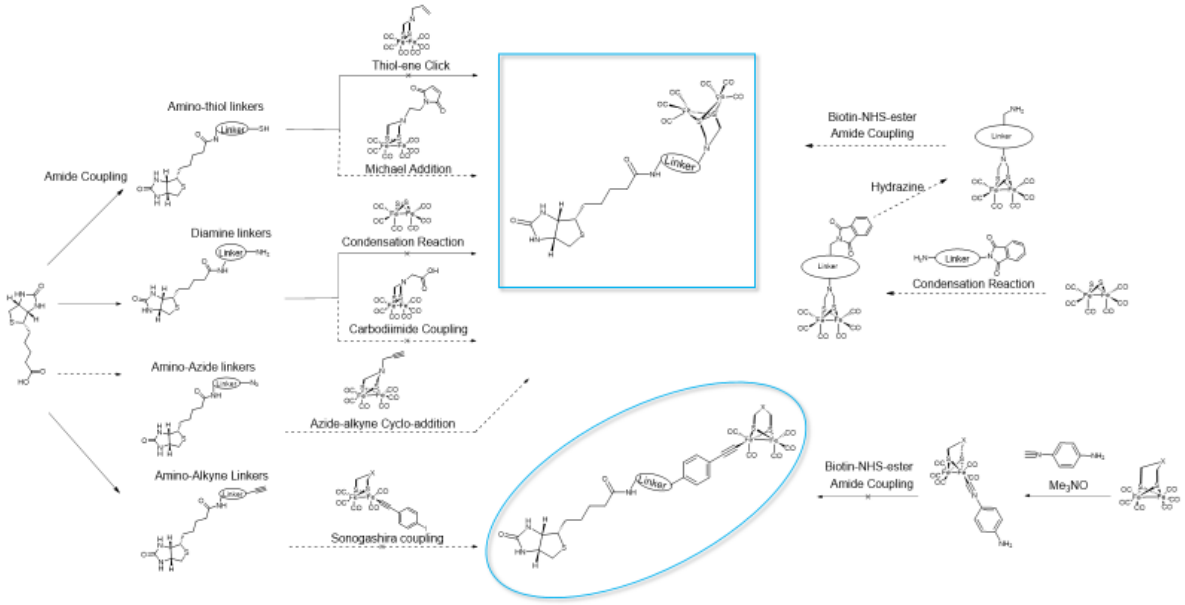

Scheme 1: Explored and proposed reaction pathways to obtain a set of tunable biotinylated diiron clusters

To synthesize a set of tunable biotinylated diiron cluster complexes compatible with a 2-factorial experimental design a variety of synthetic approaches have been explored (Scheme 1). The most promising reaction route in terms of ease of synthesis was that of generating a biotinylated thiol species then coupling it to an allyl diiron metal cluster through a photoinitiated

thiol-ene click reaction. Photo-initiated thiol-ene reactions are known for being highly efficient and robust, allowing for chain growth and transfer even under ambient conditions.[111,112] Use of biotinylated cysteamine as a mRNA tag through thiol-ene click reactions had been previously.[113] In addition, Tooley et al. had previously reported the incorporation of (μ-allylazadithiolato)diiron(I) hexacarbonyl and (μ-propargylazadithiolato)diiron(I) hexacarbonyl into polymer scaffolds through thiol-ene click reactions.[60] Thus, the synthesis of (μ-biotinylcysteamineazadithiolato)diiron(I) hexacarbonyl seemed to be a feasible first target.

In order to obtain the desired biotinylated thiol, the coupling of biotin with cysteamine using a carbodiimide coupling reagent was proposed. Coupling agents such as Dicyclohexylcarbodiimide (DCC), N,N′-Diisopropylcarbodiimide (DIC), and N-(3-Dimethylaminopropyl)-N′-ethylcarbodiimide hydrochloride (EDC) allow for facile nucleophilic acyl substitution by generating of activated ester which proceeds to react with the desired nucleophile or generating the carboxylic acid anhydride which may also proceed to react with the nucleophile.[114] DCC was chosen as the coupling agent for the first set of experiments as it is the most cost effective. Due to the prohibitive cost of biotin, octanoic acid was used as a model complex to study the reaction conditions for DCC coupling reactions with cystamine

dihydrochloride (Scheme 2). To prevent the possibility of the free thiol of cysteamine coupling to generate a thioester, cystamine was used for the DCC coupling reactions.

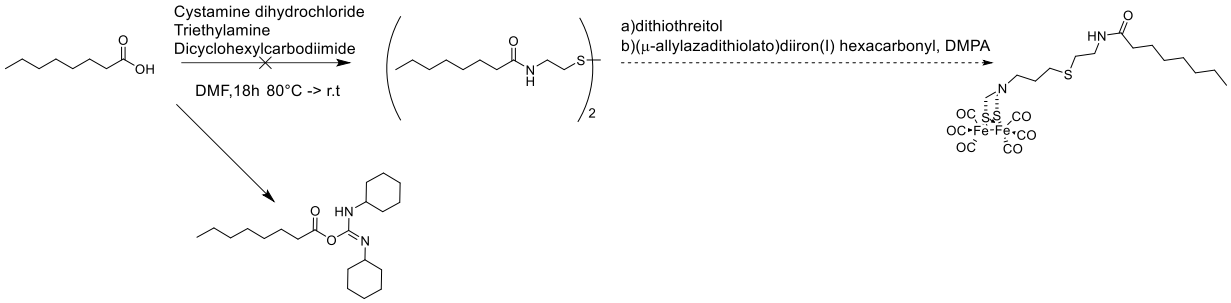

Scheme 2: Proposed synthesis route for N-(2-mercaptoehtyl)-octanamide-diironcluster model complex

The DCC coupling reaction of octanoic acid and cystamine dihydrochloride with triethylamine in dimethylformamide repeatedly resulted in the isolation of the octanoic acid – dicyclohexylcarbodiimide activated ester as large white spherical crystals (Scheme 2) (Figure A1). It is possible that the excess triethylamine needed to deprotonate the cystamine dihydrochloride may have been inhibiting the protonation of dicyclohexylcarbodiimide necessary for generation of the dicyclohexylurea as two equivalents of acid is necessary for the formation of the reactive carboxylic acid anhydride. The synthesis of an N-(2-mercaptoehtyl)-octanamide-diironcluster was abandoned for the synthesis of biotinylated-cysteamine through literature procedures as octanoic acid proved to be a poor model complex for biotin in amide coupling reactions in DMF.

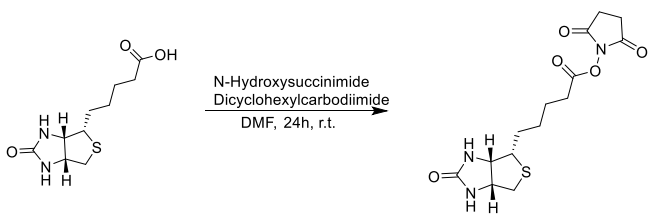

Scheme 3: Synthesis of Biotin-NHS-ester via DCC coupling.[115]

To simplify future coupling reactions, the generation of an activated biotin-n-hydroxysuccinimide ester was sought. Synthesis of Biotin N-hydroxysuccinimide ester (Biotin-NHS-ester) was completed via DCC coupling following the procedure of Singh and coworkers (Scheme 3).[115] Synthesis of biotin-NHS-ester using dicyclohexylcarbodiimide was successful but the dicyclohexylurea proved difficult to remove. Thorough trituration of the product with diethyl ether and further washing with diethyl ether appeared to give biotin-NHS-ester in greater than 100% yield. ^{1}H-NMR in DMSO-D_6 (Figure A4) confirmed the presence of the dicyclohexylurea (DCU) with a urea peak at 5.56 ppm. Adjusting for the DCU impurity the overall yield of biotin-NHS-ester was 88%.

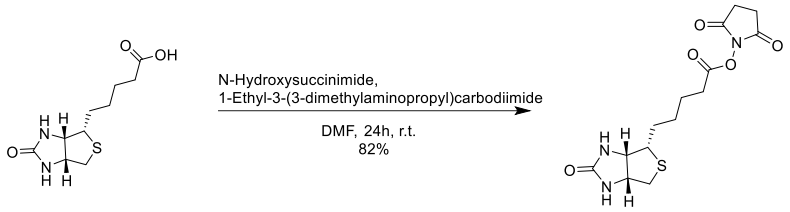

Scheme 4: Synthesis of Biotin-NHS-ester via EDC coupling [33]

To reduce waste from excessive washes, synthesis of biotin-NHS-ester was completed using 1-Ethyl-3-(3-dimethylaminopropyl)carbodiimide (EDC) as the coupling agent following the procedure of Bai He and coworkers (scheme 4).[33] Synthesis of biotin-NHS-ester using EDC as the coupling agent allowed for easy purification by the removal of the resulting urea byproduct via trituration with minimal cold methanol while maintaining a moderate yield of 82%. The synthesis of biotin-NHS-ester was characterized by ^{1}H NMR, ^{13}C NMR, and ATR-IR (Figures A5-6, A53, and A91) and the product was confirmed by the presence of a ^{1}H NMR chemical shift of 2.81 ppm correlating with the four protons of N-hydroxysuccinimide along with comparison of literature ^{1}H NMR chemical shifts.[33]

The synthesis of the biotinylated-cysteamine to be used in the thiol-ene click reactions was completed following the procedures of Mauro Lo Conte and coworkers by coupling biotin to cystamine dihydrochloride followed by the reduction of the cystamine disulfide bond (Scheme 5).[116]

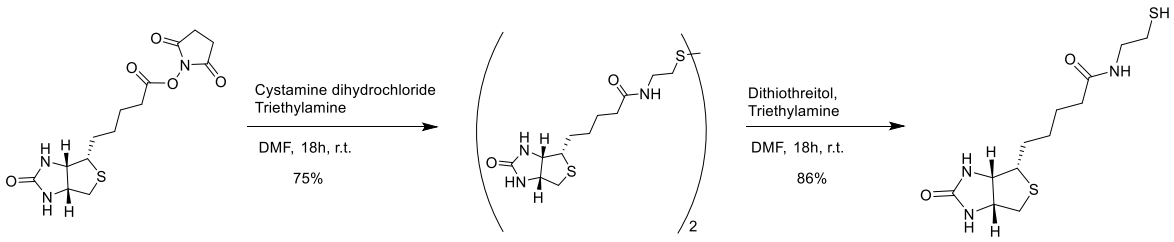

Scheme 5: Synthesis of biotinylated-cysteamine.[33]

Coupling of cystamine dihydrochloride with biotin led to a large quantity of white gel which precipitates out of solution. Removal of the solvent under high vacuum followed by trituration with water led to biotinylated-cystamine in 75% yield as a white powder. Biotinylated-cystamine was characterized by ^{1}H NMR, ^{13}C NMR, and ATR-IR (Figures A8-9, A54, and A92) and the identity of the product was confirmed by the growth of a ^{1}H NMR chemical shift at 7.99 ppm corresponding to the formation of the amide and loss of the chemical shift of 2.81 correlating to the loss of N-hydroxysuccinimide. ^{1}H NMR of biotinylated cystamine was comparative to literature ^{1}H NMR chemical shifts.[116]

The free thiol was generated under an inert atmosphere in two methods. The first method followed Mauro Lo Conte and co-workers procedures and reduced the disulfide bond with dithiothreitol followed by removal of solvent under high vacuum followed by trituration with degassed acetone to yield dithiothreitol as an off-white powder and 86% yield. Biotinylated-cysteamine was characterized by ^{1}H NMR, ^{13}C NMR, and ATR-IR (Figures A10-11, A55, and A93) and the identity of the product was confirmed by comparison of literature ^{1}H NMR chemical

shifts.[116] The second method of generating the free thiol was through reduction of the disulfide bond using excess tris(2-carboxyethyl)phosphine (TCEP). The product of the TCEP reaction was never purified and characterized but was instead used directly in the thiol-ene click reaction with (μ-allylazadithiolato)diiron(I) hexacarbonyl (aadtFe$_2$).

(μ-allylazadithiolato)diiron(I) hexacarbonyl (aadtFe$_2$) was chosen for thiol-ene click chemistry as it had been demonstrated by Christian Tooley to be compatible with radical initiation.[60] (μ-dithiolato)diiron(I) hexacarbonyl [(μ-S$_2$)Fe2(CO)$_6$] and (μ-allylazadithiolato)diiron(I) hexacarbonyl were synthesized following the procedures of Li and Rauchfuss which were modified Tooley et al (Scheme 6).[60,117]

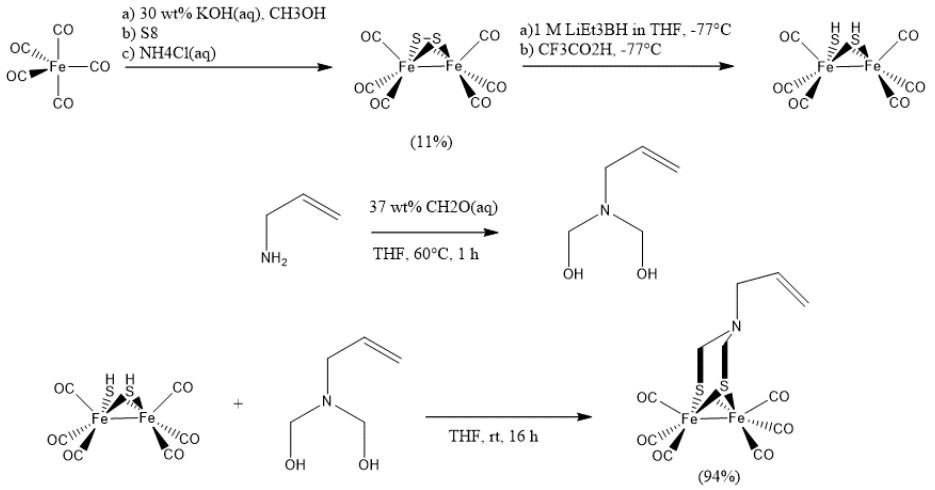

Scheme 6: Synthesis of (μ-allylazadithiolato)diiron(I) hexacarbonyl.[60]

In the first step of the reaction, iron(0)pentacarbonyl was reacted with hydroxide ions leading to the nucleophilic attack of the carbonyl and dissociation of carbon dioxide. The iron carbonyl solution was then reacted with elemental sulfur for six minutes and quenched with ammonium chloride leading to the formation of (μ-dithiolato)triiron(I) nonacarbonyl and (μ-dithiolato)diiron(I) hexacarbonyl. The mixture was purified by column chromatography resulting in (μ-dithiolato)diiron(I) hexacarbonyl with a low yield of 11% vs the literature yield of 17%.

ATR-IR shows carbonyl stretches at 2074, 2038, 1995, 1977, 1953, and 1928 cm^{-1} (figure A94) vs the literature IR(cyclohexane) carbonyl stretches at 2083, 2043, 2007, 1991, 1969, 1956 cm^{-1} (Table 4).[28] Broadened peaks in the obtained IR spectrum of (μ-dithiolato)diiron(I) hexacarbonyl may be due to impurities of the trimer but the trimer will form the same product as the dimer when used in the condensation reaction with formaldehyde and amines.[117]

To generate the (μ-allylazadithiolato)diiron(I) hexacarbonyl, a condensation reaction of protonated (μ-dithiolato)diiron(I) hexacarbonyl, formaldehyde, and allylamine was carried out. [60,118] Purification by column chromatography with hexanes eluent resulted in an 85% yield of (μ-allylazadithiolato)diiron(I) hexacarbonyl after adjusting for an 8.3 % hexane grease impurity and 0.8 % acetone impurity based on ^1H NMR (figure A13). ATR-IR resulted in carbonyl stretching frequencies of 2071, 2026, and 1963 cm^{-1} (figure A95) which were consistent the stretching frequencies of 2071, 2025, 1957 reported by Tooley et al (Table 4).[60]

Table 4: Infrared carbonyl stretching frequencies, ν_{CO}, and nitrile stretching frequencies, ν_{CN}, of synthesized and relevant previously reported Fe-S metal clusters.

Complex	Technique /Solvent	ν_{CO} (cm^{-1})	ν_{CN} (cm^{-1})	ref
Fe-S cluster {Desulfovibrio vulgaris}	FT-IR	2007.5, 1983, 1847.5	2106.5,2087	119
Fe-S cluster {Clostridium pasteurianum}		2017,1974,1971,1810	2097,2077	120
$Fe_2[\mu\text{-}S_2](CO)_6$	ATR-IR	2074, 2038, 1995, 1977, 1953, 1928	-	-
$Fe_2[\mu\text{-}S_2](CO)_6$	IR (cyclohexane)	2083, 2043, 2007, 1991, 1969, 1956		118
$Fe_2[\mu\text{-}S_2](CO)_6$ {tetrahedrane}	DFT (calc)	2075, 2039, 2010, 2005, 1989		121
$Fe_2[\mu\text{-}S_2](CO)_6$ {butterfly}	DFT (calc)	2082, 2056, 2023, 2014		121
$Fe_2[(SCH_2)_2NH)](CO)_6$	ATR-IR	2066, 2044, 2020, 1977, 1946	-	-
$Fe_2[(SCH_2)_2NH)](CO)_6$	IR (hexanes)	2075, 2035, 2007, 1989, 1979	-	118
$Fe_2[(SCH_2)_2NH)](CO)_6$	IR(KBr)	2073, 2031, 1994	-	122
$Fe_2[(SCH_2)_2NCH_2CH{=}CH_2](CO)_6$	ATR-IR	2071, 2026, 1963	-	-
$Fe_2[(SCH_2)_2NCH_2CH{=}CH_2](CO)_6$	ATR-IR	2071, 2025, 1957	-	60
$Fe_2[(SCH_2)_2NCH_2CH{=}CH_2](CO)_6$	IR (hexanes)	2076, 2038, 2003, 1999	-	123
$Fe_2[(SCH2)_2N\text{-}I]^2\text{-}CH_2CH{=}CH_2](CO)_5$	IR (hexanes)	2062, 2009, 1998, 1982, 1967	-	123

$Fe_2[(SCH_2)_2NCH_2C{\equiv}CH](CO)_6$	ATR-IR	2072, 2030, 2003, 1982, 1960, 1946	-	-
$Fe_2[(SCH_2)_2NCH_2C{\equiv}CH](CO)_6$	ATR-IR	2081, 2034, 1980	-	[60]
$Fe_2[(SCH_2)_2CH_2](CO)_6$	ATR-IR	2069, 2025, 1983, 1943	-	-
$Fe_2[(SCH_2)_2CH_2](CO)_6$	IR	2072, 2033, 1993	-	[124]
$Fe_2[(SCH_2)_2CH_2](CO)_6$	DFT (calc)	2069, 2020, 2017, 2005, 2000, 1995	-	[125]
$Fe_2[(SCH_2)_2CH_2]\ (CN)_1(CO)_5$	IR	2027, 1977, 1944, 1919	2103	[124]
$Fe_2[(SCH_2)_2CH_2]\ (CN)_2(CO)_4$	IR	1962, 1921, 1883	2076	[124]
$Fe_2[(SCH_2)_2CH_2]\ (CN)_2(CO)_4$	DFT (calc)	1958, 1912, 1893, 1875	2087, 2078	[125]
$Fe_2[(SCH_2)_2CH_2](C{\equiv}NC_6H_4\text{-}4\text{-}I)(CO)_5$	ATR-IR	2032, 1958, 1986, 1974, 1937, 1916	2115	-
$Fe_2[(SCH_2)_2CH_2](C{\equiv}NC_6H_4\text{-}4\text{-}I)_2(CO)_4$	ATR-IR	2036, 1991, 1967, 1930	2118, 2089	-
$Fe_2[(SCH_2)_2CH_2](C{\equiv}NC_6H_4\text{-}4\text{-}NH_2)(CO)_5$	ATR-IR	2033, 1979, 1970, 1974, 1950, 1921, 1898	2132	-
$Fe_2[(\mu\text{-}SCH_2)_2N(C_6H_4\text{-}4\text{-}CH_3)](C{\equiv}NC_6H_4\text{-}4\text{-}I\ )_1(CO)_5$	FT-IR	2040, 2000, 1975	2124	[126]
$Fe_2[(\mu\text{-}SCH_2)_2N(C_6H_4\text{-}4\text{-}CH_3)](C{\equiv}NC_6H_4\text{-}4\text{-}I\ )_2(CO)_4$	FT-IR	1996, 1980, 1950	2122, 2094	[126]
$C{\equiv}NC_6H_4\text{-}4\text{-}I$	ATR-IR	-	2126	-
$C{\equiv}NC6H_4\text{-}4\text{-}NH_2$	ATR-IR	-	2128	-

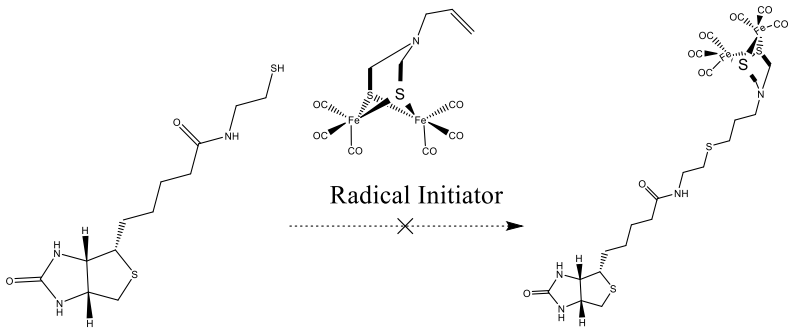

Scheme 7: General synthesis route of (μ-biotinylcysteamineazadithiolato)diiron(I) hexacarbonyl

For the first set of thiol-ene reactions biotinylated-cysteamine and (μ-allylazadithiolato)diiron(I) hexacarbonyl were chosen due to their previously reported compatibility with radical initiated click chemistry.[60,116] The decision to use biotinylated-cysteamine was based on the experiments of Mauro Lo Conte and coworkers were biotinylated-cysteamine was successfully used for thiol-ene click chemistry in process of tagging alkynyl peptides.[116] In Mauro Lo Conte's experiments the thiol-ene click reaction with biotinylated-cysteamine was successfully carried out in 2:1 MeOH−H_2O with 2,2-Dimethoxy-2-phenylacetophenone (DPAP or DMPA) as the photo initiator under 365nm light for 15 minutes.[18]

The radical initiated thiol-ene click reactions between biotinylated-cysteamine and (μ-allylazadithiolato)diiron(I) hexacarbonyl (Scheme 7) were carried out under various conditions (Table 5) without successful coupling to generate the (μ-biotinylated-cysteamine-azadithiolato)diiron hexacarbonyl product.

Table 5: Reaction conditions for thiol-ene click reactions (SM = Starting materials, Decomp = decomposed diiron cluster)

Radical initiator	**Wavelength/temp**	**Solvent**	**Disulfide reduction method**	**Result**
DMPA	254 nm	DMF	Dithiothreitol	SM, Decomp
DMPA	254 nm	Methanol	Dithiothreitol	SM, Decomp
DMPA	360 nm	DMF	Dithiothreitol	SM, Decomp
DMPA	360 nm	Methanol	Dithiothreitol	SM, Decomp
DMPA	254 nm	Methanol	Dithiothreitol, Single-pot	SM, Decomp
DMPA	254 nm	DMF	TCEP, single-pot	Fe_2-TCEP adduct
DMPA	254 nm	Methanol	TCEP, single-pot	SM, Decomp
AIBN	65°C	DMF	Dithiothreitol	SM, Decomp

All dithiothreitol reduced biotinylated-cysteamine, photoinitiated reactions resulted in the recovery of a large quantity of unreacted (μ-allylazadithiolato)diiron(I) hexacarbonyl, a small quantity of pink oil (DMPA), a small quantity of green solids, and a large quantity of brown solids (biotinylated-cysteamine with iron impurities). ^{1}H-NMR of the crude product showed no signs of a formaldehyde peak at 10 ppm or a singlet at 5.4 due to the decomposition of DMPA to benzaldehyde and (Dimethoxymethyl)benzene (figure 7).

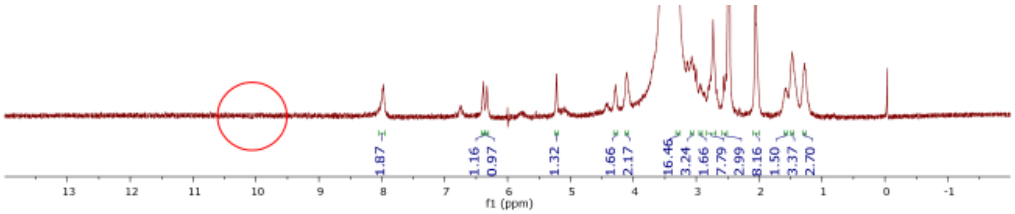

Figure 6: ^{1}H NMR (DMSO-d_6, 400MHz) spectrum of Biotinyltated-cystamine-aadtFe$_2$(CO)$_6$ crude product, Disulfide bond broken with Dithiothreitol

Recovery of unreacted (μ-allylazadithiolato)diiron(I) hexacarbonyl was completed by extracting the reaction mixture with hexanes and confirmed by ^{1}H-NMR. Isolation of unreacted DMPA by column chromatography resulted in a pink oil. The pink oil was confirmed to be unreacted DMPA by ^{1}H-NMR. The ^{1}H-NMR peaks were broadened possibly due to a paramagnetic impurity. Roughly all DMPA implemented for the reactions was recovered after adjusting for hexanes grease found in ^{1}H-NMR. ATR-IR of the pink oil showed the presence of weak carbonyl peaks at 2055, 1997, and 1954 cm^{-1} (figure 8).

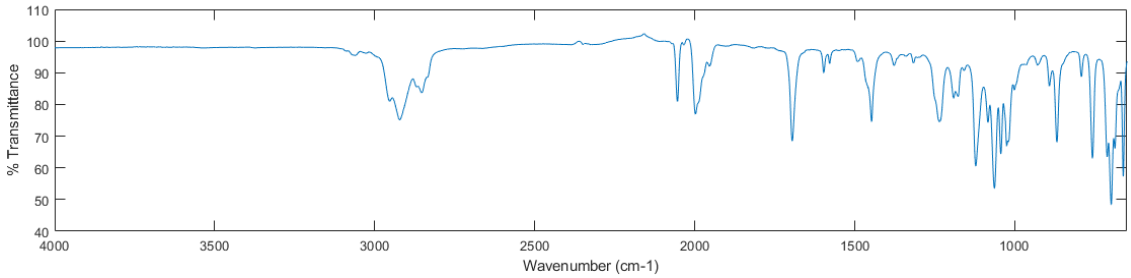

Figure 7: ATR-IR spectrum of unreacted DMPA recovered from thiol-ene reaction

The yield of green powder was too low to characterize. ^{1}H-NMR of the brown solids in DMSO-d_6 confirmed the presence of biotinylated-cysteamine but lacked a significant peak around 3.5 ppm correlating with the presence of the protons from the azadithiolato motif confirming that no product had formed. ATR-IR of the brown solids showed the presence of weak carbonyls as an impurity which was most likely decomposed (μ-allylazadithiolato)diiron(I) hexacarbonyl.

TCEP reduced biotinylated-cysteamine was used without purification or removal of excess TCEP. As such the attempt to use TCEP and biotinylated-cystamine in methanol led to solubility issues with (μ-allylazadithiolato)diiron(I) hexacarbonyl due to the extra water used in the reduction of the biotinylated-cystamine. The ^{1}H-NMR of the crude product did not show signs of the decomposition of DMPA. Dissolving the crude product in ethyl acetate and washing with saturated sodium chloride lead to a red ethyl acetate fraction and a golden aqueous solution. Purification of the ethyl acetate fraction by column chromatography lead to results consistent with the dithiothreitol trials. A majority of the starting (μ-allylazadithiolato)diiron(I) hexacarbonyl was recovered and the ^{1}H-NMR of third red fraction matched the pink fraction of the dithiothreitol trials. Biotinylated-cysteamine was not recovered as it was likely removed with the aqueous wash.

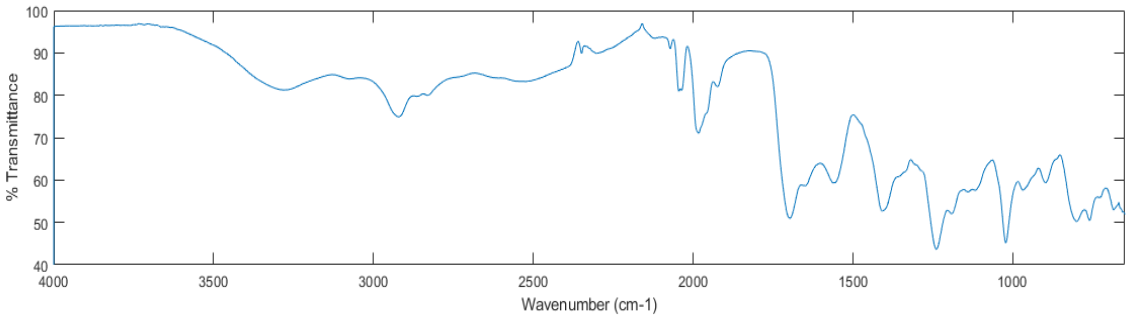

Figure 8:ATR-IR spectrum of the methanol soluble product from thiol-ene reaction using TCEP to reduce the disulfide bond of biotinylated cystamine.

Use of TCEP and biotinylated-cystamine in DMF lead to the isolation of a TCEP and (μ-allylazadithiolato)diiron(I) hexacarbonyl adduct as evidenced by ATR-IR (figure 9). The product was isolated by extracting the crude product with hexanes, dichloromethane, then methanol. The methanol fraction was filtered through celite and concentrated to yield an orange glassy tar. The phosphine of TCEP was likely able to coordinate due to the dissociation of a carbonyl due to UV activation.

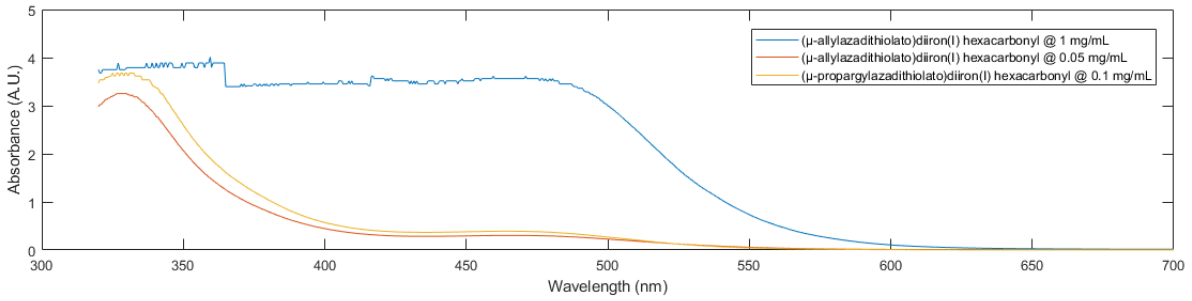

Figure 9: UV-Vis absorbance spectrum (320 to 700 nm) of (μ-allylazadithiolato)diiron(I) hexacarbonyl at 1 mg/mL in hexanes (blue) 0.05 mg/mL in hexanes (red) and (μ-propargylazadithiolato)diiron(I) hexacarbonyl at 0.1 mg/mL in hexanes (gold).

In order to elucidate the reason for DMAP not initiating with irradiation UV-Vis spectra of (μ-allylazadithiolato)diiron(I) hexacarbonyl and (μ-propargylazadithiolato)diiron(I) hexacarbonyl were obtained (figure 10). (μ-Allylazadithiolato)diiron(I) hexacarbonyl was found to have a λ_{max} of 329 nm and a molar absorptivity, ε, of 28000 $L \cdot mol^{-1} \cdot cm^{-1}$. DMPA has λ_{max} of 254 and a local maxima at 334 nm with molar absorptivity of 248.3 $L \cdot mol^{-1} \cdot cm^{-1}$.[127,128] As the reactions were run at 20 mg/mL of (μ-allylazadithiolato)diiron(I) hexacarbonyl and 2 mg/mL of DMPA it is likely that (μ-allylazadithiolato)diiron(I) hexacarbonyl was absorbing a majority of the incoming photons. Thus, DMPA would not be able to absorb the required photons to generate the desired radicals. If this reaction was to be attempted in the future it may be beneficial use 4,4'-Bis(diethylamino)benzophenone as the photoiniator as it has a λ_{max} at 363 in DMF and perform the reaction in glass rather than quartz to minimize light absorbed by the diiron cluster.[129]

The thiol-ene click reaction of biotinylated-cysteamine and (μ-allylazadithiolato)diiron(I) hexacarbonyl initiated thermally with Azobisisobutyronitrile (AIBN) at 65°C did not generate the desired product. After two hours of reacting the solution was concentrated and washed with hexanes yielding the starting material (μ-allylazadithiolato)diiron(I) hexacarbonyl and green solids. Since the reaction had not gone forward the mixture was recombined and allowed to react

for another 12 hours at 65°C. The solution was filtered to yield a large quantity of black solids and a yellow solution. The solution was concentrated to yield dull orange solids. The solids were insoluble in hexanes or ethyl acetate but were soluble in methanol. TLC of the orange solids with methanol eluent led to a single large spot Rf = 0.69. ^{1}H-NMR of the orange solids showed the presence of both biotinylated-cysteamine and (μ-allylazadithiolato)diiron(I) hexacarbonyl. In the ^{1}H-NMR the alkene peaks are present at 5.15 and 5.65 ppm signifying that the biotinylated-cysteamine is not coupled through the click reaction.

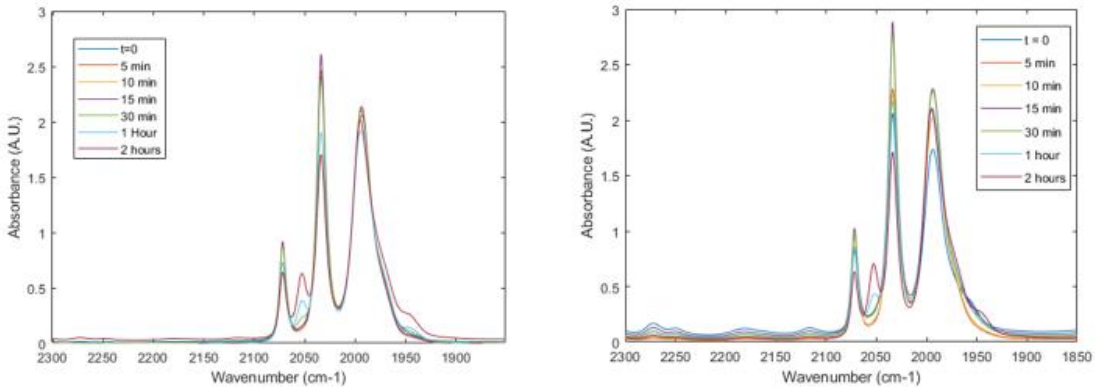

Figure 10: Comparison of IR absorbance spectra (2300 to 1850 cm^{-1}) over time of (μ-allylazadithiolato)diiron(I) hexacarbonyl at 10 mg/mL and AIBN at 1.3 mg/mL in DMF heated to 65°C (left) and allylazadithiolato)diiron(I) hexacarbonyl at 10 mg/mL in DMF heated to 65°C (right)

In order to evaluate the stability of (μ-allylazadithiolato)diiron(I) hexacarbonyl at temperatures adequate for thermal initiation of AIBN, (μ-allylazadithiolato)diiron(I) hexacarbonyl was heated in DMF to 65°C with and without AIBN with aliquots taken every 15 minutes for IR spectroscopy. Evolution of the carbonyl peaks overtime gave evidence of a new diiron carbonyl specie, forming new carbonyl absorption peaks at 2052 and 1945 cm^{-1} independent of whether AIBN was used (figure 11). It is unclear based on IR data alone if the new specie was due solely to a change in geometry or a change in ligation.

Research into other (μ-allylazadithiolato)diiron(I) hexacarbonyl homologues used with AIBN brought up the work of Daniel Heine et al, where styrene (μ-dithiolato)diiron(I) hexacarbonyl derivatives were incorporated into polymers using AIBN initiated thiol-ene click chemistry.[130] In Heine's studies it was found that copolymerization with methylene bridging ligands successfully formed polymers, while all attempts at copolymerization with amino bridging ligands failed leading to the formation of black solution and no polymer formation.[130] In the paper they attribute the black solution to the possibility of aminolysis of the dithioformates used as a thiol source but there are no primary or secondary amines present and this may be difficult with tertiary amines which are present in the reactions.[130]

Due to the ongoing difficulties with thiol-ene click chemistry a second reaction route to produce a biotinylated-diiron cluster was initiated. The goal was to use a biotinyl-diamine in place of the primary amine used in the previous (μ-azadithiolato)diiron(I) hexacarbonyl condensation reaction to generate the desired product (scheme 8).

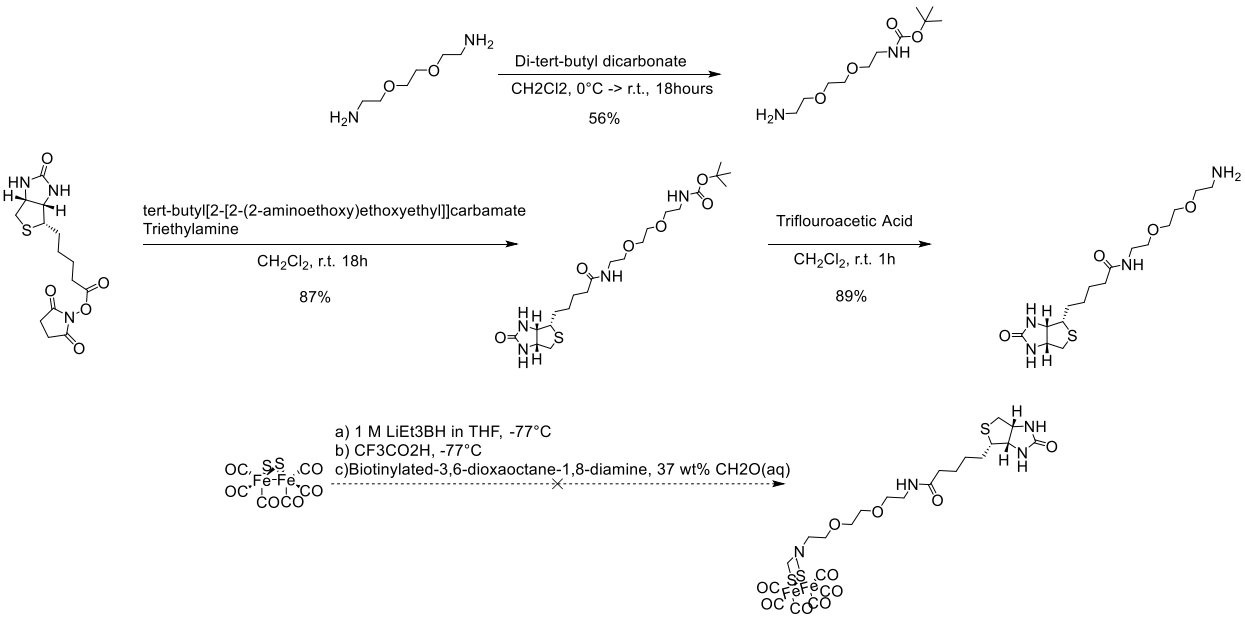

Scheme 8: Synthesis of (μ-biotinylated-3,6-dioxaoctane-1,8-diamine-azadithiolato)diiron(I) hexacarbonyl

To increase hydrophilicity of the final product 2,2-(ethylenedioxy)bis(ethylamine) was chosen as the diamine linker. Protection of 2,2-(ethylenedioxy)bis(ethylamine) to generate tert-butyl-2-[2-(2-aminoethyoxy)ethyoxyethyl]carbamate was performed following the procedure of Servinis et al.[131] The single n-Boc protection of a single side of the diamine was successfully carried out by dropwise addition of 1 equivalent of a dilute di-tert-butyldicarbonate to 3 equivalents of 2,2-(ethylenedioxy)bis(ethylamine) in dichloromethane. Work up by silica column chromatography gave tert-butyl-2-[2-(2-aminoethyoxy)ethyoxyethyl]carbamate in 56% yield. The identification of the product as tert-butyl-2-[2-(2-aminoethyoxy)ethyoxyethyl]carbamate was confirmed by comparison of obtained ^{1}H NMR (figure A15) with literature chemical shifts.[131]

Coupling of tert-butyl-2-[2-(2-aminoethyoxy)ethyoxyethyl]carbamate with Biotin-NHS-ester in dichloromethane followed by purification by column chromatography with 90:10:1 dichloromethane: methanol: ammonium hydroxide eluent resulted in the isolation of biotinylated-tert-butyl[2-[2-(2-aminoethoxy)ethoxyethyl]]carbamate in 87% yield. Biotinylated- tert-butyl[2-[2-(2-aminoethoxy)ethoxyethyl]]carbamate was characterized by ^{1}H NMR (figure A16-17).

Deprotection of n-Boc-bioitnylated-3,6-dioxaoctane-1,8-diamine was carried out with a 50:50 solution of trifluoracetic acid and dichloromethane to yield the bioitnylated-3,6-dioxaoctane-1,8-diamine-TFA salt. The salt was removed by column chromatography with 20:10:1 Dichloromethane : Methanol : triethylamine solvent. Isolation of biotinylated-3,6-dioxaoctane-1,8-diamine in 89% yield was determined by ^{1}H NMR (figure A18-19). The loss of tert-butyl protons and growth of a chemical shift at 7.86 correlating to the protonated amine matched literature ^{1}H NMR.[132]

Use of biotinylated-3,6-dioxaoctane-1,8-diamine in the condensation reaction with (μ-dithiolato)diiron(I) hexacarbonyl was unsuccessful. ^{1}H-NMR showed the absence of the peak at

6.38 and 6.45 ppm which correlate with the protons of the biotin urea (Figure 12). Furthermore, ^{13}C-NMR showed the absence of carbon peaks around 169 ppm correlating to the central carbon of the biotin urea (Figure 13). Attempts were made to replicate the decomposition of the biotin bridgehead using biotin, unfortunately non-modified biotin was not soluble in the reaction conditions used for the condensation reaction.

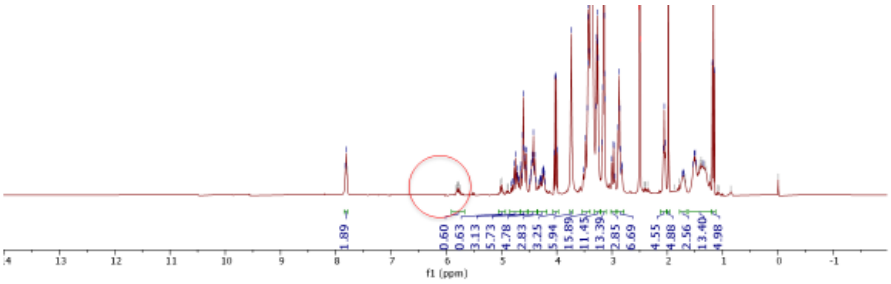

Figure 11: ^{1}H NMR spectrum of *Biotinylated-3,6-dioxaoctane-1,8-diamine-(μ-dithiolato)diiron(I) hexacarbonyl reaction crude product. Circled region around 6.38 and 6.45 ppm show absence of urea proton peaks associated with biotin.*

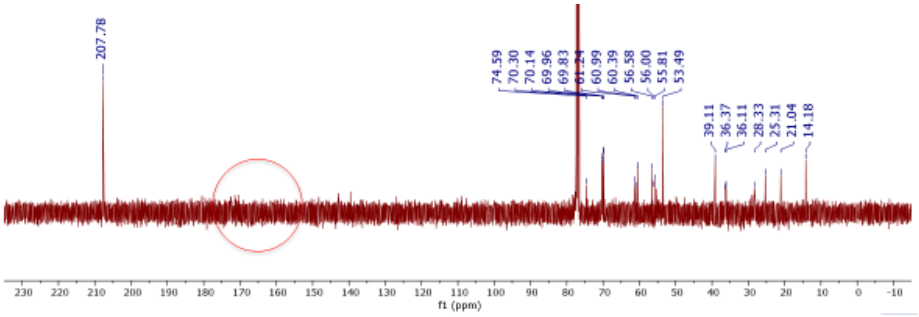

Figure 12: ^{13}C NMR spectrum of *Biotinylated-3,6-dioxaoctane-1,8-diamine-(μ-dithiolato)diiron(I) hexacarbonyl reaction crude product. Circled region around 169 ppm shows absence of urea carbon peak associated with biotin.*

A previous report by Micke Lisbjerg et al. showed that the condensation reaction of biotin with formaldehyde in the presence of acid yielded biotin[6]uril (figure).[133] Comparison of the crude Biotinylated-3,6-dioxaoctane-1,8-diamine-(μ-dithiolato)diiron(I) hexacarbonyl reaction ^{1}H NMR spectrum with that of biotin[6]uril showed evidence of the formation of a biotin macrocycle.

The chemical shifts in the range of 4.5 to 4.0 ppm of the crude product matched the proton shifts of the methylene protons connecting the urea groups found in biotin[6]uril.[133]

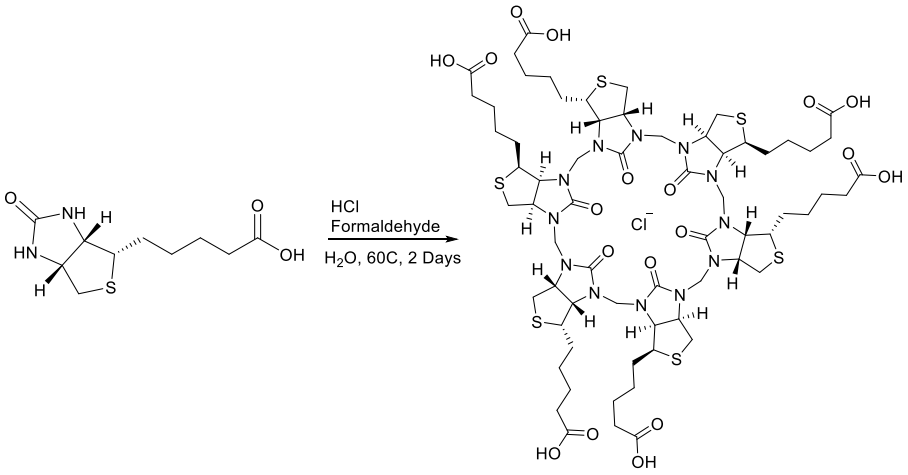

Scheme 9: Synthesis of biotin[6]uril [133]

Purification of the product using column chromatography with a 90:10 ethyl acetate / methanol eluent led to the isolation of an orange-red film. ^{1}H NMR spectrum of the film confirmed the isolation of the uril product (figure 14) due to the presence of the protons with chemical shifts in the range of 4.5 ppm to 4.0 ppm correlating with the methylene units connecting the urea groups (figure 14). ATR-IR of the fraction, while contaminated by residual methanol from the column, gave evidence that the diiron clusters were intact with carbonyl stretching frequencies of 2071, 2031, and 1991 cm^{-1} (figure 15). Based on the NMR and IR data it was proposed that a novel biotinylated-diiron cluster macrocycle had been synthesized (figure 14), but as this was not the desired product further purification and characterization was not completed.

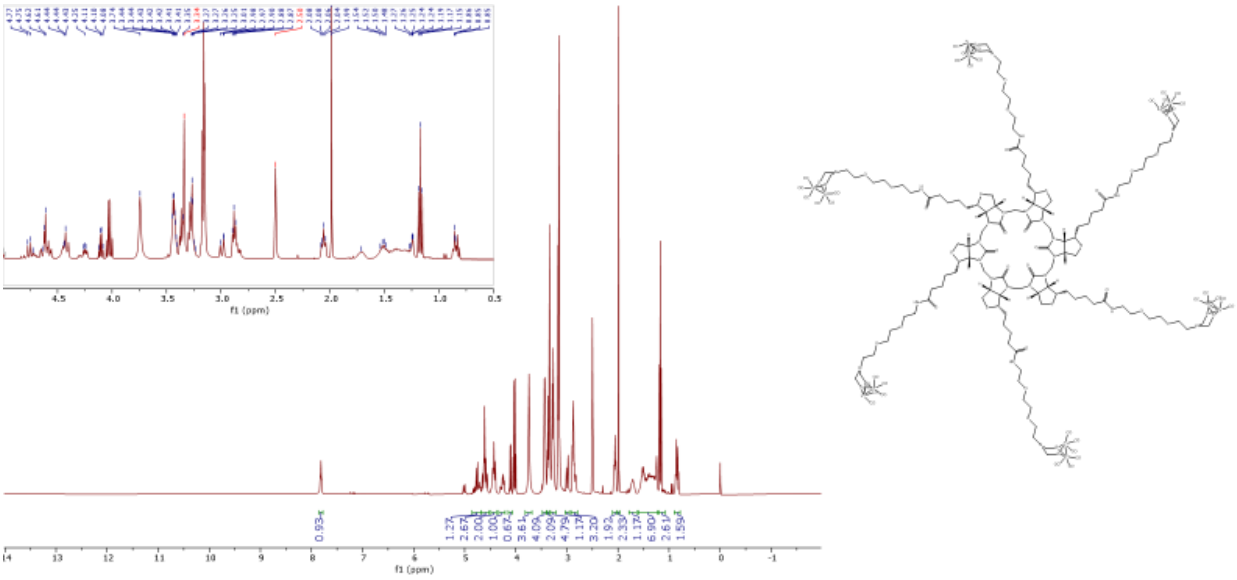

Figure 13: ^{1}H NMR spectrum of fraction 5 of 90:10 ethyl acetate: methanol silica column from biotinylated-3,6-dioxaoctane-1,8-diamine-(μ-dithiolato)diiron(I) hexacarbonyl reaction (left). Proposed structure of isolated compound (right).

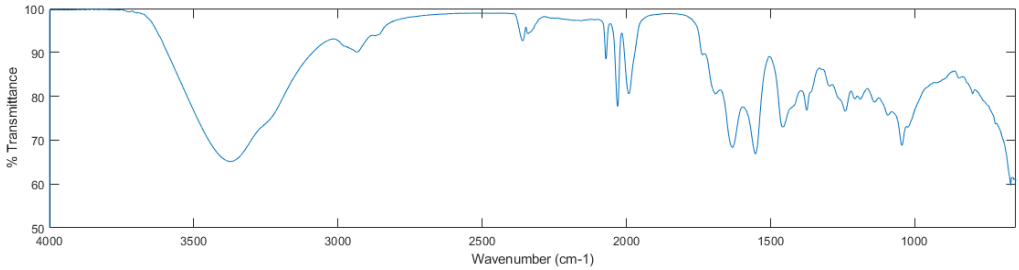

Figure 14:ATR-IR spectrum of fraction 5 of 90:10 ethyl acetate: methanol silica column from biotinylated-3,6-dioxaoctane-1,8-diamine-(μ-dithiolato)diiron(I) hexacarbonyl reaction . Large absorbance at 3373 cm^{-1} due to residual methanol.

As the urea group of biotin were incompatible with condensation reactions, a diiron cluster capable of amide coupling was sought. The amide coupling of the diiron cluster was pursued through two separate approaches (scheme 10). The first approach as to directly amide couple biotin with (μ-azadithiolato)diiron(I) hexacarbonyl by reacting the diiron cluster with the activated biotin-NHS-ester which resulted in no reaction based on TLC after several days of stirring. The second approach was to synthesize an azadithiolatodiiron cluster with an activated ester motif for coupling with biotinylated diamines (scheme 10).

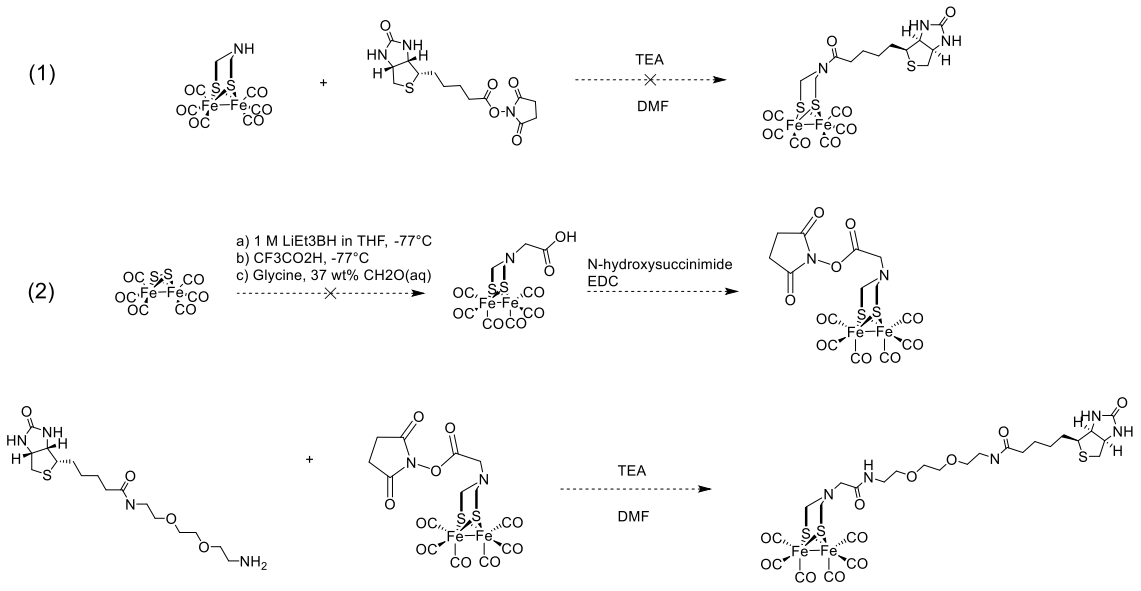

Scheme 10: Reaction routes for the synthesis of biotinylated diiron clusters through amide couplings.

In order to generate an activated ester diiron cluster, synthesis of (μ-glycine-dithiolato)diiron(I) hexacarbonyl was explored (Scheme 10). Glycine was chosen for the condensation reaction due to its short chain length which would maximize the probability of the diiron cluster remaining in the binding pocket of avidin or streptavidin. Use of glycine in the condensation reaction was unsuccessful. In the attempted synthesis of (μ-glycine-dithiolato)diiron(I) hexacarbonyl, glycine was directly reacted with the formaldehyde to generate the N,N-bis(hydroxymethyl)-glycine intermediate which may have led to several side reactions. The N,N-bis(hydroxymethyl)-glycine mixture was then added to a solution of $Fe2[(\mu\text{-}SH)_2](CO)_6$ to form (μ-glycine-dithiolato)diiron(I) hexacarbonyl through a condensation reaction. Purification of the crude (μ-glycine-dithiolato)diiron(I) hexacarbonyl mixture using column chromatography led to the separation of two fractions. The second fraction which was expected to be (μ-glycine-dithiolato)diiron(I) hexacarbonyl, based on TLC, ceased mid column requiring elution with acetone for extraction. During NMR analysis, the compound crystalized in the NMR tube, further

attempts to recrystallize the crude reaction product failed to give good recoveries. ATR-IR of the crystalized product gave a strong absorbance peak at 1671 cm^{-1} indicative of an amide C=O stretch (figure A106). Thus, it is likely the glycine polymerized during the reaction. Synthesis of (μ-glycine-dithiolato)diiron(I) hexacarbonyl may still be possible. Gao and coworkers previously reported the synthesis of carboxylate diiron clusters through the condensation reaction of $[Fe_2(CO)_6(HOCH2S)_2]$ with a premixed solution of triethylamine and 4-Aminobutyric acid or 2-Aminobutyric acid reducing the chance of polymerization of the amino acids during condensation.[134]

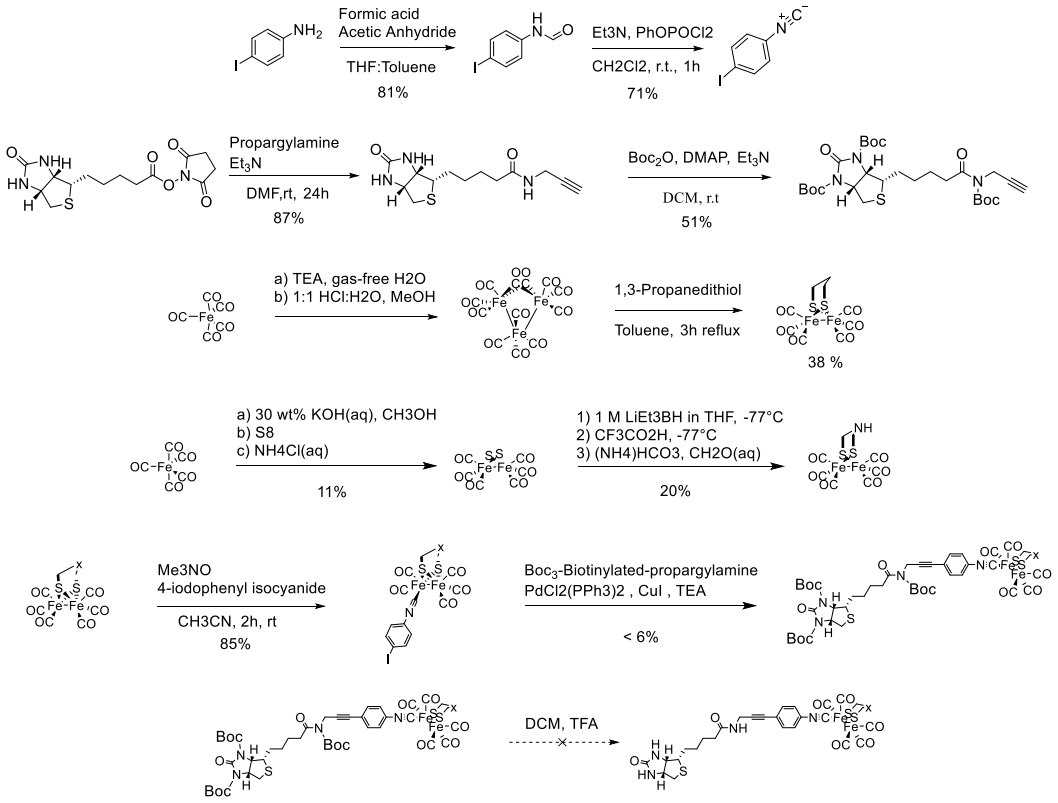

Scheme 11: Reaction route for the synthesis of biotinylated diiron clusters through Sonogashira coupling.

As it has been shown that the presence of the (μ-azadithiolato) bridging ligand is essential for an optimized diiron cluster,[95,135] research into the formation of an activated ester diiron cluster was halted. Inspired by the work of Feng Wang et al,[136] and intrigued by the potential of

Sonogashira coupling to generate a series of biotinylated diiron cluster capable of comparing the effects of bridging ligands from propanedithiolate to azadithiolate, the Sonogashira coupling of a biotinylated alkyne species with a diiron 4-iodopheynylisocyano pentacarbonyl cluster was pursued (scheme 11).

Synthesis of the 4-iodophenyl isocyanide ligand was achieved by the dehydration of N-(4-iodophenyl)-formamide which was synthesized by the reaction of 4-iodaniline with formic acid. Replicating the procedure reported by Kishor P. Dhake et al. to synthesis N-(4-iodophenyl)-formamide by a neat reaction of 4-iodoaniline and formic acid resulted in undesired products only.[137] The successful synthesis of N-(4-iodophenyl)-formamide was achieved by replicating the reaction conditions reported by Lei Zhu, Manoj Patel, Mingbao Zhang.[138] The reaction of 4-iodoaniline with a premixed solution of formic acid and acetic anhydride resulted in a 81.2% yield of N-(4-iodophenyl)-formamide as off-white solids. The isolated off-white solids were characterized by ^{1}H-NMR (figure A21), ^{13}C NMR (figure A58), and ATR-IR (figure A99) leading to the identification of N-(4-iodophenyl)-formamide through comparison of literature ^{1}H-NMR chemical shifts.[138]

Synthesis of the 4-iodophenyl isocyanide ligand for Sonogashira coupling was completed by the dehydration of N-(4-iodophenyl)-formamide using phenyl dichlorophosphate as a dehydration reagent and triethylamine as a base under conditions reported by Genki Kobayashi, Tateo Saito, Yoshikazu Kitano.[139] Purification of the reaction mixture via column chromatography led to the isolation of yellow solids. The solids were characterized via ^{1}H-NMR (figure A22) and ATR-IR (figure A100) leading to the identification of the solids as 4-iodophenyl isocyanide through comparison of literature ^{1}H-NMR chemical shifts and the presence of an IR absorbance peak at 2126 cm^{-1} corresponding with a nitrile stretch.[139]

Cesear Corona, Bj K. Bryant, and Jeffrey B. Arterburn previously reported a 6-step synthesis of a tert-butyloxycarbonyl (Boc) protected-biotin derivative which could be implemented in Sonogashira couplings while removing the chance of in vivo amide cleavage of the coupling product by the enzyme biotinidase.[140] As the biotin derivative synthesized by Corona et al. lacked the amide functional group which stabilizes biotin's binding through interactions with the ser 73 and ser 75 residues of avidin and the proposed artificial enzyme was not designed for in vivo applications,[110,140] the synthesis of a Boc-protected biotinylated amino-alkyne though amide coupling was proposed. Due to its short chain length, propargylamine was chosen as the amino-alkyne linker for the Boc-protected biotin derivative.

Synthesis of biotinylated propargylamine was completed by reaction of the activated biotin-NHS-ester with propargylamine in the presence of triethylamine as a base in N,N-dimethylformamide. Concentration of the solution under reduced pressure followed by Trituration of the crude product with diethyl ether led to the isolation of orange solids which were characterized by ^{1}H NMR (figures A23-A24) and ^{13}C NMR (figure A59). Comparison of ^{1}H NMR with literature spectra and the presence of an amide proton at with a chemical shift of 8.23 ppm resulted in the identification of the solids as biotinylated propargylamine with a 87% yield.[141]

Due to the harsh conditions implemented with Sonogashira couplings, the urea and amide groups of biotinylated propargylamine were protected through the reaction with di-tert-butyl dicarbonate, 4-dimethylaminopyridine, and triethylamine in DCM to generate a mixture of di and tri protected biotinylated-propargylamine. Isolation of the products via column chromatography after 18 hours of reaction led to an 51 % yield of the fully protected species based on the presence of 1H NMR chemicals shifts at 1.53, 1.52, and 1.51 ppm each integrating to 9H, correlating with

the t-butyl protons of each protecting group (Figure A25). Allowing for the reaction to continue for 29 hours prior to workup resulted in a decrease in yield to 16%.

In order to compare the effect of bridging ligands on the hydrogen evolution reaction turnover, two species of diiron clusters (μ-propanedithiolato)diiron(I) hexacarbonyl and (μ-azadithiolato)diiron(I) hexacarbonyl were synthesized for further ligation with 4-iodophenylisocyanide. (μ-propanedithiolato)diiron(I) hexacarbonyl was synthesized following the procedure of Benjamin Garrett et al with the triiron(I) dodecacarbonyl intermediate synthesized via the procedure of McFarlene and Wilkinson.[142,143] Triiron(I) dodecacarbonyl was synthesized by the reaction of Iron-pentacarbonyl with triethylamine, the resulting solids were isolated then refluxed with hydrochloric acid. As triiron(I) dodecacarbonyl is known to be pyrophoric if allowed to dry the resulting green solids were isolated by gravity filtration and washed with water then methanol under a nitrogen blanket then used without further characterization. Triiron(I) dodecacarbonyl was then refluxed with 1,3-propanedithiol in toluene. The resulting solution was concentrated and purified by column chromatography to isolate (μ-propanedithiolato)diiron(I) hexacarbonyl as red solids in 38% yield. ^{1}H NMR chemical shifts of 2.14 and 1.80 ppm, integrating to 4 and 2 protons respectively (Figure A27) as well as characteristic carbonyl stretching frequencies of 2069, 2025, 1983, 1943 cm^{-1} (figure A97) matched literature results confirming the identity of (μ-propanedithiolato)diiron(I) hexacarbonyl.[142]

(μ-azadithiolato)diiron(I) hexacarbonyl was synthesized following the procedures of Li and Rauchfuss.[117] In order to form the bridging ligand, ammonium carbonate reacted with formaldehyde to form bis-(hydroxymethyl)amine. Then a condensation reaction of bis-(hydroxymethyl)amine with $Fe2[(\mu\text{-}SH)_2](CO)_6$ led to the formation of (μ-azadithiolato)diiron(I) hexacarbonyl. The reaction mixture was concentrated, and the resulting residuals were extracted

with hexanes and washed with saturated bicarbonate solution to remove excess trifluoracetic acid from the formation of $Fe2[(\mu\text{-}SH)_2](CO)_6$. The organic phase was then concentrated and purified via column chromatography resulting in the isolation of a red oil. Characterization via ^{1}H NMR resulted in chemical shifts of 3.69 ppm integrating to four protons and 1.76 ppm integrating to one proton indicating that the bridging ligand was properly formed (figure A26). Carbonyl stretching frequencies of 2066, 2044, 2020, 1977, and 1946 cm^{-1} were observed via ATR-IR (figure A105). Based on comparison of the 1H NMR and IR spectra to literature value the red oil was identified as (μ-azadithiolato)diiron(I) hexacarbonyl with a 19.6% yield.[117] Attempts to protect the amine of the bridging ligand for further Sonogashira coupling reactions via a Boc-protection resulted in the decomposition of (μ-azadithiolato)diiron(I) hexacarbonyl with no evidence of product formation.

Due to the reactivity of (μ-azadithiolato)diiron(I) hexacarbonyl, Synthesis of a biotinylated diiron cluster through Sonogashira coupling was explored with the (μ-propanedithiolato)diiron(I) hexacarbonyl species first. In order to generate a diiron species capable undergoing a Sonogashira coupling, (μ-propanedithiolato)diiron(I) hexacarbonyl was decarbonylated with 1.06 equivalence of trimethylamine-N-oxide dropwise in the presence of 4-iodophenyl isocyanide. Purification via column chromatography led to the isolation of (μ-propanedithiolato)diiron 4-iodopheynylisocyano pentacarbonyl and (μ-propanedithiolato)diiron di(4-iodopheynylisocyano) tetracarbonyl in 84 and 13 % yields respectively. Formation of (μ-propanedithiolato)diiron 4-iodopheynylisocyano pentacarbonyl was confirmed by the ^{1}H NMR chemical shifts of 7.7 and 7.3 integrating to two protons each indicating the inclusion of the phenyl group, and chemical shifts of 2.15, 2.04, and 1.82-1.76 each integrating to two protons each indicating the bridging propyl group is no longer symmetric due to the change in ligation (Figure A28). ATR-IR analysis show the presence of a

nitrile stretch at 2115 cm^{-1} and carbonyl stretches at 2032, 1958, 1986, 1974, 1937, 1916 cm^{-1} (figure A101).

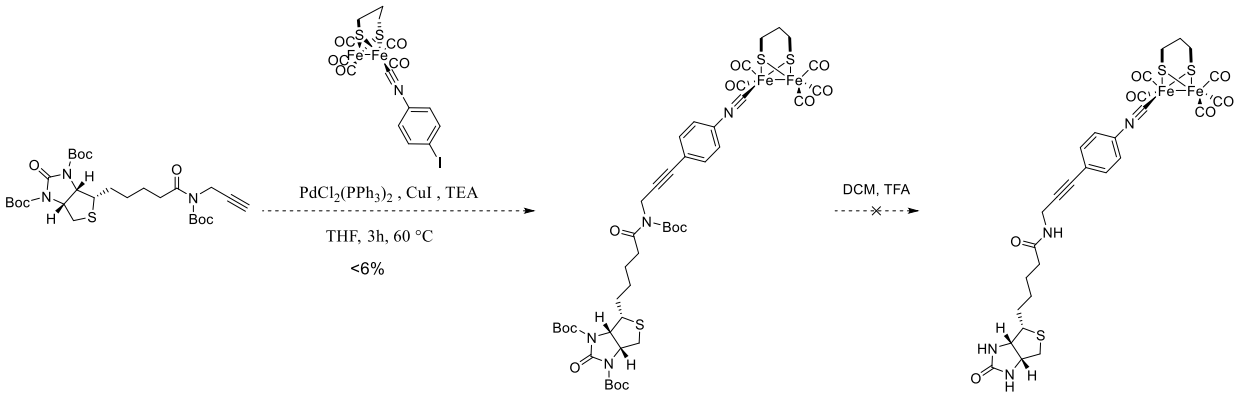

Scheme 12: Sonogashira coupling of Boc3Biotinylated Propargylamine and (μ-propanedithiolato)diiron 4-iodopheynylisocyano pentacarbonyl

Following literature reaction conditions,[140,144–146] Sonogashira coupling of Boc-protected Biotinylated Propargylamine and (μ-propanedithiolato)diiron 4-iodopheynylisocyano pentacarbonyl was carried out in dry tetrahydrofuran and triethylamine with bis(triphenylphosphine)palladium chloride and copper iodide co-catalysts (Scheme 12). After three hours of reacting at 60°C, the solution was concentrated purified via column chromatography resulting in ethyl acetate insoluble residuals and the isolation of four bands.

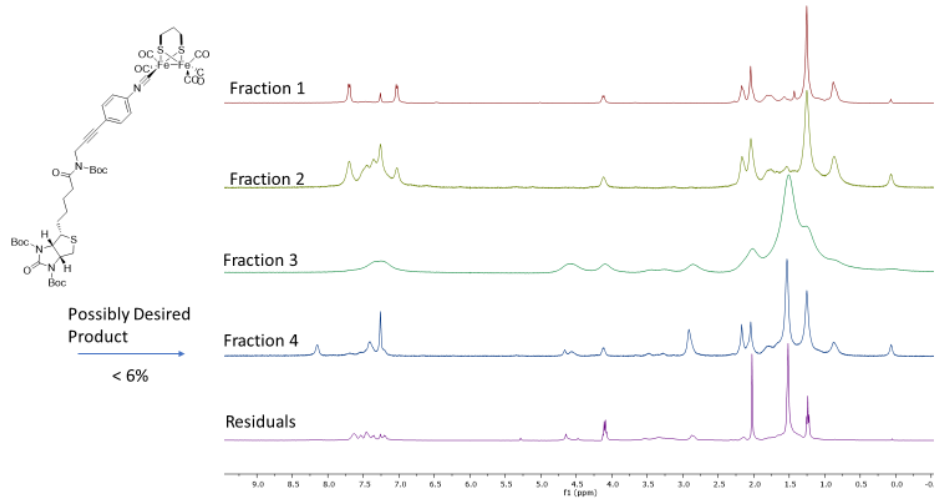

Figure 15:[1]H NMR spectra of isolated fractions from Sonogashira coupling of Boc-protected Biotinylated Propargylamine and (μ-propanedithiolato)diiron 4-iodopheynylisocyano pentacarbonyl

A change in phenyl ^{1}H NMR chemical shifts from 7.7 and 7.03 ppm to 8.15 and 7.4 ppm, along with the presence of protons at 4.66, 4.56, 3.48, and 3.28 ppm correlating to biotin, a broad peak at 1.53 ppm indicating the presence of tert-butyl groups and chemical shifts at 2.17 and 2.04 characteristic of the bridging propanedithiolato ligand led to the identification of fraction 4 as the desired coupling product in less than 6 % yield (Figure 17). All the sample obtained was used for NMR analysis. Due to the low yield the signal to noise ratio obtained during NMR experiments was too low to reliably determine relative integrations. In addition, ATR-IR analysis was not possible due to quantity of isolated product. Attempts to deprotect the Sonogashira coupling product under standard Boc-deprotection conditions with trifluoroacetic acid led to a decomposition of the diiron cluster. Further attempts to optimize the Sonogashira coupling conditions were not pursued due to a change in projects.

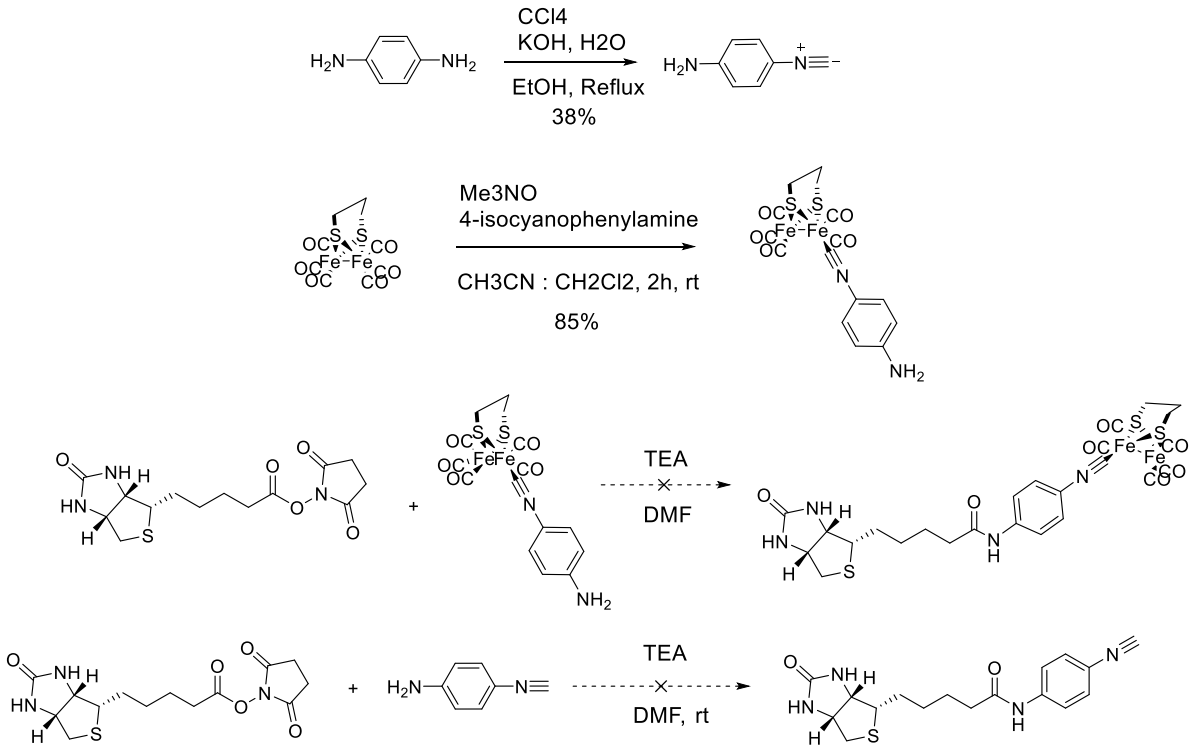

Scheme 13: Synthesis of (μ-propanedithiolato)diiron 4-aminopheynylisocyano pentacarbonyl and subsequent amide coupling reactions with biotin-NHS-ester

While pursuing the Sonogashira coupling reaction route, (μ-propanedithiolato)diiron 4-aminopheynylisocyano pentacarbonyl was synthesized as a side project in pursuit of a novel diiron cluster which would be capable of coupling with biotin through an amide coupling reaction with the activated biotin-NHS-ester (Scheme 13). The 4-Aminophenylisocyanide ligand was synthesized following the optimized procedure reported by Heinze and Jacob.[147] To synthesize 4-Aminophenylisocyanide, 1,4-diaminobenzene was reacted with dichlorocarbene in a carbylamine reaction or Hofmann isocyanide synthesis. Dichlorocarbene was generated in situ by the reaction of chloroform with potassium hydroxide. Purification by column chromatography led to the isolation of 4-Aminophenylisocyanide with a 37% yield as orange solids. Characterization of 4-Aminophenylisocyanide via ATR-IR confirmed the presence of the isocyanide functional group with a nitrile stretching frequency of 2128 cm^{-1}. Characterization via 1H NMR matched the

literature values with chemical shifts of 7.13 ppm integrating to two protons, 6.62-6.52 ppm integrating to two protons correlating to phenyl protons, and a chemical shift of 3.95 ppm integrating to two protons correlating with the amine protons.[147]

Synthesis of the novel (μ-propanedithiolato)diiron 4-aminopheynylisocyano pentacarbonyl was accomplished by decarbonylating of (μ-propanedithiolato)diiron hexacarbonyl with methylamine-N-oxide in the presence of 4-aminopheynylisocyanide. Purification via column chromatography led to the isolation of a red oil in an 85% yield. When attempting different purification techniques, it was found that the (μ-propanedithiolato)diiron 4-aminopheynylisocyano pentacarbonyl complex was water soluble. Characterization via ATR-IR showed amine N-H stretching frequencies at 3492 and 3398 cm^{-1} indicating that the amine had not been oxidized by binding (μ-propanedithiolato)diiron hexacarbonyl, a nitrile stretching frequency of 2132 cm^{-1} indicating the presence of isocyanate and a shortening of the C≡N bond compared to 4-aminopheynylisocyanide, and carbonyl stretching frequencies of 2033, 1979, 1970, 1974, 1950, 1921, 1898 cm^{-1} (figure A104). Characterization via ^{1}H-NMR in chloroform-D gave chemical shifts of 7.09 and 6.57 ppm integrating to two protons each correlating to phenyl protons, 3.88 ppm correlating integrating to two protons correlating with two amine protons, and chemical shifts of 2.15, 2.02, and 1.77 ppm integrating to two protons each correlating with the loss in symmetry of the bridging propanedithiolato ligand (figure A31). Attempts to couple (μ-propanedithiolato)diiron 4-aminopheynylisocyano pentacarbonyl or 4-aminopheynylisocyanide with biotin via the activated NHS ester or through EDC couplings led to no measurable reaction after 48 hours. Leading to the conclusion that 4-aminophenylisocyanide is a poor nucleophile.

Conclusions

In summary, several reaction routes for the formation of a biotinylated diiron cluster were explored. It was found that the use of 2,2-dimethyoxy-2-phenylacetophenone as a photo initiator for thiol-ene click reactions with diiron iron clusters failed due to the high molar absorptivity of the (μ-allylazadithiolato)diiron(I) hexacarbonyl in the ranges of light used. Further photo-initiated thiol-ene click reactions would benefit from photoiniator with a λ_{max} greater than 400 nm to avoid overlapping with the absorption range of the diiron cluster. In addition, (μ-allylazadithiolato)diiron(I) hexacarbonyl are unstable under the minimal thermal conditions required for the use of azobisisobutyronitrile as a radical initiator.

While probing additional reaction routes for generating a biotinylated diiron cluster several novel compounds were synthesized. A biotin[n]uril-diiron hexacarbonyl adduct macrocycle was synthesized when attempting to use biotinylated-3,6-dioxaoctane-1,8-diamine in a condensation reaction with formaldehyde and bishydrothiodiiron hexacarbonyl. While interesting, the complex was not useful in conjunction with the avidin artificial enzyme project. A novel water soluble (μ-propanedithiolato)diiron 4-aminopheynylisocyano pentacarbonyl complex was synthesized but was incompatible with amide coupling reactions to form the desired biotinylated diiron cluster.

Synthesis of a biotinylated diiron cluster through Sonogashira coupling was partially successful. Sonogashira coupling of Boc-protected biotinylated propargylamine with (μ-propanedithiolato)diiron 4-iodopheynylisocyano pentacarbonyl led to the isolation of a Boc-protected-biotinylated diiron cluster in extremely low yields. Unfortunately, the acidic conditions used for deprotection to yield a biotin specie capable of binding avidin lead to the decomposition of the diiron cluster. With further research, optimization of the Sonogashira conditions and use of dilute acid conditions for deprotection may someday lead to the synthesis of an artificial hydrogenase enzyme using biotin-avidin technology.

Experimental

Materials

The following reagents were obtained from the indicated commercial suppliers and used as received unless otherwise noted: Acetic anhydride (Fisher Scientific), Allylamine (Alfa Aesar), Ammonium carbonate (Alfa Aesar), Ammonium chloride (BDH), Ammonium hydroxide (Fisher Scientific), Azobisisobutyronitrile (AIBN) (Sigma-Aldrich), biotin (Sigma-Aldrich), Bis(triphenylphosphine)palladium chloride (Sigma-Aldrich), celite 503 (EMD Chemicals), Copper iodide (Alfa Aesar), Cystamine dihydrochloride (Alfa Aesar), 1,4-diaminobenzene (Sigma-Aldrich), Dicyclohexylcarbodiimide (Sigma-Aldrich), 4-dimethylaminopyridine (Sigma-Aldrich), 2,2-dimethyoxy-2-phenylacetophenone (Acros Organics), Di-tert-butyl dicarbonate (Acros Organics), Dithiothreitol (TCI America), 2,2'-(ethylenedioxy)bis(ethylamine) (Alfa Aesar), 37% aqueous Formaldehyde solution (Alfa Aesar), Formic acid (Sigma-Aldrich), Glycine (Alfa Aesar), Hydrochloric acid (Fisher Scientific), 4-Iodoaniline (Sigma-Aldrich), Iron(0) pentacarbonyl (Sigma-Aldrich), 1 M Lithium triethylborohydride in THF (Alfa Aesar), Magnesium sulfate (EMD Chemicals), N-(3-dimethylaminopropyl)-N’-ethylcarbodiimide·HCl (TCI America), N-hydroxysuccinimide (Fisher Scientific), Octanoic acid (Sigma-Aldrich), Phenyl dichlorophosphate (Sigma-Aldrich), Potassium hydroxide (EM Science), 1,3-Propanedithiol (Sigma-Aldrich), Propargylamine (Alfa Aesar), silica gel (230400 mesh) (SiliCycle), Sodium bicarbonate (EMD Chemicals), Sodium chloride (Fisher Scientific), Sodium sulfate (Fisher Scientific), Sulfur (Sigma-Aldrich), Tris(2-carboxyethyl)phosphine hydrochloride (Alfa Aesar), Triethylamine (Sigma-Aldrich), Trifluoroacetic acid (Alfa Aesar), Trimethylamine-N-oxide (Sigma-Aldrich), Acetone (Pharmco Products Inc), Chloroform ($CHCl_3$) (Pharmco Products Inc), Dichloromethane (DCM) (Fisher Scientific), Diethyl ether (Pharmco Products Inc), Ethanol (Pharmco Products Inc), Ethyl acetate (Fisher Scientific), Hexanes (Fisher Scientific), Methanol

(Fisher Scientific), N,N-dimethylformamide (DMF) (Fisher Scientific), Tetrahydrofuran (THF) (Fisher Scientific), Toluene (Acros Organics), Acetonitrile-D_3 (Cambridge Isotope Laboratories), Chloroform-D (Cambridge Isotope Laboratories), N,N-dimethylformamide-D_7 (Cambridge Isotope Laboratories), Dimethylsulfoxide-D_6 (Cambridge Isotope Laboratories), Methanol-D4 (Cambridge Isotope Laboratories). Dry toluene, DCM, DMF, and THF were obtained from an Innovative Technology solvent purification system model SPS-400-5.

Instrumentation

Photo reactions were conducted in a Luzchem photo-reactor CCP-4V equipped with 4 UVA (350 nm centered) and 4 UVC (254 nm centered) lamps. ^{1}H NMR and ^{13}C NMR Spectra were acquired with a Varian Mercury 400 BB NMR or Varian UnityINOVA 500 NMR. Chemical shifts (δ) are reported in parts per million (ppm) relative to tetramethylsilane (TMS). Solvents ($CDCl_3$ & DMF-D_7) contained 0.03% v/v TMS as an internal reference. Peak abbreviations are used as follows: s = singlet, d = doublet, t = triplet, m = multiplet, br = broad. NMR spectrums were processed with MestReNova Software by Mestrelab Research. UV-Vis spectra were obtained using a Shimadzu UV-2450 UV-Vis spectrophotometer. Infrared spectra were obtained using a Thermo Nicolet iS10 FTIR equipped with a diamond plate Smart iTR™ attenuated total reflectance (ATR) sampling accessory. UV-Vis and ATR-IR spectra were processed with Matlab R2019b software by The MathWorks, Inc.

Experimental Procedures

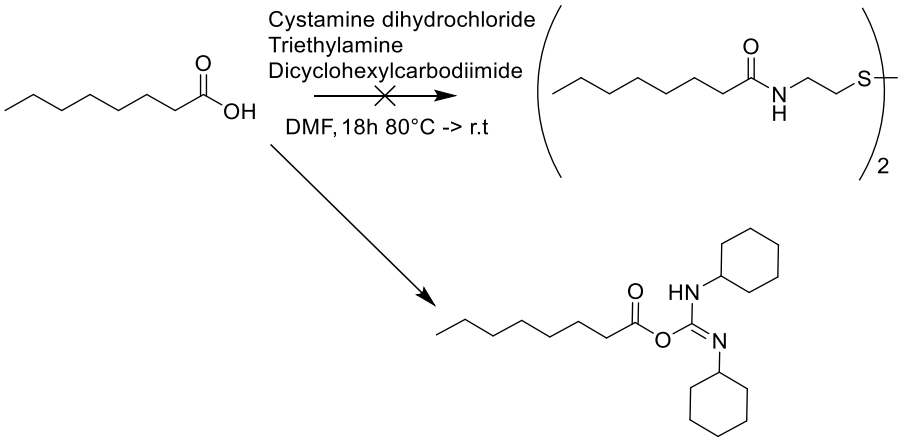

Scheme 14: Synthesis of N-(2-mercaptoethyl)-Octanamide (DDC coupling)

Procedure for synthesis of N-(2-mercaptoethyl)-Octanamide

A 100ml round bottom flask was charged with octanoic acid (200 µL, 1.262 mmol), Dicyclohexylcarbodiimide (0.264 g, 1.280 mmol), cystamine dihydrochloride (0.140 g, 0.621 mmol), and N,N-dimethylformamide (5 mls). The solution was stirred while triethylamine (582 µL, 4.20 mmol) was added. The solution was heated to 55°C and stirred for 24 hours. The solution was filtered to yield a yellow solution and a brilliant white powder (0.056 g). DMF solution extracted with ethyl acetate (50 ml). Ethyl acetate fraction washed with water (5x100 ml) then concentrated under reduced pressure to yield a waxy residue. Residue dissolved in acetone to yield a fine white powder and a yellow solution. Acetone solution concentrated under reduced pressure to yield a yellow oil. Oil was washed with hexanes to yield a white cloudy solution and beige solids. Beige solids dissolved in acetone and concentrated under reduced pressure to yield a yellow oil which crystalized into large white spherical crystals (0.240 g). ^{1}H NMR (400 MHz, CDCl3) δ 7.14 (s, 1H), 3.88 (td, J = 11.9, 5.9 Hz, 1H), 3.67 (dddd, J = 14.4, 10.4, 7.9, 4.0 Hz, 1H), 2.44 – 2.35 (m, 2H), 2.01 – 1.84 (m, 4H), 1.84 – 1.55 (m, 12H), 1.45 – 1.28 (m, 9H), 1.28 – 1.21 (m, 7H), 1.21 – 1.06 (m, 3H), 0.91 – 0.81 (m, 4H). (^{1}H NMR figure: A1)

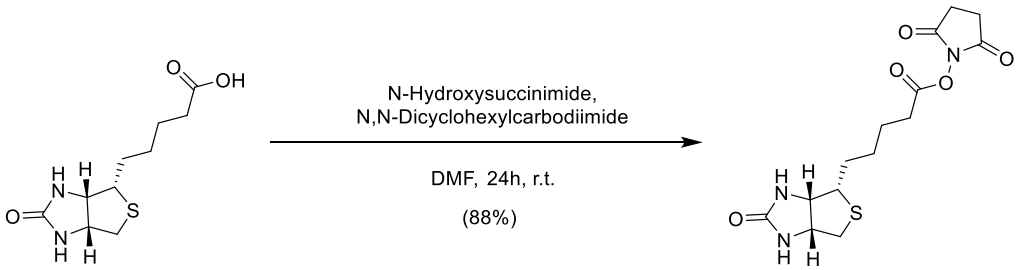

Scheme 15: Synthesis of Biotin-NHS-Ester (DDC coupling)

Synthesis of Biotin-NHS-Ester (DCC coupling)

A 25ml round bottom flask was charged with biotin (0.225 g, 0.921 mmol) and N,N-dimethylformamide (13 mls) and allowed to warm to 32°C until biotin dissolved. To the solution n-hydroxysuccinimide (0.114 g, 0.921 mmol) and Dicyclohexylcarbodiimide (0.259 g, 1.255mmol) were added and allowed to stir for 24 hours. The solution was vacuum filtered to yield dicyclohexylurea as a white powder (0.113 g, 0.504 mmol) and a clear filtrate. The solvent was evaporated under high vacuum to yield white solids. The white solids were triturated with diethyl ether to yield mixture of biotin-NHS-Ester (87% based on NMR) and dicyclohexylurea (12.4%) as a white powder (0.315 g,). ^{1}H NMR (400 MHz, DMSO-d6) δ 6.43 (s, 1H), 6.37 (s, 1H), 4.30 (dd, J = 7.8, 5.0 Hz, 1H), 4.15 (ddd, J = 7.4, 4.4, 1.8 Hz, 1H), 3.10 (td, J = 7.9, 7.1, 4.2 Hz, 1H), 2.91 – 2.72 (m, 5H), 2.67 (t, J = 7.4 Hz, 2H), 2.58 (d, J = 12.4 Hz, 1H), 1.70 – 1.36 (m, 6H). (^{1}H NMR figure: A4)

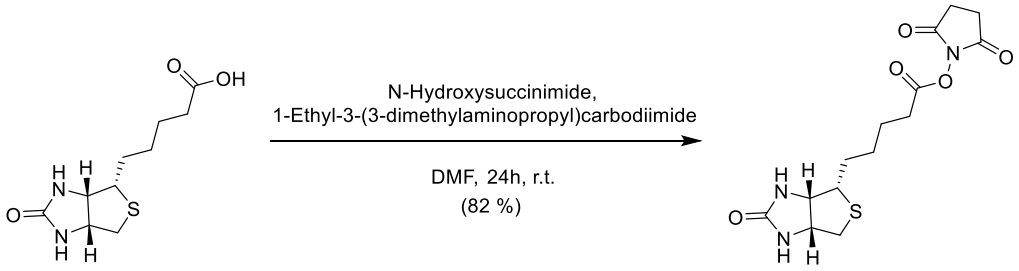

Scheme 16: Synthesis of Biotin-NHS-Ester (EDC coupling)

Synthesis of Biotin-NHS-Ester (EDC coupling)

A 50ml round bottom flask equipped with a stir bar was charged with biotin (0.5028 g, 2.058 mmol), n-hydroxysuccinimide (0.2690 g, 2.337 mmol), N-(3-dimethylaminopropyl)-N'-ethylcarbodiimide·HCl (0.4740 g, 2.473 mmol), and N,N-dimethylformamide (25 mls). The solution was stirred for 24 hours. The solvent was evaporated under vacuum to yield white solids. The solids were triturated with cold methanol to yield biotin-NHS-ester as a white solid (0.5764 g, 1.688 mmol, 82% yield). ^{1}H NMR (400 MHz, DMSO-d6) δ 6.43 (s, 1H), 6.37 (s, 1H), 4.30 (dd, J = 7.8, 5.0 Hz, 1H), 4.15 (ddd, J = 7.4, 4.4, 1.8 Hz, 1H), 3.10 (td, J = 7.9, 7.1, 4.2 Hz, 1H), 2.91 – 2.72 (m, 5H), 2.67 (t, J = 7.4 Hz, 2H), 2.58 (d, J = 12.4 Hz, 1H), 1.70 – 1.36 (m, 6H). ^{13}C NMR (101 MHz, DMSO) δ 170.26, 168.93, 162.68, 60.98, 59.17, 55.23, 30.69, 29.99, 27.83, 27.57, 25.44, 24.31. (^{1}H NMR figure A5-6, ^{13}C NMR figure A53, ATR-IR figure A91)

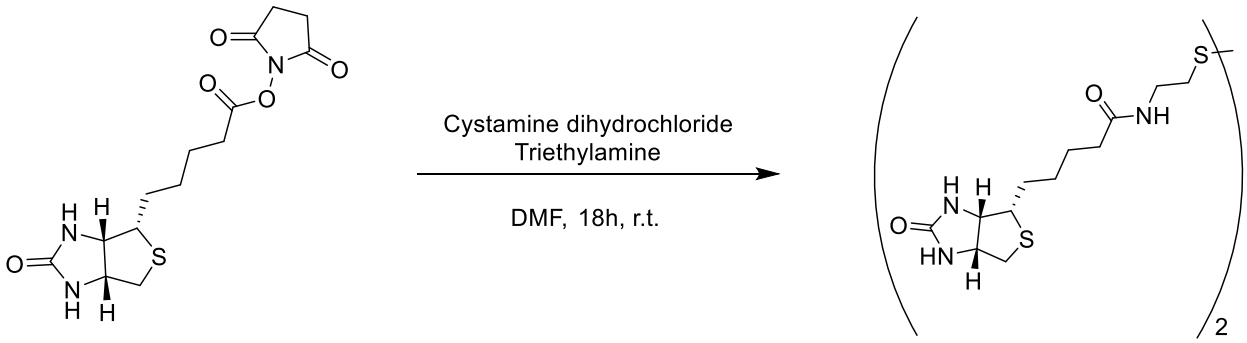

Scheme 17: Synthesis of Biotinylated-Cystamine

Synthesis of Biotinylated-Cystamine

A 50ml round bottom flask equipped with a stir bar was charged with biotin-NHS-ester (0.346 g, 1.014 mmol), cystamine dihydrochloride (0.118 g, 0.524 mmol), and N,N-dimethylformamide (18 mls) and allowed to stir. To the solution triethylamine (420 µL, 3.03 mmol) was added and allowed to stir for 18 hours. The solvent was evaporated under high vacuum to yield a white gel. The gel was triturated with cold water to yield biotinylated-cystamine as a white powder (0.2307 g, 0.381 mmol, 75% yield). ^{1}H NMR (400 MHz, DMSO-d6) δ 7.99 (t, J =

5.6 Hz, 1H), 6.44 (s, 1H), 6.37 (s, 1H), 4.30 (t, J = 6.4 Hz, 1H), 4.12 (t, J = 6.1 Hz, 1H), 3.34 – 3.26 (m, 3H), 3.10 (q, J = 4.9 Hz, 1H), 2.78 (dt, J = 13.7, 9.5 Hz, 4H), 2.57 (d, J = 12.5 Hz, 1H), 2.06 (t, J = 7.3 Hz, 2H), 1.60 (q, J = 7.4, 6.4 Hz, 1H), 1.48 (dt, J = 16.9, 8.2 Hz, 4H), 1.31 (dq, J = 14.9, 7.4, 6.8 Hz, 2H).[13]C-NMR (400 MHz, DMSO-D6), δ: 172.24, 162.73, 61.04, 59.21, 55.43, 39.88, 37.88, 37.32, 35.16, 28.20, 28.04, 25.25. ([1]H NMR figure A8-9, [13]C NMR figure A54, ATR-IR figure A92)

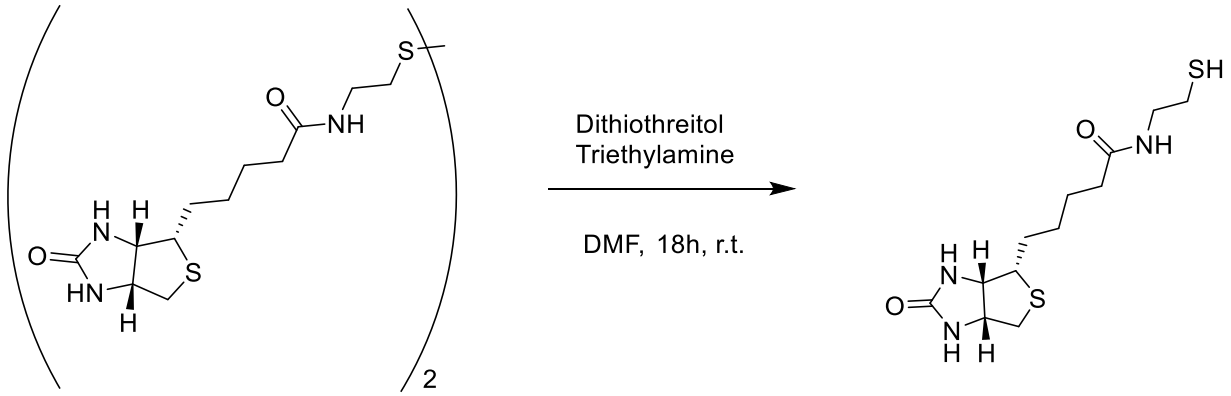

Scheme 18: Synthesis of Biotinylated-cysteamine

Synthesis of Biotinylated-Cysteamine

A 50ml round bottom flask equipped with a stir bar was charged with biotinylated-cystamine (0.1058 g, 0.175 mmol), dithiothreitol (0.1352 g, 0.876 mmol) and dry, degassed N,N-dimethylformamide (10 mls) and allowed to stir. The flask was purged with nitrogen. To the solution triethylamine (46 µL, 0.332 mmol) was added to yield a pink solution and was stirred for 18 hours. The solvent was removed under high vacuum to yield an off-white powder. The round bottom flask was then backfilled with nitrogen and the solids were triturated with dry, degassed acetone under nitrogen flow. The triturated solids were collected with vacuum filtration to yield biotinylated-cysteamine as white solids (0.1146 g, 0.378 mmol, 108% yield). The solids were quickly returned a 50ml round bottom flask and purged with nitrogen to be used immediately in

thiol-ene click reaction. ^{1}H-NMR (400 MHz, DMSO-D6), δ: 7.96 (t, J = 5.7 Hz, 1H), 6.43 (s, 1H), 6.37 (s, 1H), 4.30 (dd, J = 7.7, 4.9 Hz, 1H), 4.16 – 4.09 (m, 1H), 3.23 – 3.02 (m, 3H), 2.91 – 2.70 (m, 1H), 2.57 (d, J = 12.4 Hz, 1H), 2.50 (q, J = 7.8 Hz, 3H), 2.34 (t, J = 8.0 Hz, 1H), 2.14 – 1.99 (m, 3H), 1.68 – 1.38 (m, 4H), 1.40 – 1.22 (m, 2H).^{13}C-NMR (400 MHz, DMSO-D6), δ: 172.18, 162.78, 61.08, 59.24, 55.46, 42.08, 39.90, 35.17, 30.75, 28.24, 28.07, 25.28, 23.58. (^{1}H NMR figure A10-11, ^{13}C NMR figure A55, ATR-IR figure A93)

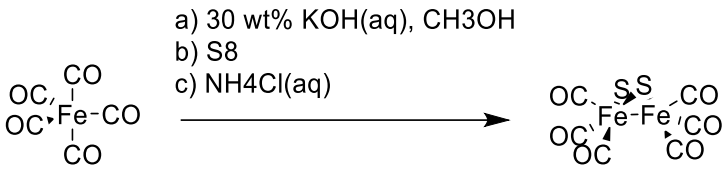

Scheme 19: Synthesis of (μ-dithiolato)diiron(I) hexacarbonyl

Synthesis of (μ-dithiolato)diiron(I) hexacarbonyl, $Fe_2[\mu\text{-}S_2](CO)_6$

A 500ml schlenck flask equipped with a stir bar was charged with potassium hydroxide (30% wt., 20 ml) and methanol (35 ml). The solution was stirred while it was cooled to 0°C and purged with nitrogen. Iron(0) pentacarbonyl (7.5 ml, 56 mmol) was added dropwise and was stirred three minutes yielding a deep red solution. Elemental sulfur (10.0293 g, 39.1 mmol) was added scoop wise with a nitrogen counter flow and vigorous mixing generating a black mixture. After six minutes of stirring water (80 ml), hexanes (200 ml) and ammonium chloride (25.2685g, mmol) were added and allowed to stir vigorously for an hour and a half. The top layer was decanted, and the residual black layer was extracted with hexanes (3x150 ml). The decanted solution and extracted hexanes were filtered through celite, combined, washed with equivalent portions of water, then dried over magnesium sulfate. The solvent was evaporated under reduced pressure to yield a dark red oil. The red oil was purified with silica column chromatography with hexanes eluent. The first red-orange fraction was collected, and the second maroon fraction was

discarded. The solvent of the red-orange fraction was removed under reduced pressure to yield (μ-dithiolato)diiron(I) hexacarbonyl as a red solid (1.0826 g, 3.156 mmol, 11% yield); ATR-IR ν_{CO} = 2074, 2038, 1995, 1977, 1953, and 1928 cm^{-1} (ATR-IR figure A94)

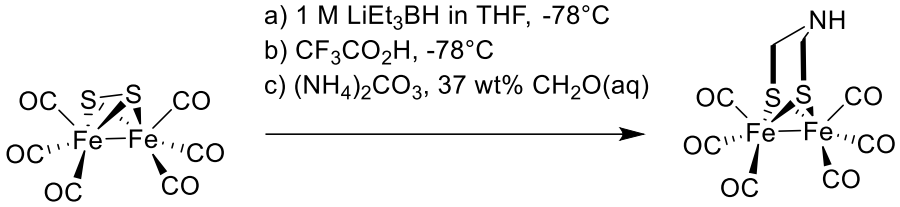

Scheme 20: Synthesis of (μ-azadithiolato)diiron(I) hexacarbonyl

Synthesis of (μ-azadithiolato)diiron(I) hexacarbonyl, $Fe_2[(SCH_2)_2NH)](CO)_6$

A 100 ml schlenk flask was charged with tetrahydrofuran (30 ml) and ammonium carbonate (1.6777 g, 17.460 mmol). The solution was degassed by bubbling nitrogen. To the degassed solution 37% aqueous formaldehyde solution (2.85 ml, 38.274 mmol) was added. The solution was heated to 60°C for one hour then allowed to cool to room temperature.

A separate 100 ml schlenk flask was charged with (μ-dithiolato)diiron(I) hexacarbonyl (1.2006 g, 3.4914 mmol) and tetrahydrofuran (24 ml). The solution was degassed by bubbling nitrogen and cooled to -78°C. 1 M lithium triethylborohydride in THF (7.9 ml, 7.9 mmol) was added dropwise then allowed to stir for 15 minutes. Trifluoroacetic acid (1.1 ml, 15 mmol) was then added dropwise and allowed to stir for 15 minutes. The solution was then allowed to warm to room temperature. The ammonium carbonate solution was then cannula transferred to the (μ-dithiolato)diiron(I) hexacarbonyl solution and allowed to stir for 16 hours. The solution was then concentrated under reduced pressure to yield a dark red oil. The dark red oil was dissolved in hexanes (200ml) and sonicated for 2 hours. The organic solution was washed with water (2 x 150 mL) followed by saturated sodium bicarbonate solution (150 mL). The red hexanes solution was dried over magnesium sulfate then concentrated under reduced pressure to yield a red oil. The oil

was then purified column chromatography with silica and 95:5 hexanes/ethyl acetate eluent. Five bands were observed. The 5th band was collected and concentrated to yield (μ-azadithiolato)diiron(I) hexacarbonyl as a red oil (0.2923g, 0.6845 mmol, 19.605 %yield). ^{1}H NMR (500 MHz, cdcl3) δ 3.69 (s, 4H), 1.76 (s, 1H). ATR-IR ν_{CO} = 2066, 2044, 2020, 1977, and 1946 cm^{-1} (^{1}H NMR figure A26, ATR-IR figure A105)

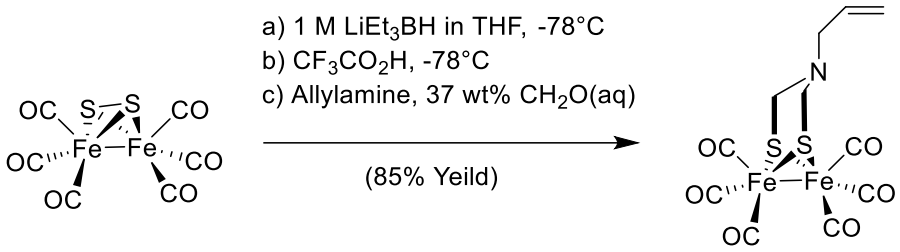

Scheme 21: Synthesis of (μ-allylazadithiolato)diiron(I) hexacarbonyl

Synthesis of (μ-allylazadithiolato)diiron(I) hexacarbonyl, $Fe_2[(SCH_2)_2NCH_2CH{=}CH_2](CO)_6$

A 100 ml schlenk flask was charged with tetrahydrofuran (34 ml) and allylamine (150 μL, 2.00 mmol). The solution was degassed by bubbling nitrogen. To the degassed solution 37% aqueous formaldehyde solution (1.5 ml, 18.5 mmol) was added. The solution was heated at 60°C for one hour then allowed to cool to room temperature.

A separate 100 ml schlenk flask was charged with (μ-dithiolato)diiron(I) hexacarbonyl (0.6845 g, 1.996 mmol) and tetrahydrofuran (14 ml). The solution was degassed by bubbling nitrogen and cooled to -78°C. 1 M lithium triethylborohydride in THF (4.5 ml, 4.5 mmol) was added dropwise then allowed to stir for 15 minutes to yield a green solution. Trifluoroacetic acid (0.63 ml, 8.2 mmol) was then added dropwise and allowed to stir for 15 minutes to yield a dark red solution. The solution was then allowed to warm to room temperature. The allylamine solution was then cannula transferred to the (μ-dithiolato)diiron(I) hexacarbonyl solution and allowed to

stir for 16 hours. The solution was then concentrated under reduced pressure to yield a dark red oil. The dark red oil was dissolved in hexanes (100ml) then was washed with equal portions water followed by equal portions saturated sodium bicarbonate solution. The red hexanes solution was dried over magnesium sulfate then concentrated under reduced pressure to yield a red oil. The oil was then purified via column chromatography with silica and hexanes eluent. Four bands were observed, a yellow band (unreacted (μ-dithiolato)diiron(I) hexacarbonyl), an unknown purple band, a thin unknown gold band, then a dark orange band. The dark orange band was collected and concentrated to yield (μ-allylazadithiolato)diiron(I) hexacarbonyl as a red oil.(0.7605 g, 1.712 mmol, 85% yield). Molar quantity and yield adjusted for hexanes grease impurity based on NMR. ^{1}H-NMR (400 MHz, $CDCl_3$), δ 5.63 (ddt, J = 16.7, 10.2, 6.3 Hz, 1H), 5.19 – 5.06 (m, 2H), 3.32 (s, 4H), 3.16 (d, J = 6.3 Hz, 2H). δ: ATR-IR ν_{CO} = 2071, 2026, and 1963 cm^{-1}. (^{1}H NMR figure A13, ATR-IR figure A95)

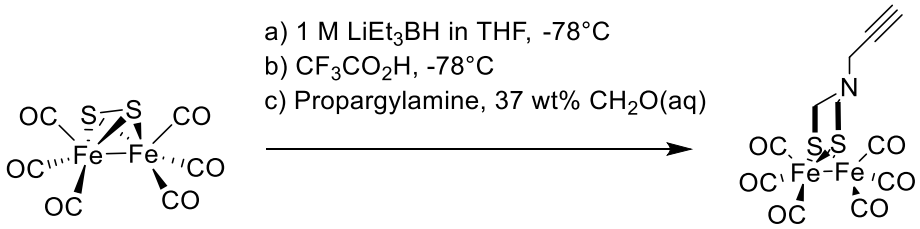

Scheme 22: Synthesis of (μ-propargylazadithiolato)diiron(I) hexacarbonyl

Synthesis of (μ-propargylazadithiolato)diiron(I) hexacarbonyl, $Fe_2[(SCH_2)_2NCH_2C{\equiv}CH](CO)_6$

A 100 ml schlenk flask was charged with tetrahydrofuran (50 ml) and propargylamine (186 μL, 2.91 mmol). The solution was degassed by bubbling nitrogen. To the degassed solution 37% aqueous formaldehyde solution (2.25 ml, 30.2 mmol) was added. The solution was heated at 60°C for one hour then allowed to cool to room temperature.

A separate 100 ml schlenk flask was charged with (μ-dithiolato)diiron(I) hexacarbonyl (1.0013 g, 2.9119 mmol) and tetrahydrofuran (20 ml). The solution was degassed by bubbling

nitrogen and cooled to -78°C. 1 M lithium triethylborohydride in THF (6.5 ml, 6.5 mmol) was added dropwise then allowed to stir for 15 minutes to yield a green solution. Trifluoroacetic acid (0.9 mL, 12 mmol) was then added dropwise and allowed to stir for 15 minutes to yield a dark red solution. The solution was then allowed to warm to room temperature. The propargylamine solution was then cannula transferred to the (μ-dithiolato)diiron(I) hexacarbonyl solution and allowed to stir for 16 hours. The solution was then concentrated under reduced pressure to yield a dark red oil. The dark red oil was dissolved in hexanes (125ml) then was washed with water (90 mL) followed by saturated sodium bicarbonate solution (90 mL). The red hexanes solution was dried over magnesium sulfate then concentrated under reduced pressure to yield a red oil. The oil was then purified via column chromatography with silica substrate and hexanes eluent. Four bands were observed, a yellow band (unreacted (μ-dithiolato)diiron(I) hexacarbonyl), an unknown purple band, an unknown gold band, then a red band. The red band was collected and concentrated to yield (μ-propargylazadithiolato)diiron(I) hexacarbonyl as a red oil.(0.7654 g, 1.8010 mmol, 61.850 % yield). NMR showed signs of hexane grease. ^{1}H-NMR (400 MHz, CDCl3), δ: 3.33 (s, 2H), 3.22 (s, 4H), 2.29 (s, 1H). ^{13}C NMR (101 MHz, $CDCl_3$) δ 207.81, 77.03, 74.75, 51.92, 47.87. ATR-IR ν_{CO} = 2072, 2030, 2003, 1982, 1960, 1946 cm^{-1}. (^{1}H NMR figure A14, ^{13}C NMR figure A56, ATR-IR figure A96)

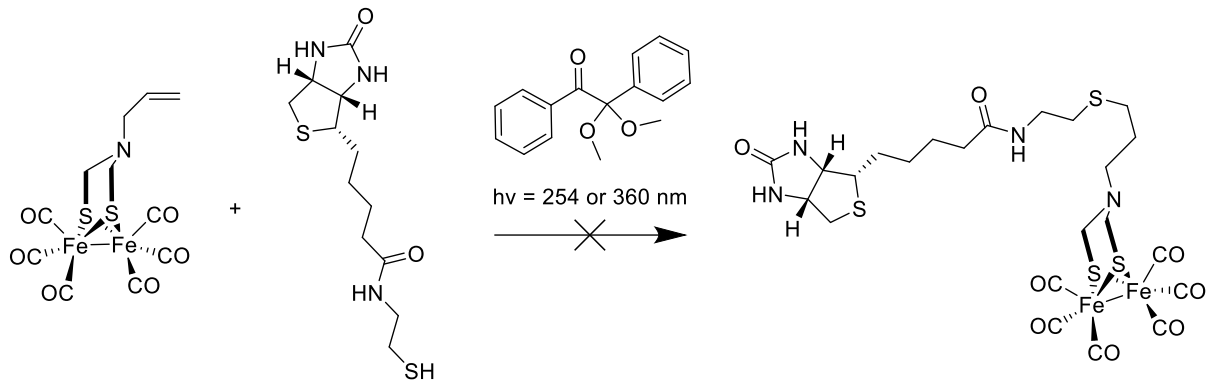

Scheme 23: Synthesis of (μ-biotinylcysteamineazadithiolato)diiron(I) hexacarbonyl via a photo-initiated thiol-ene click reaction

Procedure for the synthesis of (μ-biotinylcysteamineazadithiolato)diiron(I) hexacarbonyl (2,2-dimethyoxy-2-phenylacetophenone)

A 250-ml quartz round bottom flask equipped with a stir bar was charged with (μ-allylazadithiolato)diiron(I) hexacarbonyl (0.103g, 0.241 mmol), biotinylated-cysteamine (0.062 g, 0.205 mmol), 2,2-dimethyoxy-2-phenylacetophenone (13 mg, 0.08 mmol) and either methanol or N,N-dimethylformamide (5 ml). The quartz flask was purged with nitrogen while stirring. The solution was irradiated with either 254 or 360 nm light for 10 minutes while stirring yielding an orange solution with dark precipitates. The solution was concentrated to yield dark red oil. The oil was rinsed with hexanes yielding a red solution and blue/green solids. The solution was concentrated to yield a red oil. The blue/green solids were washed in methanol to yield a green solution. The solution was concentrated to yield green solids. Green solids once crystallized are insoluble in DMSO-D6 and Methanol-D4. NMR of red oil shows presence of DMPA and (μ-allylazadithiolato)diiron(I) hexacarbonyl starting materials only. TLC of green solids and biotinylated-cysteamine with methanol eluent match with a Rf range of 0.44 to 0.88 (streaked spots).

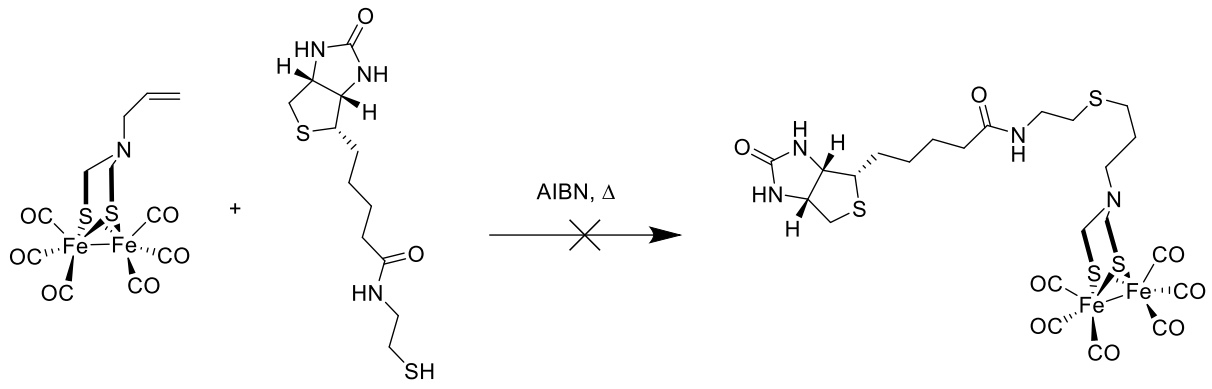

Scheme 24: Synthesis of (μ-biotinylcysteamineazadithiolato)diiron(I) hexacarbonyl via a thermal initiated thiol-ene click reaction

Procedure for the synthesis of (μ-biotinylcysteamineazadithiolato)diiron(I) hexacarbonyl (AIBN)

A 100 ml round bottom flask equipped with a magnetic stir bar was charged with allylazadithiolato)diiron(I) hexacarbonyl (0.0622 g, 0.1456 mmol), biotinylated-cysteamine (0.0492 g, 0.1623 mmol) , azobisisobutyronitrile (0.026 g, 0.158 mmol), and degassed methanol (10 ml). The flask was equipped with a condenser sealed with a septum and the system was purged with nitrogen. The flask was lowered into an oil bath at 60C and stirred for 2 hours. The reaction mixture was stripped of solvent under reduced pressure. Solids were washed with hexanes to yield red solution and green solids (0.0404 g). The hexanes solution was tested against allylazadithiolato)diiron(I) hexacarbonyl using TLC (hexanes eluent) , resulting in the identical Rf values of (0, 0.14 dark red, 0.45 faint). The hexanes solution was concentrated under reduced pressure to yield a red oil with white crystals visible (0.0786g). All fractions were recombined and dissolved in N,N-dimethylformamide (15mls) and methanol (1 ml) in a 100 ml round bottom flask equipped with a septum sealed condenser and was purged with nitrogen. The solution was heated to 65C and was stirred for 12 hours. The solution was vacuum filtered yielding a dull orange solution and black solids (0.0363g). The solution was concentrated under high vacuum to yield

light orange solids (0.0564). The solids were not soluble in hexanes or ethyl acetate, were slightly soluble methanol. TLC with methanol eluent yielded a single spot with a Rf range of 0.5 to 0.875 with a faint tail streaking back to the baseline. Black solids were insoluble in methanol-d4, acetonitrile-d3, or dimethylsulfoxide-D6.

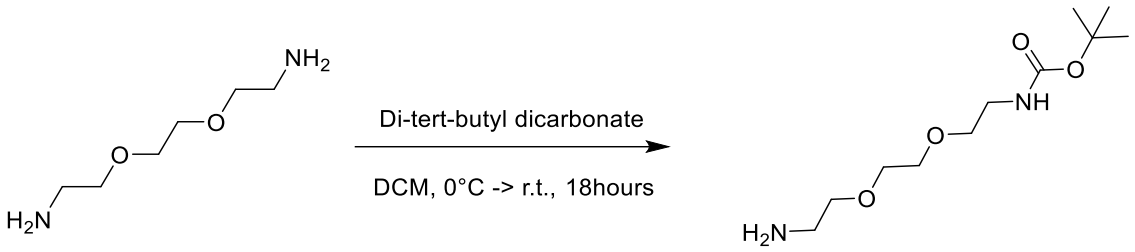

Scheme 25: Synthesis of tert-butyl[2-[2-(2-aminoethoxy)ethoxyethyl]]carbamate

Synthesis of tert-butyl[2-[2-(2-aminoethoxy)ethoxyethyl]]carbamate

A 100ml round bottom flask equipped with a stir bar was charged with dichloromethane (25 ml) and 2,2-(ethylenedioxy)bis(ethylamine) (1.009ml, 6.910 mmol) and was cooled to 0°C. A separate 100 ml round bottom flask cooled to 0°C was charged with dichloromethane (17 ml) and di-tert-butyldicarbonate (0.501 g, 2.2955 mmol). The di-tert-butyldicarbonate solution was transferred to 2,2-(ethylenedioxy)bis(ethylamine) solution dropwise over 1 hour and 45 minutes then allowed to stir at room temperature for 18 hours. The solution was washed with saturated sodium chloride solution (5x10ml) then dried over magnesium sulfate. The solution was then filtered into a 100 ml round bottom flask then concentrated under reduced pressure to yield a yellow viscous oil. The oil was purified with column chromatography with 1:2 ethyl acetate: hexanes followed by 2:1 ethyl acetate: hexanes generating two fractions. Each fraction was concentrated under reduced pressure. Fraction 1 yielded an off-white oil (0.0486g) and fraction 2 yielded tert-butyl[2-[2-(2-aminoethoxy)ethoxyethyl]]carbamate as a clear yellow tinted oil (0.3199 g, 1.288 mmol, 56% yield). ^{1}H-NMR (400 MHz, CDCl3), δ: 5.17 (s, 1H), 3.62-3.59 (m,

4H), 3.55-3.50 (m, 4H), 3.32-3.28 (m, 2H), 2.88 (t, J= 8 Hz, 2H), 1.81 (s, 3H), 1.42 (s, 9H). (^{1}H NMR figure A15)

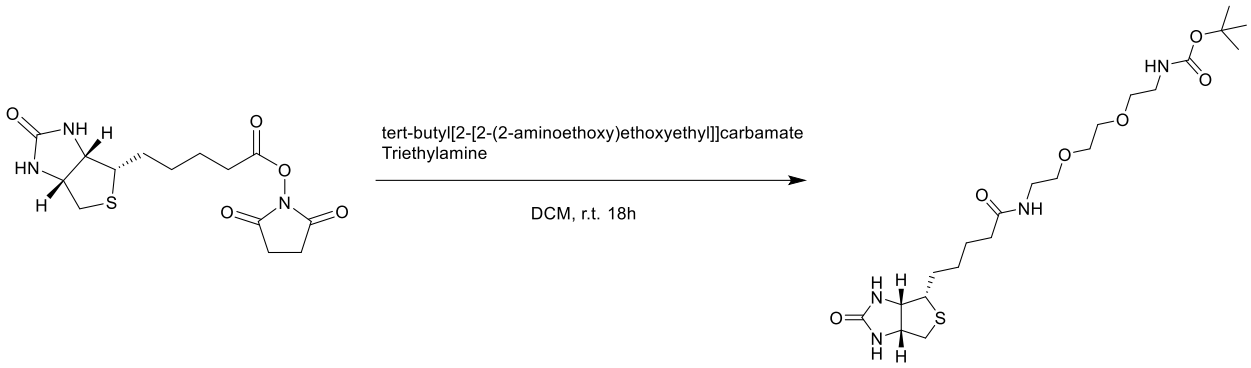

Scheme 26: Synthesis of biotinylated- tert-butyl[2-[2-(2-aminoethoxy)ethoxyethyl]]carbamate

Synthesis of biotinylated- tert-butyl[2-[2-(2-aminoethoxy)ethoxyethyl]]carbamate

A 50 ml round bottom flask equipped with a stir bar was charged with biotin-NHS-ester (0.1969 g, 0.5767 mmol), tert-butyl[2-[2-(2-aminoethoxy)ethoxyethyl]]carbamate (0.155g, 0.624 mmol), dichloromethane (20 mls) and triethylamine (100µL, 0.721 mmol) and allowed to stir at room temperature for 24 hours. The solution was concentrated under reduced pressure then dissolved in dichloromethane to yield a tan solution. The solution was purified by column chromatography with silica substrate and 90:10:1 dichloromethane: methanol: ammonium hydroxide eluent to yield two fractions. Fraction 1 was concentrated to yield n-Boc-Biotinylated -3,6-dioxaoctane-1,8-diamine as an off-white solid (0.2373g, 0.5003 mmol, 87% yield). ^{1}H NMR (400 MHz, $CDCl_3$) δ 6.71 (s, 1H), 6.54 (s, 1H), 5.59 (s, 1H), 5.15 (s, 1H), 4.49 (ddt, J = 6.3, 4.9, 1.2 Hz, 1H), 4.30 (ddd, J = 7.8, 4.6, 1.4 Hz, 1H), 3.60 (s, 4H), 3.55 (dt, J = 7.4, 5.0 Hz, 4H), 3.43 (td, J = 5.6, 4.3 Hz, 2H), 3.31 (d, J = 5.9 Hz, 2H), 3.13 (td, J = 7.4, 4.5 Hz, 1H), 2.89 (dd, J = 12.7, 4.8 Hz, 1H), 2.73 (d, J = 12.8 Hz, 1H), 2.23 (t, J = 7.5 Hz, 2H), 2.04 (s, 2H), 1.70 (dddd, J = 24.1, 16.4, 13.4, 7.5 Hz, 4H), 1.43 (m, 11H). (^{1}H NMR figure A16-17)

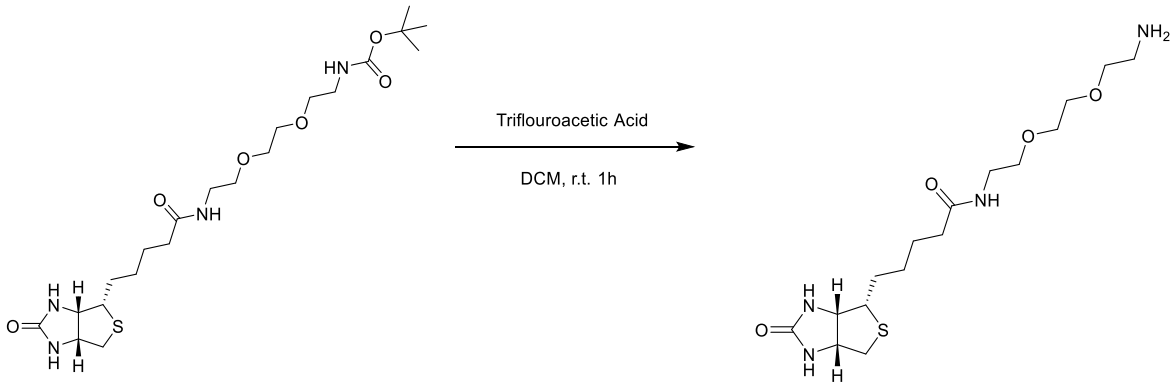

Scheme 27: Synthesis of Biotinylated -3,6-dioxaoctane-1,8-diamine

Synthesis of Biotinylated -3,6-dioxaoctane-1,8-diamine

A 50ml round bottom flask equipped with a stir bar was charged with n-Boc-Biotinylated -3,6-dioxaoctane-1,8-diamine (0.2373g, mmol) and dichloromethane (5 ml) and was allowed to stir. Trifluoroacetic acid (5 ml) was slowly added and allowed to stir for 1 hour. The solution was concentrated under reduced pressure to yield a tan oil (0.5379). Purified by column chromatography 20:10:1 Dichloromethane : Methanol : triethylamine to yield a clear oil (0.5182g). NMR showed high concentration of methanol. Attempted to concentrate under reduced pressure at 40°C for one hour. Attempting solvent exchange with ethyl acetate yielded Biotinylated -3,6-dioxaoctane-1,8-diamine as an ethyl acetate insoluble oil (0.193g, 0.5153 mmol, 89% yield). ^{1}H-NMR (400 MHz, DMSO-D6), δ: 7.86 (t, J = 5.7 Hz, 3H), 6.42 (s, 1H), 6.38 (s, 1H), 4.31 (dd, J = 7.7, 5.0 Hz, 1H), 4.15 – 4.10 (m, 1H), 3.62 – 3.49 (m, 6H), 3.19 (q, J = 5.9 Hz, 2H), 3.09 (q, J = 7.2 Hz, 5H), 2.97 (t, J = 5.2 Hz, 2H), 2.81 (dd, J = 12.5, 5.1 Hz, 1H), 2.57 (d, J = 12.4 Hz, 1H), 2.06 (t, J = 7.4 Hz, 2H), 1.67 – 1.38 (m, 4H), 1.36 – 1.24 (m, 2H), 1.17 (t, J = 7.3 Hz, 5H). (^{1}H NMR figure A18-19)

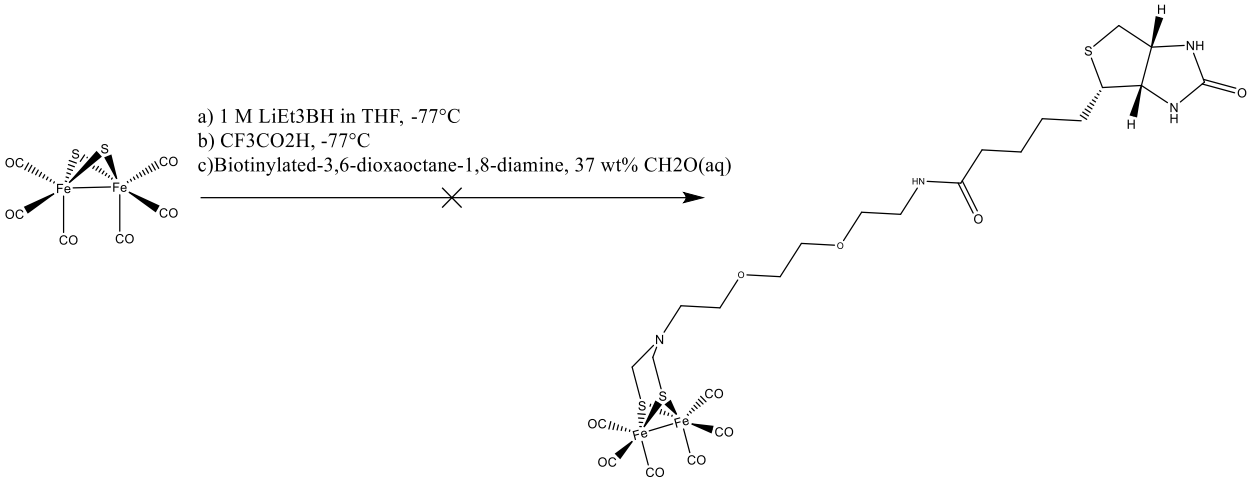

Scheme 28: Synthesis of Biotinylated-3,6-dioxaoctane-1,8-diamine -(μ-dithiolato)diiron(I) hexacarbonyl

Procedure for Biotinylated-3,6-dioxaoctane-1,8-diamine -(μ-dithiolato)diiron(I) hexacarbonyl

A 100 ml schlenk flask equipped with a stir bar was charged with biotinylated-3,6-dioxaoctane-1,8-diamine (0.193g, 0.515 mmol), tetrahydrofuran (10 ml), and methanol (1 ml) and was allowed to stir while degassing by bubbling nitrogen. 37% formaldehyde solution (0.5 ml, 6.16 mmol) was added and the solution was heated to 60°C for 1 hour. The solution was then cooled to room temperature. Some white precipitate formed.

A second 100 ml schlenk flask was charged with dithiolatodiiron(I) hexacarbonyl (0.2103 g, 0.6117 mmol) and tetrahydrofuran (4 ml), chilled to -78°C, and degassed by bubbling nitrogen. 1M lithium triethylborohydride in THF (1.3 ml, 1.3 mmol) was added dropwise and allowed to mix 15 minutes to yield a dark green solution. Trifluoroacetic acid (0.19 ml, 2.48 mmol) was added dropwise and allowed to stir for 15 minutes before warming to room temperature to yield a deep red solution. The biotinylated-3,6-dioxaoctane-1,8-diamine solution was cannula transferred to the dithiolatodiiron(I) hexacarbonyl solution and allowed to stir for 16 hours. The solution was concentrated under reduced pressure then dissolved in hexanes (3x25 mls) to yield two layers. The

solution was concentrated a second time then dissolved in ethyl acetate (50 ml) and washed with brine solution (40 ml) then saturated aqueous sodium bicarbonate solution (2x20 ml). Red ethyl acetate solution dried over magnesium sulfate then concentrated to yield a deep red oil (0.2062 g). The oil was purified with column chromatography 100% ethyl acetate followed by 100% methanol. The methanol fraction was collected and concentrated to yield a dark red oil (0.1311 g). Sample (0.026g) taken for NMR in chloroform-D. Dissolved oil in ethyl acetate and washed with brine (2x25 ml) and dried over magnesium sulfate. Concentrated solution under reduced pressure to yield dark red oil (0.0596g). Oil purified by column chromatography 90:10 ethyl acetate: methanol to yield six fractions as follows, fraction #1 tan, fraction #2 orange solution, fraction #3 orange, fraction #4 orange, fraction #5 red, fraction #6 orange. The fractions were concentrated to yield fraction #1 as an orange/brown film (0.0156 g), fraction #2 as an orange film (0.0013 g), fraction #3 orange film (0.0030 g), fraction #4 orange film (0.0091 g), fraction #5 as a red/orange film (0.0306 g), and fraction #6 as an orange film (0.0159 g). ^{1}H-NMR of fractions #5 and #6 are identical. Fraction #5 ^{1}H NMR (400 MHz, DMSO-d6) δ 7.81 (t, J = 5.6 Hz, 1H), 4.86 – 4.67 (m, 2H), 4.67 – 4.52 (m, 4H), 4.43 (td, J = 10.6, 9.7, 4.7 Hz, 3H), 4.27 (ddd, J = 19.3, 8.5, 4.8 Hz, 2H), 4.10 (q, J = 5.3 Hz, 1H), 3.74 (s, 5H), 3.43 (tt, J = 5.3, 2.6 Hz, 6H), 3.37 (t, J = 5.9 Hz, 3H), 3.32 – 3.21 (m, 7H), 3.03 – 2.95 (m, 2H), 2.87 (dt, J = 13.0, 6.6 Hz, 5H), 2.10 – 2.02 (m, 3H), 1.99 (s, 3H), 1.71 (s, 2H), 1.60 – 1.22 (m, 10H), 1.17 (t, J = 7.1 Hz, 4H), 0.90 – 0.79 (m, 2H).

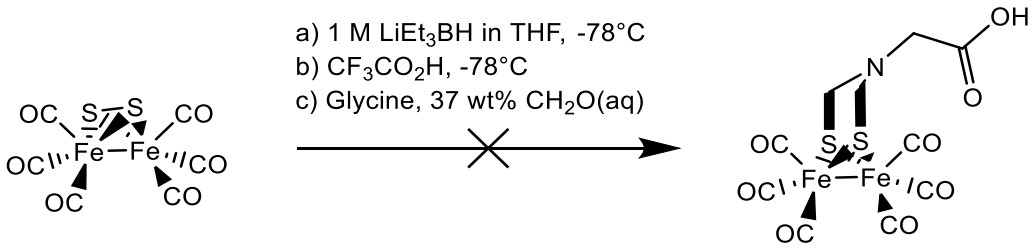

Scheme 29: Synthesis of (μ-glycineazadithiolato)diiron(I) hexacarbonyl

Procedure for Synthesis of (μ-glycineazadithiolato)diiron(I) hexacarbonyl

A 50 ml schlenk flask equipped with a stir bar was charged with glycine (0.0849 g, 1.131 mmol), 37% formaldehyde solution (868 μL, 10.7 mmol) and water (5 ml). The vessel was purged with nitrogen. The solution was heated to 60°C for 1 hour with stirring then allowed to cool to room temperature.

A separate 50 ml schlenk flask equipped with a stir bar was charged with dithiolatodiiron(I) hexacarbonyl (0.3988g, 1.160 mmol) and tetrahydrofuran (10 ml), chilled to -78°C, and degassed by bubbling nitrogen. 1 M lithium triethylborohydride in THF (2.6 ml, 2.6 mmol) was added dropwise then allowed to stir for 15 minutes to yield a dark green solution. Trifluoroacetic acid (0.37 ml, 4.83 mmol) was added dropwise then allowed to stir for 15 minutes to yield a dark red solution. The solution was then allowed to warm to room temperature. The glycine solution was transferred and allowed to stir for 16 hours. The solution was filtered with celite to yield dark red solution. The celite was washed with 10:1 Dichloromethane: Acetone (3x100 ml) to recover red crystals which formed during filtration. Solution concentrated under reduced pressure then purified with column chromatography 10:1 Dichloromethane: Acetone to yield two fractions. Fraction 1 dense red came off quickly while fraction 2 which was bright orange became stuck in the column once separated from fraction 1 and needed to be washed off the column with 100% acetone. Both fractions were concentrated to yield fraction 1 as a dark red oil (0.1320 g) and fraction 2 as an orange oil (0.312 g). It was noticed that fraction 2 crystallized in chloroform-D during NMR. Attempted recrystallization of fraction 2 in chloroform to yield orange crystals (0.0142 g). (ATR-IR figure A106)

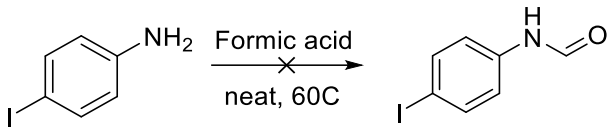

Scheme 30: Synthesis of N-(4-iodophenyl)-formamide route 1

Procedure for synthesis of N-(4-iodophenyl)-formamide route 1

A 16x100 mm test tube equipped with a stir bar was charged with 4-iodoaniline (0.4411 g, 2.0140 mmol) and formic acid (105 µL, 2.78 mmol). The mixture was stirred for 3 hours at 60 °C and was then dissolved in dichloromethane (20 mL) resulting in a red solution. The red solution was washed with saturated sodium bicarbonate solution (2 x 10 mL) and dried over sodium sulfate. The organic solution was concentrated under reduced pressure and isolation of N-(4-iodophenyl)-formamide was attempted via column chromatography with silica substrate and 50:50 ethyl acetate/ hexanes eluent. Purification lead to isolation of 4-iodoaniline starting material only.

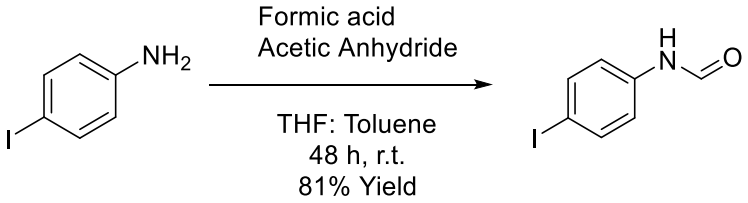

Scheme 31: Synthesis of N-(4-iodophenyl)-formamide route 2

Synthesis of N-(4-iodophenyl)-formamide route 2

A 5 mL round bottom flask equipped with a magnetic stir bar was charged acetic anhydride (978 µL, 9.77 mmol) and formic acid (590 µL, 15.6 mmol). The mixture was degassed by bubbling nitrogen and allowed to stir for 30 minutes.

A 100 mL round bottom flask equipped with a magnetic stir bar was charged with 4-iodoaniline (2.0058g, 9.1581 mmol), tetrahydrofuran (6.6 mL), and toluene (6.6 mL). The flask was purged with nitrogen and cooled to 0°C with stirring. To the 100 mL round bottom flask, the acetic anhydride and formic acid solution was added dropwise. The solution was then allowed to stir for 48 hours at room temperature. The solution was then diluted with ethyl acetate (14 mL)

and water (20 mL) resulting in a purple organic phase. The organic layer was separated and washed with water (2 x 14 mL) followed by saturated sodium bicarbonate solution (14 mL). The organic layer was then dried with sodium sulfate and concentrated under reduced pressure. The resulting off-white solids were further dried under vacuum to yield N-(4-iodophenyl)-formamide (1.838 g, 7.440 mmol, 81.2% yield). ^{1}H NMR (400 MHz, DMSO-d_6) Mixture of rotamers δ 10.29 (s, 1H), 8.29 (d, J = 1.9 Hz, 1H), 7.69 – 7.57 (m, 2H), 7.47 – 7.37 (m, 2H). ^{13}C NMR (101 MHz, DMSO-d6) Mixture of rotamers δ 168.49, 162.43, 159.79, 139.15, 138.31, 138.03, 137.94, 137.52, 137.31, 121.33, 121.15, 119.59, 87.15, 24.07. (^{1}H NMR figure A21, ^{13}C NMR figure A58, ATR-IF figure A99)

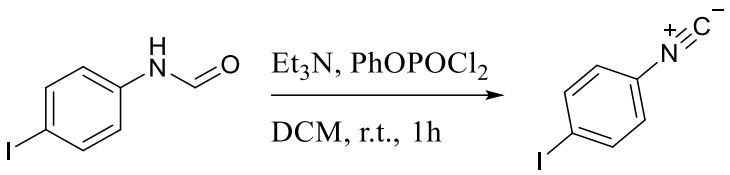

Scheme 32: Synthesis of 4-iodophenyl isocyanide

Synthesis of 4-iodophenyl isocyanide, $C{\equiv}NC_6H_4I$

A 50 mL round bottom flask equipped with a stir bar was charged with N-(4-iodophenyl)-formamide (1.2358 g, 5.0024 mmol), dichloromethane (5 mL) and triethylamine (5 mL). The solution was stirred for 10 minutes then phenyl dichlorophosphate (2 x 747 µL, 10.0 mmol) was added slowly, generating a white slurry. Dichloromethane (5 mL) was added and the mixture was stirred for 2 hours to generate a dark orange solution. The orange solution was diluted with brine (200 mL) and was extracted with ethyl acetate (3 x 200 mL). The organic layer was washed with brine (200 mL) followed by 1 M hydrogen chloride solution (200 mL) then saturated sodium bicarbonate solution (200 mL). The organic layer was dried over sodium sulfate and concentrated under reduced pressure. The product was isolated via column chromatography with silica substrate and 50:50 ethyl acetate/hexanes eluent. The first fraction was concentrated to yield 4-iodophenyl

isocyanide as yellow solids (0.8211 g, 3.570 mmol, 71.36% Yield). ^{1}H NMR (400 MHz, cdcl3) δ 7.77 – 7.70 (m, 2H), 7.15 – 7.08 (m, 2H). ATR-IR ν_{CN} = 2126 cm^{-1}. (^{1}H NMR figure A22, ATR-IR figure A100)

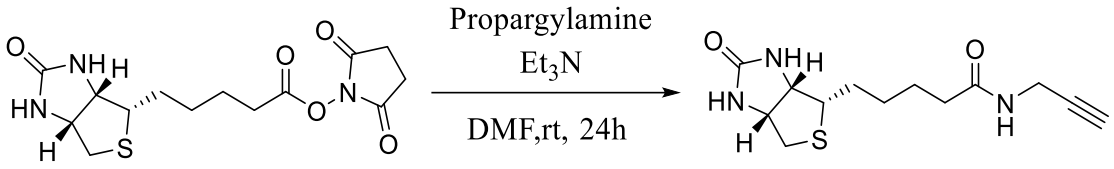

Scheme 33: Synthesis of biotinylated-propargylamine

Synthesis of biotinylated-propargylamine

A 25 mL round bottom flask equipped with a stir bar was charged with biotin-NHS-ester (0.2012 g, 0.5894 mmol), N,N-Dimethylformamide (10 mL), propargylamine (41.8 µL, 0.653 mmol), and triethylamine (208 µL, mmol). The solution was stirred for 24 hours at room temperature. The solution was concentrated under reduced pressure and the resulting solids were triturated against diethyl ether. The slurry was vacuum filtered to yield biotinylated-propargylamine as light orange solids (0.1637 g, 0.5185 mmol*, 87% yield*). *Molar quantity and yield adjusted for 11% water content found in NMR. ^{1}H NMR (400 MHz, DMSO-d$_6$) δ 8.23 (s, 1H), 6.43 (s, 1H), 6.37 (s, 1H), 4.30 (t, J = 6.1 Hz, 1H), 4.12 (t, J = 6.0 Hz, 1H), 3.86 – 3.79 (m, 2H), 3.09 (d, J = 7.9 Hz, 2H), 2.91 – 2.71 (m, 1H), 2.57 (d, J = 13.2 Hz, 2H), 2.07 (t, J = 7.5 Hz, 2H), 1.70 – 0.92 (m, 7H). ^{13}C NMR (101 MHz, DMSO-d$_6$) δ 171.83, 162.74, 81.38, 72.83, 61.05, 59.20, 55.41, 39.88, 34.87, 28.20, 28.03, 27.73, 25.24, 25.14. (^{1}H NMR figure A23-24, ^{13}C NMR figure A59)

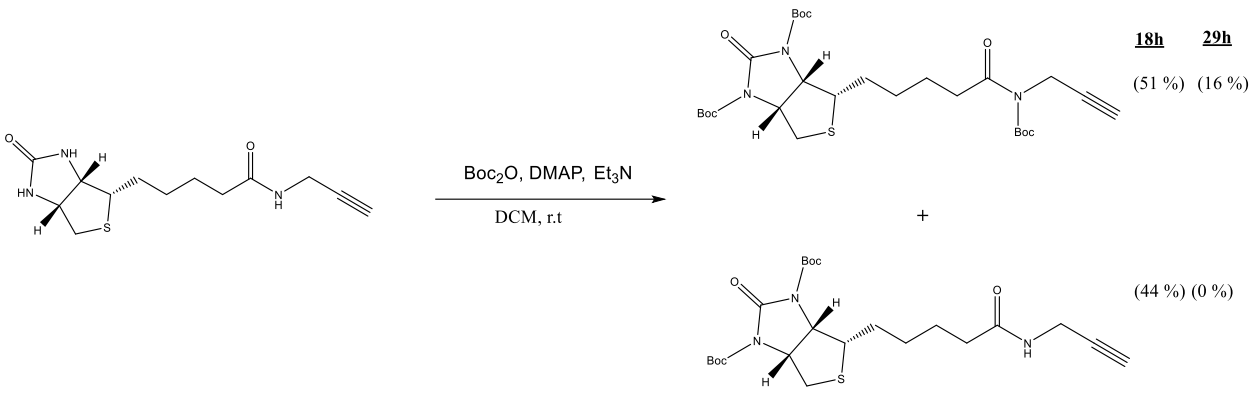

Scheme 34: Synthesis of Boc-biotinylated propargylamine

Synthesis of Boc-biotinylated propargylamine

A 50 mL round bottom flask equipped with a magnetic stir rod was charged with biotinylated-propargylamine (0.1056 g, 0.3753 mmol), dichloromethane (10 mL), di-tert-butyl dicarbonate (0.4645 g, 2.1283 mmol), 4-dimethylaminopyridine (0.1377 g, 1.1271 mmol), and triethylamine (148 μL, 1.06 mmol). The mixture was sparged with nitrogen and was stirred for 18 hours. The solution was diluted with ethyl acetate (100 mL) then washed with a 2% Acetic acid solution (100 mL). The organic phase was dried over sodium sulfate and concentrated under reduced pressure. The products were separated via column chromatography with silica substrate and a gradient of 25:75 to 60:40 ethyl acetate/ hexanes eluent. Fraction 1 was concentrated to yield the tri-protected Boc-biotinylated propargylamine (0.1124 g, 0.1932 mmol, 51.48 % yield). ^{1}H NMR (400 MHz, $CDCl_3$) δ 4.62 – 4.47 (m, 2H), 4.43 (d, J = 2.5 Hz, 2H), 3.46 (ddd, J = 12.1, 6.0, 3.3 Hz, 1H), 3.26 (dd, J = 12.8, 6.6 Hz, 1H), 2.90 – 2.79 (m, 4H), 2.72 (s, 3H), 2.15 – 2.00 (m, 5H), 1.70 – 1.54 (m, 4H), 1.53 (s, 9H), 1.52 (s, 9H), 1.51 (s, 9H), 1.42 (d, J = 0.6 Hz, 1H), 1.35 – 1.32 (m, 1H), 1.30 – 1.19 (m, 2H). (^{1}H NMR figure). Fraction 2 was concentrated to yield the di-protected Boc-biotinylated propargylamine (0.0795 g, 0.1651 mmol, 43.98 % yield). ^{1}H NMR (400 MHz, $CDCl_3$) δ 5.84 (d, J = 6.6 Hz, 1H), 4.64 – 4.48 (m, 2H), 4.03 (dd, J = 5.3, 2.6 Hz, 2H), 3.46 (ddd, J = 12.0, 6.0, 3.4 Hz, 1H), 3.31 – 3.24 (m, 1H), 2.90 – 2.79 (m, 1H), 2.26 – 2.10 (m,

3H), 2.07 (s, 1H), 2.03 (s, 1H), 1.73 – 1.55 (m, 3H), 1.52 (s, 9H), 1.52 (s, 9H), 1.50 – 1.42 (m, 1H), 1.40 – 1.30 (m, 1H), 1.30 – 1.22 (m, 2H). (^{1}H NMR figure A25)

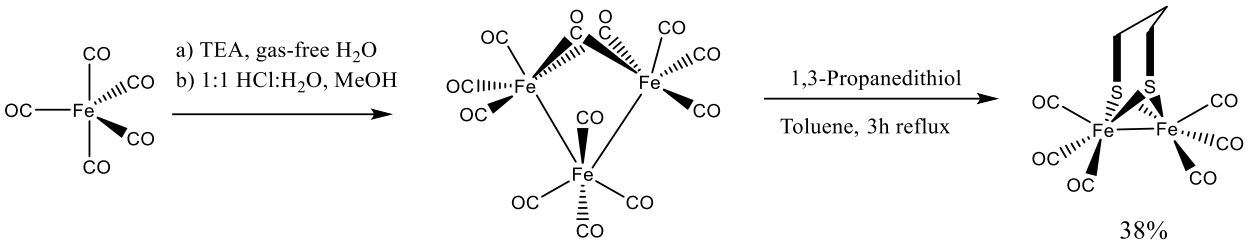

Scheme 35:Synthesis of (μ-propanedithiolato)diiron(I) hexacarbonyl

Synthesis of (μ-propanedithiolato)diiron(I) hexacarbonyl, $Fe_2[(SCH_2)_2CH_2](CO)_6$

A 50 mL three neck flask equipped with a magnetic stir bar and a condenser was charged was charged with water (20 mL) and was sparged by bubbling nitrogen. Iron-pentacarbonyl (9.2 mL, 68 mmol) was added followed by the dropwise addition of triethylamine (6.8 mL, 48 mmol). While stirring the solution was heated to 80°C for 18 hours. After cooling, the mixture was vacuum filtered, and the solids were washed with water. The solids were transferred to a new 250 mL three neck flask equipped with a magnetic stir bar and a condenser and dissolved in methanol (50 mL). To the solution 6 M hydrochloric acid (60 mL) was very slowly added with stirring. After evolution of gas subsided the solution was refluxed for 3 hours resulting in a clear solution with green solids. The solution was gravity filtered under a nitrogen blanket, and the solids were washed with water then methanol yielding green solids (4.522 g). Without further drying, the solids were transferred to a 500 mL schlenck flask equipped with a magnetic stir bar and were dissolved in dry degassed toluene (64 mL). The flask was purged with nitrogen then 1,3-propanedithiol (1 mL, 10 mmol) was added to the solution. The flask was then equipped with a condenser while maintaining nitrogen flow and the solution was refluxed for 3 hours. Solution was then concentrated under reduced pressure. The product was isolated via column chromatography with silica substrate and hexanes eluent. The first fraction was concentrated and dried under vacuum to yield (μ-

propanedithiolato)diiron hexacarbonyl as red solids (3.2947 g, 8.5366 mmol, 38% yield). ^{1}H NMR (500 MHz, $CDCl_3$) δ 2.14 (s, 4H), 1.80 (s, 2H). ATR-IR ν_{CO} = 2069, 2025, 1983, 1943 cm^{-1}. (^{1}H NMR figure A27, ATR-IR figure A97)

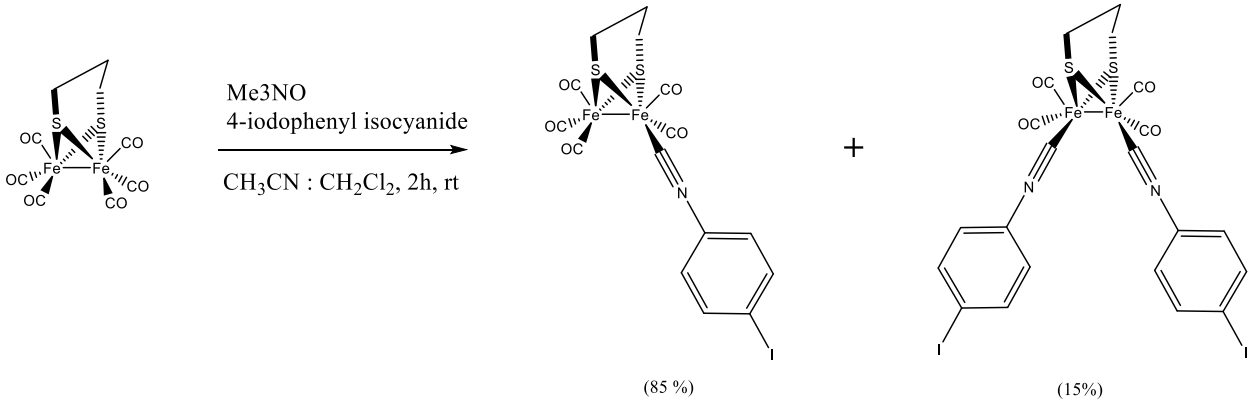

Scheme 36: Synthesis of (μ-propanedithiolato)diiron 4-iodopheynylisocyano pentacarbonyl

Synthesis of (μ-propanedithiolato)diiron 4-iodopheynylisocyano pentacarbonyl, $Fe_2[(SCH_2)_2CH_2](C{\equiv}NC_6H_4I)(CO)_5$

A 50 mL round bottom flask equipped with a stir bar was charged with (μ-propanedithiolato)diiron(I) hexacarbonyl (0.2009 g, 0.5205 mmol), 4-iodophenyl isocyanide (0.1348 g, 0.5860 mmol) and dichloromethane (8 mL). The mixture was stirred for 20 minutes and sparged with nitrogen, then trimethylamine-N-oxide (0.0466 g, 0.6204 mmol) dissolved in acetonitrile (5 mL) was added dropwise. After 30 minutes of stirring the solution was concentrated under reduced pressure. The product was isolated via silica column chromatography with 95:5 hexanes/ethyl acetate eluent. Two orange fractions were isolated. Solvent was evaporated in vacuo from the samples to yield (μ-propanedithiolato)diiron 4-iodopheynylisocyano pentacarbonyl as dark red solids (0.2495 g, 0.4215 mmol*, 84% yield*, $R_{f,\ hexanes}$= 0.27) ^{1}H NMR (400 MHz, cdcl3) δ 7.70 (d, J = 8.3 Hz, 2H), 7.03 (d, J = 8.3 Hz, 2H), 2.22 – 2.10 (m, 2H), 2.09 – 1.98 (m, 2H), 1.89 – 1.69 (m, 2H). ATR-IR ν_{CN} = 2115 cm^{-1}. ATR-IR ν_{CO} = 2032, 1958, 1986, 1974, 1937, 1916 cm^{-1}. (^{1}H NMR figure A28, ATR-IR figure A101) and (μ-propanedithiolato)diiron di(4-iodopheynylisocyano) tetracarbonyl (0.0614 g, 0.0717 mmol*, 13.8% yield*, $R_{f,\ hexanes}$= 0.13).

*Molar quantity and % yield adjusted for ethyl acetate and water impurities found in NMR. ^{1}H NMR (400 MHz, $CDCl_3$) δ 7.83 – 7.43 (m, 4H), 7.18 – 6.70 (m, 4H), 2.24 – 1.92 (m, 4H), 1.78 (s, 2H). ATR-IR ν_{CN} = 2118, 2089 cm^{-1}. ATR-IR ν_{CO} = 2036, 1991, 1967, 1930 cm^{-1}. (^{1}H NMR figure A29, ATR-IR figure A102)

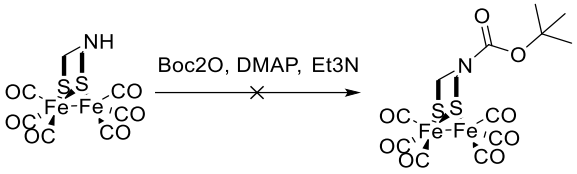

Scheme 37: Synthesis of Boc protection of (μ-azadithiolato)diiron(I) hexacarbonyl

Procedure for the Boc protection of (μ-azadithiolato)diiron(I) hexacarbonyl,

A 50 mL schlenk flask equipped with a magnetic stir bar was charged with (μ-azadithiolato)diiron(I) hexacarbonyl (0.1911 g, mmol), tetrahydrofuran (20 mL), di-tert-butyl dicarbonate (0.2180 g, mmol), and 4-dimethylaminopyridine (0.0702 g, mmol). The solution was sparged with nitrogen then cooled to 0°C. To the solution, triethylamine (76 μL, mmol) was added and the solution was stirred for 18 hours at room temperature. The reaction progress was monitored by thin layer chromatography (95:5 hexanes/ ethyl acetate). The solution was concentrated under reduced pressure resulting in a brown residue. The brown residue was dissolved in ethyl acetate (100 mL) and washed with water (2 x 150 mL). The organic layer was dried over sodium sulfate and concentrated under reduced pressure resulting in brown residue (0.0751 g). NMR of brown was paramagnetic without evidence of tert-butyl protons. No evidence of product formation by TLC.

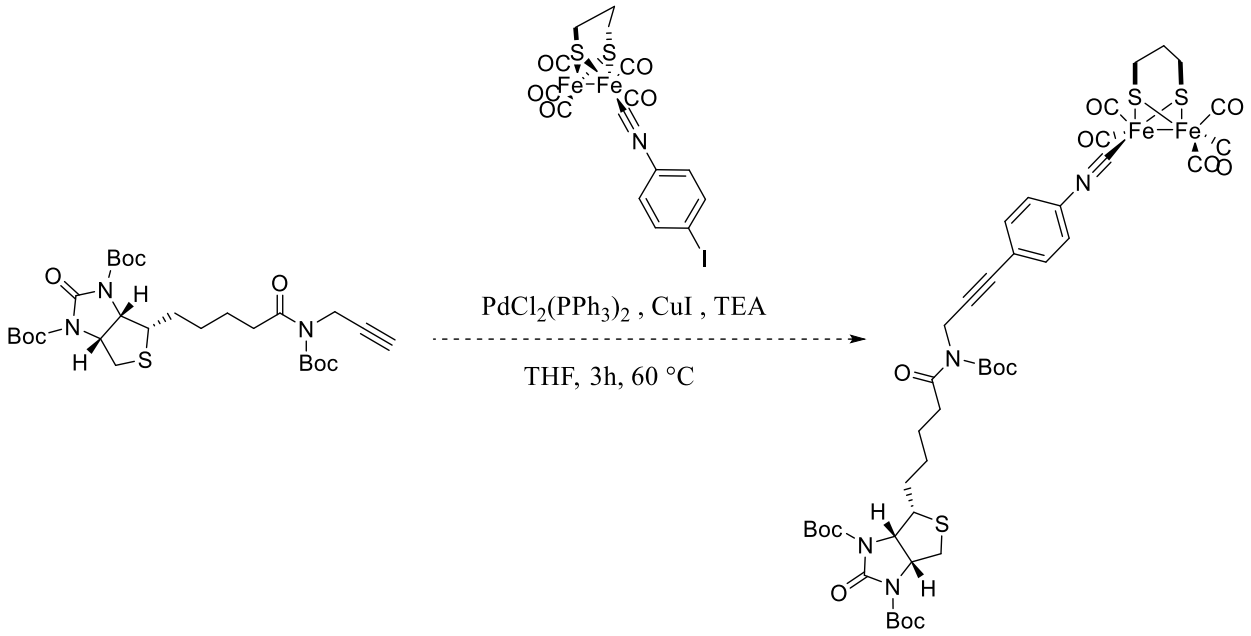

Scheme 38: Sonogashira coupling of Boc protected biotinylated propargylamine and

Procedure for Sonogashira coupling of Boc protected biotinylated propargylamine and (μ-propanedithiolato)diiron 4-iodopheynylisocyano pentacarbonyl

A 100 mL round bottom flask equipped with a magnetic stir bar was charged with Boc-protected biotinylated-propargylamine (0.0731 g, 0.125 mmol), (μ-propanedithiolato)diiron 4-iodopheynylisocyano pentacarbonyl (0.0739 g, 0.125 mmol), tetrahydrofuran (7.5 mL), and triethylamine (2 mL). The round bottom flask was equipped with a condenser and the solution was sparged with nitrogen for 20 minutes with stirring. Bis(triphenylphosphine)palladium chloride (17 mg, mmol) and copper iodide (9 mg, mmol) were added to the solution while maintaining a nitrogen blanket. The solution was stirred at 60 °C for 3 hours. The solution was concentrated under reduced pressure and the resulting oil was dissolved in ethyl acetate resulting in a red solution and an insoluble brown residue (0.0702 g). Silica column chromatography (70:30 Hexanes/ ethyl acetate) of the red solution resulted in 4 fractions. Fraction 1- unreacted (μ-propanedithiolato)diiron 4-iodopheynylisocyano pentacarbonyl. Fraction 4 (0.0089 g) : ^{1}H NMR (400 MHz, cdcl3) δ 8.15 (s, 2H), 7.79 – 7.33 (m, 6H), 4.61 (d, J = 39.9 Hz, 2H), 3.38 (d, J = 80.3 Hz, 1H), 2.91 (s, 6H), 2.17 (s, 4H), 1.79 (s, 6H), 0.87 (s, 5H).

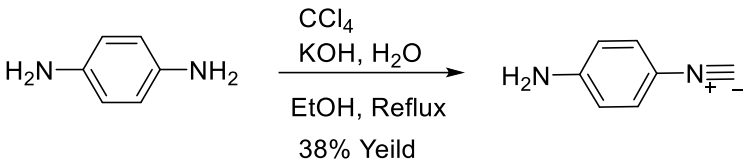

Scheme 39: synthesis of 4-Aminophenylisocyanide

Synthesis of 4-Aminophenylisocyanide, $C{\equiv}NC_6H_4NH_2$

A 500 mL round bottom flask equipped with a magnetic stir bar was charged with 1,4-diaminobenzene (4.03 g, 37.3 mmol), ethanol (16 mL), and chloroform (54 mL) and allowed to stir. In a separate flask potassium hydroxide (26.617 g, 474.41 mmol) was dissolved in water (110 mL) and allowed to cool. The Potassium hydroxide solution was slowly added to the reaction mixture then heated to reflux for 2.5 hours. Once cooled, the resulting layers were separated, and the aqueous layer was extracted with dichloromethane (3 x 75 mL). The organic layers were combined and washed with equal portions of water then dried over magnesium sulfate. The solution was filtered and concentrated under reduced pressure to yield a red oil. The red oil was purified via Alumina column chromatography (diethyl ether eluent) to yield four fractions. The fractions were concentrated to yield fraction 1 (0.1843 g) as white solids, 4-Aminophenylisocyanide from fraction 2 (1.6538, 13.999 mmol, 37.6% yield) as orange solids, fraction 3 (0.1388 g) as a yellow/brown oil, and fraction 4 (0.130 g) as a yellow/orange oil. ^{1}H NMR (400 MHz, $CDCl_3$) δ 7.13 (d, 2H), 6.62 – 6.52 (m, 2H), 3.95 (s, 2H). ATR-IR ν_{CN} = 2128 cm^{-1}. (^{1}H NMR figure A30, ATR-IR figure A103)

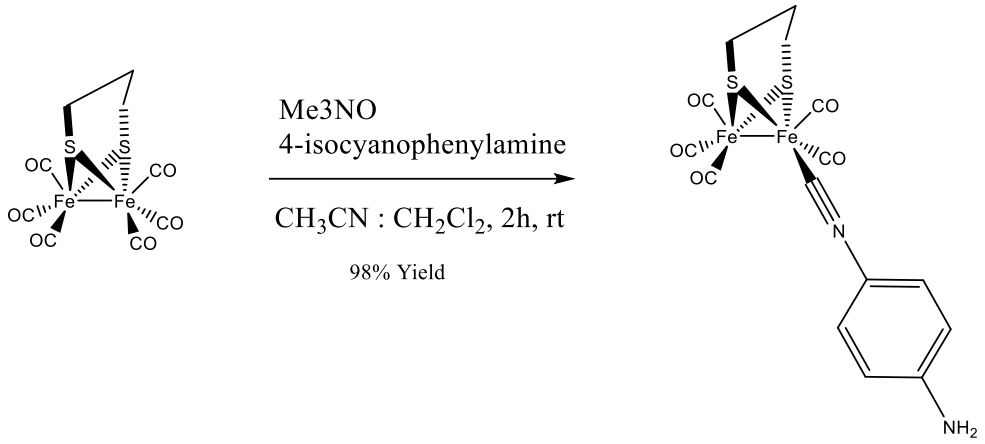

Scheme 40: Synthesis of (μ-propanedithiolato)diiron 4-aminopheynylisocyano pentacarbonyl

Synthesis of (μ-propanedithiolato)diiron 4-aminopheynylisocyano pentacarbonyl, $Fe_2[(SCH_2)_2CH_2](C{\equiv}NC_6H_4NH_2)(CO)_5$

A 50 mL round bottom flask equipped with a magnetic stir bar was charged with (μ-propanedithiolato)diiron(I) hexacarbonyl (0.1682 g, 0.436 mmol), 4-aminophenylisocyanide (0.0588 g, 0.498 mmol), and dichloromethane (6.5 mL). The solution was stirred and degassed by bubbling N_2. A premixed solution of trimethylamine-N-oxide (0.0369 g, 0.4913 mmol) in acetonitrile (5 mL) was added to the reaction mixture dropwise to yield a deep red solution. The solution was stirred for 2 hours then concentrated under reduced pressure. The concentrate was purified via silica column chromatography (1:1 ethyl acetate/hexanes eluent) to yield 5 fractions. The second fraction was concentrated under reduced pressure to yield (μ-propanedithiolato)diiron 4-aminopheynylisocyano pentacarbonyl as a red oil (0.2034 g, 0.3688 mmol*, 84.59% yield*) *Molar quantity and yield adjusted for ethyl acetate and water impurities found in NMR. ^{1}H NMR (400 MHz, cdcl3) δ 7.09 (d, J = 8.2 Hz, 2H), 6.57 (d, J = 8.0 Hz, 2H), 3.88 (s, 2H), 2.15 (s, 2H), 2.02 (d, J = 12.7 Hz, 2H), 1.77 (d, J = 25.9 Hz, 2H). ATR-IR ν_{CN} = 2132 cm^{-1}. ATR-IR ν_{CO} = 2033, 1979, 1970, 1974, 1950, 1921, 1898 cm^{-1}. (^{1}H NMR figure A31, ATR-IR figure A104)

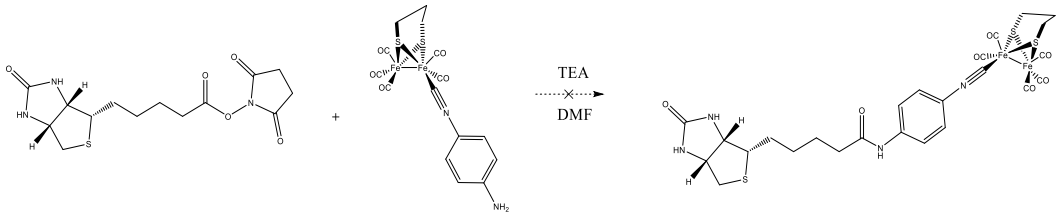

Scheme 41: coupling of biotin-NHS-ester and (μ-propanedithiolato)diiron 4-aminopheynlisocyano pentacarbonyl

Procedure for the coupling of biotin-NHS-ester and (μ-propanedithiolato)diiron 4-aminopheynlisocyano pentacarbonyl

A 25 mL round bottom flask equipped with a magnetic stir bar was charged with (μ-propanedithiolato)diiron 4-aminopheynlisocyano pentacarbonyl (0.1002 g, 0.2105 mmol) and N,N-dimethylformamide (10 mL). The solution was sparged with N_2 then biotin-NHS-ester (0.0703 g, 0.2059 mmol) and triethylamine (28 μL) were added to the mixture under a nitrogen blanket. The solution was stirred for 18 hours then concentrated under high vac. The resulting solids were triturated with diethyl ether then vacuum filtered to yield biotin-NHS-ester (0.0520 g) as tan solids and the presence of (μ-propanedithiolato)diiron 4-aminopheynlisocyano pentacarbonyl in the red filtrate solution was confirmed by thin layer chromatography (1:1 ethyl acetate/ hexanes). Dissolving the tan solids in DMSO-d6 for NMR resulted in the evolution of gas and the formation of a black precipitate. IR of the precipitate showed no carbonyl stretching signatures.

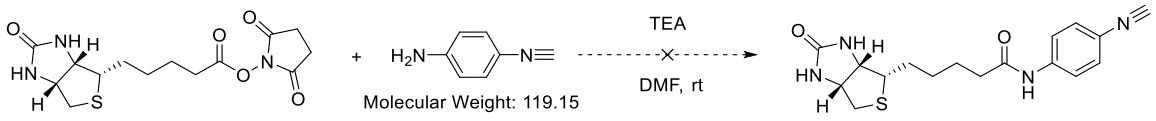

Scheme 42: Amide coupling of biotin-NHS-ester and 4-aminopheynlisocyanide

Procedure for the coupling of biotin-NHS-ester and 4-aminopheynlisocyanide

A 50 mL round bottom flask equipped with a magnetic stir bar was charged with biotin-NHS-ester (0.1014 g, 0.2970 mmol), 4-aminophenylisocyanide (0.0404 g, 0.3391 mmol) and N,N-

dimethylformamide (20 mL). Triethylamine (50 µL, 0.36 mmol) was added and the solution was stirred for 18 hours at room temp resulting in a clear orange solution. The solution was concentrated under high vac and the resulting solids were triturated with diethyl ether to yield biotin-NHS-ester as tan solids (0.0891 g) and 4-aminophenylisocyanide in diethyl ether solution.

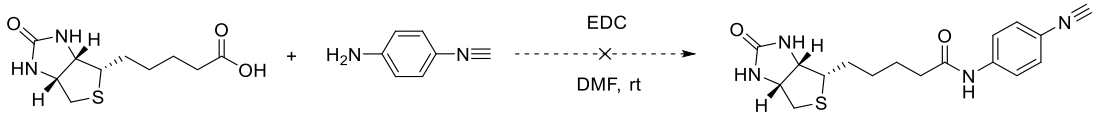

Scheme 43:EDC coupling of biotin and 4-aminopheynlisocyanide

Procedure for the EDC coupling of biotin and 4-aminopheynlisocyanide

A 50 mL round bottom flask equipped with a stir bar was charged with biotin (0.1022 g, 0.4183 mmol), 4-aminophenylisocyanide (0.1063 g, mmol), N-(3-Dimethylaminopropyl)-N′-ethylcarbodiimide hydrochloride (0.1081 g, mmol) and N,N-dimethylformamide (10 mL) . The solution was stirred for 48 hours then concentrated under reduced pressure. The resulting solids were triturated with methanol then diethyl ether. Methanol and Diethyl ether filtrates from trituration were combined and concentrated under reduced pressure. Desired product was not found in either fraction via NMR or IR.

Chapter III. Secondary Sphere Interactions Studied within Porphyrin-Cored Nanoparticles

Introduction

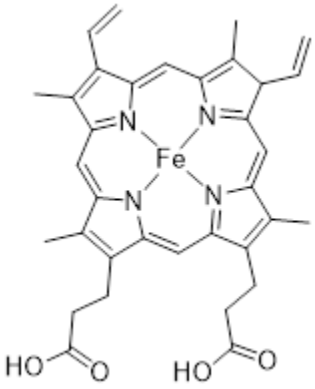

Figure 16: Structure of iron protoporphyrin IX (Heme)

In nature, iron protoporphyrin IX cofactors (Figure 18) within heme enzymes allow for a wide variety of functions including oxygen transfer (myoglobin, hemoglobin), electron transfer (cytochrome c, cytochrome b_5), catalysis (peroxidase and cytochrome P450), and signaling (CooA).[148–150] While the function of heme enzymes are often governed by the axial ligands of the iron porphyrin cofactor,[149] non-covalent secondary coordination sphere interactions play a significant role in the activity of these metalloenzymes.[151] In myoglobin (Figure 19) and hemoglobin, secondary coordination sphere interactions of the distal amino acid residues enhance the reversible binding of O_2 while lowering CO affinity.[152–154] In cytochrome P450 (figure 19), the proton shuttling channel of the I-helix leads the localization of water molecules adjacent to the heme active site which are theorized to stabilize oxidation intermediates through secondary coordination sphere interactions.[155–158] As subtle changes in the cofactor's local environments can alter the overall reactivity of the enzyme it is of particular interest to researchers to further study the secondary coordination sphere interactions responsible for heme enzyme functionality.

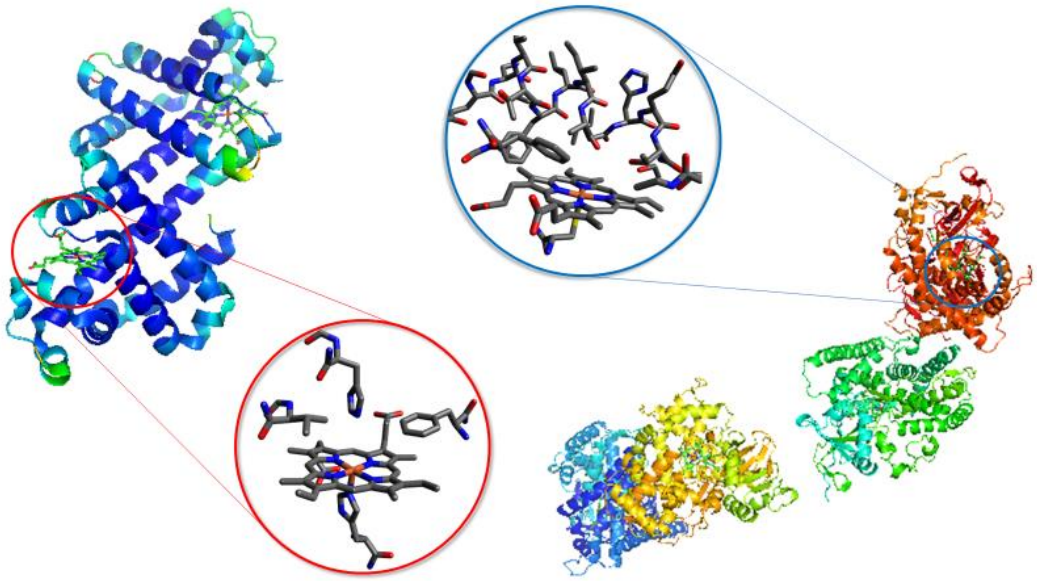

Figure 17: Protein structures of horse myoglobin dimer PDB 3VM9 (left)[159] *and cytochrome p450BM-3 tetramer PDB 1FAG (right)*[160] *With myoglobin binding site (left inset) and cytochrome p450BM-3 active site (right inset). Protein structures plotted with PyMol*[29] *and structure insets plotted with Avogadro*[99].

The stabilization of dioxygen coordination in hemoglobin through a secondary coordination sphere interaction via hydrogen bonding of a distal histidine was first suggested by the Pauling in 1964.[161] Early attempts to synthesize dioxygen bound iron porphyrin were met with some success,[162–167] but the isolation of a dioxygen bound model complex was not reported until 1975, with the synthesis of meso-tetra(α,α,α',α-o-pivalamidophenyl)porphyrin, "Picket fence" porphyrin, by Collman and coworkers (Figure 20).[168] The steric bulk of the pivalamide groups of the picket fence porphyrins generate a non-protic cavity allowing for the preferential binding of a bulky imidazole to the unhindered side of the porphyrin while reversibly binding O_2 in the cavity. X-ray crystallography of the picket fence porphyrin showed the N-H groups of pivalamide facing inward toward dioxygen but the distance to the terminal oxygen was too great to allow for hydrogen bonding.[168]

In 1981, Phillips and Schoenborn reported the resolution of an oxygen histidine hydrogen bond in oxymyoglobin through neutron diffraction. In the study, oxymyoglobin from sperm-whale skeletal muscle were deuterated and submitted to a neutron team for 21 days at -5°C. The resulting in the elucidation of an oxygen-deuterium hydrogen bond length of 1.98 Å between the iron bound dioxygen and the distal histidine indicating a medium secondary coordination sphere interaction, similar bonding was not observed when carbon monoxide was bound.

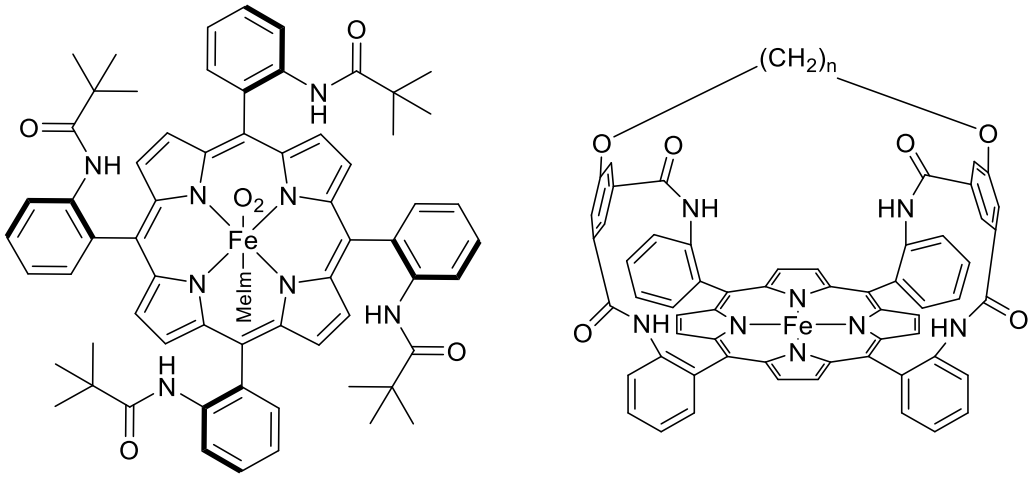

Figure 18: Collman and coworkers "Picket fence" porphyrin (left)[168] *and "Picnic Basket" porphyrin (right)*[169]

Further work by Collman and coworkers in 1994, sought to elucidate the role of H-bond and dipole-dipole interactions in the heme enzymes through the binding of O_2 to "Picnic Basket" porphyrins of varying cavity size (Figure 20). Collman and coworkers were able to indicate a dipole-dipole interaction between the amide protons and the bound O_2 by an increase in O_2 affinity as "Picnic Basket" cavity size decreased.[169] While the "picket fence" and "Picnic Basket" porphyrins allowed for the study of secondary coordination sphere interactions, the proximity of the amide protons did not allow for H-bonding nor did their designs fully replicate the enveloping macromolecular environment found in the native proteins.

While macromolecular heme-peptide models and site-directed mutagenesis have been previously been studied, their synthesis are complex and challenging.[154,170,171] An alternative method to incorporate porphyrin into a macromolecular environment is the inclusion of porphyrin into a polymer scaffold. Porphyrin has previously been incorporated into several polymeric systems.[172,173] Of particular interest to this study is Rodriguez and coworkers' design and synthesis of a series of tetra functionalized iron porphyrin cored star polymers (PCSP) capable of post polymerization modification to form nanoparticles which were shown to have similar redox and ligand binding to that of native systems.[61,174] While the polymer scaffold of the porphyrin cored polymeric nanoparticles (PCPN) were shown to protect the iron-porphyrin core from dimerization there was little evidence of secondary coordination sphere interactions.

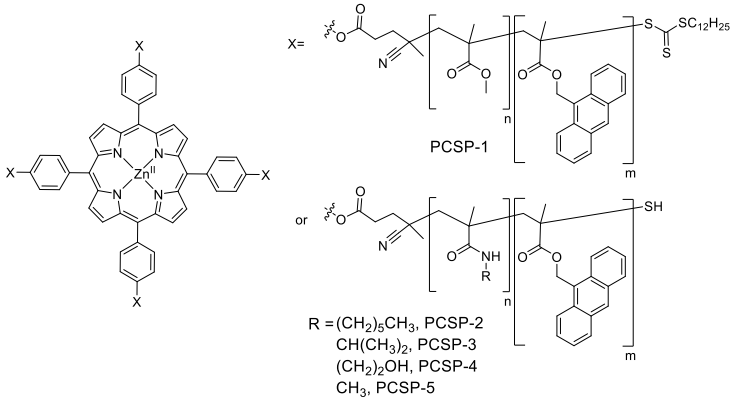

Figure 19: Suite of zinc porphyrin cored star polymers of varying degrees of possible hydrogen bonding character and steric hindrance for probing secondary sphere interactions

In the present study a series of porphyrin cored star polymers and polymeric nanoparticles of varying degrees of potential hydrogen bonding character, including Zn^{II}(Por(MMA-co-AMMA)$_4$) {PCSP-1 : PCPN-1}, Zn^{II}(Por(HexMAAm-co-AMMA)$_4$) {PCSP-2 : PCPN-2}, Zn^{II}(Por(iPMAAm-co-AMMA)$_4$) {PCSP-3 : PCPN-3}, Zn^{II}(Por(HEMA-co-AMMA)$_4$) {PCSP-4 : PCPN-4}, and Zn^{II}(Por(MMAAm-co-AMMA)$_4$) {PCSP-5 : PCPN-5} and were synthesized as abstractions of heme enzymes (figure 21). Originally the polymeric systems were designed such

that isotope labeled cyanide could be a molecular probe for secondary coordination sphere interactions using ^{15}N -NMR (figure 22).

Figure 20: Comparison of the possible secondary coordination sphere interactions generated by the polymer scaffolds.

The cyanide bound porphyrin cored polymers were found to have varying rates of reactivity with N,N-dimethylformamide which was to be used as the NMR solvent for the hydrogen bonding experiments. By monitoring the change in the absorbance spectra associated with the zinc porphyrin - cyanide adduct via UV-vis spectroscopy, sodium cyanide could still be used as a molecular probe to study the secondary coordination sphere interactions of the metallo-organic core within the polymeric scaffolds and elucidate newly discovered structure-function relationships of the porphyrin cored polymers.

Results and Discussion

In order to generate the polymeric scaffolds for probing secondary sphere interactions, Por(MMA-co-AMMA)$_4$ and Por(PFPMA-co-AMMA)$_4$ were synthesized by reversible addition−fragmentation chain transfer (RAFT) with 5,10,15,20-tetrakis(4-(4-cyano-4-

[(dodecylsulfanylthiocarbonyl)sulfanyl]-phenyl pentanoate)-21H,23H-porphine (PorCTA) as the chain transfer agent and Azobisisobutyronitrile (AIBN) as the radical initiator. The method of RAFT polymerization using a thiocarbonyl-thio chain transfer agent was chosen for this study as this method of polymerization allows for predictable molecular weights and narrow polydispersities.[175,176] 9-Anthracenylmethyl methacrylate was incorporated into the polymer scaffold to allow for nanoparticle formation through the photo induced dimerization of the anthracene units.[177] Methyl methacrylate was chosen to allow for a polymer scaffold which is capable of acting as a hydrogen bond acceptor only. Pentafluorophenyl methacrylate was incorporated as it has previously been shown to allow for post-polymerization modification through nucleophilic acyl substitution with amines leading to polymer scaffolds with possible hydrogen bond acceptors and donors.[174,178] All polymer species were characterized by absorption spectroscopy and ^{1}H NMR. Several Por(MMA-co-AMMA)$_4$ and Por(PFPMA-co-AMMA)$_4$ were synthesized for the purpose of a molecular weight calibration curve for DOSY NMR (Table 6). Unfortunately, deviations in % AMMA incorporation lead to large variations in diffusion constants indicating that use of DOSY for predicting molecular weight of the amide functionalized star polymers based on methyl methacrylate polymers would be impractical. Use of size exclusion chromatography (SEC) in conjunction with a polystyrene molecular weight calibration curves and the of dn/dc of PMMA (0.089) lead to large discrepancies between the SEC predicted molecular weights and NMR estimated molecular weights due to the incorporation of AMMA and the topology of the star polymers (example: $M_{n,SEC}$ = 2437 kDa vs $M_{n,NMR}$ = 37.3 kDa). Due to the discrepancies all polymer molecular weights were estimated using ^{1}H NMR and 100% conversion of the PFPMA species to the corresponding amide when relevant.

Table 6: Synthesized Por(MMA-co-AMMA)$_4$ and Por(PFPMA-co-AMMA)$_4$ porphyrin cored star polymers.

Por(Polymer) scaffold	PorCTA (µmol)	Monomer (mmol)	AMMA (mmol)	Yield (g)	M_n (kDa) (NMR)	%AMMA	$\bar{D}$ (cm^2/s) ($CDCl_3$)	$\bar{D}$ (cm^2/s) (DMF)
PorCTA	-	-	-	-	2.2	-	4.63e-6	-
MMA-co-AMMA	50.0	2.30	0.57	0.236	8.8	29.6	3.02e-6	-
MMA-co-AMMA	25.0	1.15	0.29	0.101	11.4	15.1	2.42e-6	1.72e-6
MMA-co-AMMA	104	6.05	1.51	0.882	17.2	22.8	2.80e-6	1.76e-6
MMA-co-AMMA	25.0	2.63	0.66	0.229	17.6	36.9	2.63e-6	-
MMA-co-AMMA	12.5	1.31	0.33	0.073	19.1	16.8	2.11e-6	1.61e-6
MMA-co-AMMA	6.26	1.40	0.35	0.048	21.3	15.3	2.46e-6	2.02e-6
MMA-co-AMMA	16.7	2.74	0.68	0.239	25.5	33.8	2.34e-6	-
MMA-co-AMMA	83.3	13.7	3.42	1.836	36.3	23.6	1.92e-6	-
MMA-co-AMMA	12.5	2.79	0.70	0.108	36.9	57.8	2.15e-6	-
MMA-co-AMMA	80.1	13.5	3.37	1.024	37.3	31.2	-	-
MMA-co-AMMA	8.33	1.37	0.34	0.103	40.3	9.49	2.20e-6	2.11e-6
MMA-co-AMMA	6.26	1.40	0.35	0.060	593.6	7.18	2.82e-6	2.06e-6
MMA-co-AMMA	80.1	13.5	3.37	1.024	37.3	31.2	-	-
PFPMA-co-AMMA	208	12.0	3.01	4.186	33.2	14.6	2.34e-6	-
PFPMA-co-AMMA	80.1	7.10	1.77	1.515	69.0	15.1	-	-
PFPMA-co-AMMA	83.3	13.7	3.42	4.033	88.4	14.9	1.80e-6	-

The molecular weight of Por(MMA-co-AMMA)$_4$ for the ^{15}N-NMR cyanide binding study was chosen to match the molecular weight of horse myoglobin, 16.95 kDa.[179] Por(MMA-co-AMMA)$_4$ was obtained at M_n = 17.2 kDa with a 22.8% AMMA incorporation, 26.5 monomer units per arm on average based on ^{1}H NMR (Figure A36). Por(PFPMA-co-AMMA)$_4$ was obtained at 33.2 kDa with a 14.6% AMMA incorporation and 30.2 monomer units per arm on average based on ^{1}H NMR (Figure A37). Por(PFPMA-co-AMMA)$_4$ was formulated such that the AMMA incorporation and number of monomer units in each arm would be similar to those of the aforementioned Por(MMA-co-AMMA)$_4$ species.

Zinc was chosen as the coordinating metal for this study as Zinc Porphin is known to be diamagnetic allowing for NMR studies and Zinc Porphin systems have previously been shown to bind cyanide and amines.[180–182] Insertion of Zn^{II} into Por(MMA-co-AMMA)$_4$ and Por(PFPMA-

co-AMMA)$_4$ using Zinc Acetate was confirmed by the contact shift of the pyrrole ^{1}H-NMR signal (from 8.87 to 8.93 ppm, Figures A39 & A40) and the anticipated change in the Soret (418 to 426 nm), and α,β absorbance signatures (514, 549, 592, and 649 nm to 559 and 599 nm) (Figures A119 & A121,Table 7).

PCSP-2, PCSP-3, PCSP-4, PCSP-5 were synthesized by the post-polymerization modification of Zn^{II}(Por(PFPMA-co-AMMA)$_4$) through nucleophilic acyl substitution carried out in dimethyl sulfoxide (DMSO) using hexan-1-amine, propan-2-amine, 2-Aminoethan-1-ol, and methylamine respectively. Completion of nucleophilic acyl substitution was confirmed by the loss of pentafluorophenol via ^{19}F NMR (Figures A65 – A68) and the growth of the associated amide proton ^{1}H-NMR signals (Figures A41 - A45).

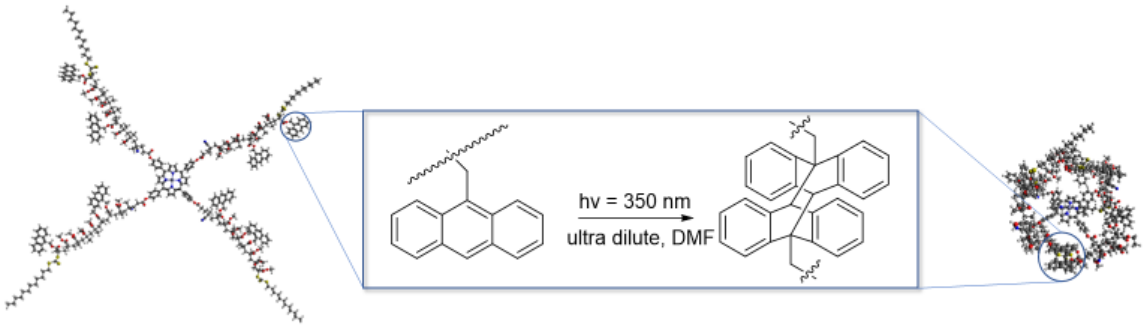

Figure 21: Collapse of polymeric scaffold via photo-induced [4+4] cycloaddition of anthracene to form polymeric nanoparticles. Polymer and Nanoparticles images built in Avogadro software.[99] *The nanoparticle image (right) was formed by manually making bonds between anthracene units of adjacent polymer arms. Geometries Optimized via universal force fields (UFF) in Avogadro.*

PCPN's were synthesized from the parent polymers by the dimerization of the anthracene units under dilute conditions in N,N-dimethylformamide (0.1 mg/mL) through a photoinduced [4π + 4π] cycloaddition (λ = 350 nm) (figure 23).[177] Collapse of the polymer species were monitored by the decrease in methyl anthracenyl UV-Vis absorption signature as well as through ^{1}H-NMR, gCOSY, and DOSY NMR. Two hours of UV exposure (λ = 350 nm) lead to a 52 ± 2 % conversion

of anthracene to the anthracene dimer in PCPN-1, 47 ± 3 % in PCPN-2, 40.8 ± 0.02 % in PCPN-3, and 70 ± 4 % in PCPN-4, calculated from the change in absorbance at 366.5 nm (Figures A127 – A132). Formation of the anthracene dimer indicating nanoparticle formation was confirmed by the change in coupled aromatic proton ^{1}H NMR chemical shifts ({8.34, 7.70}, {8.29, 8.00}, {8.19, 7.60} and {7.63, 7.40} to {8.38, 8.28}, {8.30, 8.00}, {8.23, 8.17} and {8.15, 8.06}, gCOSY NMR, 400 MHz, DMF-d_7, Figures A46 - A47).

Exposure of the polymer species to UV radiation over 2 hours generated several nanoparticle species of varying size. Due to the Zn^{II}(Por(HexMAAm-co-AMMA)$_4$) and Zn^{II}(Por(iPMAAm-co-AMMA)$_4$) having low solubility in THF and Zn^{II}(Por(HEMA-co-AMMA)$_4$ as well as Zn^{II}(Por(MMAAm-co-AMMA)$_4$ being insoluble in THF, Size-exclusion chromatography (SEC) characterization of the polymers and nanoparticles were not possible without exchanging the column set. In order to characterize the size of the complexes diffusion ordered spectroscopy (DOSY) was applied. The Stokes or hydrodynamic radius, R_H, of the parent polymers and nanoparticles were calculated using the Stokes-Einstein equation (Equation 1).[183,184] Where k_b is the Boltzmann constant, T is the absolute temperature, D is the diffusion constant, and η is the solutions viscosity. The diffusion constants, D, were obtained through Bayesian transformation of DOSY NMR experiments in DMF-D7 at 298 K (Equation 1).

$$R_H = \frac{k_B T}{6\pi\eta D} \qquad (1)$$

Based on DMF's viscosity, η, of 0.802 cP at 25 °C,[185] R_H of PCSP-1 decreased from 31.3 to 15.5 Å during the formation of PCPN-1 (figures A70 & A71). R_H of PCSP-2 decreased from 20.5 to 17.0 Å during the formation of PCPN-2 (figures A72 & A73). R_H of PCSP-3 changed from 27.5 to 27.7 Å during the formation of PCPN-3 (figures A74 & A75). R_H of PCSP-4 decreased

from 31.8 to 21.1 Å during the formation of PCPN-4 (figures A76 & A77). Comparative stokes radii in DMF for PCSP-5 and PCPN-5 could not be accurately obtained due to lack of adequate phase locking when DOSY-NMR was performed (figures A78 and A79). Phase lock could not be obtained due to the methyl peaks of the amide overlapping with the NMR solvent peaks.

In order to study the stability of the zinc porphyrin systems in DMF prior to more costly ^{15}N-NMR cyanide binding studies, the binding of cyanide was confirmed and monitored via UV-vis spectroscopy. Binding of cyanide was completed by spiking a stock solution of sodium cyanide in DMF (4.4 mg/mL) into aliquots of polymer in DMF solution with a final concentration of ~2.9 μM Polymer and 0.5 mM NaCN. Binding of cyanide was confirmed and monitored by anticipated changes in the Soret, α, and β absorbances signatures. Upon addition of sodium cyanide solution to the polymer solutions the Soret peak immediately shifted from 429 to 439 nm. The α,β peaks shifted from 562 and 604 to 581 and 625 nm matching previously reported systems (Table 7) and indicating the formation of a Zn-Porphyrin cyanide adduct (figures A133 to A148).[180,181] Observing the UV-vis spectrum of PCSP-1,PCPN-1, and PCSP-2 peak over several hours (figures S54 to S56) it was found that the zinc-cyanide adduct was unstable over time with decreases in absorbance at 439, 581 and 625 nm and increases in absorbance at 428.5, 562 and 604 nm with isosbestic points occurring at 433.5, 569.5, 595.5 and 611.5 nm (figure A136).

Table 7: Absorbance spectral data for synthesized complexes and relevant complexes which have been previously reported.

Complex	Solvent	Soret	α,β	ref
ZnTPP	MeCN	420.7	-	[181]
ZnTPP(CN)	MeCN	432.4	-	[181]
ZnTPP-1	MeCN	428.7	-	[181]
ZnTPP-1(CN)	MeCN	439.3	-	[181]
ZnTPP-15C5(p)	Toluene	422	512, 548, 588, 629	[180]
ZnTPP-15C5(p)(Na)(CN)	Toluene	437	575, 617	[180]
ZnTPP-15C5(p)	Water/DMSO	428	-	[180]
ZnTPP-15C5(p)(Na)(CN)	Water/DMSO	438	-	[180]
Por(MMA-co-AMMA)$_4$	THF	418	514, 548, 592, 648	-

Zn[Por(MMA-co-AMMA)$_4$]	THF	426	521, 559, 599	-
Zn[Por(MMA-co-AMMA)$_4$]	DMF	429	562, 604	-
Zn[Por(MMA-co-AMMA)$_4$](CN)	DMF	439	581, 625	-
Por(PFPMA-co-AMMA)$_4$	THF	418	514, 549, 592, 648	-
Zn[Por(PFPMA-co-AMMA)$_4$]	THF	424	556, 596	-
Zn[Por(HexMAAm-co-AMMA)$_4$]	DMF	428	562, 604	-
Zn[Por(HexMAAm-co-AMMA)$_4$](CN)	DMF	439	580, 624	-
Zn[Por(iPMAAm-co-AMMA)$_4$]	DMF	428	561, 603	-
Zn[Por(iPMAAm-co-AMMA)$_4$](CN)	DMF	439	580, 624	-
Zn[Por(MMAAm-co-AMMA)$_4$]	DMF	429	562, 604	-
Zn[Por(MMAAm-co-AMMA)$_4$](CN)	DMF	439	581, 624	-
Zn[Por(HEMA-co-AMMA)$_4$]	DMF	429	562, 603	-
Zn[Por(HEMA-co-AMMA)$_4$](CN)	DMF	439	-	-

Ram Chand Paul and B. R. Sreenathan have previously shown that metal cyanides slowly react with dimethylformamide to form metal dimethylamines, carbon dioxide, and hydrogen cyanide under reflux conditions (equation 2).[186]

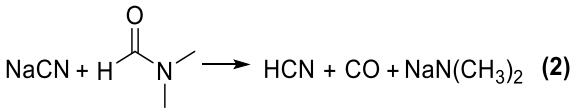

Testing for the presence of HCN via the titration of PCPN-4 test solution two weeks after sodium cyanide addition with sodium acetate lead to the partial recovery of the characteristic 439, 581 and 625 nm absorption peaks associated with the cyanide adduct (Figure A149). Based on the initial UV-Vis binding studies and the recovery of the characteristic absorbance signatures of cyanide binding, it was hypothesized that the zinc porphyrin substrates were acting as catalysts for the reaction of cyanide and DMF at room temperature.

In order to elucidate the reaction kinetics, the UV-Vis absorbances at 428.5 and 439 nm were monitored for 24 hours after sodium cyanide addition to a degassed solution of polymer at 25 °C with absorbance measurements taken every 15 minutes. Replicating the experiments in triplicate for each polymer species resulted in the intensity of absorbance at 439 nm diminished at varying rates depending on polymer scaffold functionality and topology (figure 24). Twenty-four

hours after sodium cyanide addition the absorbance at 439 nm decreased by 4.0 ± 0.1 % for PCSP-1, 9 ± 2 % PCPN-1, 18 ± 7 % for PCSP-2, 30 ± 10 % for PCPN-2, 36 ± 7 % for PCSP-3, 50 ± 10 % for PCPN-3, 33 ± 9 % for PCSP-4, and 43 ± 2 % for PCPN-4 (Table 8). Indicating that polymers with a greater number of potential hydrogen bond donors and greater steric bulk increased the rate of the observed reaction and nanoparticles decreased in measured absorbance faster than their random coil parent species. The absorbance data at 439 nm for these reactions could not be linearly fit for 1st or 2nd order kinetic models, presenting the possibility of concurrent reactions.

Table 8: Diffusion constants, Stokes radius, and average percent change in Soret UV-Vis absorbance at 439 nm associated with the Zn-Porphyrin-CN adduct 24 hours after cyanide addition for the random coil and folded particle polymer species

Polymer Species	Random Coil (PCSP)			Folded Particle (PCPN)		
	$\bar{D}$ (cm^2/s)	$\bar{R}_H$ (Å)	-Δ Abs @ 439 nm [24 h]	$\bar{D}$ (cm^2/s)	$\bar{R}_H$ (Å)	-Δ Abs @ 439 nm [24 h]
Zn^{II}(Por(MMA-co-AMMA)$_4$)	8.70e-7	31.3	4.0 ± 0.1 %	1.76e-6	15.5	9 ± 2 %
Zn^{II}(Por(HexMAAm-co-AMMA)$_4$)	1.33e-6	20.5	18 ± 7 %	1.60e-6	17.0	30 ± 10 %
Zn^{II}(Por(iPMAAm-co-AMMA)$_4$)	9.92e-7	27.5	36 ± 7 %	9.82e-7	27.7	50 ± 10 %
Zn^{II}(Por((HEMA-co-AMMA)$_4$)	8.57e-7	31.8	33 ± 9 %	1.29e-6	21.1	43 ± 2 %

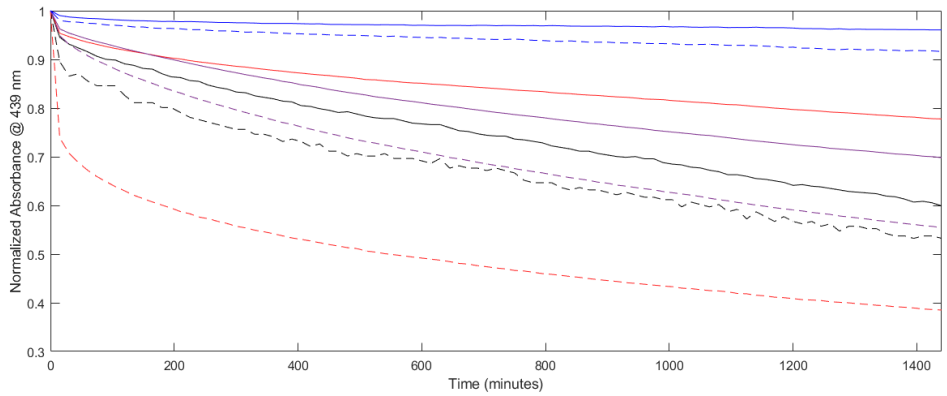

Figure 22: Normalized absorbance over 24 hours after cyanide addition to PCSP-1 (blue line), PCPN-1 (dashed blue line), PCSP-2 (red line), PCPN-2 (dashed red line), PCSP-3 (purple line), PCNP-3 (dashed purple line), PCSP-4 (Black line), PCPN-4 (dashed black line) for a single set of experiments.

To isolate the products of the reaction between NaCN and DMF in the presence of the zinc porphyrin polymers, a large excess of sodium cyanide was added to a dilute solution of PCPN-2 in N,N-Dimethylformamide and stirred under ambient conditions. 48 hours after the sodium cyanide addition a white precipitate was isolated and characterized by ^{1}H NMR, ^{13}C NMR and ATR-IR. A lack of a ^{1}H NMR signal (Figure A52) in conjunction with a single 168.08 ppm ^{13}C NMR (figure A62) chemical shift in D_2O indicated that sodium dimethylamine was not present. Comparison of the IR spectrums of the precipitate (Figure A114) with commercially available sodium carbonate (Figure A115) lead to the identification of the solids as sodium carbonate.

The reaction of hydroxide ions with carbon dioxide leading to the subsequent generation of carbonate in aqueous media (equations 5 and 6) has been previously studied by Pohorecki and Moniuk.[187] Due to the possible absorption of atmospheric moisture and carbon dioxide into DMF under ambient conditions it is proposed that the following cascade of reactions occurred following the reaction of cyanide and DMF resulting in the accelerated formation of sodium carbonate.

$$NaN(CH_3)_2 + H_2O \rightleftharpoons HN(CH_3)_2 + NaOH \quad \textbf{(3)}$$

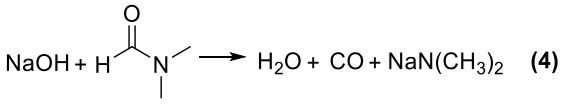

(4)

$$NaOH + CO_2 \rightleftharpoons NaHCO_3 \quad \textbf{(5)}$$

$$NaHCO_3 + NaOH \rightleftharpoons Na_2CO_3 + H_2O \quad \textbf{(6)}$$

Scheme 44: Subsequent reactions occurring during the reaction of sodium cyanide and DMF in the presence of zinc porphyrins under ambient conditions.

In order to test the hypothesis that the polymer species were catalyzing the reaction of cyanide with DMF, the folded particles of each polymer species and a control of DMF were reacted with large excesses of cyanide over 48 hours under ambient conditions in triplicate. The resulting

percent yields of sodium carbonate were 78.7 ± 0.7, 81 ± 6, 83 ± 2, and 74 ± 1 % for PCPN-1, PCPN-2, PCPN-3, and PCPN-4 respectively. And a yield of 68 ± 2 % of sodium carbonate for the control containing only DMF and cyanide. Replication of the experiments replacing cyanide with acetate lead to the recovery of starting material only. Indicating that the cyanide does react with DMF at room temperature and the polymers are increasing the rate of dimethylamine generation resulting in larger yields of sodium carbonate.

Conclusions

In summary, the series of porphyrin cored polymers and nanoparticles synthesized in order to study the secondary coordination sphere interactions of the metallo-organic core and polymeric scaffold formed adducts with sodium cyanide which were unstable on a ^{15}N NMR timescale in DMF. While unable to gain direct evidence of hydrogen bonding via observing the ^{15}N NMR chemical shift of isotope labeled cyanide, studying the reaction of cyanide and DMF in the presence of PCSP and PCPN species elucidated the significant roll the functionalization and topology of the polymer scaffold played in the reactivity of the zinc porphyrin cyanide adduct. While all species catalyzed the reaction of sodium cyanide and DMF, the ester backboned PCSP and PCPN species formed the least reactive adducts of the series with the amide and ethanolamide species containing a greater number of potential hydrogen bond donors and greater steric bulk increasing the reactivity. In addition, for all polymer species tested the folded particle topology formed more reactive cyanide adducts than the random coil topologies.

Experimental

Materials

The following reagents were obtained from the indicated commercial suppliers and used as received unless otherwise noted: 5,10,15,20-Tetrakis(4-hydroxyphenyl)-21H,23H-porphine (THPP) (Sigma Aldrich), 4-cyano-4-[(dodecyl-sulfanylthiocarbonyl)sulfanyl]-penatanoic acid (Sigma Aldrich), N,N'-dicyclohexylcarbodiimide (DCC) (Sigma Aldrich), 4-(Dimethylamino)pyridine (DMAP) (Sigma Aldrich), sodium sulfate (Fisher Scientific), 9-anthraldehyde (Sigma Aldrich), sodium borohydride (Sigma Aldrich), methacrylic acid (Sigma Aldrich), ethyl acetate (Fisher Scientific), pentafluorophenol (Oakwood Products, Inc), methacrylol chloride (Sigma Aldrich), methyl methacrylate (MMA) (Sigma Aldrich), azobisisobutyronitrile (AIBN) (Sigma Aldrich), Chloroform (Fisher Scientific), zinc acetate hydrate (Sigma Aldrich), n-hexylamine (Sigma Aldrich), Acetone (Pharmco Products Inc), isopropylamine (Alfa Aesar), 2-aminoethanol (TCI America), N,N-dimethylformamide (DMF) (Fisher Scientific), sodium cyanide (Sigma Aldrich), dimethyl sulfoxide (DMSO) (Fisher Scientific), dichloromethane (DCM) (Fisher Scientific), methanol (Fisher Scientific), tetrahydrofuran (THF) (Fisher Scientific), silica gel (230400 mesh) (SiliCycle), chloroform-d (Cambridge Isotope Laboratories), and N,N-dimethylformamide-d_7(Cambridge Isotope Laboratories). Dry toluene, DCM, DMF, and THF were obtained from an Innovative Technology solvent purification system model SPS-400-5.

Instrumentation

Photodimerization reactions were conducted in a Luzchem photo-reactor CCP-4V equipped with 4 UVA (350 nm centered) and 4 UVC (254 nm centered) lamps. ^{1}H NMR and ^{13}C NMR Spectra were acquired with a Varian Mercury 400 BB NMR or Varian UnityINOVA 500

NMR. Chemical shifts (δ) are reported in parts per million (ppm) relative to tetramethylsilane (TMS). Solvents ($CDCl_3$ & DMF-D_7) contained 0.03% v/v TMS as an internal reference. Peak abbreviations are used as follows: s = singlet, d = doublet, t = triplet, m = multiplet, br = broad. NMR spectra were processed with MestReNova Software (Ver. 14.0.0). Size exclusion chromatography (SEC) was performed on a Tosoh EcoSEC dual detection (RI and UV) SEC system coupled to an external Wyatt Technologies miniDAWN Treos multi angle light scattering (MALS) detector and a Wyatt Technologies ViscoStarII differential viscometer. Samples were run in THF at 40 ºC at a flow rate of 0.35 mL/min. The column set was two Tosoh TSKgel SuperMultipore HZ-M columns (4.6×150 mm), one Tosoh TSKgel SuperH3000 column (6×150 mm) and one Tosoh TSKgel SuperH4000 column (6×150 mm). ^{1}H DOSY NMR were acquired with a Varian UnityINOVA 500 NMR using a ledbpgp2s pulse pattern with 25 gradient steps (2% to 95% gradient amplitude) and 8 scans per step. Varian UnityINOVA 500 NMR magnetic field gradient calibrated against D_2O. ^{1}H DOSY NMR spectra were processed in MestReNova Software (Ver. 14.0.0) using Bayesian transformations with 2 repetitions, 0.1 resolution, and 256 points in the diffusion dimension. Viscosity of DOSY solutions were assumed to be that of pure DMF (0.802 cP at 25 °C).[185] UV-Vis spectra were obtained using a Shimadzu UV-2450 UV-Vis spectrophotometer equipped with a S-1700 thermoelectric single cell holder and a Lauda RE 200 chiller. Infrared spectra were obtained using a Thermo Nicolet iS10 FTIR equipped with a diamond plate Smart iTR™ attenuated total reflectance (ATR) sampling accessory. UV-Vis and ATR-IR spectra were processed with Matlab R2019b software by The MathWorks, Inc.

Experimental Procedures

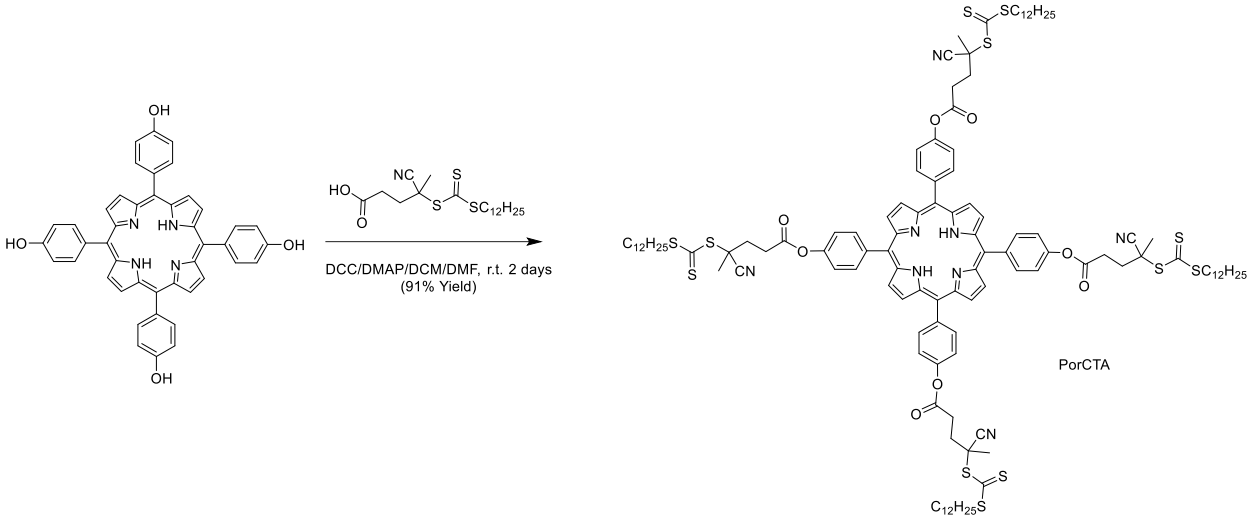

Scheme 1: Synthesis of PorCTA

Synthesis of 5,10,15,20-tetrakis(4-(4-cyano-4[(dodecylsulfanylthiocarbonyl)sulfanyl]phenyl pentanoate)-21H,23H-porphine (PorCTA)[61]

A 100 mL round bottom flask equipped with a magnetic stir bar was charged with dry dichloromethane (30 mL), dry N,N-dimethylformamide (1 mL), 5,10,15,20-tetrakis(4-hydroxyphenol)-21H,23H-porphine (0.1790 g, 0.2637 mmol), 4-cyano-4-[(dodecyl-sulfanylthiocarbonyl)sulfanyl]-pentanoic acid (0.5414g, 1.341 mmol), Dicyclohexylcarbodiimide (0.2980 g, 1.444 mmol) , and 4-Dimethylaminopyridine (0.0283 g, 0.1883 mmol). The solution sparged with nitrogen then allowed to stir for 20 hours at room temperature. The solution was then vacuum filtered. The filtrate was then washed with water (4 x 50 mL) and dried with sodium sulfate. The solution was then concentrated under reduced pressure and the product was isolated by column chromatography using silica (9:1 toluene/ ethyl acetate, Rf = 0.7). The product fraction was concentrated under reduced pressure to yield 5,10,15,20-tetrakis(4-(4-cyano 4[(dodecylsulfanylthiocarbonyl)sulfanyl]phenyl pentanoate)-21H,23H-porphine as a purple tar (0.5323 g, 0.2396 mmol, 90.86% yield). ^{1}H NMR ($CDCl_3$, 400 MHz): δ 8.90 (s, 8H), 8.25 (d, 8H), 7.55 (d, 8H), 3.43-3.40 (m, 8H), 3.14-3.11 (m, 8H), 2.86-2.66 (m, 8H), 2.07 (s, 12H), 1.79-

1.68 (m, 8H), 1.47-1.25 (m, 72H), 0.92-0.89 (m, 12H), -2.80 (br s, 2NH) 13C NMR (101 MHz, cdcl3) δ 216.99, 170.39, 150.56, 139.95, 138.01, 135.52, 129.17, 128.36, 125.43, 119.88, 119.28, 119.21, 61.12, 46.56, 37.29, 34.05, 32.05, 30.39, 29.76, 29.69, 29.57, 29.48, 29.23, 29.10, 27.84, 25.27, 22.83, 21.60, 14.27. (^{1}H NMR figure A32, ^{13}C NMR figure A60, UV-Vis figure A116)

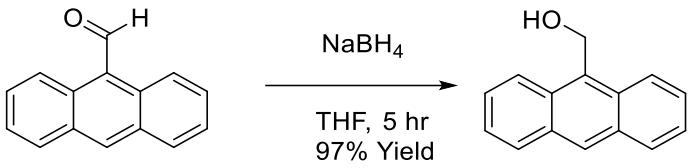

Scheme 2: Synthesis of 9-Anthracene methanol

Synthesis of 9-anthracene methanol[188]

A 500 mL round bottom flask equipped with a magnetic stir bar was charged with dry tetrahydrofuran (120 mL), 9-anthraldehyde (3.0199 g, 14.643 mmol) and sodium borohydride (0.6475 g, 17.116 mmol). The solution was stirred under nitrogen at room temperature for 5 hours. The solution was then poured into 1 L beaker containing 500 mL of cold water. The resulting yellow precipitate was isolated by vacuum filtration and dried under vacuum to yield 9-antrhacene methanol as a yellow powder (2.962 g, 14.223 mmol, 97.131% yield). ^{1}H NMR ($CDCl_3$, 500 MHz): δ 8.48 (s, 1H), 8.42 (dq, *J* = 8.9, 1.0 Hz, 2H), 8.04 (ddt, J = 8.4, 1.4, 0.7 Hz, 2H), 7.58 (ddd, , J = 8.9, 6.5, 1.4 Hz, 2H), 7.51 (ddd, , J = 8.4, 6.5, 1.1 Hz, 2H), 5.66 (d, J = 5.6 Hz, 2H), 1.81 (t, J = 5.6 Hz, OH). (^{1}H NMR figure A33, ATR-IR figure A107)

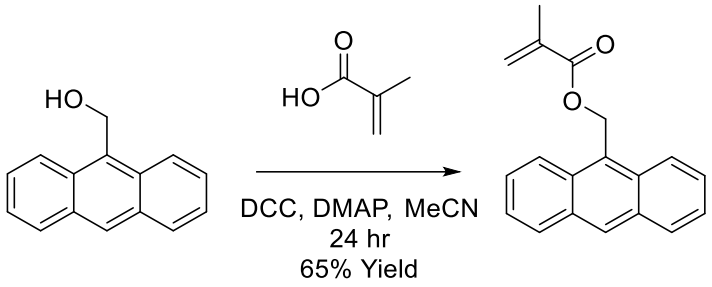

Scheme 3: Synthesis of 9-Anthraceynlmethyl methacrylate

Synthesis of 9-anthracynlmethyl methacrylate (AMMA)[188]

A 500 mL round bottom flask equipped with a magnetic stir bar was charged with dry acetonitrile (60 mL), 9-anthracene methanol (2.5068 g, 12.037 mmol), methacrylic acid (2.06 mL, 24.4 mmol), N,N-Dicyclohexylcarbodiimide (5.0407 g, 24.430 mmol), and 4-Dimethylaminopyridine (0.2314 g, 1.8941 mmol). The mixture was stirred at room temperature for 24 hours under nitrogen. The solution was vacuum filtered, and the filtrate was concentrated under reduced pressure. The product was isolated via column chromatography using silica (5:1 toluene/ ethyl acetate). The product fraction was concentrated under reduced pressure and precipitated in methanol. The resulting precipitate was vacuum filtered and dried under vacuum to yield 9-anthracynlmethyl methacrylate as a pale-yellow powder (2.1736 g, 7.8657 mmol, 65.346% yield). ^{1}H NMR (500 MHz, $CDCl_3$) δ 8.52 (s, 1H), 8.38 (dq, J = 8.9, 1.0 Hz, 2H), 8.04 (ddt, J = 8.5, 1.4, 0.7 Hz, 2H), 7.58 (ddd, J = 8.9, 6.5, 1.4 Hz, 2H), 7.50 (ddd, J = 8.4, 6.5, 1.1 Hz, 2H), 6.23 (s, 2H), 6.06 (dq, J = 2.0, 1.0 Hz, 1H), 5.51 (p, J = 1.6 Hz, 1H), 1.93 (dd, J = 1.6, 0.9 Hz, 3H). ^{13}C NMR (126 MHz, $CDCl_3$) δ 167.75, 136.28, 131.54, 131.26, 129.27, 129.22, 126.73, 126.55, 126.15, 125.24, 124.19, 59.29, 18.49. (^{1}H NMR figure A34, ^{13}C NMR figure A61, ATR-IR figure A108, UV-Vis figure A117)

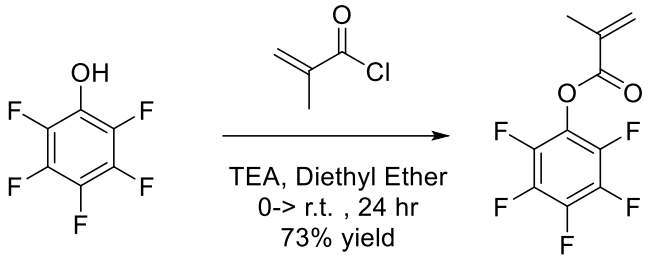

Scheme 4: Synthesis of Pentafluorophenyl methacrylate

Synthesis of pentafluorophenyl methacrylate (PFPMA)[174]

A 250 mL round bottom flask equipped with a magnetic stir bar was charged with diethyl ether (100 mL), Pentafluorophenol (4.3537 g, 23.652 mmol), and triethylamine (3.9 mL, 28 mmol). The solution was sparged with nitrogen and cooled to 0°C. While stirring methacryloyl chloride (2.8 mL, 29 mmol) was added dropwise to the solution. The solution was then stirred for an additional 24 hours at room temperature under nitrogen. The solution was vacuum filtered, and the filtrate was then concentrated under reduced pressure. The product was isolated via column chromatography using silica (petroleum ether). The product fraction was concentrated under reduced pressure to yield pentafluorophenol methacrylate as a clear oil (4.3404 g, 17.214 mmol, 72.780% yield). ^{1}H NMR (400 MHz, $CDCl_3$) δ 6.45 (p, J = 1.0 Hz, 1H), 5.92 – 5.90 (m, 1H), 2.08 (dd, J = 1.6, 1.0 Hz, 3H). ^{19}F NMR ($CDCl_3$, 376.1 MHz): δ -152.86 (d, 2F), -158.31 (t, 1F), -162.59 (t, 2F). (^{1}H NMR figure A35, ^{19}F NMR figure A63)

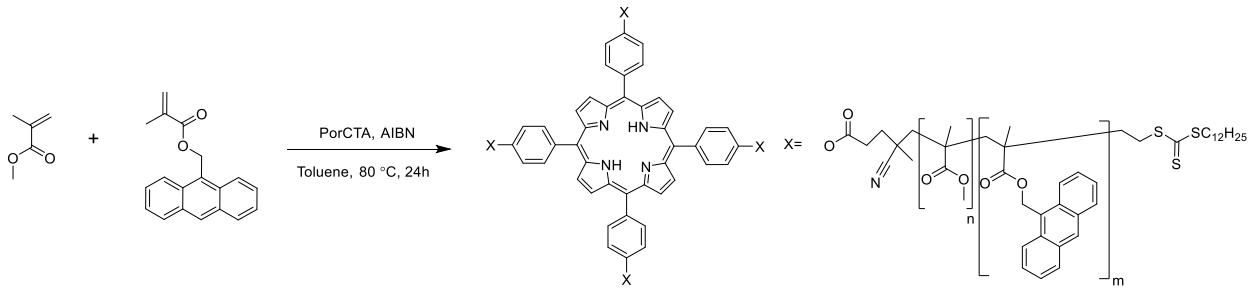

Scheme 45: Synthesis of Por(MMA-co-AMMA)$_4$

Synthesis of Por(MMA-co-AMMA)$_4$ [61]

A 50 mL round bottom flask equipped with a magnetic stir bar was charged with PorCTA in toluene solution (1.079 ml, 0.176g PorCTA, 0.079 mmol), 9-anthracynlmethyl methacrylate (0.4160 g, 1.5054 mmol), methyl methacrylate (0.6060 g, 6.0529 mmol), and azobisisobutyronitrile (0.0145 g, 0.0883 mmol). The mixture was sparged with argon for 1 hour while stirring. After, the flask was placed in an oil bath preheated to 80°C and the solution was stirred under argon for 18 hours. The solution was then concentrated under reduced pressure, dissolved in minimal dichloromethane, then precipitated in cold methanol. The collected solids were dialyzed against tetrahydrofuran. The polymer solution was then concentrated under reduced pressure, dissolved in minimal dichloromethane, and precipitated in cold methanol. The precipitate was collected via vacuum filtration and dried under vacuum to yield Por(MMA-co-AMMA)$_4$ as a tan powder (0.8819 g, M_n = 17.2 kDa, AMMA incorporation = 22.8%). M_n calculated based on Equation 1. %AMMA incorporation calculated based on Equation 2. ^{1}H NMR ($CDCl_3$, 500 MHz): δ 8.87 (br s), 8.55-8.10 (br m), 8.10-7.70 (br m), 7.67-7.10 (br m), 6.32-5.60 (br m), 3.86-3.00 (br m), 2.50-0.36 (br m), -2.85 (br s). (^{1}H NMR figure A36, UV-Vis figure A118)

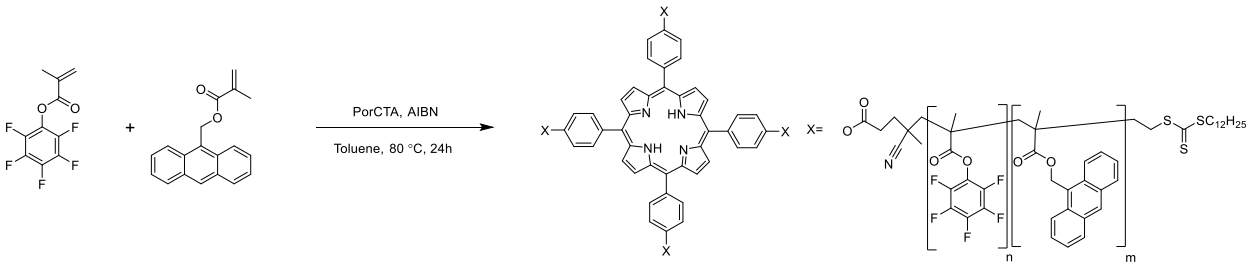

Scheme 46: Synthesis of Por(PFPMA-co-AMMA)$_4$

Synthesis of Por(PFPMA-co-AMMA)$_4$ [174]

A 50 mL round bottom flask equipped with a stir bar was charged with PorCTA (0.4550 g, 0.2049 mmol) , toluene (2 mL), 9-anthracenylmethyl methacrylate (0.8350 g, 3.022 mmol), pentafluorophenyl methacrylate (3.0444 g, 12.074 mmol) and azobisisobutyronitrile (0.0261 g,

0.1589 mmol). The mixture was sparged with argon for 1 hour while stirring. After, the flask was placed in an oil bath preheated to 80°C and the solution was stirred under argon for 18 hours. The solution was then concentrated under reduced pressure, dissolved in minimal dichloromethane, then precipitated in cold methanol. The collected solids were dialyzed against tetrahydrofuran. The polymer solution was then concentrated under reduced pressure, dissolved in minimal dichloromethane, and precipitated in cold methanol. The precipitate was collected via vacuum filtration and dried under vacuum to yield Por(PFPMA-co-AMMA)$_4$ as a red powder. (4.1863 g, M_n = 33.2 kDa, AMMA incorporation = 14.6%) M_n Calculated based on equation 3. ^{1}H NMR ($CDCl_3$, 500 MHz): δ 8.87 (br s), 8.54 -8.06 (br m), 8.06-7.65 (br m), 7.65-7.00 (br m), 6.49-5.62 (br m), 2.75 -0.6 (br m), -2.84 (br s) ^{19}F NMR ($CDCl_3$, 376.1 MHz): δ -149.2 to -152.5(br m), -156.5 to -158.2 (br m), -161.2 to -163.0 (br m). (^{1}H NMR figure A37, ^{19}F NMR figure A64, UV-Vis figure A121)

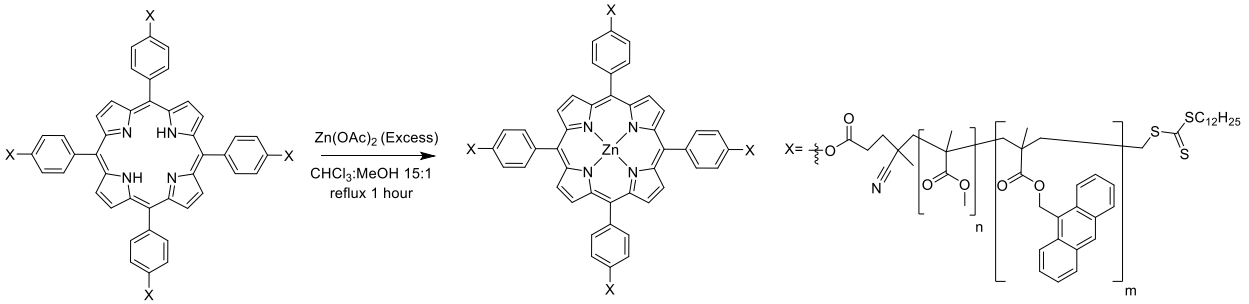

Scheme 47: Synthesis of Zn^{II}(Por(MMA-co-AMMA)$_4$)

Synthesis of Zn^{II}(Por(MMA-co-AMMA)$_4$)

A 1 L round bottom flask equipped with a magnetic stir bar was charged with Por(MMA-co-AMMA (0.5014 g, 0.0292 mmol), chloroform (140 mL), methanol (10 mL), and zinc acetate hydrate (0.1283 g, 0.5886 mmol). The solution was refluxed with stirring for 1 hour. The solution was concentrated under reduced pressure, dissolved in minimal dichloromethane, and precipitated in cold methanol. The precipitate was collected via vacuum filtration then dried under vacuum to

yield Zn^{II}(Por(MMA-co-AMMA)$_4$) as a red powder (0.4537g). ^{1}H NMR ($CDCl_3$, 500 MHz): δ 8.93 (br s), 8.55-8.10 (br m), 8.10-7.70 (br m), 7.67-7.10 (br m), 6.32-5.60 (br m), 3.86-3.00 (br m), 2.50-0.36 (br m). (^{1}H NMR figure A38-39, ^{1}H DOSY NMR figure A70, ATR-IR figure A109, UV-Vis figure A119-A120)

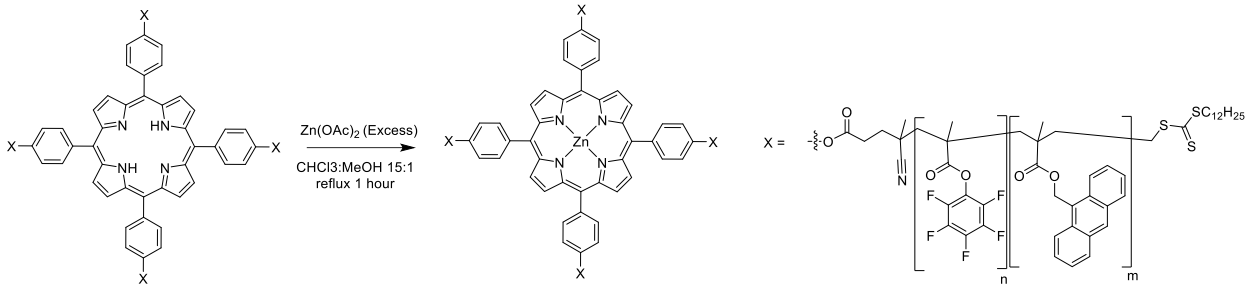

Scheme 48: Synthesis of Zn^{II}(Por(PFPMA-co-AMMA)$_4$)

Synthesis of Zn^{II}(Por(PFPMA-co-AMMA)$_4$)

A 1 L round bottom flask equipped with a magnetic stir bar was charged with Por(PFPMA-co-AMMA (1.2173 g, 0.0429 mmol), chloroform (337 mL), methanol (24 mL), and zinc acetate hydrate (0.3101 g, 1.4226 mmol). The solution was refluxed with stirring for 1 hour. The solution was concentrated under reduced pressure, dissolved in minimal dichloromethane, and precipitated in cold methanol. The precipitate was collected via vacuum filtration then dried under vacuum to yield Zn^{II}(Por(PFPMA-co-AMMA)$_4$) as a pink powder (1.0447 g). . ^{1}H NMR ($CDCl_3$, 500 MHz): δ 8.96 (br s), 8.54 -8.06 (br m), 8.06-7.65 (br m), 7.65-7.00 (br m), 6.49-5.62 (br m), 2.75 -0.60 (br m). (^{1}H NMR figure A40-41, ^{19}F NMR figure A65, UV-Vis figure A121)

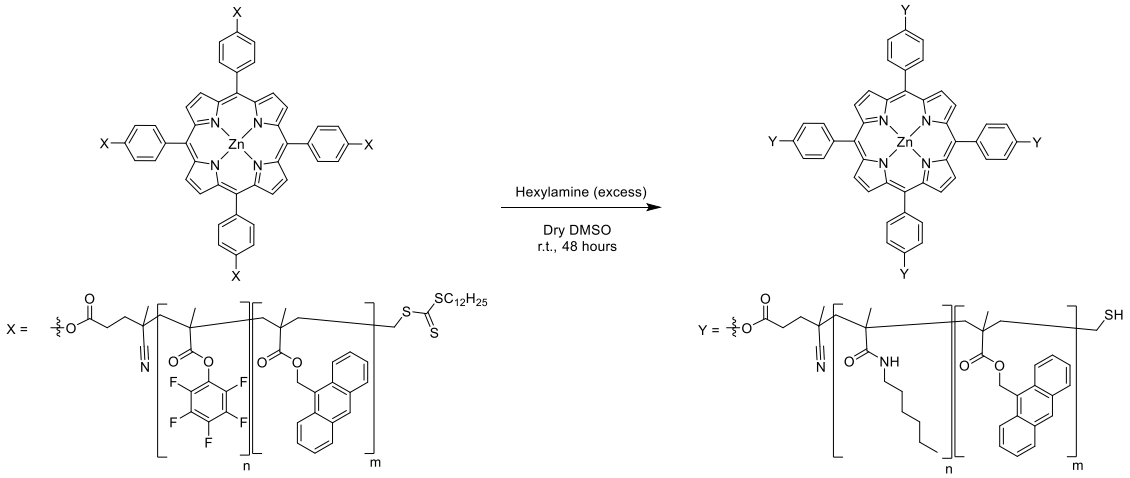

Scheme 49: Synthesis of Zn^{II}(Por(HexMAAm-co-AMMA)$_4$)

Synthesis of Zn^{II}(Por(HexMAAm-co-AMMA)$_4$)

A 50 mL round bottom flask equipped with a magnetic stir bar was charged with Zn^{II}(Por(PFPMA-co-AMMA)$_4$) (0.3992 g, mmol), dry dimethyl sulfoxide (15.5 mL), and hexylamine (800 μL, mmol). The mixture was allowed to stir for 48 hours at room temperature under nitrogen to yield a green solution. The solution was dialyzed against acetone for 3 hours, replacing the dialysis tube every 30 minutes. The solution was then concentrated under reduced pressure and dialyzed against tetrahydrofuran for 24 hours to yield a reddish tan solution. The solution was concentrated under reduced pressure and dried under vacuum to yield Zn^{II}(Por(HexMAAm-co-AMMA)$_4$) as green solids (0.3385 g). ^{1}H NMR ($CDCl_3$, 500 MHz): δ 8.87 (br s), 8.60-8.12 (br m), 8.12-7.71 (br m), 7.71-6.99 (br m), 6.42-4.90 (br m), 3.86-0.16 (br m). (^{1}H NMR figure A42, ^{19}F NMR figure A65, ^{1}H DOSY NMR figure A72, ATR-IR figure A110, UV-Vis figure A122)

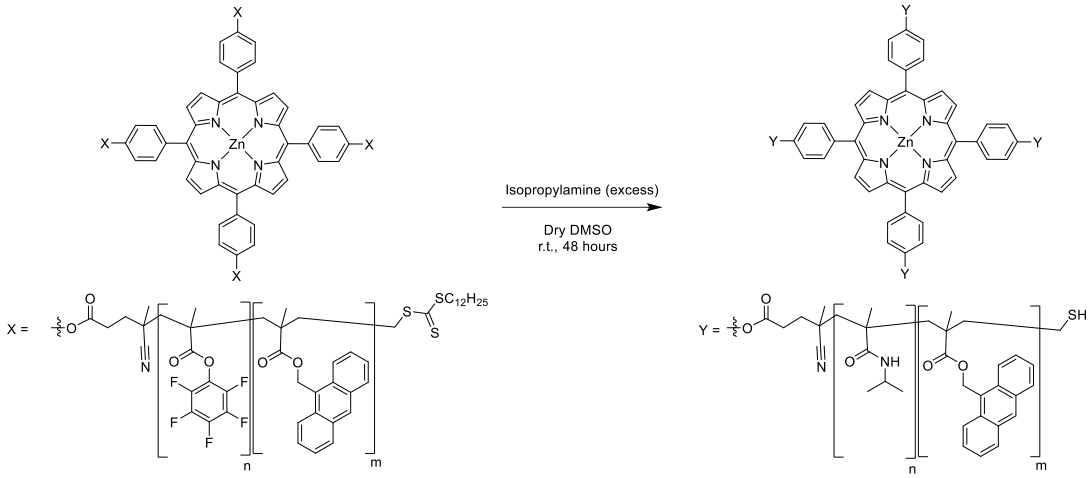

Scheme 50: Synthesis of Zn^{II}(Por(iPMAAm-co-AMMA)$_4$)

Synthesis of Zn^{II}(Por(iPMAAm-co-AMMA)$_4$)

A 50 mL round bottom flask equipped with a magnetic stir bar was charged with Zn^{II}(Por(PFPMA-co-AMMA)$_4$) (0.4019 g, mmol), dry dimethyl sulfoxide (16 mL), and isopropylamine (800 μL, mmol). The mixture was stirred for 48 hours at room temperature under nitrogen. The solution was dialyzed against acetone for 5 hours, replacing the dialysis tube every hour. The solution was then concentrated under reduced pressure and dialyzed against tetrahydrofuran for 48 hours to yield a reddish tan solution. The solution was concentrated under reduced pressure and dried under vacuum to yield Zn^{II}(Por(iPMAAm-co-AMMA)$_4$) as green solids (0.2686 g) ^{1}H NMR ($CDCl_3$, 500 MHz): δ 8.88 (br s), 8.60-8.12 (br m), 8.12-7.71 (br m), 7.71-6.99 (br m), 6.48-4.88 (br m), 4.30-3.26 (br m), 2.71-0.15 (br m). (^{1}H NMR figure A43, ^{19}F NMR figure A66, ^{1}H DOSY NMR figure A74, ATR-IR figure A111, UV-Vis figure A123)

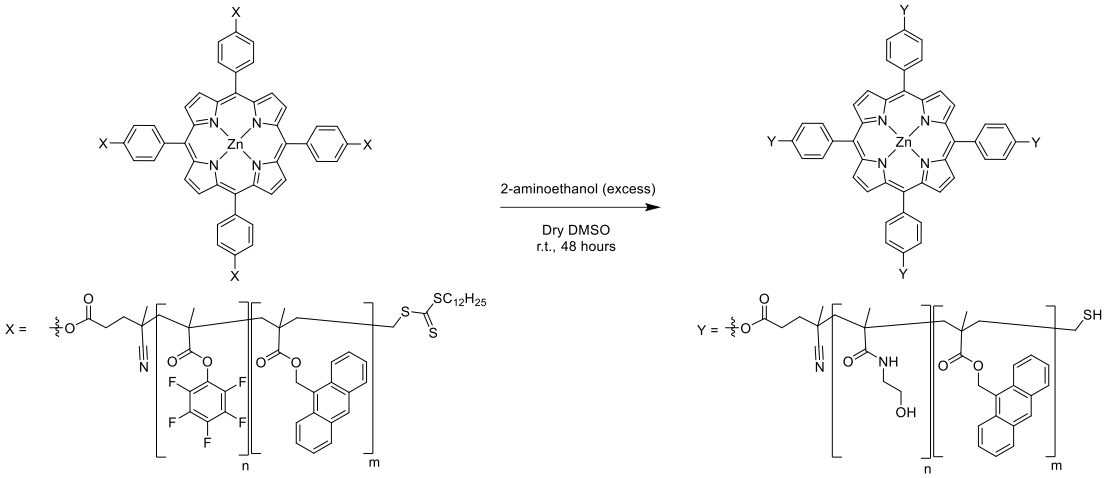

Scheme 51: Synthesis of Zn^{II}(Por((HEMA-co-AMMA)$_4$)

Synthesis of Zn^{II}(Por((HEMA-co-AMMA)$_4$)

A 50 mL round bottom flask equipped with a magnetic stir bar was charged with Zn^{II}(Por(PFPMA-co-AMMA)$_4$) (0.4007 g, mmol), dry dimethyl sulfoxide (16 mL), and 2-aminoethanol (360 μL, 5.9 mmol). The mixture was stirred for 24 hours at room temperature under nitrogen. The solution was dialyzed against acetone for 48 hours, replacing the dialysis tube every 30 minutes for the first 3 hours, and again after 24 hours resulting in green solids plated to the dialysis tubes and a purple solution. The solids were collected from the dialysis bags and dried under vacuum to yield Zn^{II}(Por((HEMA-co-AMMA)$_4$) as green solids (0.1291 g) ^{1}H NMR (DMF-d_7, 400 MHz): δ 8.93 (br s), 8.82-8.29 (br m) 8.29-7.93 (br m) 7.93-7.10 (br m) 6.43-5.60 (br m) 5.05-4.58 (br m), 4.16-3.00 (br m), 2.51-0.26 (br m). (^{1}H NMR figure A44, ^{19}F NMR figure A67, ^{1}H DOSY NMR figure A76, ATR-IR figure A112, UV-Vis figure A124)

Synthesis of Zn^{II}(Por((MMAAm-co-AMMA)$_4$)

A 50 mL round bottom flask equipped with a magnetic stir bar was charged with Zn^{II}(Por(PFPMA-co-AMMA)$_4$) (0.3989 g, mmol), dry dimethyl sulfoxide (16 mL), and methylamine in ethanol 8 M (800 μL, mmol). The mixture was stirred for 24 hours at room

temperature under nitrogen. The solution was dialyzed against acetone for 72 hours, replacing the dialysis tube every 30 minutes for the first 3 hours resulting in a biphasic mixture with a red solution phase and a blue gel. The mixture was then concentrated under reduced pressure and dried under vacuum to yield Zn^{II}(Por((MMAAm-co-AMMA)$_4$) as green solids (0.2279 g) . (^{1}H NMR figure A45, ^{19}F NMR figure A68, ^{1}H DOSY NMR figure A78, ATR-IR figure A113, UV-Vis figure A125)

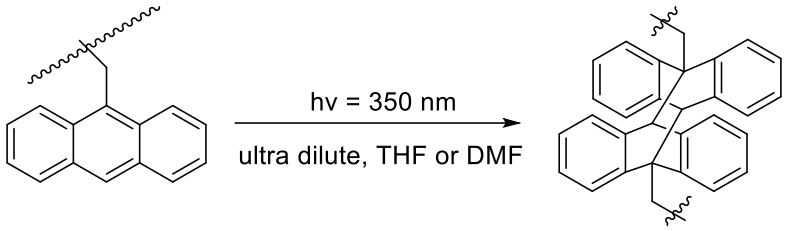

Scheme 52:Photo-induced [4+4] cycloaddition of anthracene

General procedure for photoinduced dimerization of anthracene

A 250 mL quartz round bottom flask equipped with a stir bar was charged with polymer (15 mg) and either tetrahydrofuran or N,N-dimethylformamide (150 mL). The solution was stirred for 1 hour and a 10 mL aliquot was taken. The bulk solution was then submitted to 350 nm light for 2 hours at room temperature with stirring. A second 10 mL aliquot was taken then the bulk was concentrated under reduced pressure. Collapse of the polymers to nanoparticles were monitored by UV-Vis spectroscopy and DOSY NMR. Percent conversion of Anthracene to the anthracene dimer calculated based on the UV-Vis absorbance at 366.5 nm. (gCOSY NMR figures A46-A47, ^{1}H NMR figures A48-A51, ^{1}H DOSY NMR figure A71, A73, A75, A77, and A79, UV-Vis Figures A126 – A132)

General procedure for CN binding

Stock polymer in DMF solution (0.1 mg/mL) was diluted to ~2.9 µM in a quartz cuvette. Initial spectrum (700 to 320 nm) was obtained, then stock sodium cyanide in DMF solution (4.4 mg/mL) was spiked into the cuvette and kinetics was immediately monitored at 428.5 and 439 nm. Shimadzu kinetics module was set to collect spectra every 15 minutes for 24 hours. After 24 hours a full spectrum (700 to 320 nm) scan was performed and the solution was transferred to a scintillation vial and stored at room temperature. (UV-Vis figures A133 – A149)

Procedure for isolating Zn-CN adduct precipitate

Sodium cyanide (75 mg, mmol) and DMF (2 mL) were added to a 20 mL scintillation vial equipped with a magnetic stir bar. The sodium cyanide was crushed with a spatula then stock Zn^{II}(Por(HexMAAm -co-AMMA)$_4$) solution in DMF solution (0.1 mg/mL, 2 mL) was added and the solution was stirred for 48 hours. The solution was vacuum filtered, and the white precipitate was rinsed with dry DCM (10 mL). The precipitate was dried under vacuum to yield sodium carbonate as a white powder (g, mmol). ^{13}C NMR (101 MHz, d2o) δ 168.08. ATR-IR v = 1422, 1413, 878, 702, 695 cm^{-1}. (^{1}H NMR figure A52, ^{13}C NMR figure A62, ATR-IR figure A114)

Chapter IV: Summary of the Current State of the Fields of [FeFe]-Hydrogenase and Polymer Catalysts and This Work's Contributions to Science

Current State of the Field of Diiron Hydrogenase Enzymes

Research into the fields of [FeFe]-Hydrogenase and [FeFe] model complexes are currently relevant due to their efficacy as hydrogen evolution catalysts and the push to generate a clean hydrogen fuel economy.[189] Current research into the native enzymes have been focused on elucidating the active species present during catalysis, the role hydrogen bonding networks in the proton transfer pathway, and the mechanism of enzyme deactivation in the presence of oxygen with several break throughs in the field over the last few years.

Research by Ratzloff and coworkers in 2018 investigated the presence of μ-CO bridging ligands in the active sites of *Clostridium acetobutylicum* (CaI) and *Chlamydomonas reinhardtii* (CrHydA1) throughout the catalytic process. Characterization of CaI and CrHydA1 via Fourier-transform infrared (FTIR) spectroscopy with temperature annealing and H/D isotope exchange led to the identification of a bridging CO ligand remains during all steps in the catalytic process of hydrogen evolution.[190]

The competency of the proposed H_{ox}, H_{red}, $H_{red}H^+$, $H_{sred}H^+$, and H_{hyd} reaction intermediates of the CrHydA1 catalytic cycle have been recently tested by Sanchez and coworkers. The lifetimes of the proposed intermediates were measured with time-resolved IR (TRIR) spectroscopy with the catalytic cycles initiated by a pulsed laser induces a potential jump via a CdSe/CdS dot-in-rod (DIR) nanocrystalline semiconductor intermediary. Each of the observed reaction intermediates were found to be kinetically competent to be part of the proposed catalytic cycle with formation and decay rates within the experimental turn over frequency of CrHydA1. In addition, Sanchez and coworkers found that proton transfer was not the limiting step in the catalytic process but

instead the rate limiting step was proposed to be the physical release of H_2 from the protein structure.[191]

A more recent study by Lorent and coworkers, published in 2020, elucidated two additional reaction intermediates of CrHydA1 via cryogenic infrared and electron paramagnetic resonance spectroscopy. In addition to the previously reported H_{ox}, H_{red}, $H_{red}H^+$, $H_{sred}H^+$, and H_{hyd} states, Lorent and coworkers reported the presence of $H_{hyd:red}$ and $H_{hyd:ox}$ catalytic intermediates. The presence of these two states indicates that the reaction pathway may additional reaction channels leading to the H_{hyd} state.[192]

In a recent publication by Artz and Coworkers in 2020, [FeFe]-hydrogenases CpI, CpII, and CpIII of Clostridium pasteurianum were compared by EPR spectroscopy, protein film electrochemistry, FTIR spectroscopy, and computational modeling in order to investigate the variables which effect the catalytic bias of proton reduction versus hydrogen oxidation. While X-ray structures of CpII and CpIII have yet to be obtained, homology structures generated based on CpI elucidated the role of secondary coordination sphere interactions via amino acids at the Met353 and Ser357 position. The differences in stabilization of catalytic intermediates through secondary interactions of Met353 with the carbonyls of the diiron cluster and Ser357 with the [4Fe4S] cubane or lack thereof were shown to attribute to the large range in catalytic biases in CpI, CpII, and CpIII.[193]

In addition to IR studies, ^{1}H NMR studies of the active site of Chlamydomonas reinhardtii (HydA1) has been successfully achieved for the first time. In a report from Rumpel and coworkers, apo-HydA1 and HydA1 were analyzed via paramagnetic NMR. Rumpel and coworkers found that the cysteine and bridging azadithiolate protons are contact shifted outside of the diamagnetic envelope (-1 to 11 ppm) to a range of (-30 to 80 ppm) with the degree of the contact shift dependent

on spin state of the attached iron cluster, spin density at the nucleus, the dihedral angle of Fe−S−Cβ−$\beta$$CH_2$, as well as the temperature of the sample. The capability to analyze the native hydrogenase enzyme via NMR allows for novel insights into the electronic and geometric states required for catalysis.[194]

In addition to researching the geometric and electronic conditions of the native enzyme's active site which allows for hydrogen reduction research has been increasingly focused on the proton transfer pathway. In 2018 Duan and coworkers were able to assign the proton transfer pathway to cysteine C169, water 826, glutamic acids E141 and E144, serine residue S189, and arginine R148 in HydA1 through extensive site directed mutagenesis of CpI and HydA1 and characterization via in situ attenuated total reflection Fourier transform infrared spectroscopy and x-ray crystallography.[195] Further research by Senger and coworkers in 2019 suggests that glutamic acid residue E141 and arginine R148 are essential for the facilitation of bidirectional proton transfer influencing the catalytic bias of hydrogen evolution.[196]

While [FeFe]-hydrogenases are excellent catalysts for the reduction of protons to generate hydrogen, [FeFe]-hydrogenases are known to be extremely sensitive to oxygen. Recent studies by Esselborn and coworkers has led to the first isolation and structural characterization of CpI which have undergone degradation via oxygen interactions. Esselborn and coworkers found that the active site of CpI when exposed to oxygen undergoes degradation through two distinct pathways. The first pathway involves the dissociation of the distal iron atom potentially caused by the formation of a Fe(IV)=O^{2-} specie intermediate at the distal iron. The second pathway involves the formation of H2O2 and OOH radicals intermediates at the distal Fe which diffuse and react with the distal [4Fe4S] cluster which result in the conversion of the [4Fe4S] cluster to a [2Fe- 2S] cluster. The illumination of the degradation pathways allows for a greater perspective in the

challenges required to engineer oxygen resistant [FeFe]-hydrogenases and [FeFe] model complexes.[197]

While extensive research has occurred in the native [FeFe]-hydrogenases, synthetic chemists have continued to tune the electronics of [FeFe] model complexes. Within the last two years there has a been an increase in the use of phosphine ligands to replicate the electronics of the native cyanide ligands, including the use of 4-diphenylphosphinopyridine, 1,3,5-triaza-7-phosphaadamantane, 1,1-Bis(diphenylphosphino)-methane, amongst others.[198–201] While capable of catalytically reducing protons to hydrogen these model complexes lack proton shuttling motifs which allow for efficient catalysis.

In research of effective bridging ligands, the field of biomimetic model complexes has diverged from current findings in native enzymes. To rationalize the proton shuttling behavior of the aza bridging ligands, Aster and coworkers reported the characterization of (μ-aza)diiron(I) hexacarbonyl and (μ-aza)diiron(I) tetracarbonyl bis(trimethylphosphine) via real-time infrared and UV-Vis spectroscopies during electron and proton transfers in 2019. Aster and coworkers hypothesized that the aza bridging ligand may not be acting as a proton shuttle but rather is changing the geometry of the diiron cluster upon protonation and thus reducing the reorganization energy for hydride formation.[202]

Thus, new bridging ligands published which have focused on the decrease in overpotentials required for proton reduction rather than the inclusion of proton shuttling motifs have been justified. Research published by Watanabe and coworkers in 2019, presented the first set of hydrogenase mimic complexes to incorporate tetracene motifs into the bridging ligand of the diiron complex. These complexes were found to have turn over frequencies in the range of 2.2 to 2.7 h^{-1} which is lower than the turn over frequencies found in (μ-pdt)$Fe_2(CO)_6$ under similar

conditions.[203] Research by Schippers and coworkers in 2019 resulted in the synthesis of a set of κ^2-C,N-Pyridine bridged model complexes which were able to catalyze proton reduction with an overpotential of 120 mV.[204] Thus, Schippers and coworkers reported the lowest overpotential for a [FeFe] model complex.

In addition to small molecules, a novel artificial [FeFe]-hydrogenase enzyme has been reported in 2019 by the incorporation of a $[Fe_2\{(\mu\text{-}SC_2H_4)(\mu\text{-}SCH)(CH_2)_4COOH\}(CO)_6]$ model complex and rubidium photosensitizer into horse spleen apoferritin. It was found that the incorporation of $[Fe_2\{(\mu\text{-}SC_2H_4)(\mu\text{-}SCH)(CH_2)_4COOH\}(CO)_6]$ into the non-native protein led to a one order of magnitude increase in the catalysis of proton reduction in comparison to the homogenous photocatalytic system.[205]

In 2018, Brezinski and coworkers improved upon the work of Tooley et al.[60] and generated the first water soluble, single active site [FeFe]-metallopolymer synthesized by atom-transfer radical polymerization (ATRP). The new [2Fe-2S] cored poly 2-(dimethylamino)ethyl methacrylate (DMAEMA) was shown to be stable under aerobic conditions during catalysis with turnover frequencies extrapolated to 250,000 s^{-1} and mild overpotential of 0.3V.[206] The synthesis of this polymeric model complex marked a turning point in the use of diiron hydrogenase mimics as viable hydrogen evolution catalysts for use in a hydrogen economy.

Thus in the last two years, the field of [FeFe]-Hydrogenase and [FeFe] model complexes has seen the elucidation of catalytic intermediates of the native *Clostridium acetobutylicum* (CaI) and *Chlamydomonas reinhardtii* (CrHydA1) enzymes, the identification of the residues of native enzymes comprising the proton transfer pathway, the isolation and characterization of the[FeFe]-Hydrogenase post oxygen degradation, and the elucidation of alternative mechanisms for the increase in catalytic activity of aza bridged clusters over their alkyl homologs. While small

molecule complexes have yet exceeded the catalytic activity of the native enzymes under mild conditions, insights from the research in the native enzymes may pave the way forward for generating synthetic hydrogen reduction catalysts such as in the case of the [2Fe-2S] cored poly 2-(dimethylamino)ethyl methacrylate polymers which may be used to sustain a hydrogen fuel economy in the future.

Summary of Contributions to the Field of Diiron Hydrogenase Enzymes

In the attempt to synthesize an artificial biotinylated diiron cluster, several reaction routes for the formation of a biotinylated diiron cluster were explored. These attempted synthesis led to the identification of roadblocks in the proposed synthetic pathways as well as the isolation of novel [FeFe] complexes.

It was found that photoreactions involving (μ-allylazadithiolato)diiron(I) hexacarbonyl in the 254 to 360 nm light range will predominately result in decomposition of the diiron cluster due to its high molar absorptivity in this range. In order to successfully complete a photoreaction involving (μ-allylazadithiolato)diiron(I) hexacarbonyl the excitation wavelength should be greater than 400 nm based on UV-vis spectroscopy of (μ-allylazadithiolato)diiron(I) hexacarbonyl or the solution must be ultra-dilute. In addition (μ-allylazadithiolato)diiron(I) hexacarbonyl were found to be thermally unstable at temperatures greater than 60°C, limiting the possible chemistries involved in the coupling of (μ-allylazadithiolato)diiron(I) hexacarbonyl to other chemical system.

In addition to elucidating the road blocks involved with radical initiated reactions of (μ-allylazadithiolato)diiron(I) hexacarbonyl, a novel biotin[n]uril-diiron hexacarbonyl adduct macrocycle was may have been synthesized when attempting to use biotinylated-3,6-dioxaoctane-1,8-diamine in a condensation reaction with formaldehyde and bishydrothiodiiron hexacarbonyl. Due to biotin[n]uril-diiron hexacarbonyl adduct being an undesired product for the biotin-avidin

artificial hydrogenase project, full characterization was not achieved though it has potential to be an interesting model complex. In an alternative reaction pathway to obtain a biotinylated diiron cluster, a novel water soluble (μ-propanedithiolato)diiron 4-aminopheynylisocyano pentacarbonyl complex was synthesized. As the (μ-propanedithiolato)diiron 4-aminopheynylisocyano pentacarbonyl complex was synthesized at the end of the artificial hydrogenation project lifeline and the 4-aminophenylisocyanide was shown to be incompatible with amide coupling chemistry, further characterization of (μ-propanedithiolato)diiron 4-aminopheynylisocyano pentacarbonyl through x-ray crystallography and electrochemistry was not sought. In futures studies it may be of interest it may be worthwhile to collect electrochemical data of aza diiron clusters with 4-aminopheynylisocyanide and 4-iodophenylisocyanide ligands as cyanide analogs for the study of tuning the electronic environment of the diiron cluster.

The most successful synthetic strategy pursued was the Sonogashira coupling of Boc-protected biotinylated propargylamine with (μ-propanedithiolato)diiron 4-iodopheynylisocyano pentacarbonyl which led to the isolation of a Boc-protected-biotinylated diiron cluster in extremely low yields. With further research, optimization of the Sonogashira conditions and variation of acid conditions for deprotection may eventually lead to the synthesis of a biotinylated diiron cluster compatible with avidin binding for the generation of artificial hydrogenase enzyme.

As an additional potential alternative route to generate biotinylated diiron cluster, Merinero and coworkers has reported the synthesis of triazole containing [FeFe] hydrogenase mimics which have been shown to undergo azide-alkyne click reactions in moderate to good yields (43-85%).[207] Future attempts to synthesize biotinylated diiron clusters may result from the azide-alkyne click reaction of one of these triazole containing [FeFe] hydrogenase mimics with biotinylated propargylamine.

While unsuccessful in the synthesis of an artificial hydrogenase enzyme based on biotin-avidin technology, these attempted synthesis led to the identification of roadblocks in the proposed synthetic pathways as well as the isolation of novel [FeFe] complexes. (μ-Propanedithiolato)diiron 4-aminopheynylisocyano pentacarbonyl which was synthesized to generate a biotinylated diiron cluster through amide coupling holds potential interest as an analog to μ-Propanedithiolato)diiron(I) pentacarbonyl cyano in electrochemical studies in comparison to the current phosphine analogs explored in the past few years. In addition, several modifications which may increase the viability of the various reaction pathways have been suggested based on experimental data.

Current State of the Field of Polymeric Catalysts

The field of polymeric catalysts is continuing to flourish. The goal of designing polymeric catalysts has extended past the modeling of specific enzymes and has grown to encompass a broader scope of catalysis. In this section the most recent developments in the field of polymeric catalysts will be reviewed.

As noted in the current state of the field of diiron hydrogenase section, In 2018, Brezinski and coworkers improved upon the work of Tooley et al.[60] and generated the first water soluble, single active site [FeFe]-metallopolymer synthesized by atom-transfer radical polymerization (ATRP). The new [2Fe-2S] cored poly 2-(dimethylamino)ethyl methacrylate (DMAEMA) polymer took advantage of the polymer scaffold to imbed the active catalyst in an amine rich environment which was hypothesized by Dey and coworkers[208] to reduce the deactivation of diiron clusters by oxygen. The new [2Fe-2S] cored poly(DMAEMA) polymer was shown to be stable

under aerobic conditions during catalysis with turnover frequencies extrapolated to 250,000 s^{-1}.[206] Marking a vast improvement of the polymeric enzyme model over small molecule models.

Research by Zimmerman group of the University of Illinois reported the development of a series of copper cross-linked single-chain organic nanoparticles for the catalysis of alkyne-azide cycloaddition reactions.[209,210] In the research published in 2018, Chen and coworkers of the Zimmerman group reported the first iteration of the copper cross-linked single-chain organic nanoparticles with cationic, anionic, zwitterionic, and neutral water-solubilizing groups. By systematically varying the size and copper content of the polymer system as well as the charge and hydrophobicity of the substrates Chen and coworkers were able to probe structure-activity relationships of the SCNP systems. The optimization of artificial enzyme -substrate interactions resulting in the conclusion that the rate of reaction is more dependent on the substrate binding interactions than the size of the polymer or copper content.[209] In 2019, Chen and coworkers reported a second generation of copper containing single-chain organic nanoparticle capable of catalyzing alkyne-azide cycloaddition reactions. Chen and coworkers unexpectedly discovered that in addition to the observation that polymeric catalyst selectively bound small molecule substrates, the new generation of alkyne-azide catalyst adaptively and reversibly bound protein surfaces allowing for dramatic accelerations of protein surface modifications.[210]

In addition to mimicking enzyme activity, research into polymer enzymes as multifunctional catalytic systems has been reported with the last few years. Recently a bifunctional polymeric catalyst was designed by Sun and coworkers for a one-pot deacetalization-Knoevenagel reaction. In their 2019 publication Sun and Coworkers reported the synthesis of a poly((divinylbenzene)–amine–styrenesulfonic acid) copolymer via two separate synthetic routes. Sun and Coworkers found that the use of solvothermal synthesis of the poly((divinylbenzene)–

styrenesulfonic acid) copolymer followed by post-polymerization resulting in a porous derivative which led to an increase in catalytic efficiency and reusability. Whereas solvothermal synthesis of the poly((divinylbenzene) derivative followed by sequential post polymerization to incorporate sulfonic and amine groups led to poor yields in the catalysis of the one-pot deacetalization-Knoevenagel reaction.

In the past two years, two new polymeric porphyrin catalysts have been reported. In 2018, Banerjee and Nabee reported the synthesis and characterization of a series of poly(5,10,15,20-Tetrakis(4-aminophenyl)porphyrin iron(III) chloride) polymers (PFeTAPP) with dialdehyde linkers for the reduction of oxygen. Banerjee and Nabee found that while the polymerization process lacked the desired control of porosity, the resulting PFeTAPP derivatives show moderate to high oxygen reduction activity.[211]

The most recently reported polymeric porphyrin catalyst was designed by Rajendiran, Ganesan, and Yoon. In their 2019 report, Rajendiran, Ganesan, and Yoon presented the synthesis of a series of porous organic polymer porphyrin chromium tetracarbonyl cobaltate POP-[TPPCr][Co(CO)4] with the goal of heterogenization of the homogeneous catalyst tetraphenylporphyrin chromium tetracarbonyl cobaltate [TPPCr][Co(CO)4]. Rajendiran, Ganesan, and Yoon found that lower molecular weight porous polymers functioned at similar reaction rates to the homogeneous [TPPCr][Co(CO)4] for the formation of lactones from epoxides and carbon monoxide, whereas the higher molecular weight polymers suffered a slightly lower turnover frequency but benefitted from increased stability, recyclability, and reusability.[212]

In summary, recently reported polymeric catalysts have been used in a diverse range of catalytic reactions. An increase in interest in the structure-function relationship of has led to the synthesis of a polymeric artificial hydrogenase enzyme which protects the diiron core from

degradation by oxygen and outperforms small molecule analogs as well as optimization of an alkyne-azide cycloaddition catalyst. While there have been few reports of polymeric porphyrin catalysts over the last two years, the new reports provided evidence of increased stability of the catalysts due to incorporation into polymer scaffolds.

Summary of Contributions to the Field of Polymeric Catalysts

The research in this dissertation in the field of polymeric catalysts focused on the study of secondary coordination sphere interactions and structure-function relationships within polymeric systems. In order to elucidate the hydrogen bonding environment surrounding the binding pocket within porphyrin cored polymers via a cyanide molecular probe in conjunction with ^{15}N NMR spectroscopy of a series of porphyrin cored star polymers and polymeric nanoparticles of varying degrees of potential hydrogen bonding character. The novel series of zinc porphyrin cored polymers (PCSP) and polymeric nanoparticles (PCPN) synthesized and characterized for this study included Zn^{II}(Por(MMA-co-AMMA)$_4$) {PCSP-1 : PCPN-1}, Zn^{II}(Por(HexMAAm-co-AMMA)$_4$) {PCSP-2 : PCPN-2}, Zn^{II}(Por(iPMAAm-co-AMMA)$_4$) {PCSP-3 : PCPN-3}, Zn^{II}(Por(HEMA-co-AMMA)$_4$) {PCSP-4 : PCPN-4}, and Zn^{II}(Por(MMAAm-co-AMMA)$_4$) {PCSP-5 : PCPN-5}.

UV-vis spectroscopy studies of the series of the cyanide bound porphyrin cored polymers and nanoparticles revealed varying degrees of instability when solvated by N,N-dimethylformamide which was to be used as the NMR solvent for the hydrogen bonding experiments. While the Zn-cyanide adducts were not stable in the desired NMR solvent on a ^{15}N NMR timescale, studying the reaction of cyanide and DMF in the presence of the PCSP and PCPN species via UV-Vis spectroscopy elucidated the significant roll the functionalization and topology of the polymer scaffold played in the reactivity at the porphyrin core.

In the study all zinc PCSP and PCPN species catalyzed the reaction of sodium cyanide and DMF to generate dimethylamine and in the presence of atmospheric carbon dioxide and water subsequently generated sodium carbonate. The ester backboned PCSP and PCPN species were found to form the least reactive Zn-cyanide adducts of the series while the amide and ethanolamide species containing a greater number of potential hydrogen bond donors and greater steric bulk showed the greatest reactivity. In addition, for all polymer species studied the folded particle topology formed more reactive cyanide adducts than the random coil topologies leading to higher yields of sodium carbonate under ambient conditions and shorter Zn-cyanide adduct lifetimes.

This project was the first study which was able to systematically reveal structure function relationships due to differences in polymer topologies (random coil vs nanoparticle) and hydrogen bonding environments afforded by the polymer scaffold.

LIST OF REFERENCES

(1) Manchester, K. L. The Crystallization of Enzymes and Virus Proteins: Laying to Rest the Colloidal Concept of Living Systems. *Endeavour* **2004**, *28* (1), 25–29.

(2) Katchalski, E.; Fasman, G. D.; Simons, E.; Blout, E. R.; Gurd, F. R. N.; Koltun, W. L. Synthetic Histidine-Containing Polypeptides as Catalysts for the Hydrolysis of p-Nitrophenyl Acetate. *Arch. Biochem. Biophys.* **1960**, *88* (2), 361–365.

(3) Hennrich, N.; Cramer, F. Inclusion Compounds. XVIII. The Catalysis of the Fission of Pyrophosphates by Cyclodextrin. A Model Reaction for the Mechanism of Enzymes. *J. Am. Chem. Soc.* **1965**, *87* (5), 1121–1126.

(4) Cramer, F.; Kampe, W. Inclusion Compounds. XVII. Catalysis of Decarboxylation by Cyclodextrins. A Model Reaction for the Mechanism of Enzymes. *J. Am. Chem. Soc.* **1965**, *87* (5), 1115–1120.

(5) Breslow, R.; Overman, L. E. An "Artificial Enzyme" Combining a Metal Catalytic Group and a Hydrophobic Binding Cavity. *J. Am. Chem. Soc.* **1970**, *92* (4), 1075–1077.

(6) Letsinger, R. L.; Savereide, T. J. Selectivity in Solvolyses Catalyzed by Poly-(4-Vinylpyridine). *J. Am. Chem. Soc.* **1962**, *84* (16), 3122–3127.

(7) Sheehan, J. C.; Bennett, G. B.; Schneider, J. A. Synthetic Peptide Models of Enzyme Active Sites. III. Stereoselective Esterase Models. *J. Am. Chem. Soc.* **1966**, *88* (14), 3455–3456.

(8) Sakurada, I.; Sakaguchi, Y.; Ono, T.; Ueda, T. Homogeneous Hydrolysis of Esters with Polymer Sulfonic Acids. *Die Makromol. Chemie* **1966**, *91* (1), 243–263.

(9) Morawetz, H.; Overberger, C. G.; Salamone, J. C.; Yaroslavsky, S. Selective Catalytic Effects of Strongly Ionizing Polycations on Ester Solvolysis. *J. Am. Chem. Soc.* **1968**, *90* (3), 651–656.

(10) Klotz, I. M.; Stryker, V. H. Macromolecule-Small Molecule Interactions. A Synthetic Macromolecule with High Esterolytic Activity. *J. Am. Chem. Soc.* **1968**, *90* (10), 2717–2719.

(11) Klotz, I. M.; Royer, G. P.; Scarpa, I. S. Synthetic Derivatives of Polyethyleneimine with Enzyme-Like Catalytic Activity (Synzymes). *Proc. Natl. Acad. Sci.* **1971**, *68* (2), 263–264.

(12) Breslow, B. R. CENTENARYLECTURE Biomimetic Chemistry. *Chem. Soc. Rev.* **1972**, *1*, 553–580.

(13) Breslow, R. Biomimetic Control of Chemical Selectivity. *Acc. Chem. Res.* **1980**, *13* (6), 170–177.

(14) Hutchison, A.; Phillips, S.; Edge, H.; Vt, W. Mutagenesis at a Specific Position in a DNA

Sequence. *J. Biol. Chem.* **1978**, *253* (18), 6551–6560.

(15) Gerlt, J. A. Relationships between Enzymatic Catalysis and Active Site Structure Revealed by Applications of Site-Directed Mutagenesis. *Chem. Rev.* **1987**, *87*, 1079–1105.

(16) Goldsmith, M.; Tawfik, D. S. Directed Enzyme Evolution : Beyond the Low-Hanging Fruit. *Curr. Opin. Struct. Biol.* **2012**, *22* (4), 406–412.

(17) Schwizer, F.; Okamoto, Y.; Heinisch, T.; Gu, Y.; Pellizzoni, M. M.; Lebrun, V.; Reuter, R.; Köhler, V.; Lewis, J. C.; Ward, T. R. Artificial Metalloenzymes: Reaction Scope and Optimization Strategies. *Chem. Rev.* **2018**, *118* (1), 142–231.

(18) Pollack, S. J.; Jacobs, J. W.; Schultz, P. G. Selective Chemical Catalysis by an Antibody. *Science (80-.).* **1986**, *234* (4783), 1570–1573.

(19) Lerner, R. A.; Benkovic, S. J.; Schultz, P. G. At the Crossroads of Chemistry and Immunology : Catalytic Antibodies. *Science.* **1991**, *252* (5006), 659–667.

(20) Prudent, J. R.; Uno, T.; Schultz, P. G. Expanding the Scope of RNA Catalysis. *Science.* **1994**, *264* (June), 1924-1927.

(21) Li, Y.; Sen, D. Toward an Efficient DNAzyme †. **1997**, *2960* (96), 5589–5599. https://doi.org/10.1021/bi962694n.

(22) Lu, Y. Metalloprotein and Metallo-DNA/RNAzyme Design: Current Approaches, Success Measures, and Future Challenges. *Inorg. Chem.* **2006**, *45* (25), 155–158. https://doi.org/10.1021/ic052007t.

(23) Manea, F.; Houillon, F. B.; Pasquato, L.; Scrimin, P. Nanozymes: Gold-Nanoparticle-Based Transphosphorylation Catalysts. *Angew. Chem. Int. Ed. 2004*, **2004**, *43* (45), 6165–6169. https://doi.org/10.1002/anie.200460649.

(24) Green, N. M. Avidin. *Adv. Protein Chem.* **1975**, *29*, 85–133.

(25) Flower, D. R. The Lipocalin Protein Family : Structure and Function. **1996**, *14*, 1–14.

(26) Rosano, C.; Arosio, P.; Bolognesi, M. The X-Ray Three-Dimensional Structure of Avidin. *Biomol. Eng.* **1999**, *16* (1–4), 5–12.

(27) Eakin, R. E.; Snell, E. E.; Williams, R. J. Concentration and Assay of Avidin, The Injury-Producing Protein in Raw Egg White. *J. Biol. Chem. 1941*, **1941**, *140*, 535–543.

(28) Livnah, O.; Bayer, E. A.; Wilchek, M.; Sussman, J. L. Three-Dimensional Structures of Avidin and the Avidin-Biotin Complex. *Proc. Natl. Acad. Sci. U. S. A.* **1993**, *90* (11), 5076–5080.

(29) PyMol,The PyMOL Molecular Graphics System, Version 2.0. Schrödinger, LLC.

(30) Diamandis, E. P.; Christopoulos, T. K. The Biotin-(Strept)Avidin System: Principles and Applications in Biotechnology. *Clin. Chem.* **1991**, *37* (5), 625–636.

(31) Wilcheck, M.; Bayer, E. A. The Avidin-Biotin Complex in Bioanalytical Appications. *Anal. Biochem.* **1988**, *171*, 1–32.

(32) Sakahara, H.; Saga, T. Avidin-Biotin System for Delivery of Diagnostic Agents. *Adv. Drug Deliv. Rev.* **1999**, *37* (1–3), 89–101.

(33) He, B.; Velaparthi, S.; Pieffet, G.; Pennington, C.; Mahesh, A.; Holzle, D. L.; Brunsteiner, M.; Van Breemen, R.; Blond, S. Y.; Petukhov, P. A. Binding Ensemble Profiling with Photoaffinity Labeling (BEProFL) Approach: Mapping the Binding Poses of HDAC8 Inhibitors. *J. Med. Chem.* **2009**, *52* (22), 7003–7013.

(34) Heinisch, T.; Ward, T. R. Design Strategies for the Creation of Artificial Metalloenzymes. *Curr. Opin. Chem. Biol.* **2010**, *14* (2), 184–199.

(35) Collot, J.; Gradinaru, J.; Humbert, N.; Skander, M.; Zocchi, A.; Ward, T. R. Artificial Metalloenzymes for Enantioselective Catalysis Based on Biotin−Avidin. *J. Am. Chem. Soc.* **2003**, *125* (30), 9030–9031.

(36) Letondor, C.; Pordea, A.; Humbert, N.; Ivanova, A.; Mazurek, S.; Novic, M.; Ward, T. R. Artificial Transfer Hydrogenases Based on the Biotin−(Strept)Avidin Technology: Fine Tuning the Selectivity by Saturation Mutagenesis of the Host Protein. *J. Am. Chem. Soc.* **2006**, *128* (25), 8320–8328.

(37) Ward, T. R. Artificial Metalloenzymes Based on the Biotin−Avidin Technology: Enantioselective Catalysis and Beyond. *Acc. Chem. Res.* **2011**, *44* (1), 47–57.

(38) Liang, A. D.; Serrano-Plana, J.; Peterson, R. L.; Ward, T. R. Artificial Metalloenzymes Based on the Biotin–Streptavidin Technology: Enzymatic Cascades and Directed Evolution. *Acc. Chem. Res.* **2019**, *52* (3), 585–595.

(39) Wilson, M. E.; Whitesides, G. M. Conversion of a Protein to a Homogeneous Asymmetric Hydrogenation Catalyst by Site-Specific Modification with a Diphosphinerhodium(I) Moiety. *J. Am. Chem. Soc.* **1978**, *100*, 306–307.

(40) Klein, G.; Humbert, N.; Gradinaru, J.; Ivanova, A.; Gilardoni, F.; Rusbandi, U. E.; Ward, T. R. Tailoring the Active Site of Chemzymes by Using a Chemogenetic-Optimization Procedure: Towards Substrate-Specific Artificial Hydrogenases Based on the Biotin–Avidin Technology. *Angew. Chemie - Int. Ed.* **2005**, *44* (47), 7764–7767.

(41) Letondor, C.; Humbert, N.; Ward, T. R. Artificial Metalloenzymes Based on Biotin-Avidin Technology for the Enantioselective Reduction of Ketones by Transfer Hydrogenation. *Proc. Natl. Acad. Sci. U. S. A.* **2005**, *102* (13), 4683–4687.

(42) Schwizer, F.; Köhler, V.; Dürrenberger, M.; Knörr, L.; Ward, T. R. Genetic Optimization of the Catalytic Efficiency of Artificial Imine Reductases Based on Biotin-Streptavidin Technology. *ACS Catal.* **2013**, *3* (8), 1752–1755.

(43) Dürrenberger, M.; Heinisch, T.; Wilson, Y. M.; Rossel, T.; Nogueira, E.; Knörr, L.; Mutschler, A.; Kersten, K.; Zimbron, M. J.; Pierron, J.; et al. Artificial Transfer Hydrogenases for the Enantioselective Reduction of Cyclic Imines. *Angew. Chemie - Int. Ed.* **2011**, *50* (13), 3026–3029.

(44) Okamoto, Y.; Köhler, V.; Paul, C. E.; Hollmann, F.; Ward, T. R. Efficient in Situ Regeneration of NADH Mimics by an Artificial Metalloenzyme. *ACS Catal.* **2016**, *6* (6), 3553–3557.

(45) Betanzos-Lara, S.; Liu, Z.; Habtemariam, A.; Pizarro, A. M.; Qamar, B.; Sadler, P. J. Organometallic Ruthenium and Iridium Transfer-Hydrogenation Catalysts Using Coenzyme NADH as a Cofactor. *Angew. Chemie - Int. Ed.* **2012**, *51* (16), 3897–3900.

(46) Pierron, J.; Malan, C.; Creus, M.; Gradinaru, J.; Hafner, I.; Ivanova, A.; Sardo, A.; Ward, T. R. Artificial Metalloenzymes for Asymmetric Allylic Alkylation on the Basis of the Biotin-Avidin Technology. *Angew. Chemie - Int. Ed.* **2008**, *47* (4), 701–705.

(47) Pordea, A.; Mathis, D.; Ward, T. R. Incorporation of Biotinylated Manganese-Salen Complexes into Streptavidin: New Artificial Metalloenzymes for Enantioselective Sulfoxidation. *J. Organomet. Chem.* **2009**, *694* (6), 930–936.

(48) Thomas, C. M.; Letondor, C.; Humbert, N.; Ward, T. R. Aqueous Oxidation of Alcohols Catalyzed by Artificial Metalloenzymes Based on the Biotin-Avidin Technology. *J. Organomet. Chem.* **2005**, *690* (20 SPEC. ISS.), 4488–4491.

(49) Lo, C.; Ringenberg, M. R.; Gnandt, D.; Wilson, Y.; Ward, T. R. Artificial Metalloenzymes for Olefin Metathesis Based on the Biotin-(Strept)Avidin Technology. *Chem. Commun.* **2011**, *47* (44), 12065–12067.

(50) Merguet, M.; Bonduelle, C.; Lecommandoux, S. Multicompartmentalized Polymeric Systems : Towards Biomimetic Cellular Structure and Function. *Chem Soc Rev* **2013**, *42* (2), 512–529.

(51) Palivan, C. G.; Fischer-Onaca, O.; Delcea, M.; Itel, F.; Wolfgang, M. Protein–Polymer Nanoreactors for Medical Applications. *Chem Soc Rev* **2012**, *41*, 2800–2823.

(52) Drotleff, S.; Lungwitz, U.; Breunig, M.; Dennis, A.; Blunk, T.; Tessmar, J.; Go, A. Biomimetic Polymers in Pharmaceutical and Biomedical Sciences. *Eur. J. Pharm. Biopharm.* **2004**, *58*, 385–407.

(53) Wen, G.; Guo, Z.; Liu, W. Biomimetic Polymeric Superhydrophobic Surfaces and Nanostructures: From Fabrication to Applications. *Nanoscale* **2017**, *9*, 3338–3366.

(54) Pomposo, A. Bioinspired Single-Chain Polymer Nanoparticles. *Polym Int* **2014**, *63*, 589–592.

(55) Kofoed, J.; Reymond, J. Dendrimers as Artificial Enzymes. *Curr. Opin. Chem. Biol.* **2005**, *9*, 656–664.

(56) Latorre-Sánchez, A.; Pomposo, J. A. Recent Bioinspired Applications of Single-Chain Nanoparticles. *Polym. Int.* **2016**, *65* (8), 855–860.

(57) Kiefer, H. C.; Congdon, W. I.; Scarpa, I. S.; Klotz, I. M. Catalytic Accelerations of 1012-Fold by an Enzyme-Like Synthetic Polymer. *Proc. Natl. Acad. Sci.* **1972**, *69* (8), 2155–2159.

(58) Sanchez-sanchez, A.; Akbari, S.; Etxeberria, A.; Arbe, A.; Gasser, U.; Moreno, A. J.; Colmenero, J.; Pomposo, J. A. " Michael " Nanocarriers Mimicking Transient-Binding Disordered Proteins. *ACS Macro Lett.* **2013**, *2*, 491–495.

(59) Colmenero, J.; Pomposo, J. A. Endowing Single-Chain Polymer Nanoparticles with

Enzyme-Mimetic Activity. *ACS Macro Lett.* **2013**, *2*, 775–779.

(60) Tooley, C. A.; Pazicni, S.; Berda, E. B. Toward a Tunable Synthetic [FeFe] Hydrogenase Mimic: Single-Chain Nanoparticles Functionalized with a Single Diiron Cluster. *Polym. Chem.* **2015**, *6* (44), 7646–7651.

(61) Rodriguez, K. J.; Hanlon, A. M.; Lyon, C. K.; Cole, J. P.; Tuten, B. T.; Tooley, C. A.; Berda, E. B.; Pazicni, S. Porphyrin-Cored Polymer Nanoparticles: Macromolecular Models for Heme Iron Coordination. *Inorg. Chem.* **2016**, *55* (19), 9493–9496.

(62) Lubitz, W.; Ogata, H.; Rüdiger, O.; Reijerse, E. Hydrogenases. *Chem. Rev.* **2014**, *114* (8), 4081–4148.

(63) Adams, M. W. W.; Mortenson, L. E.; Chen, J.-S. HYDROGENASE. *Biochem. Biophys. Acta* **1981**, *594*, 105–176.

(64) Adams, M. W. W. The Structure and Mechanism of Iron-Hydrogenases. *Biochim. Biophys. Acta* **1990**, *1020*, 115–145.

(65) Frey, M. Hydrogenases: Hydrogen-Activating Enzymes. *ChemBioChem* **2002**, *3* (2–3), 153–160.

(66) Fontecilla-Camps, J. C.; Volbeda, A.; Cavazza, C.; Nicolet, Y. Structure/Function Relationships of [NiFe]- and [FeFe]-Hydrogenases. *Chem. Rev.* **2007**, *107* (10), 4273–4303.

(67) Vignais, P. M.; Billoud, B.; Meyer, J. Classification and Phylogeny of Hydrogenases. *FEMS Microbiol. Rev.* **2001**, *25*, 455–501.

(68) Vignais, P. M.; Billoud, B. Occurrence , Classification , and Biological Function of Hydrogenases : An Overview. *Chem. Rev.* **2007**, *107*, 4206–4272.

(69) Tamagnini, P.; Axelsson, R.; Lindberg, P.; Oxelfelt, F.; Wünschiers, R.; Lindblad, P. Hydrogenases and Hydrogen Metabolism of Cyanobacteria. *Microbiol. Mol. Biol. Rev.* **2002**, *66* (1), 1–20.

(70) Tamagnini, P.; Leita, E.; Oliveira, P.; Ferreira, D.; Pinto, F.; Harris, D. J.; Heidorn, T.; Lindblad, P. Cyanobacterial Hydrogenases : Diversity , Regulation and Applications. *FEMS Microbiol Rev* **2007**, *31*, 692–720.

(71) Kaserer, H. Die Oxydation Des Wasser-Stoffes Durch Mikroorganismen. *Centr. Bakt. Par.* **1906**, *16* (II), 681–696.

(72) Stephenson, M.; Stickland, L. H. Hydrogenase: A Bacterial Enzyme Activating Molecular Hydrogen. *Biochem. J.* **1931**, *25* (1), 205–214.

(73) Volbeda, A.; Garcin, E.; Piras, C.; Lacey, A. L. De; Fernandez, V. M.; Hatchikian, E. C.; Frey, M.; Fontecilla-camps, J. C. Structure of the [NiFe] Hydrogenase Active Site : Evidence for Biologically Uncommon Fe Ligands. *J. Am. Chem. Soc.* **1996**, *118*, 12989–12996.

(74) Garcin, E.; Vernede, X.; Hatchikian, E. C.; Volbeda, A.; Frey, M.; Fontecilla-Camps, J. C. The Crystal Structure of a Reduced [NiFeSe] Hydrogenase Provides an Image of the

Activated Catalytic Center. *Struct.* **1999**, *7* (5), 557–566.

(75) Nicolet, Y.; Rubach, J. K.; Posewitz, M. C.; Amara, P.; Mathevon, C.; Atta, M.; Fontecave, M.; Fontecilla-camps, J. C. X-Ray Structure of the [FeFe] -Hydrogenase Maturase HydE from Thermotoga Maritima. *J. Biol. Chem.* **2008**, *283* (27), 18861–18872.

(76) Shima, S.; Pilak, O.; Vogt, S.; Schick, M.; Stagni, M.; Meyer-klaucke, W.; Warkentin, E.; Thauer, rudolf k; Ermler, U. The Crystal Structure of [Fe]-Hydrogenase Reveals the Geometry of the Active Site. *Science (80-.).* **2008**, *321* (July), 572–576.

(77) Wombwell, C.; Caputo, C. A.; Reisner, E. [NiFeSe]-Hydrogenase Chemistry. *Acc. Chem. Res.* **2015**, *48* (11), 2858–2865.

(78) Schlegel, H. G.; Schneider, K. Hydrogenases: Their Catalytic Activity, Structure and Function. In *Workshop Meeting Held in Goettingen, Germany*; 1978; p 452.

(79) Marbán, G.; Valdés-Solís, T. Towards the Hydrogen Economy? *Int. J. Hydrogen Energy* **2007**, *32* (12), 1625–1637.

(80) Crabtree, G. W.; Dresselhaus, M. S.; Buchanan, M. V. The Hydrogen Economy. *Phys. Today* **2004**, *57*, 39–44.

(81) Abbott, D. Keeping the Energy Debate Clean: How Do We Supply the World's Energy Needs? *Proc. IEEE* **2010**, *98* (1), 42–66.

(82) Esswein, A. J.; Nocera, D. G. Hydrogen Production by Molecular Photocatalysis. *Chem. Rev.* **2007**, *107* (10), 4022–4047.

(83) Melis, A.; Happe, T. Hydrogen Production . Green Algae as a Source of Energy. *Plant Physiol.* **2001**, *127*, 740–748.

(84) Lubitz, W.; Reijerse, E. J.; Messinger, J. Solar Water-Splitting into H2 and O2: Design Principles of Photosystem II and Hydrogenases. *Energy Environ. Sci.* **2008**, *1* (1), 15.

(85) Sun, L.; ??kermark, B.; Ott, S. Iron Hydrogenase Active Site Mimics in Supramolecular Systems Aiming for Light-Driven Hydrogen Production. *Coord. Chem. Rev.* **2005**, *249* (15-16 SPEC. ISS.), 1653–1663.

(86) Navarro, R. M.; Sanchez-Sanchez, M. C.; Alvarez-Galvan, M. C.; Valle, F. del; Fierro, J. L. G. Hydrogen Production from Renewable Sources: Biomass and Photocatalytic Opportunities. *Energy Environ. Sci.* **2009**, *2* (1), 35–54.

(87) Magnuson, A.; Anderlund, M.; Johansson, O.; Lindblad, P.; Lomoth, R.; Polivka, T.; Ott, S.; Stensjö, K.; Styring, S.; Sundström, V.; et al. Biomimetic and Microbial Approaches to Solar Fuel Generation. *Acc. Chem. Res.* **2009**, *42* (12), 1899–1909.

(88) Cook, T. R.; Dogutan, D. K.; Reece, S. Y.; Surendranath, Y.; Teets, T. S.; Nocera, D. G. Solar Energy Supply and Storage for the Legacy and Non Legacy Worlds. *Chem. Rev.* **2010**, *110* (11), 6474–6502.

(89) Vignais, P. M.; Billoud, B. Occurrence , Classification , and Biological Function of Hydrogenases : An Overview. **2007**, No. 0, 4206–4272.

(90) Hatchikian, E. C.; Forget, N.; Fernandez, V. M.; Williams, R.; Cammack, R. Further Characterization of the [Fe]-Hydrogenase from Desulfovibrio Desulfuricans ATCC 7757. *Eur. J. Biochem.* **1992**, *209* (1), 357–365.

(91) Kuchenreuther, J. M.; Grady-Smith, C. S.; Bingham, A. S.; George, S. J.; Cramer, S. P.; Swartz, J. R. High-Yield Expression of Heterologous [FeFe] Hydrogenases in Escherichia Coli. *PLoS One* **2010**, *5* (11), 4–11.

(92) Adamska-venkatesh, A.; Krawietz, D.; Siebel, J.; Weber, K.; Happe, T.; Reijerse, E.; Lubitz, W. New Redox States Observed in [FeFe] Hydrogenases Reveal Redox Coupling Within the H - Cluster. *J. Am. Chem. Soc.* **2014**, *136*, 11339–11346.

(93) Madden, C.; Vaughn, M. D.; Díez-p, I.; Brown, K. A.; King, P. W.; Gust, D.; Moore, A. L.; Moore, T. A. Catalytic Turnover of [FeFe] -Hydrogenase Based on Single-Molecule Imaging. *J. Am. Chem. Soc* **2012**, *134* (3), 1577–1582.

(94) Siebel, J. F.; Adamska-Venkatesh, A.; Weber, K.; Rumpel, S.; Reijerse, E.; Lubitz, W. Hybrid [FeFe]-Hydrogenases with Modified Active Sites Show Remarkable Residual Enzymatic Activity. *Biochemistry* **2015**, *54* (7), 1474–1483.

(95) Carroll, M. E.; Barton, B. E.; Rauchfuss, T. B.; Carroll, P. J. Synthetic Models for the Active Site of the [FeFe]-Hydrogenase: Catalytic Proton Reduction and the Structure of the Doubly Protonated Intermediate. *J. Am. Chem. Soc.* **2012**, *134* (45), 18843–18852.

(96) Nicolet, Y.; Piras, C.; Legrand, P.; Hatchikian, C. E.; Fontecilla-camps, J. C. Desulfovibrio Desulfuricans Iron Hydrogenase : The Structure Shows Unusual Coordination to an Active Site Fe Binuclear Center. *Structure* **1999**, *7* (1), 13–23.

(97) Peters, J. W.; Lanzilotta, W. N.; Lemon, B. J.; Seefeldt, L. C. X-Ray Crystal Structure of the Fe-Only Hydrogenase (CpI) from Clostridium Pasteurianum to 1 . 8 Angstrom Resolution. *Science (80-.).* **1998**, *282* (December), 1853–1859.

(98) Nicolet, Y.; Lacey, A. L. De; Verne, X.; Fernandez, V. M.; Hatchikian, E. C.; Fontecilla-camps, J. C. Crystallographic and FTIR Spectroscopic Evidence of Changes in Fe Coordination Upon Reduction of the Active Site of the Fe-Only Hydrogenase from Desulfo V Ibrio Desulfuricans. *J. Am. Chem. Soc.* **2001**, *123*, 1596–1601.

(99) Hanwell, M. D.; Curtis, D. E.; Lonie, D. C.; Vandermeersch, T.; Zurek, E.; Hutchison, G. R. Avogadro: An Advanced Semantic Chemical Editor, Visualization, and Analysis Platform. *J. Cheminform.* **2012**, *4* (1), 17.

(100) Berggren, G.; Adamska, A.; Lambertz, C.; Simmons, T. R.; Esselborn, J.; Atta, M.; Gambarelli, S.; Mouesca, J.; Reijerse, E.; Lubitz, W.; et al. Biomimetic Assembly and Activation of [FeFe]-Hydrogenases. *Nature* **2013**, *498* (7456), 66–69.

(101) Tard, C.; Pickett, C. J. Structural and Functional Analogues of the Active Sites of the [Fe]-,[NiFe]-, and [FeFe]-Hydrogenases. *Chem. Rev.* **2009**, *109* (6), 2245.

(102) Yu, Z.; Wang, M.; Li, P.; Dong, W.; Wang, F.; Sun, L. Diiron Dithiolate Complexes Containing Intra-Ligand NH ... S Hydrogen Bonds: [FeFe] Hydrogenase Active Site Models for the Electrochemical Proton Reduction of HOAc with Low Overpotential. *Dalton Trans.* **2008**, No. 18, 2400–2406.

(103) Li, Y.; Rauchfuss, T. B. Synthesis of Diiron(I) Dithiolato Carbonyl Complexes. *Chem. Rev.* **2016**, *116* (12), 7043–7077.

(104) Simmons, T. R.; Berggren, G.; Bacchi, M.; Fontecave, M.; Artero, V. Mimicking Hydrogenases : From Biomimetics to Artificial Enzymes. *Coord. Chem. Rev.* **2014**, *270–271* (January), 127–150.

(105) Barton, B. E.; Olsen, M. T.; Rauchfuss, T. B. Artificial Hydrogenases. *Curr. Opin. Biotechnol.* **2010**, *21* (3), 292–297.

(106) Gloaguen, F.; Rauchfuss, T. B. Small Molecule Mimics of Hydrogenases: Hydrides and Redox. *Chem. Soc. Rev.* **2009**, *38*, 100–108.

(107) Gao, S.; Fan, W.; Liu, Y.; Jiang, D.; Duan, Q. Artificial Water-Soluble Systems Inspired by [FeFe] -Hydrogenases for Electro- and Photocatalytic Hydrogen Production. *Int. J. Hydrogen Energy* **2019**, *45* (7), 4305–4327.

(108) Faiella, M.; Roy, A.; Sommer, D.; Ghirlanda, G. De Novo Design of Functional Proteins: Toward Artificial Hydrogenases. *Pept. Sci.* **2013**, *100* (6), 11–14.

(109) Onoda, A.; Kihara, Y.; Fukumoto, K.; Sano, Y.; Hayashi, T. Photoinduced Hydrogen Evolution Catalyzed by a Synthetic Diiron Dithiolate Complex Embedded within a Protein Matrix. *ACS Catal.* **2014**, *4* (8), 2645–2648.

(110) Pazy, Y.; Kulik, T.; Bayer, E. A.; Wilchek, M.; Livnah, O. Ligand Exchange between Proteins: Exchange of Biotin and Biotin Derivatives between Avidin and Streptavidin. *J. Biol. Chem.* **2002**, *277* (34), 30892–30900.

(111) Hoyle, C. E.; Bowman, C. N. Thiol-Ene Click Chemistry. *Angew. Chemie - Int. Ed.* **2010**, *49* (9), 1540–1573.

(112) Lowe, A. B. Thiol-Ene "Click" Reactions and Recent Applications in Polymer and Materials Synthesis. *Polym. Chem.* **2010**, *1* (1), 17–36.

(113) Schulz, D.; Holstein, J. M.; Rentmeister, A. A Chemo-Enzymatic Approach for Site-Specific Modification of the RNA Cap. *Angew. Chemie Int. Ed.* **2013**, *52* (30), 7874–7878.

(114) Valeur, E.; Bradley, M. Amide Bond Formation: Beyond the Myth of Coupling Reagents. *Chem Soc Rev* **2009**, *38* (2), 606–631.

(115) Singh, S.; Tiwari, A. K.; Varshney, R.; Mathur, R.; Shukla, G.; Bag, N.; Singh, B.; Mishra, A. K. Comparative Evaluation of Bis(Thiosemicarbazone)- Biotin and Met-Ac-TE3A for Tumor Imaging. *Spectrochim. Acta - Part A Mol. Biomol. Spectrosc.* **2016**, *153*, 566–571.

(116) Lo Conte, M.; Pacifico, S.; Chambery, A.; Marra, A.; Dondoni, A. Photoinduced Addition of Glycosyl Thiols to Alkynyl Peptides: Use of Free-Radical Thiol-Yne Coupling for Post-Translational Double-Glycosylation of Peptides. *J. Org. Chem.* **2010**, *75* (13), 4644–4647.

(117) Li, H.; Rauchfuss, T. B. Iron Carbonyl Sulfides, Formaldehyde, and Amines Condense to

Give the Proposed Azadithiolate Cofactor of the Fe-Only Hydrogenases. *J. Am. Chem. Soc.* **2002**, *124* (5), 726–727.

(118) Stanley, J. L.; Rauchfuss, T. B.; Wilson, S. R. Studies on the Condensation Pathway to and Properties of Diiron Azadithiolate Carbonyls. *Organometallics* **2007**, *26* (8), 1907–1911.

(119) Pierik, A. J.; Hulstein, M.; Hagen, W. R.; Albracht, S. P. J. A Low-Spin Iron with CN and CO as Intrinsic Ligands Forms the Core of the Active Site in [Fe]-Hydrogenases. *Eur. J. Biochem.* **1998**, *258* (2), 572–578.

(120) Chen, Z.; Lemon, B. J.; Huang, S.; Swartz, D. J.; Peters, J. W.; Bagley, K. A. Infrared Studies of the CO-Inhibited Form of the Fe-Only Hydrogenase from Clostridium Pasteurianum I: Examination of Its Light Sensitivity at Cryogenic Temperatures. *Biochemistry* **2002**, *41* (6), 2036–2043.

(121) Silaghi-Dumitrescu, I.; Bitterwolf, T. E.; King, R. B. Butterfly Diradical Intermediates in Photochemical Reactions of Fe 2(CO)6(??-S2). *J. Am. Chem. Soc.* **2006**, *128* (16), 5342–5343.

(122) Wang, Z.; Liu, J. Azadithiolates Cofactor of the Iron-Only Hydrogenase and Its PR 3 - Monosubstituted Derivatives : Synthesis , Structure , Electrochemistry and Protonation. *J. Organomet. Chem.* **2007**, *692* (2), 5501–5507.

(123) Lawrence, J. D.; Li, H.; Rauchfuss, T. B. Beyond Fe-Only Hydrogenases: N-Functionalized 2-Aza-1,3-Dithiolates Fe 2 [(SCH 2) 2 NR](CO) x (x = 5, 6). *Chem. Commun.* **2001**, *1* (16), 1482–1483.

(124) Lyon, E. J.; Georgakaki, I. P.; Reibenspies, J. H.; Darensbourg, M. Y. Carbon Monoxide and Cyanide Ligands in a Classical Organometallic Complex Model for Fe-Only Hydrogenase. *Angew. Chemie - Int. Ed.* **1999**, *38* (21), 3178–3180.

(125) Cao, Z.; Hall, M. B. Modeling the Active Sites in Metalloenzymes. 3. Density Functional Calculations on Models for [Fe]-Hydrogenase: Structures and Vibrational Frequencies of the Observed Redox Forms and the Reaction Mechanism at the Diiron Active Center. *J. Am. Chem. Soc.* **2001**, *123* (16), 3734–3742.

(126) Hou, J.; Peng, X.; Liu, J.; Gao, Y.; Zhao, X.; Gao, S.; Han, K. A Binuclear Isocyanide Azadithiolatoiron Complex Relevant to the Active Site of Fe-Only Hydrogenases: Synthesis, Structure and Electrochemical Properties. *Eur. J. Inorg. Chem.* **2006**, No. 22, 4679–4686.

(127) Schafer, K. J.; Hales, J. M.; Balu, M.; Belfield, K. D.; Van Stryland, E. W.; Hagan, D. J. Two-Photon Absorption Cross-Sections of Common Photoinitiators. *J. Photochem. Photobiol. A Chem.* **2004**, *162* (2–3), 497–502.

(128) Teixeira, S.; Giudici, R.; Bossmann, S. H.; Lang, J.; Braun, A. M. Approaches towards a Technically Feasible Photoinitiated Prepolymerization of Methyl Methacrylate. *Chem. Eng. Process. Process Intensif.* **2004**, *43* (10), 1317–1328.

(129) Spang, S.; El-Sayed, M.; Muller, H.; Rheinwald, G.; Lang, H.; Poppitz, W. Solid-State Structures of N -Substituted Michler ' s Ketones and Their Relation to Solvatochromism.

Eur. J. Org. Chem. **2002**, 4159–4168.

(130) Heine, D.; Pietsch, C.; Schubert, U. S.; Weigand, W. Controlled Radical Polymerization of Styrene-Based Models of the Active Site of the [FeFe] -Hydrogenase. *J. Polym. Sci. PART A Polym. Chem.* **2013**, *51*, 2171–2180.

(131) Servinis, L.; Gengenbach, T. R.; Huson, M. G.; Henderson, L. C.; Fox, B. L. A Novel Approach to the Functionalisation of Pristine Carbon Fibre Using Azomethine 1,3-Dipolar Cycloaddition. *Aust. J. Chem.* **2015**, *68* (2), 335–344.

(132) Gnaccarini, C.; Ben-Tahar, W.; Lubell, W. D.; Pelletier, J. N.; Keillor, J. W. Fluorometric Assay for Tissue Transglutaminase-Mediated Transamidation Activity. *Bioorganic Med. Chem.* **2009**, *17* (17), 6354–6359.

(133) Lisbjerg, M.; Jessen, B. M.; Rasmussen, B.; Nielsen, B.; Madsen, A. Ø.; Pittelkow, M. Discovery of a Cyclic 6+6 Hexamer of D-Biotin and Formaldehyde. *Chem. Sci.* **2014**, *5* (7), 2591–2908.

(134) Gao, W.; Sun, J.; Li, M.; Eriksson, L. Attachment of a Hydrogen-Bonding Carboxylate Side Chain to an [FeFe] - Hydrogenase Model Complex : Influence on the Catalytic Mechanism. *Chem. Eur. J.* **2010**, *16*, 2537–2546.

(135) Siebel, J. F.; Adamska-Venkatesh, A.; Weber, K.; Rumpel, S.; Reijerse, E.; Lubitz, W. Hybrid [FeFe]-Hydrogenases with Modified Active Sites Show Remarkable Residual Enzymatic Activity. *Biochemistry* **2015**, *54* (7), 1474–1483.

(136) Wang, F.; Wang, W. G.; Wang, X. J.; Wang, H. Y.; Tung, C. H.; Wu, L. Z. A Highly Efficient Photocatalytic System for Hydrogen Production by a Robust Hydrogenase Mimic in an Aqueous Solution. *Angew. Chemie - Int. Ed.* **2011**, *50* (14), 3193–3197.

(137) Dhake, K. P.; Tambade, P. J.; Singhal, R. S.; Bhanage, B. M. An Efficient, Catalyst- and Solvent-Free *N* -Formylation of Aromatic and Aliphatic Amines. *Green Chem. Lett. Rev.* **2011**, *4* (2), 151–157.

(138) Zhu, L.; Patel, M.; Zhang, M. Synthesis of Biphenyl Anilines Using Iodo Phenylformamides via a One-Pot Suzuki Coupling Reaction. *Tetrahedron Lett.* **2008**, *49* (17), 2734–2737.

(139) Kobayashi, G.; Saito, T.; Kitano, Y. A Novel Method for Preparing Isocyanides from N-Substituted Formamides with Chlorophosphate Compounds. *Synthesis (Stuttg).* **2011**, No. 20, 3225–3234.

(140) Corona, C.; Bryant, B. K.; Arterburn, J. B. Synthesis of a Biotin-Derived Alkyne for Pd-Catalyzed Coupling Reactions. *Org. Lett.* **2006**, *8* (9), 1883–1886.

(141) Villemin, E.; Gravel, E.; Izard, N.; Filoramo, A.; Vivien, L.; Doris, E. Polymer-Decorated Carbon Nanotubes as Transducers for Label-Free Photonic Biosensors. *Chem. - A Eur. J.* **2015**, *21* (51), 18649–18653.

(142) Garrett, B. R.; Awad, A.; He, M.; Click, K. A.; Durr, C. B.; Gallucci, J. C.; Hadad, C. M.; Wu, Y. Dimeric FeFe-Hydrogenase Mimics Bearing Carboxylic Acids : Synthesis and Electrochemical Investigation. *Polyhedron* **2016**, *103*, 21–27.

(143) McFarlene, W.; Wilkinson, G. Triiron Dodecacarbonyl. *Inorg. Synth.* **1966**, *8*, 181–183.

(144) Sonogashira, K.; Tohda, Y.; Hagihara, N. A Convenient Synthesis of Acetylenes: Catalytic Substitutions of Acetylenic Hydrogen with Bromoalkenes, Iodoarenes and Bromopyridines. *Tetrahedron Lett.* **1975**, *16* (50), 4467–4470.

(145) Chinchilla, R.; N??jera, C. The Sonogashira Reaction: A Booming Methodology in Synthetic Organic Chemistry. *Chem. Rev.* **2007**, *107* (3), 874–922.

(146) Grosshenny, V.; Romero, F. M.; Ziessel, R. Construction of Preorganized Polytopic Ligands via Palladium-Promoted Cross-Coupling Reactions. *J. Org. Chem.* **1997**, *62* (5), 1491–1500.

(147) Heinze, K.; Jacob, V. Stepwise Assembly of Mixed Metal Dinuclear Carbonyl Complexes. *Eur. J. Inorg. Chem.* **2003**, *2003* (21), 3918–3923.

(148) Poulos, T. L. Heme Enzyme Structure and Function. *Chem. Rev.* **2014**, *114* (7), 3919–3962.

(149) Smith, A. T.; Pazicni, S.; Marvin, K. A.; Stevens, D. J.; Paulsen, K. M.; Burstyn, J. N. Functional Divergence of Heme-Thiolate Proteins: A Classification Based on Spectroscopic Attributes. *Chem. Rev.* **2015**, *115* (7), 2532–2558.

(150) Lin, Y. W. Structure and Function of Heme Proteins Regulated by Diverse Post-Translational Modifications. *Arch. Biochem. Biophys.* **2018**, *641* (November 2017), 1–30.

(151) Zhao, M.; Wang, H. B.; Ji, L. N.; Mao, Z. W. Insights into Metalloenzyme Microenvironments: Biomimetic Metal Complexes with a Functional Second Coordination Sphere. *Chem. Soc. Rev.* **2013**, *42* (21), 8360–8375.

(152) Collman, J. P.; Fu, L. Synthetic Models for Hemoglobin and Myoglobin. *Acc. Chem. Res.* **1999**, *32* (6), 455–463.

(153) Phillips, S. E. V.; Schoenborn, B. P. Neutron Diffraction Reveals Oxygen-Histidine Hydrogen Bond in Oxymyoglobin. *Nature* **1981**, *5818*, 81-82.

(154) Springer, B. A.; Egeberg, K. D.; Sligar, S. G.; Rohlfs, R. J.; Mathews, A. J.; Olson, J. S. Discrimination between Oxygen and Carbon Monoxide and Inhibition of Autooxidation by Myoglobin. Site-Directed Mutagenesis of the Distal Histidine. *J. Biol. Chem.* **1989**, *264* (6), 3057–3060.

(155) Poulos, T. L. Cytochrome P450. *Curr. Opin. Struct. Biol.* **1995**, *5* (6), 767–774.

(156) Martinis, S. A.; Atkins, W. M.; Stayton, P. S.; Sligar, S. G. A Conserved Residue of Cytochrome P-450 Is Involved The Dehydrophenyl Anion and the Gas Phase Ion Chemistry of Benzyne. *J. Am. Chem. Soc* **1989**, *111*, 9252–9253.

(157) Altarsha, M.; Benighaus, T. Coupling and Uncoupling Mechanisms in the Methoxythreonine Mutant of Cytochrome P450cam : A Quantum Mechanical / Molecular Mechanical Study. *J Biol Inorg Chem* **2010**, *15*, 361–372.

(158) Schlichting, I.; Berendzen, J.; Chu, K.; Stock, A. M.; Maves, S. A.; Benson, D. E.; Sweet, R. M.; Ringe, D.; Petsko, G. A.; Sligar, S. G. The Catalytic Pathway of Cytochrome

P450cam at Atomic Resolution. *Science.* **2000**, *287* (March), 1615–1623.

(159) Nagao, S.; Osuka, H.; Yamada, T.; Uni, T.; Shomura, Y.; Imai, K.; Higuchi, Y.; Hirota, S. Structural and Oxygen Binding Properties of Dimeric Horse Myoglobin. *Dalt. Trans.* **2012**, *41* (37), 11378.

(160) Li, H.; Poulos, T. L. The Structure of the Cytochrome P450BM-3 Haem Domain Complexed with the Fatty Acid Substrate, Palmitoleic Aciditle. *Nat. Struct. Biol.* **1997**, *4* (2), 140–146.

(161) Pauling, L. Nature of the Iron-Oxygen Bond in Oxyhemoglobin. *Nature* **1964**, *203* (4941), 182–183.

(162) Corwin, A. H.; Reyes, Z. Preparation and Properties of Imidazole Ferro- and Ferriprotoporphyrin Complexes 1. *J. Am. Chem. Soc.* **1956**, *78* (11), 2437–2439.

(163) Wang, J. H. HEMOGLOBIN STUDIES. II. A SYNTHETIC MATERIAL WITH HEMOGLOBIN-LIKE PROPERTY 1. *J. Am. Chem. Soc.* **1958**, *80* (12), 3168–3169.

(164) Alben, J. O.; Fuchsman, W. H.; Beaudreau, C. A.; Caughey, W. S. Substituted Deuteroporphyrins. III. Iron(II) Derivatives. Reactions with Oxygen and Preparations from Chloro- and Methoxohemins. *Biochemistry* **1968**, *7* (2), 624–635.

(165) Chang, C. K.; Traylor, T. G. Solution Behavior of a Synthetic Myoglobin Active Site. *J. Am. Chem. Soc.* **1973**, *95* (17), 5810–5811.

(166) Anderson, D. L.; Weschler, C. J.; Basolo, F. Reversible Reaction of Simple Ferrous Porphyrins with Molecular Oxygen at Low Temperatures. *J. Am. Chem. Soc.* **1974**, *96* (17), 5599–5600.

(167) Almog, J.; Baldwin, J. E.; Dyer, R. L.; Huff, J.; Wilkerson, C. J. Reversible Binding of Dioxygen to Mesoporphyrin IX Derivatives at Low Temperatures. *J. Am. Chem. Soc.* **1974**, *96* (17), 5600–5601.

(168) Coliman, J. P.; Gagne, R. R.; Reed, C. A.; Halbert, T. R.; Robinson, W. T.; Lang, G. "Picket Fence Porphyrins". Synthetic Models for Oxygen Binding Hemoproteins. *J. Am. Chem. Soc.* **1975**, *97* (6), 1427–1439.

(169) Collman, J. P.; Zhang, X.; Wong, K.; Brauman, J. I. Dioxygen Binding in Iron and Cobalt Picnic Basket Porphyrins. *J. Am. Chem. Soc.* **1994**, *116* (14), 6245–6251.

(170) Lombardi, A.; Nastri, F.; Pavone, V. Peptide-Based Heme-Protein Models. *Chem. Rev.* **2001**, *101* (10), 3165–3189.

(171) Zhao, Z.; Wang, D.; Wang, M.; Sun, X.; Wang, L.; Huang, X.; Ma, L.; Li, Z. Proximal Environment Controlling the Reactivity between Inorganic Sulfide and Heme-Peptide Model. *RSC Adv.* **2016**, *6* (82), 78858–78864.

(172) Tian, J.; Zhang, W. Synthesis, Self-Assembly and Applications of Functional Polymers Based on Porphyrins. *Prog. Polym. Sci.* **2019**, *95*, 65–117.

(173) Jin, R. H.; Motoyoshi, K. I. Porphyrin-Centered Water-Soluble Star-Shaped Polymers: Poly(N-Acetylethylenimine) and Poly(Ethylenimine) Arms. *J. Porphyr. Phthalocyanines*

1999, *3* (1), 60–64.

(174) Rodriguez, K. J. Modeling Secondary Coordination Sphere Interactions in Heme Proteins: From Small Molecule Ligands to Macromolecular Porphyrin-Cored Polymer Nanoparticles, University of New Hampshire, 2017.

(175) Chiefari, J.; Chong, Y. K. B.; Ercole, F.; Krstina, J.; Jeffery, J.; Le, T. P. T.; Mayadunne, R. T. A.; Meijs, G. F.; Moad, C. L.; Moad, G.; et al. Living Free-Radical Polymerization by Reversible Addition−Fragmentation Chain Transfer: The RAFT Process. *Macromolecules* **1998**, *31* (16), 5559–5562.

(176) Perrier, S.; Takolpuckdee, P. Macromolecular Design via Reversible Addition-Fragmentation Chain Transfer (RAFT)/Xanthates (MADIX) Polymerization. *J. Polym. Sci. Part A Polym. Chem.* **2005**, *43* (22), 5347–5393.

(177) Frank, P. G.; Tuten, B. T.; Prasher, A.; Chao, D.; Berda, E. B. Intra-Chain Photodimerization of Pendant Anthracene Units as an Efficient Route to Single-Chain Nanoparticle Fabrication. *Macromol. Rapid Commun.* **2014**, *35* (2), 249–253.

(178) Liu, Y.; Pauloehrl, T.; Presolski, S. I.; Albertazzi, L.; Palmans, A. R. A.; Meijer, E. W. Modular Synthetic Platform for the Construction of Functional Single-Chain Polymeric Nanoparticles: From Aqueous Catalysis to Photosensitization. **2015**, *137*(40),13096-13105

(179) Zaia, J.; Annan, R. S.; Biemann, K. The Correct Molecular Weight of Myoglobin, a Common Calibrant for Mass Spectrometry. *Rapid Commun. Mass Spectrom.* **1992**, *6* (1), 32–36.

(180) Kim, Y.-H.; Hong, J.-I. Ion Pair Recognition by Zn-Porphyrin/Crown Ether Conjugates: Visible Sensing of Sodium Cyanide. *Chem. Commun. (Camb).* **2002**, No. 5, 512–513.

(181) Yoon, H.; Lee, C. H.; Jeong, Y. H.; Gee, H. C.; Jang, W. D. A Zinc Porphyrin-Based Molecular Probe for the Determination of Contamination in Commercial Acetonitrile. *Chem. Commun.* **2012**, *48* (42), 5109–5111.

(182) Andreev, V. P.; Sobolev, P. S.; Zaitsev, D. O.; Remizova, L. A.; Tunina, S. G. Tetraphenylporphine Zinc(II) Coordination with Primary Amines and Alcohols in Chloroform. *Russ. J. Gen. Chem.* **2012**, *82* (6), 1157–1166.

(183) Groves, P. Diffusion Ordered Spectroscopy (DOSY) as Applied to Polymers. *Polym. Chem.* **2017**, *8* (44), 6700–6708.

(184) Einstein, A. Motion of Suspended Particles in Stationary Liquids Required from the Molecular Kinetic Theory of Heat. *Ann. Phys.* **1905**, No. 17, 549–560.

(185) N,N-Dimethylformamide | HCON(CH3)2 - PubChem https://pubchem.ncbi.nlm.nih.gov/compound/dimethylformamide (accessed Feb 18, 2020).

(186) Paul, R. C.; Sreenathan, B. R. Dimethylformamide as a Polar Solvent: Part IV - Solubility, Solvate Formation & Solvolytic Reactions Of Substances in Dimethylformamide. *Indian J. Chem.* **1966**, *4* (9), 382–386.

(187) Pohorecki, R.; Moniuk, W. Kinetics of Reaction between Carbon Dioxide and Hydroxyl Ions in Aqueous Electrolyte Solutions. *Chem. Eng. Sci.* **1988**, *43* (7), 1677–1684.

(188) Frank, P. G.; Tuten, B. T.; Prasher, A.; Chao, D.; Berda, E. B. Intra-Chain Photodimerization of Pendant Anthracene Units as an Efficient Route to Single-Chain Nanoparticle Fabrication. *Macromol. Rapid Commun.* **2014**, *35* (2), 249–253.

(189) Dawood, F.; Anda, M.; Shafiullah, G. M. Hydrogen Production for Energy : An Overview. *Int. J. Hydrogen Energy* **2019**, *45* (7), 3847–3869.

(190) Ratzloff, M. W.; Artz, J. H.; Mulder, D. W.; Collins, R. T.; Furtak, T. E.; King, P. W. CO-Bridged H-Cluster Intermediates in the Catalytic Mechanism of [FeFe]-Hydrogenase CaI. *J. Am. Chem. Soc.* **2018**, *140* (24), 7623–7628.

(191) Sanchez, M. L. K.; Sommer, C.; Reijerse, E.; Birrell, J. A.; Lubitz, W.; Dyer, R. B. Investigating the Kinetic Competency of Cr HydA1 [FeFe] Hydrogenase Intermediate States via Time-Resolved Infrared Spectroscopy. *J. Am. Chem. Soc.* **2019**, *141* (40), 16064–16070.

(192) Lorent, C.; Katz, S.; Duan, J.; Kulka, C. J.; Caserta, G.; Teutloff, C.; Yadav, S.; Apfel, U.; Winkler, M.; Happe, T.; et al. Shedding Light on Proton and Electron Dynamics in [FeFe] Hydrogenases. *J. Am. Chem. Soc.* **2020**, *142* (12), 5493–5497.

(193) Artz, J. H.; Zadvornyy, O. A.; Mulder, D. W.; Keable, S. M.; Cohen, A. E.; Ratzloff, M. W.; Williams, S. G.; Ginovska, B.; Kumar, N.; Song, J.; et al. Tuning Catalytic Bias of Hydrogen Gas Producing Hydrogenases. *J. Am. Chem. Soc.* **2020**, *142* (3), 1227–1235.

(194) Rumpel, S.; Ravera, E.; Sommer, C.; Reijerse, E.; Farès, C.; Luchinat, C.; Lubitz, W. 1 H NMR Spectroscopy of [FeFe] Hydrogenase: Insight into the Electronic Structure of the Active Site. *J. Am. Chem. Soc.* **2018**, *140* (1), 131–134.

(195) Duan, J.; Senger, M.; Esselborn, J.; Engelbrecht, V.; Wittkamp, F.; Apfel, U.-P.; Hofmann, E.; Stripp, S. T.; Happe, T.; Winkler, M. Crystallographic and Spectroscopic Assignment of the Proton Transfer Pathway in [FeFe]-Hydrogenases. *Nat. Commun.* **2018**, *9* (1), 4726.

(196) Senger, M.; Eichmann, V.; Laun, K.; Duan, J.; Wittkamp, F.; Knör, G.; Apfel, U.; Happe, T.; Winkler, M.; Heberle, J.; et al. How [FeFe]-Hydrogenase Facilitates Bidirectional Proton Transfer. *J. Am. Chem. Soc.* **2019**, *141* (43), 17394–17403.

(197) Esselborn, J.; Kertess, L.; Apfel, U.; Hofmann, E.; Happe, T. Loss of Specific Active-Site Iron Atoms in Oxygen-Exposed [FeFe]-Hydrogenase Determined by Detailed X-Ray Structure Analyses. *J. Am. Chem. Soc.* **2019**, *141* (44), 17721–17728.

(198) Hu, S.; Zhang, L.; Wu, Y.; Feng, J.; Wu, S.; Xie, B.; Zou, L. [FeFe]-Hydrogenase Active Site Mimics Containing Pyridyl-Functionalized Phosphine Ligands: Synthesis, Characterization and Electrochemical Investigation. *Inorganica Chim. Acta* **2020**, *504* (October 2019), 119435.

(199) Agarwal, T.; Kaur-Ghumaan, S. Mono- and Dinuclear Mimics of the [FeFe] Hydrogenase Enzyme Featuring Bis(Monothiolato) and 1,3,5-Triaza-7-Phosphaadamantane Ligands. *Inorganica Chim. Acta* **2020**, *504* (January), 119442.

(200) Hai, L.; Zhang, T.; Jiang, S.; Zhang, X.; Zhang, G.; Ma, X.; Li, B. Model Compound of [FeFe]-Hydrogenase Active Site Employing [2Fe–2S] Subunit as Non-Innocent [4Fe–4S] Cluster and Its Proton Reduction Performance. *Int. J. Hydrogen Energy* **2020**, *45* (21), 11995–11999.

(201) Wen, N.; Zhang, L.; Lin, J.; Feng, Y.; Cao, J.; Wen, C.; Wei, Y. Diiron Models for Active Site of FeFe-Hydrogenase Armed with One or Two Chlorine Butynyl Groups: Synthesis, Structures and Electrochemistry. *Inorganica Chim. Acta* **2019**, *486* (September 2018), 508–517.

(202) Aster, A.; Wang, S.; Mirmohades, M.; Esmieu, C.; Berggren, G.; Hammarström, L.; Lomoth, R. Metal vs. Ligand Protonation and the Alleged Proton-Shuttling Role of the Azadithiolate Ligand in Catalytic H 2 Formation with FeFe Hydrogenase Model Complexes. *Chem. Sci.* **2019**, *10* (21), 5582–5588.

(203) Watanabe, M.; Goto, K.; Miyazaki, T.; Shibahara, M.; Chang, Y. J.; Chow, T. J.; Ishihara, T. Electrocatalytic Hydrogen Production Using [FeFe]-Hydrogenase Mimics Based on Tetracene Derivatives. *New J. Chem.* **2019**, *43* (35), 13810–13815.

(204) Schippers, E. C. F.; Nurttila, S. S.; Oudsen, J. H.; Tromp, M.; Dzik, W. I.; van der Vlugt, J. I.; Reek, J. N. H. [FeFe]-Hydrogenase Mimic Employing κ 2 - C , N -Pyridine Bridgehead Catalyzes Proton Reduction at Mild Overpotential. *Eur. J. Inorg. Chem.* **2019**, *2019* (20), 2510–2517.

(205) Chen, W.; Cai, X.; Ji, L.; Li, X.; Wang, X.; Zhang, X.; Gao, Y.; Feng, F. A Photosynthesis-Inspired Supramolecular System: Caging Photosensitizer and Photocatalyst in Apoferritin. *Photosynth. Res.* **2019**, *142* (2), 169–180.

(206) Brezinski, W. P.; Karayilan, M.; Clary, K. E.; Pavlopoulos, N. G.; Li, S.; Fu, L.; Matyjaszewski, K.; Evans, D. H.; Glass, R. S.; Lichtenberger, D. L.; et al. [FeFe]-Hydrogenase Mimetic Metallopolymers with Enhanced Catalytic Activity for Hydrogen Production in Water. *Angew. Chemie Int. Ed.* **2018**, *57* (37), 11898–11902.

(207) Merinero, A. D.; Collado, A.; Casarrubios, L.; Gómez-Gallego, M.; Ramírez de Arellano, C.; Caballero, A.; Zapata, F.; Sierra, M. A. Triazole-Containing [FeFe] Hydrogenase Mimics: Synthesis and Electrocatalytic Behavior. *Inorg. Chem.* **2019**, *58* (23), 16267–16278.

(208) Dey, S.; Rana, A.; Crouthers, D.; Mondal, B.; Das, P. K. uma.; Darensbourg, M. Y.; Dey, A. Electrocatalytic O 2 Reduction by [Fe-Fe]-Hydrogenase Active Site Models. *J. Am. Chem. Soc.* **2014**, *136* (25), 8847–8850.

(209) Chen, J.; Wang, J.; Bai, Y.; Li, K.; Garcia, E. S.; Ferguson, A. L.; Zimmerman, S. C. Enzyme-like Click Catalysis by a Copper-Containing Single-Chain Nanoparticle. *J. Am. Chem. Soc.* **2018**, *140* (42), 13695–13702.

(210) Chen, J.; Wang, J.; Li, K.; Wang, Y.; Gruebele, M.; Ferguson, A. L.; Zimmerman, S. C. Polymeric "Clickase" Accelerates the Copper Click Reaction of Small Molecules, Proteins, and Cells. *J. Am. Chem. Soc.* **2019**, *141* (24), 9693–9700.

(211) Banerjee, S.; Nabae, Y. Ferric Porphyrin–Based Polymers for Electrochemical Oxygen

Reduction. *Catal. Today* **2019**, *332* (July 2018), 109–114.

(212) Rajendiran, S.; Ganesan, V.; Yoon, S. Balancing between Heterogeneity and Reactivity in Porphyrin Chromium-Cobaltate Catalyzed Ring Expansion Carbonylation of Epoxide into β-Lactone. *Inorg. Chem.* **2019**, *58* (5), 3283–3289.

APPENDICES

APPENDIX A: ^{1}H NMR Spectra

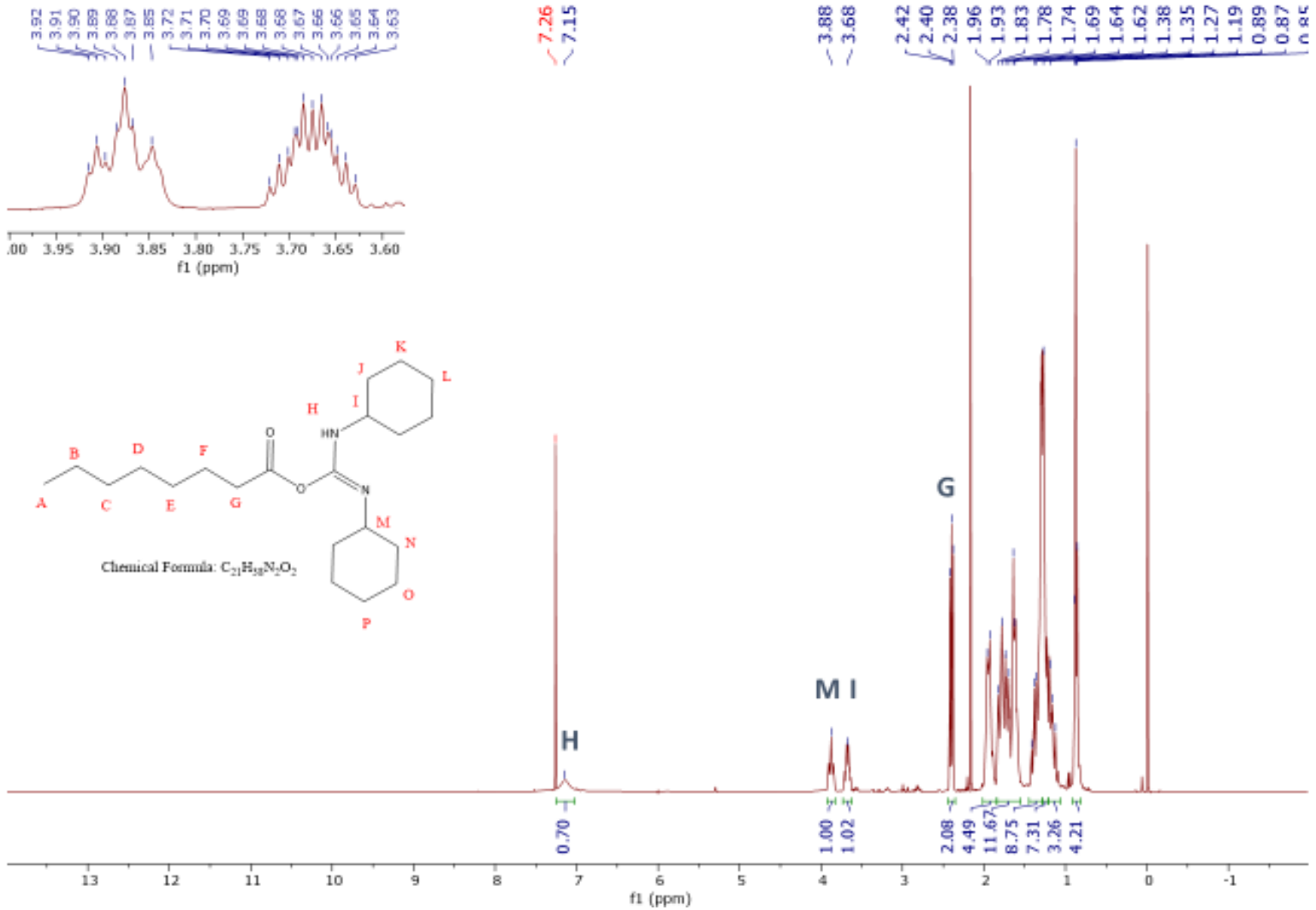

Figure A1: ^{1}H NMR ($CDCl_3$, 400 MHz) spectrum of crystallized product from the attempted synthesis of N-(2-mercaptoethyl)-Octanamide

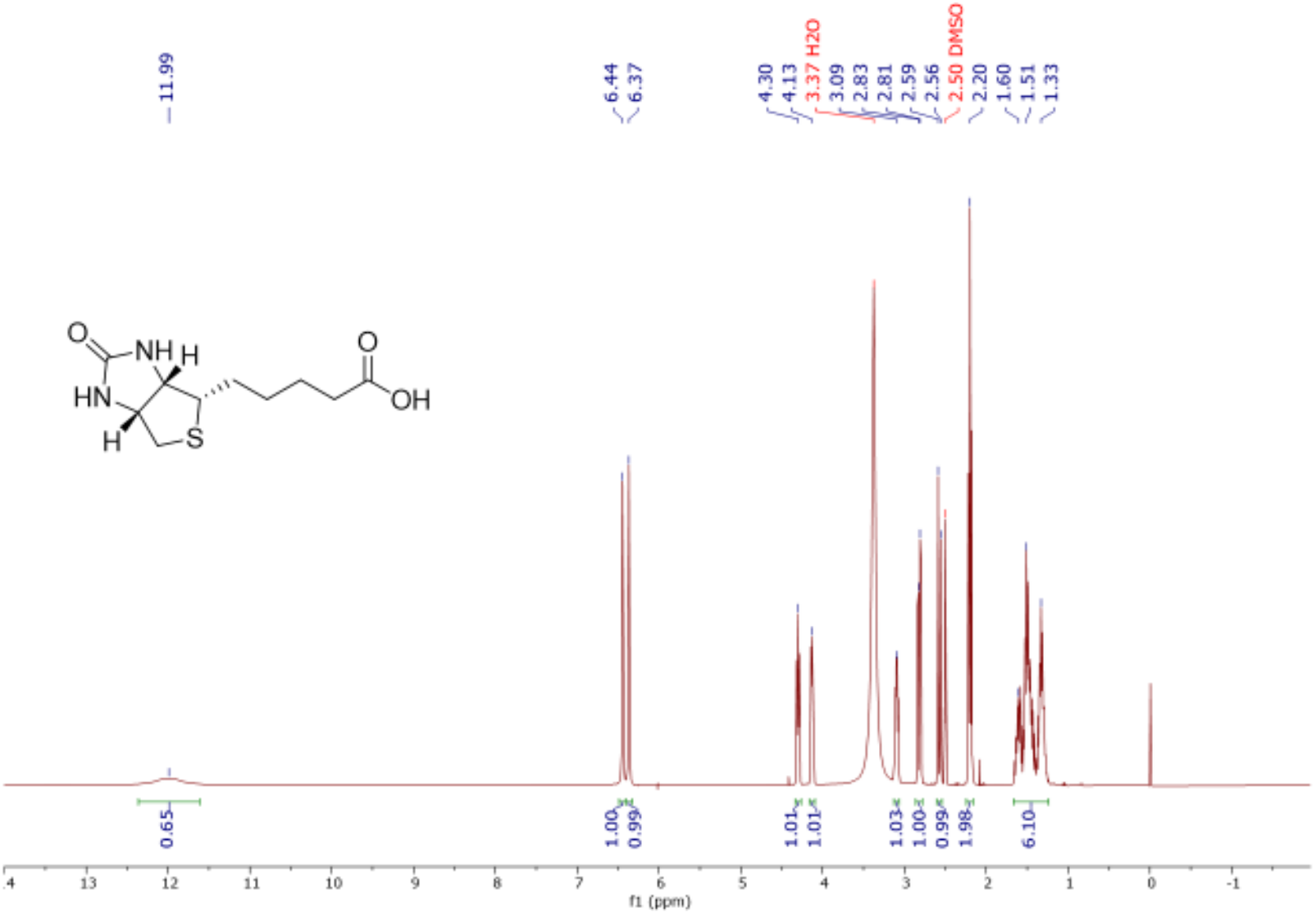

Figure A2: ^{1}H NMR (DMSO-d_6, 400 MHz) spectrum of biotin

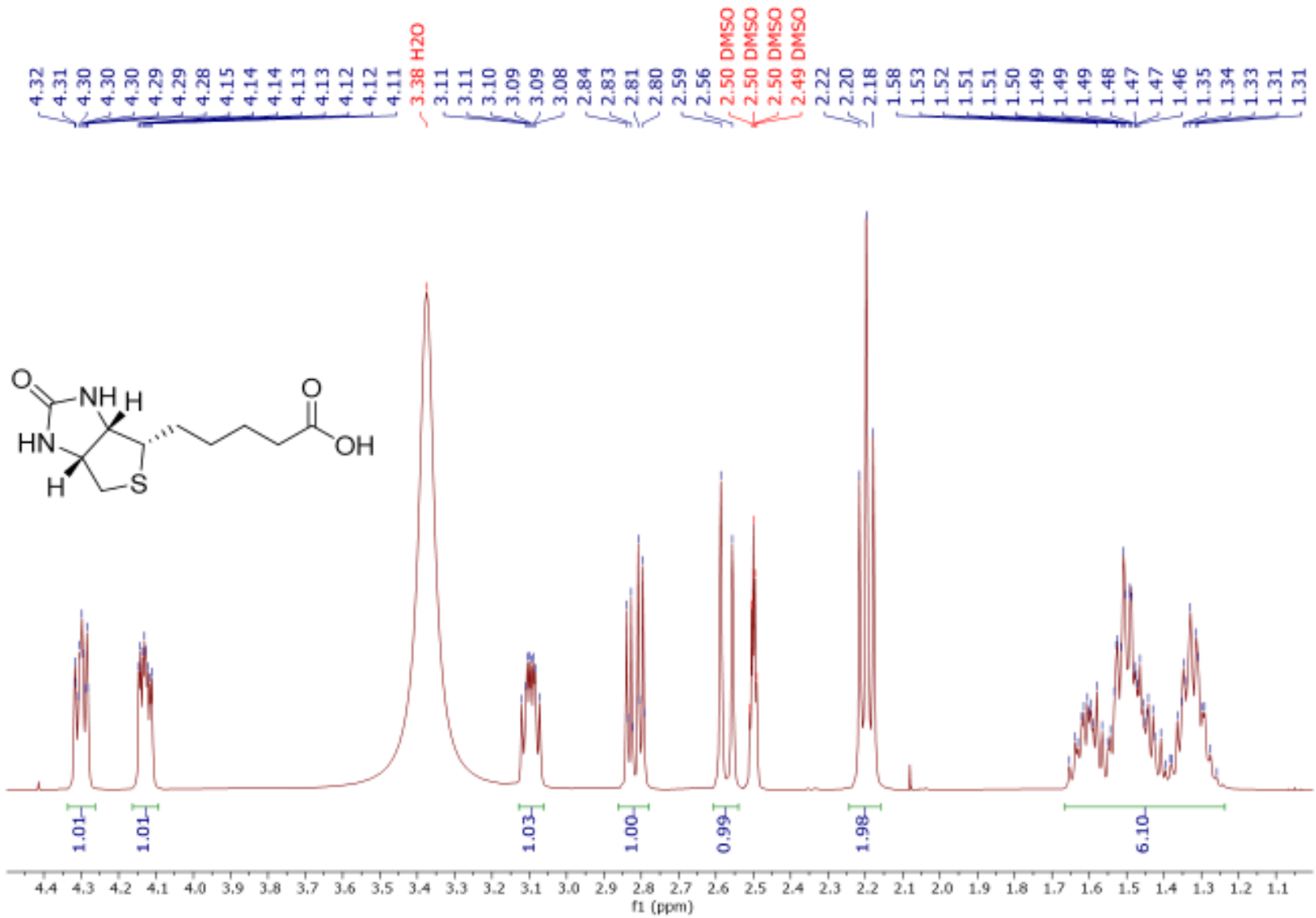

Figure A3:Expansion of ^{1}H NMR (DMSO-d_6, 400 MHz) spectrum of biotin [4.5 to 1.0 ppm]

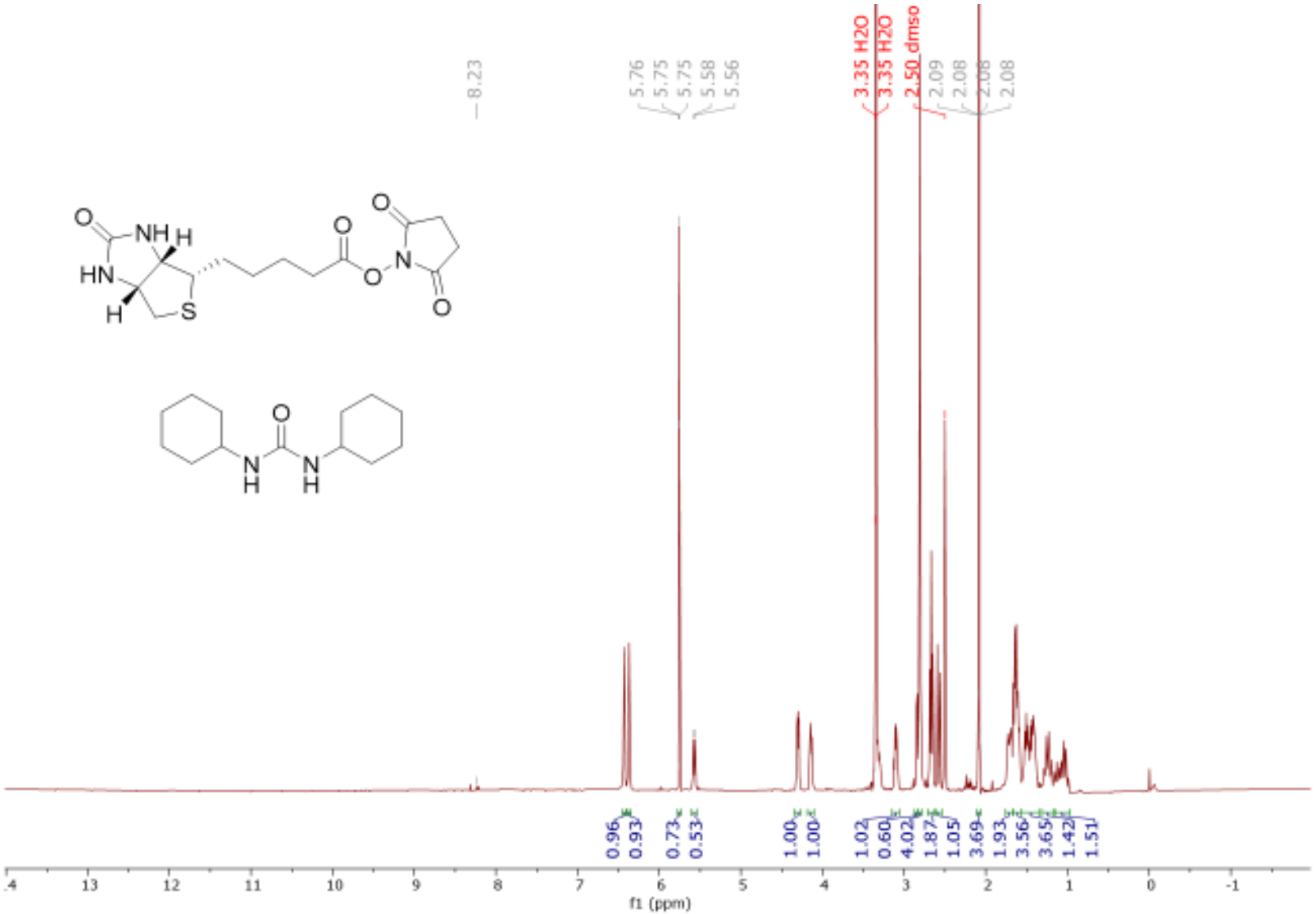

Figure A4: ^{1}H NMR (DMSO-d_6, 400 MHz) spectrum of a mixture of Biotin-NHS-ester and N,N-dicyclohexylurea

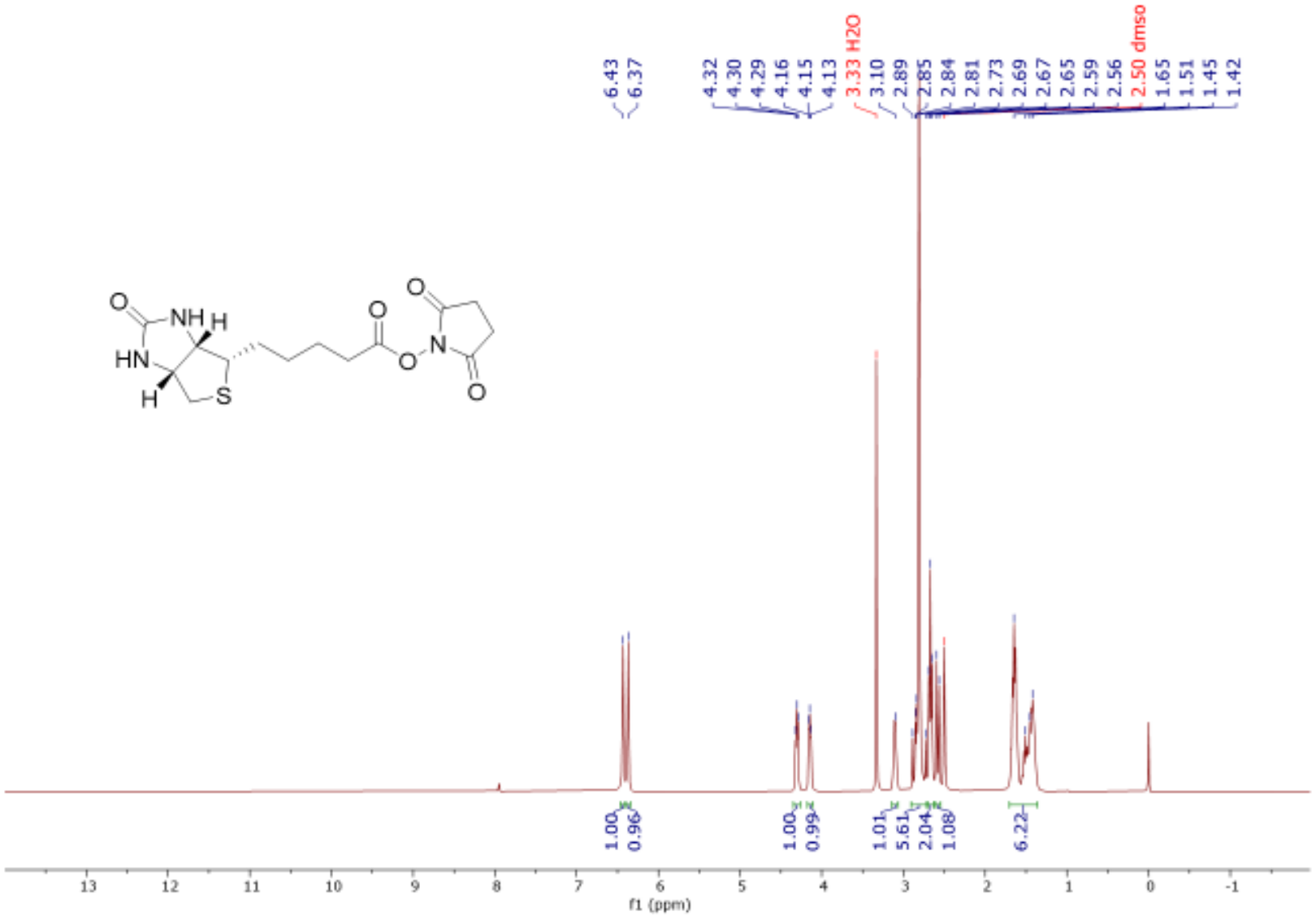

Figure A5: ^{1}H NMR (DMSO-d_6, 400 MHz) spectrum of Biotin-NHS-ester

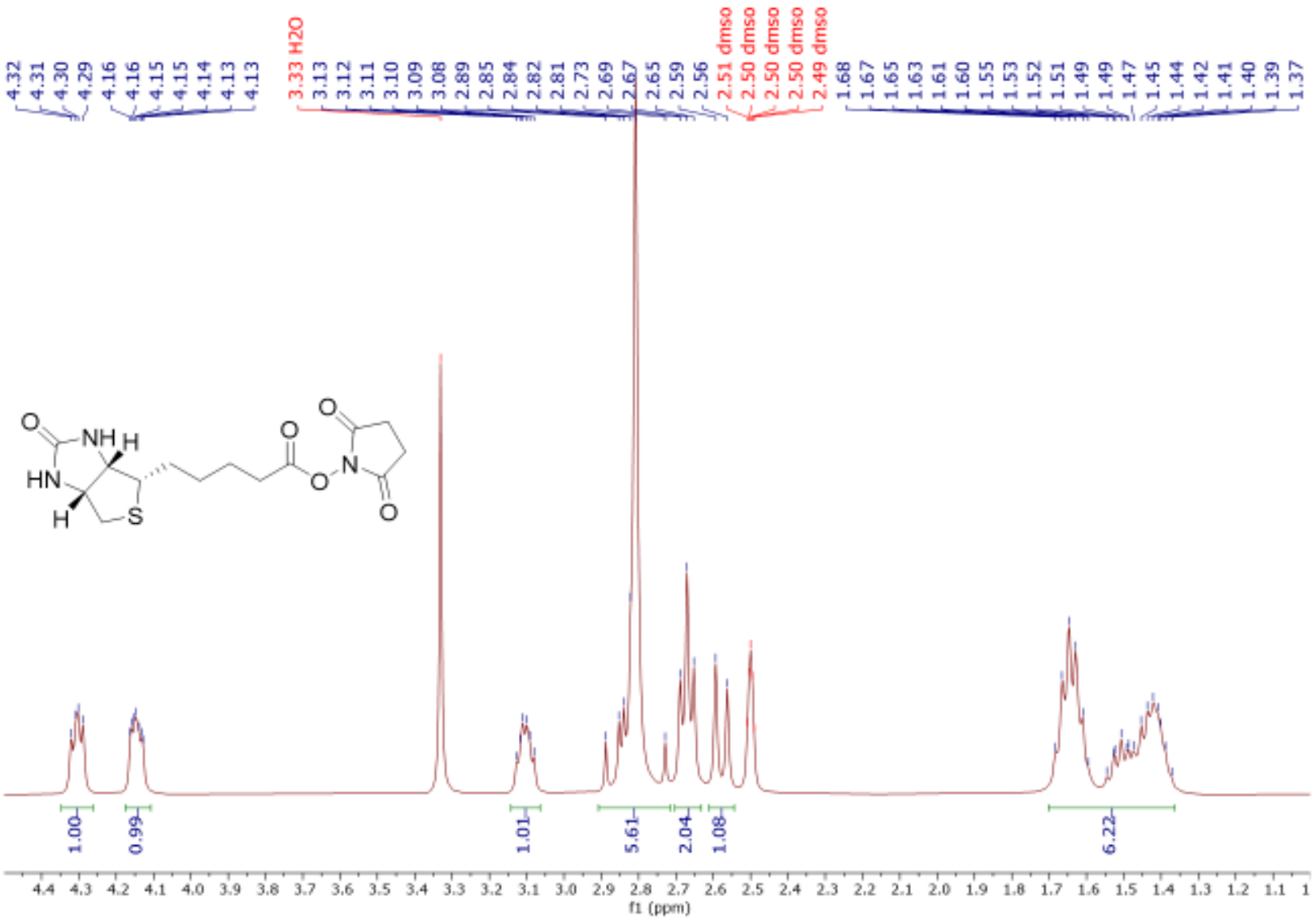

Figure A6:Expansion of ^{1}H NMR (DMSO-d_6, 400 MHz) spectrum of Biotin-NHS-ester [4.5 to 1.0 ppm]

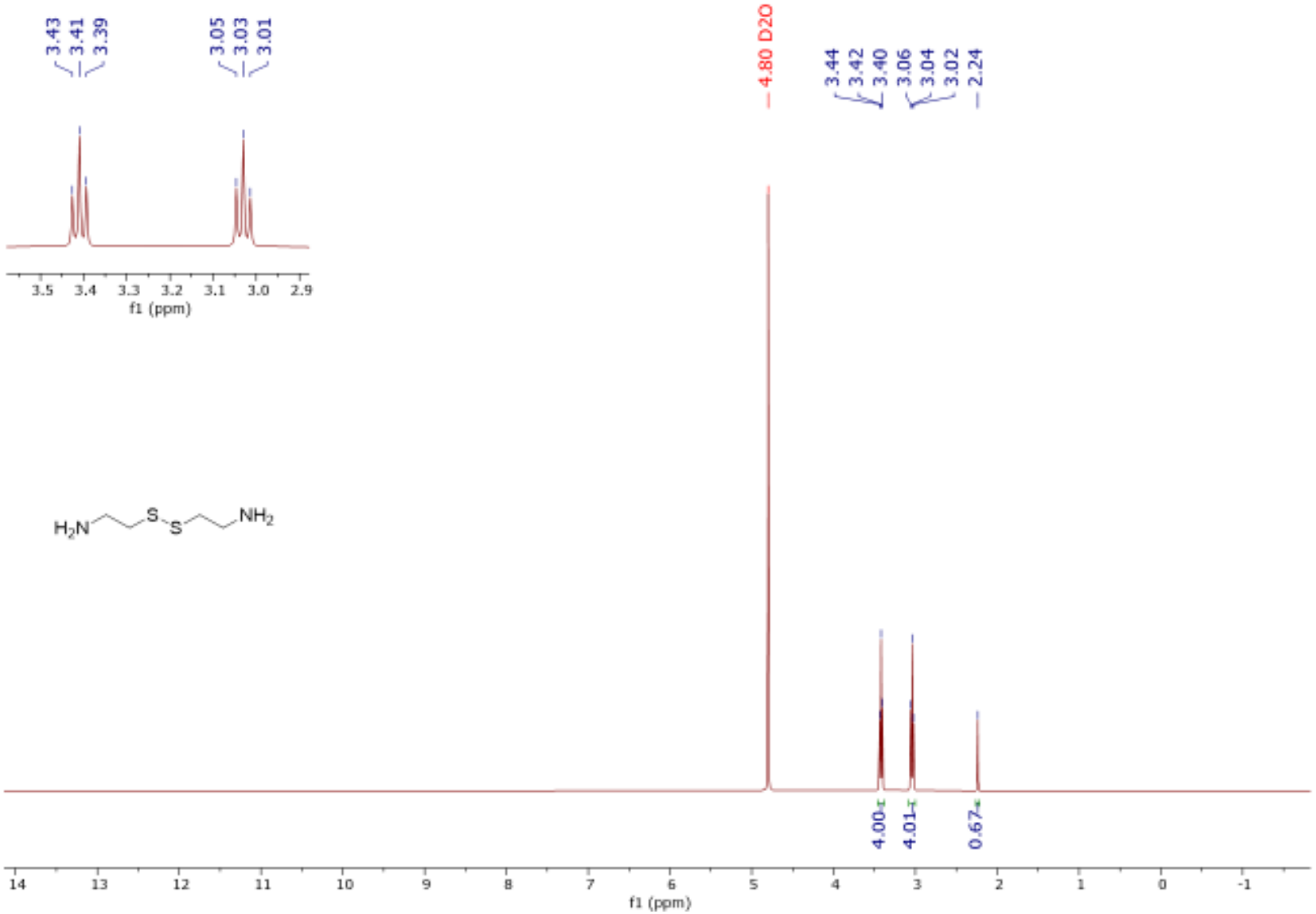

Figure A7: ^{1}H NMR (D_2O, 400 MHz) spectrum of cystamine

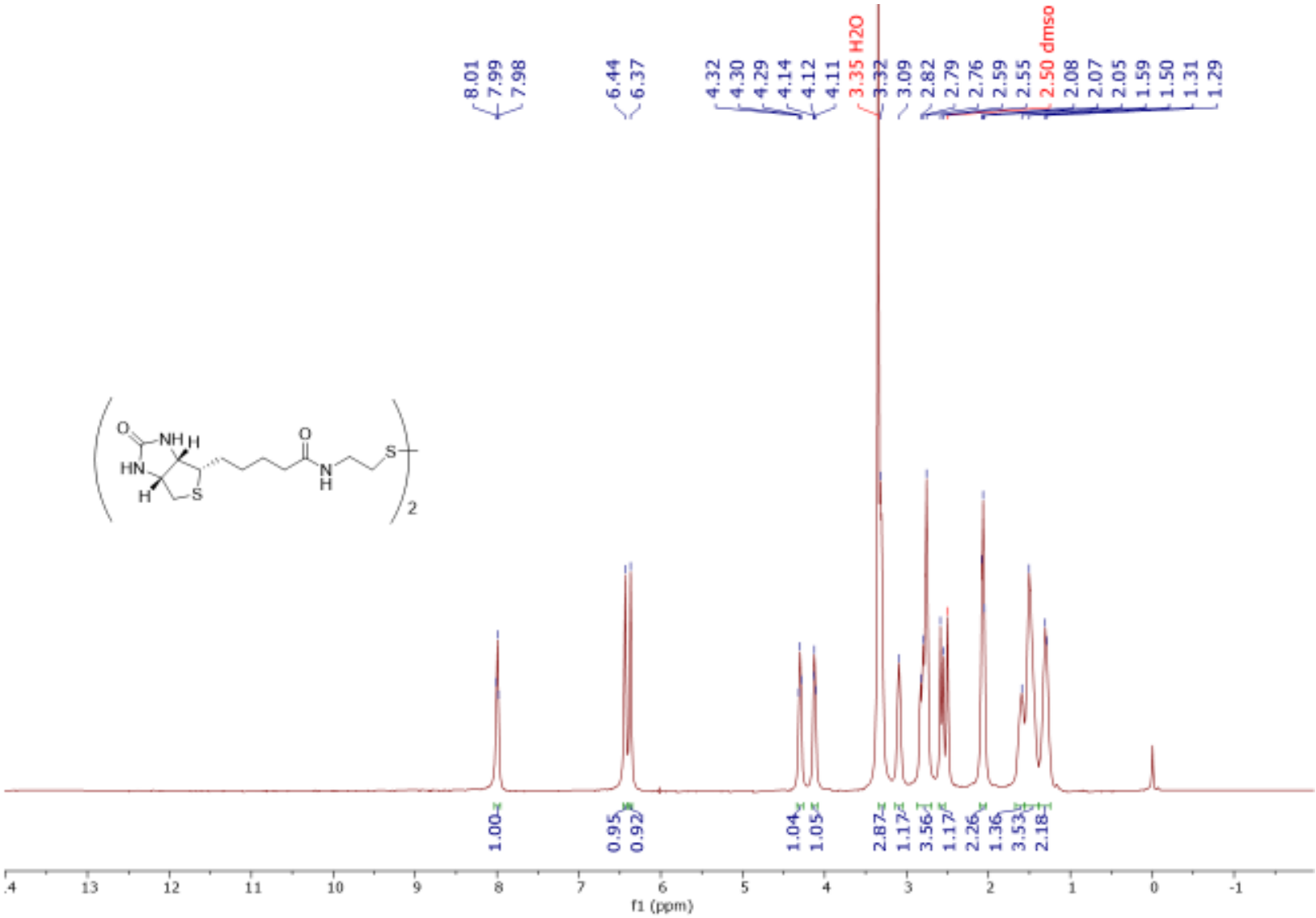

Figure A8: ^{1}H NMR (DMSO-d_6, 400 MHz) spectrum of biotinylated-cystamine

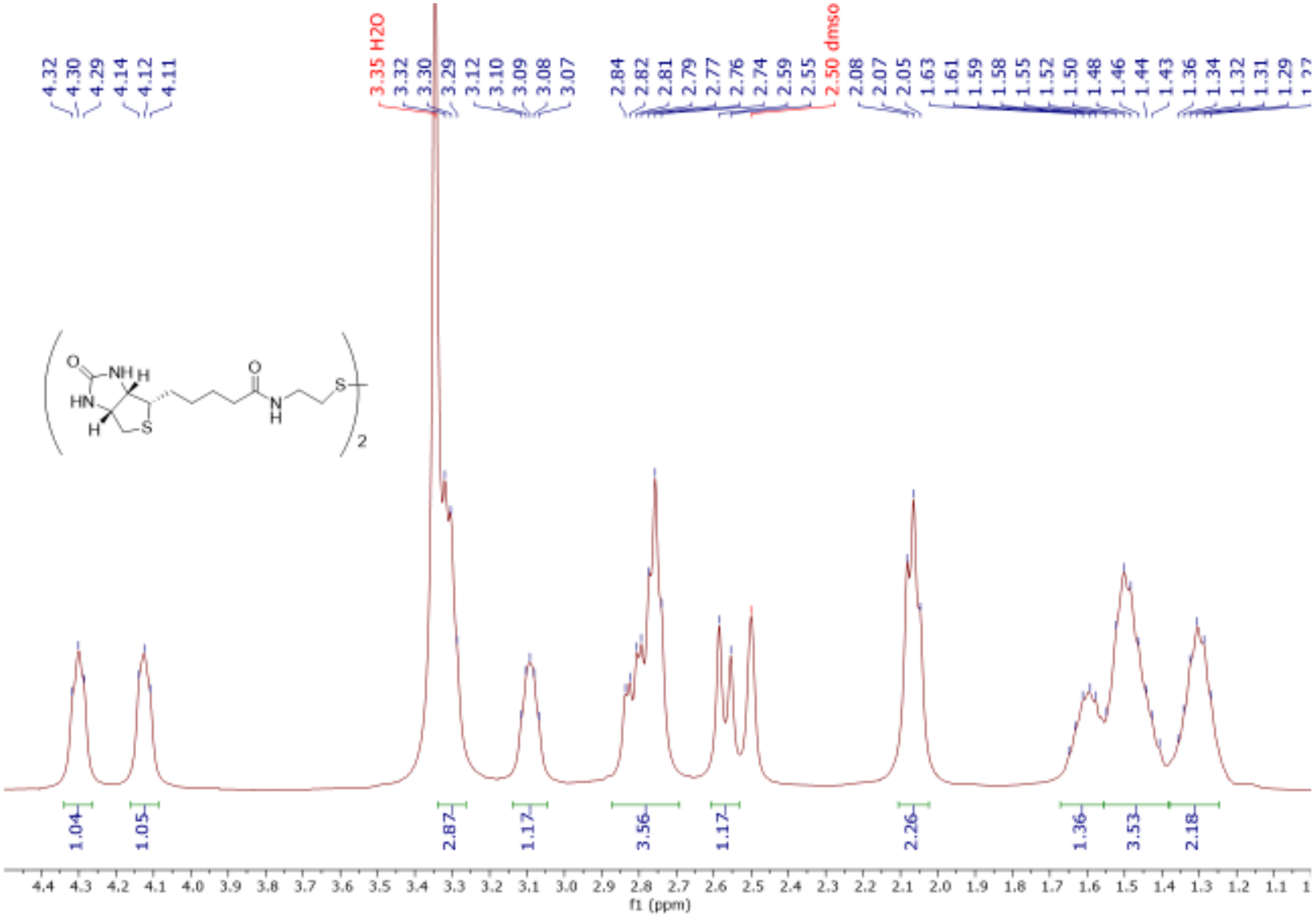

Figure A9:Expansion of ^{1}H NMR (DMSO-d_6, 400 MHz) spectrum of biotinylated-cystamine [4.5 to 1.0 ppm]

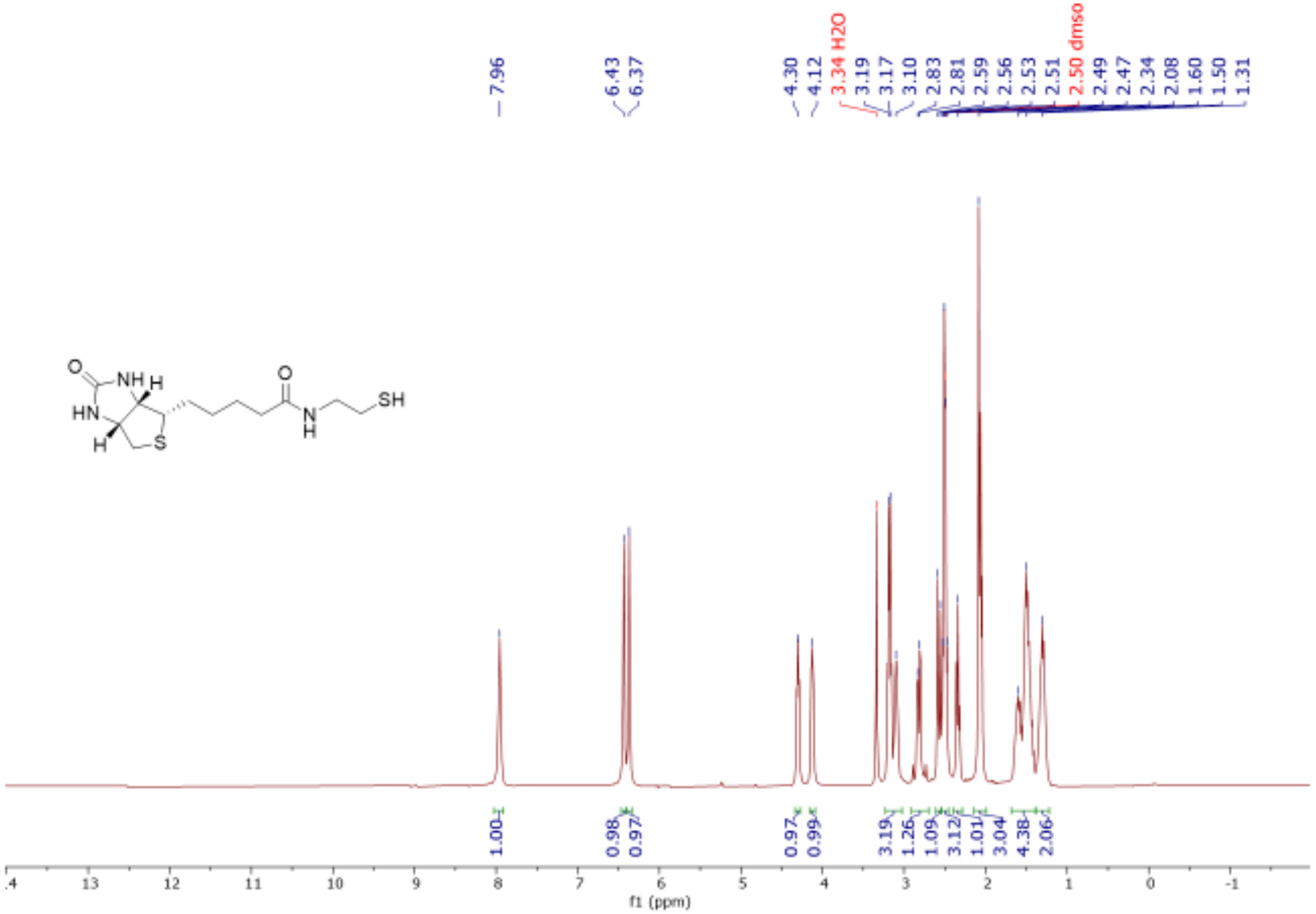

Figure A10: ^{1}H NMR (DMSO-d_6, 400 MHz) spectrum of biotinylated-cysteamine

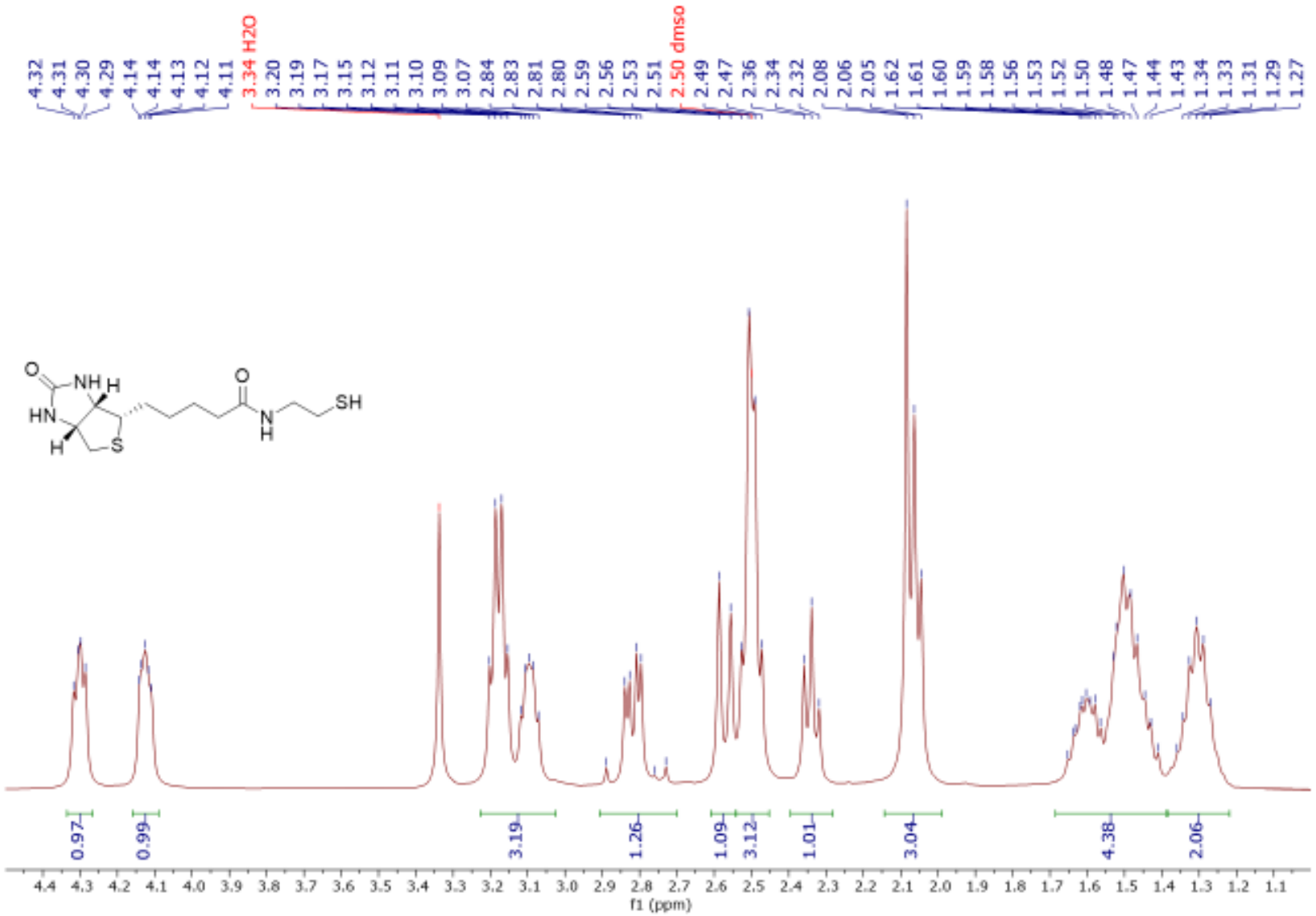

Figure A11:Expansion of ^{1}H NMR (DMSO-d_6, 400 MHz) spectrum of biotinylated-cysteamine [4.5 to 1.0 ppm]

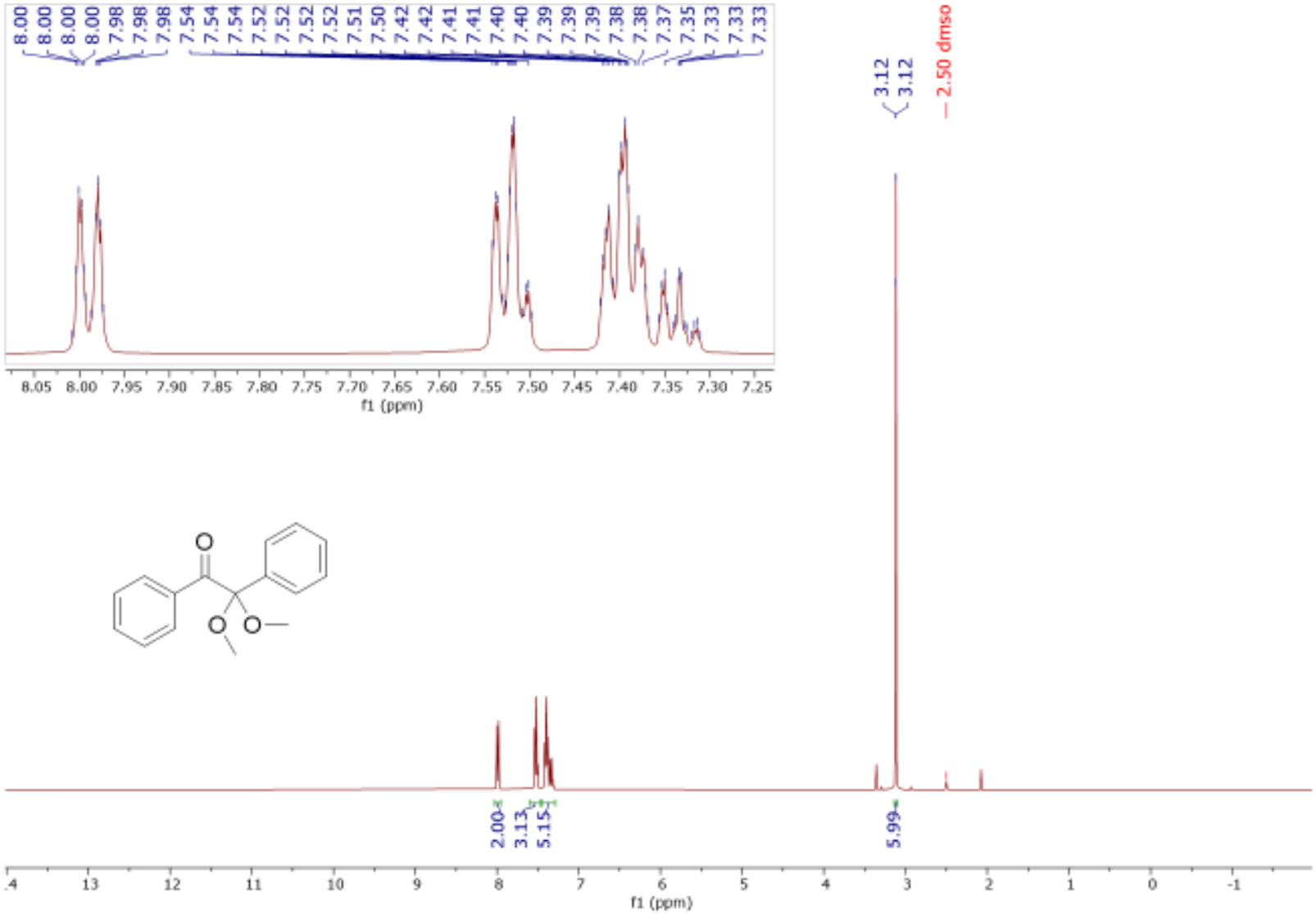

Figure A12: ^{1}H NMR (DMSO-d_6, 400 MHz) spectrum of 2,2-dimethoxy-2-phenoacetophenone

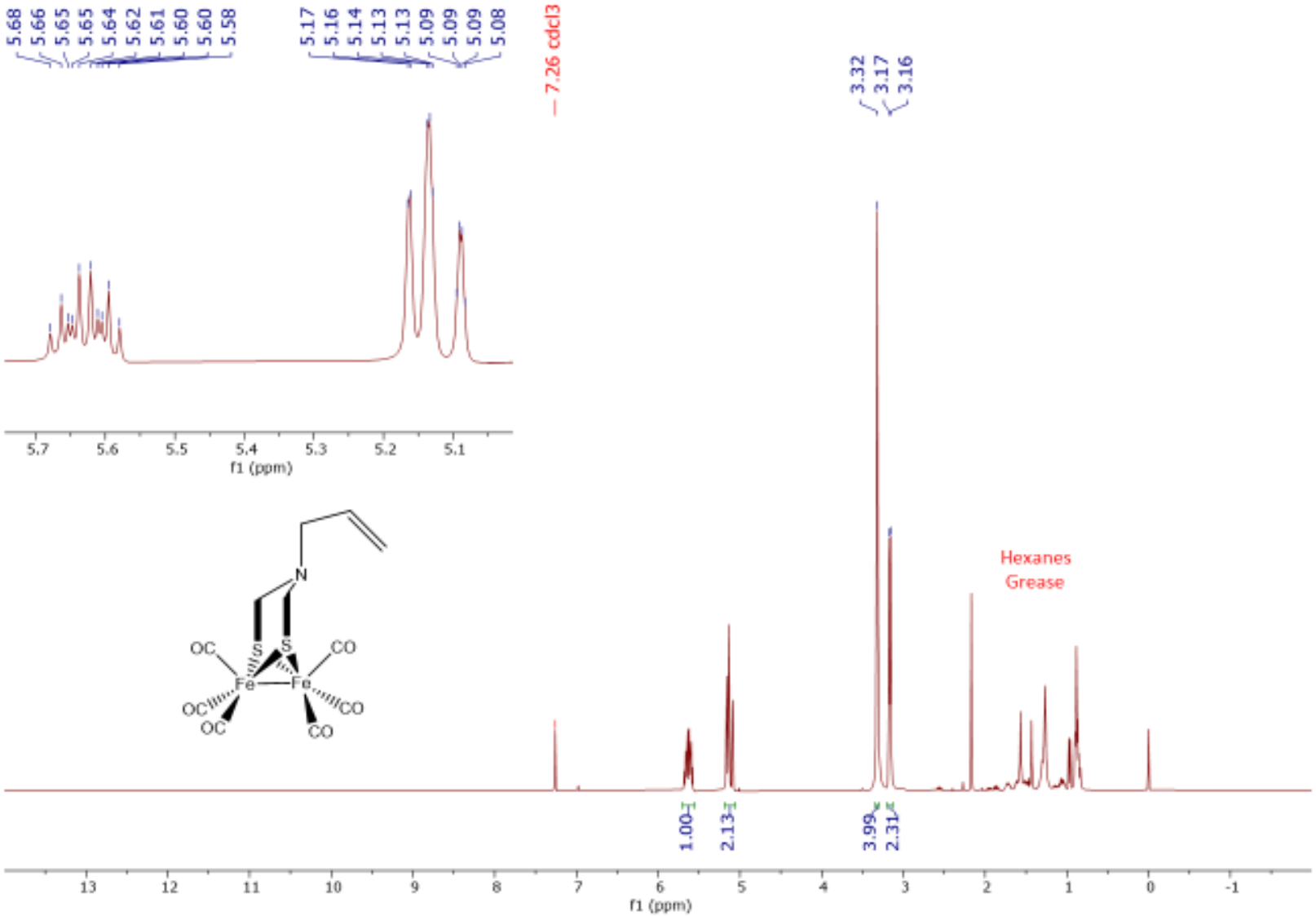

Figure A13: ^{1}H NMR ($CDCl_3$, 400 MHz) spectrum of (μ-allylazadithiolato)diiron(I) hexacarbonyl

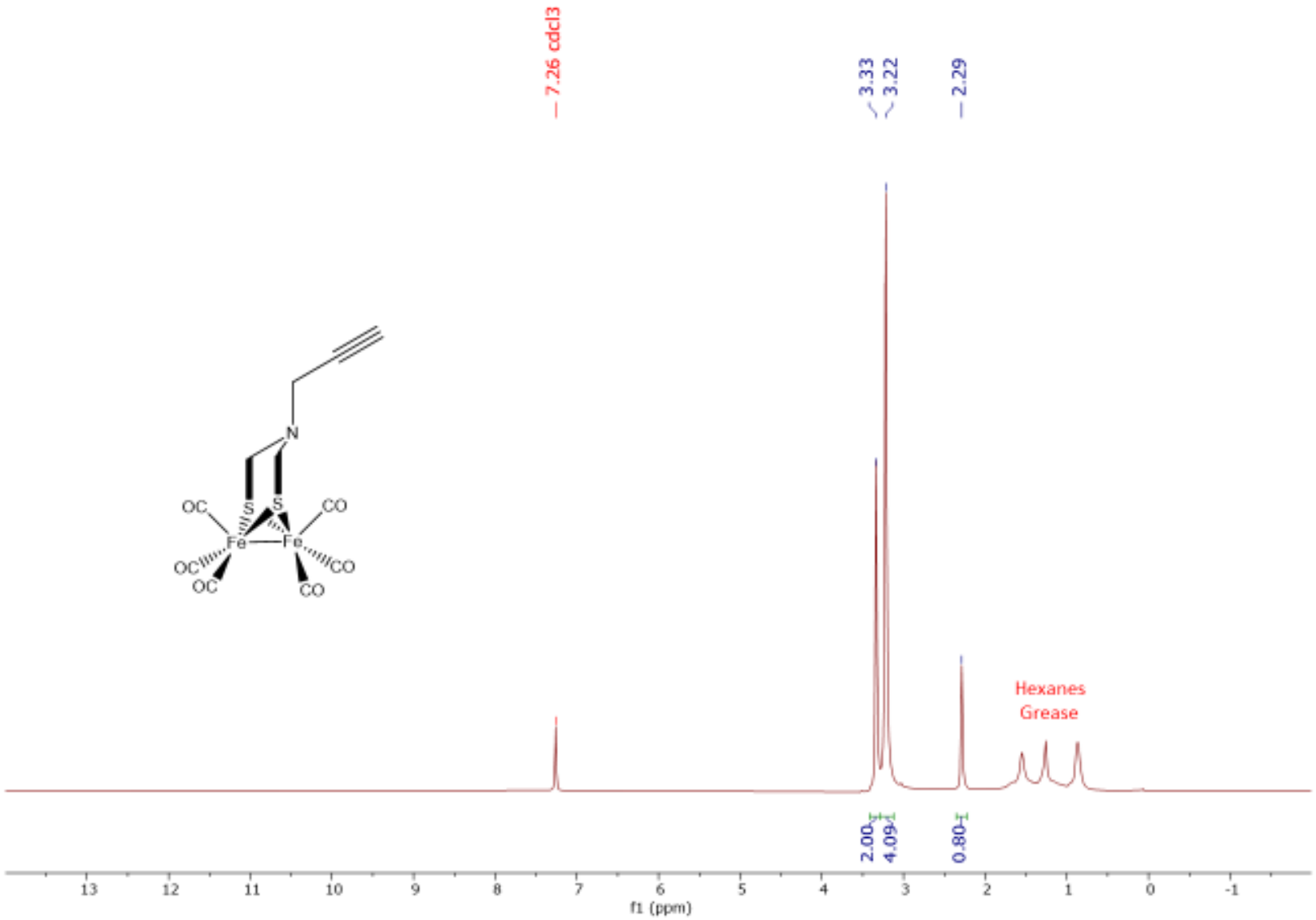

Figure A14: ^{1}H NMR ($CDCl_3$, 400 MHz) spectrum of (μ-propargylazadithiolato)diiron(I) hexacarbonyl

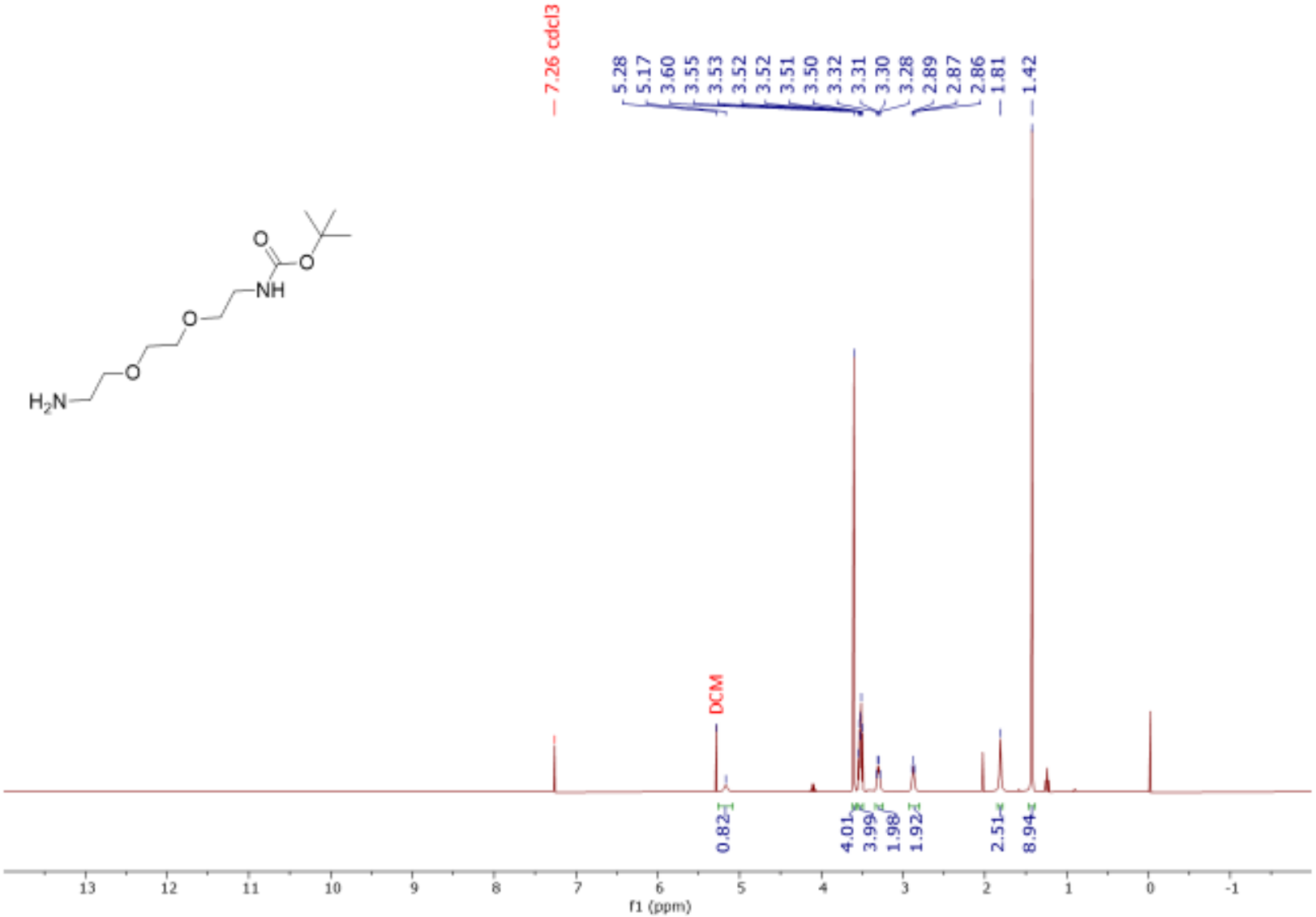

Figure A15: ^{1}H NMR ($CDCl_3$, 400 MHz) spectrum of tert-butyl[2-[2-(2-aminoethoxy)ethoxyethyl]]carbamate

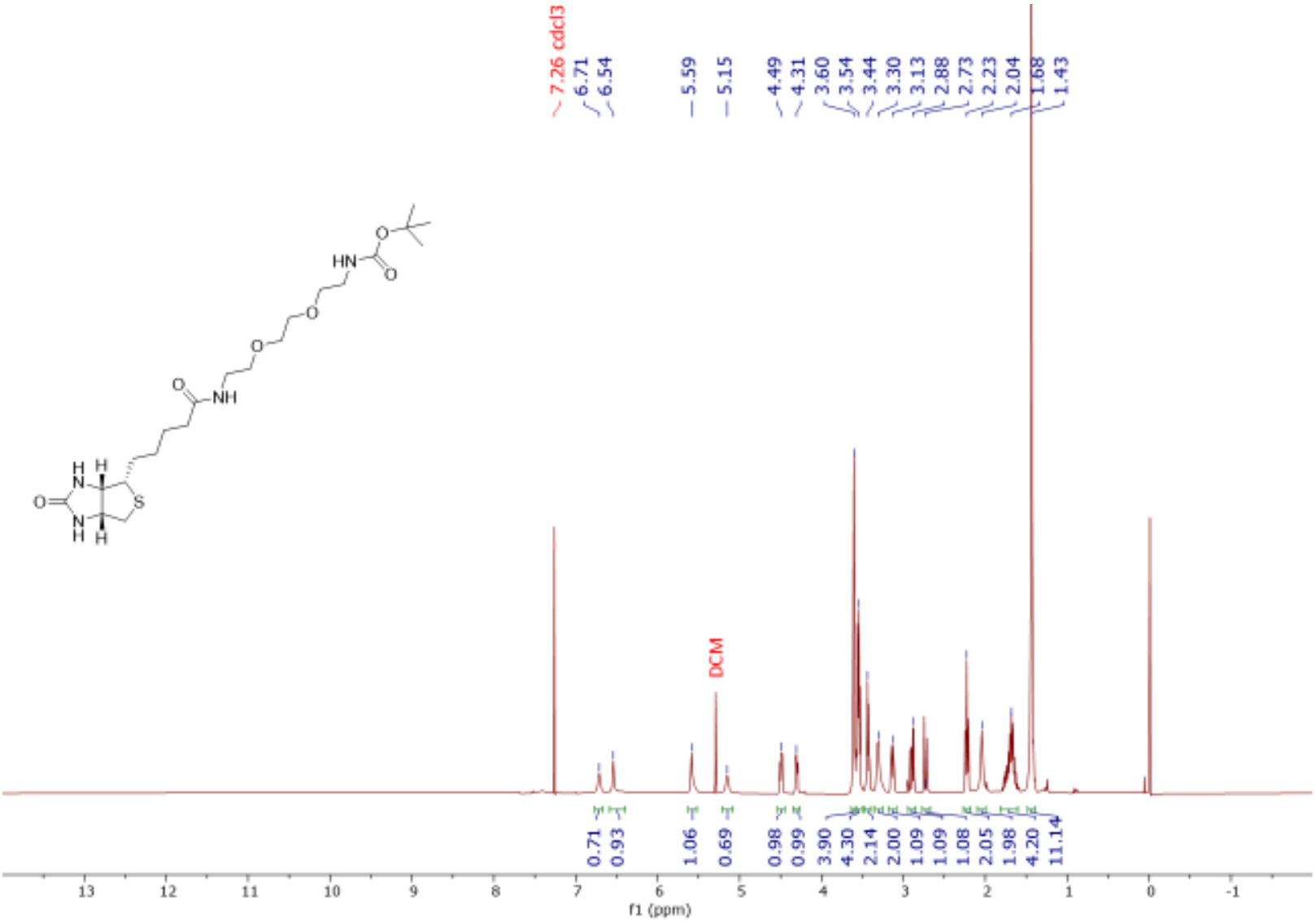

Figure A16: ^{1}H NMR ($CDCl_3$, 400 MHz) spectrum of biotinylated- tert-butyl[2-[2-(2-aminoethoxy)ethoxyethyl]]carbamate

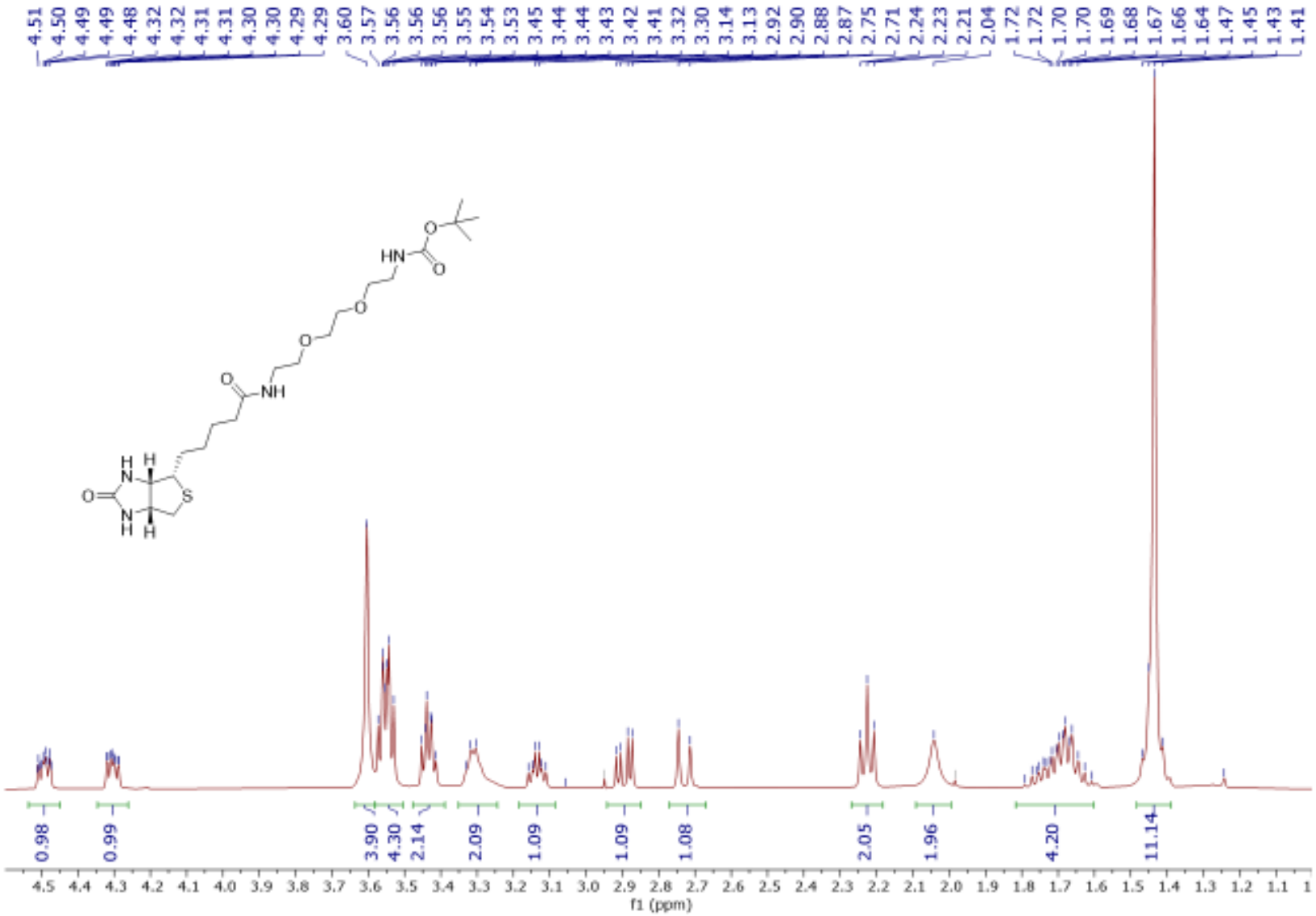

Figure A17:Expansion of ^{1}H NMR ($CDCl_3$, 400 MHz) spectrum of biotinylated- tert-butyl[2-[2-(2-aminoethoxy)ethoxyethyl]]carbamate [4.6 to 1.0 ppm]

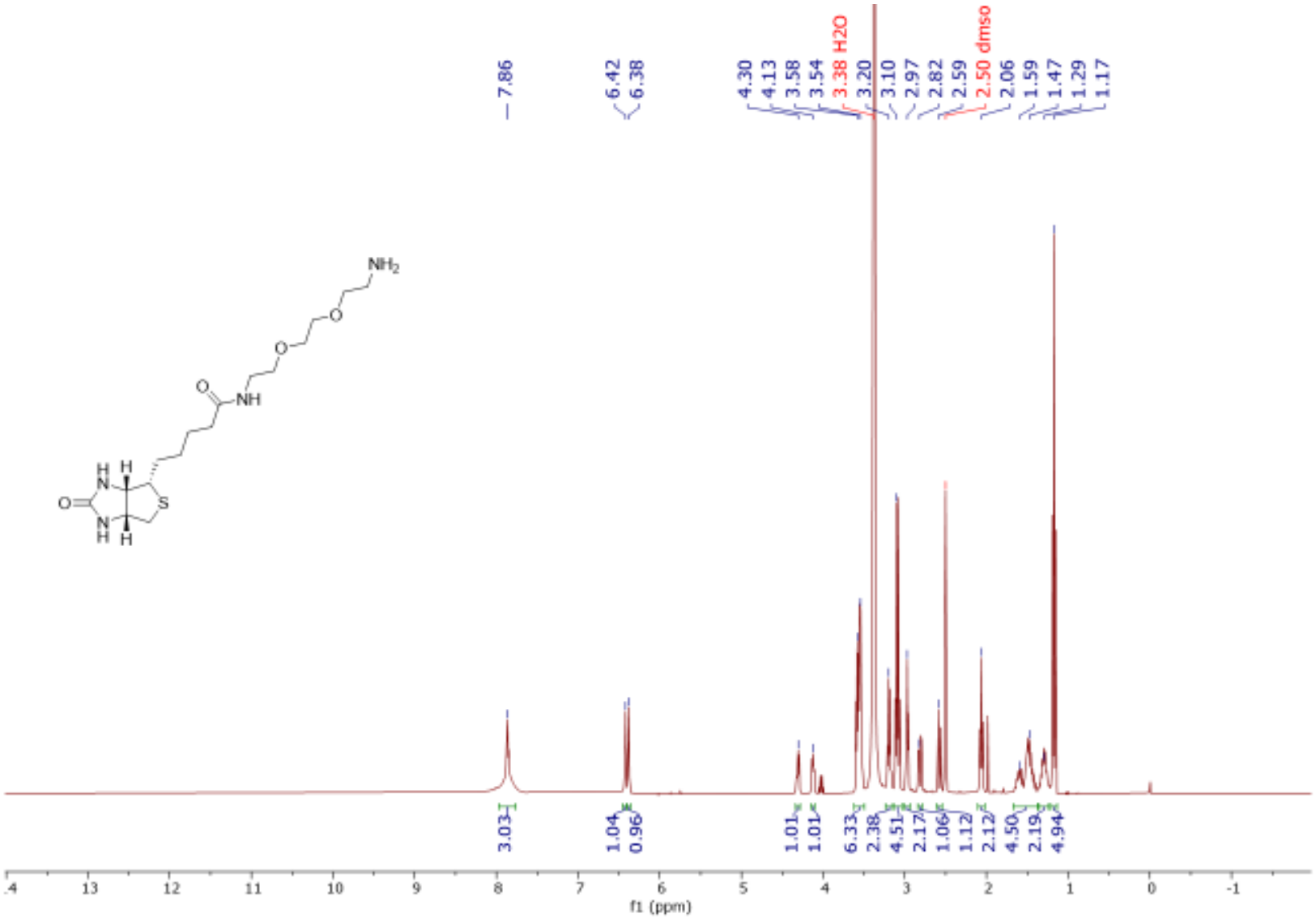

Figure A18: ^{1}H NMR (DMSO-d_6, 400 MHz) spectrum of Biotinylated -3,6-dioxaoctane-1,8-diamine

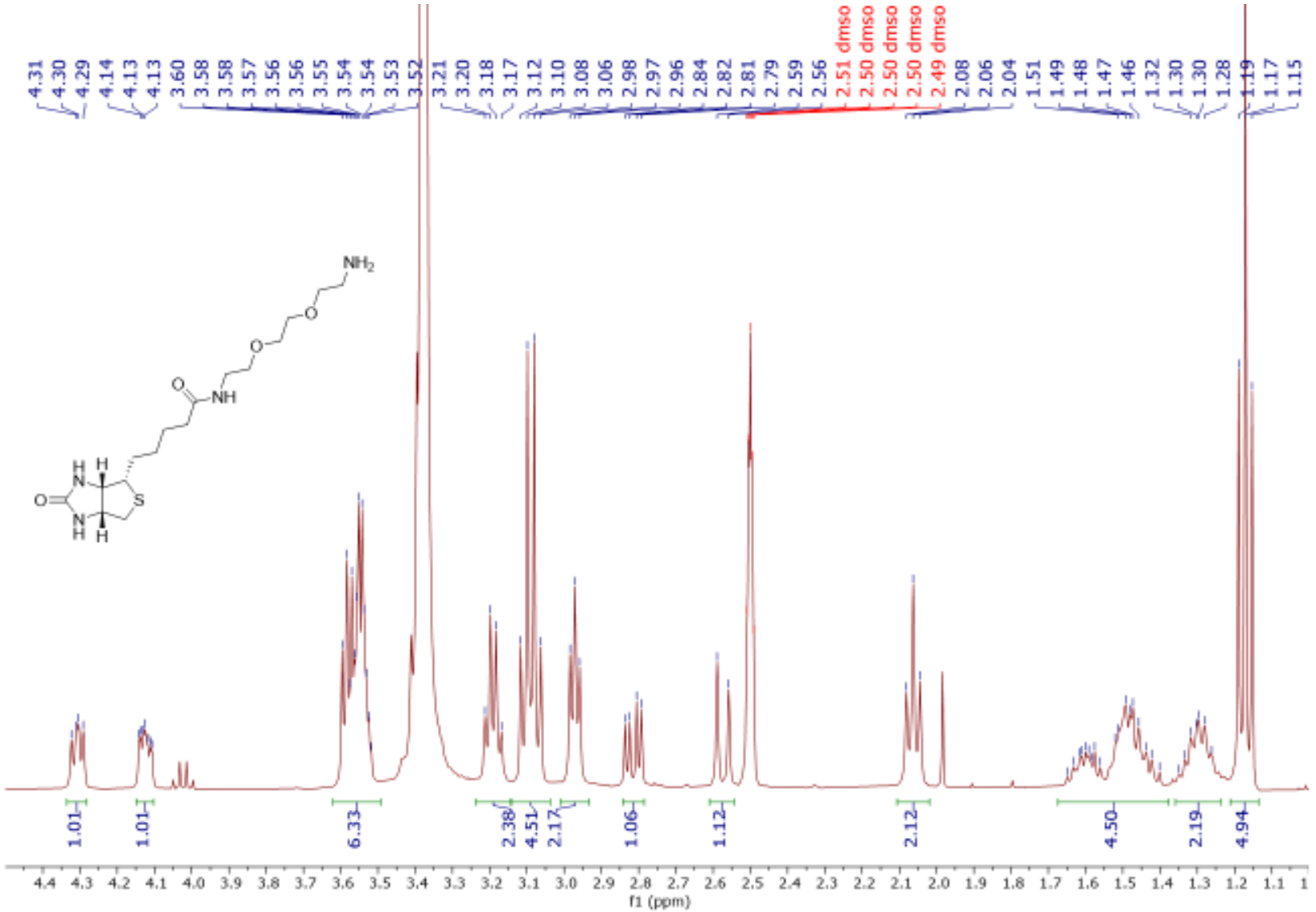

Figure A19:Expansion of ^{1}H NMR (DMSO-d_6, 400 MHz) spectrum of Biotinylated -3,6-dioxaoctane-1,8-diamine [4.5 to 1.0 ppm]

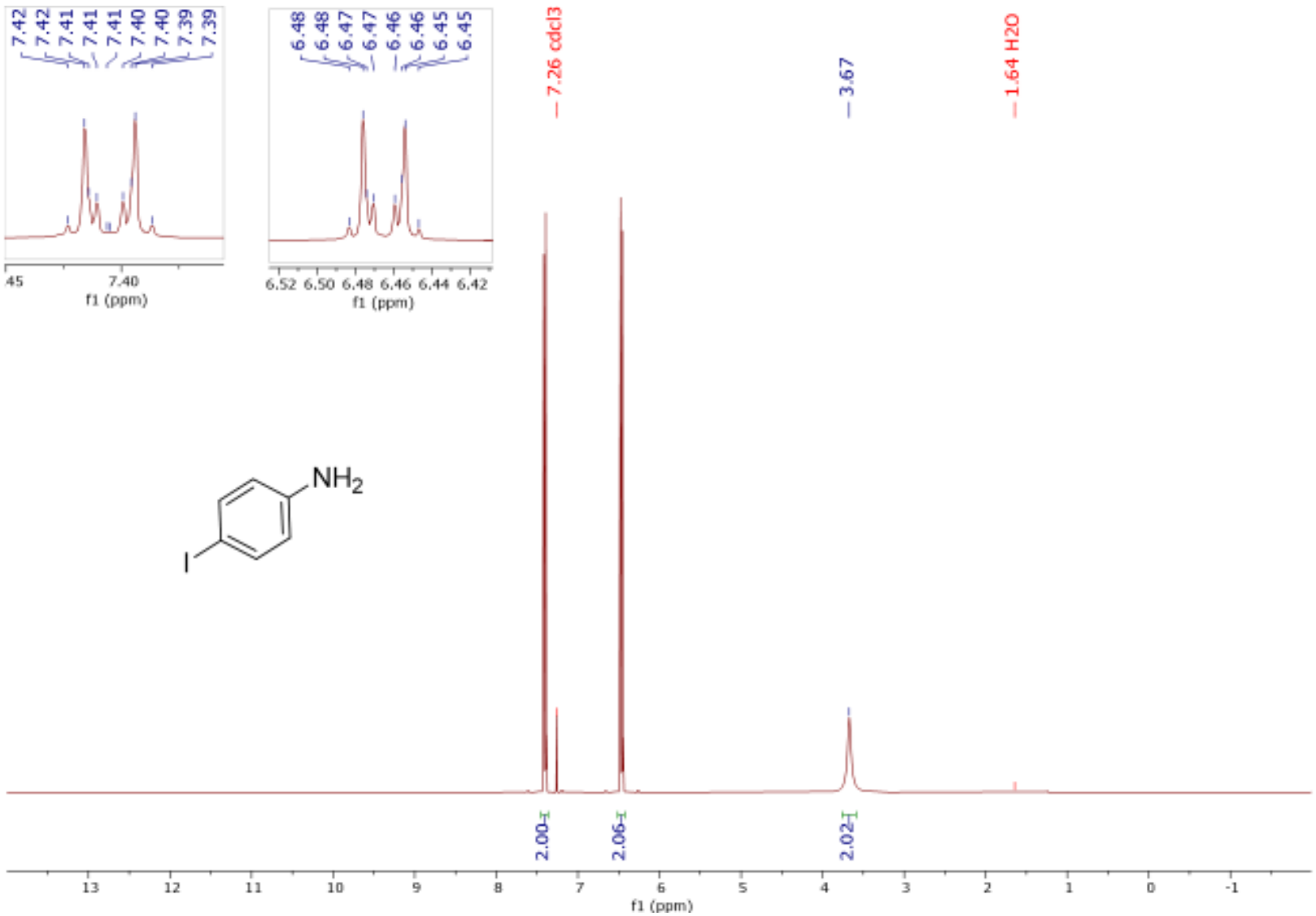

Figure A20: ^{1}H NMR ($CDCl_3$, 400 MHz) spectrum of 4-iodoanaline

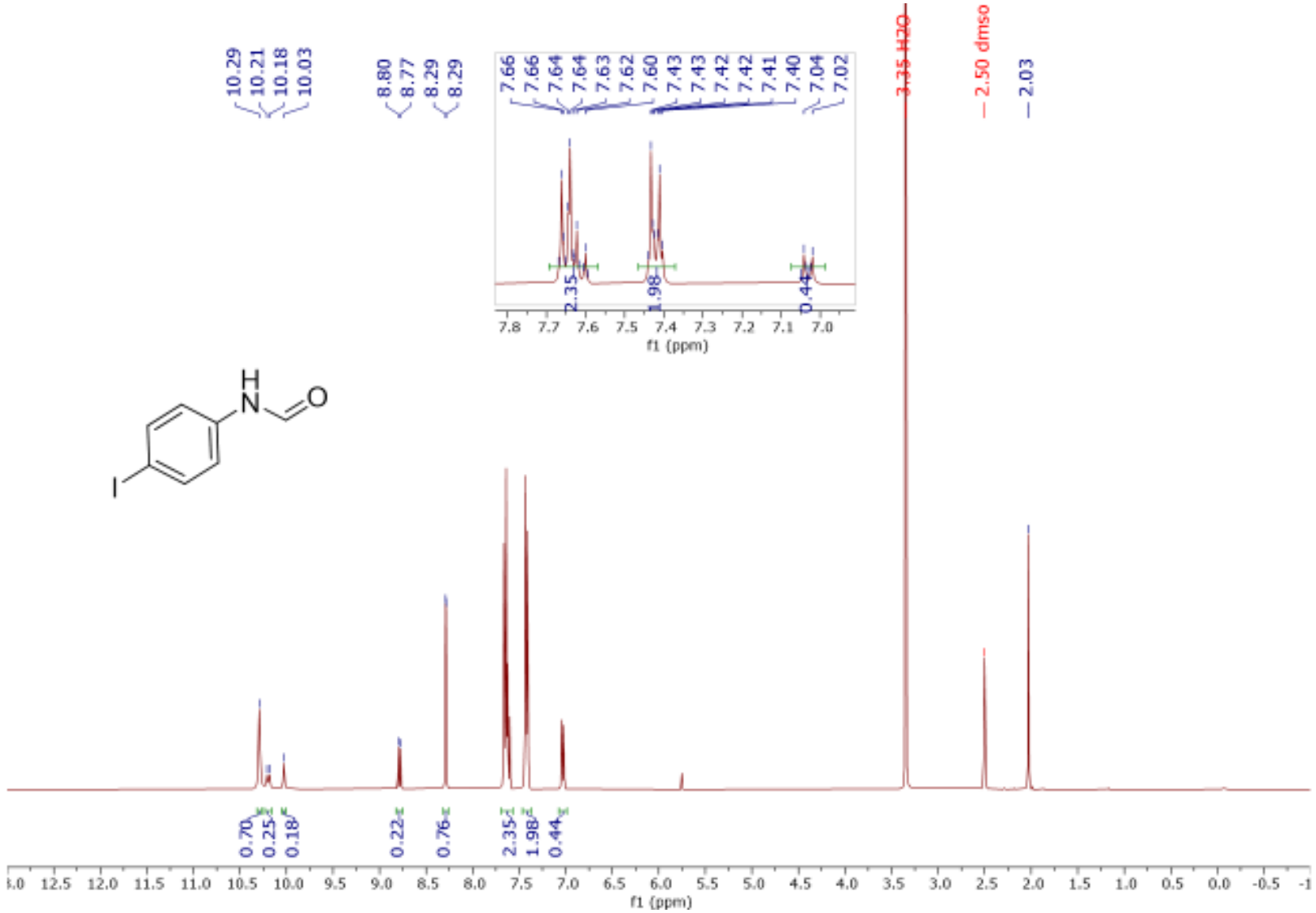

Figure A21: ^{1}H NMR ($CDCl_3$, 400 MHz) spectrum of N-(4-iodophenyl)-formamide (mixture of rotamers)

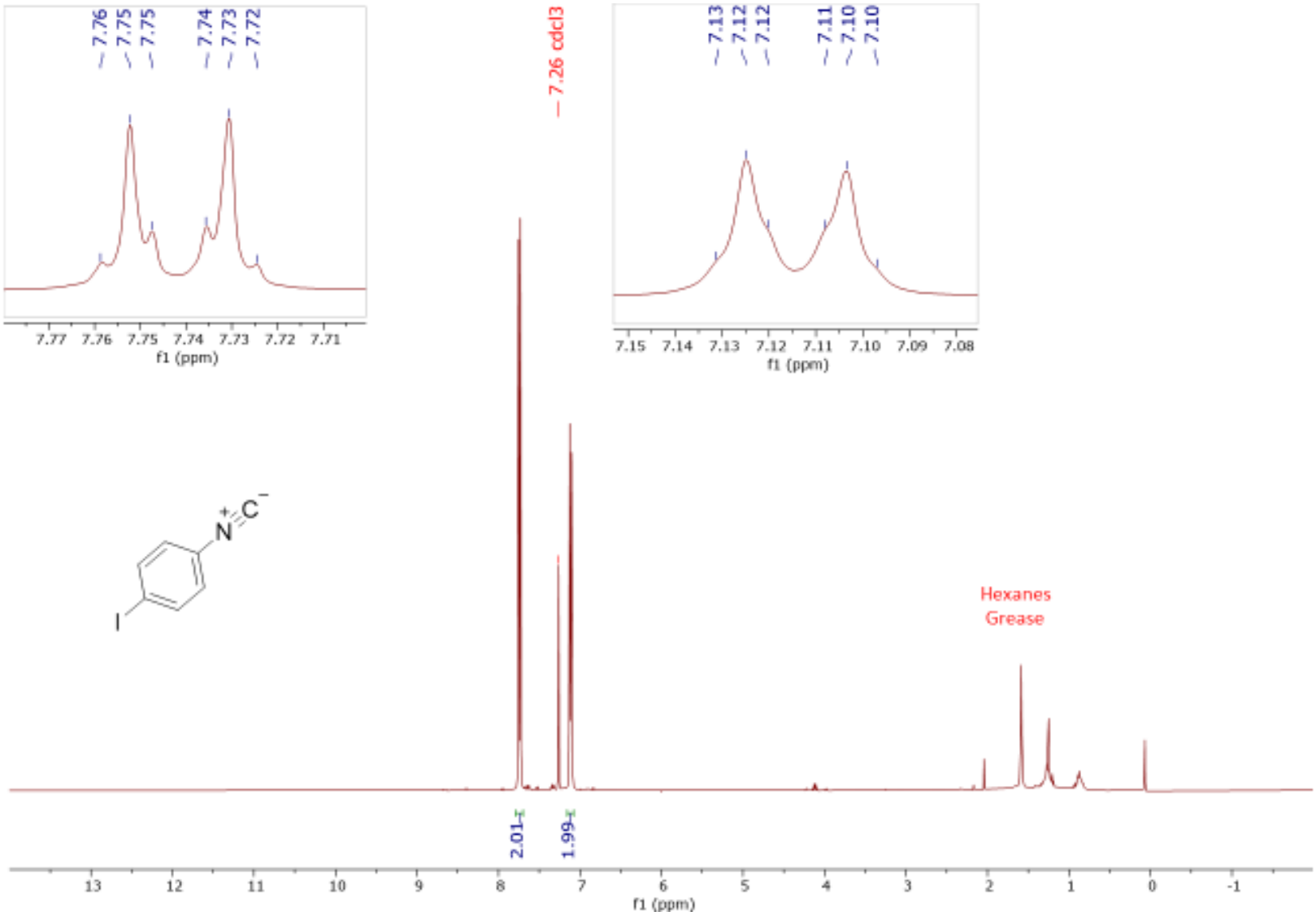

Figure A22: ^{1}H NMR ($CDCl_3$, 400 MHz) spectrum of 4-iodophenyl isocyanide

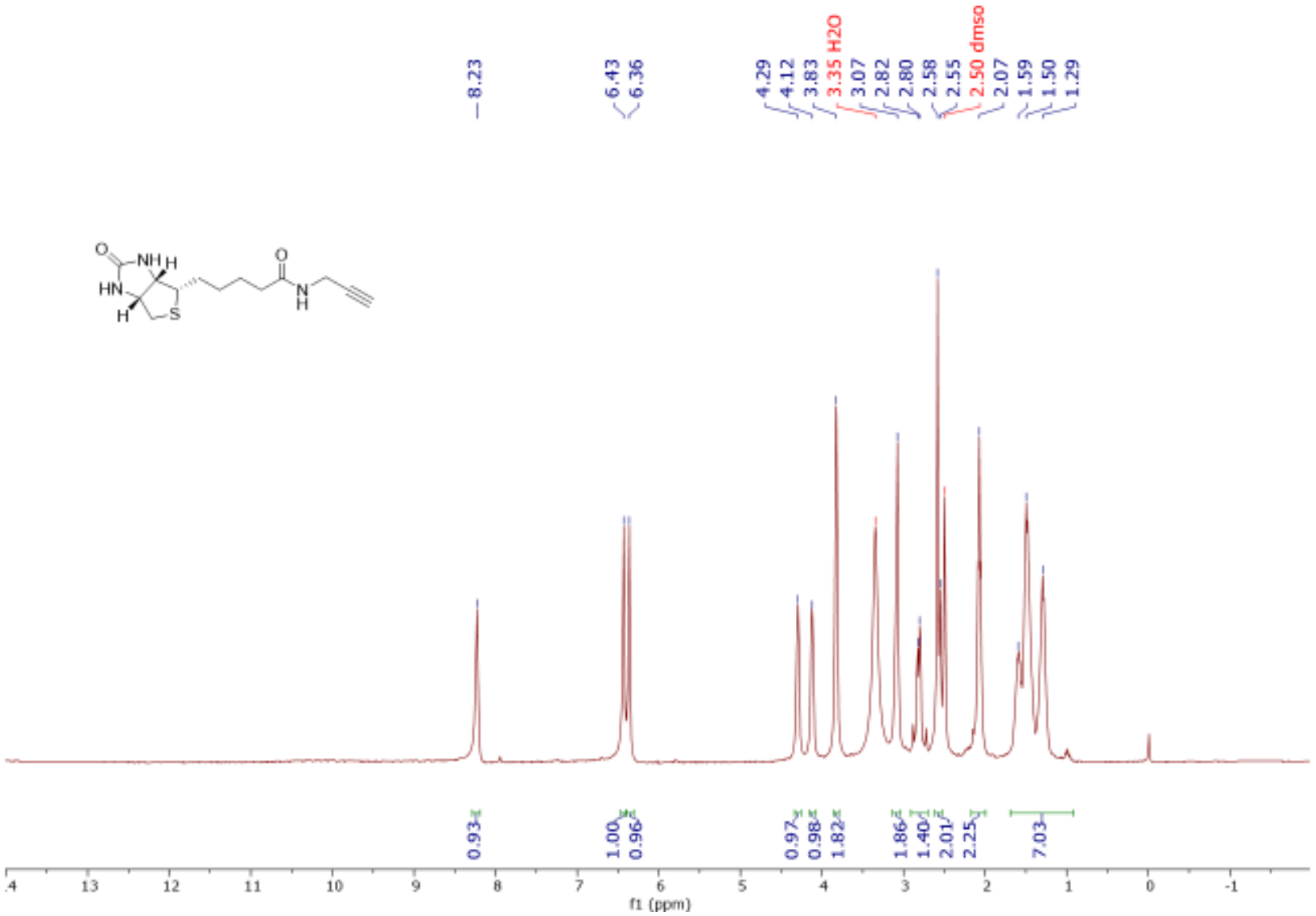

Figure A23: ^{1}H NMR (DMSO-d_6, 400 MHz) spectrum of Biotinylated-propargylamine

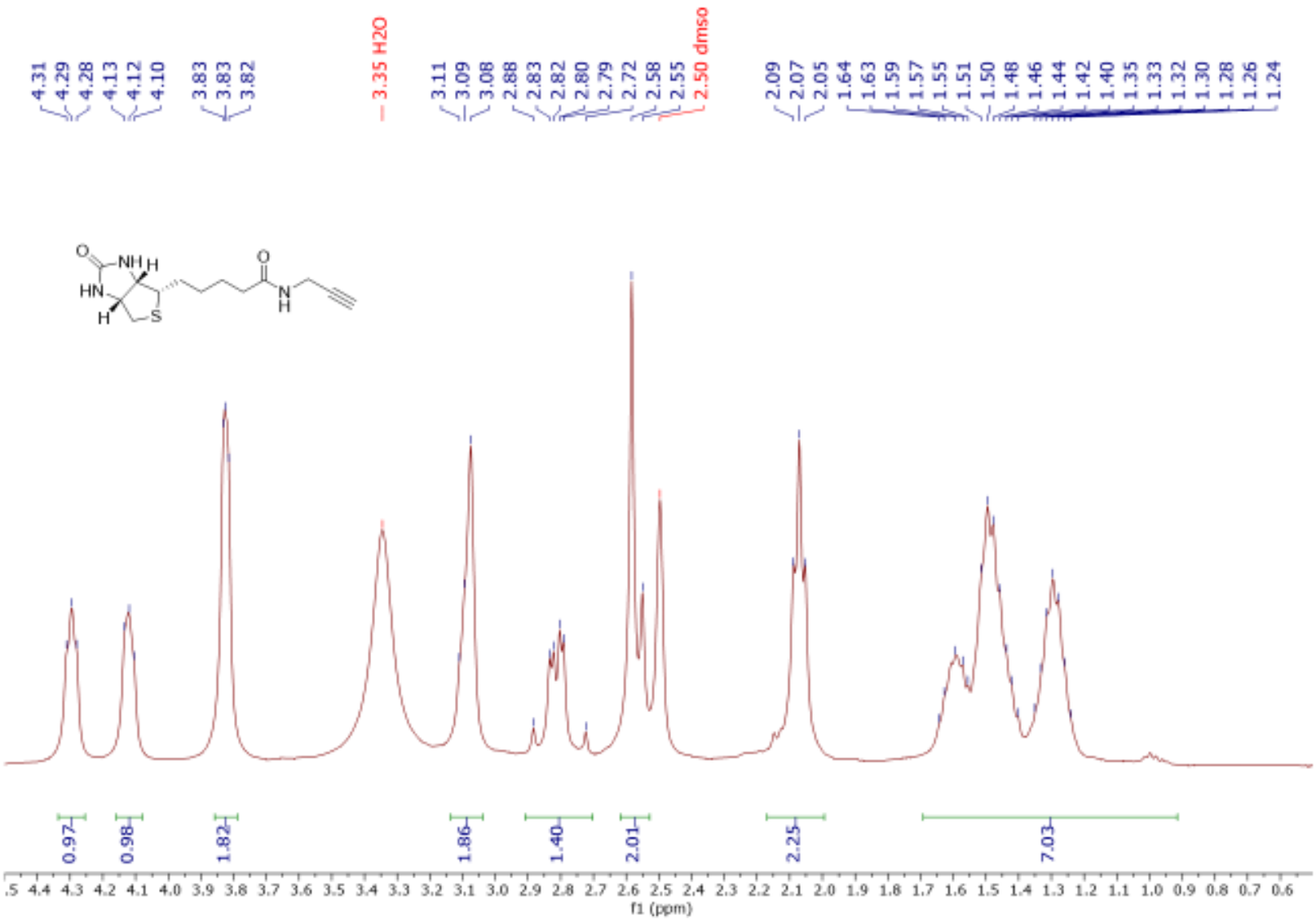

Figure A24:Expansion of ^{1}H NMR (DMSO-d_6, 400 MHz) spectrum of Biotinylated-propargylamine [4.5 to 0.5 ppm]

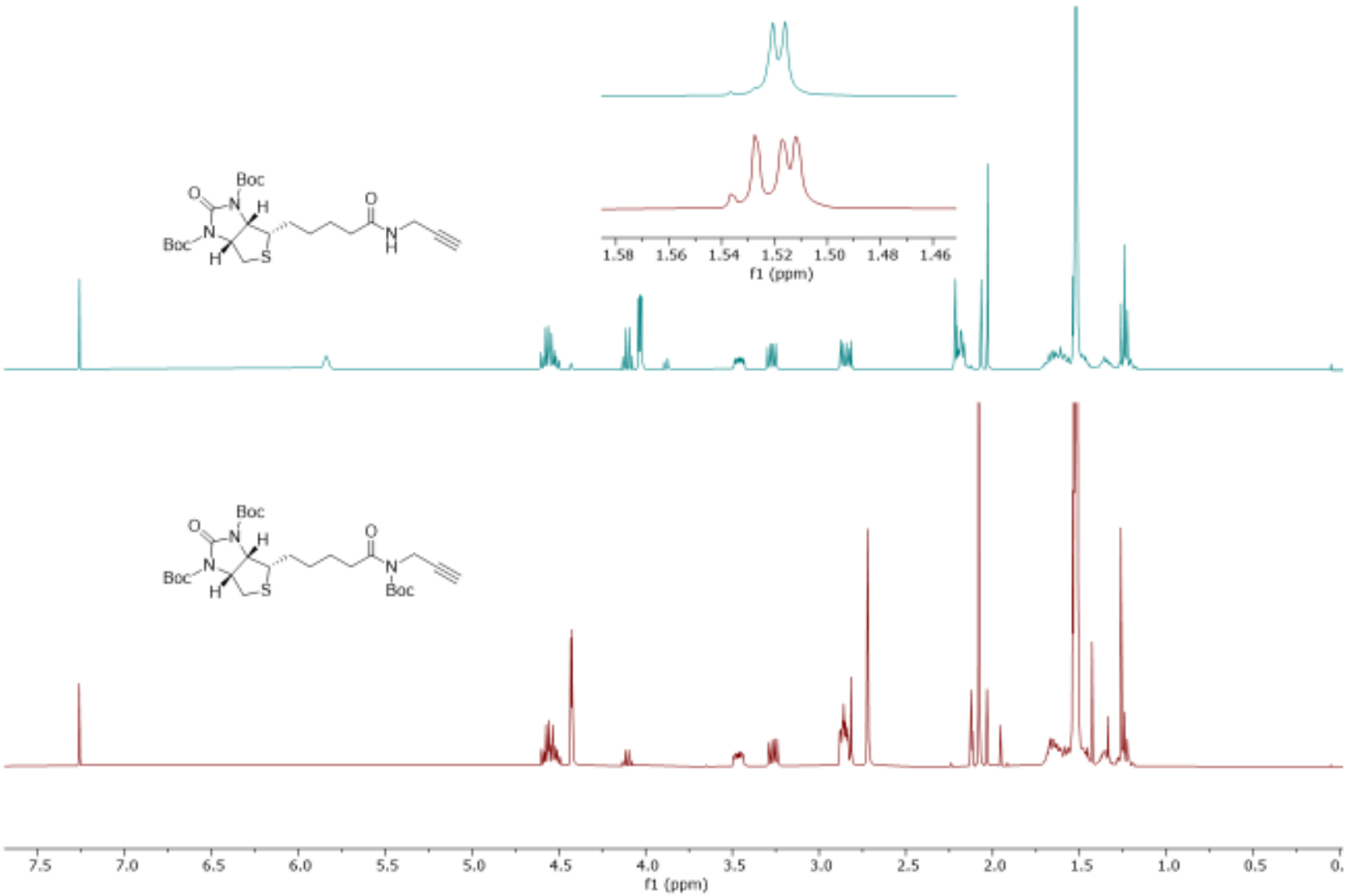

Figure A25: ^{1}H NMR ($CDCl_3$, 400 MHz) spectrums of Boc protected Biotinylated-propargylamine

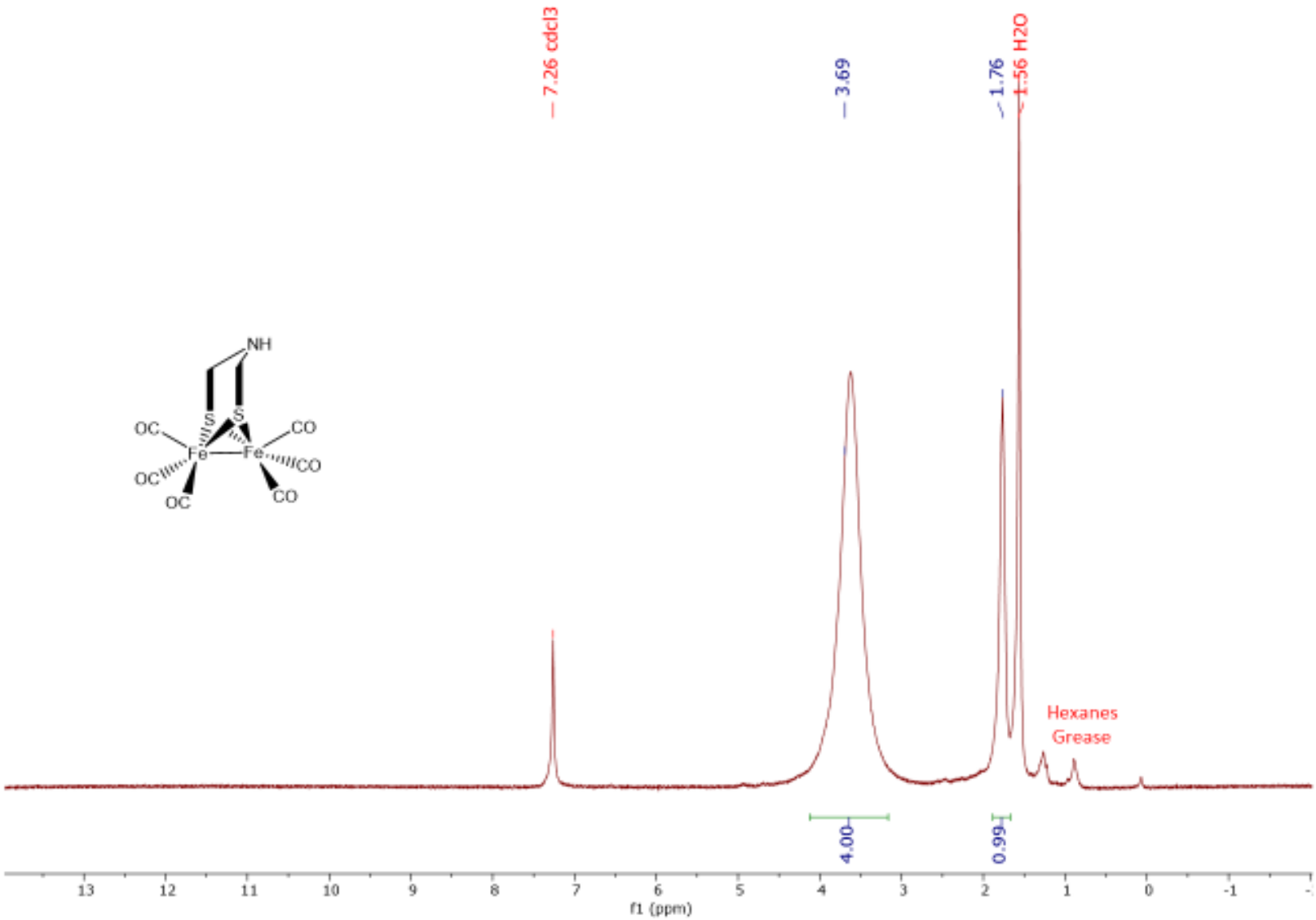

Figure A26: ^{1}H NMR ($CDCl_3$, 400 MHz) spectrum of (μ-azadithiolato)diiron(I) hexacarbonyl

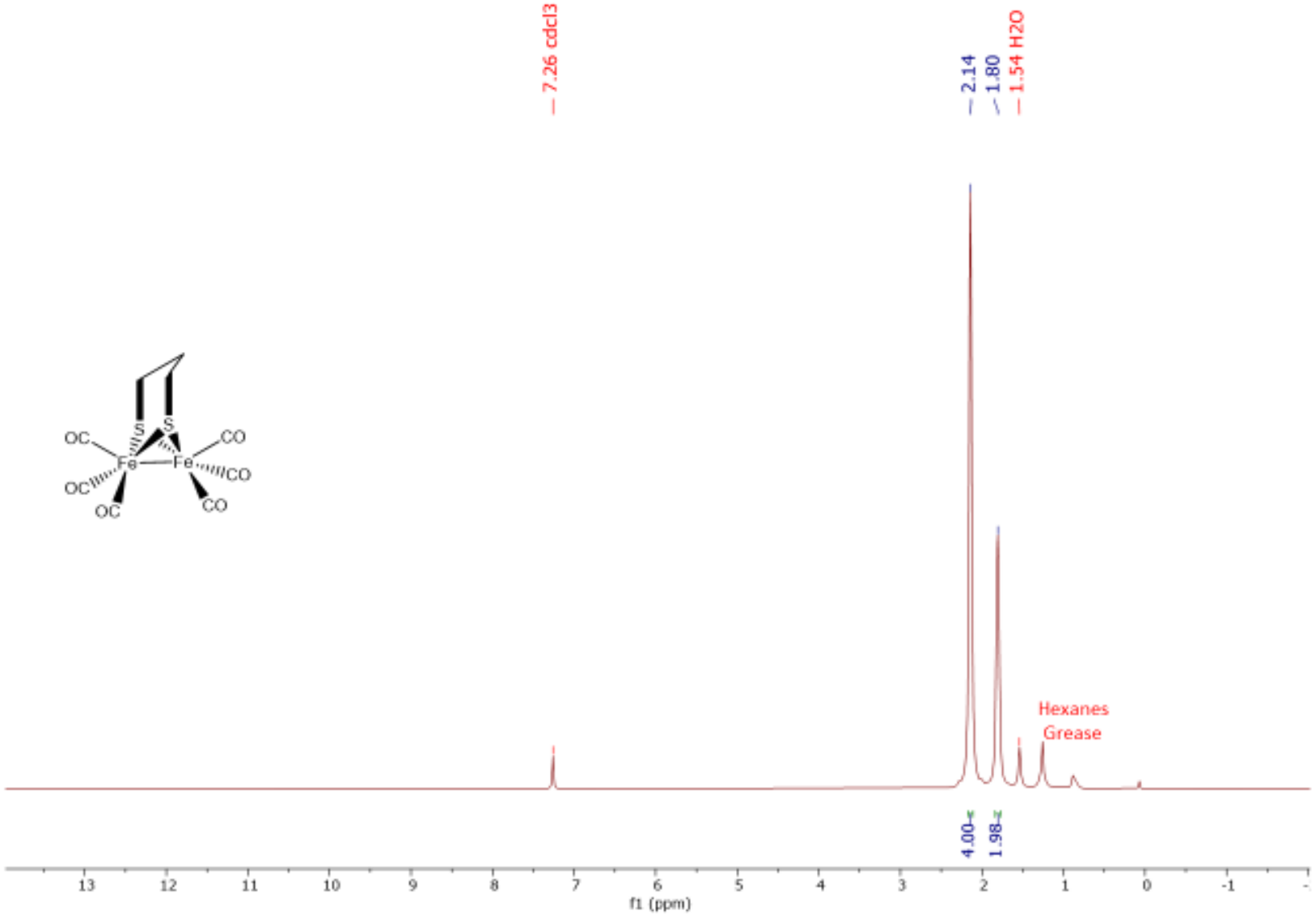

Figure A27: ^{1}H NMR ($CDCl_3$, 400 MHz) spectrum of (μ-propanedithiolato)diiron(I) hexacarbonyl

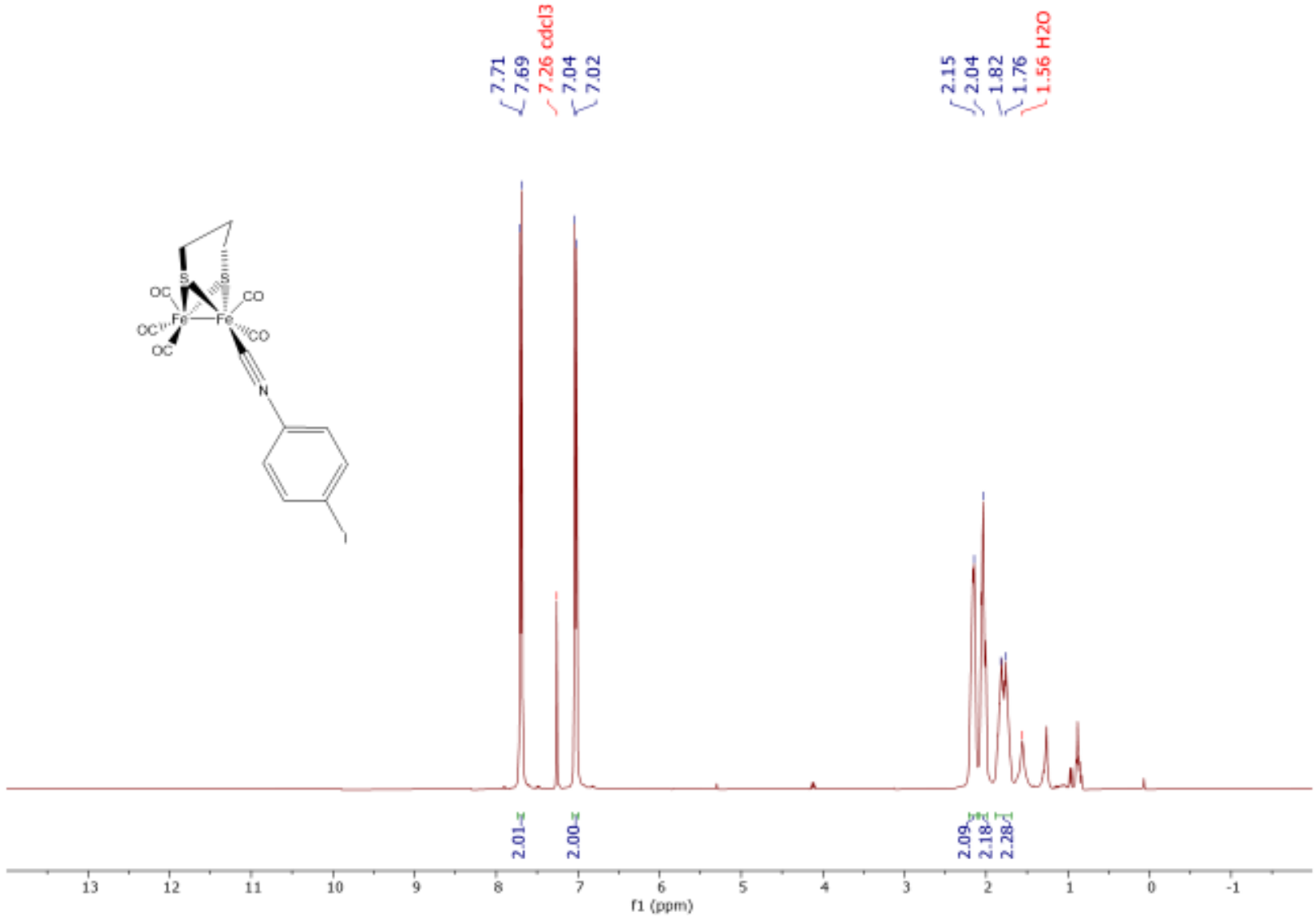

Figure A28: ^{1}H NMR ($CDCl_3$, 400 MHz) spectrum of (μ-propanedithiolato)diiron 4-iodopheynylisocyano pentacarbonyl

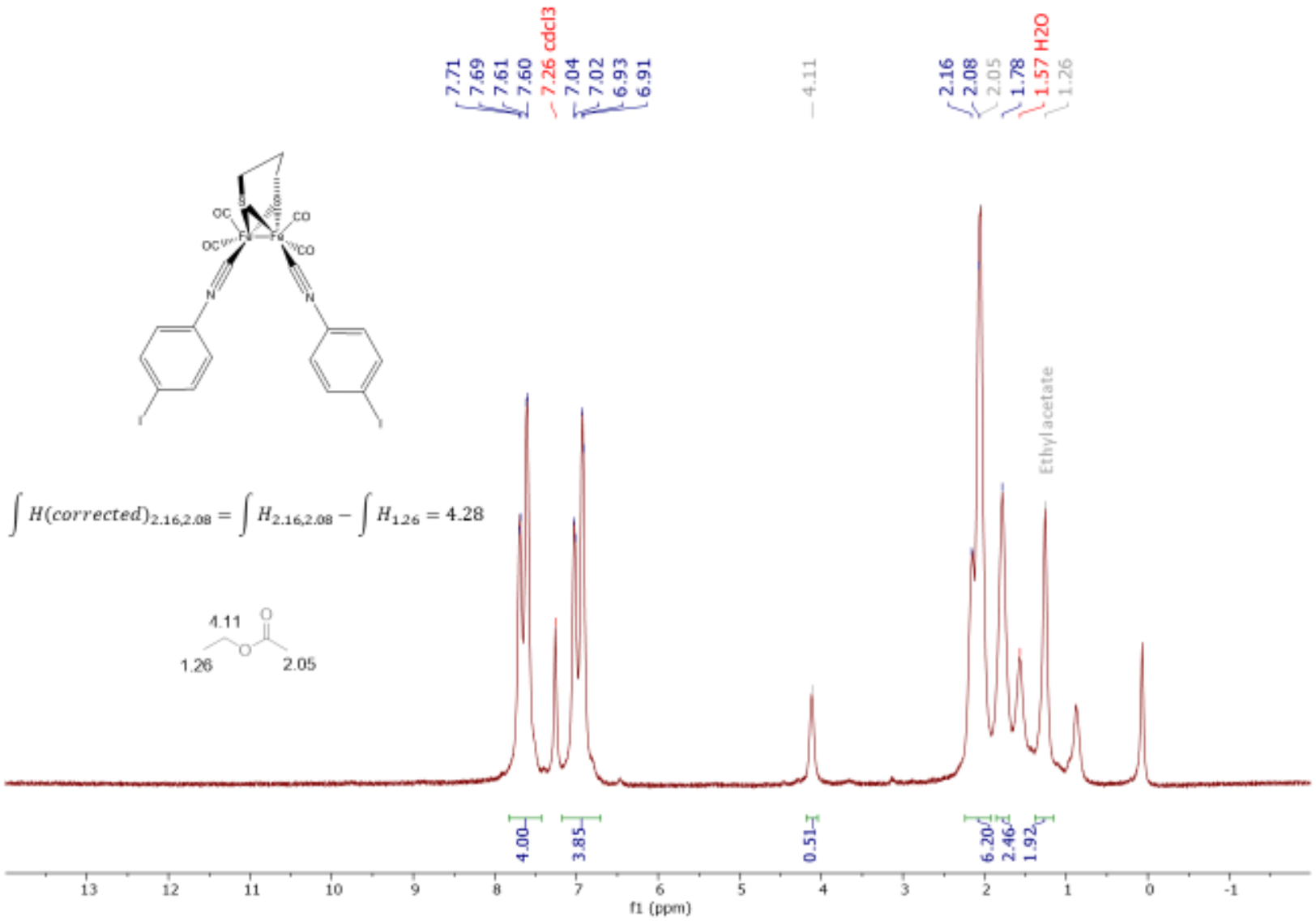

Figure A29: ^{1}H NMR ($CDCl_3$, 400 MHz) spectrum of (μ-propanedithiolato)diiron di(4-iodopheynylisocyano) tetracarbonyl

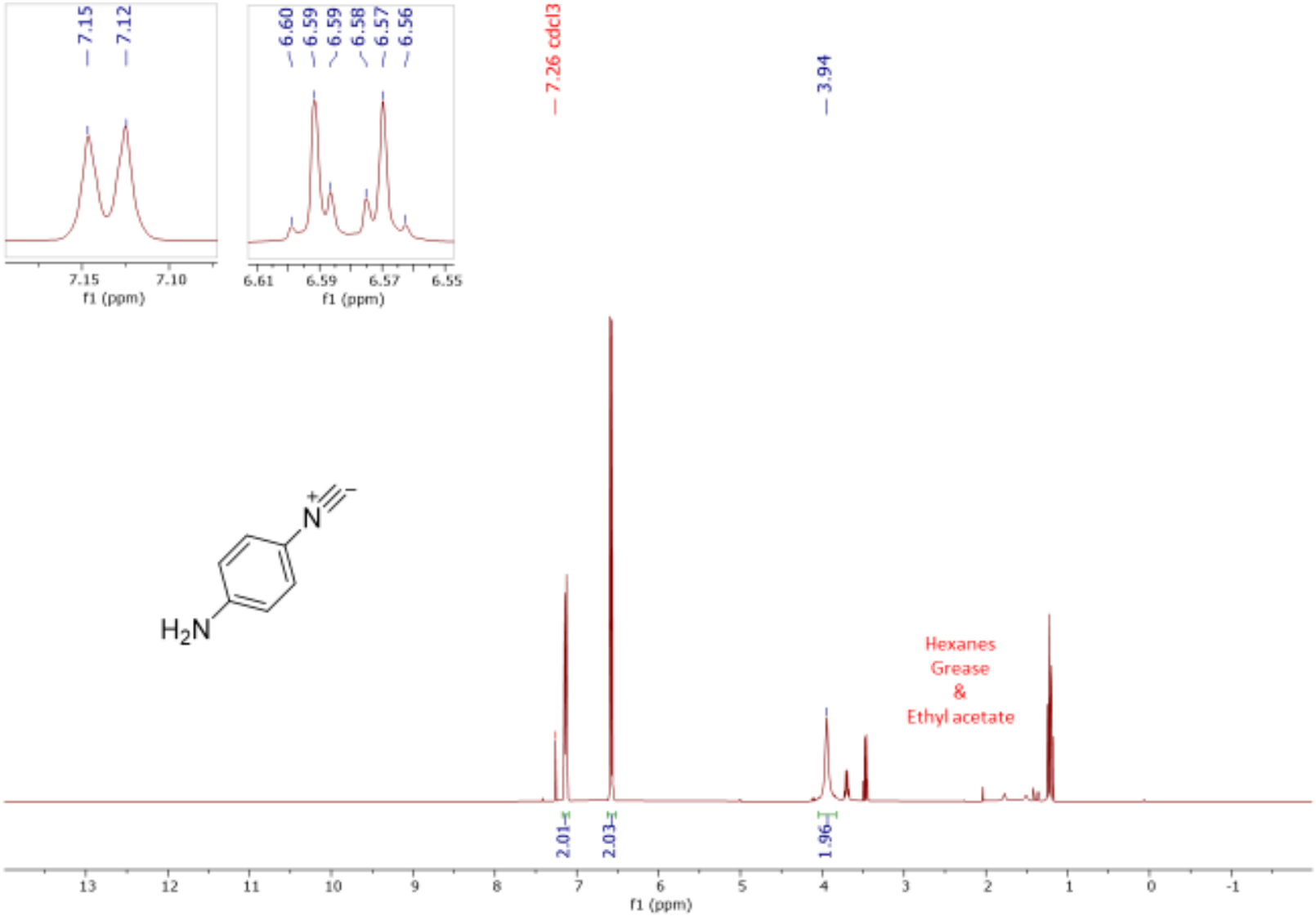

Figure A30: ^1H NMR ($CDCl_3$, 400 MHz) spectrum of 4-Aminophenylisocyanide

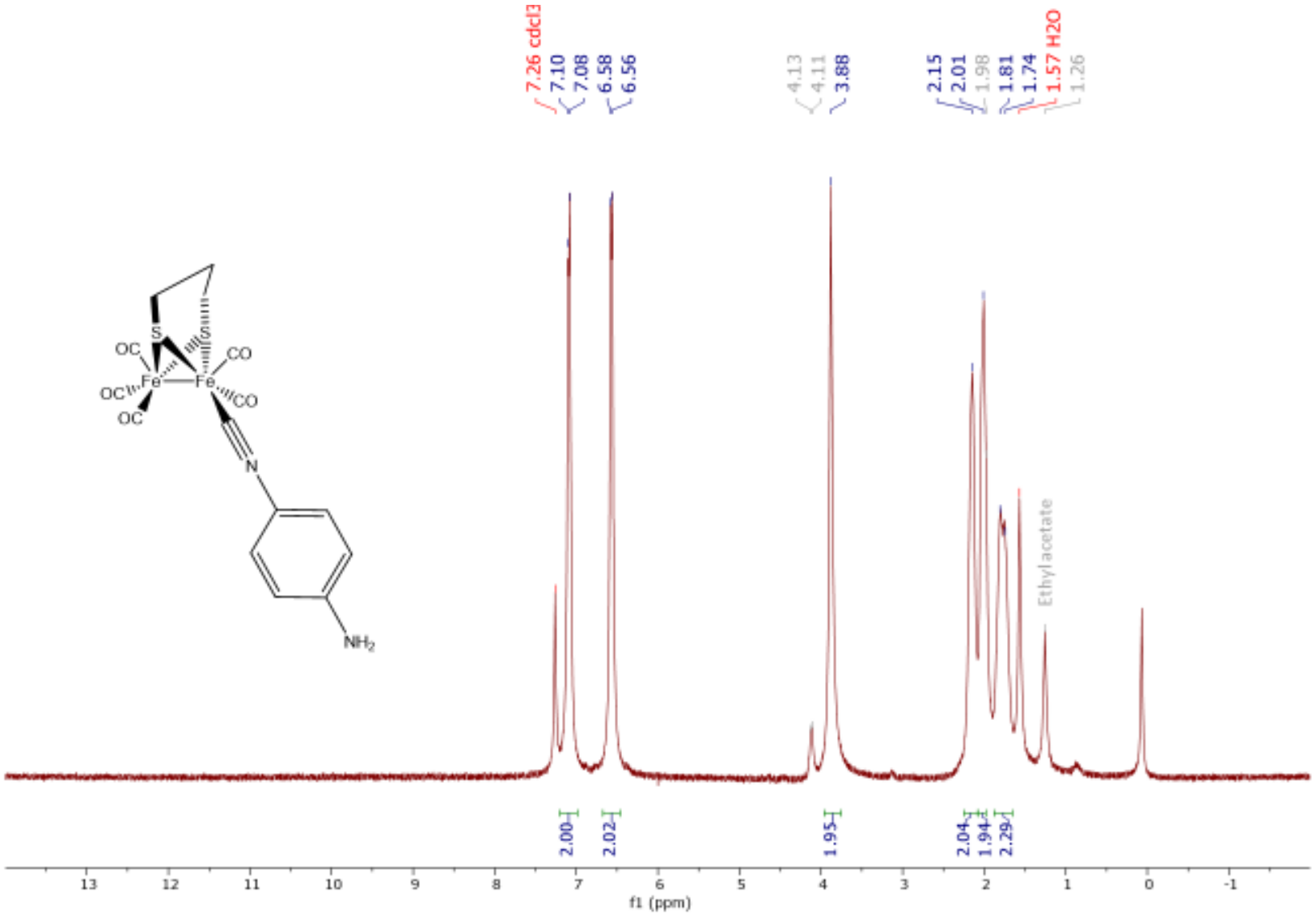

Figure A31: ^{1}H NMR ($CDCl_3$, 400 MHz) spectrum of (μ-propanedithiolato)diiron 4-aminopheynylisocyano pentacarbonyl

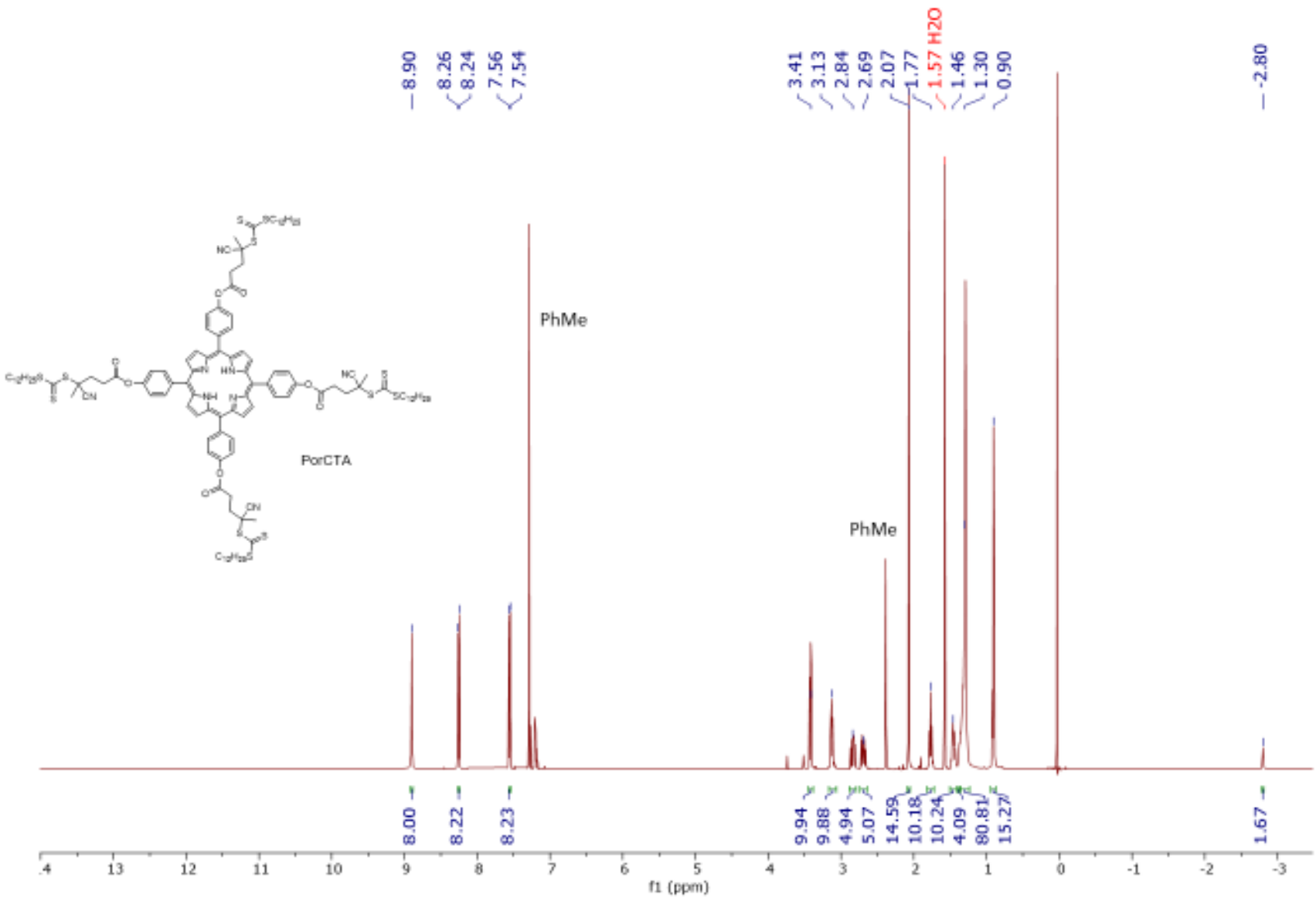

Figure A32: ^{1}H NMR ($CDCl_3$, 400 MHz) spectrum of PorCTA

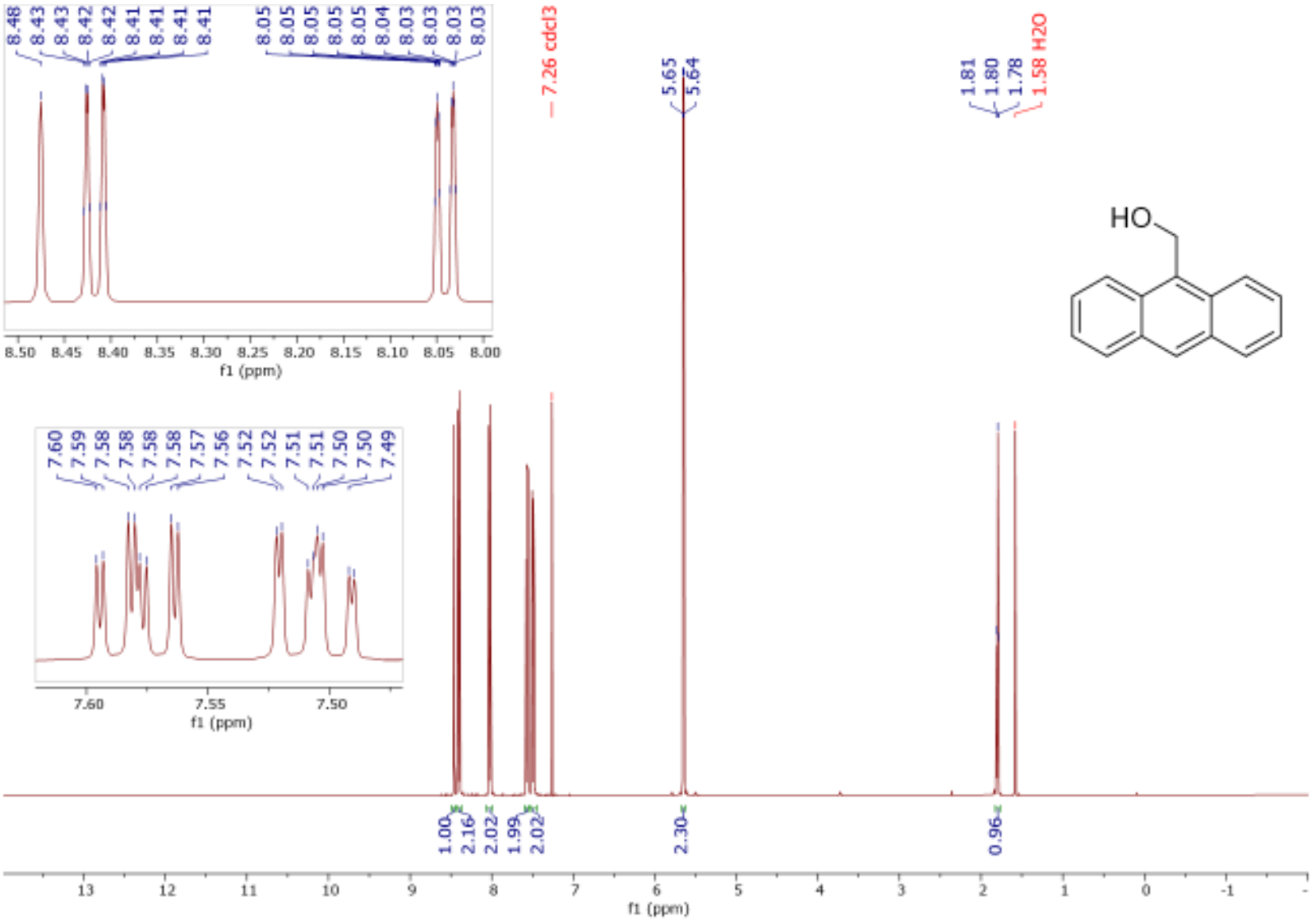

Figure A33: ^{1}H NMR ($CDCl_3$, 500 MHz) spectrum of 9-anthracenemethanol

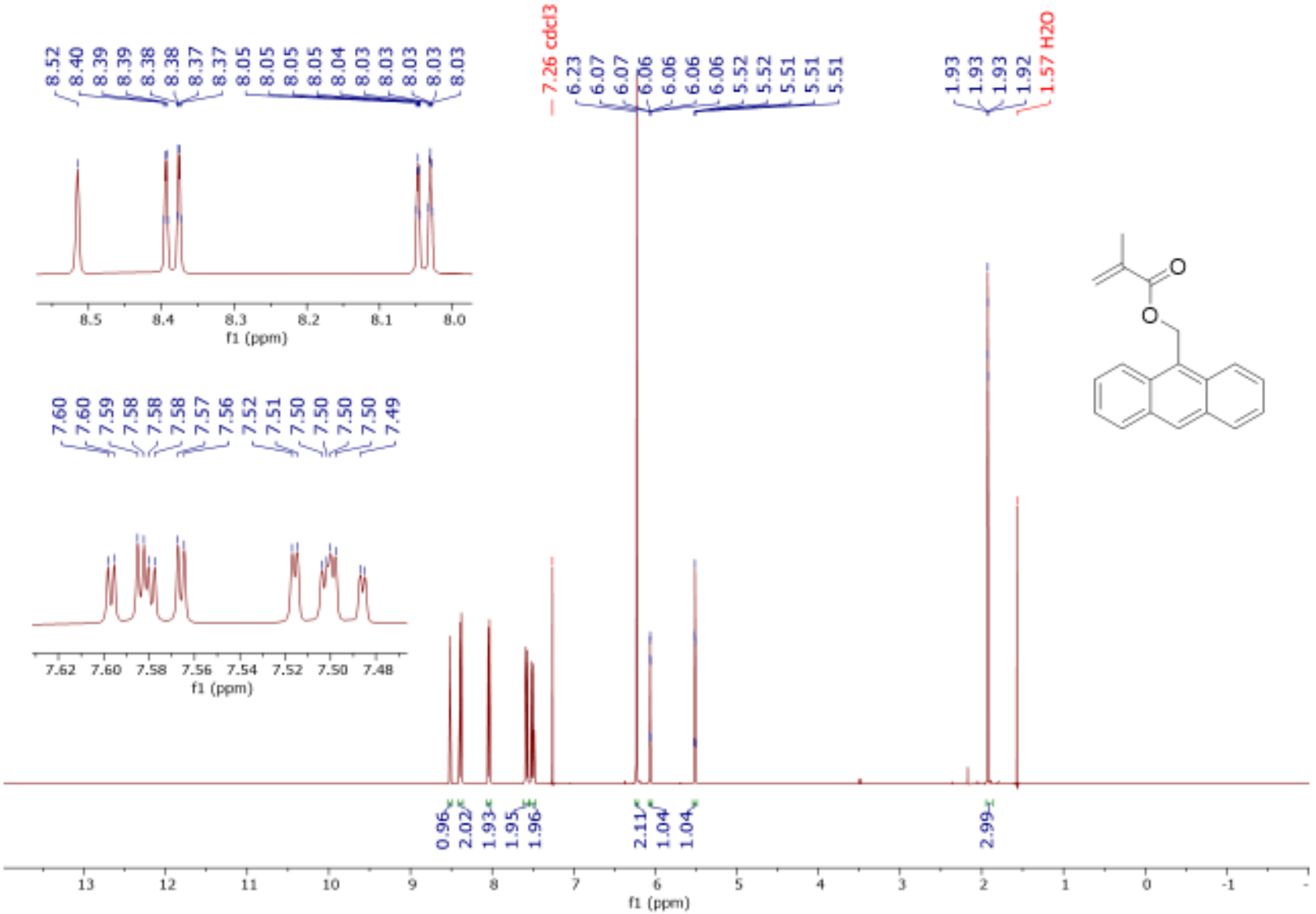

Figure A34: ^{1}H NMR ($CDCl_3$, 500 MHz) spectrum of AMMA

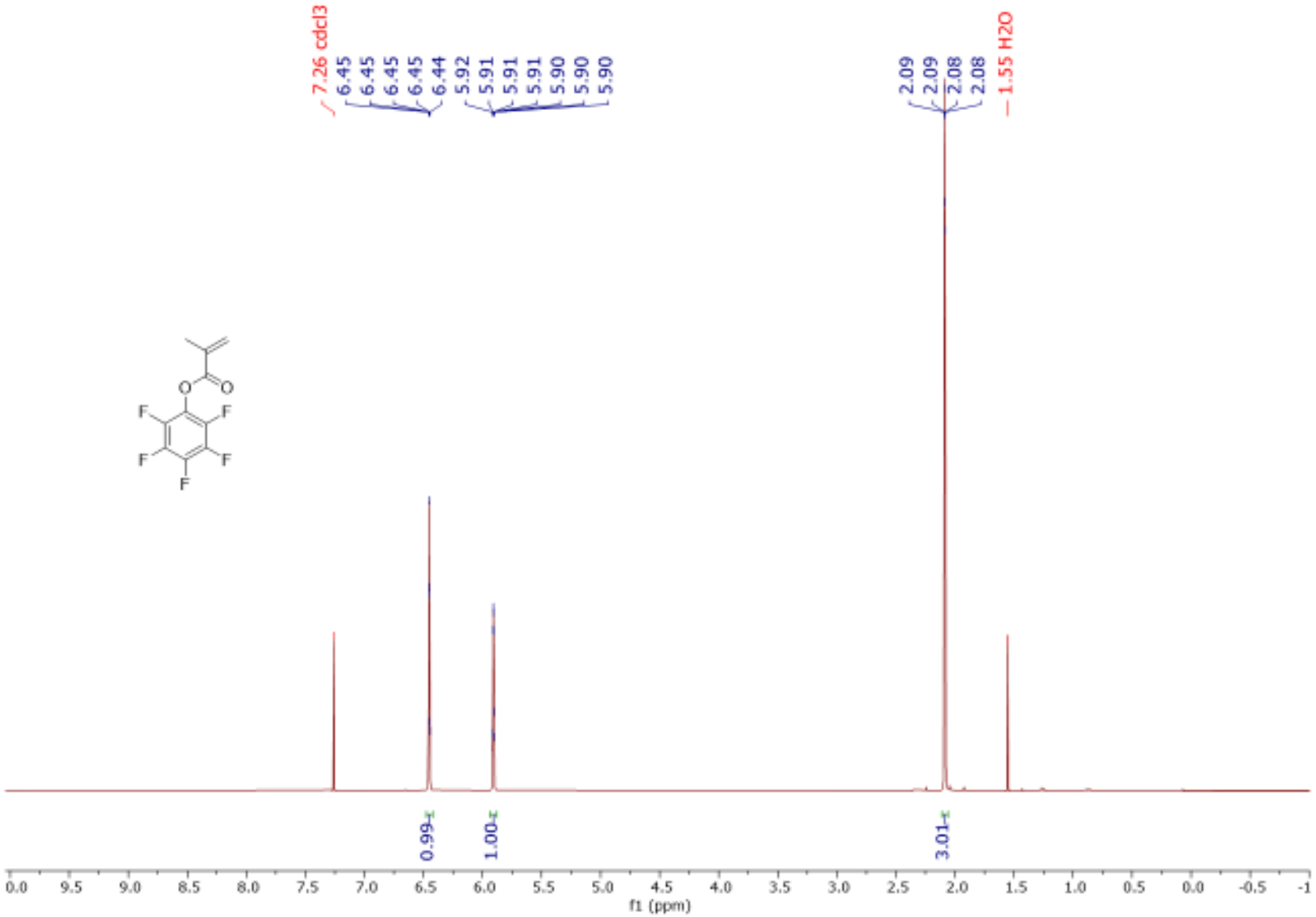

Figure A35: ^{1}H NMR ($CDCl_3$, 400 MHz) spectrum of PFPMA

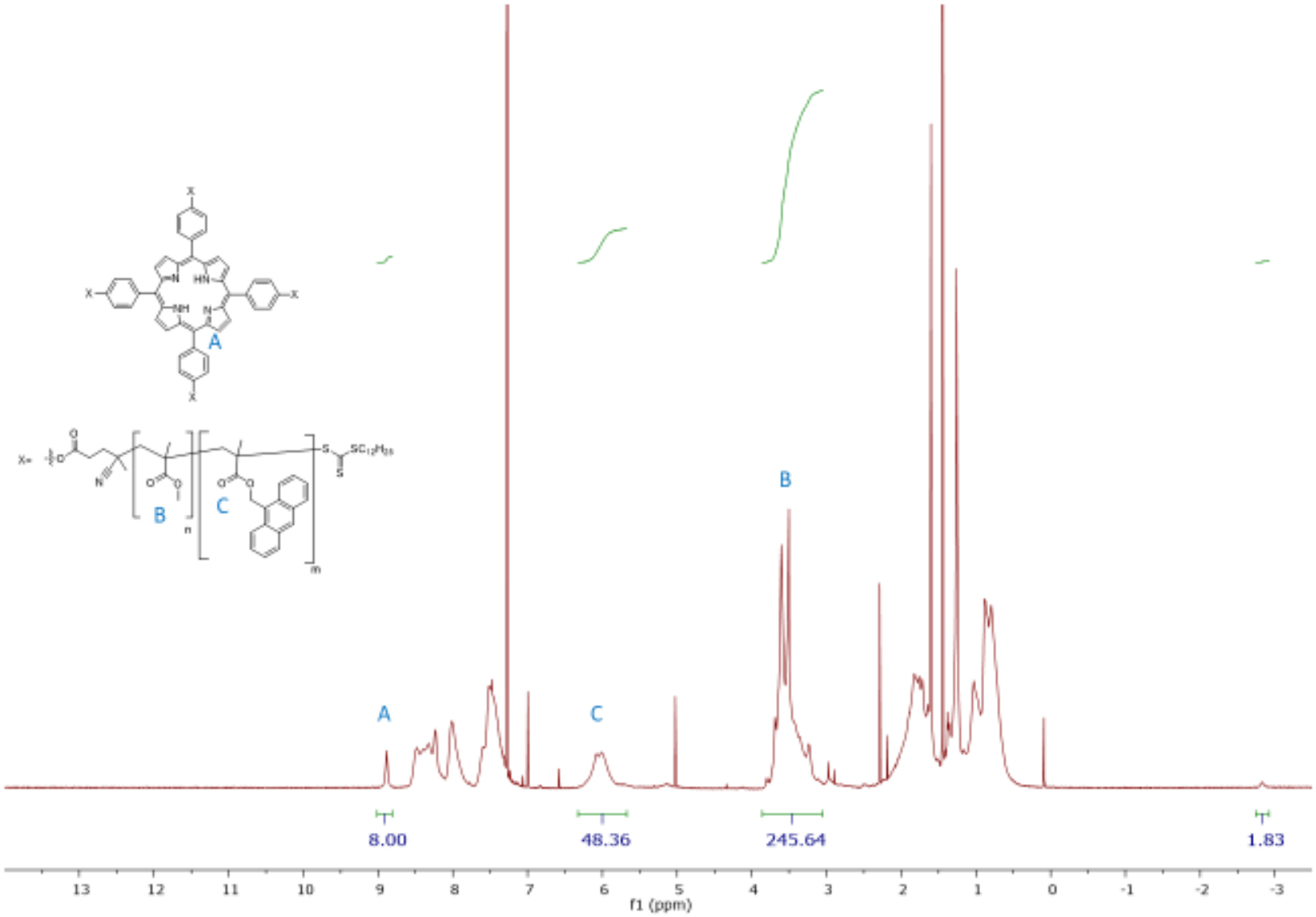

Figure A36: ^{1}H NMR ($CDCl_3$, 500 MHz) spectrum of Por(MMA-co-AMMA)$_4$

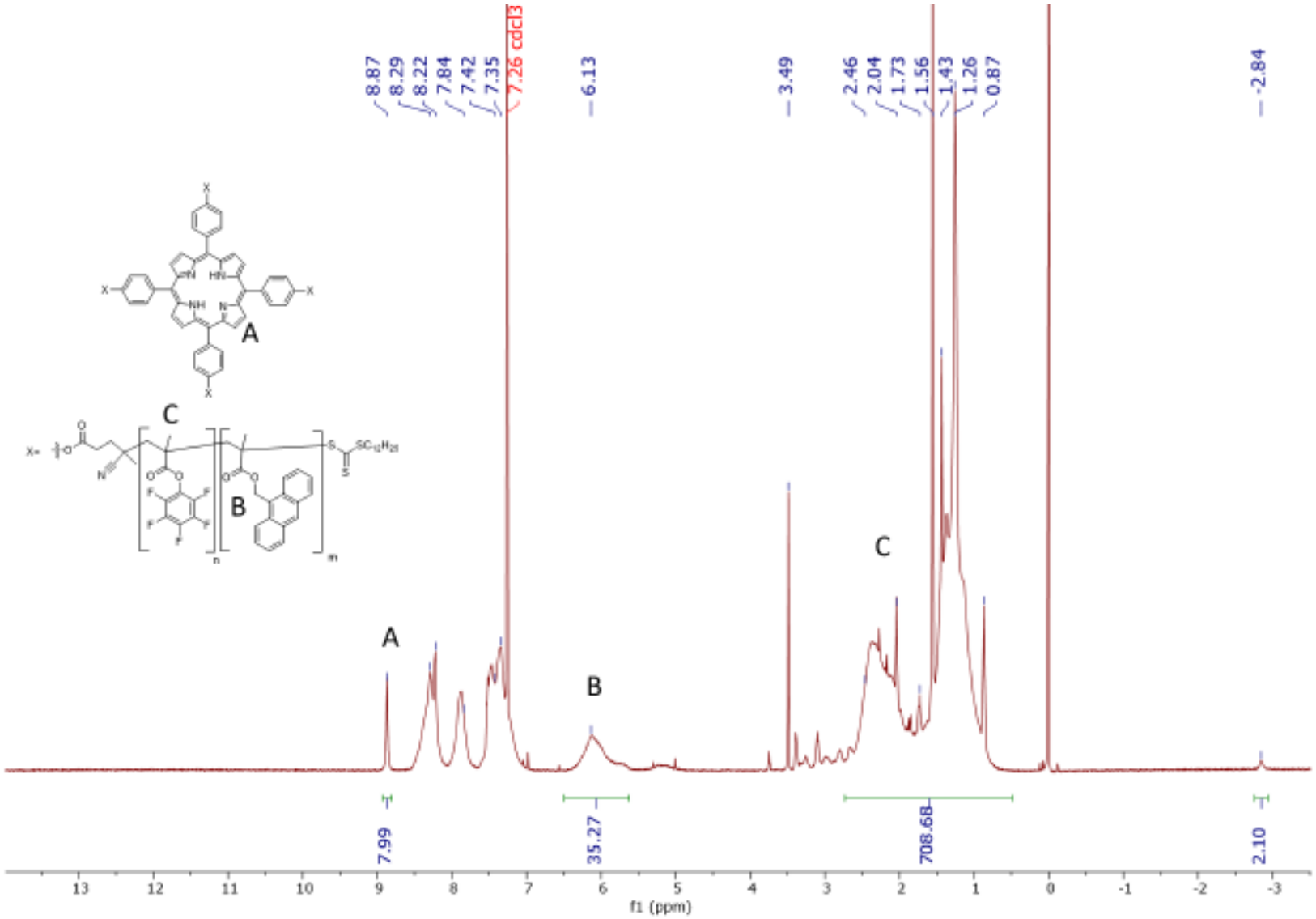

Figure A37: ^{1}H NMR ($CDCl_3$, 500 MHz) spectrum of Por(PFPMA-co-AMMA)$_4$

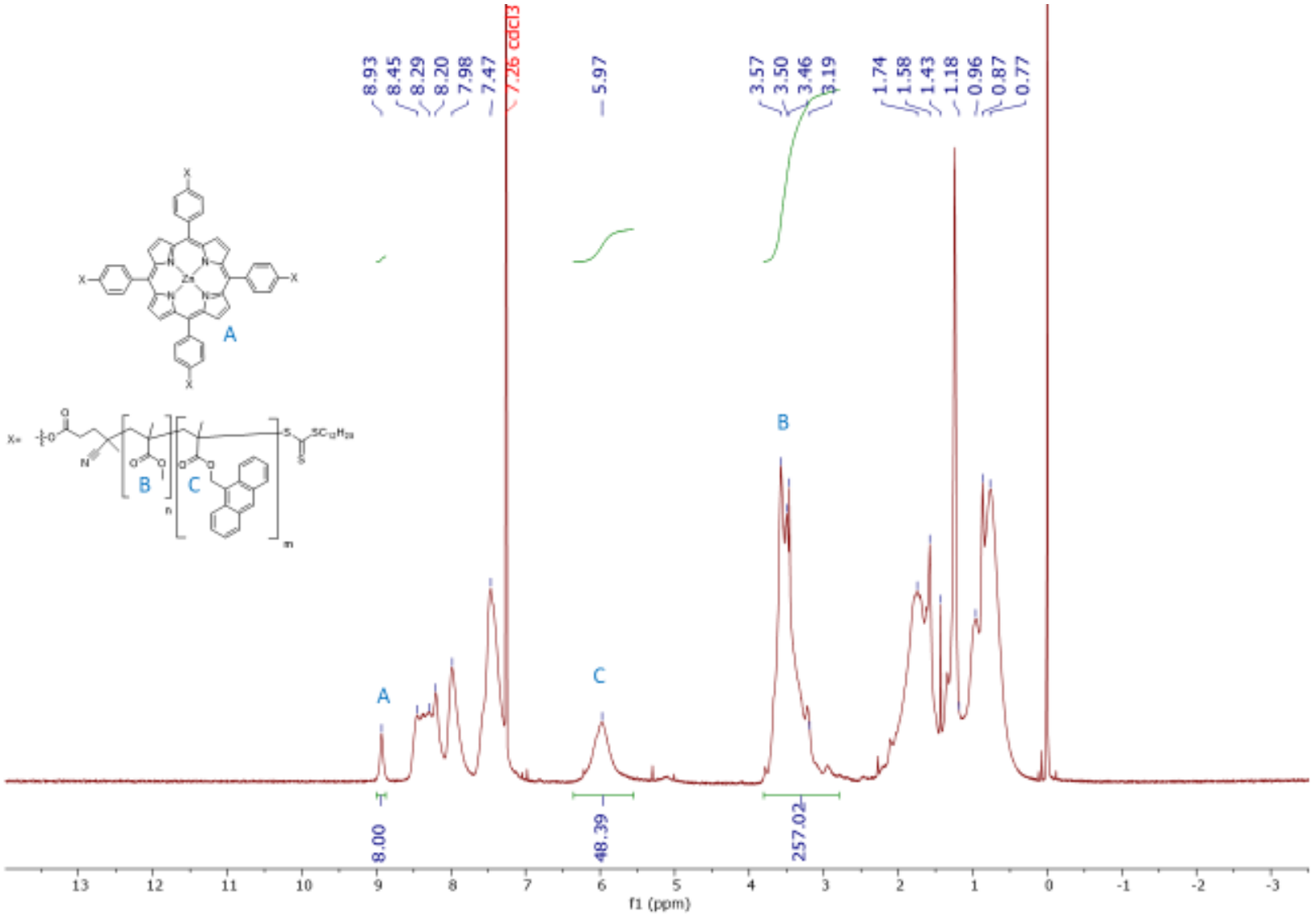

Figure A38: ^{1}H NMR ($CDCl_3$, 500 MHz) spectrum of Zn^{II}(Por(MMA-co-AMMA)$_4$)

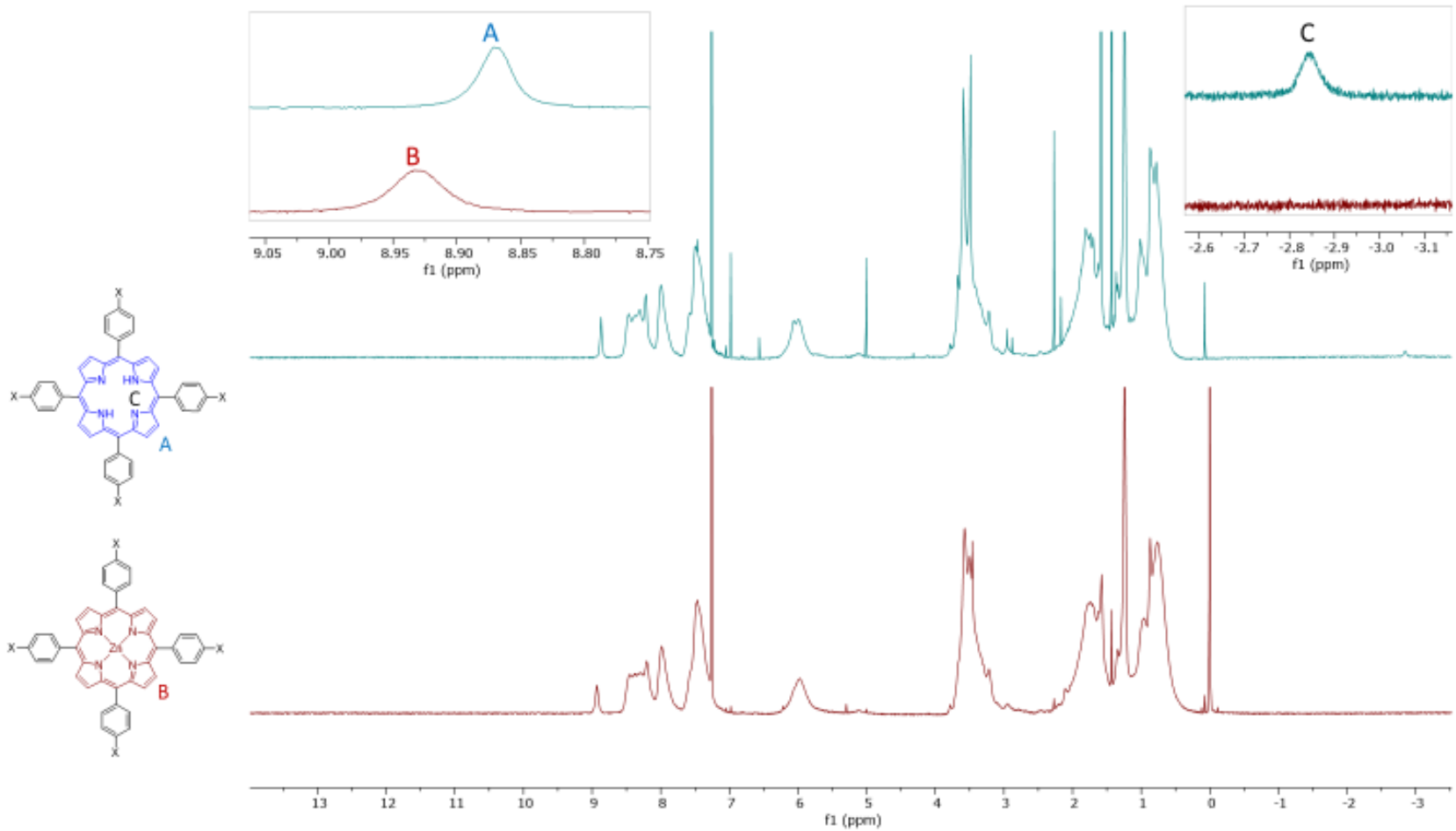

Figure A39: Comparison of ^{1}H NMR ($CDCl_3$, 500 MHz) spectrums for Por(MMA-co-AMMA)$_4$ (Blue) and Zn^{II}(Por(MMA-co-AMMA)$_4$) (Red)

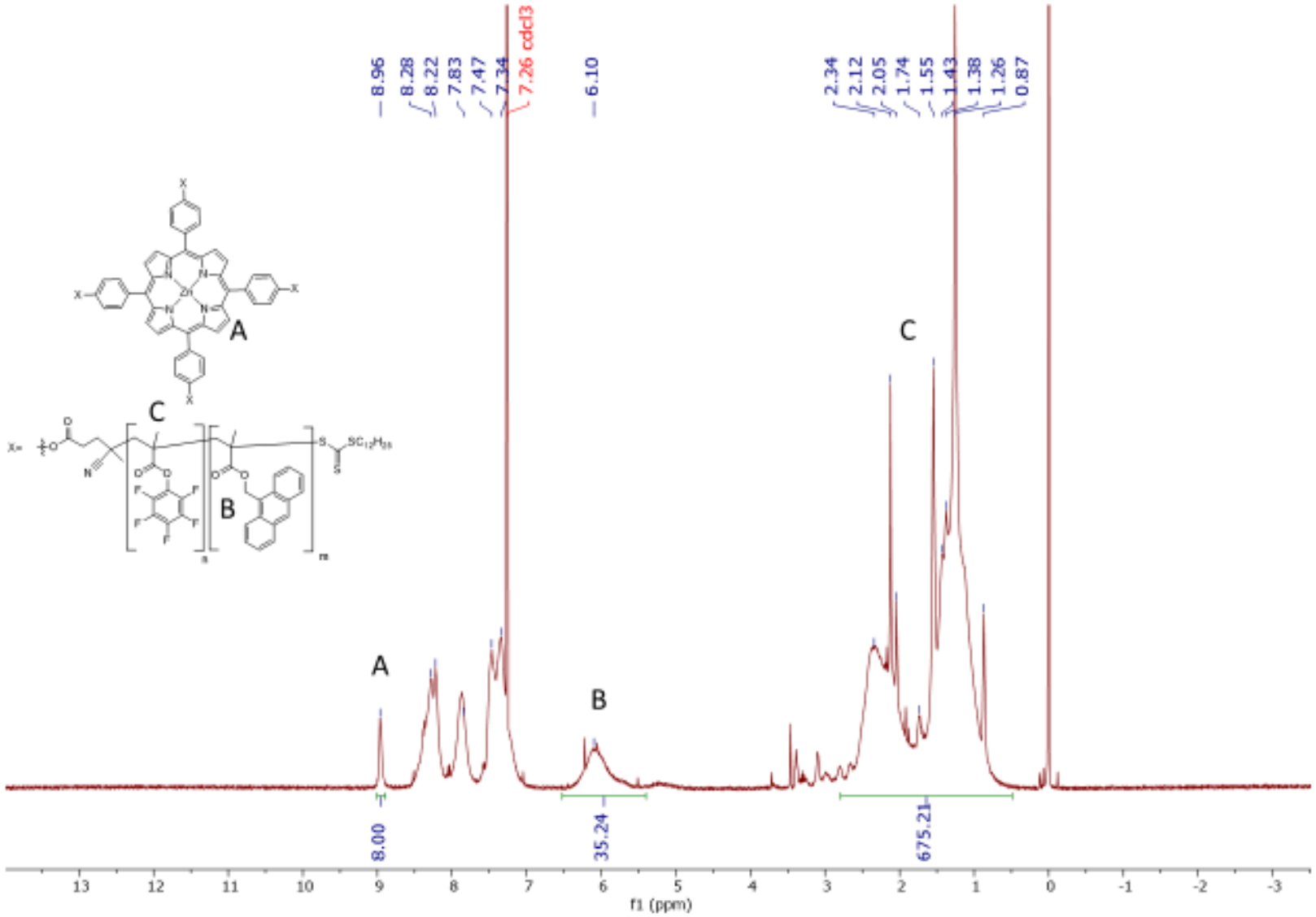

Figure A40: ^{1}H NMR ($CDCl_3$, 500 MHz) spectrum of Zn^{II}(Por(PFPMA-co-AMMA)$_4$)

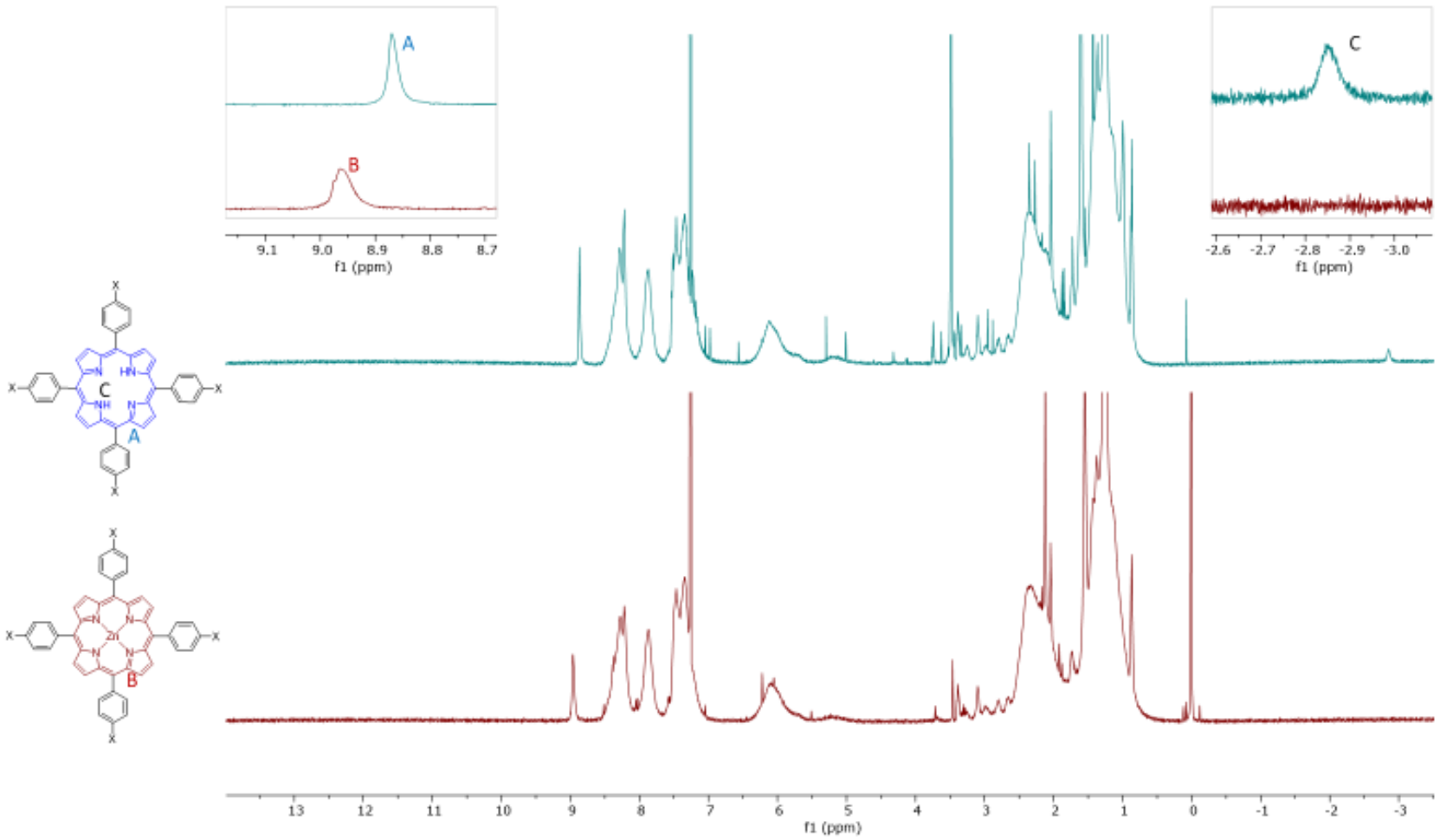

Figure A41:Comparison of ^{1}H NMR ($CDCl_3$, 500 MHz) spectrums for Por(PFPMA-co-AMMA)$_4$ (Blue) and Zn^{II}(Por(PFPMA-co-AMMA)$_4$) (Red)

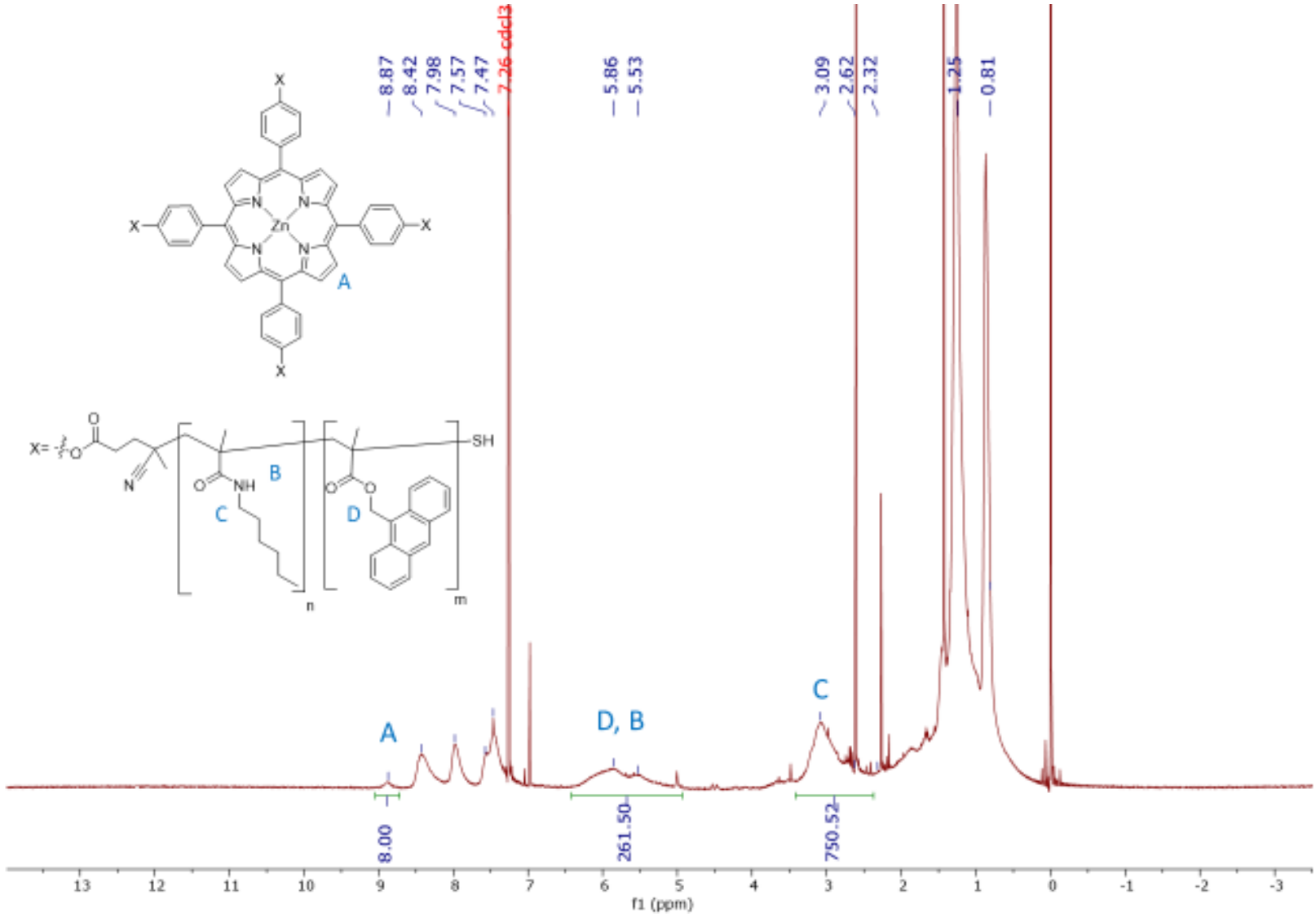

Figure A42: ^{1}H NMR ($CDCl_3$, 500 MHz) spectrum of Zn^{II}(Por(HexMAAm -co-AMMA)$_4$)

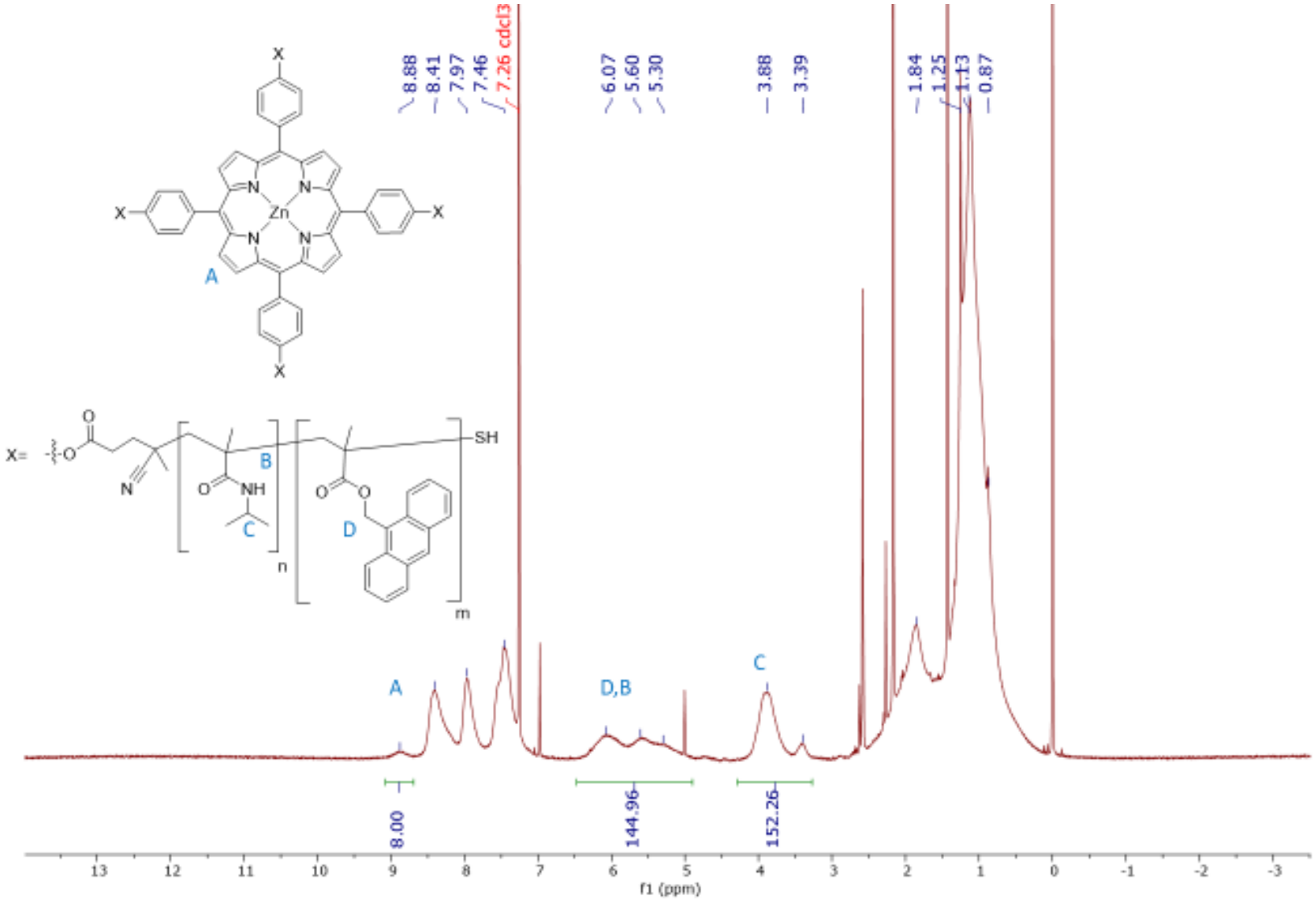

Figure A43: ^{1}H NMR ($CDCl_3$, 500 MHz) spectrum of Zn^{II}(Por(iPMAAm-co-AMMA)$_4$)

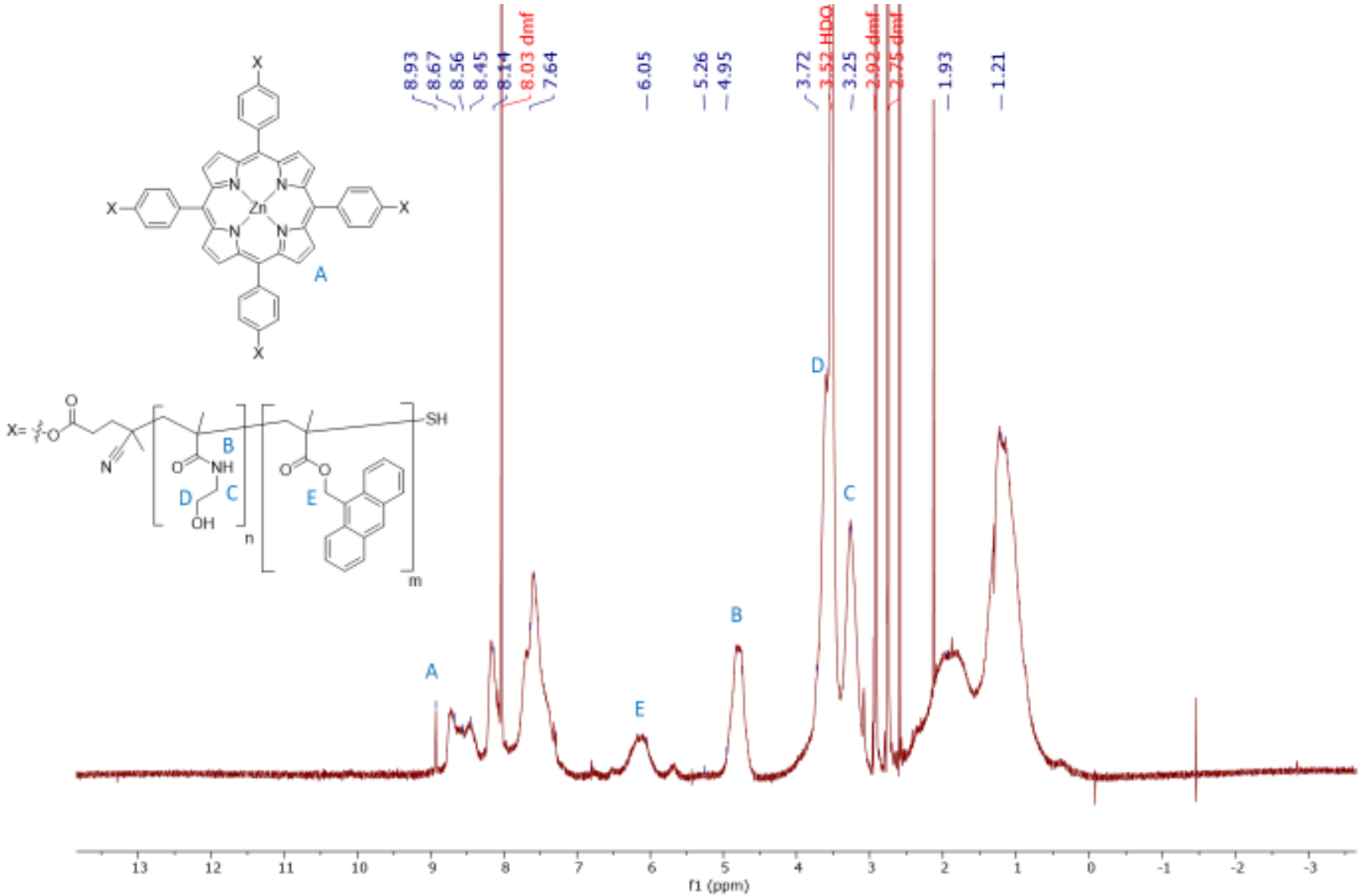

Figure A44:[1]H NMR (DMF-d_7, 400 MHz) spectrum of Zn^{II}(Por((HEMA-co-AMMA)$_4$)

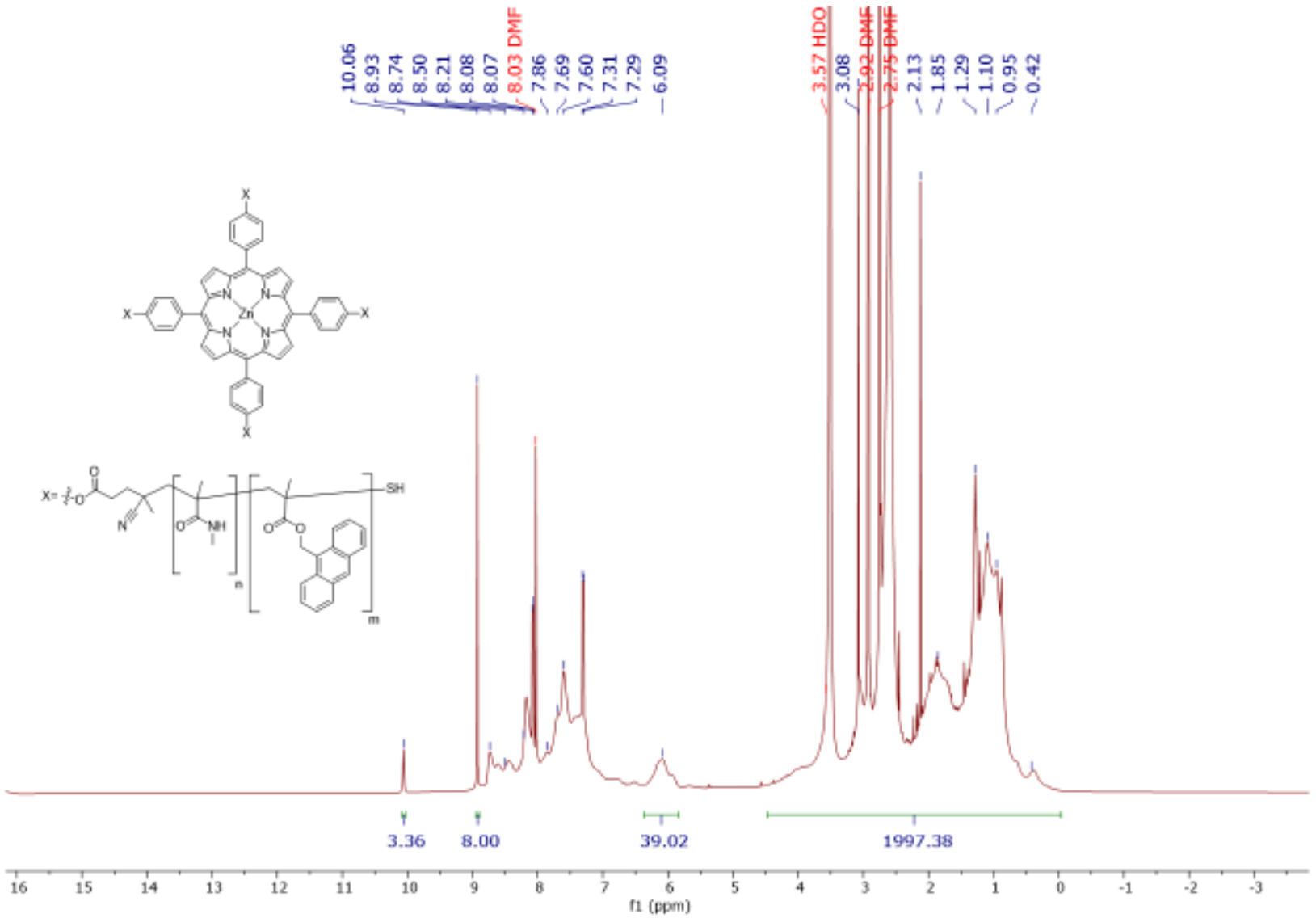

Figure A45: ^{1}H NMR (DMF-d_7, 400 MHz) spectrum of Zn^{II}(Por((MMAAm-co-AMMA)$_4$)

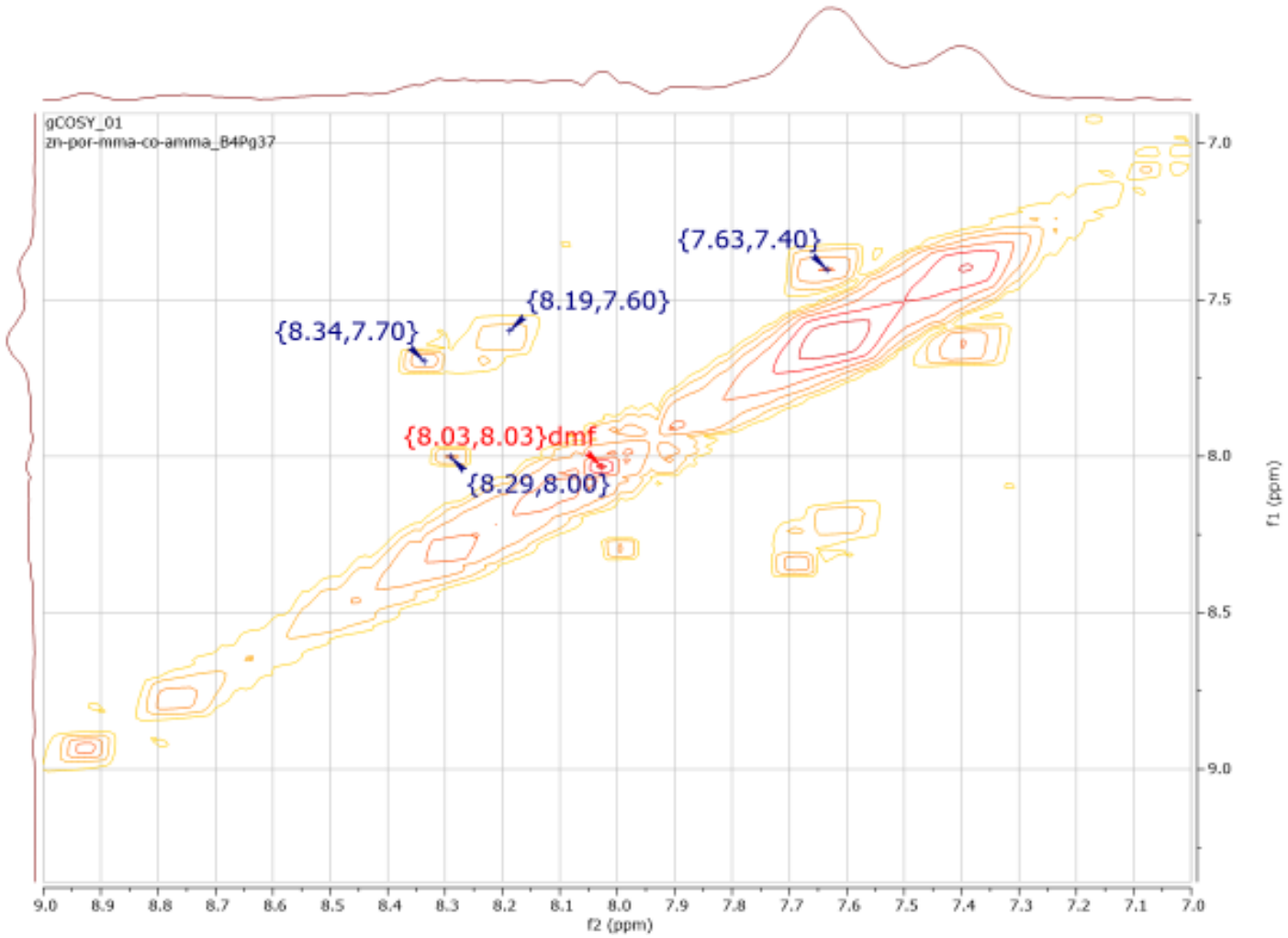

Figure A46: gCOSY NMR (DMF-d_7, 400 MHz) spectrum [δ 9.0 to 7.0] of Zn^{II}(Por(MMA-co-AMMA)$_4$)

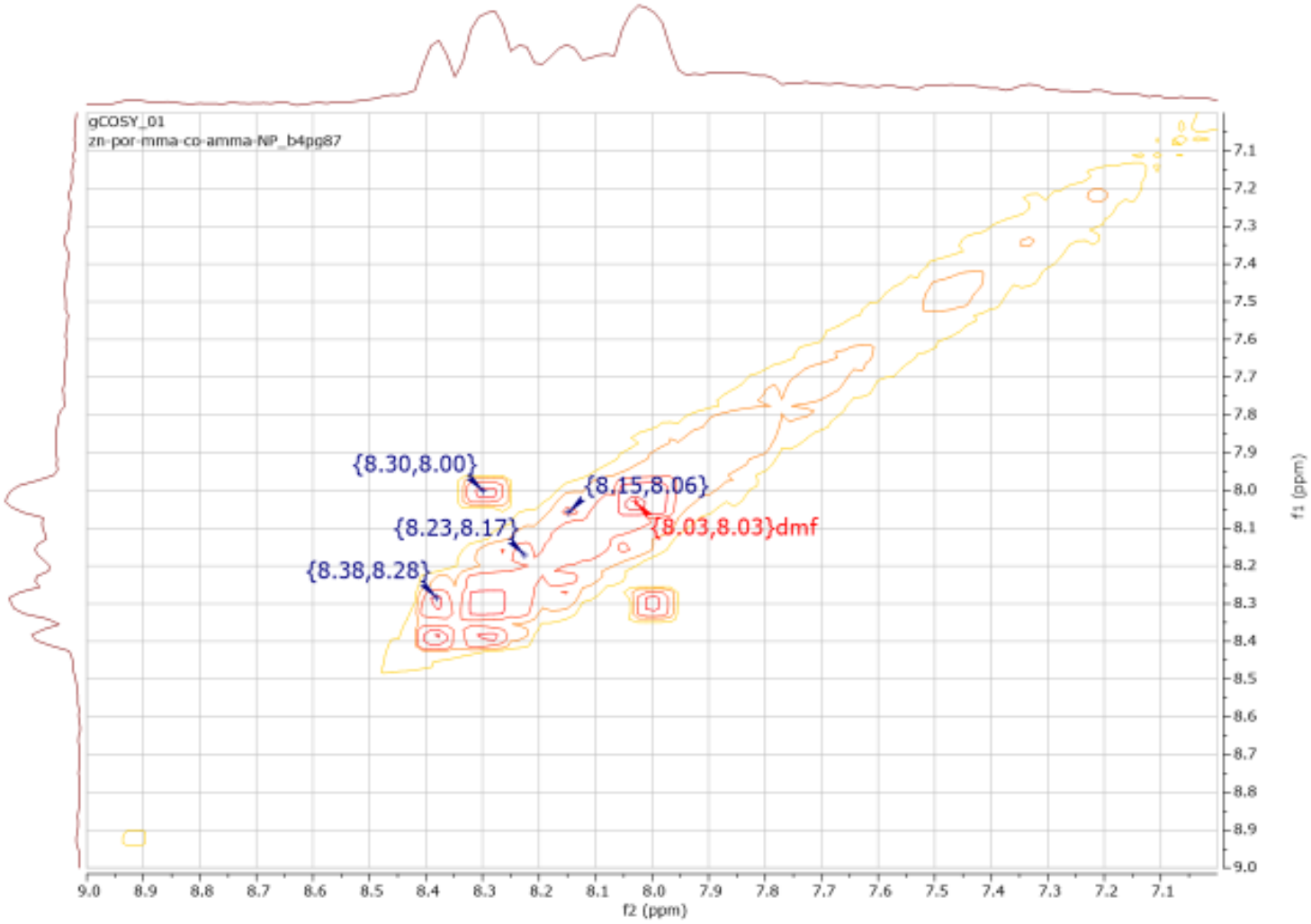

Figure A47: gCOSY NMR (DMF-d_7, 400 MHz) spectrum [δ 9.0 to 7.0] of Zn^{II}(Por(MMA-co-AMMA)$_4$)-NP

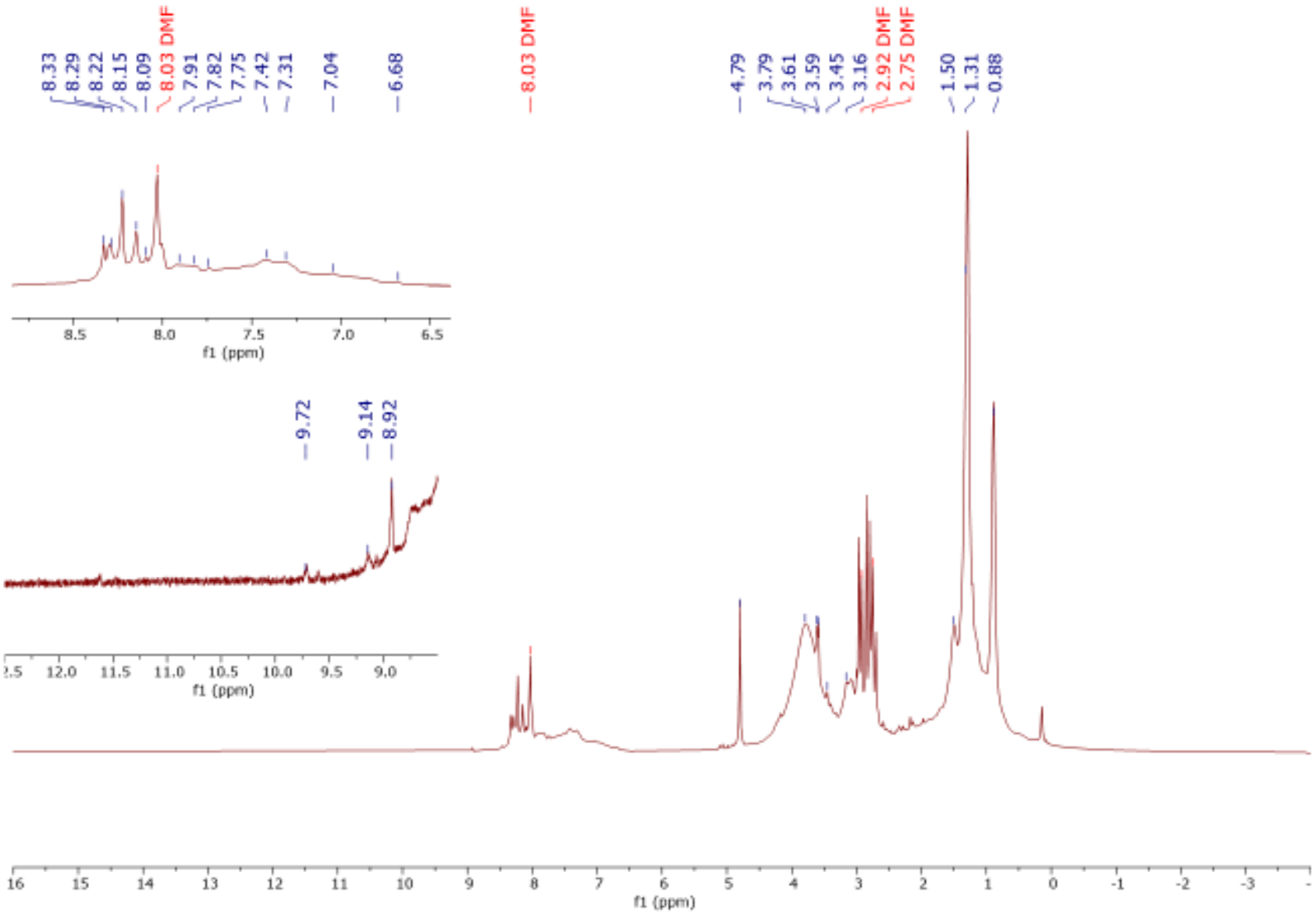

Figure A48: ^{1}H NMR (DMF-d7, 500 MHz) spectrum of Zn^{II}(Por(HexMAAm-co-AMMA)$_4$)-NP

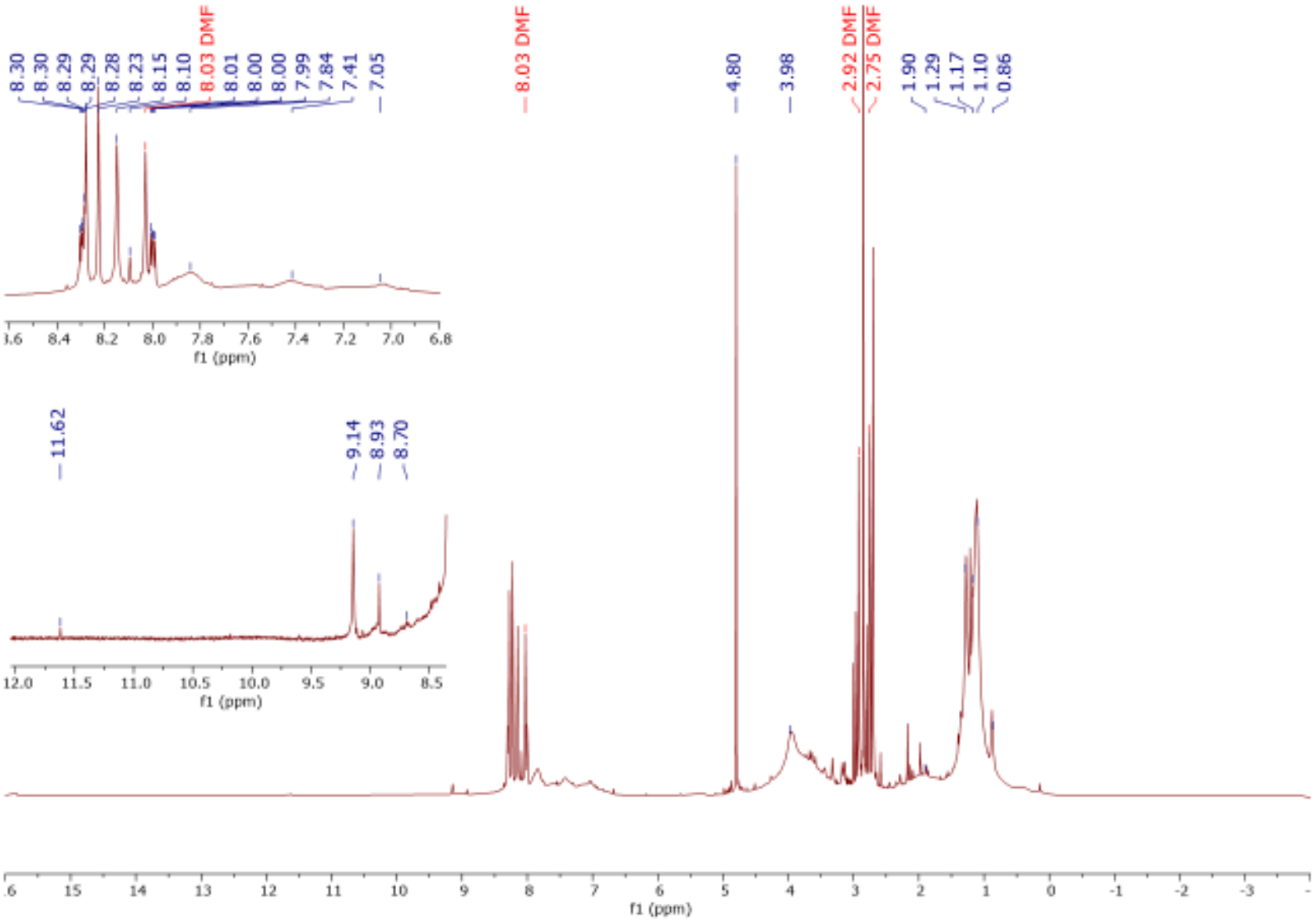

Figure A49: 1H NMR (DMF-d7, 500 MHz) spectrum of Zn^{II}(Por(iPMAAm -co-AMMA)$_4$)-NP

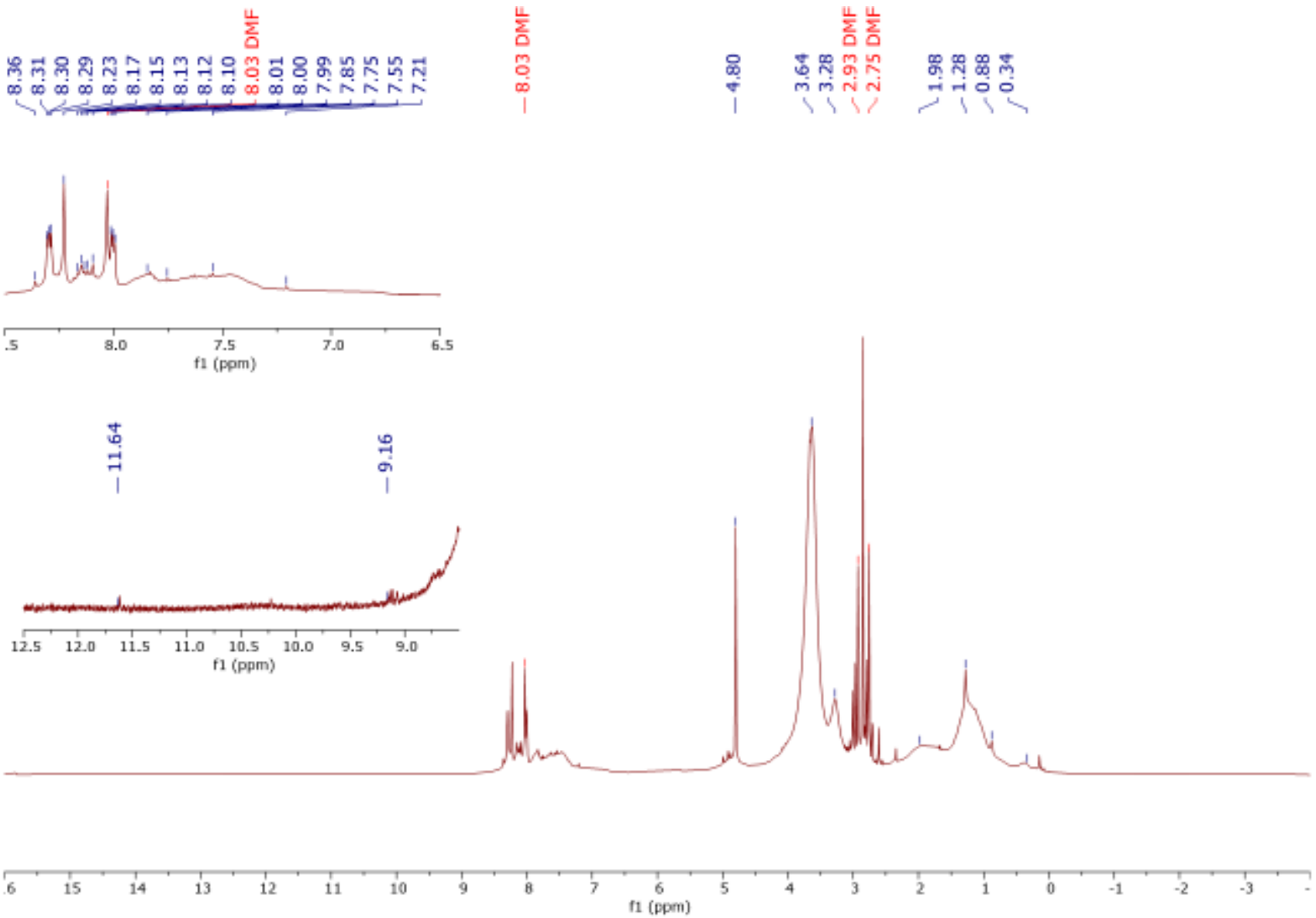

Figure A50: ^{1}H NMR (DMF-d7, 500 MHz) spectrum of Zn^{II}(Por(HEMA-co-AMMA)$_4$)-NP

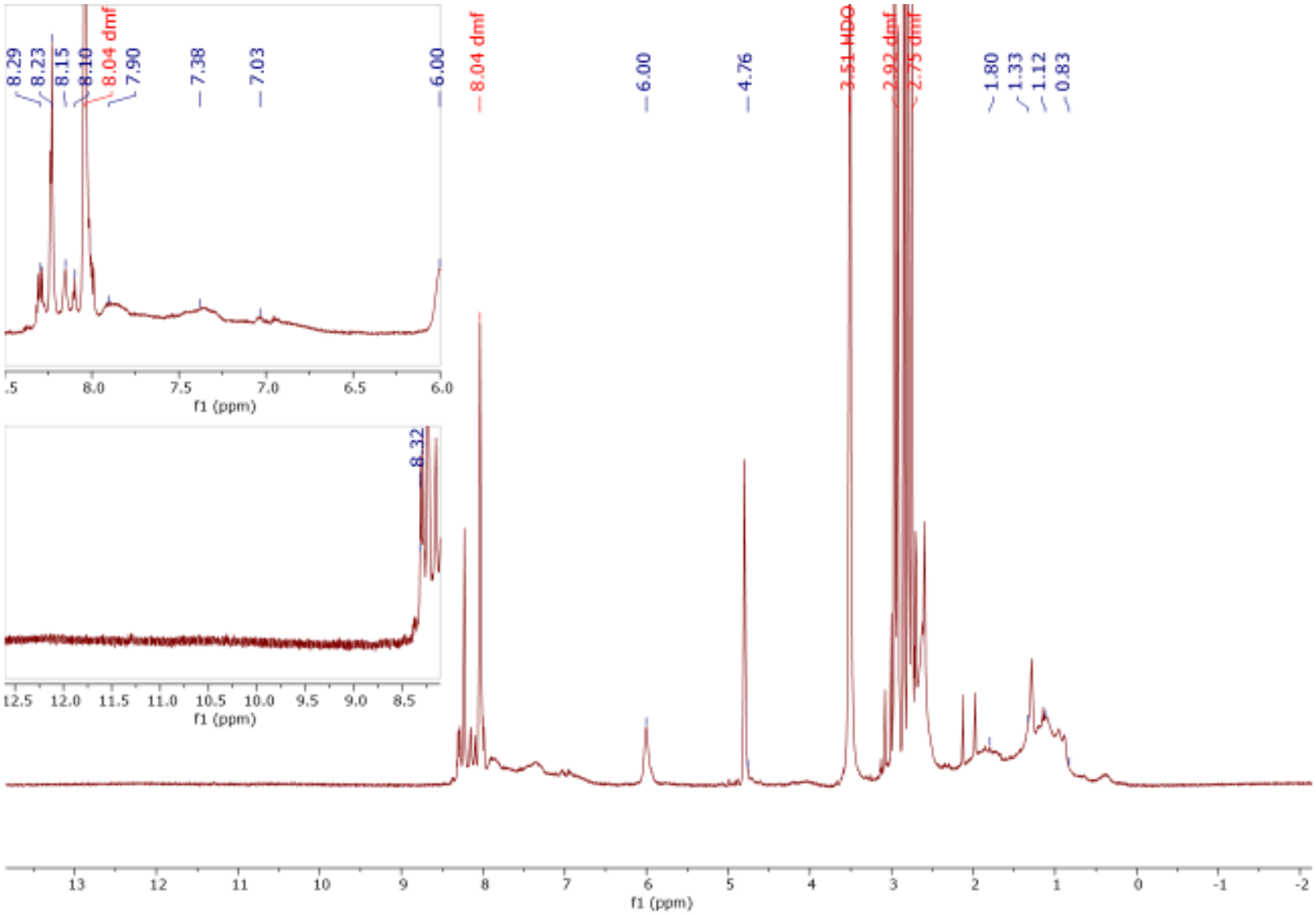

Figure A51: ^{1}H NMR (DMF-d7, 500 MHz) spectrum of Zn^{II}(Por(MMAAm-co-AMMA)$_4$)-NP

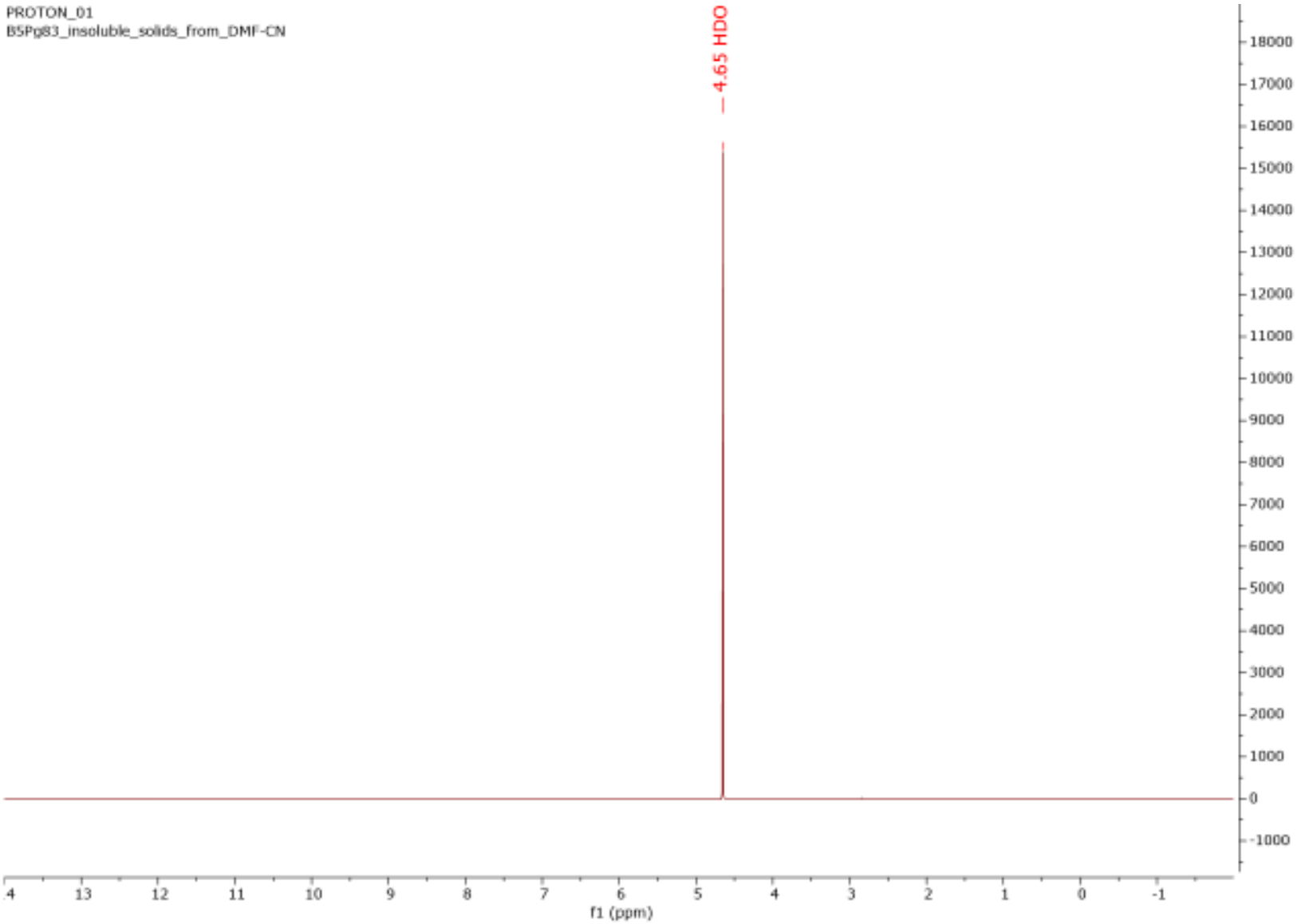

Figure A52: ^{1}H NMR (D_2O, 400 MHz) spectrum of white precipitate from reaction of Zn^{II}(Por(HexMAAm -co-AMMA)$_4$), NaCN, and DMF under ambient conditions.

APPENDIX B: ^{13}C NMR Spectra

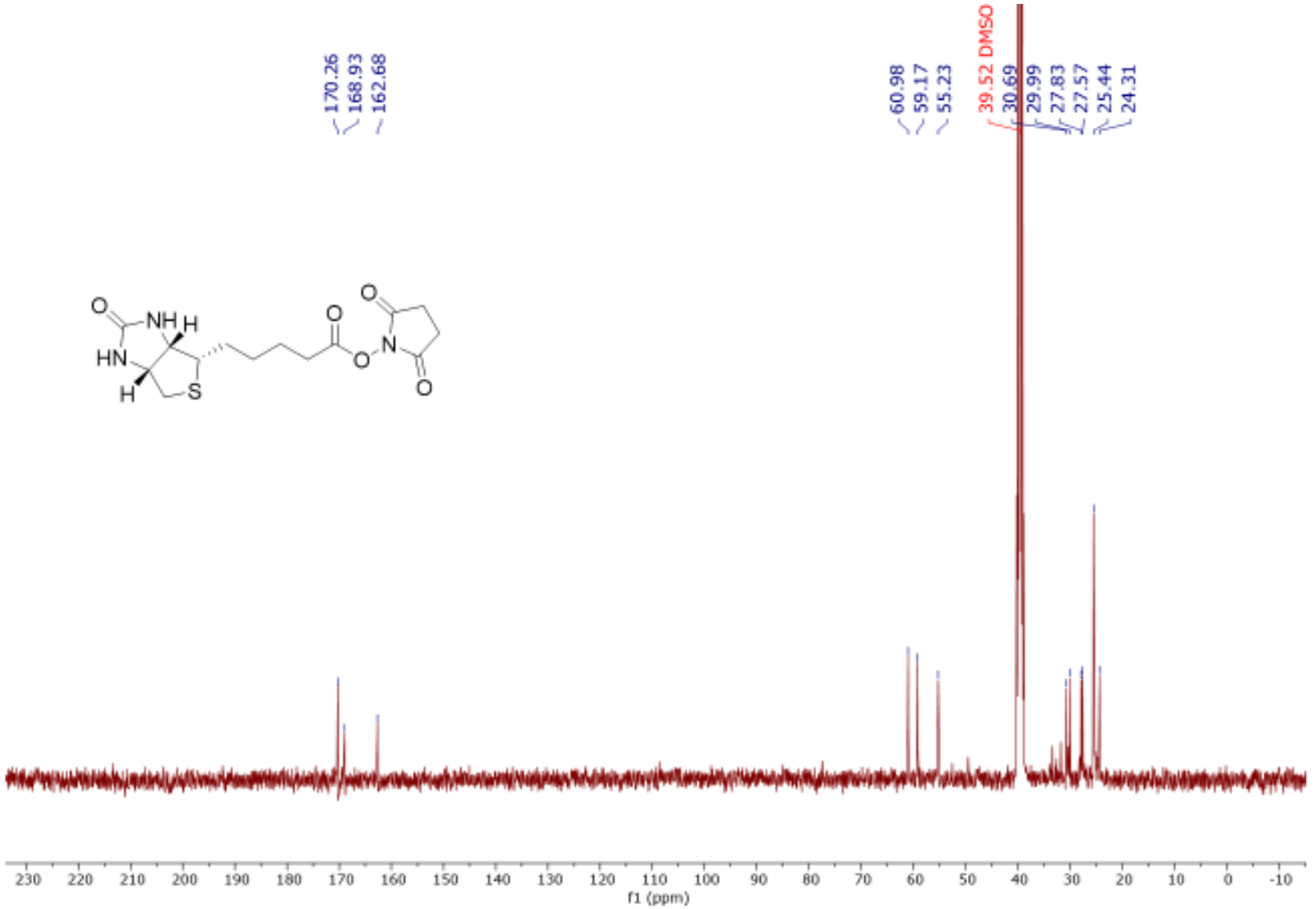

A-55

Figure A53: ^{13}C NMR (101 MHz, DMSO-d_6) spectrum of Biotin-NHS-ester

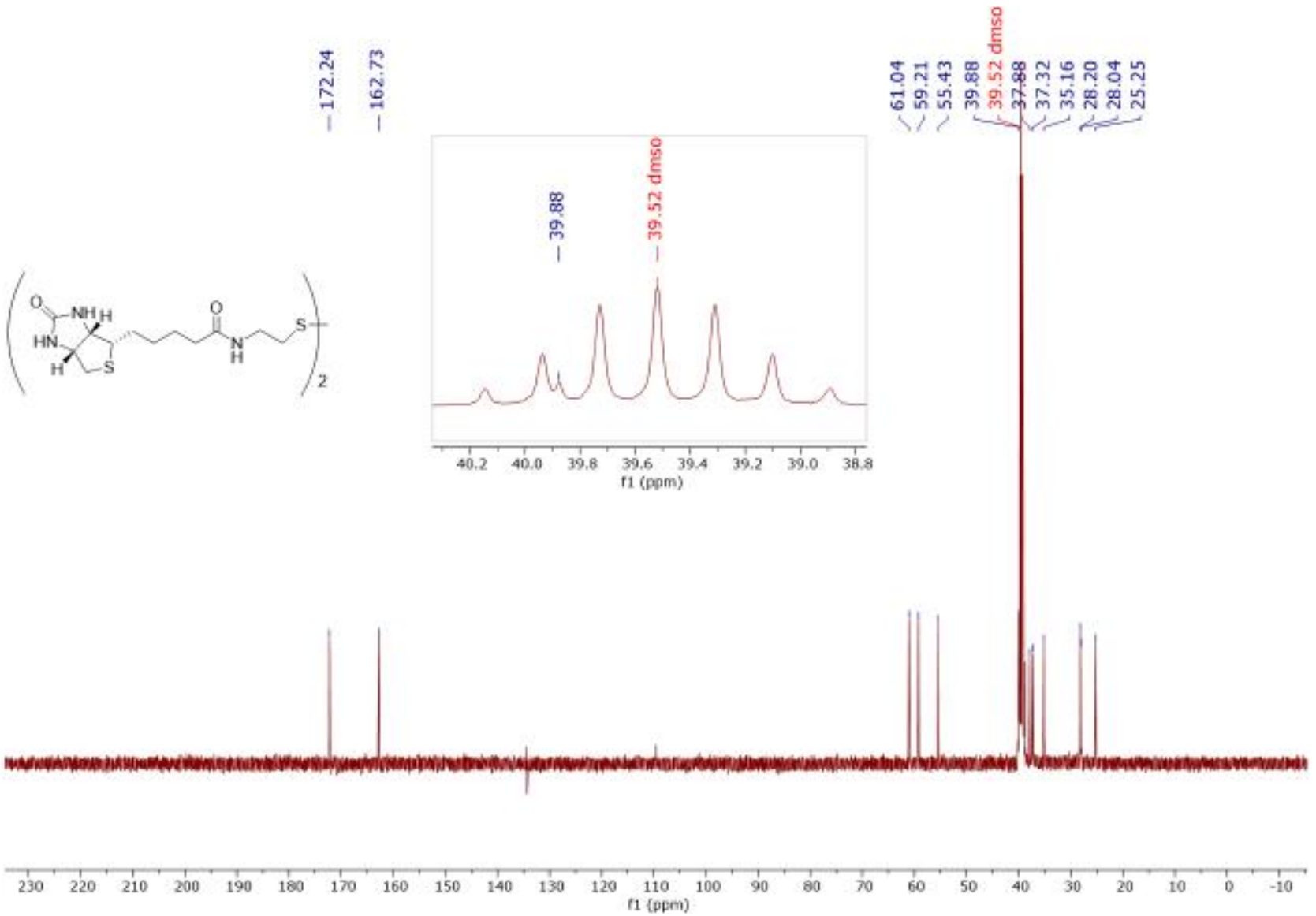

Figure A54: ^{13}C NMR (101 MHz, DMSO-d_6) spectrum of Biotinylated-cystamine

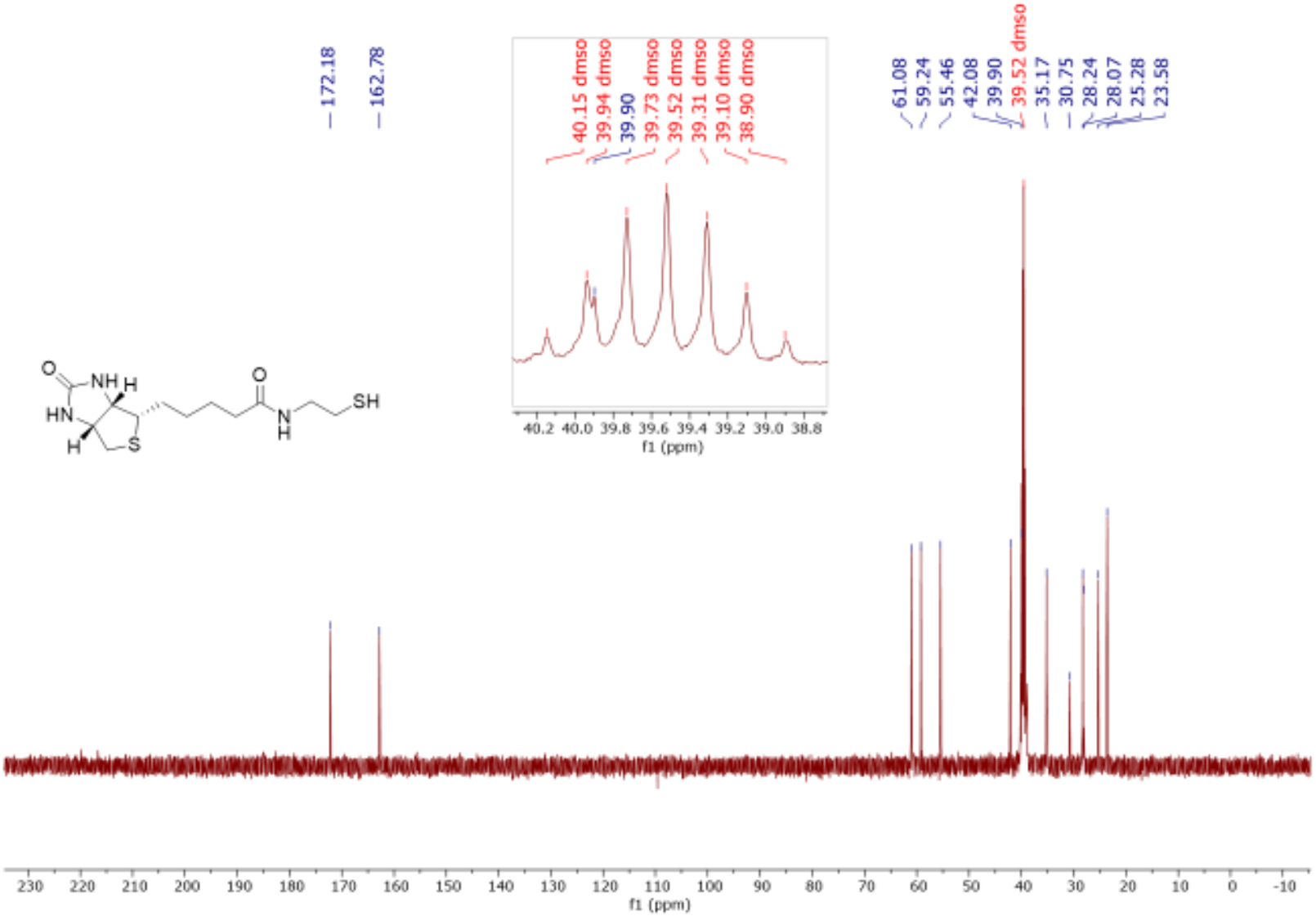

Figure A55: ^{13}C NMR (101 MHz, DMSO-d_6) spectrum of Biotinylated-cysteamine

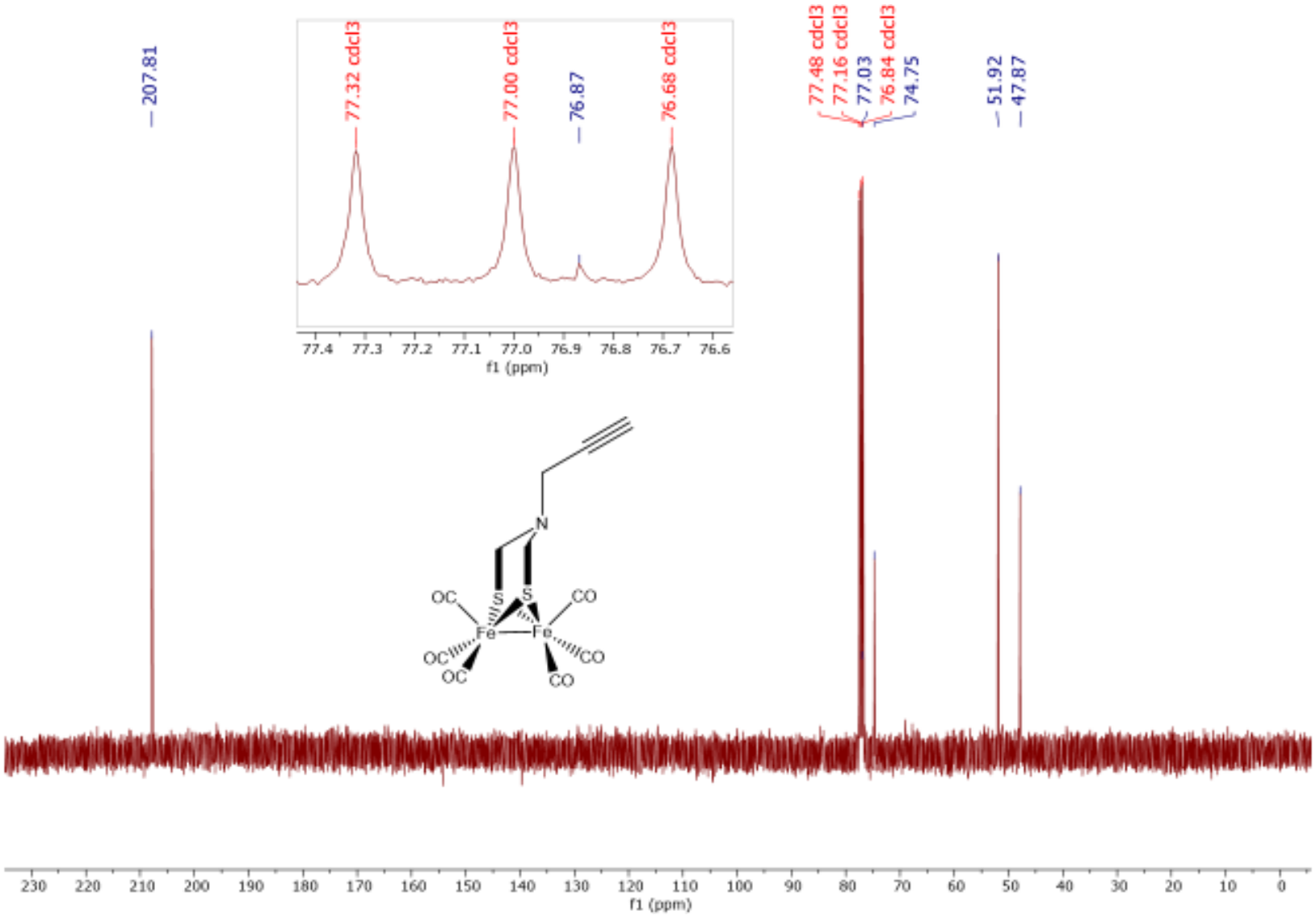

Figure A56: ^{13}C NMR (101 MHz, $CDCl_3$) spectrum of (μ-propargylazadithiolato)diiron(I) hexacarbonyl

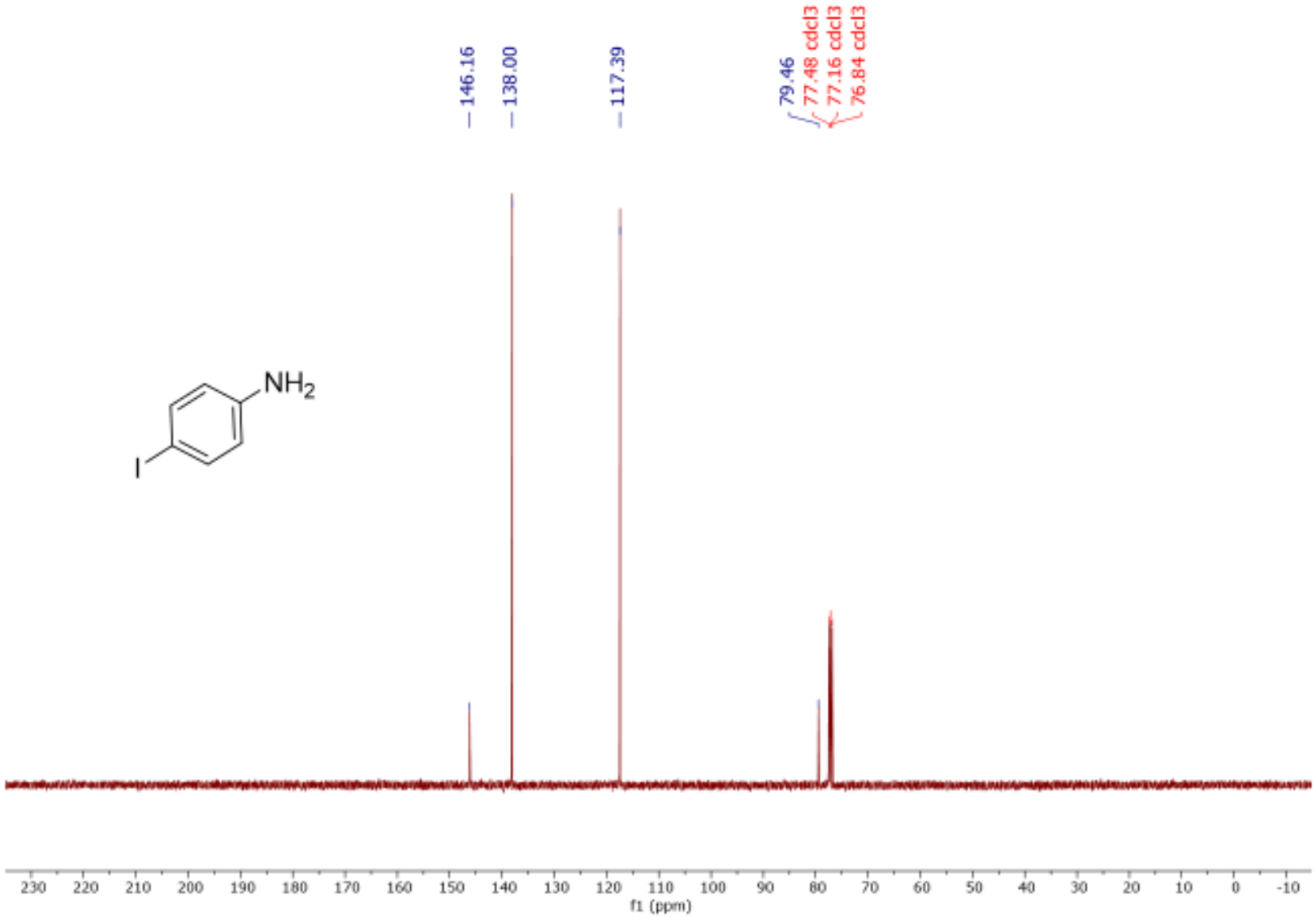

Figure A57: ^{13}C NMR (101 MHz, $CDCl_3$) spectrum of 4-iodoaniline

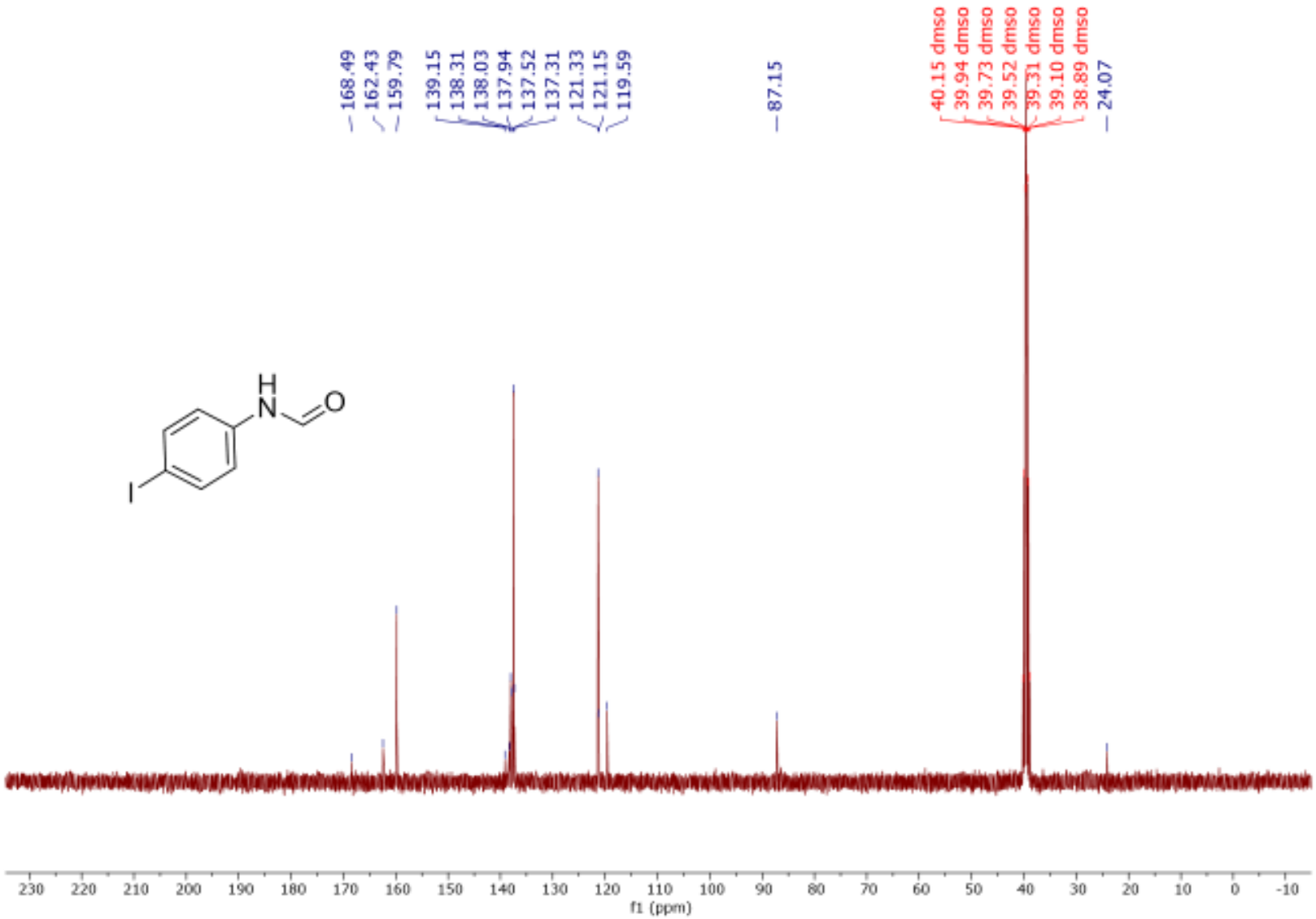

Figure A58: ^{13}C NMR (101 MHz, $CDCl_3$) spectrum of N-(4-iodophenyl)-formamide

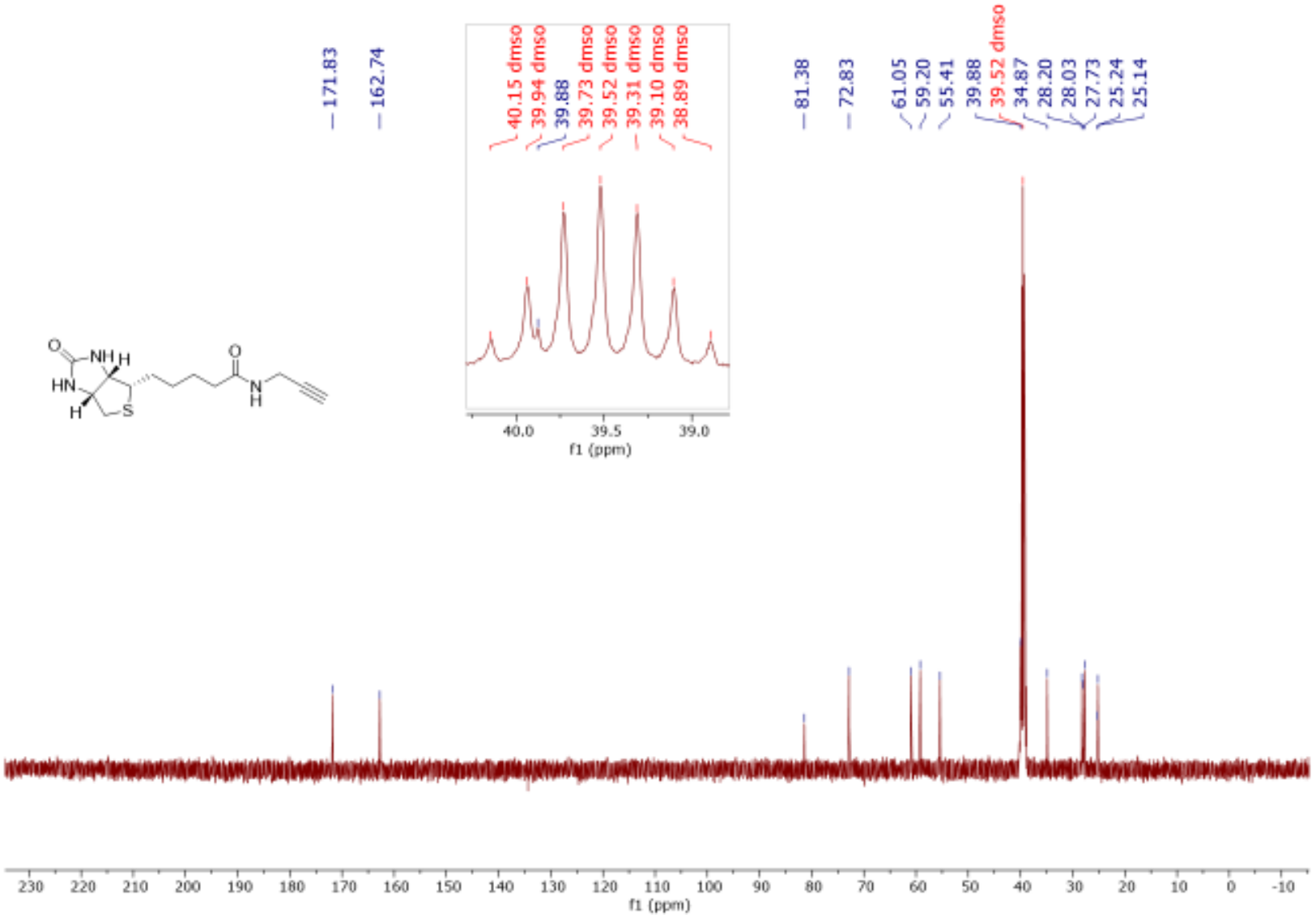

Figure A59: ^{13}C NMR (101 MHz, DMSO-d_6) spectrum of Biotinylated propargylamine

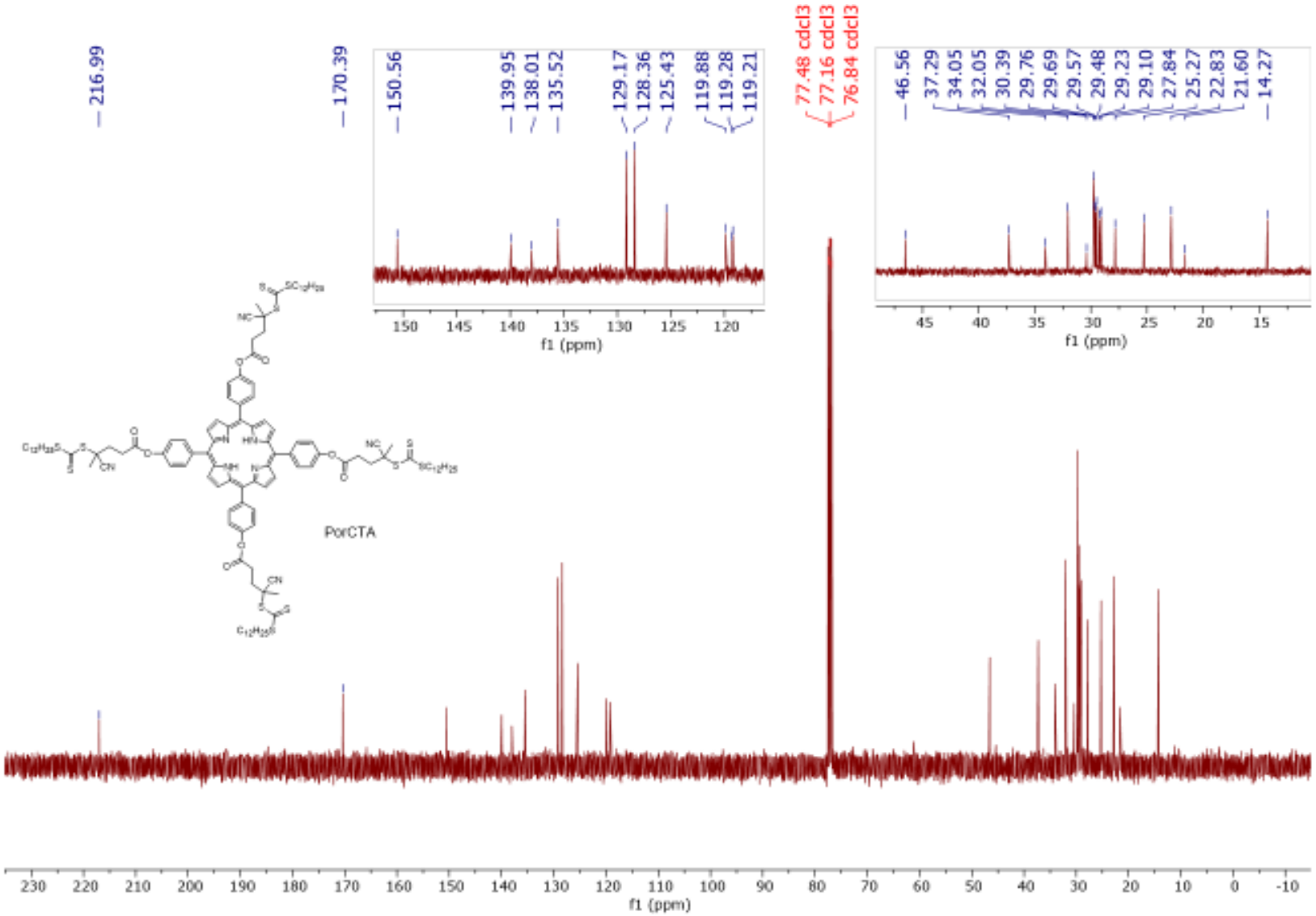

Figure A60: ^{13}C NMR (126 MHz, $CDCl_3$) spectrum of PorCTA

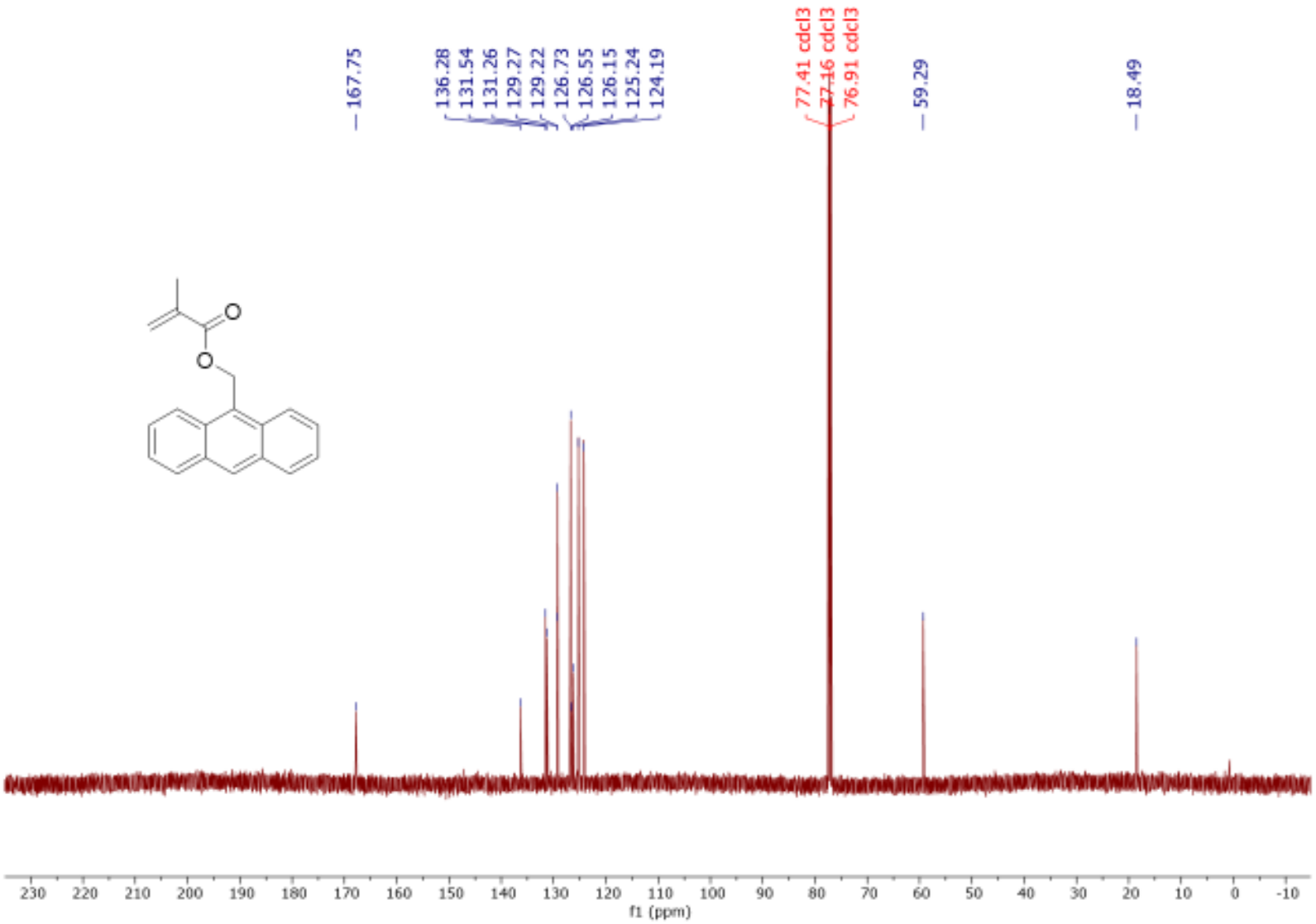

Figure A61: ^{13}C NMR (126 MHz, $CDCl_3$) spectrum of AMMA

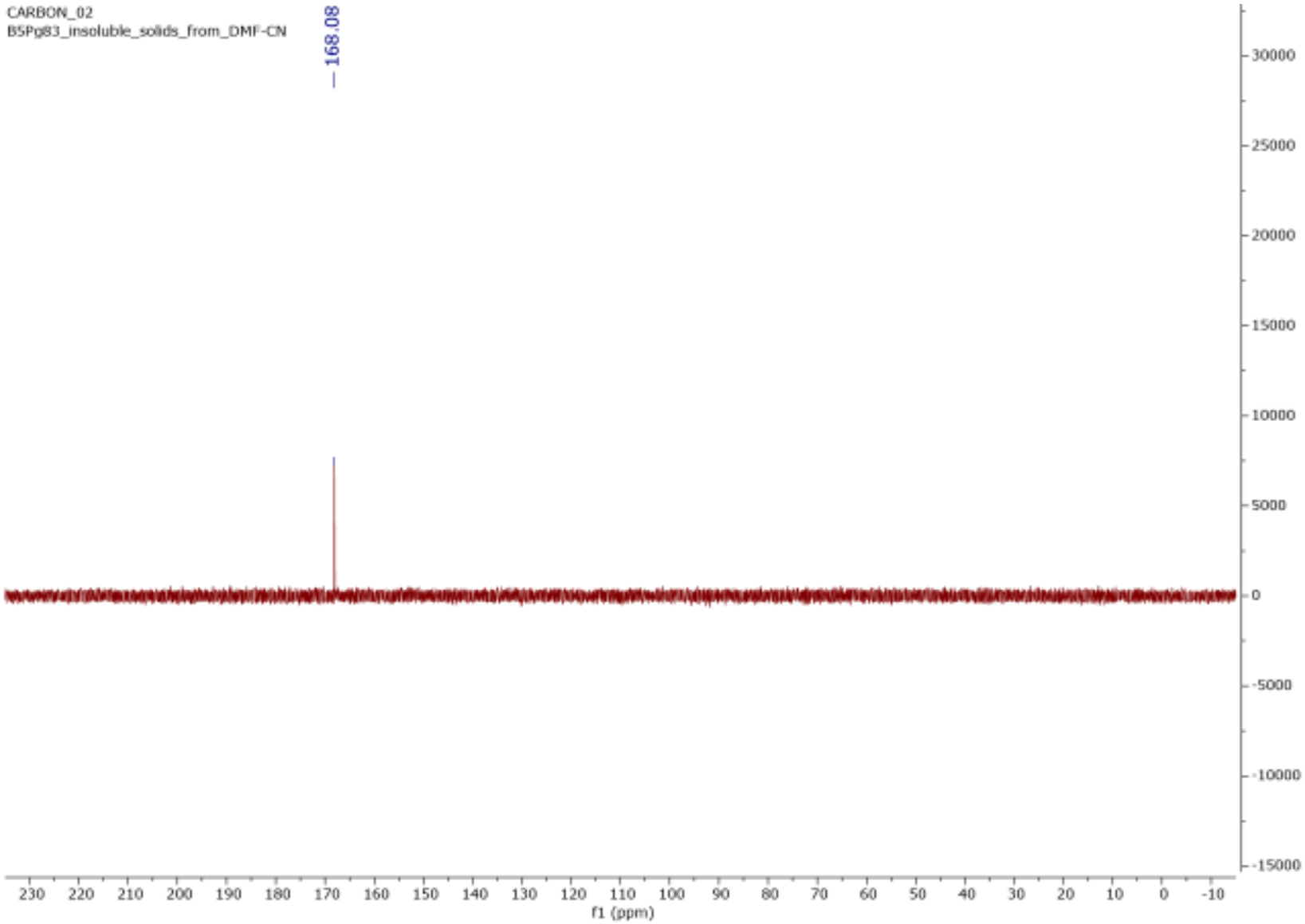

Figure A62: ^{13}C NMR (D_2O, 101 MHz) spectrum of white precipitates from reaction of Zn^{II}(Por(HexMAAm -co-AMMA)$_4$), NaCN, and DMF under ambient conditions.

APPENDIX C: ^{19}F NMR spectra

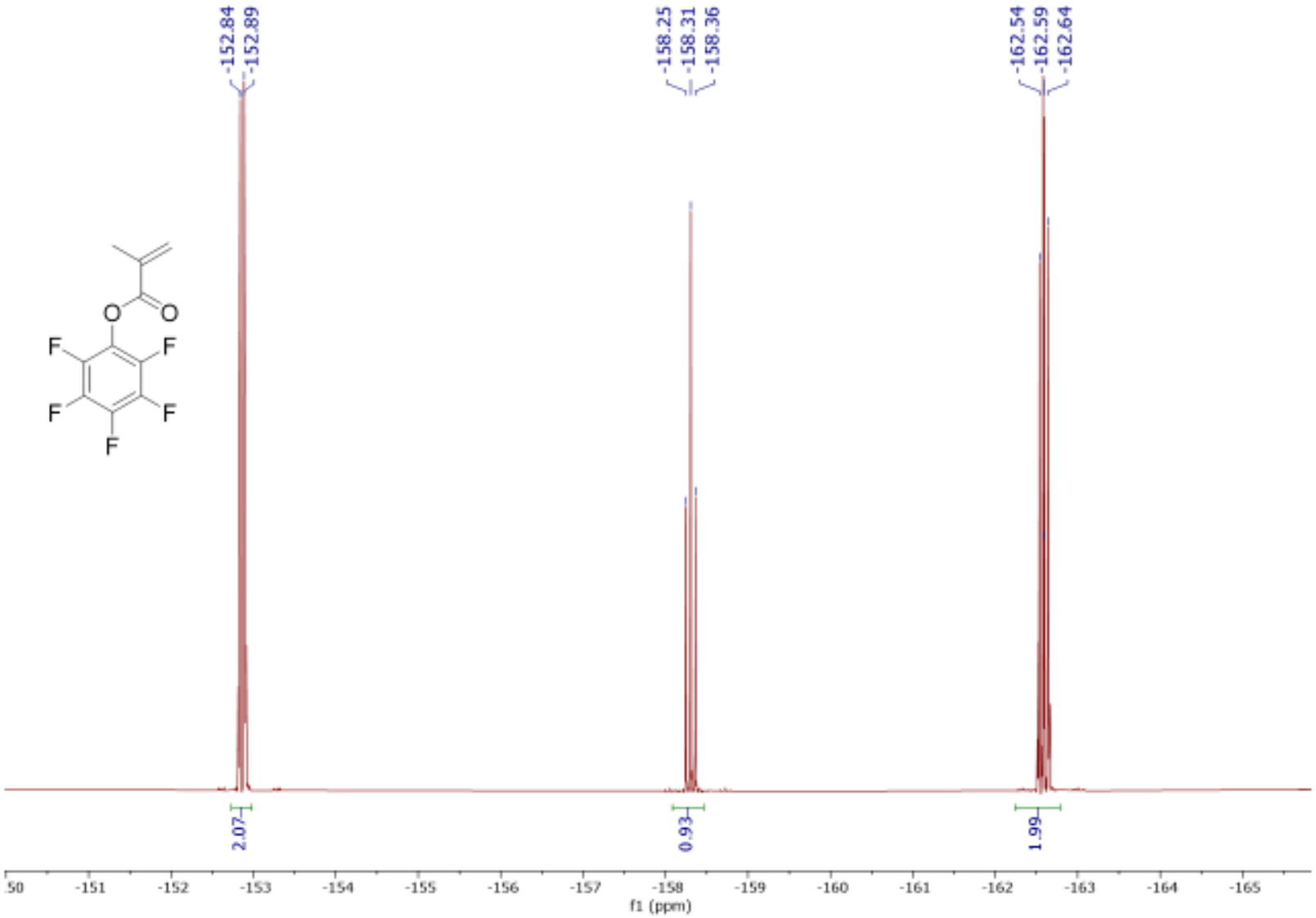

Figure A63: ^{19}F NMR ($CDCl_3$, 376.1 MHz) spectrum of PFPMA

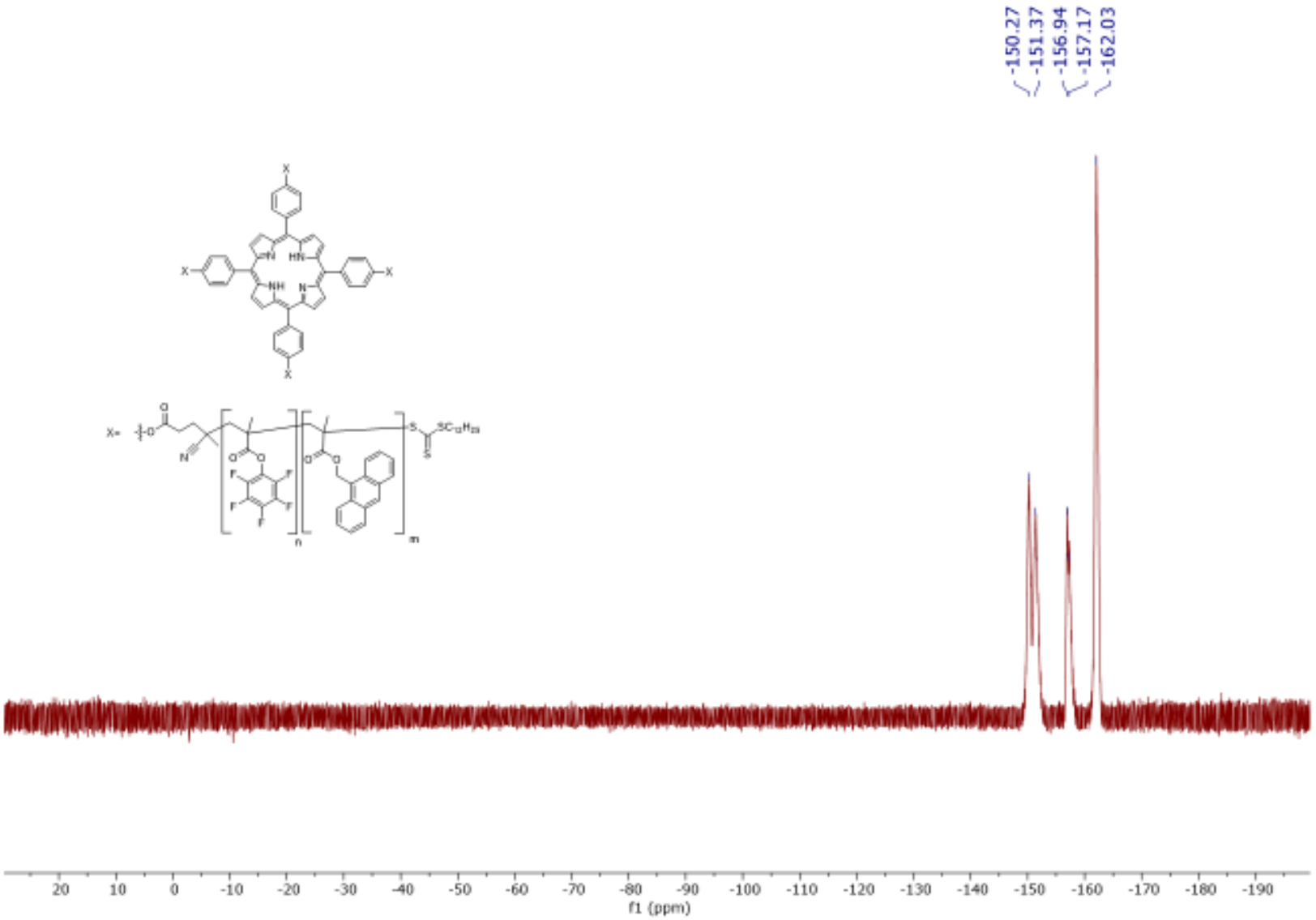

Figure A64: ^{19}F NMR ($CDCl_3$, 376.1 MHz) spectrum of Por(PFPMA-co-AMMA)$_4$

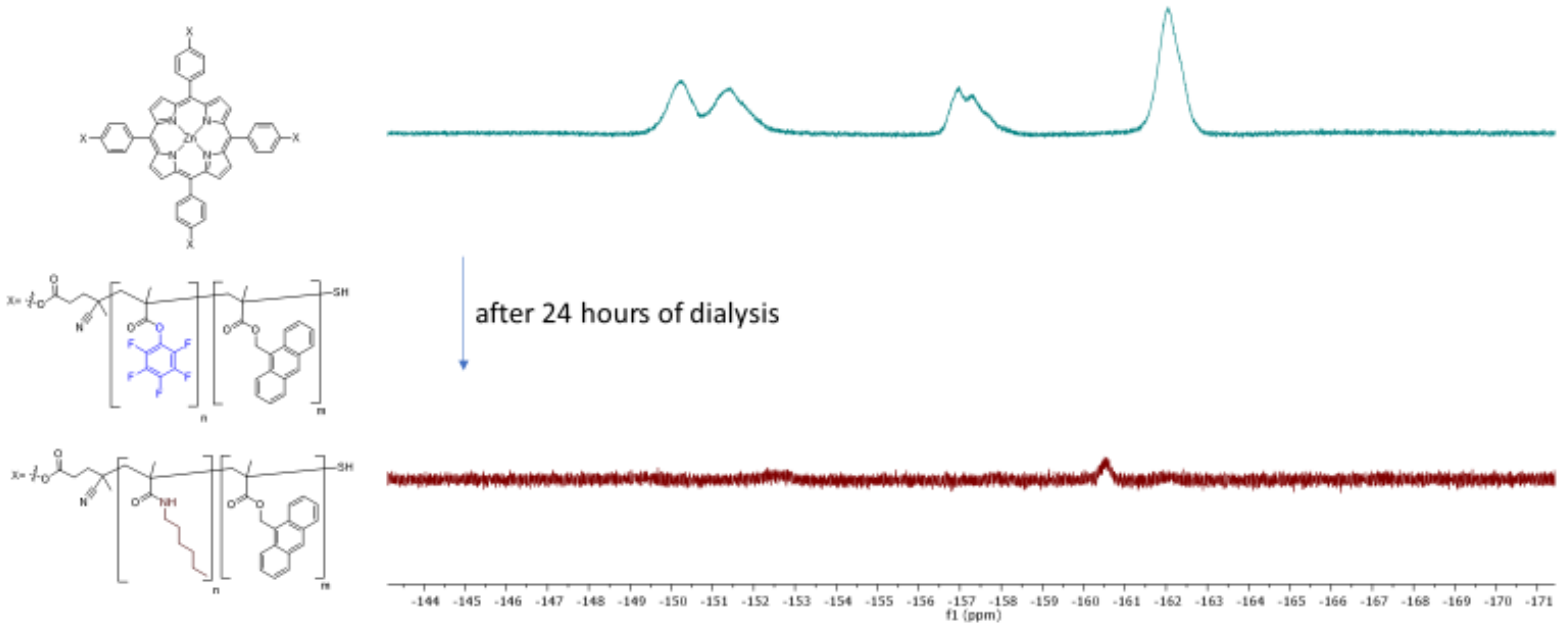

Figure A65: (Top) ^{19}F NMR ($CDCl_3$, 376.1 MHz) spectrum of Zn^{II}(Por(PFPMA-co-AMMA)$_4$), (Bottom) ^{19}F NMR ($CDCl_3$, 376.1 MHz) spectrum of Zn^{II}(Por(HexMAAm-co-AMMA)$_4$) after dialysis.

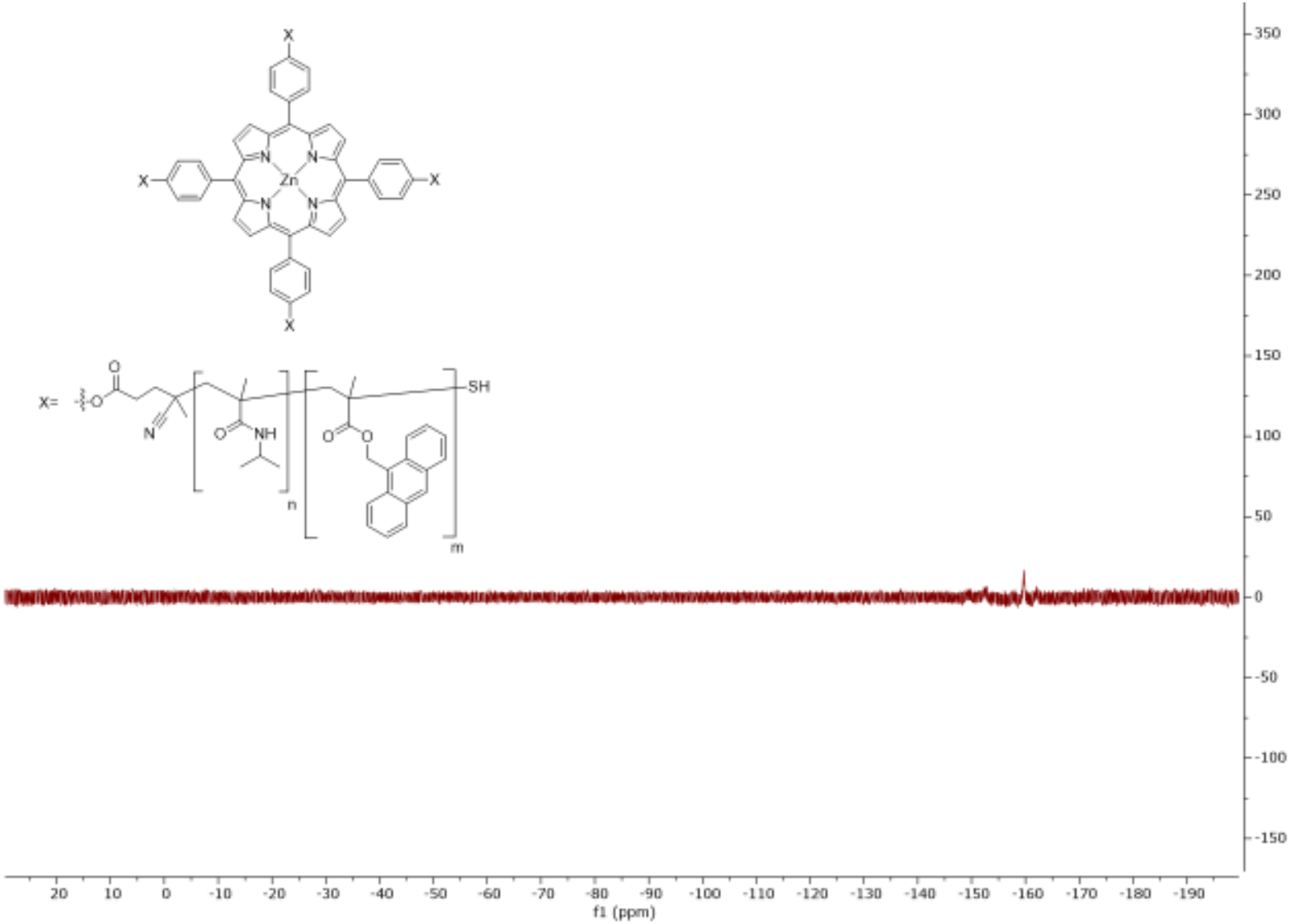

Figure A66: ^{19}F NMR ($CDCl_3$, 376.1 MHz) spectrum of Zn^{II}(Por(iPMAAm-co-AMMA)$_4$)

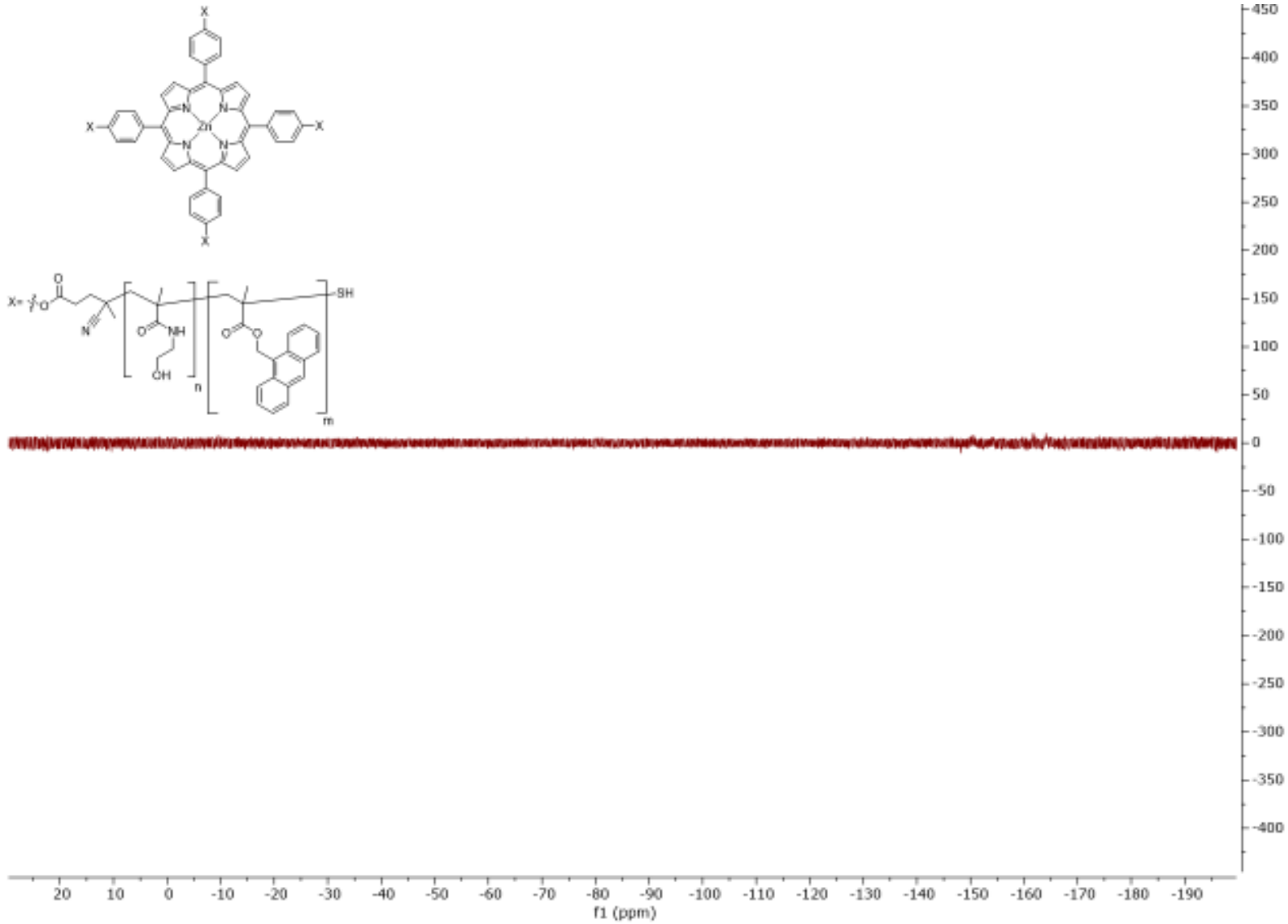

Figure A67:[19]F NMR (DMF-d_7, 376.1 MHz) spectrum of Zn^{II}(Por((HEMA-co-AMMA)$_4$)

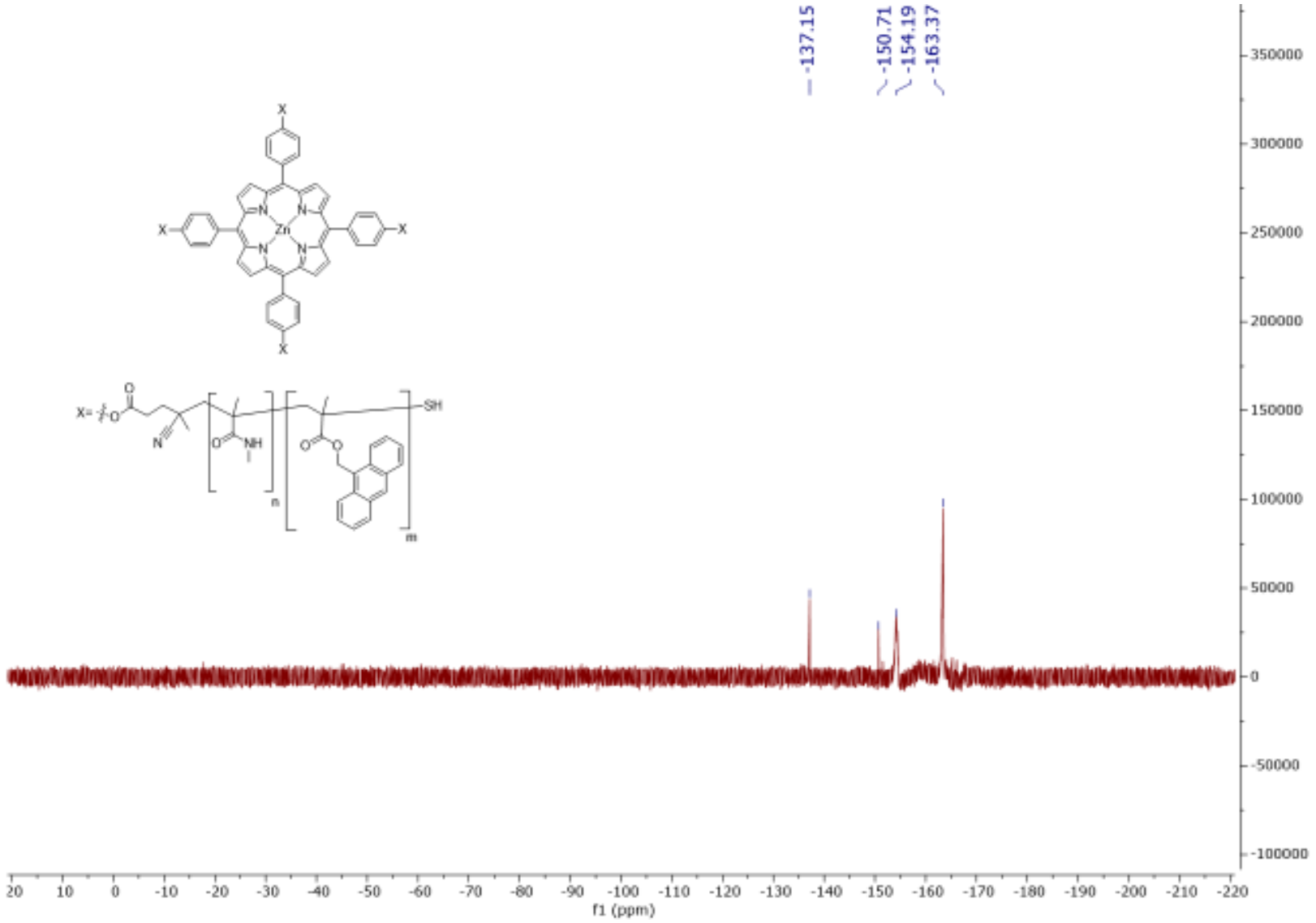

Figure A68: ^{19}F NMR (DMF-d_7, 470.14 MHz) spectrum of Zn^{II}(Por((MMAAm-co-AMMA)$_4$)

APPENDIX D: ^{1}H DOSY NMR Spectra

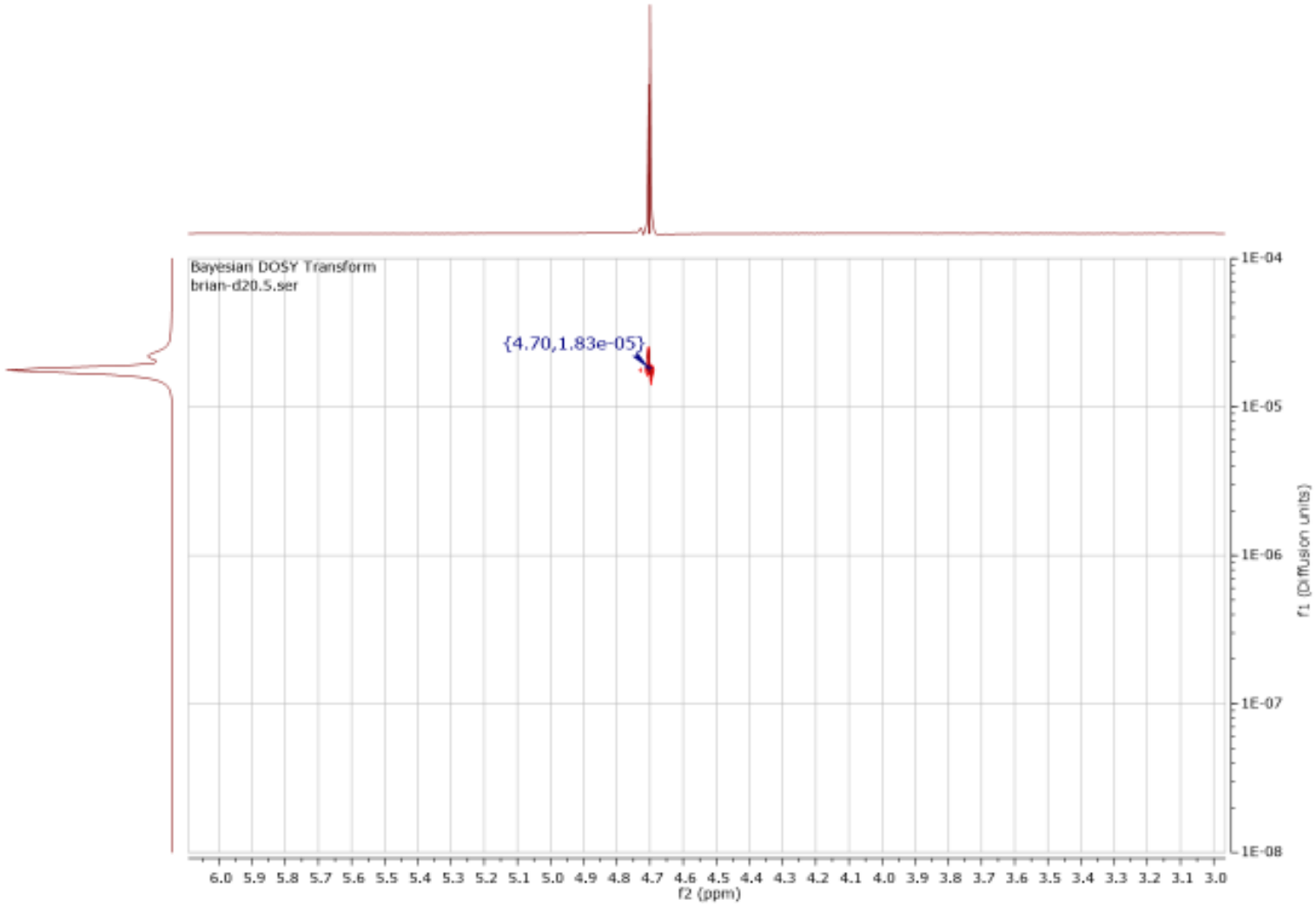

Figure A69: ^{1}H DOSY NMR (D_2O, 500 MHz, 298 K) spectrum of HDO and H_2O used for magnetic field calibration

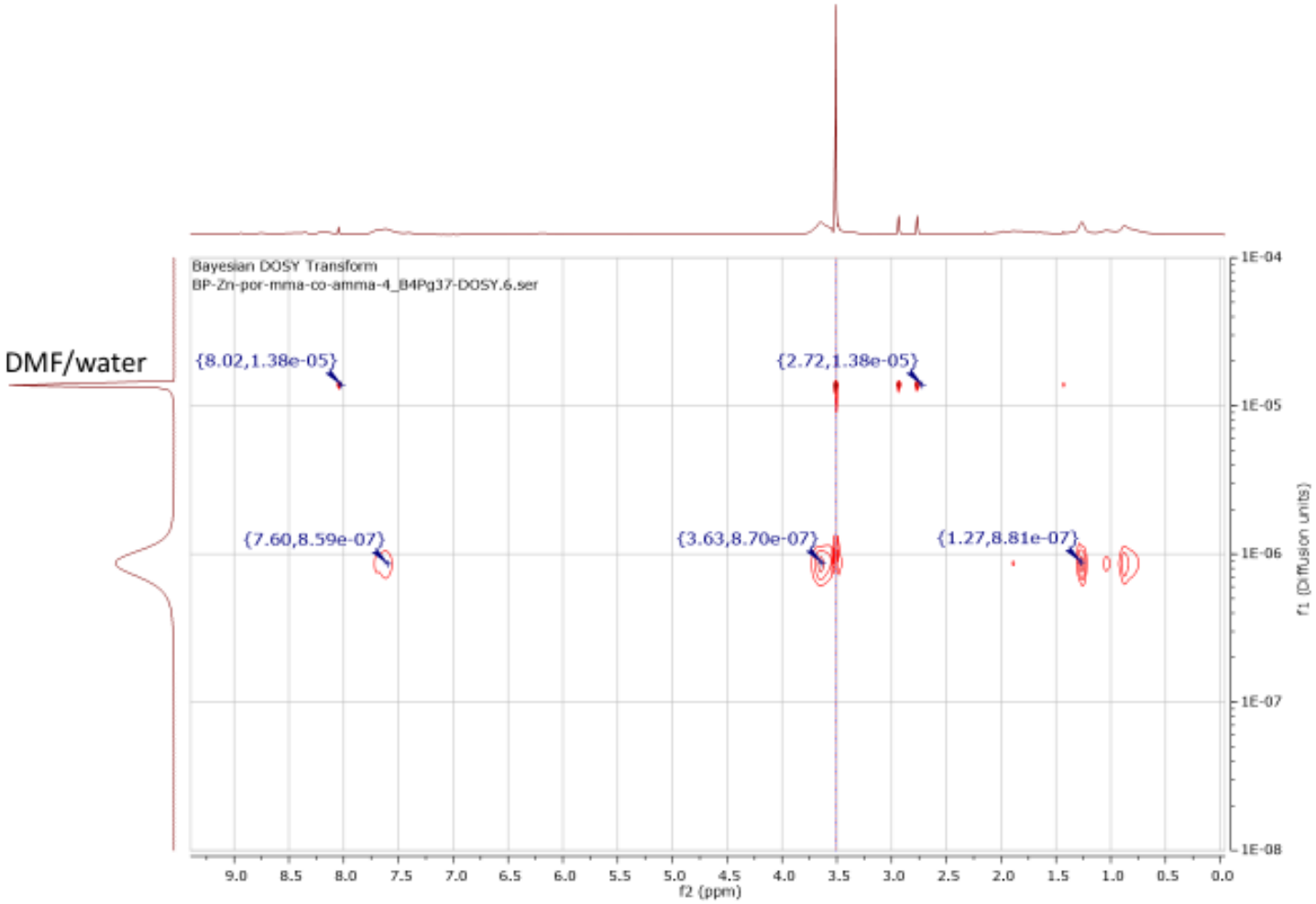

Figure A70: ^{1}H DOSY NMR (DMF-d_7, 500 MHz, 298 K) spectrum of Zn^{II}(Por(MMA-co-AMMA)$_4$)

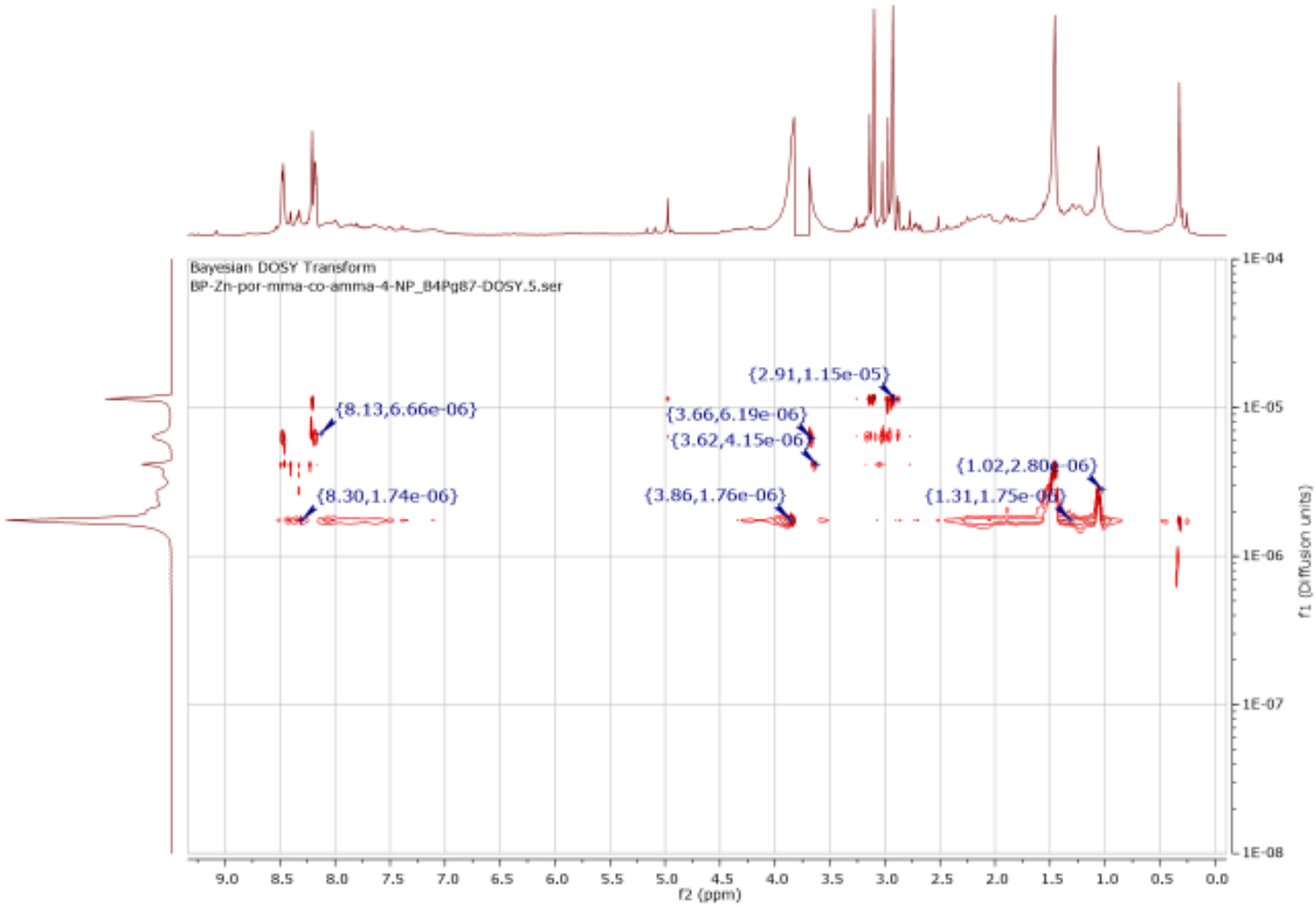

Figure A71: ^{1}H DOSY NMR (DMF-d_7, 500 MHz, 298 K) spectrum of Zn^{II}(Por(MMA-co-AMMA)$_4$)-NP

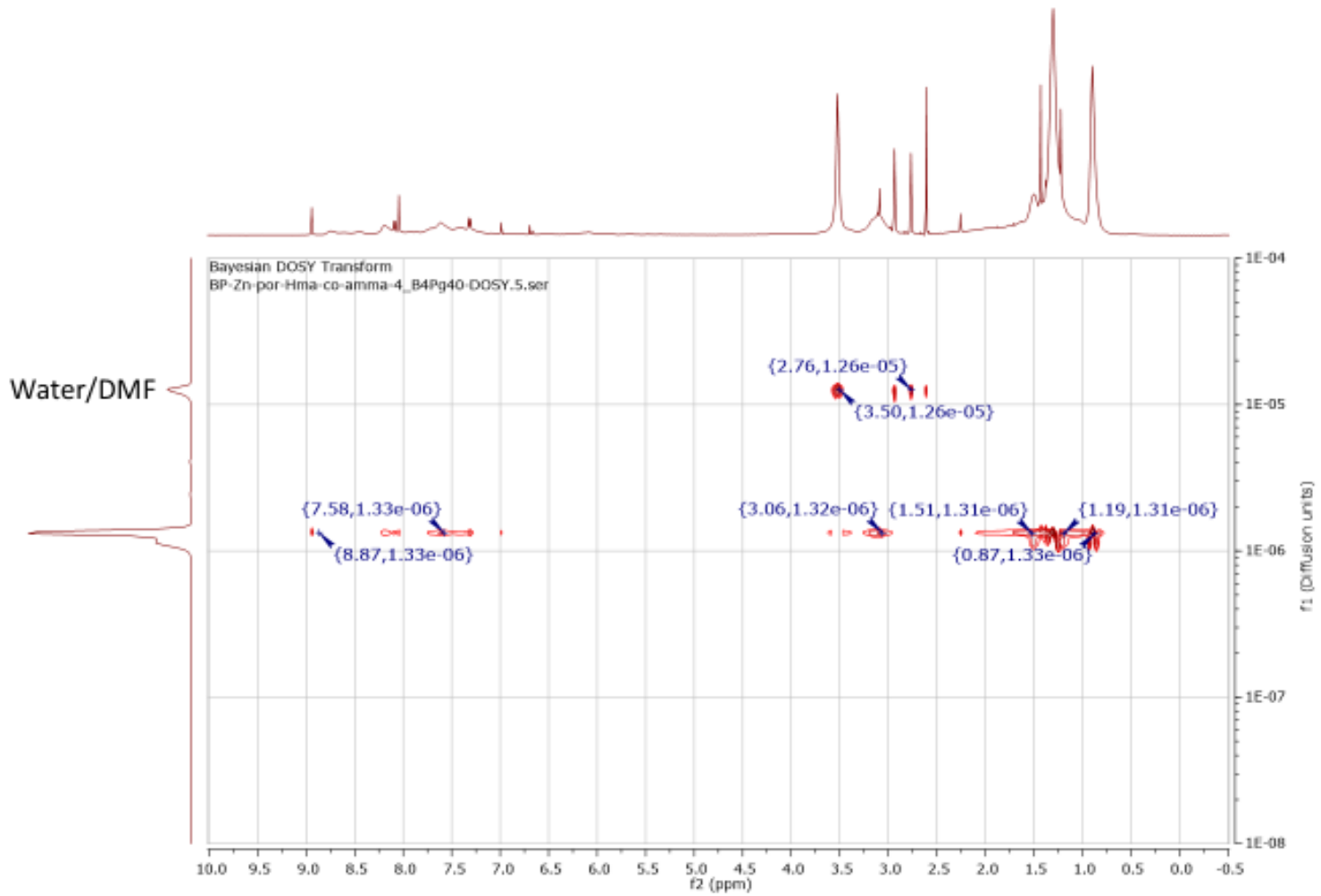

Figure A72: ^{1}H DOSY NMR (DMF-d_7, 500 MHz, 298 K) spectrum of Zn^{II}(Por(HexMAAm-co-AMMA)$_4$)

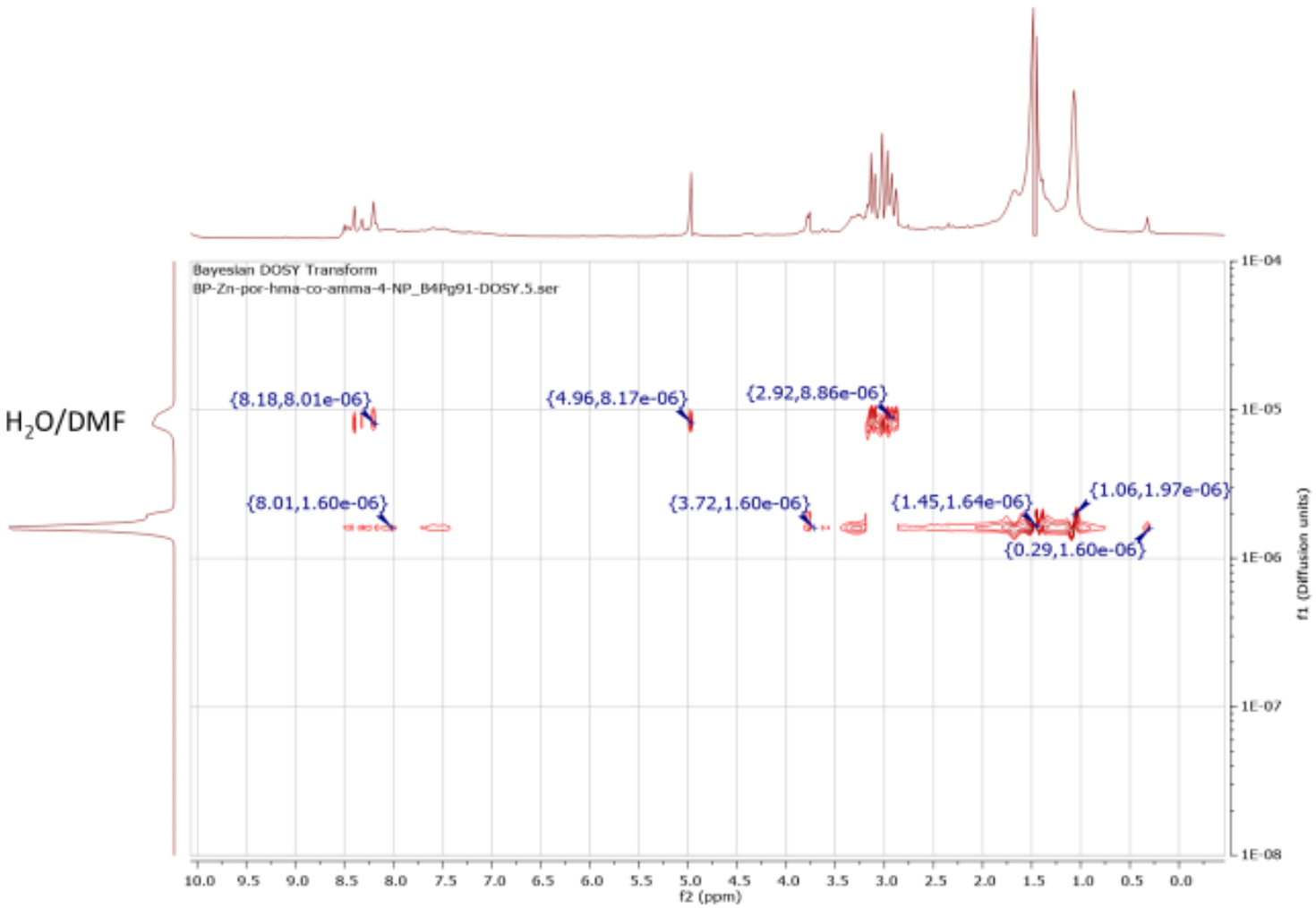

Figure A73: ^{1}H DOSY NMR (DMF-d_7, 500 MHz, 298 K) spectrum of Zn^{II}(Por(HexMAAm-co-AMMA)$_4$)-NP

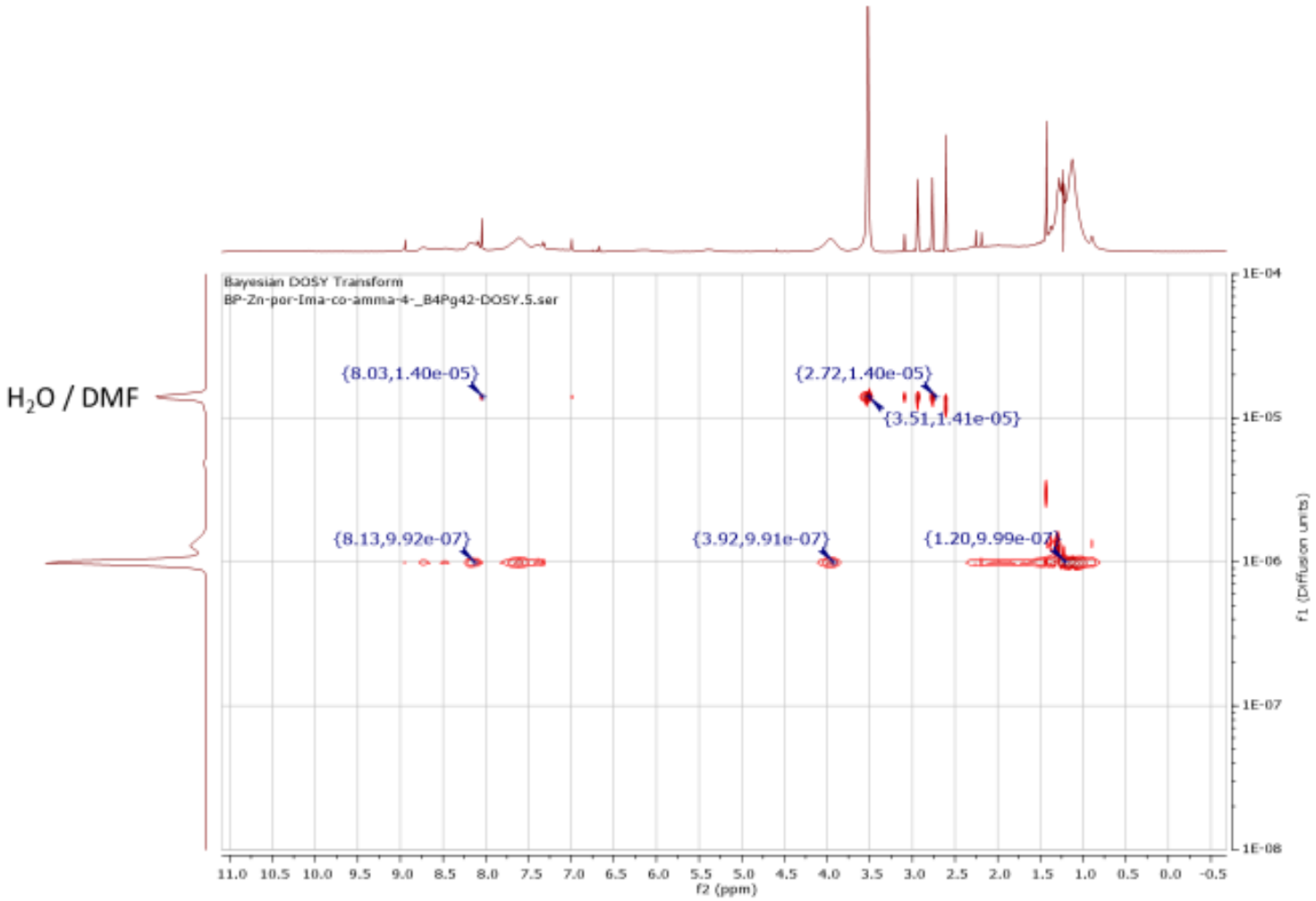

Figure A74: ^{1}H DOSY NMR (DMF-d_7, 500 MHz, 298 K) spectrum of Zn^{II}(Por(iPMAAm-co-AMMA)$_4$)

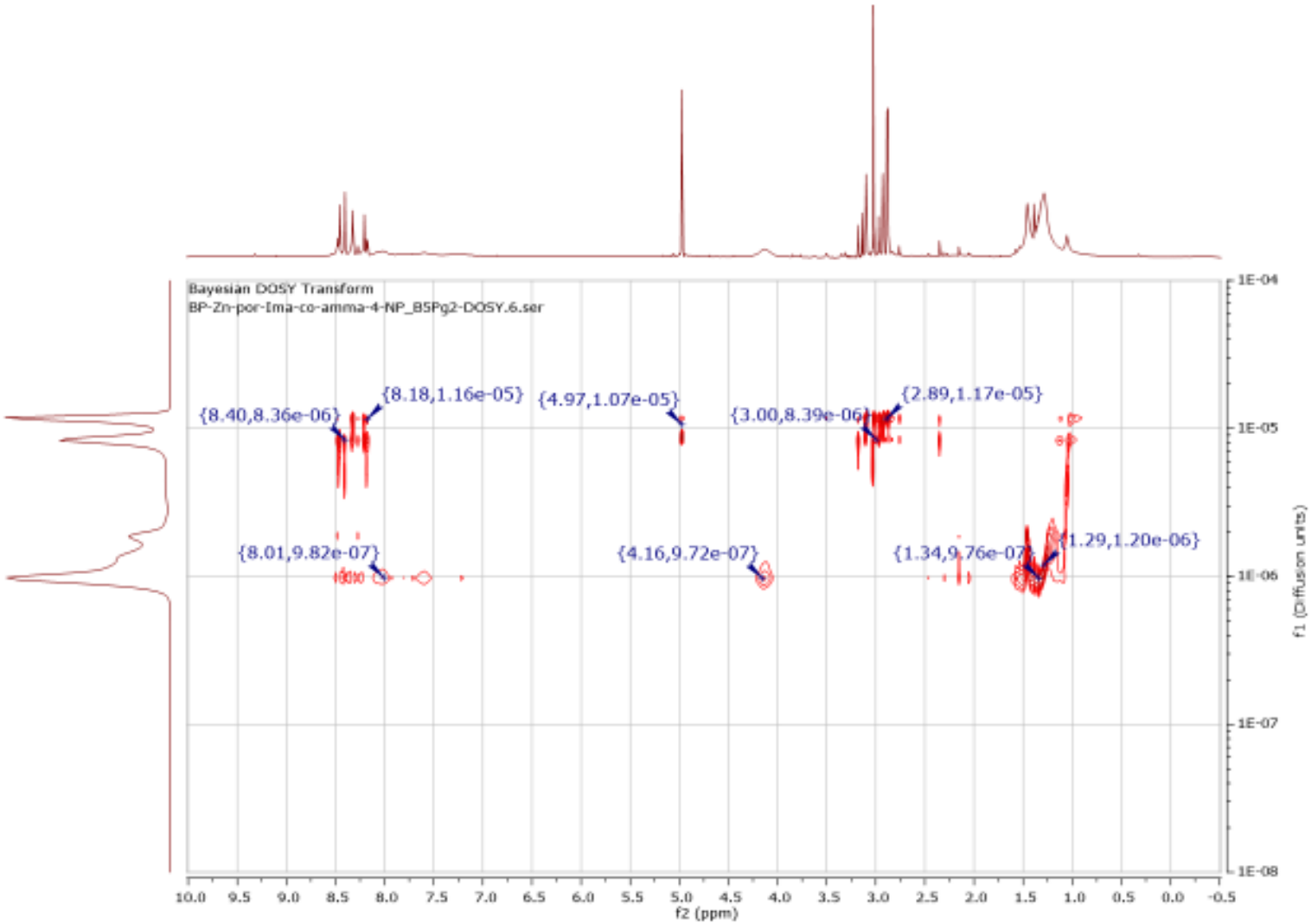

Figure A75: ^{1}H DOSY NMR (DMF-d_7, 500 MHz, 298 K) spectrum of Zn^{II}(Por(iPMAAm-co-AMMA)$_4$)-NP

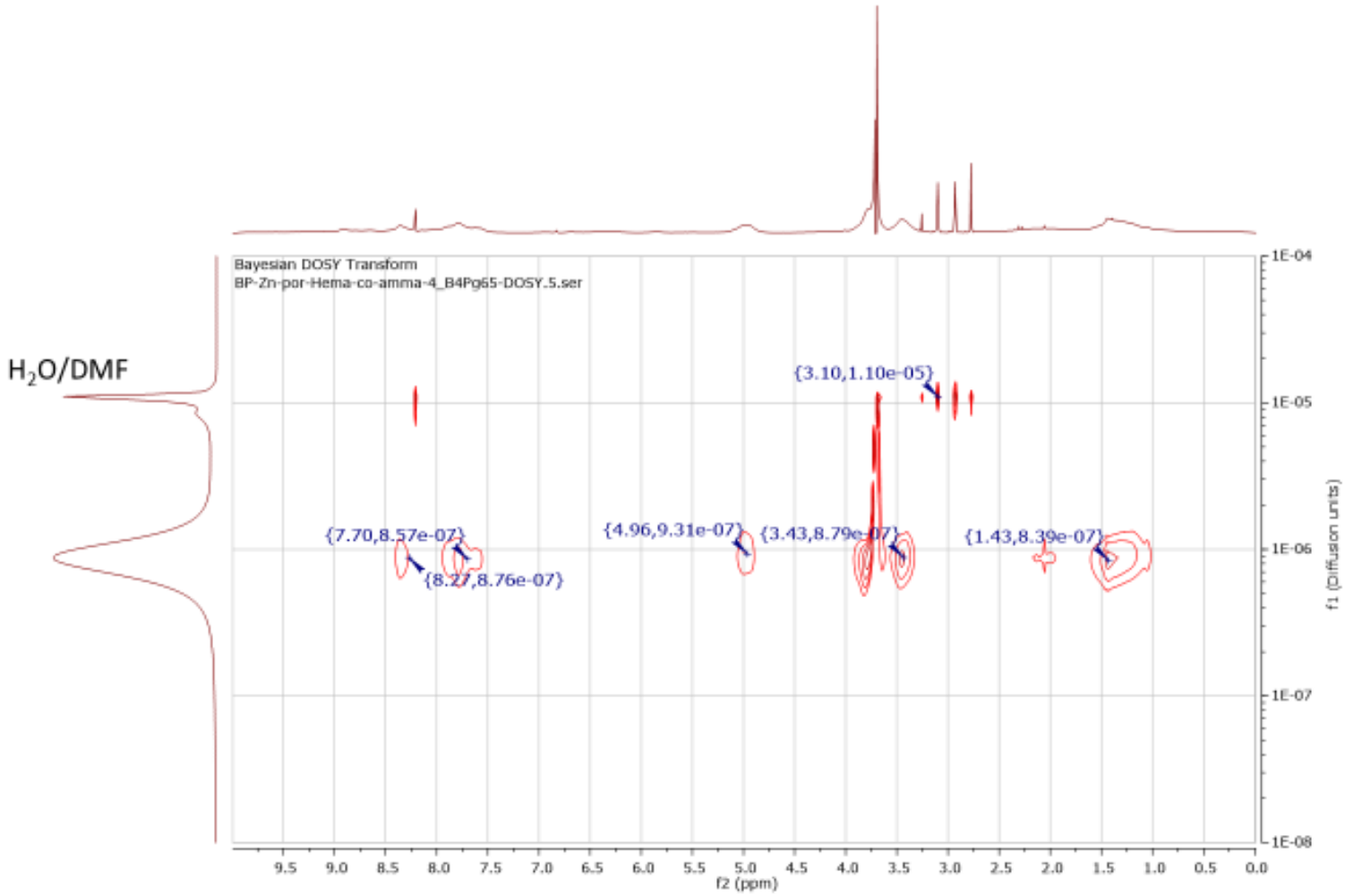

Figure A76: ^{1}H DOSY NMR (DMF-d_7, 500 MHz, 298 K) spectrum of Zn^{II}(Por((HEMA-co-AMMA)$_4$)

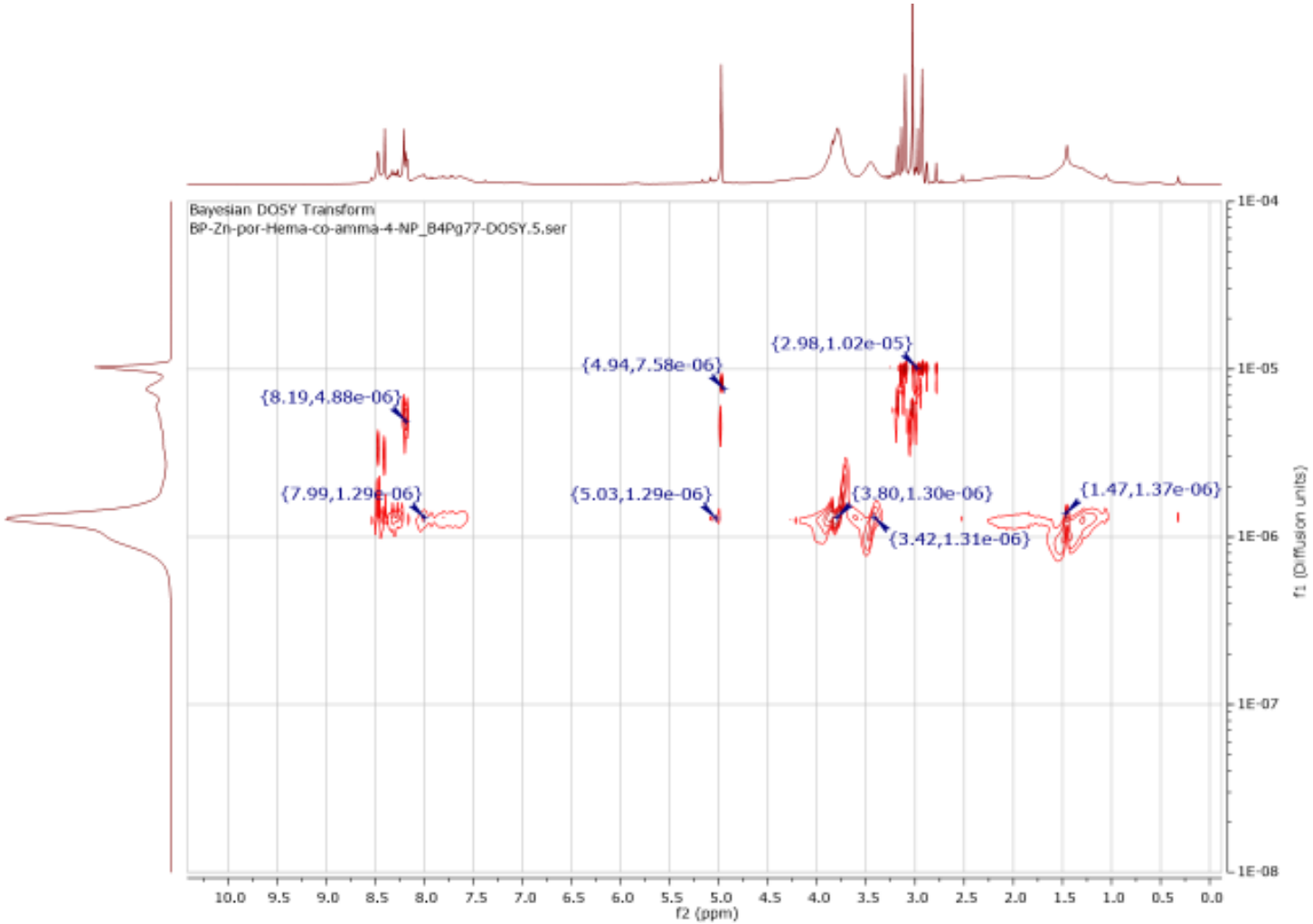

Figure A77: ^{1}H DOSY NMR (DMF-d_7, 500 MHz, 298 K) spectrum of Zn^{II}(Por(HEMA-co-AMMA)$_4$)-NP

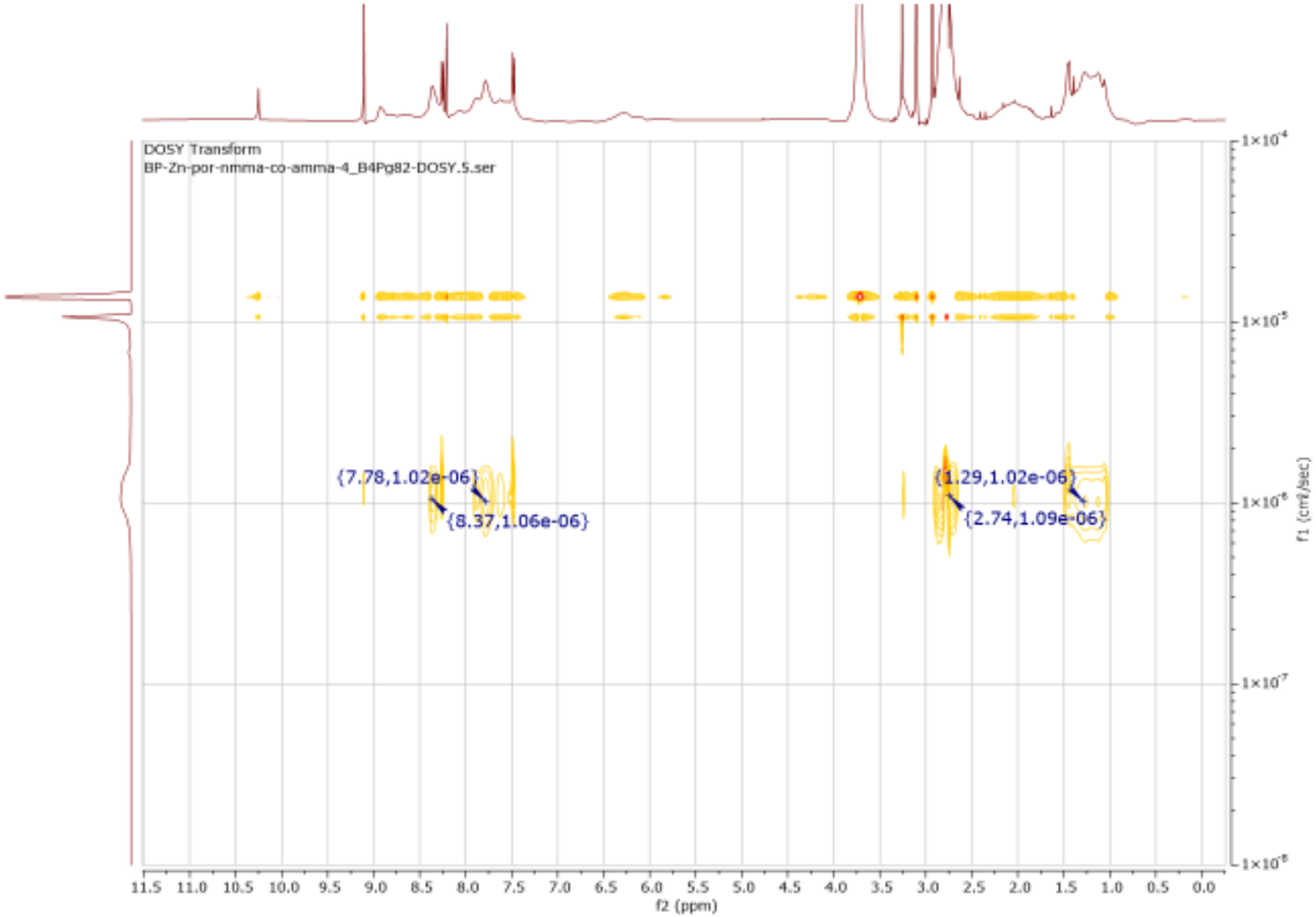

Figure A78: ^{1}H DOSY NMR (DMF-d7, 500 MHz, 298 K) spectrum of Zn^{II}(Por(MMAAm-co-AMMA)$_4$)

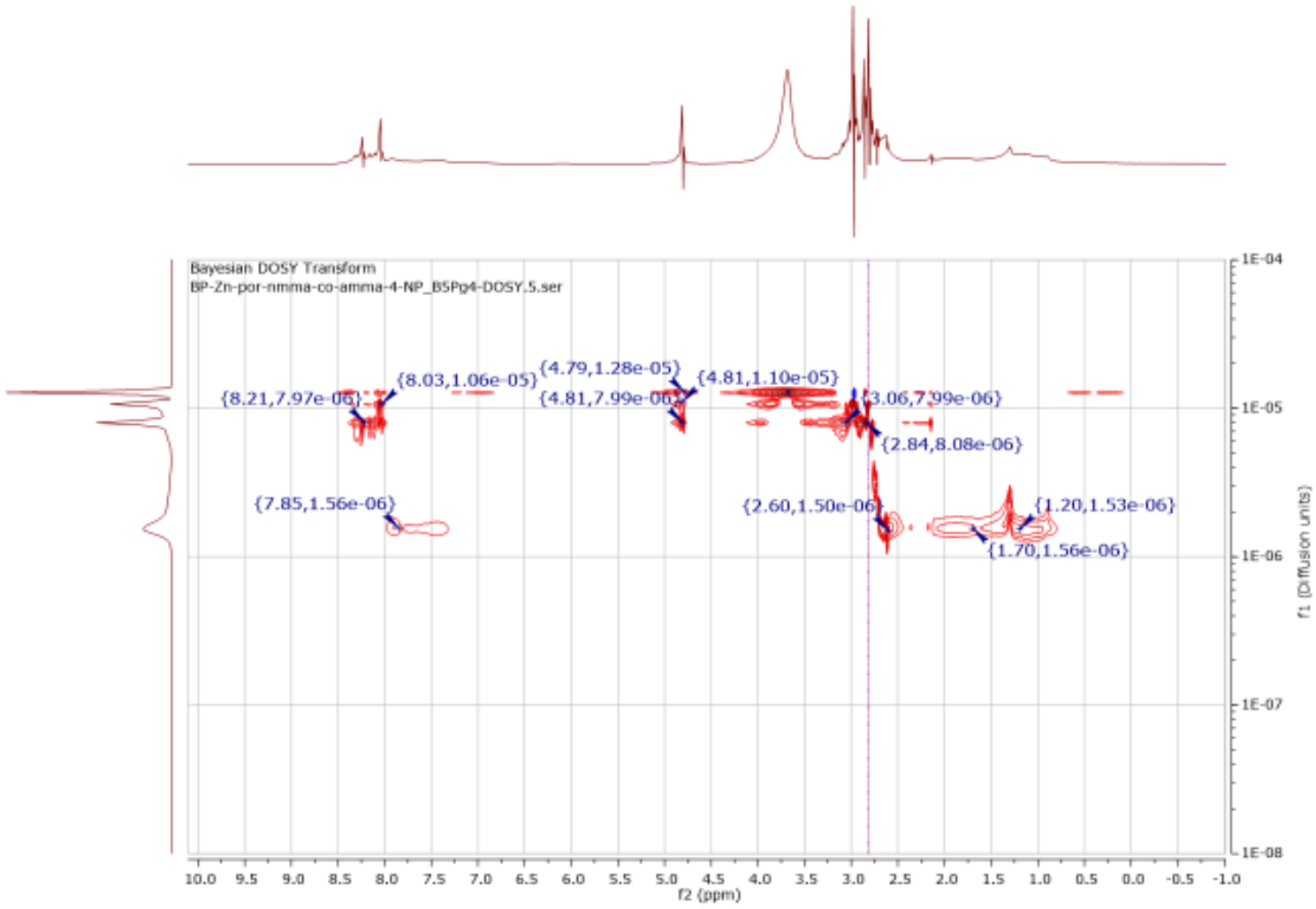

Figure A79: ^{1}H DOSY NMR (DMF-d7, 500 MHz, 298 K) spectrum of Zn^{II}(Por(MMAAm-co-AMMA)$_4$)-NP

APPENDIX F: IR Spectra

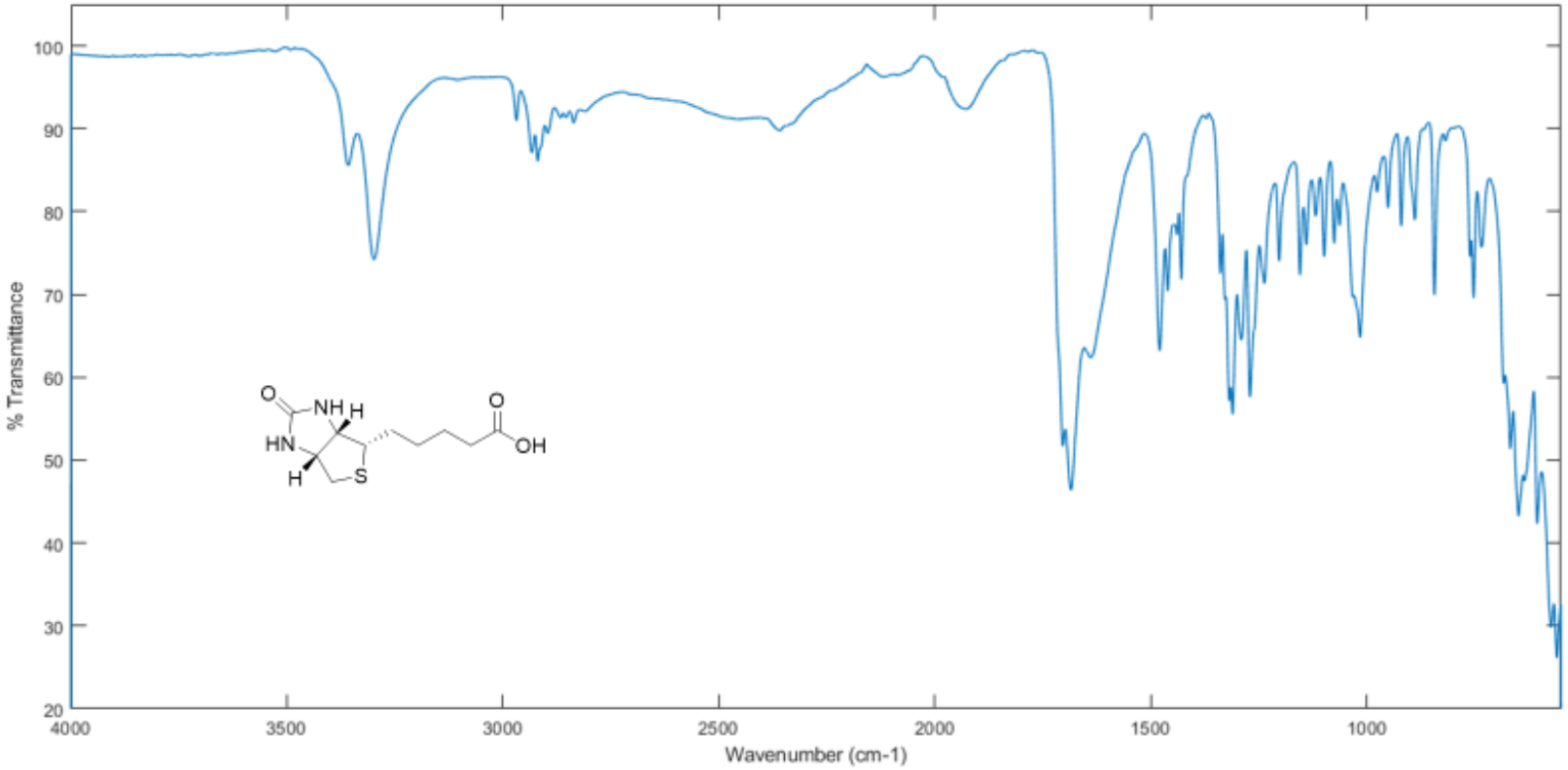

Figure A80: ATR-IR spectrum of Biotin

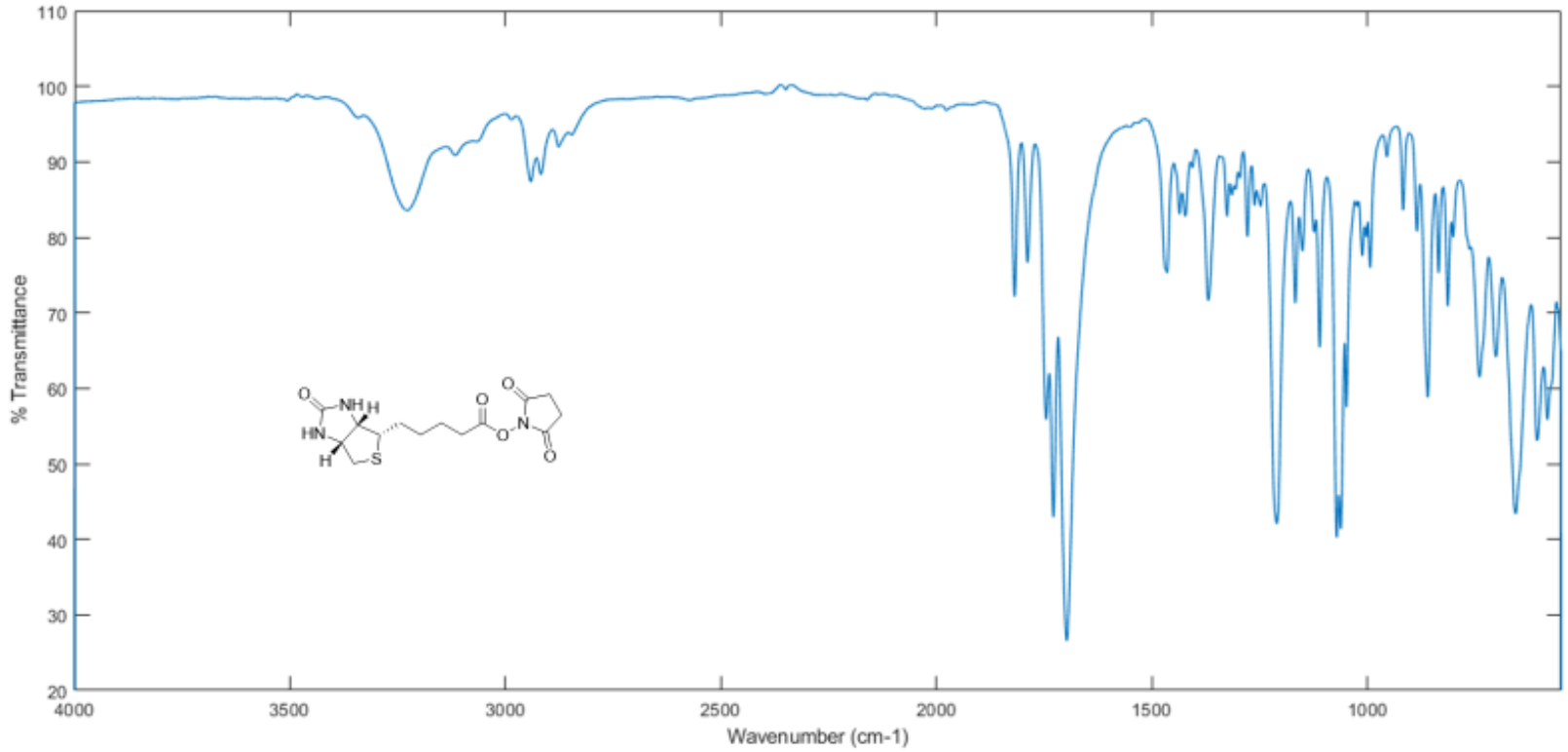

Figure A81: ATR-IR spectrum of Biotin-NHS-ester

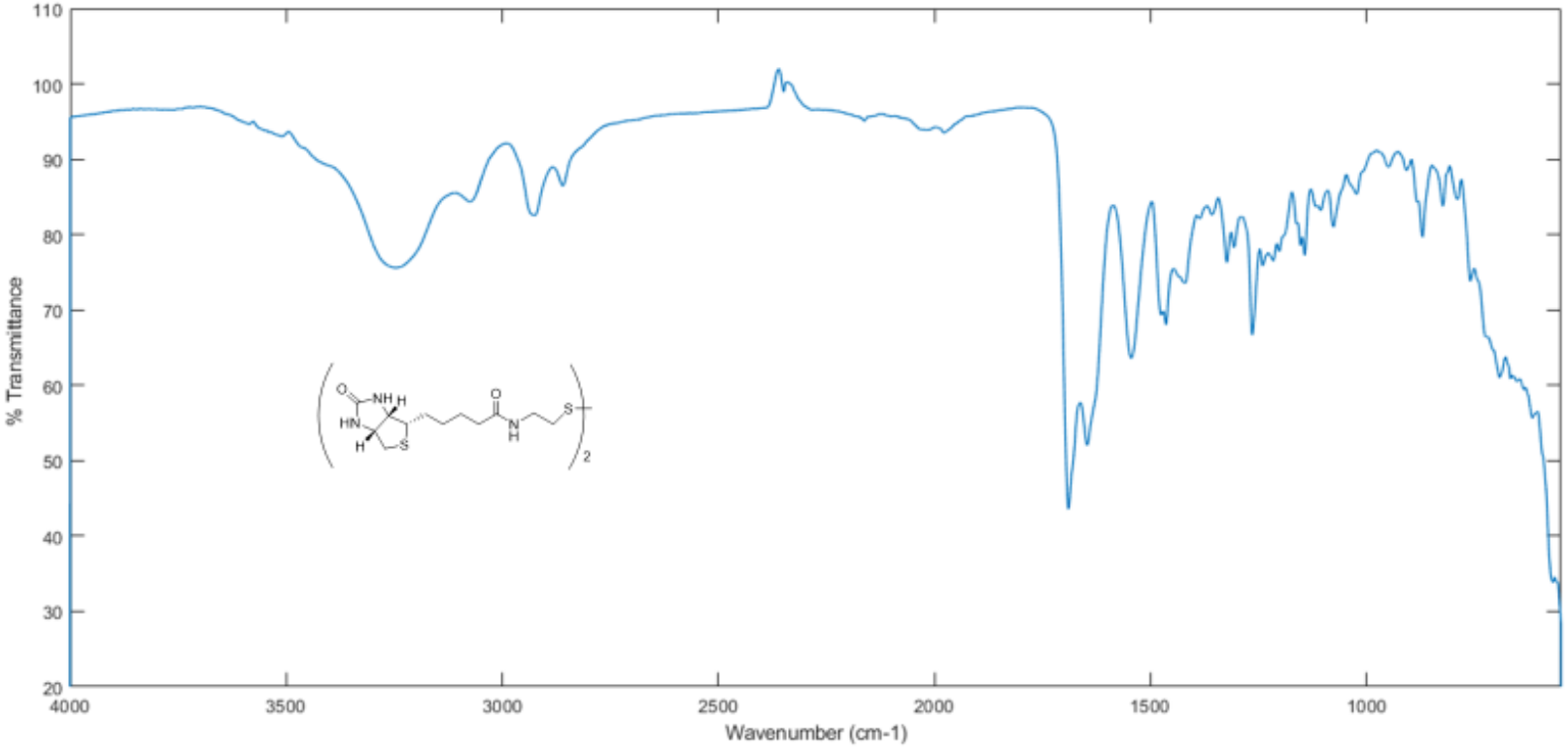

Figure A82: ATR-IR of Biotinylated -cystamine

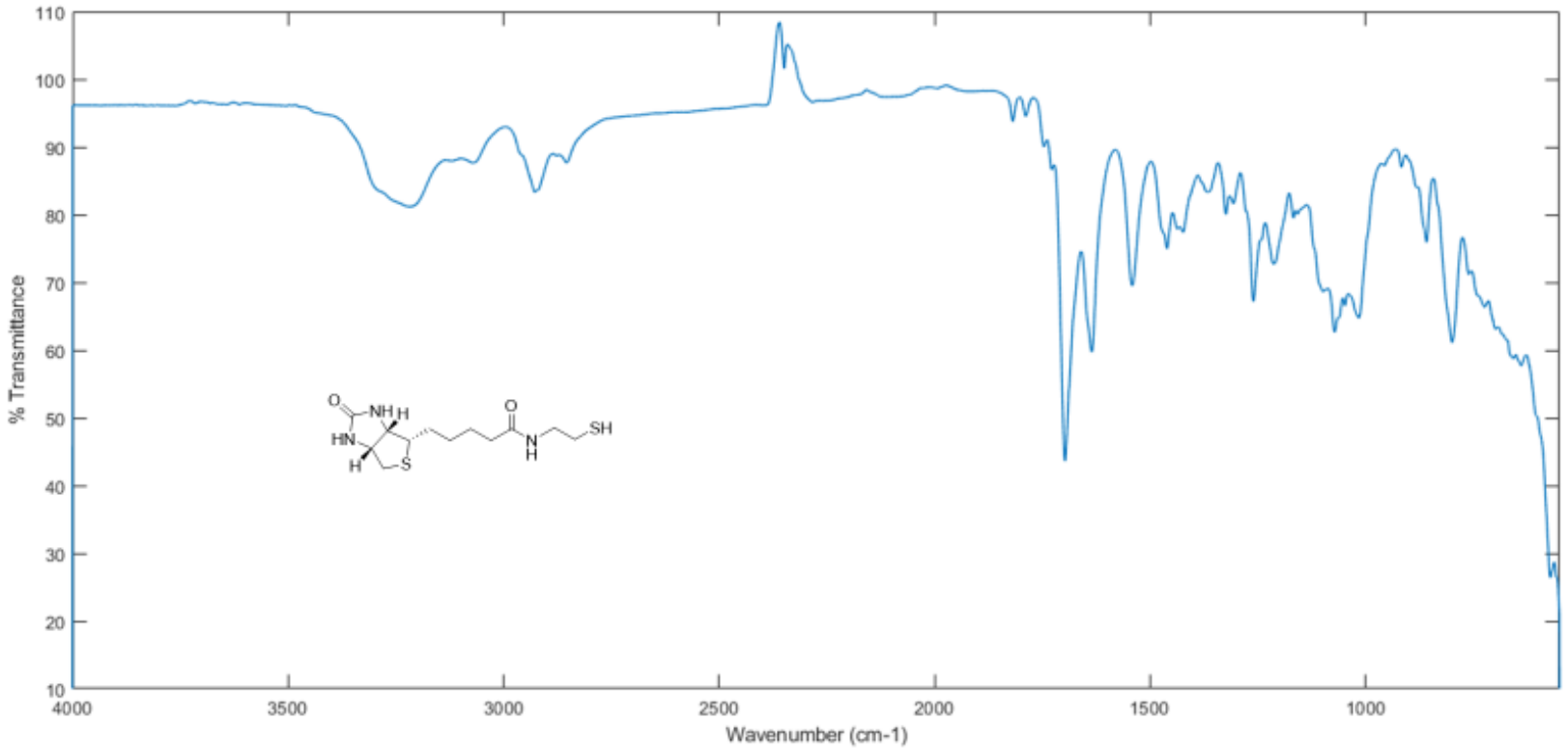

Figure A83: ATR-IR spectrum of Biotinylated cysteamine

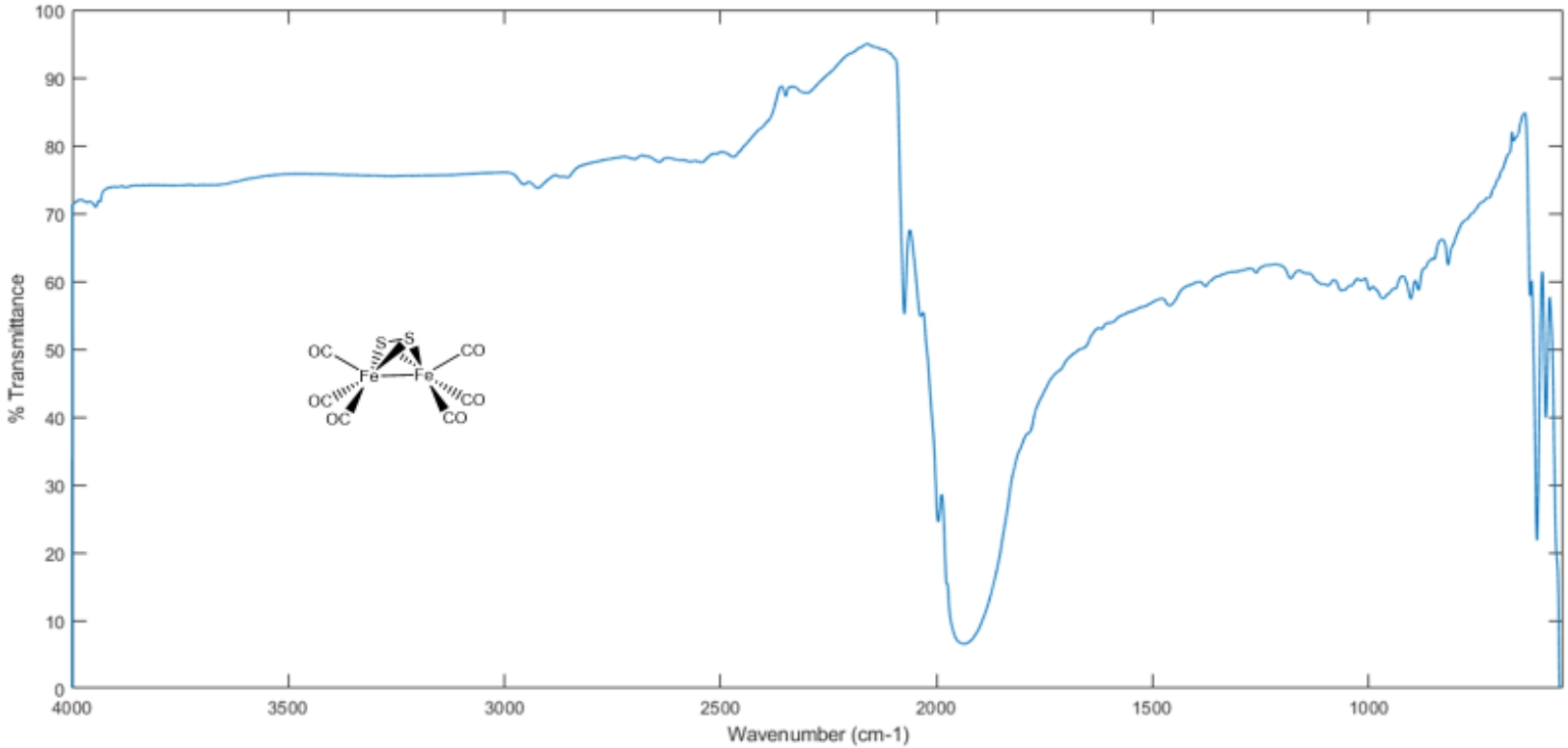

Figure A84: ATR-IR spectrum of (μ-dithiolato)diiron(I) hexacarbonyl

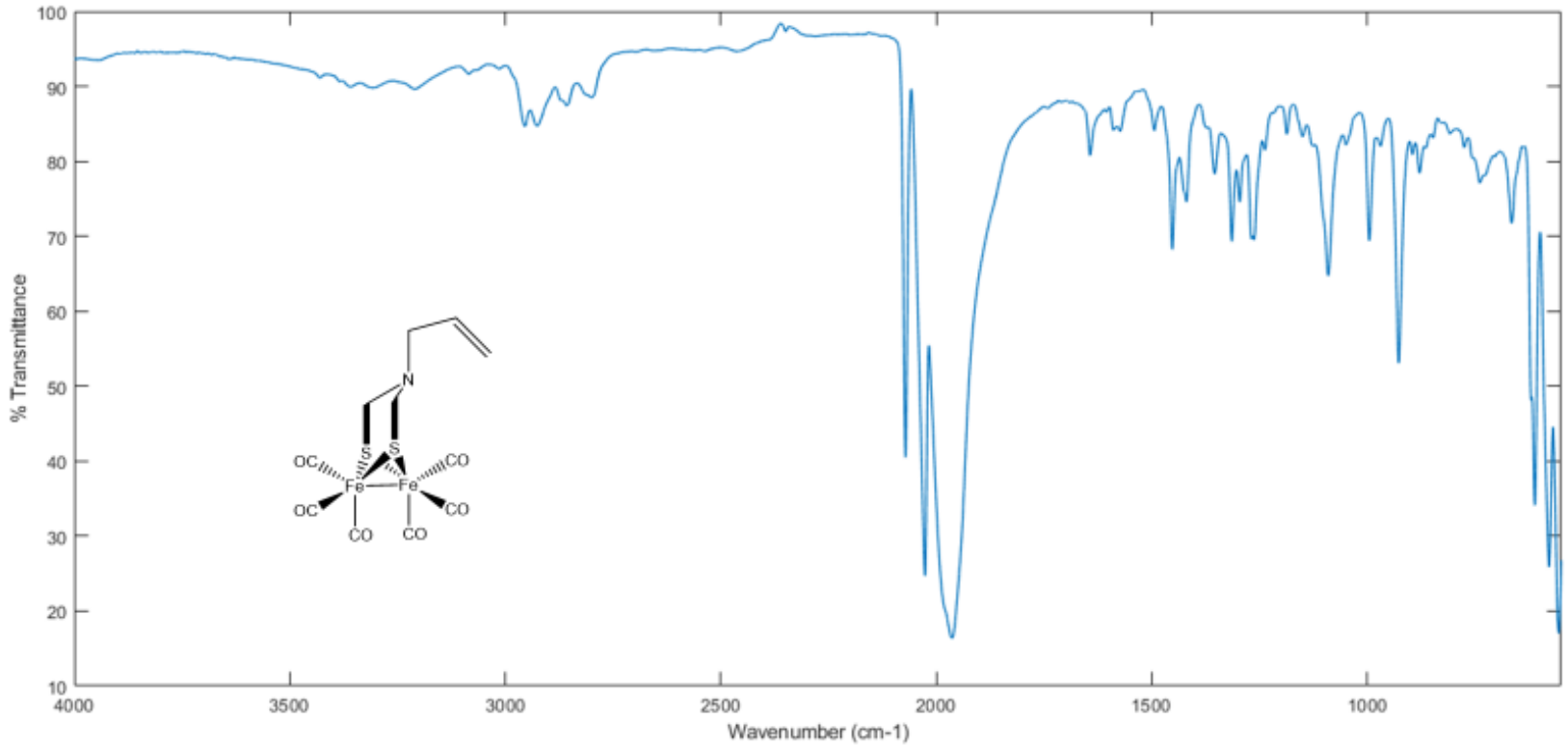

Figure A85: ATR-IR spectrum of (μ-allylazadithiolato)diiron(I) hexacarbonyl

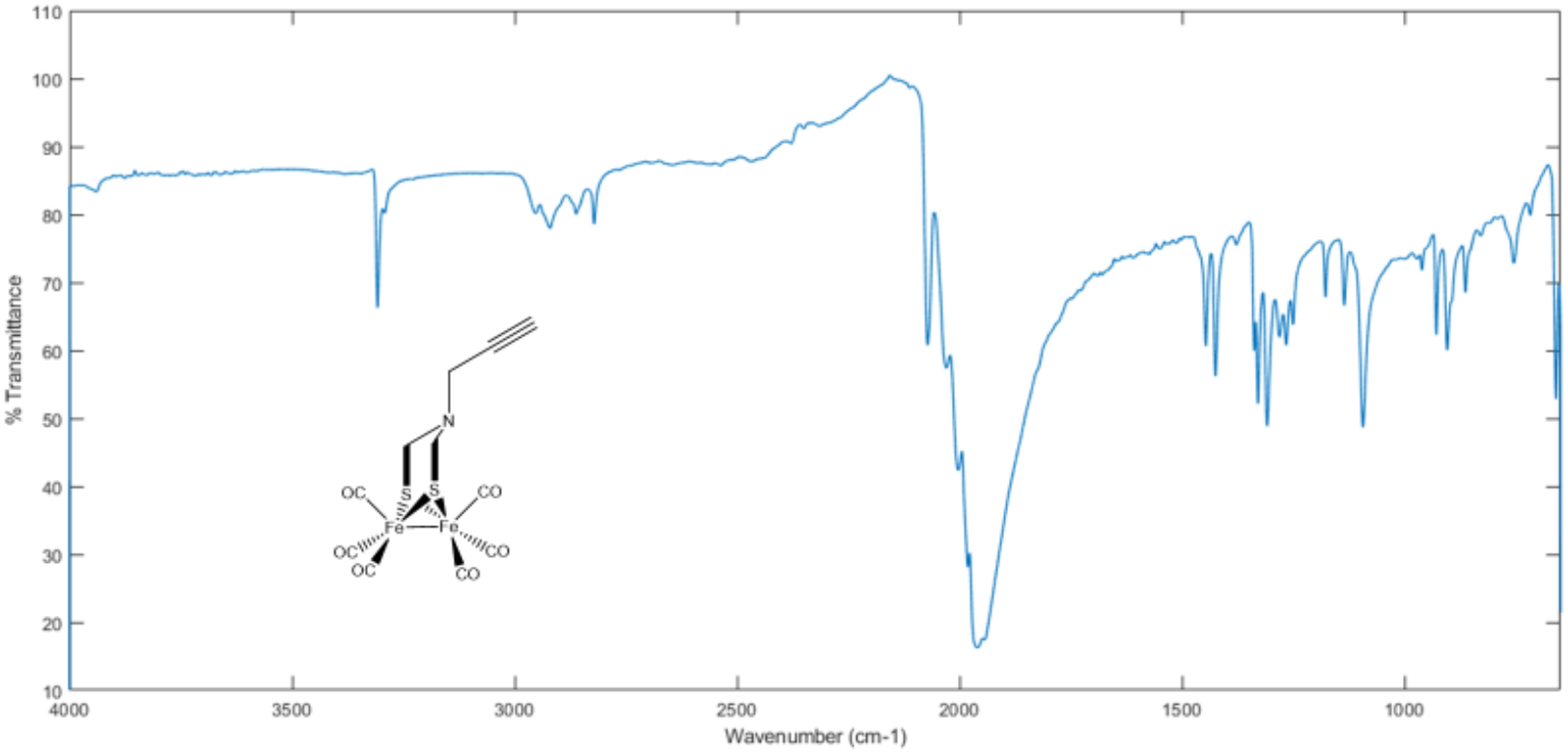

Figure A86: ATR-IR spectrum of (μ-propargylazadithiolato)diiron(I) hexacarbonyl

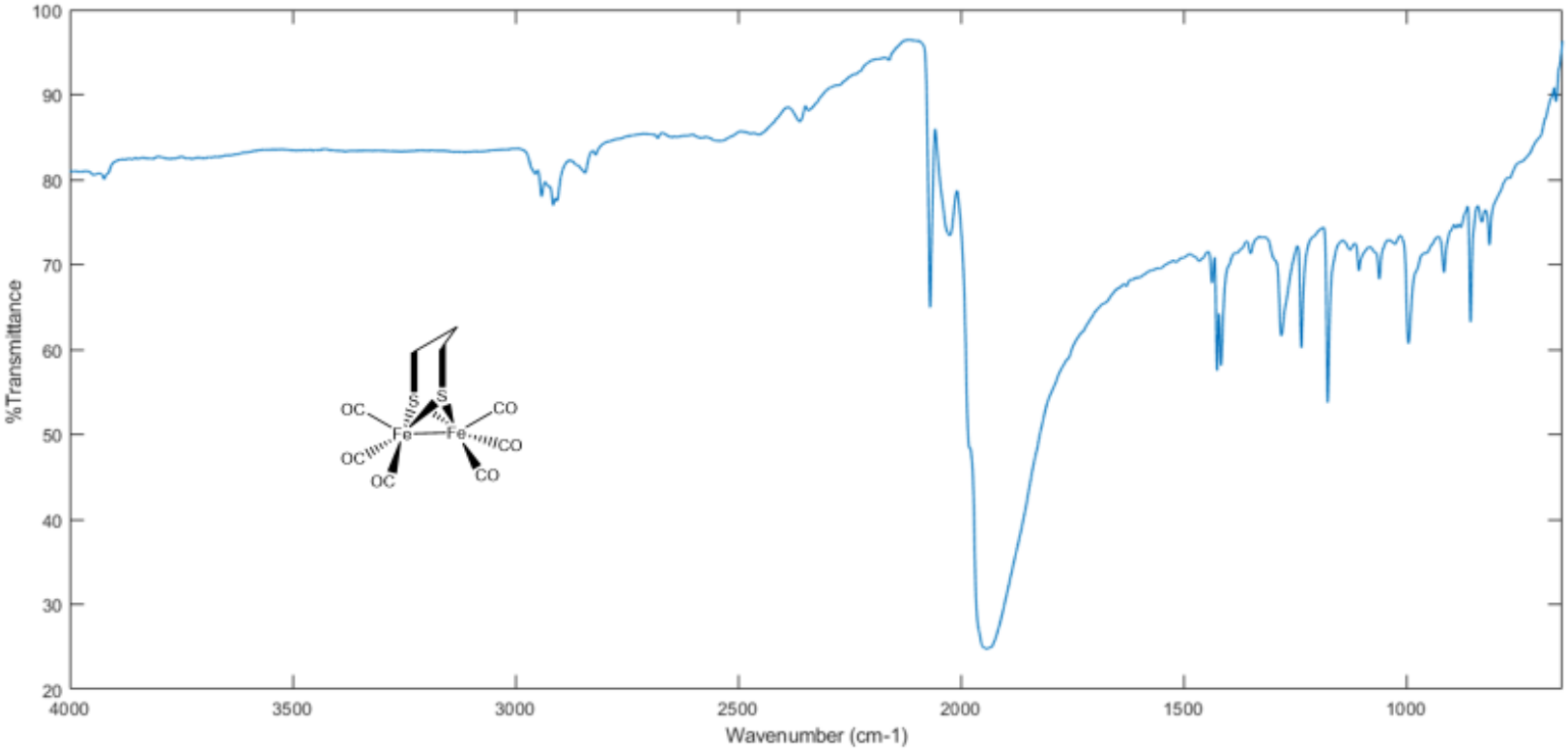

Figure A87: ATR-IR spectrum of (μ-propanedithiolato)diiron(I) hexacarbonyl

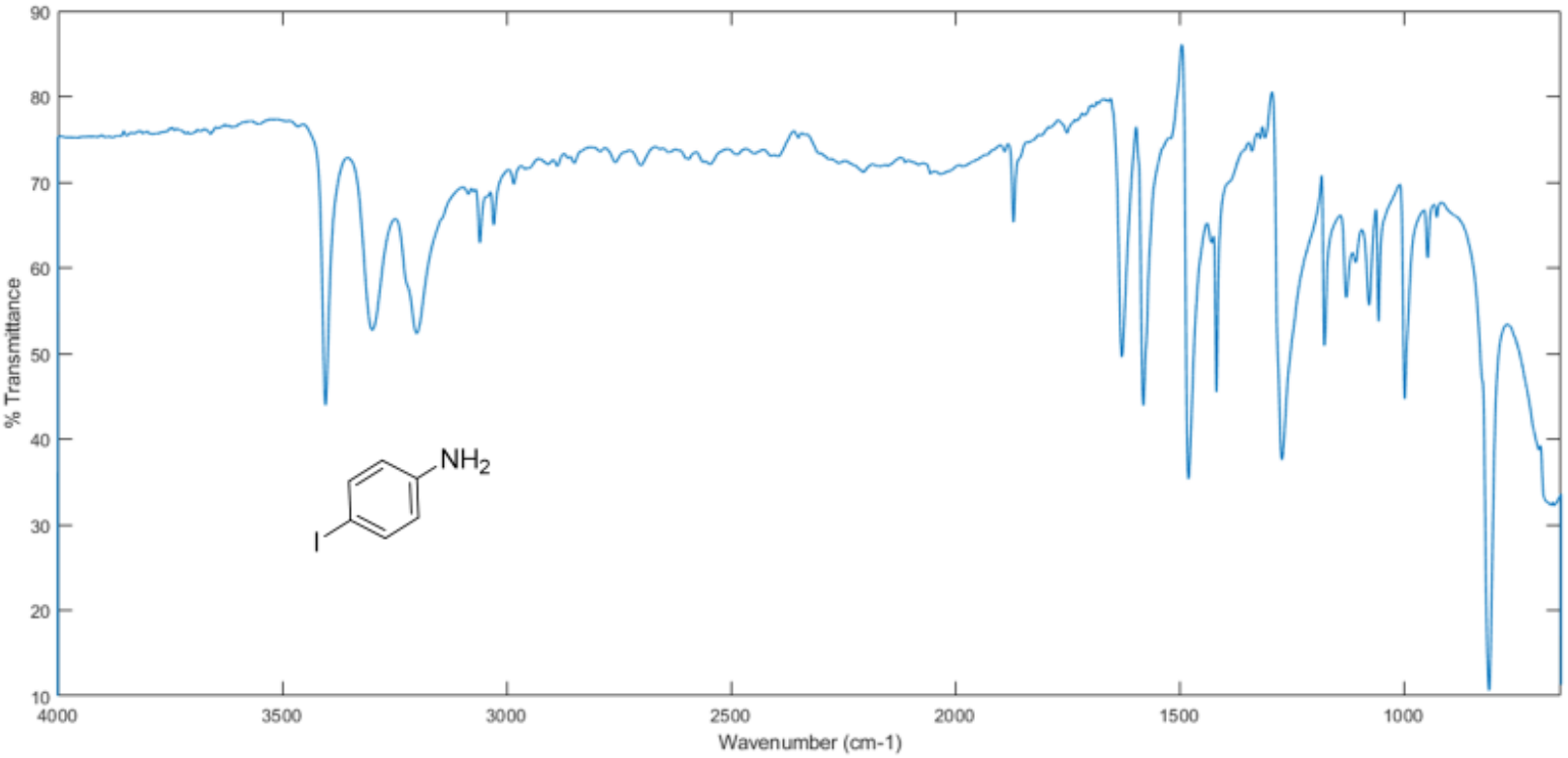

Figure A88: ATR-IR spectrum of 4-iodoanaline

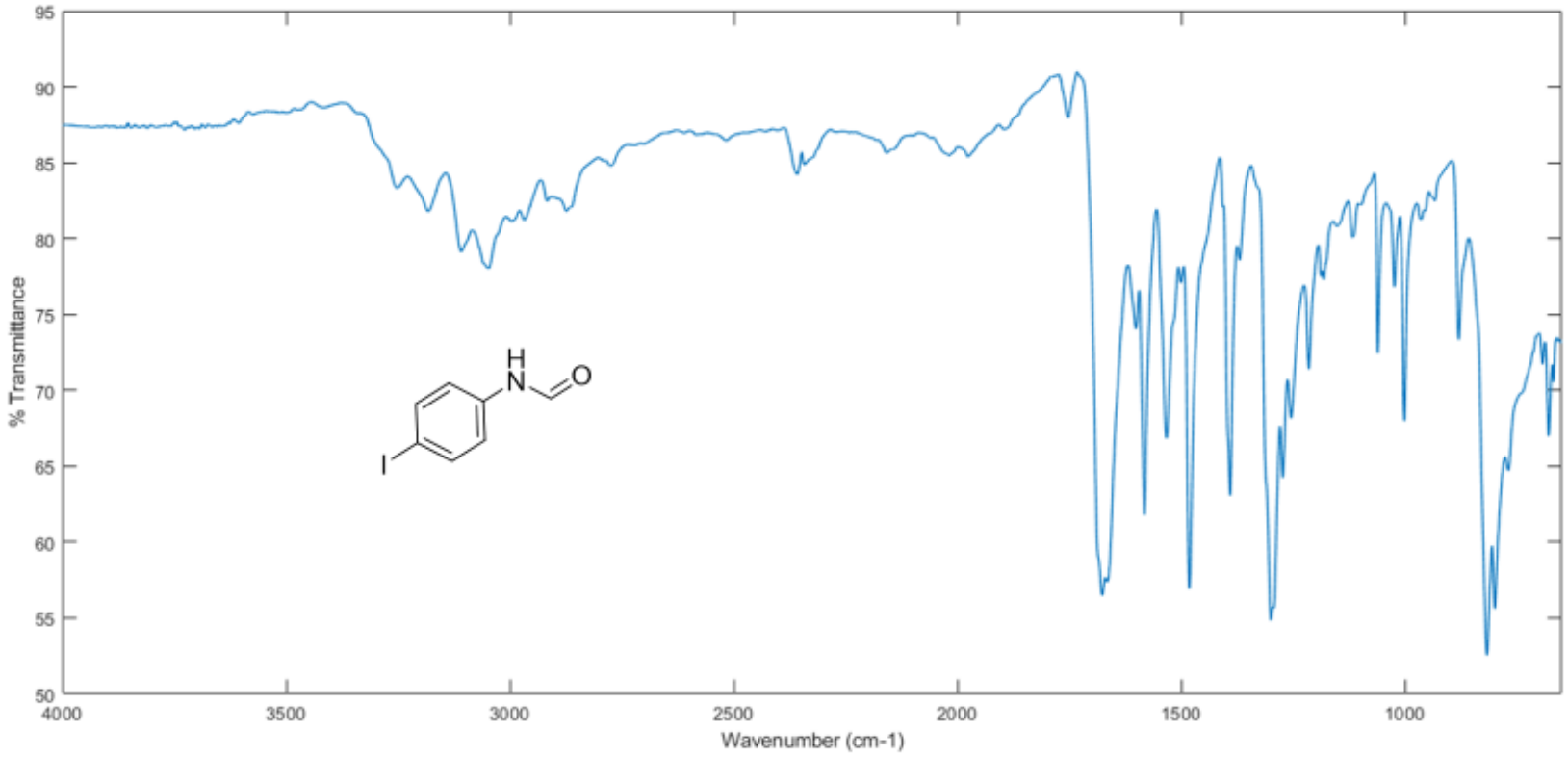

Figure A89: ATR-IR spectrum of N-(4-iodophenyl)-formamide

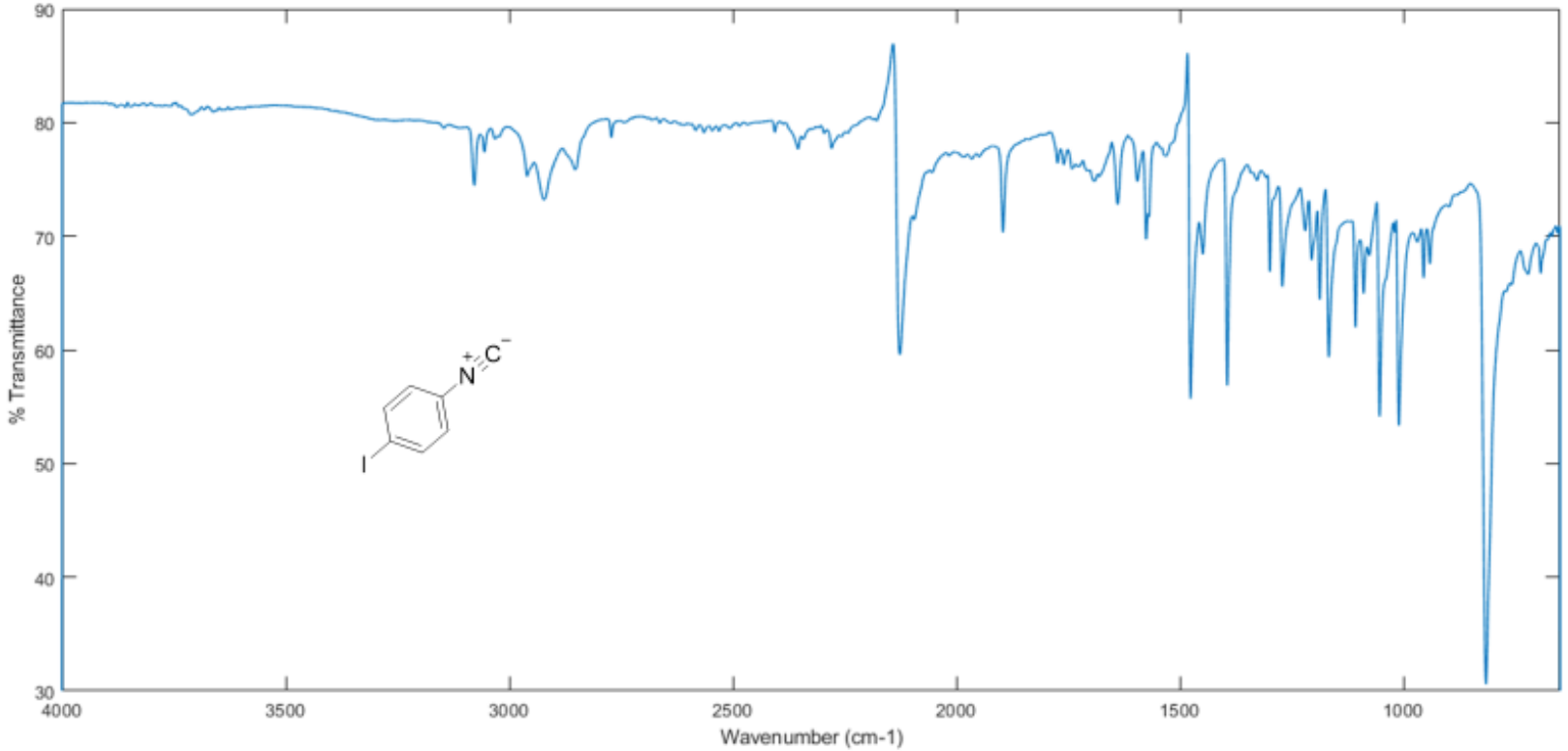

Figure A90: ATR-IR spectrum of 4-iodophenyl isocyanide

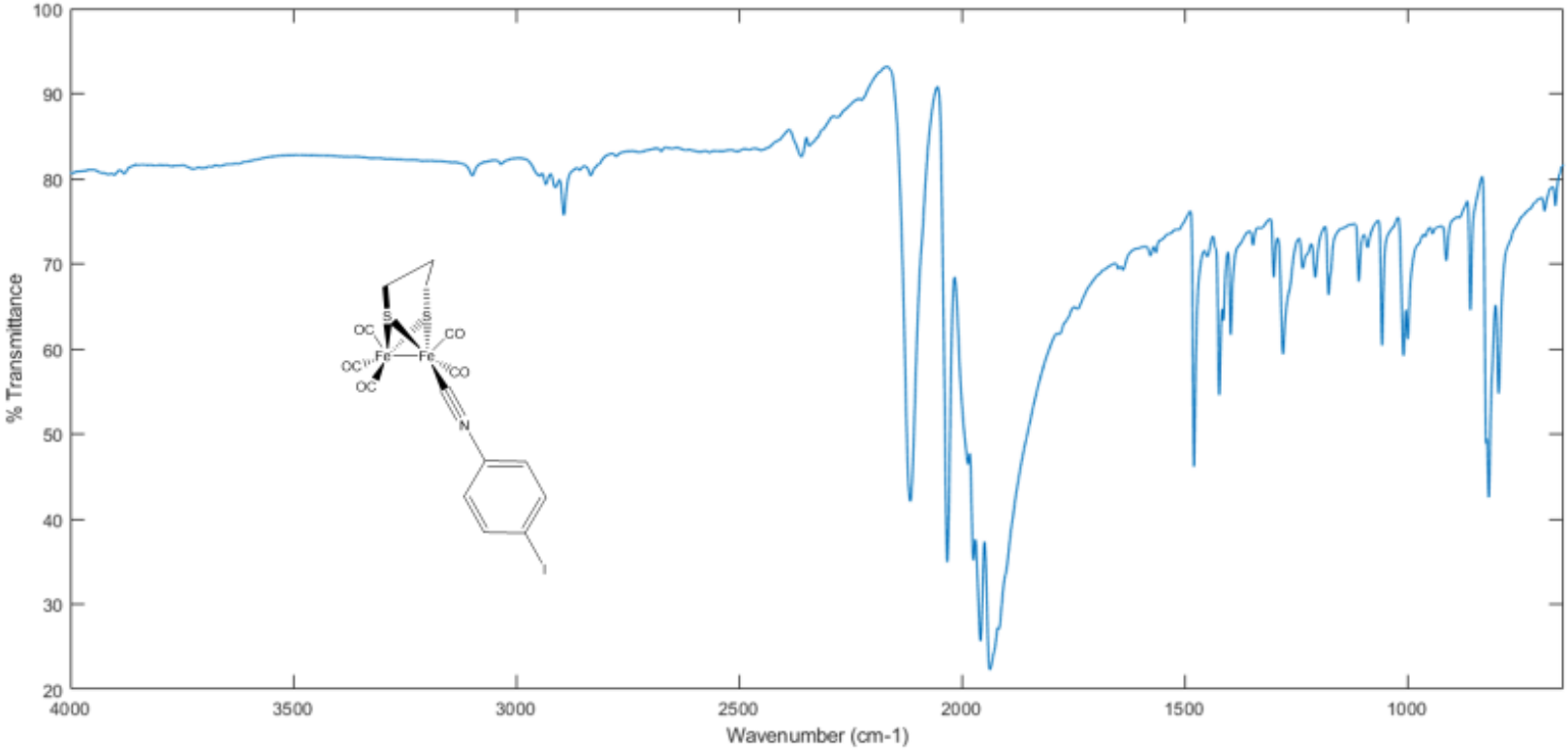

Figure A91: ATR-IR spectrum of (μ-propanedithiolato)diiron 4-iodopheynylisocyano pentacarbonyl

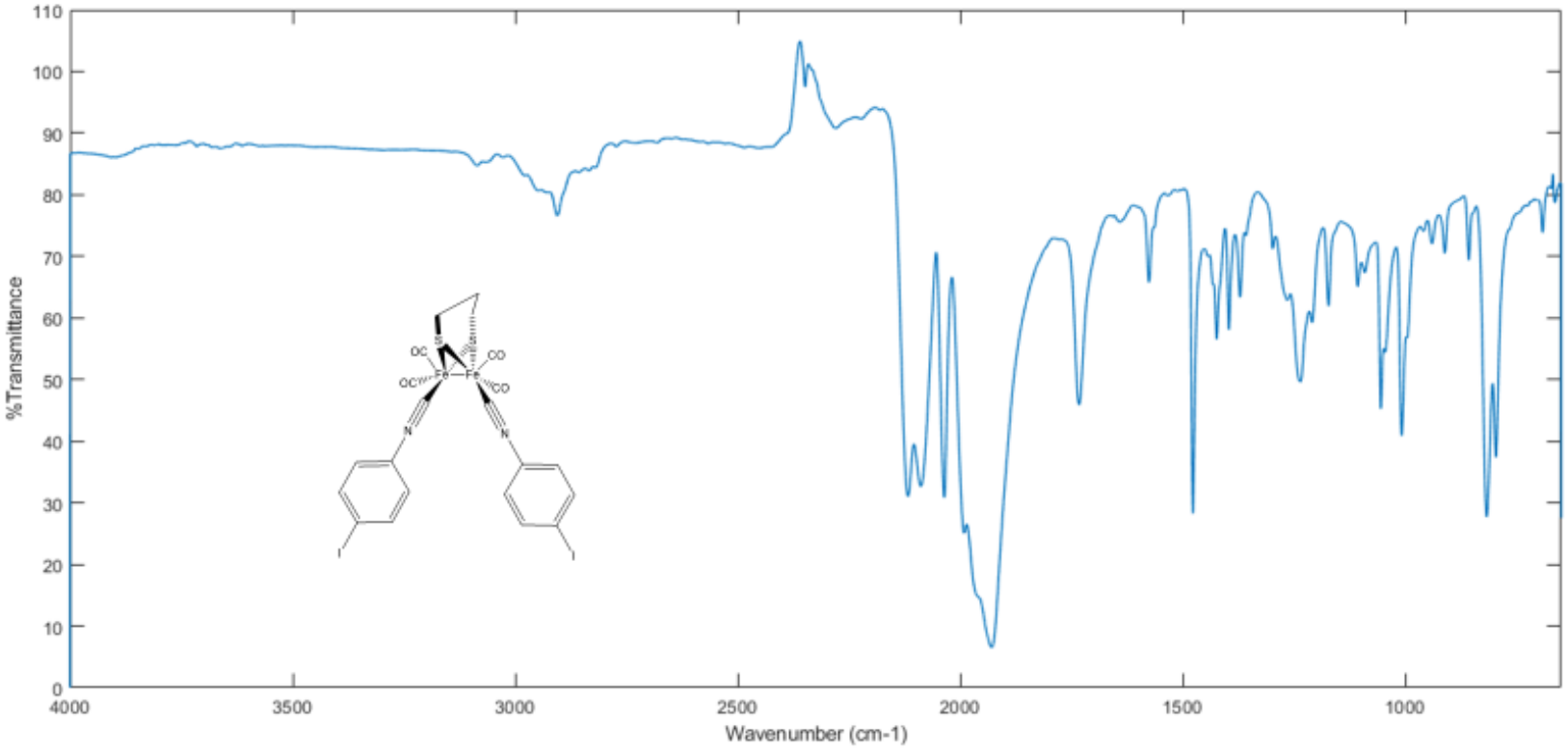

Figure A92: ATR-IR spectrum of (μ-propanedithiolato)diiron di(4-iodopheynylisocyano) tetracarbonyl

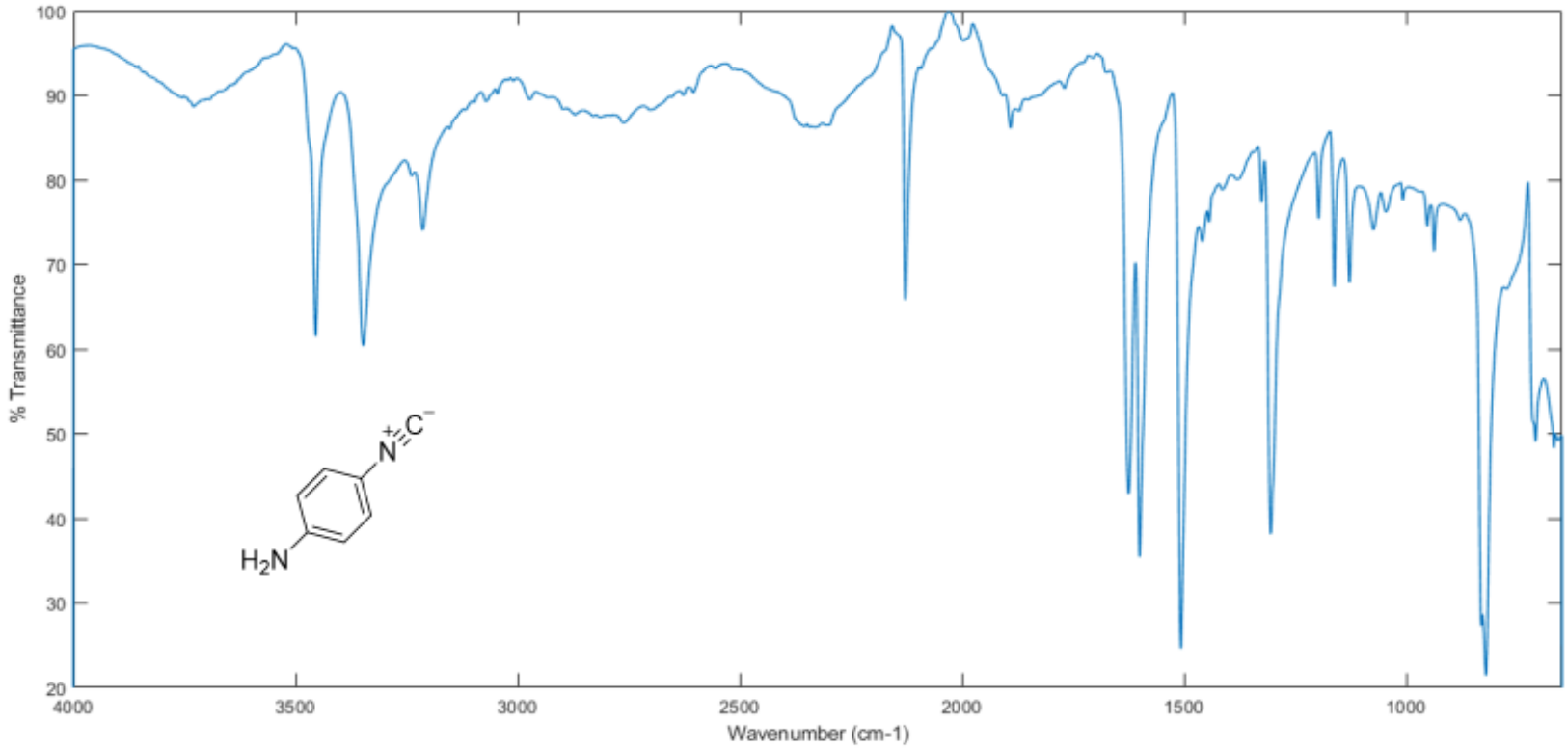

Figure A93: ATR-IR spectrum of 4-Aminophenylisocyanide

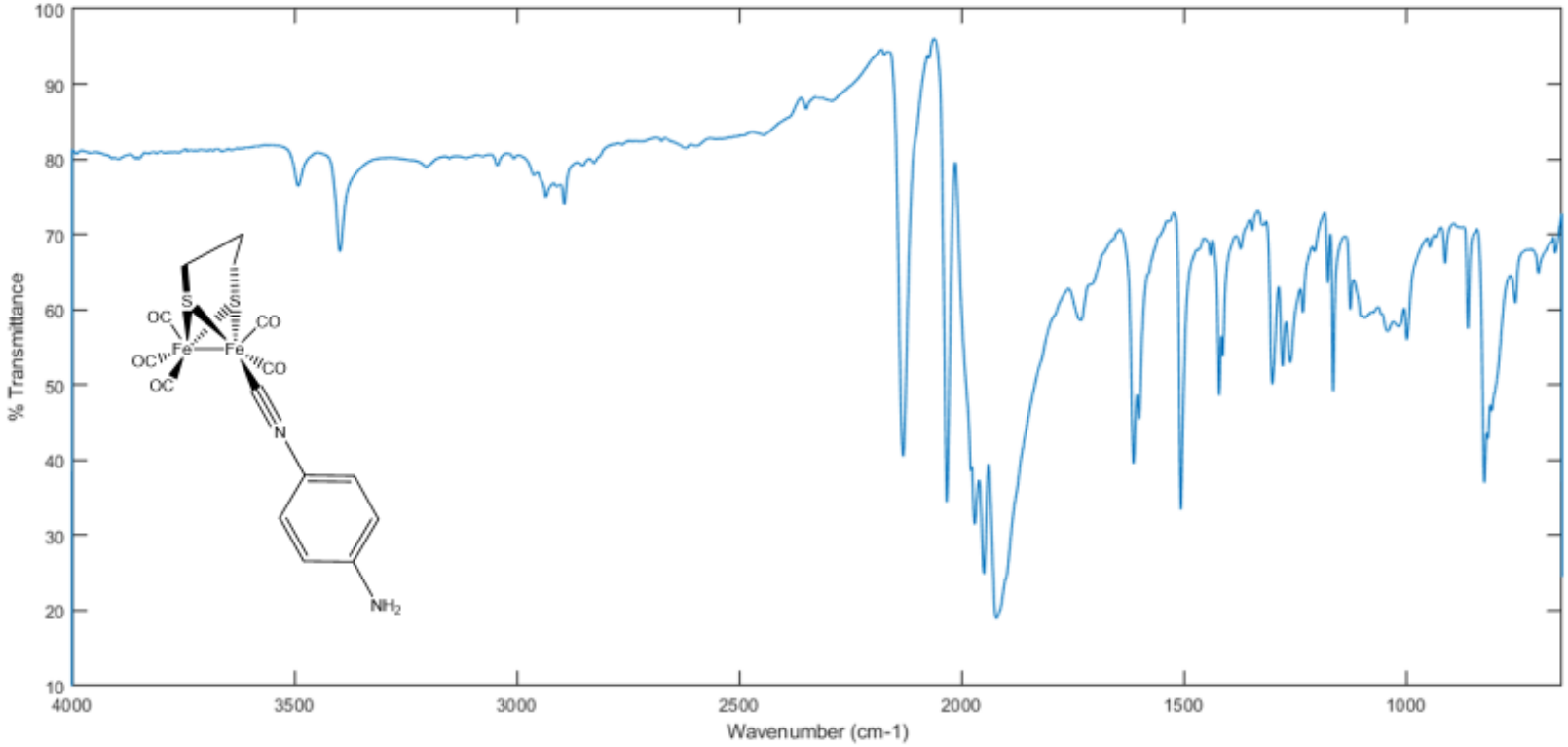

Figure A94: ATR-IR spectrum of (μ-propanedithiolato)diiron 4-aminopheynylisocyano pentacarbonyl

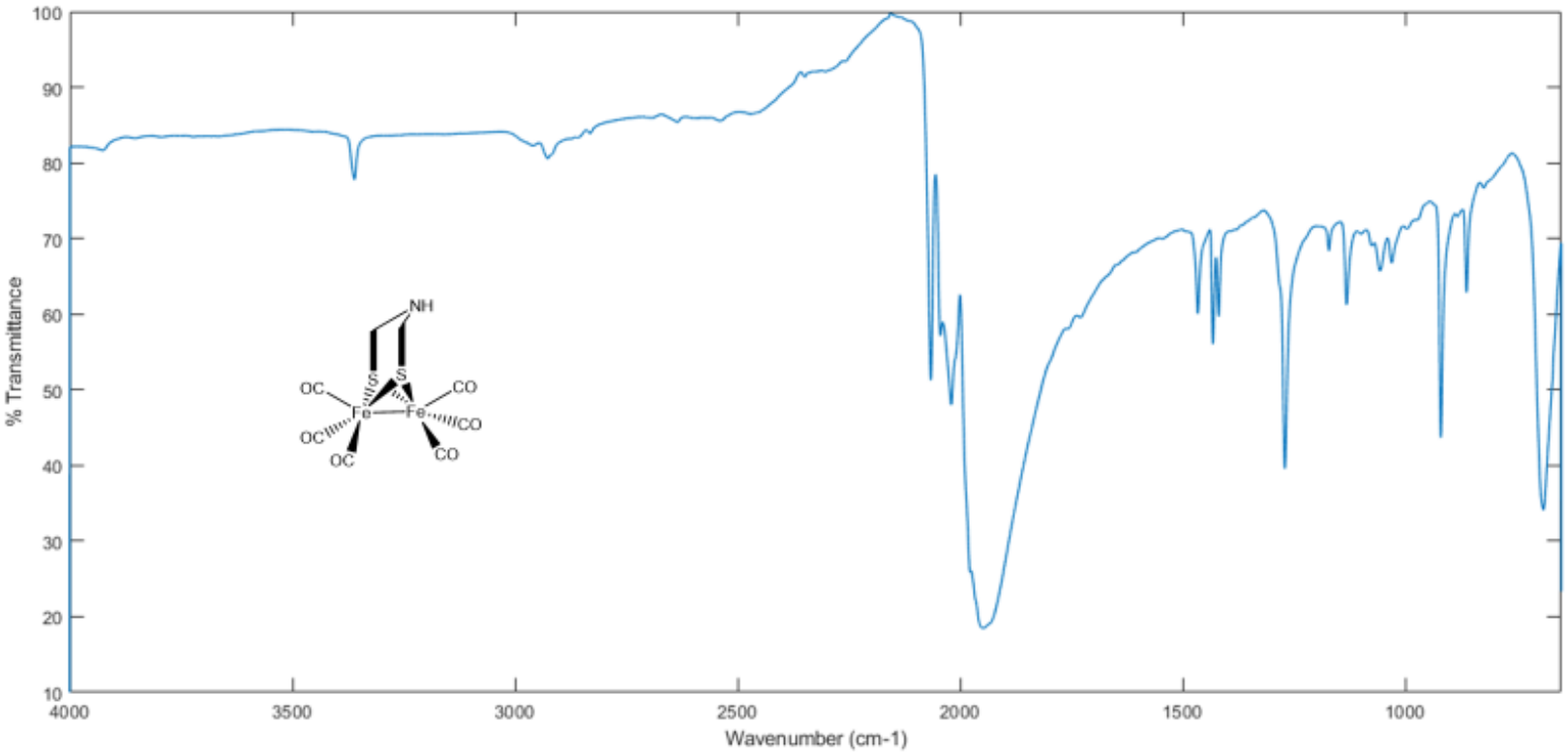

Figure A95: ATR-IR spectrum of (μ-azadithiolato)diiron(I) hexacarbonyl

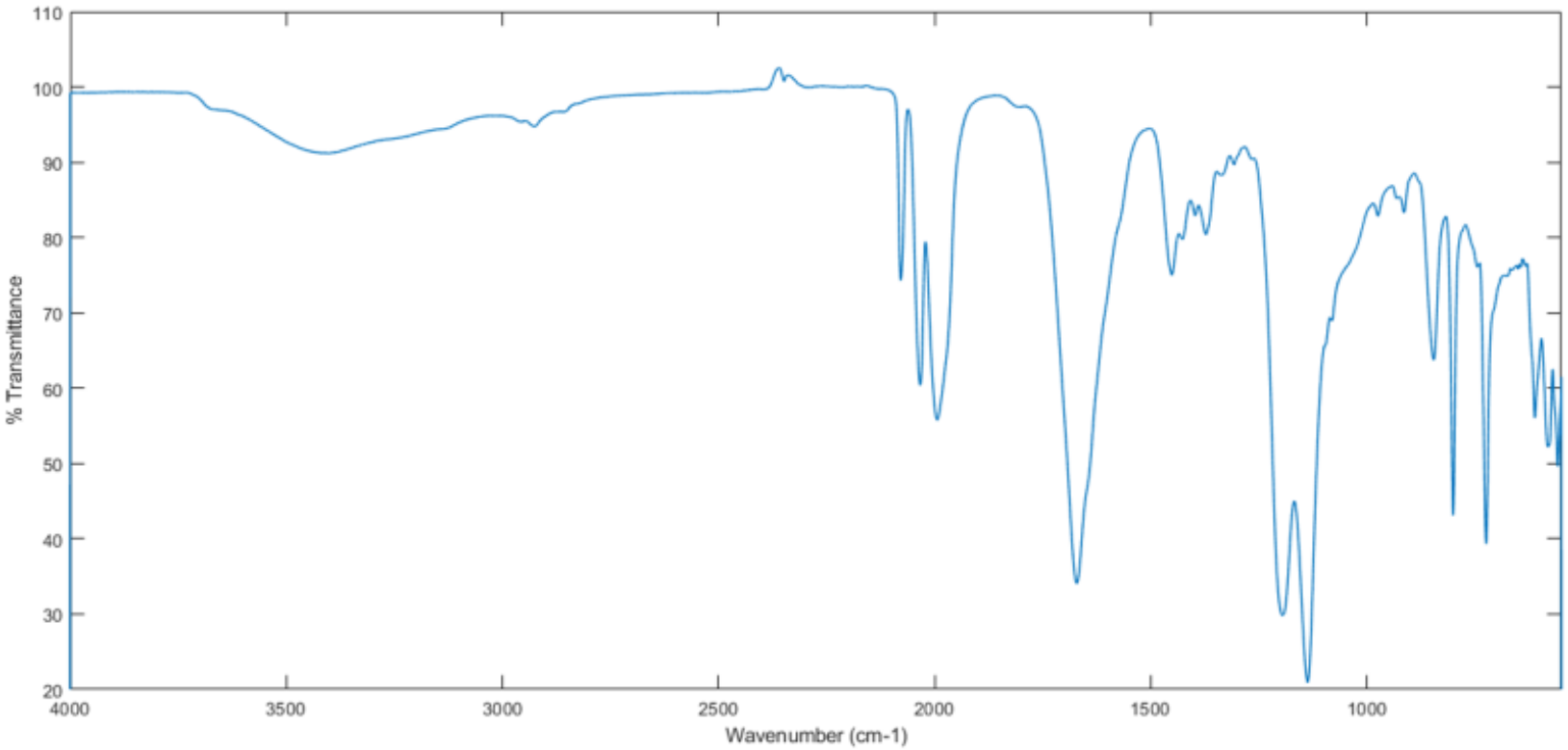

Figure A96: ATR-IR spectra of recrystallized fraction 3 of (μ-glycineazadithiolato)diiron(I) hexacarbonyl reaction

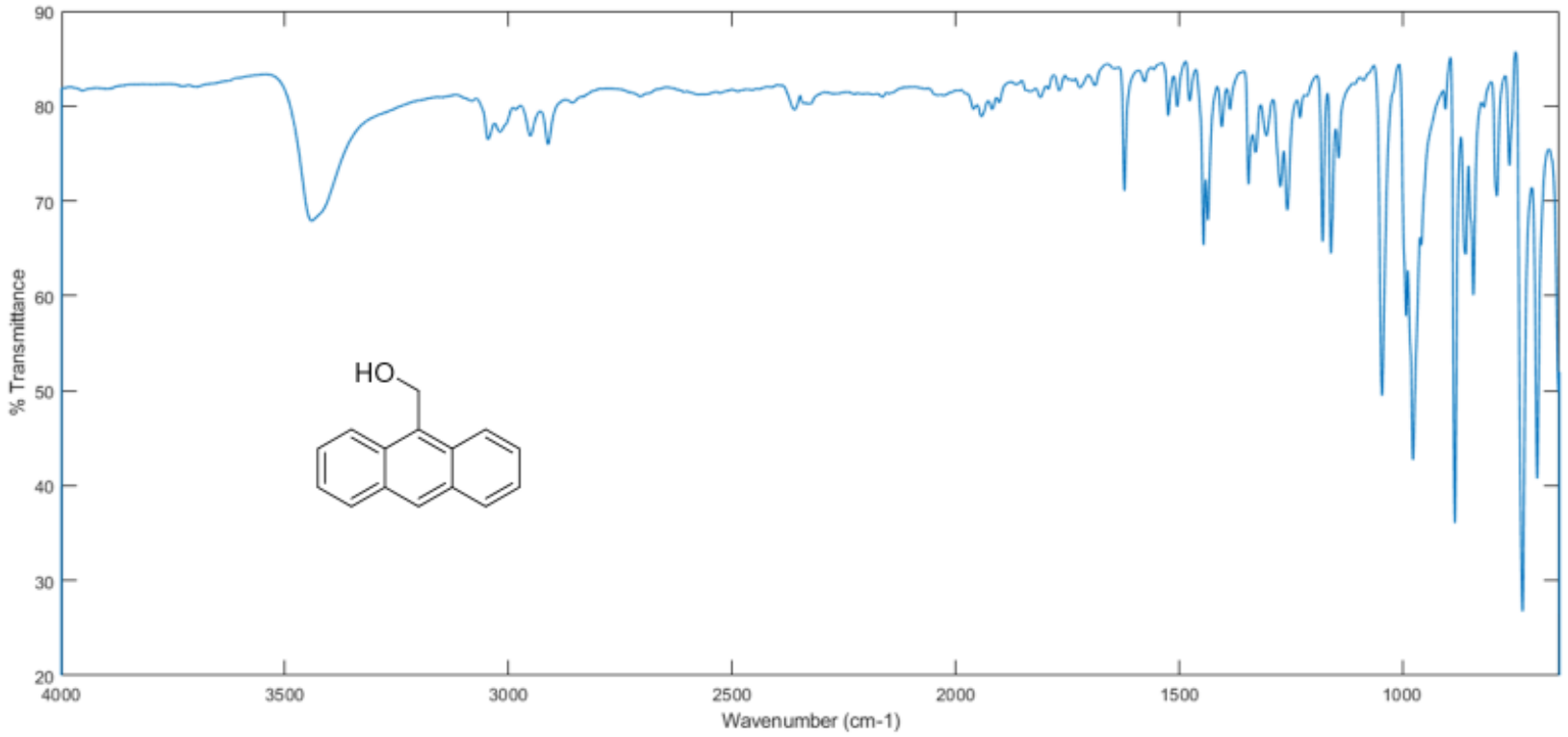

Figure A97: ATR-IR spectrum of 9-anthracene methanol

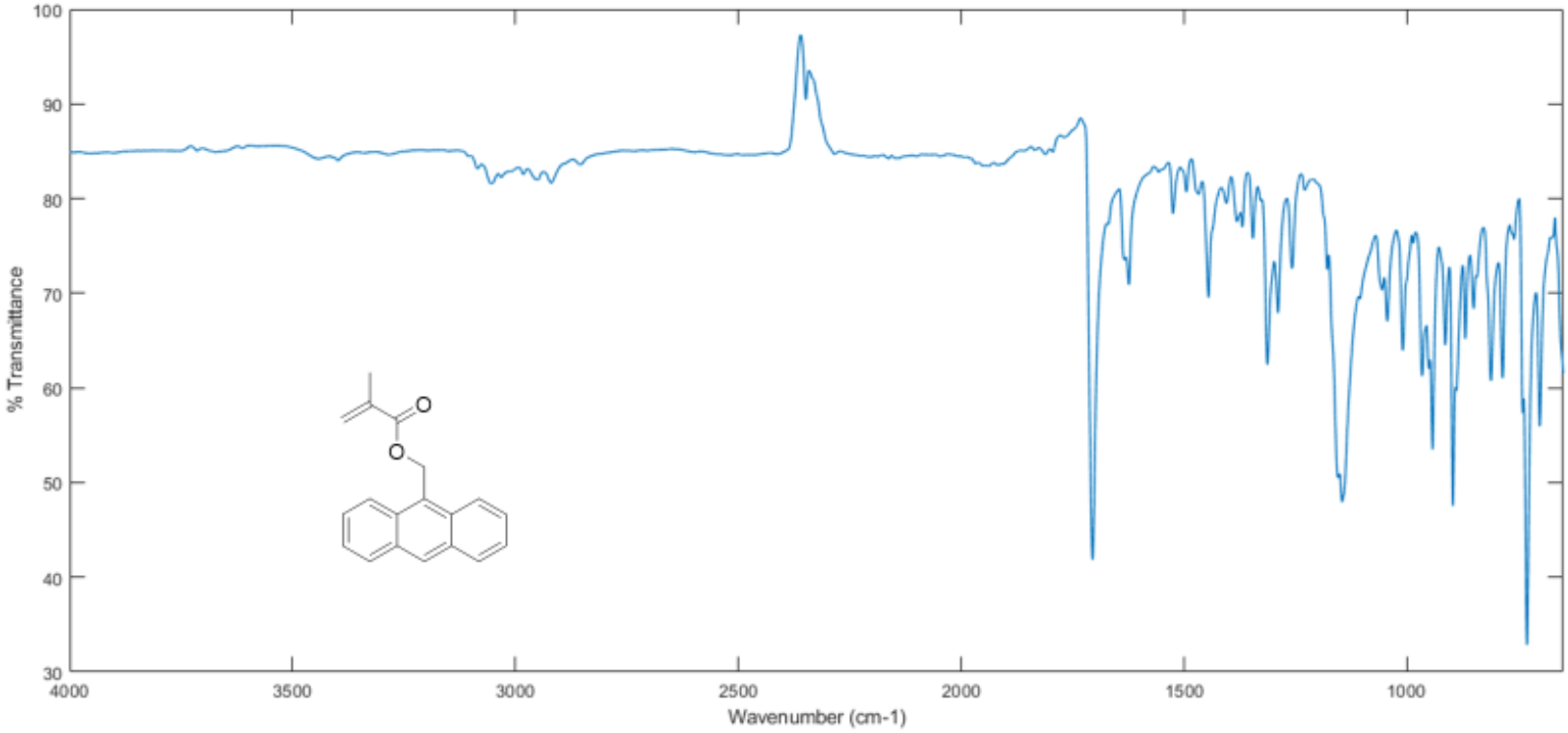

Figure A98: ATR-IR spectrum of 9-anthracynlmethyl methacrylate

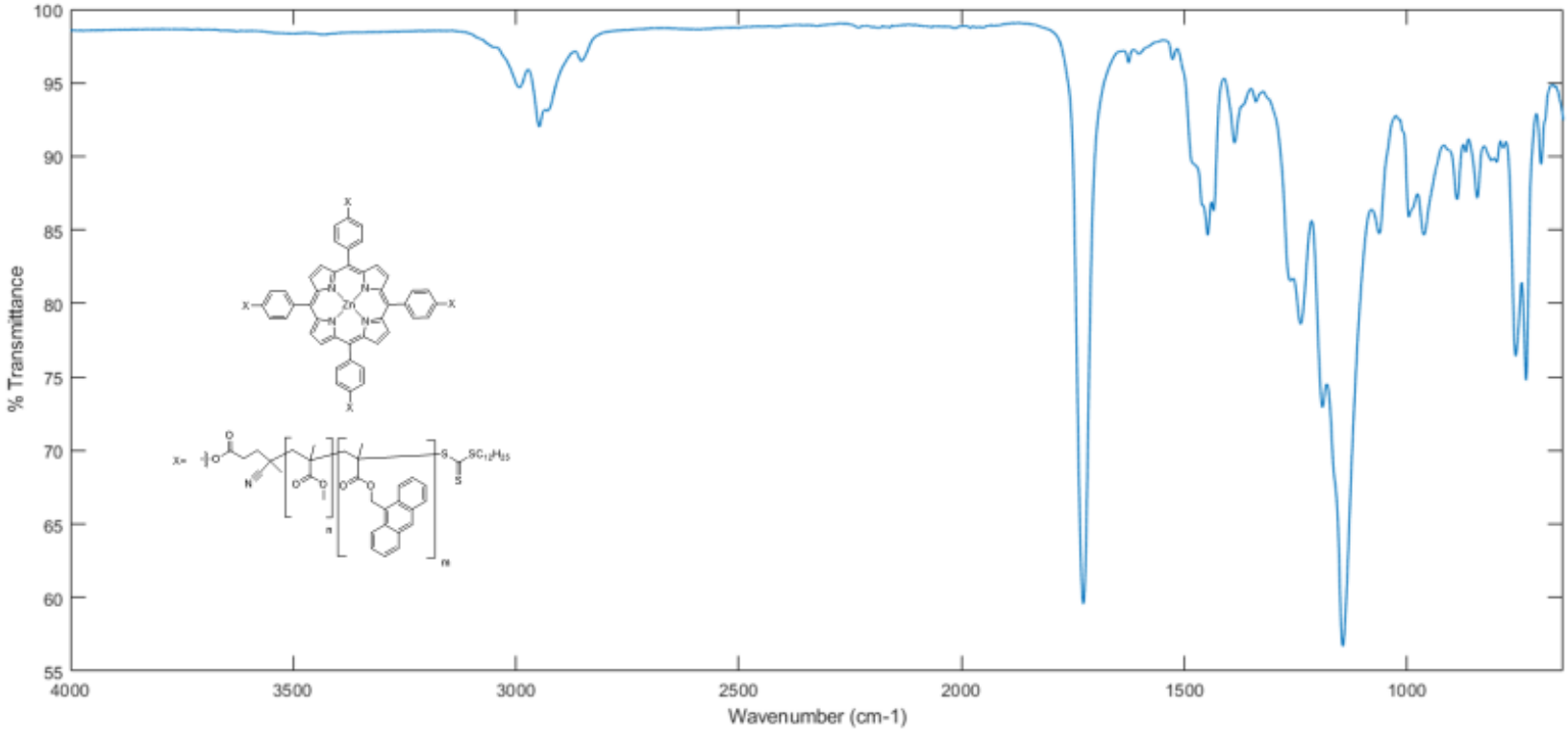

Figure A99: ATR-IR spectrum of Zn^{II}(Por(MMA-co-AMMA)$_4$)

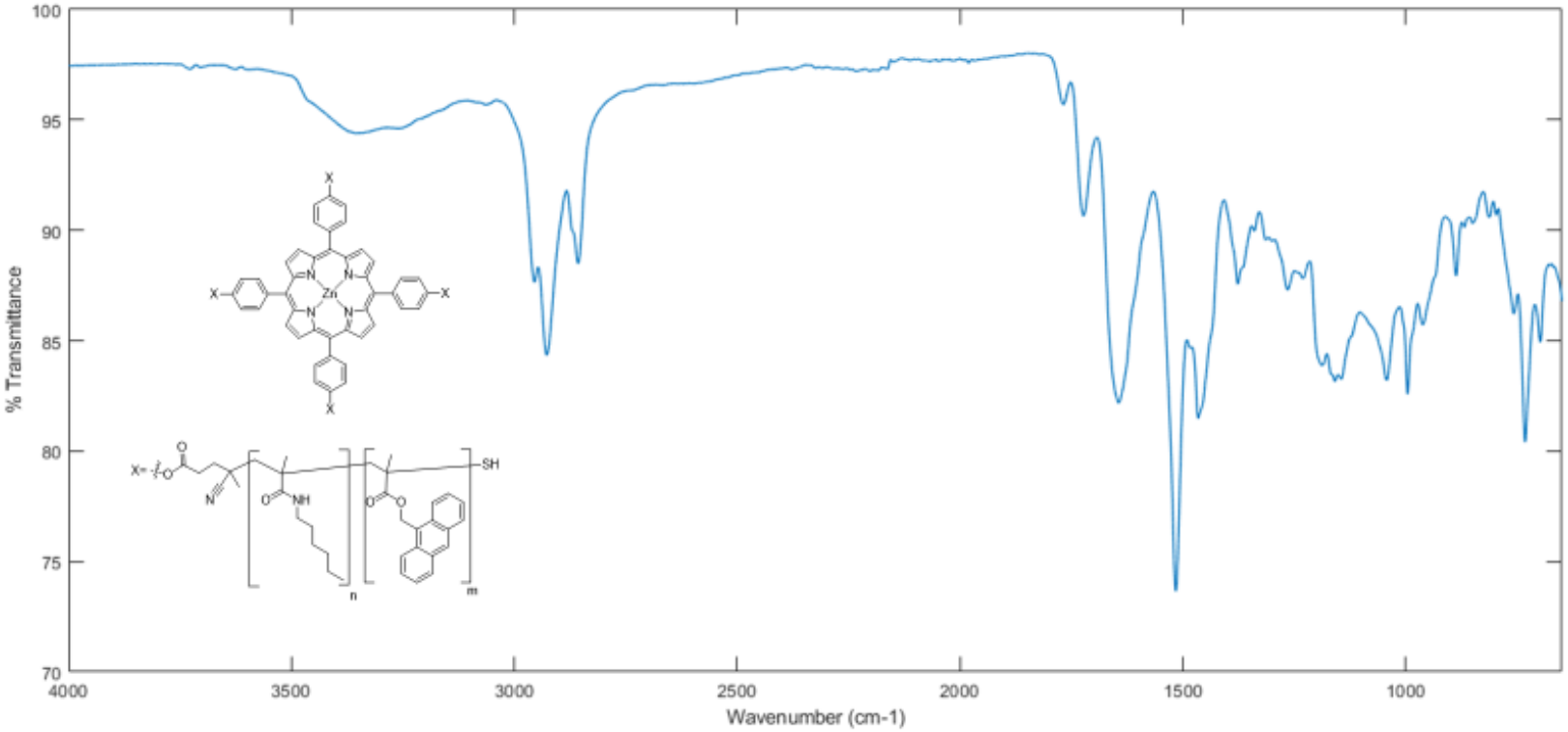

Figure A100: ATR-IR spectrum of Zn^{II}(Por(HexMAAm-co-AMMA)$_4$)

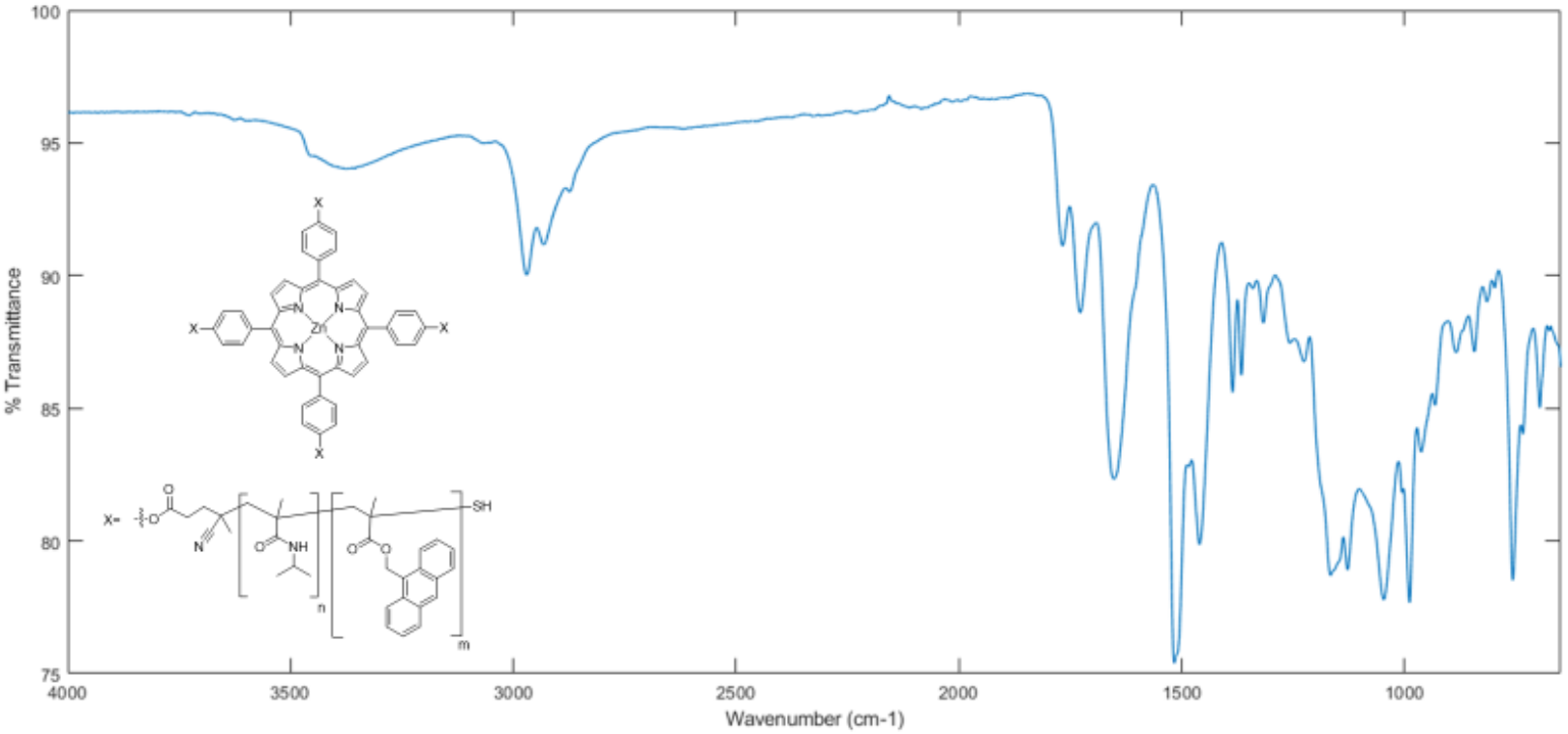

Figure A101: ATR-IR spectrum of Zn^{II}(Por(iPMAAm-co-AMMA)$_4$)

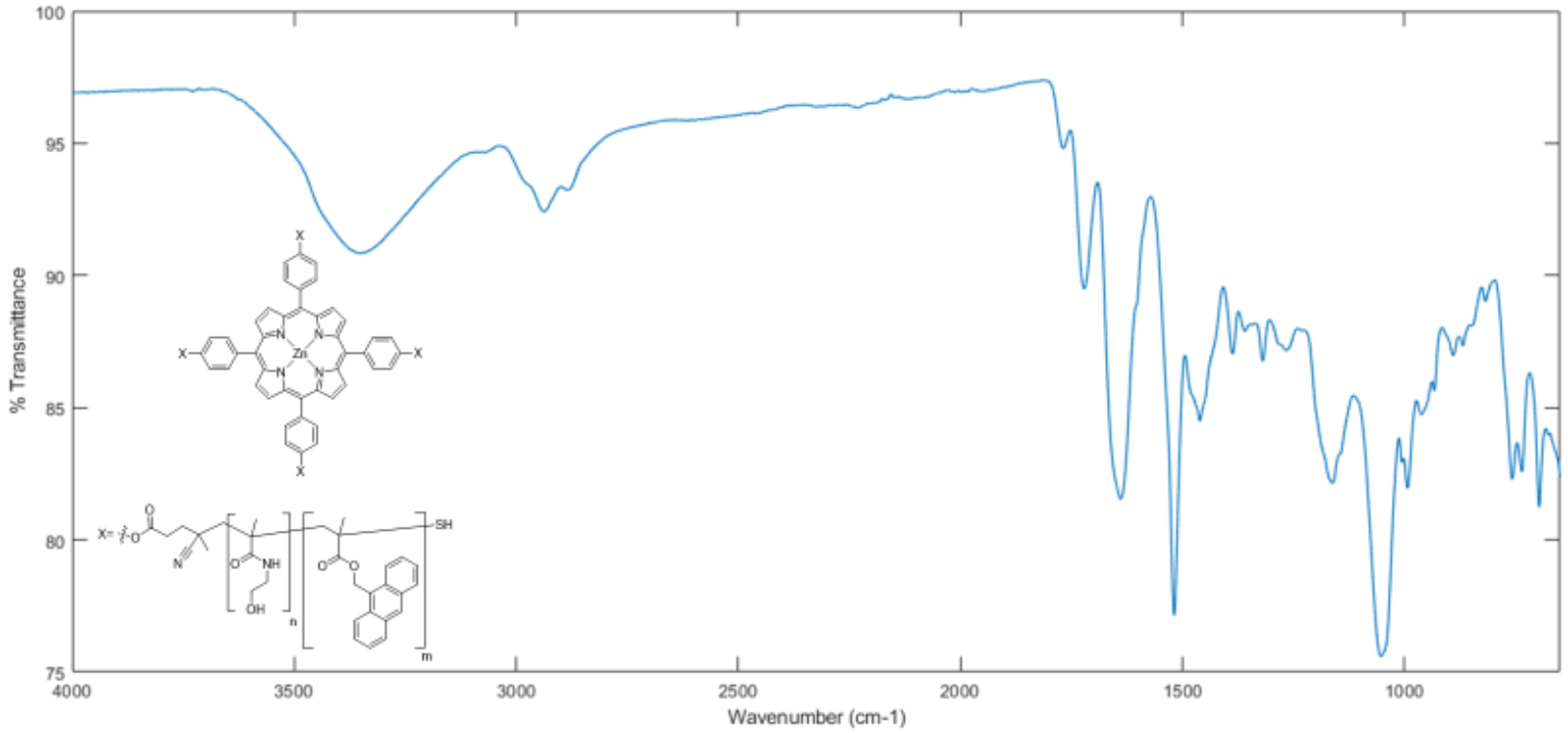

Figure A102: ATR-IR of Zn^{II}(Por(HEMA-co-AMMA)$_4$)

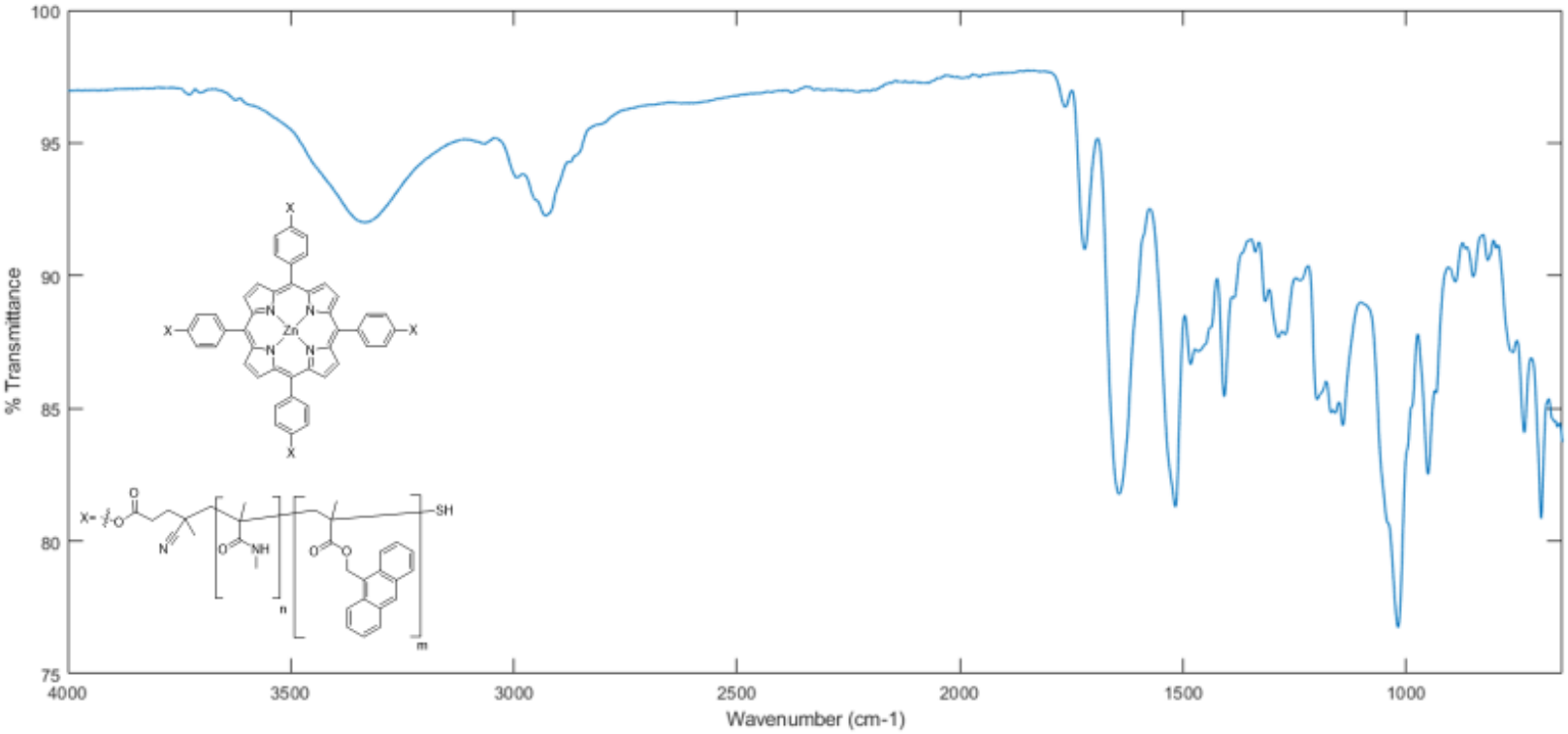

Figure A103: ATR-IR spectrum of Zn^{II}(Por(MMAAm-co-AMMA)$_4$)

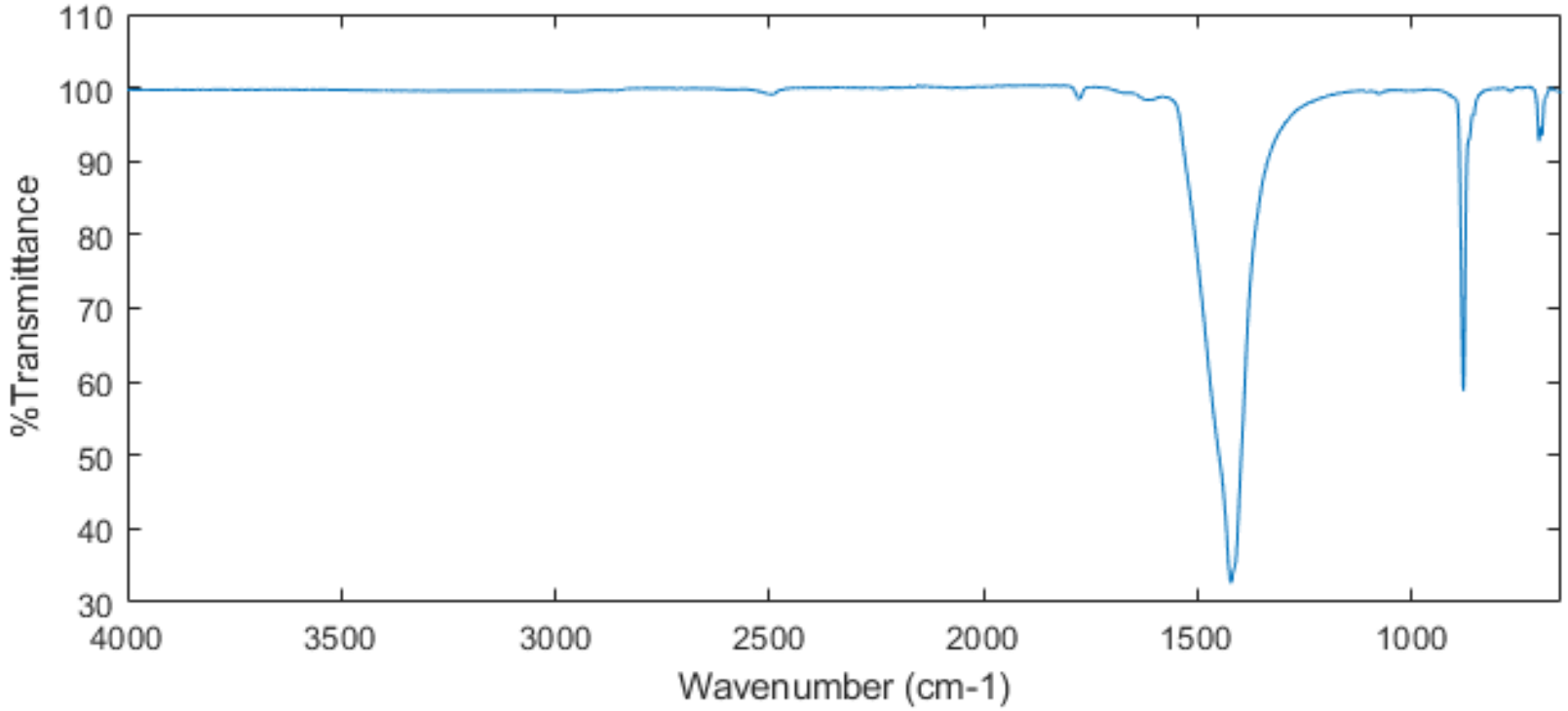

Figure A104: ATR-IR spectrum of white precipitates from reaction of Zn^{II}(Por(HexMAAm -co-AMMA)$_4$), NaCN, and DMF under ambient conditions

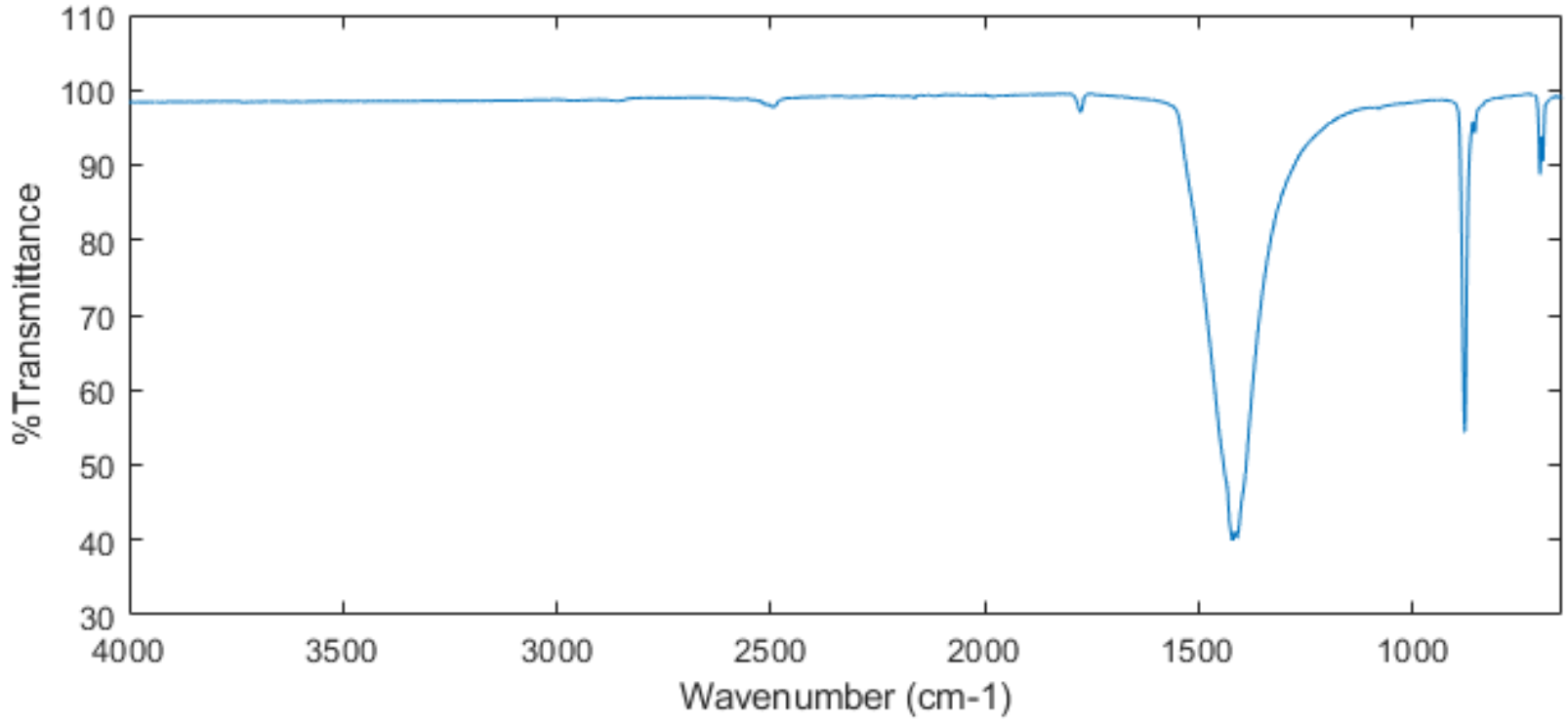

Figure A105: ATR-IR spectrum of Sodium Carbonate, 98% purity from Alfa Aesar

APPENDIX E: SEC Traces

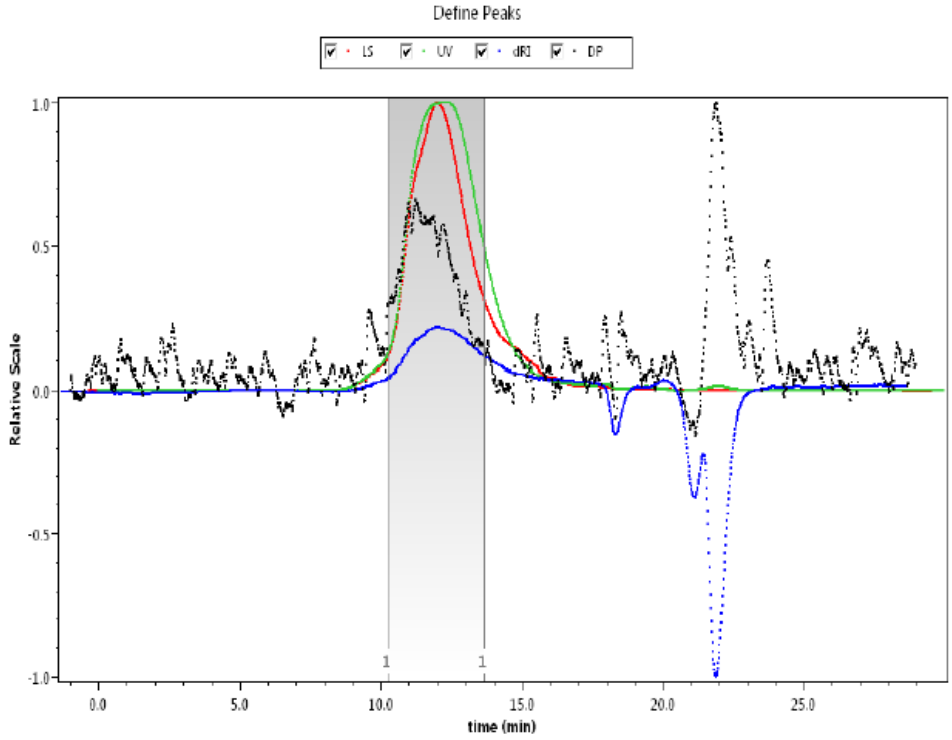

Figure A106: SEC traces of Por(PFPMA-co-AMMA)$_4$ [$M_{n,H\text{-}NMR}$ = 51.2 kDa, 16 % AMMA incorporation]

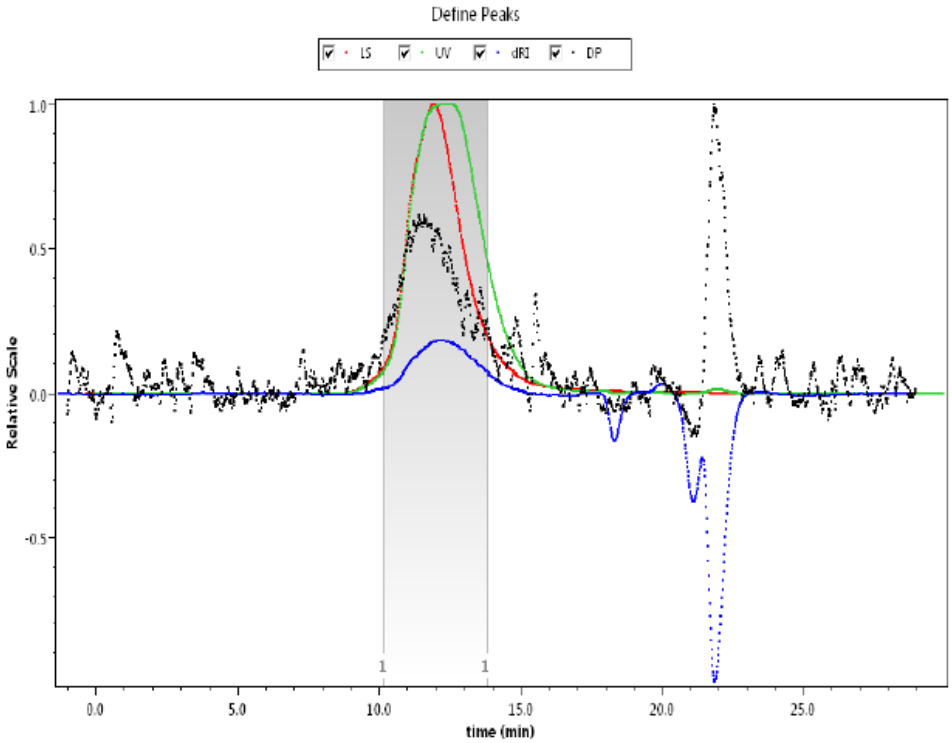

Figure A107: SEC traces of Zn^{II}(Por(PFPMA-co-AMMA)$_4$ [$M_{n,H\text{-}NMR}$ = 51.2 kDa, 16 % AMMA incorporation]

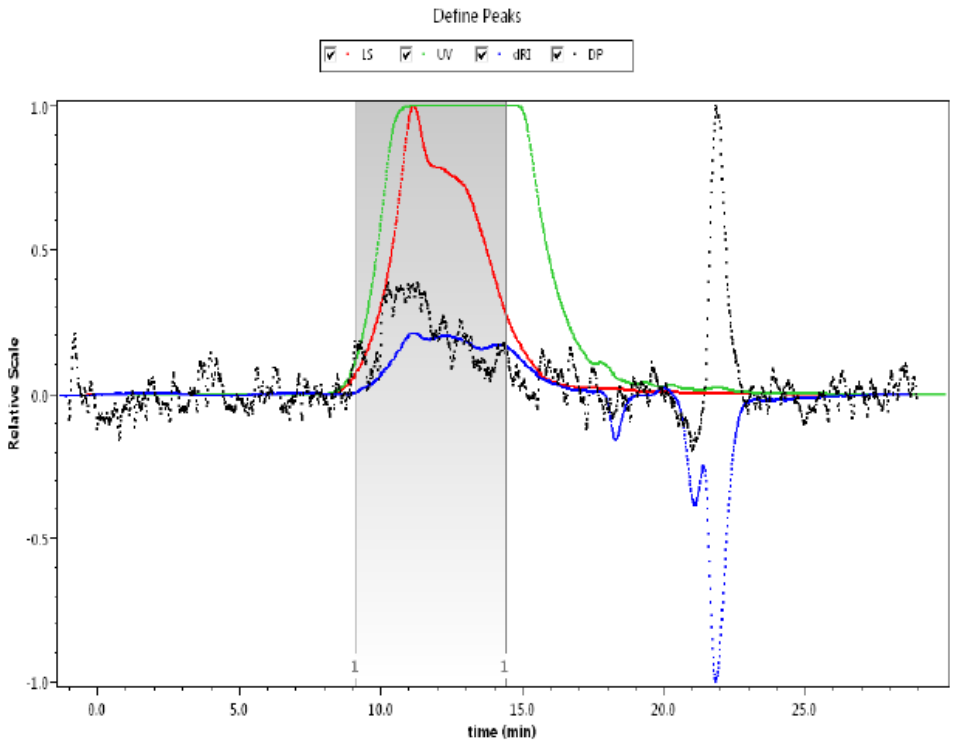

Figure A108: SEC traces of Por(MMA-co-AMMA)$_4$ [$M_{n,H\text{-}NMR}$ = 18.5 kDa, 31 % AMMA incorporation]

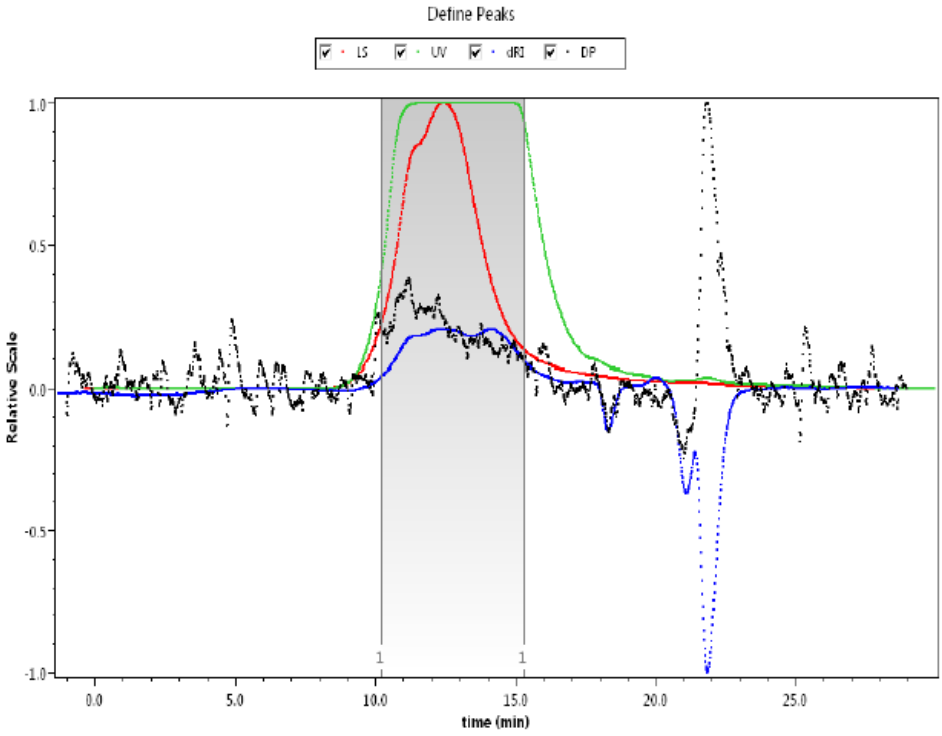

Figure A109: SEC traces of Zn^{II}(Por(MMA-co-AMMA)$_4$ [$M_{n,H\text{-}NMR}$ = 18.5 kDa, 31 % AMMA incorporation]

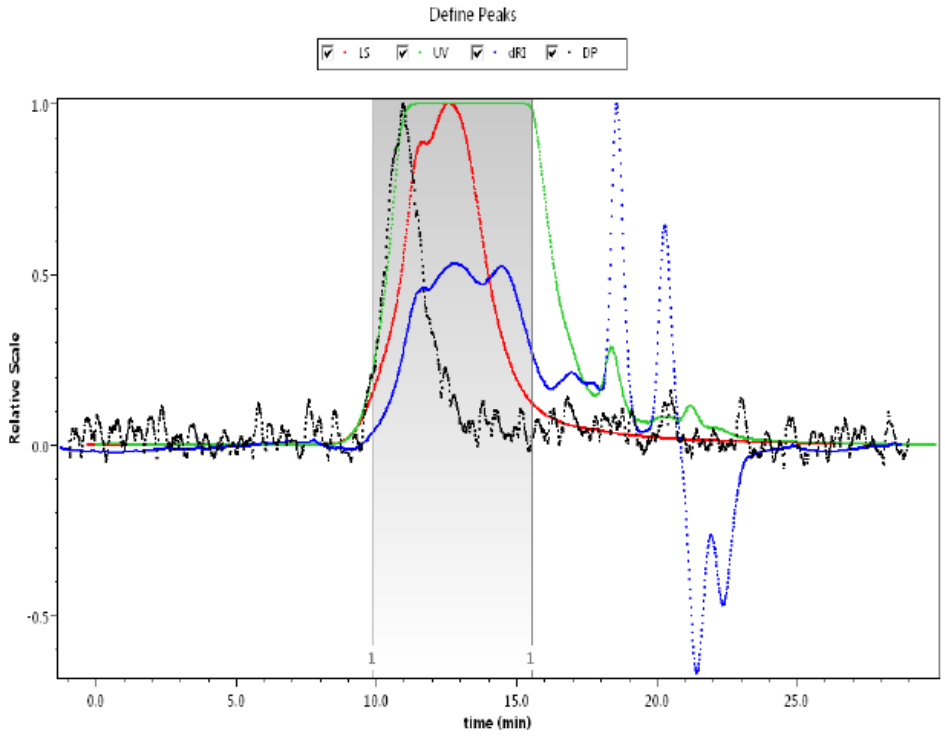

Figure A110: SEC traces of Zn^{II}(Por(MMA-co-AMMA)$_4$-NP [$M_{n,H\text{-}NMR}$ = 18.5 kDa, 31 % AMMA incorporation]

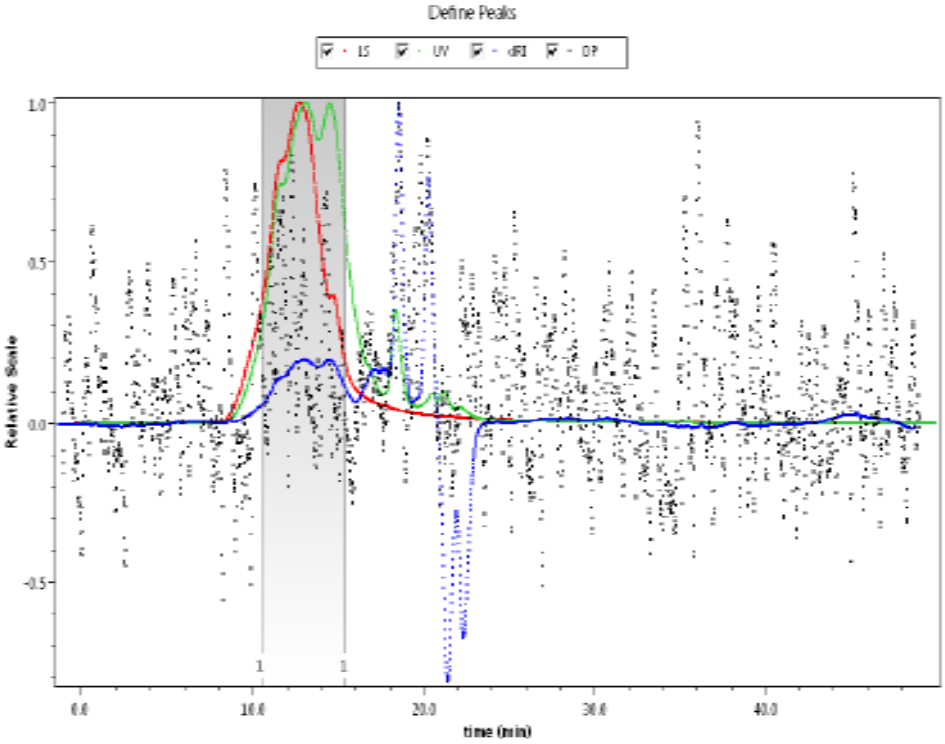

Figure A111: SEC traces of Zn^{II}(Por(MMA-co-AMMA)$_4$-NP [$M_{n,H\text{-}NMR}$ = 18.5 kDa, 31 % AMMA incorporation]

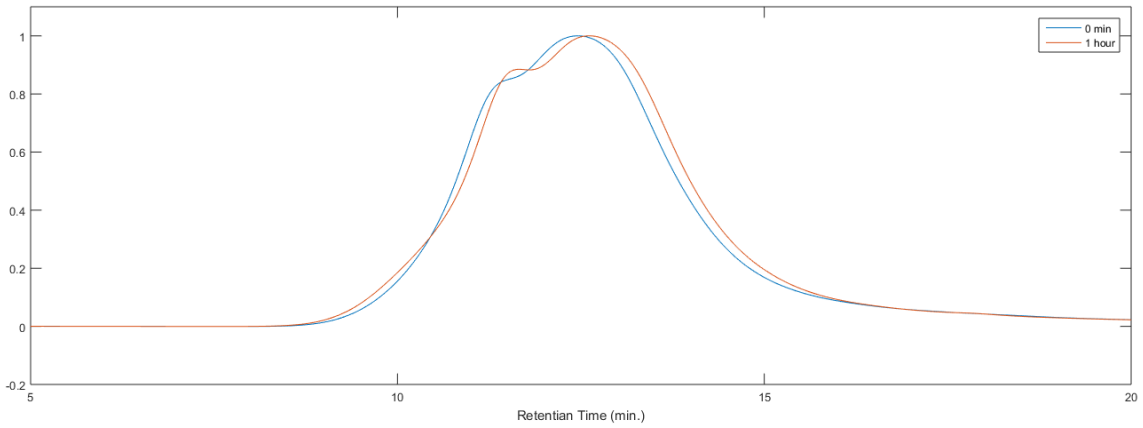

Figure A112: SEC traces (MALS detector) of Zn^{II}(Por(MMA-co-AMMA)$_4$ before (blue) and after exposure to 350 nm light for 1 hour (red) [$M_{n,H\text{-}NMR}$ = 18.5 kDa, 31 % AMMA incorporation]

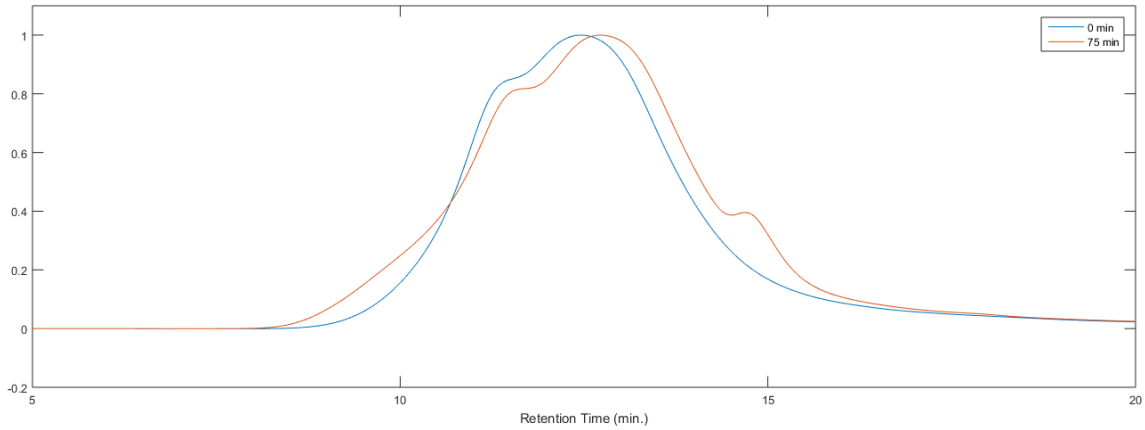

Figure A113: SEC traces (MALS detector) of Zn^{II}(Por(MMA-co-AMMA)$_4$ before (blue) and after exposure to 350 nm light for 1.25 hours (red) [$M_{n,H\text{-}NMR}$ = 18.5 kDa, 31 % AMMA incorporation]

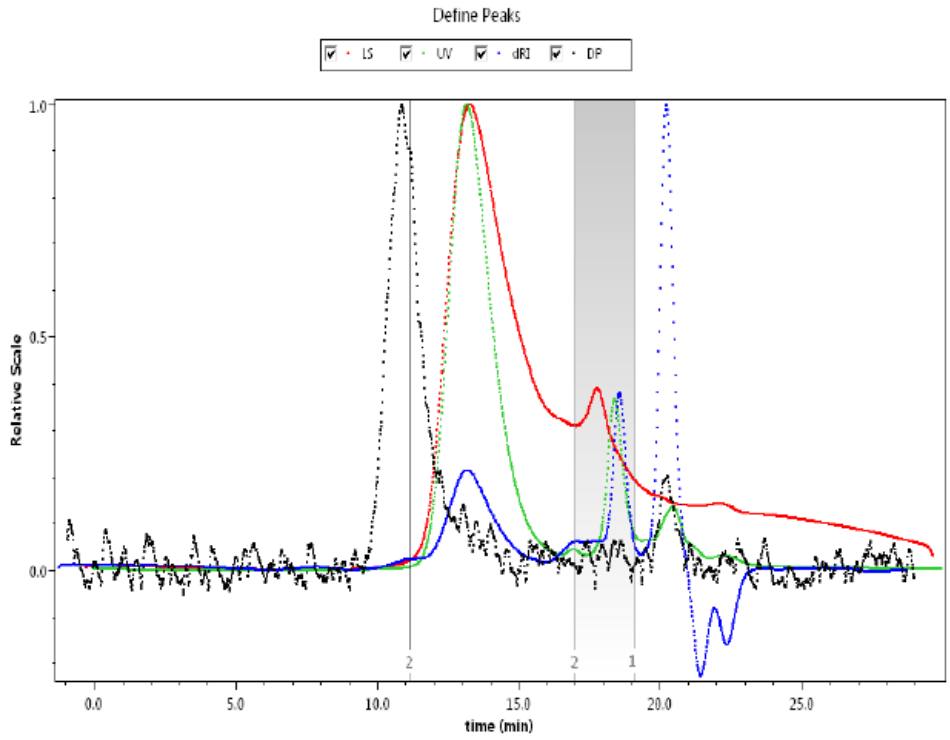

Figure A114: SEC traces of Zn^{II}(Por(HMA-co-AMMA)$_4$ -NP [$M_{n,estimated}$ = 14.4 kDa, 16 % AMMA incorporation]

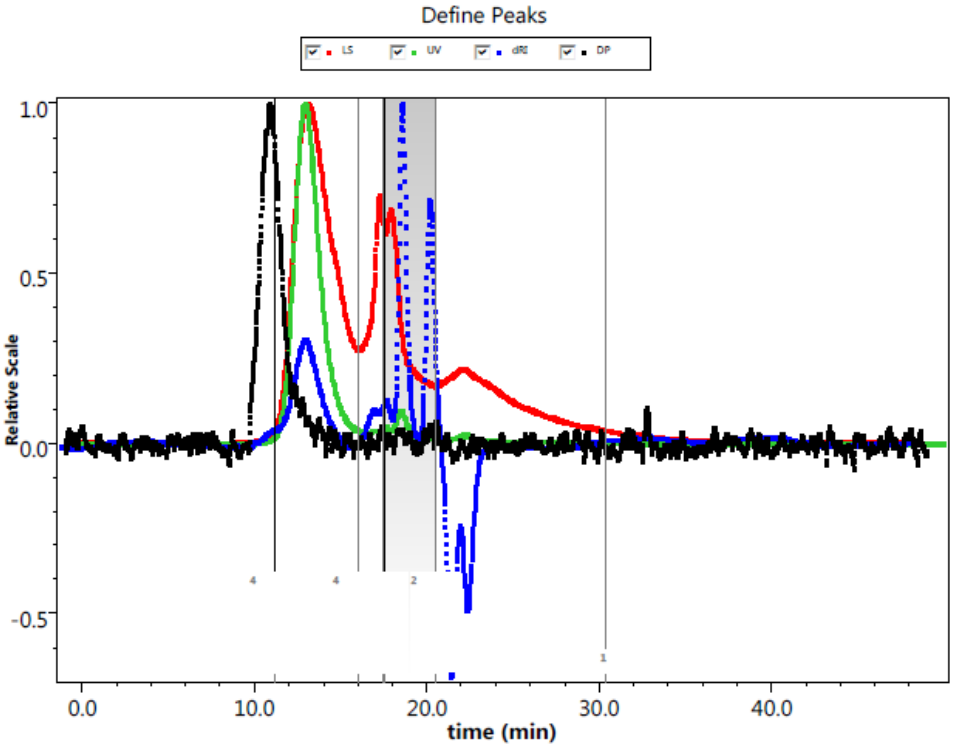

Figure A115: SEC traces of Zn^{II}(Por(HMA-co-AMMA)$_4$-NP [$M_{n,estimated}$ = 14.4 kDa, 16 % AMMA incorporation]

APPENDIX G: UV-Vis Absorbance Spectra

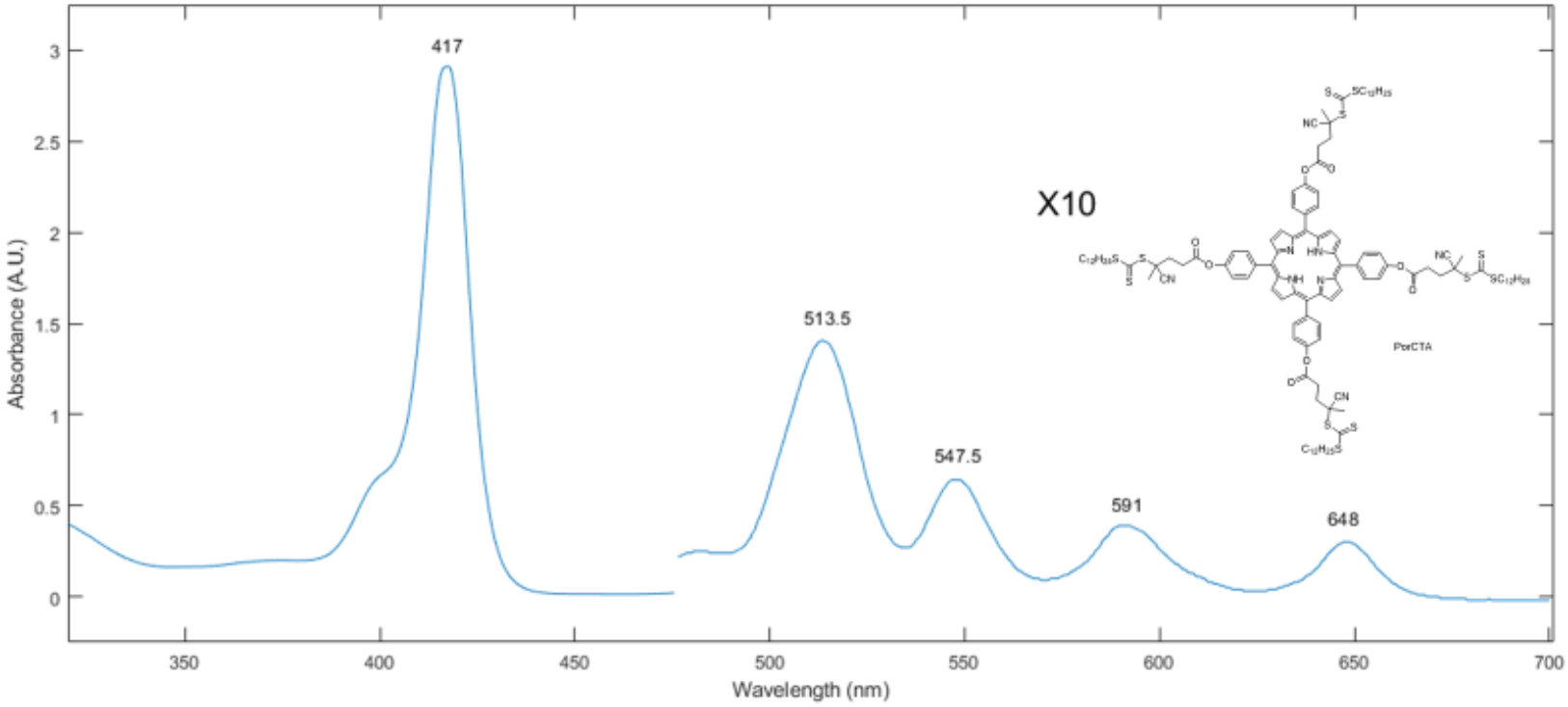

Figure A116: UV-Vis absorbance spectra of PorCTA at 0.02 mg/mL in THF

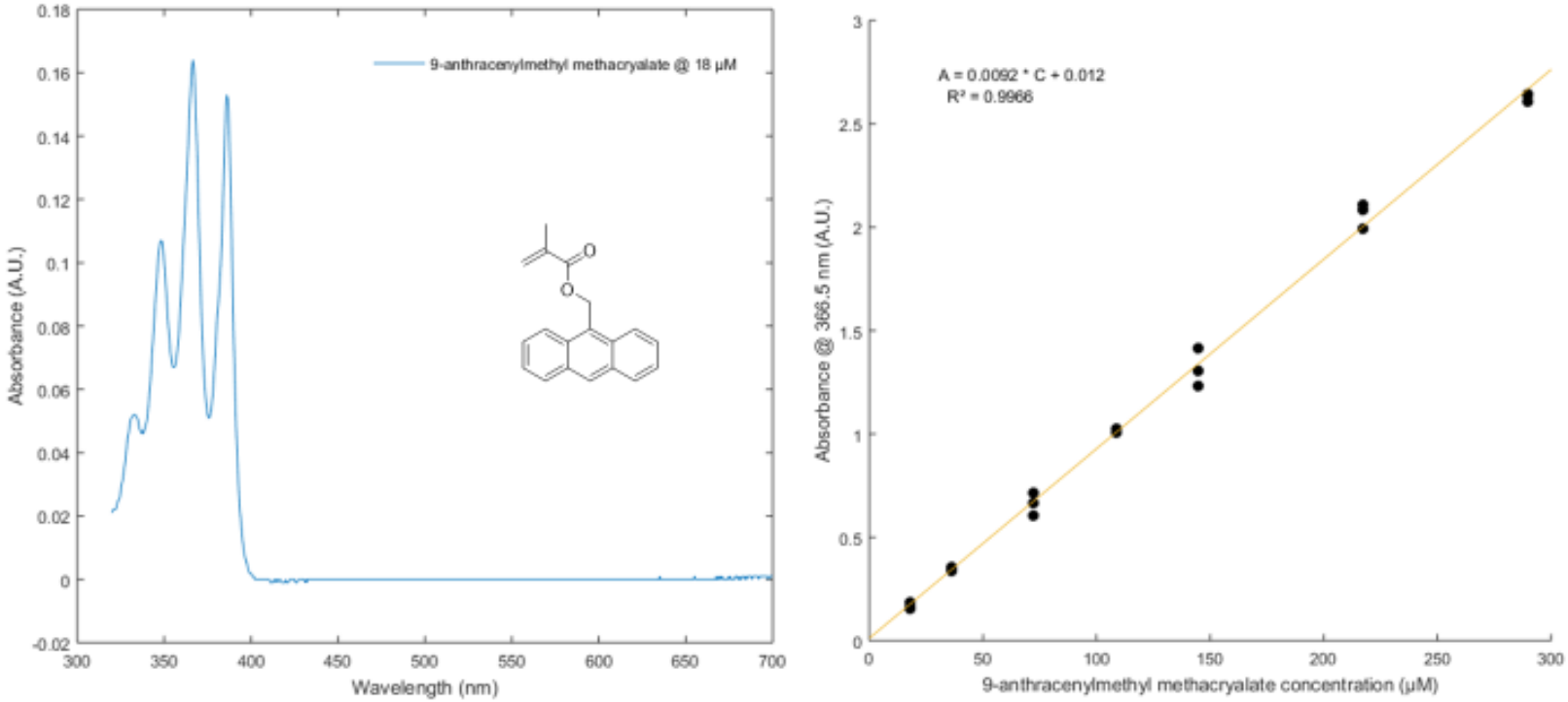

Figure A117: (Left) UV-Vis absorbance spectra of 18µM AMMA in THF, (Right) Concentration curve of AMMA at 366.5 nm

*Absorbance = 0.0092 * Concentration (µM) + 0.012, R^2 = 0.9966*

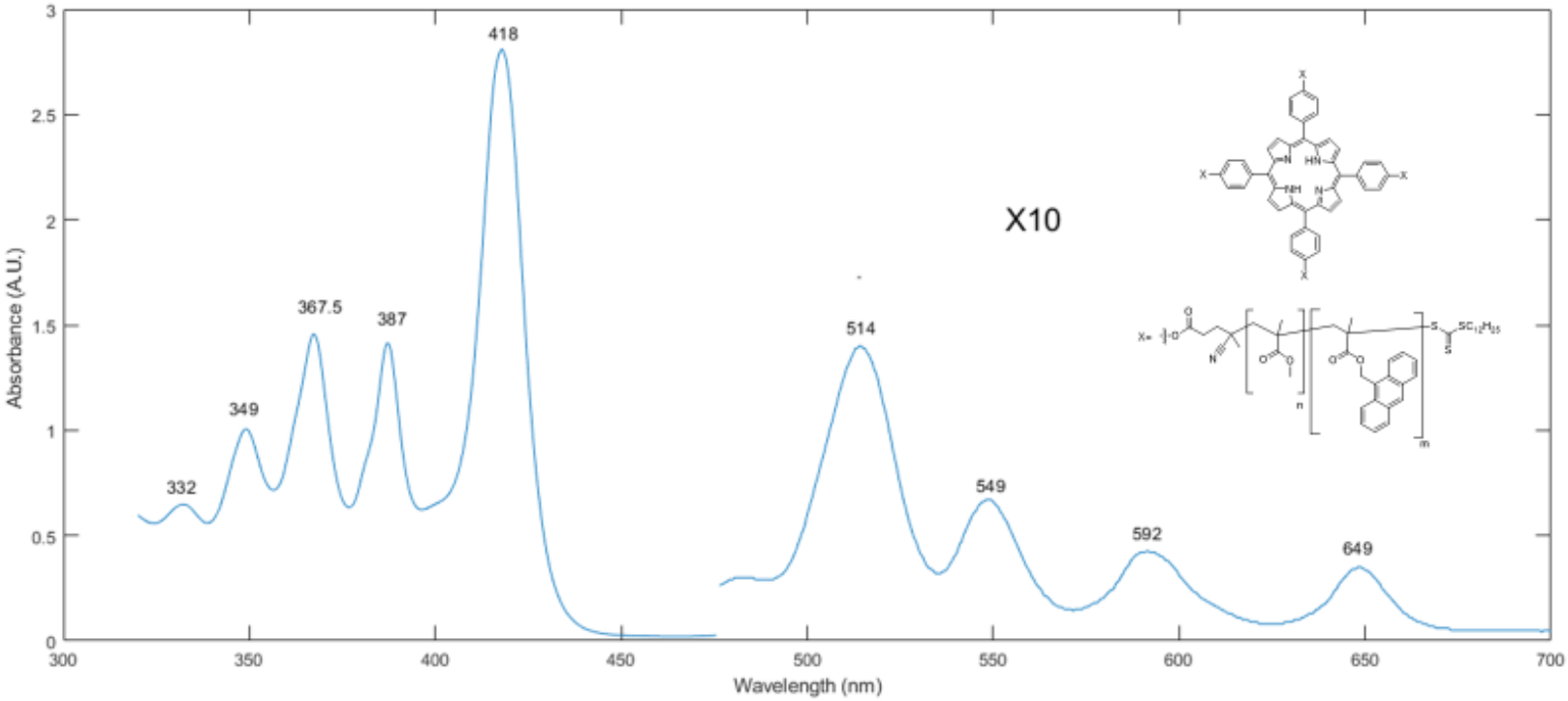

Figure A118: UV-Vis absorbance spectra of Por(MMA-co-AMMA)4 at 0.1 mg/mL in THF. Absorbance from 475 to 700 nm magnified X 10

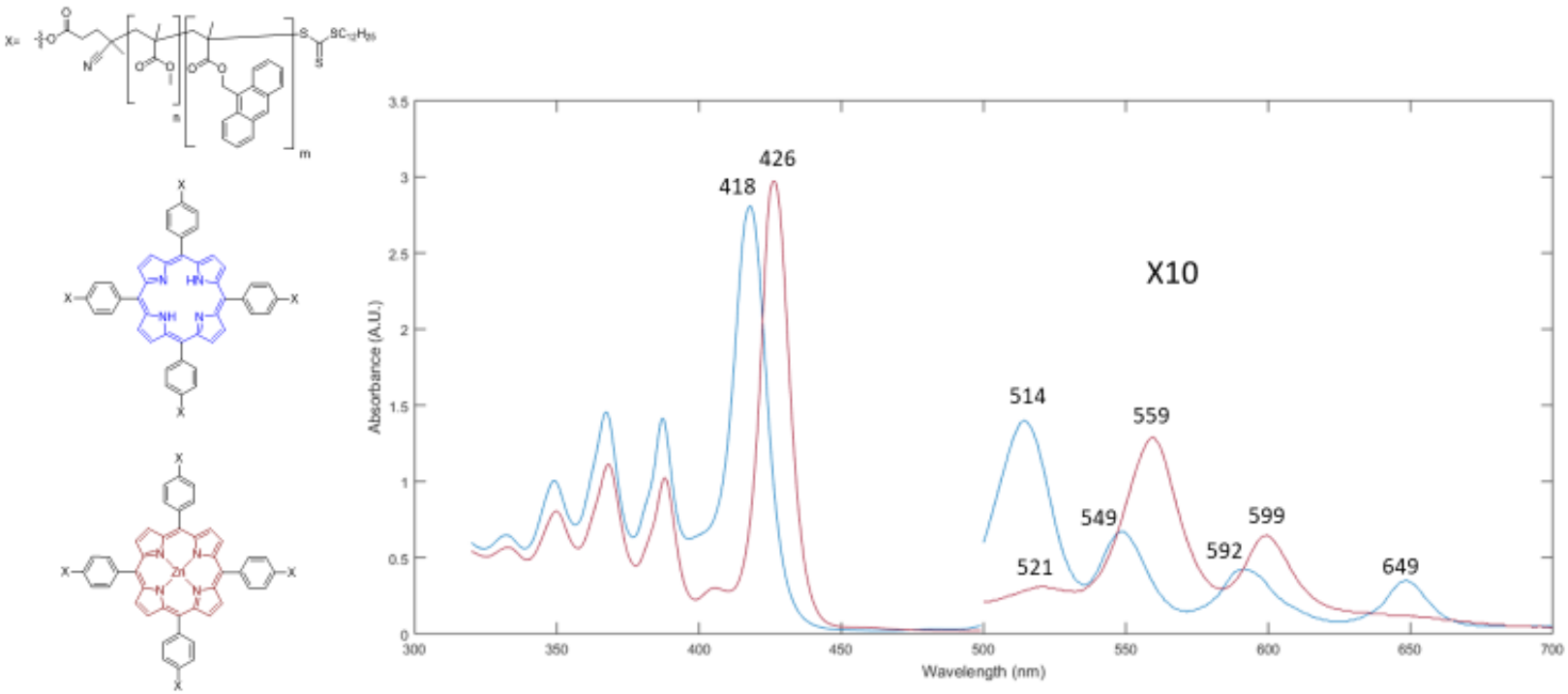

Figure A119: Comparison of UV vis absorbance spectra of Por(MMA-co-AMMA)$_4$ (Blue) and Zn^{II}(Por(MMA-co-AMMA)$_4$) (Red) at 0.1 mg/mL in THF

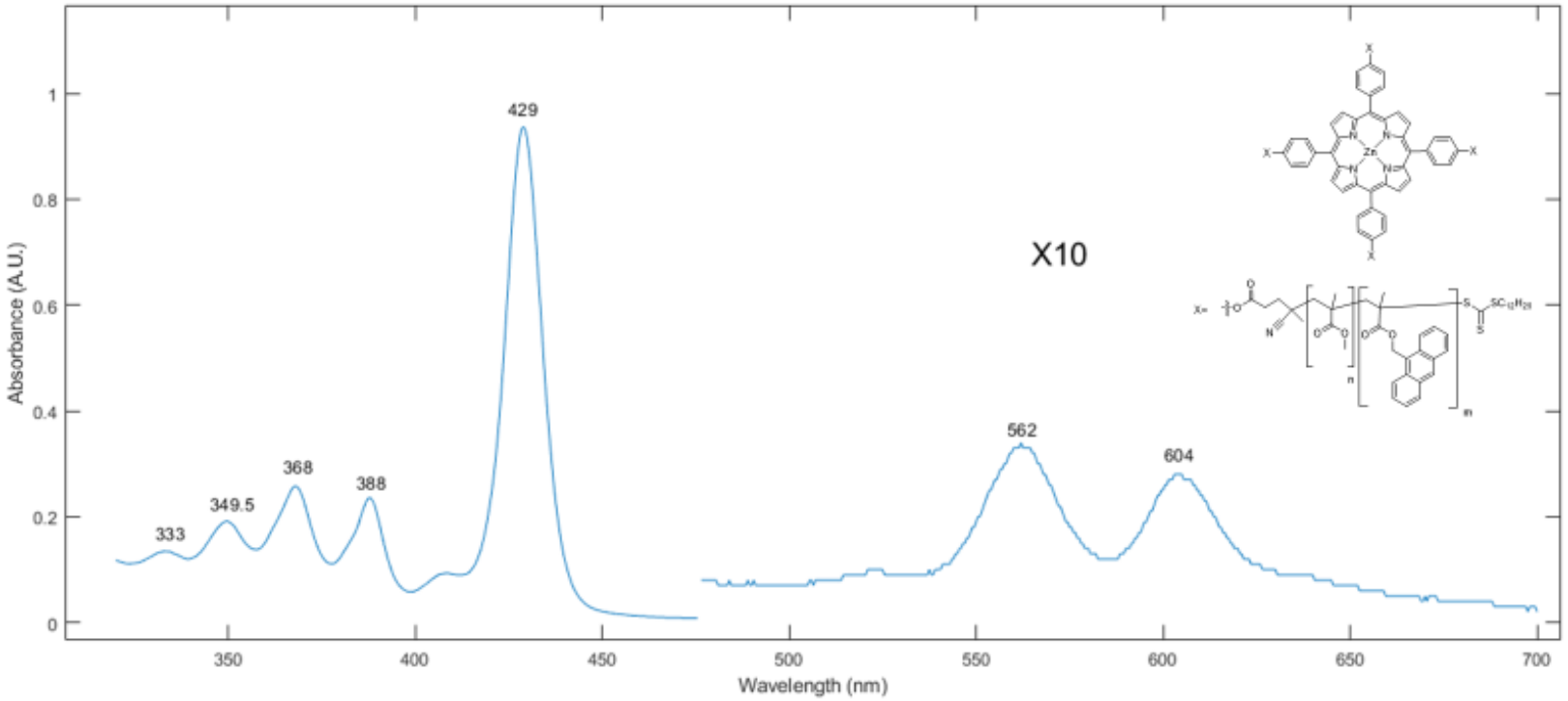

Figure A120: UV-Vis absorbance spectra of Zn^{II}(Por(MMA-co-AMMA)$_4$) at ~2.9 µM in DMF. Absorbance from 475 to 700 nm magnified X 10

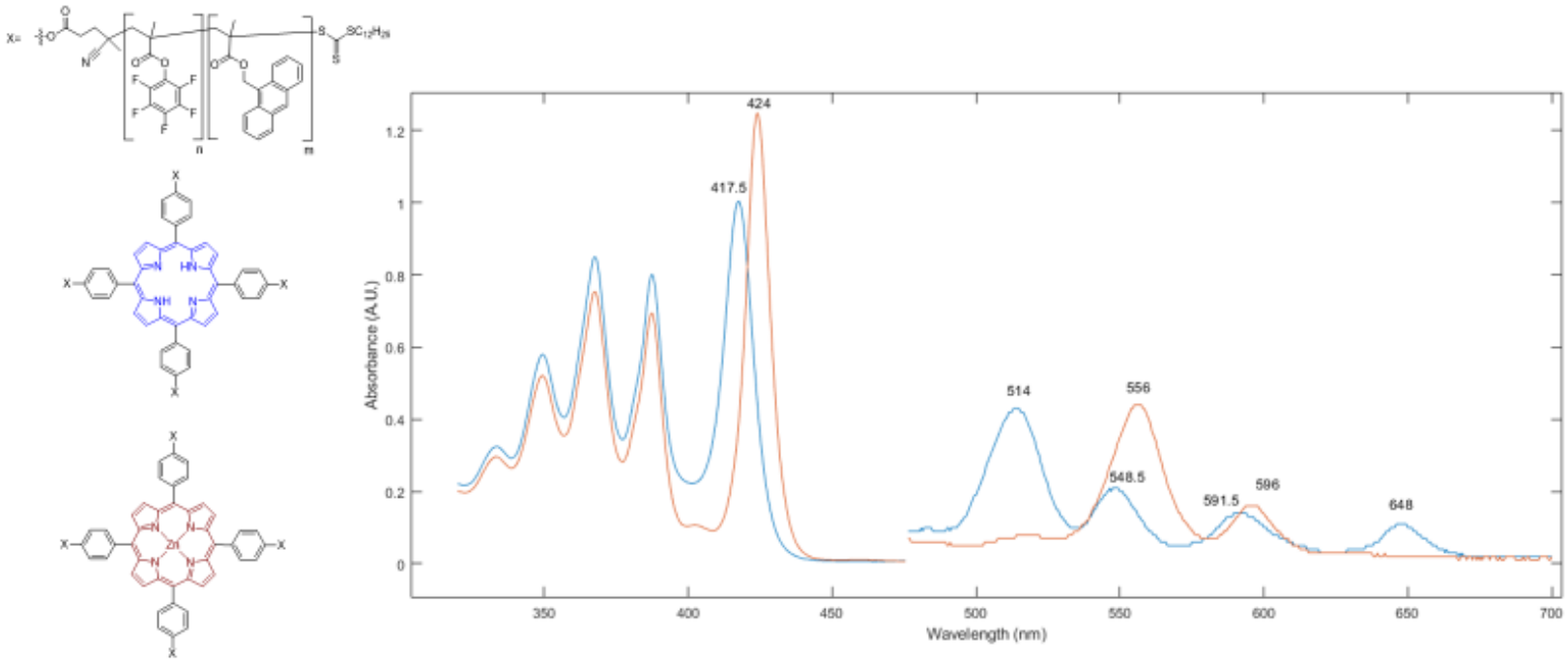

Figure A121: Comparison of UV vis spectra of Por(MMA-co-AMMA)$_4$ (Blue) at 0.20 mg/mL in THF and Zn^{II}(Por(MMA-co-AMMA)$_4$) (Red) at 0.17 mg/mL in THF, Absorbance from 475 to 700 nm magnified X 10

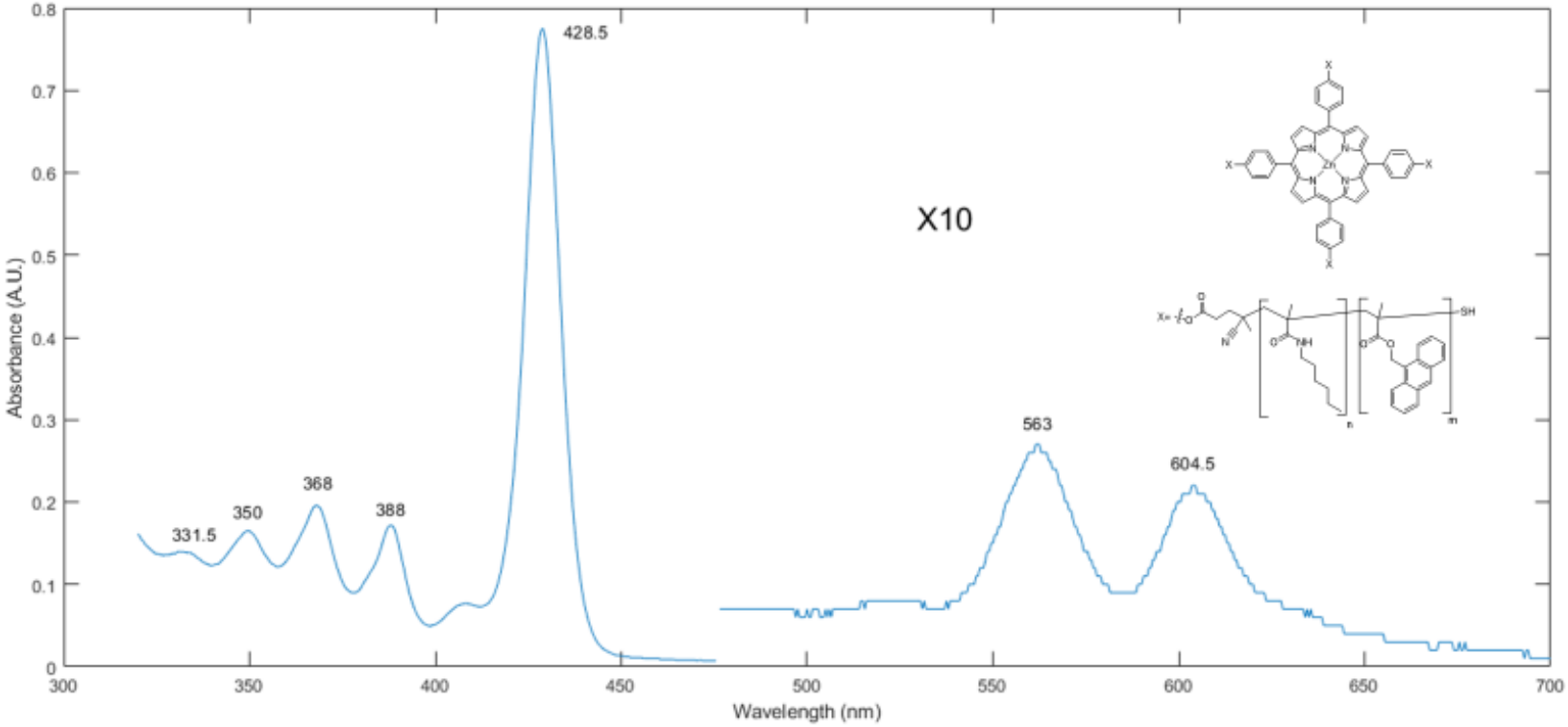

Figure A122: UV-Vis absorbance spectra of Zn^{II}(Por(HexMAAm-co-AMMA)$_4$) at ~2.9 µM in DMF. Absorbance from 475 to 700 nm magnified X 10

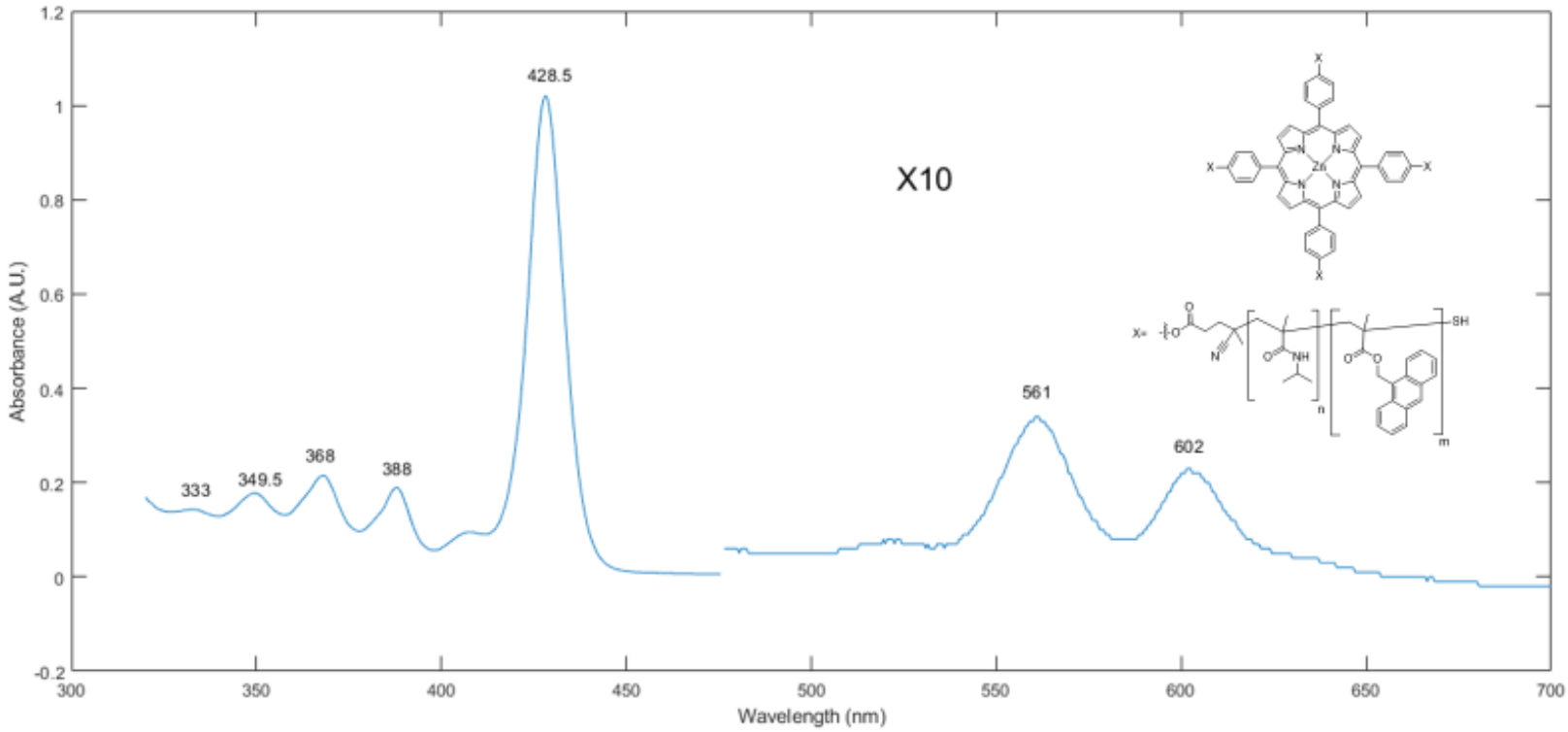

Figure A123: UV-Vis absorbance spectra of Zn^{II}(Por(iPMAAm-co-AMMA)$_4$) at ~2.9 µM in DMF. Absorbance from 475 to 700 nm magnified X 10

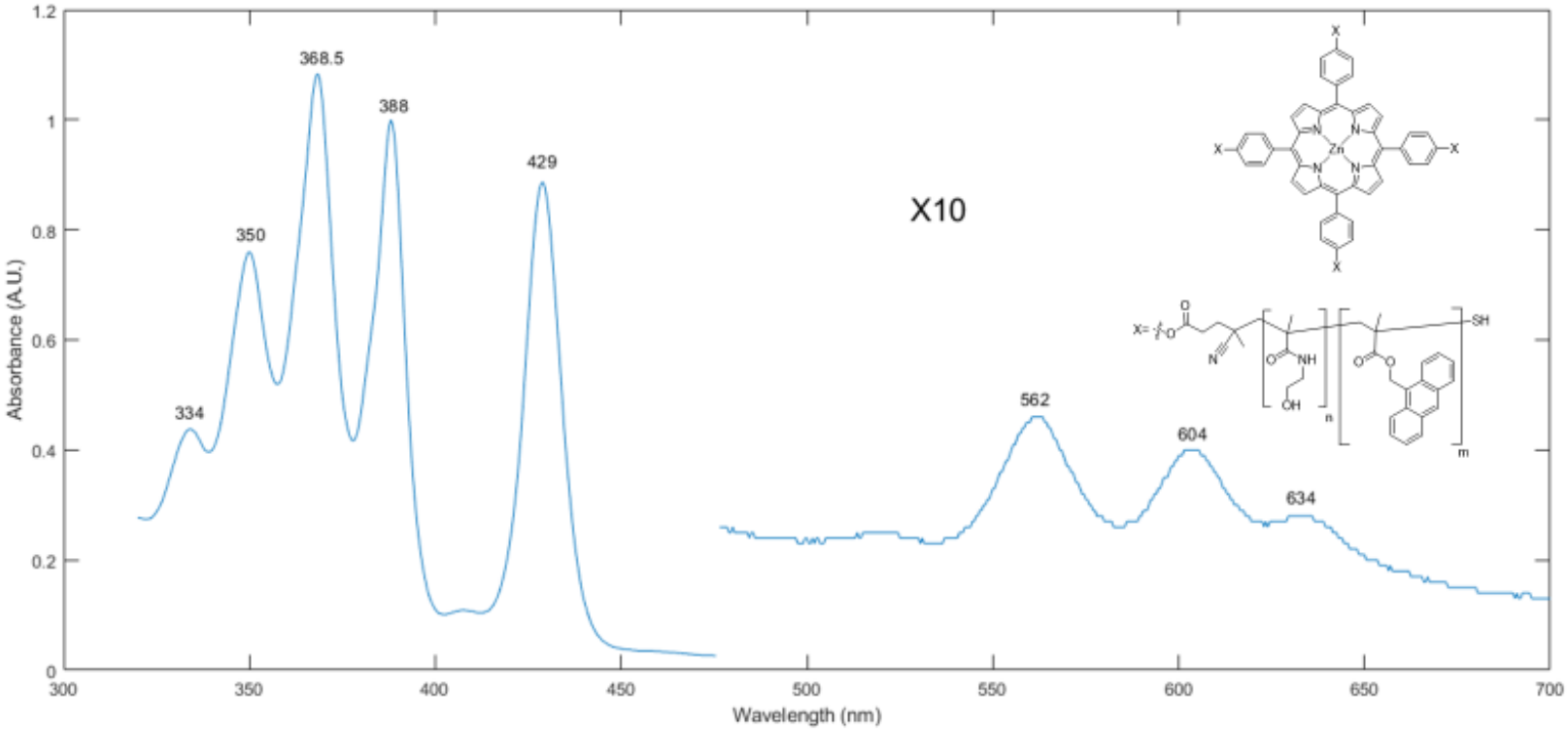

Figure A124: UV-Vis absorbance spectra of Zn^{II}(Por(HEMA-co-AMMA)$_4$) at ~2.9 µM in DMF. Absorbance from 475 to 700 nm magnified X10

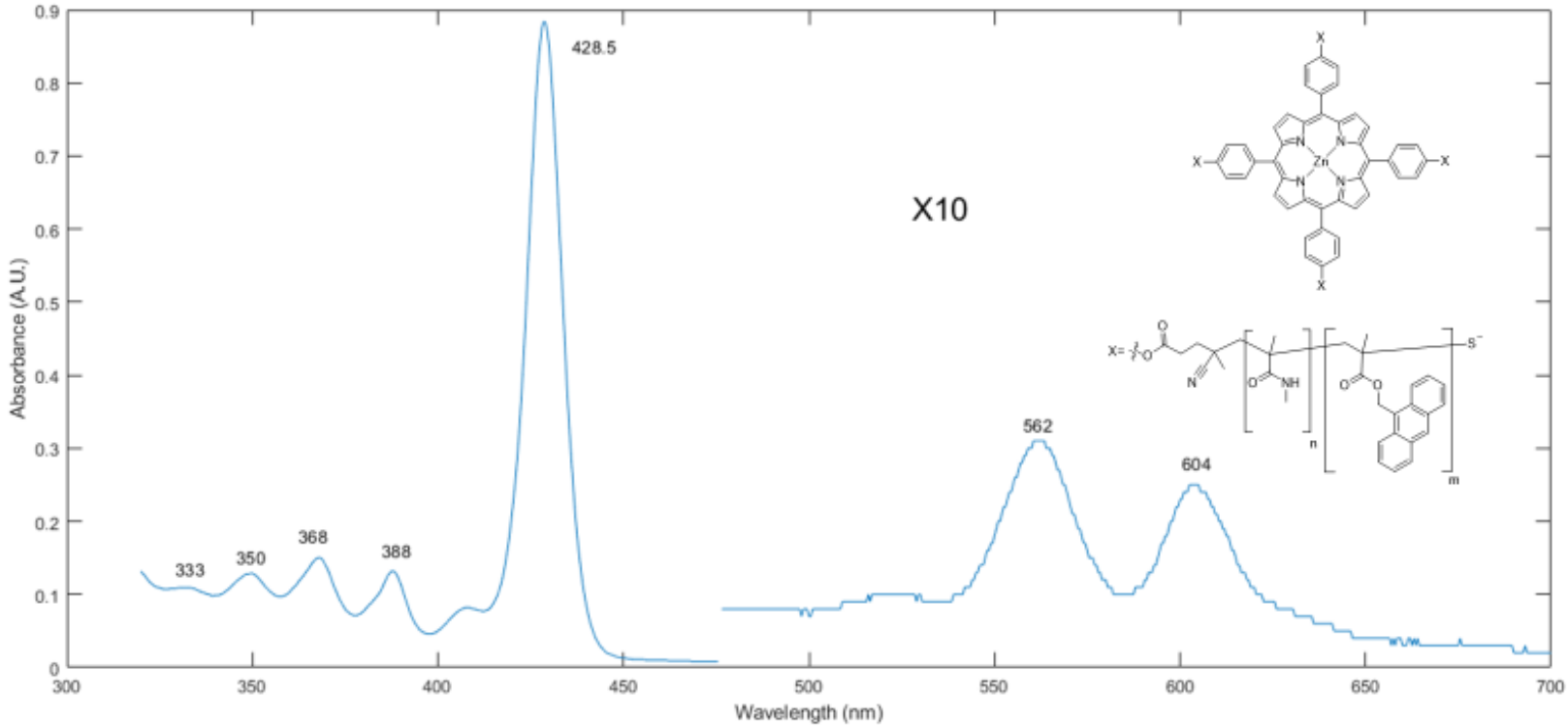

Figure A125: UV-Vis absorbance spectra of Zn^{II}(Por(MMAAm-co-AMMA)$_4$) at ~2.9 µM in DMF. Absorbance from 475 to 700 nm magnified X10

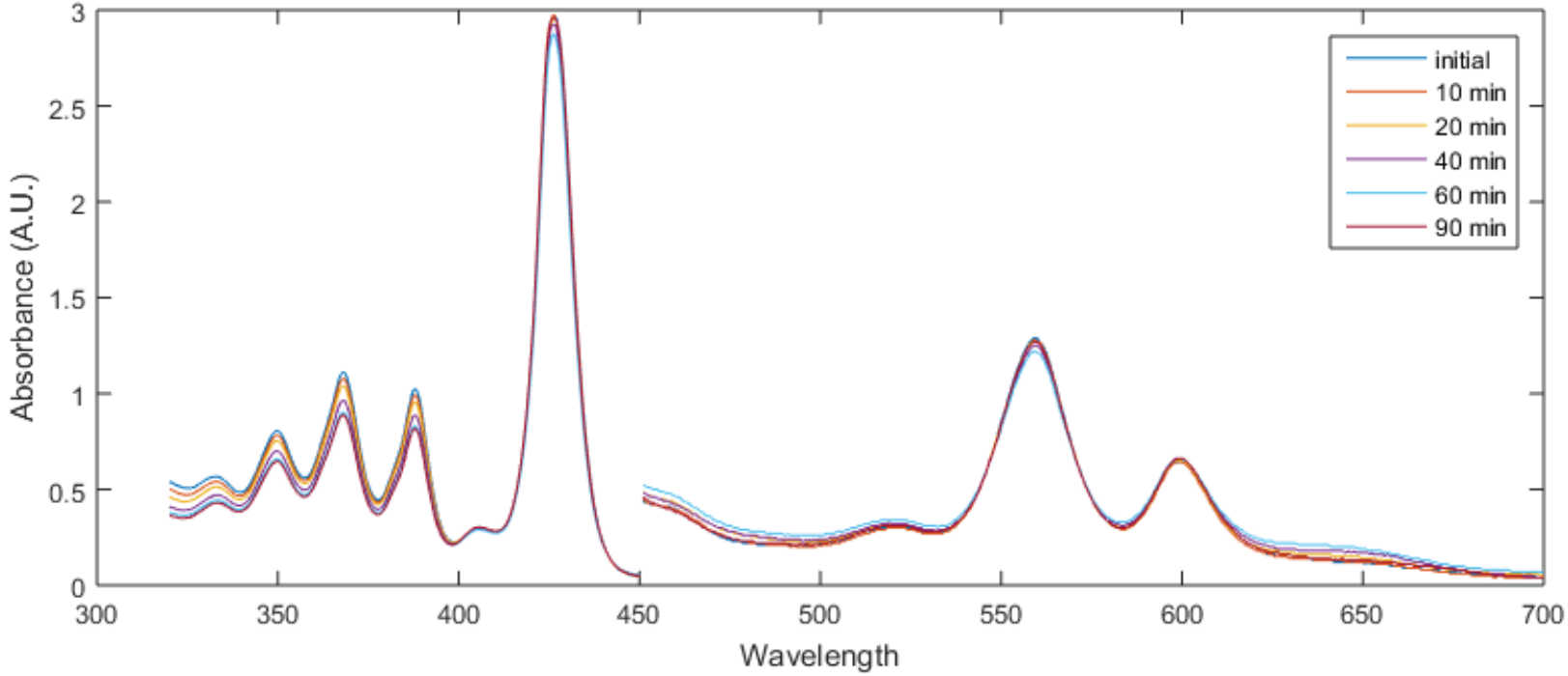

Figure A126: Evolution of UV-Vis absorbance spectra for Por(MMA-co-AMMA)$_4$) at 0.1 mg/mL in THF over time after exposure to 350 nm light.. Absorbance from 450 to 700 nm magnified X 10

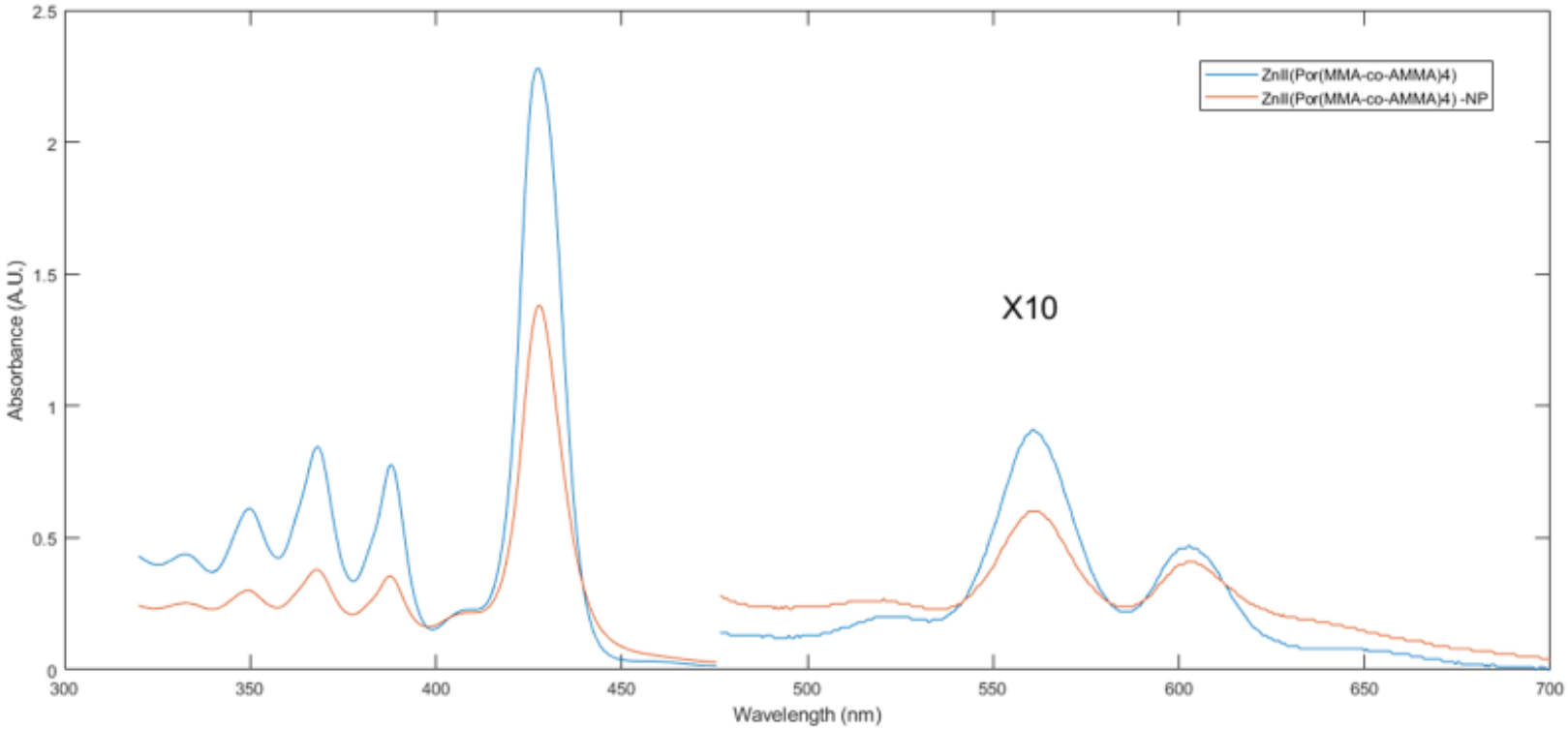

Figure A127: Comparison of UV-Vis absorbance spectra for Zn^{II}(Por(MMA-co-AMMA)$_4$) (blue) and Zn^{II}(Por(MMA-co-AMMA)$_4$)-NP (red) at 0.1 mg/mL in DMF. Absorbance from 475 to 700 nm magnified X 10

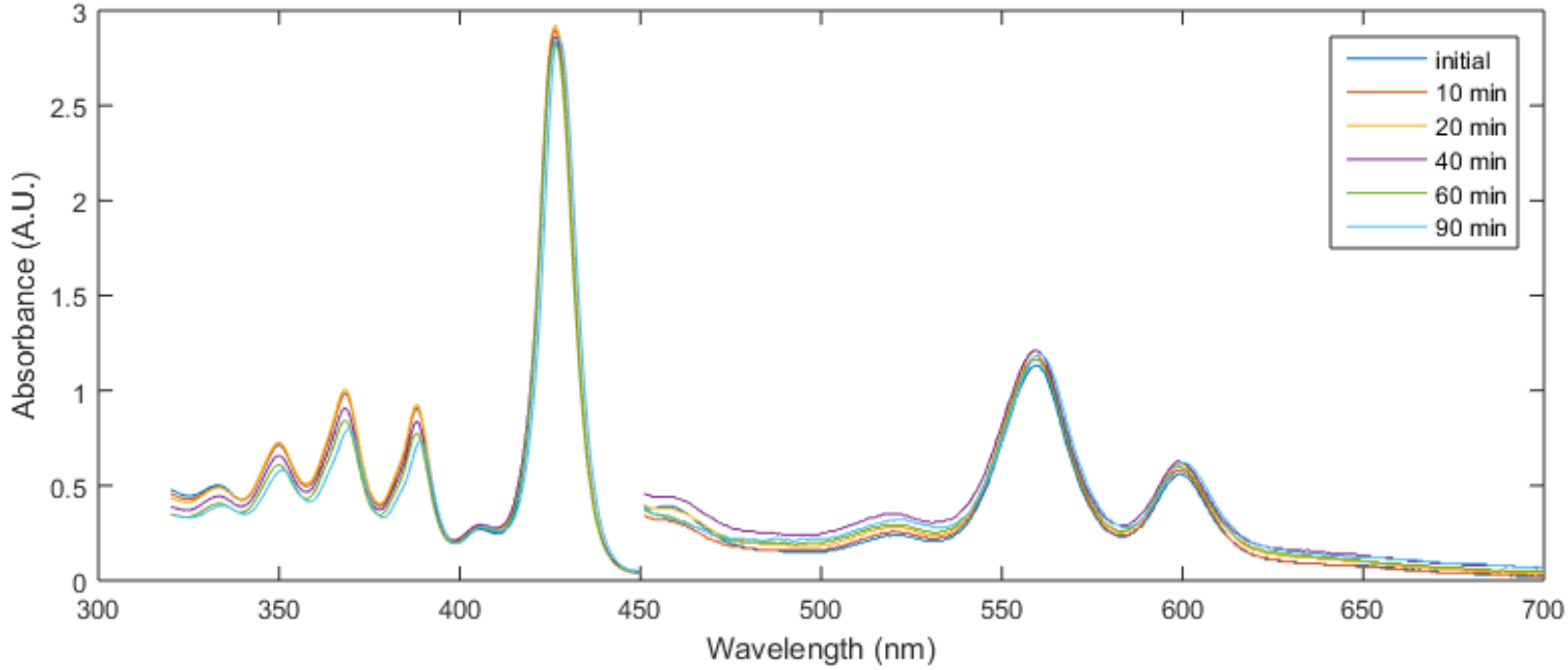

Figure A128: Evolution of UV-Vis absorbance spectra for Por(MMA-co-AMMA)$_4$) at 0.1 mg/mL in THF over time after exposure to 350 nm light. Absorbance from 450 to 700 nm magnified X 10

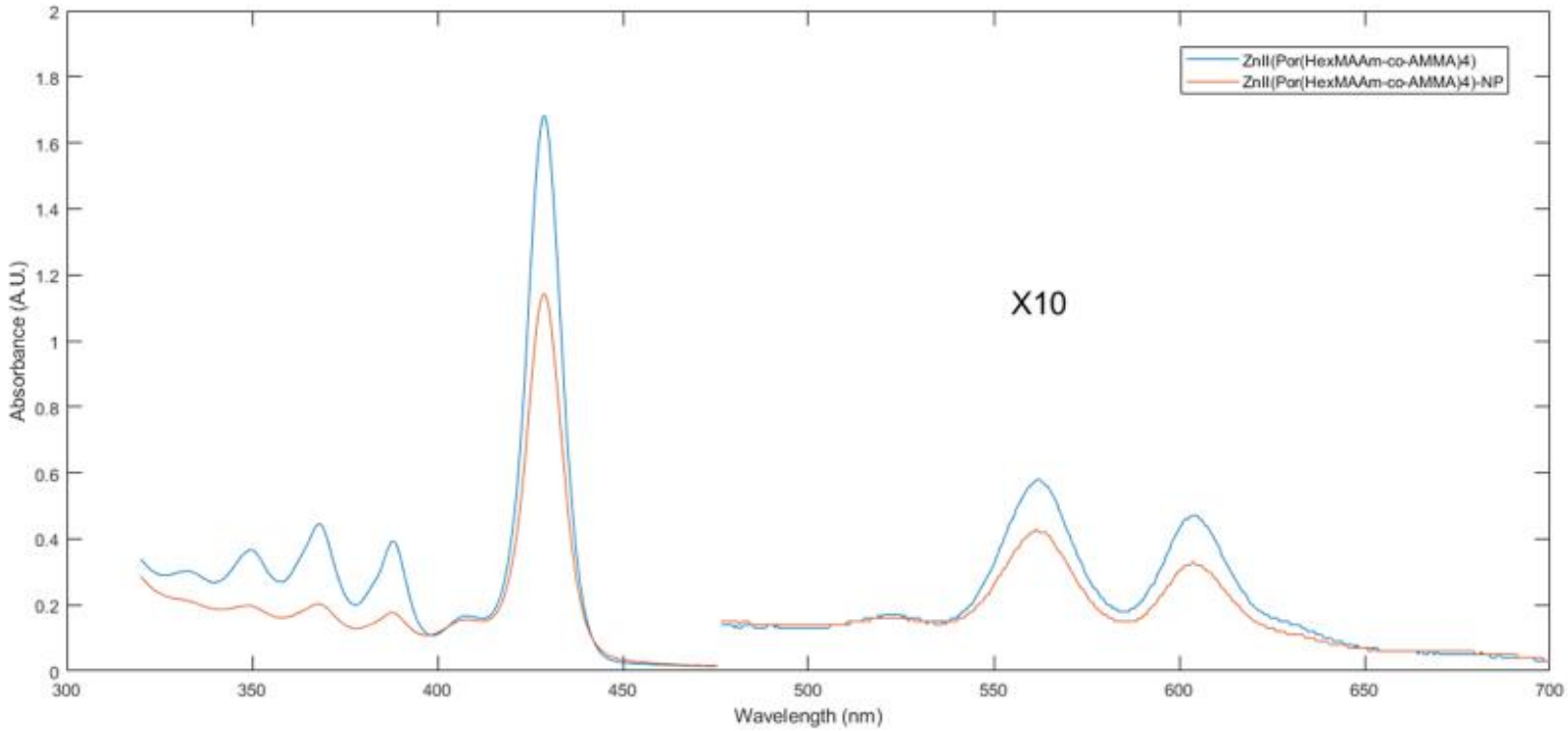

Figure A129: Comparison of UV-Vis absorbance spectra for Zn^{II}(Por(HexMAAm-co-AMMA)$_4$) (blue) and Zn^{II}(Por(HexMAAm -co-AMMA)$_4$)-NP (red) at 0.1 mg/mL in DMF. Absorbance from 475 to 700 nm magnified X 10

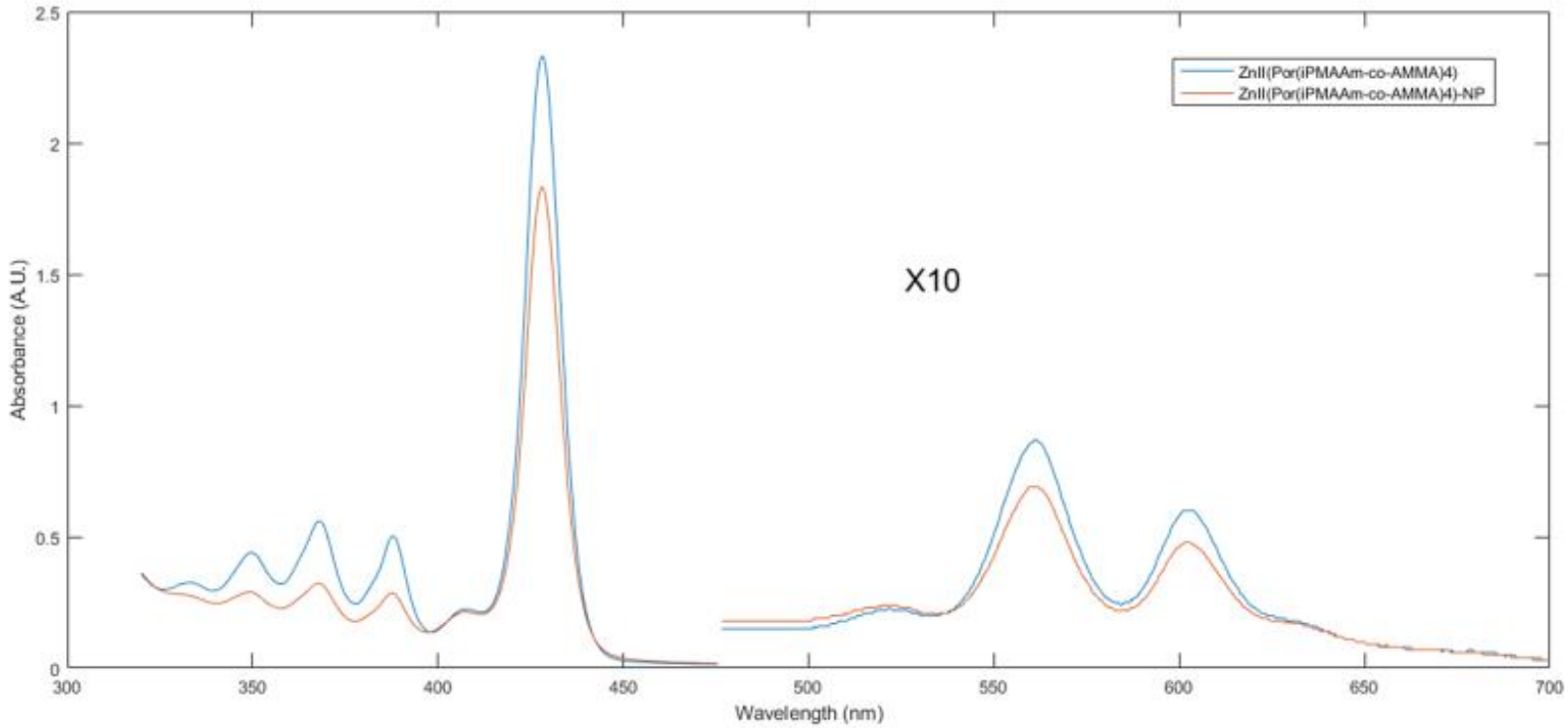

Figure A130: Comparison of UV-Vis absorbance spectra for Zn^{II}(Por(iPMAAm-co-AMMA)$_4$) (blue) and Zn^{II}(Por(iPMAAm -co-AMMA)$_4$)-NP (red) at 0.1 mg/mL in DMF. Absorbance from 475 to 700 nm magnified X 10

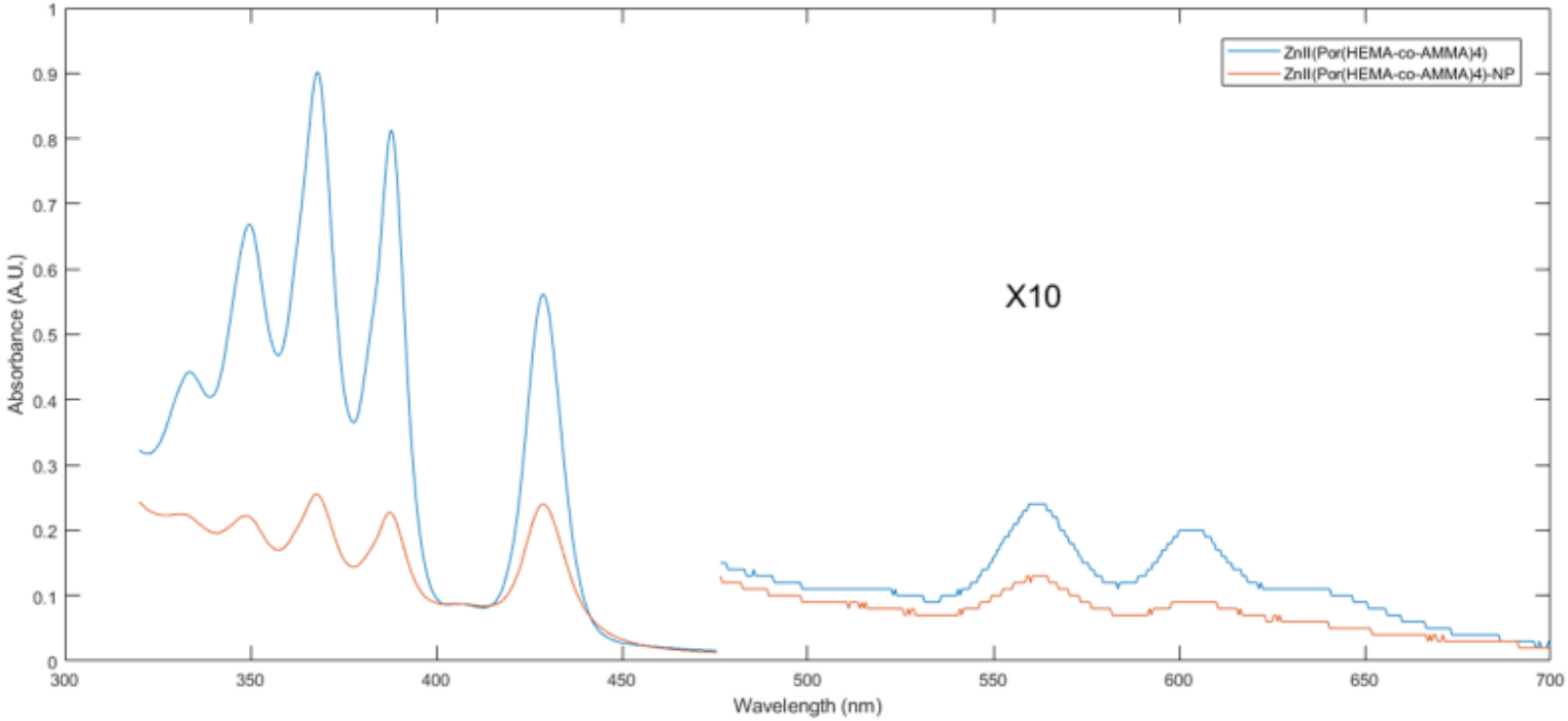

Figure A131: Comparison of UV-Vis absorbance spectra for Zn^{II}(Por(HEMA-co-AMMA)$_4$) (blue) and Zn^{II}(Por(HEMA-co-AMMA)$_4$)-NP (red) at 0.1 mg/mL in DMF. Absorbance from 475 to 700 nm magnified X 10

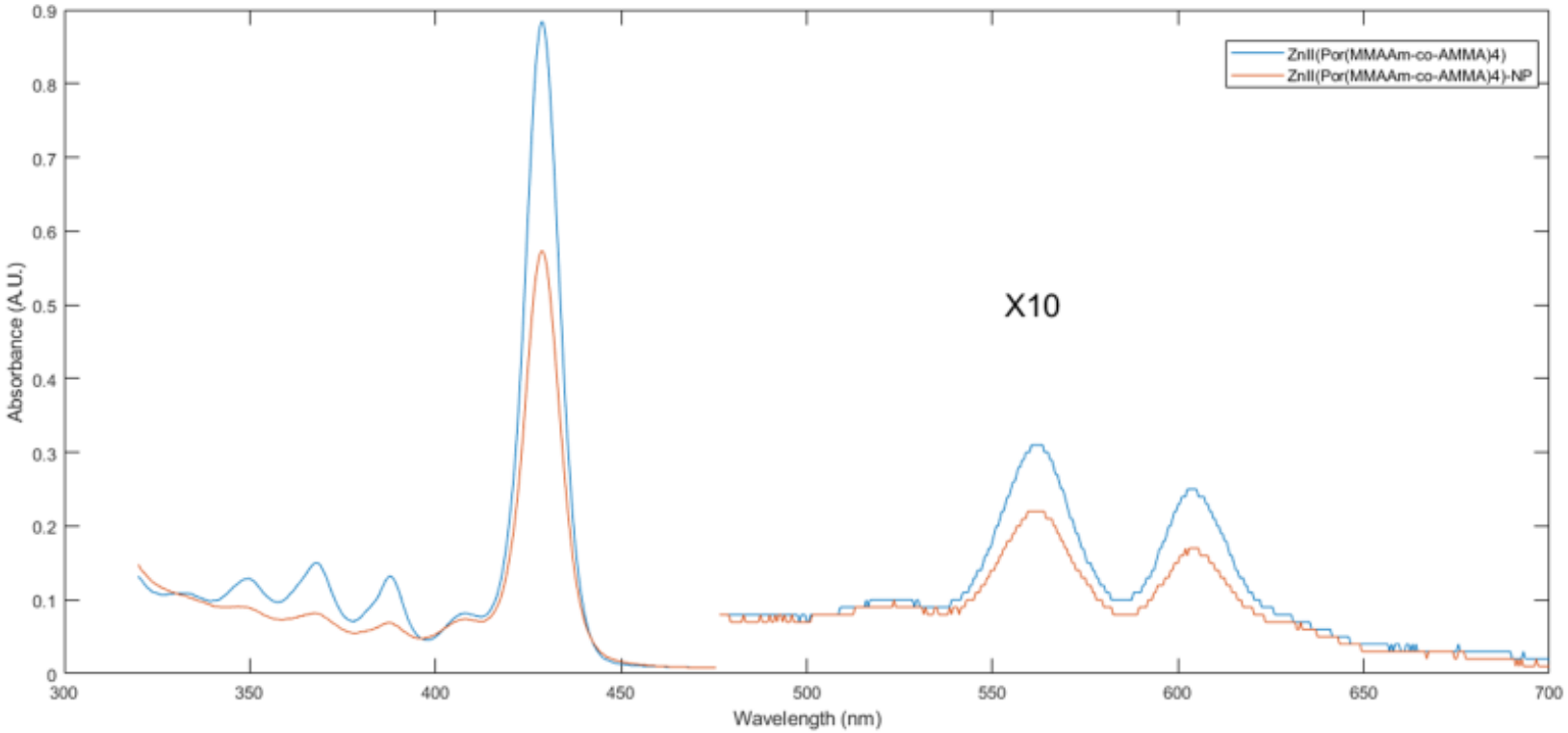

Figure A132: Comparison of UV-Vis absorbance spectra for Zn^{II}(Por(MMAAm-co-AMMA)$_4$) (blue) and Zn^{II}(Por(MMAAm-co-AMMA)$_4$)-NP (red) at ~2.9 µM in DMF. Absorbance from 475 to 700 nm magnified X 10

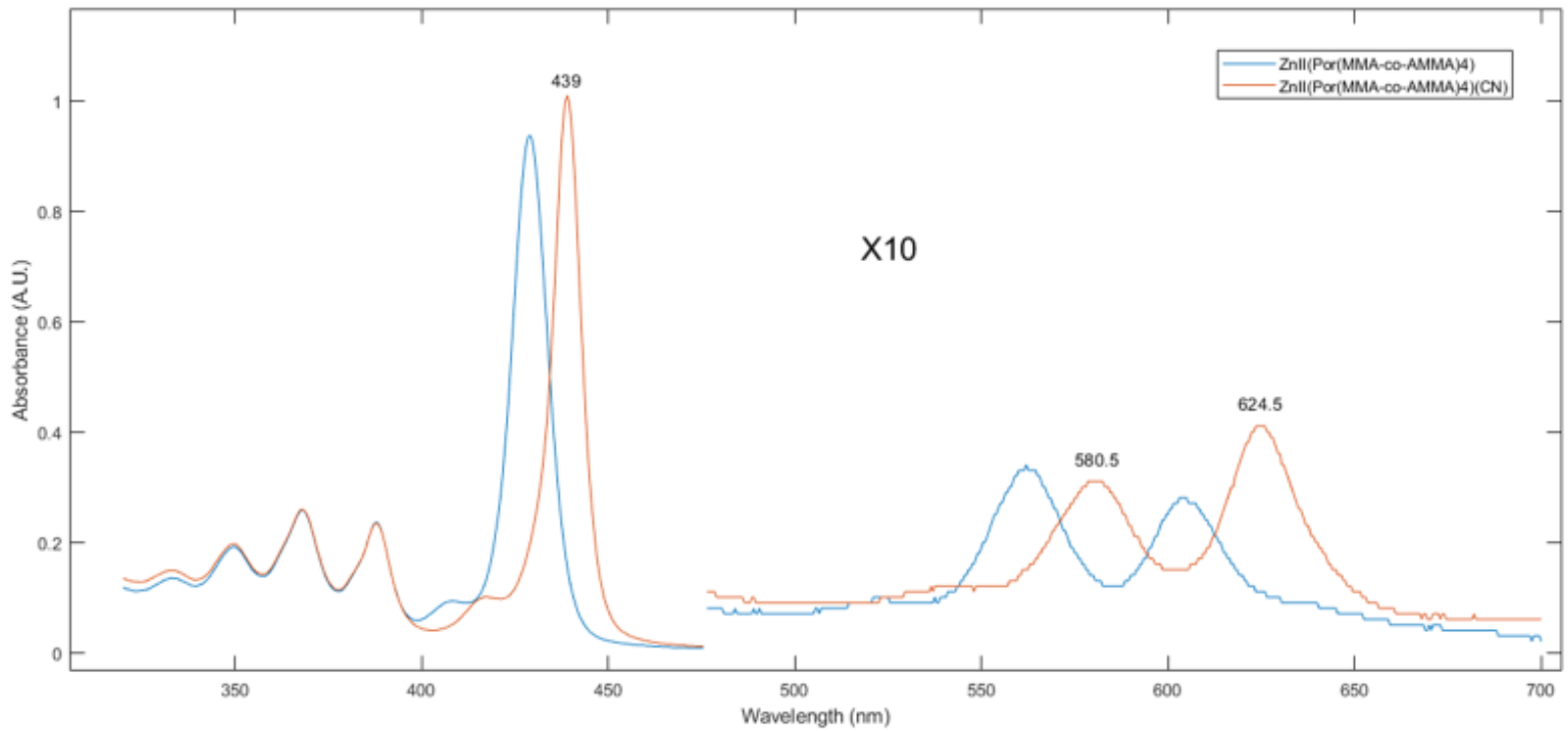

Figure A133: Comparison of UV-Vis absorbance spectra for Zn^{II}(Por(MMA-co-AMMA)$_4$) (blue) and Zn^{II}(Por(MMA-co-AMMA)$_4$)(CN) (red) at ~2.9 µM in DMF. Absorbance from 475 to 700 nm magnified X 10

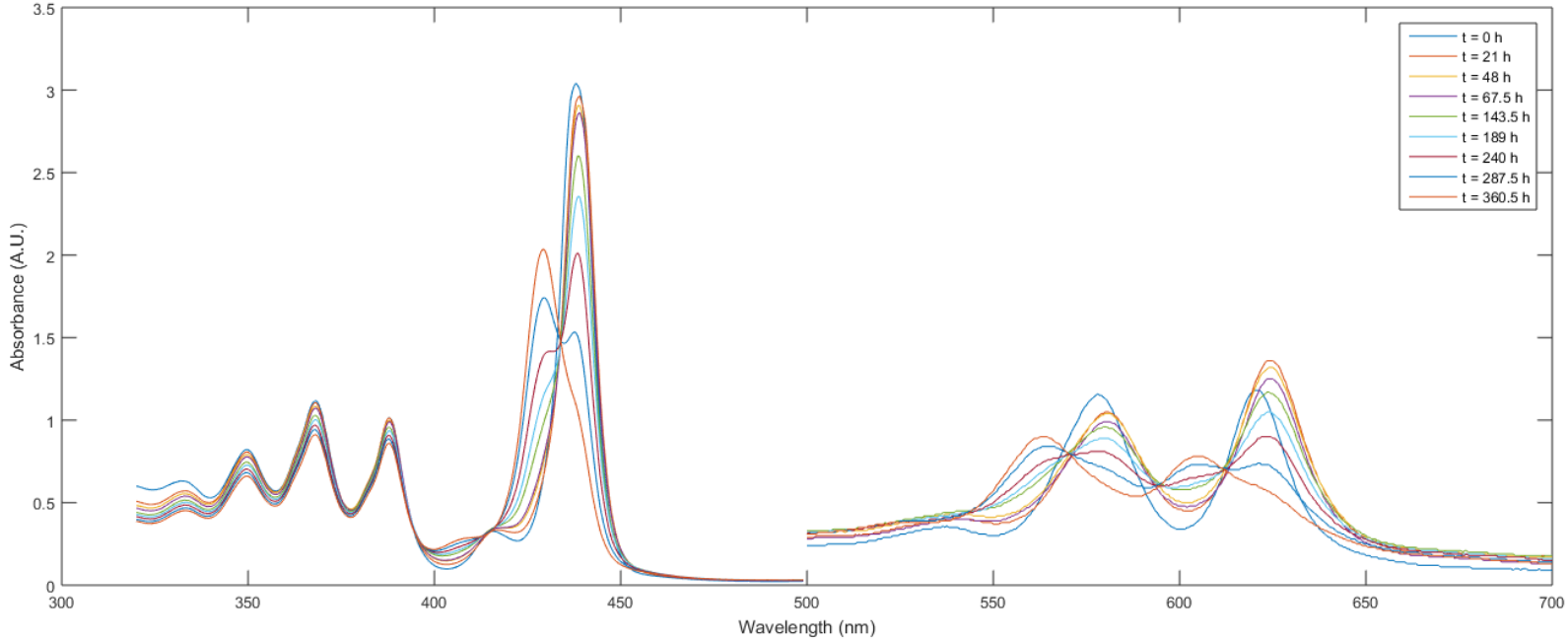

Figure A134: UV-Vis absorbance spectra of the evolution of Zn^{II}(Por(MMA-co-AMMA)$_4$) at 0.1 mg/ml and 0.5 mM in DMF over time after cyanide addition. Solutions exposed to ambient air when transferring between scintillation vial to cuvette at each time interval. Absorbance from 500 to 700 nm magnified X 10

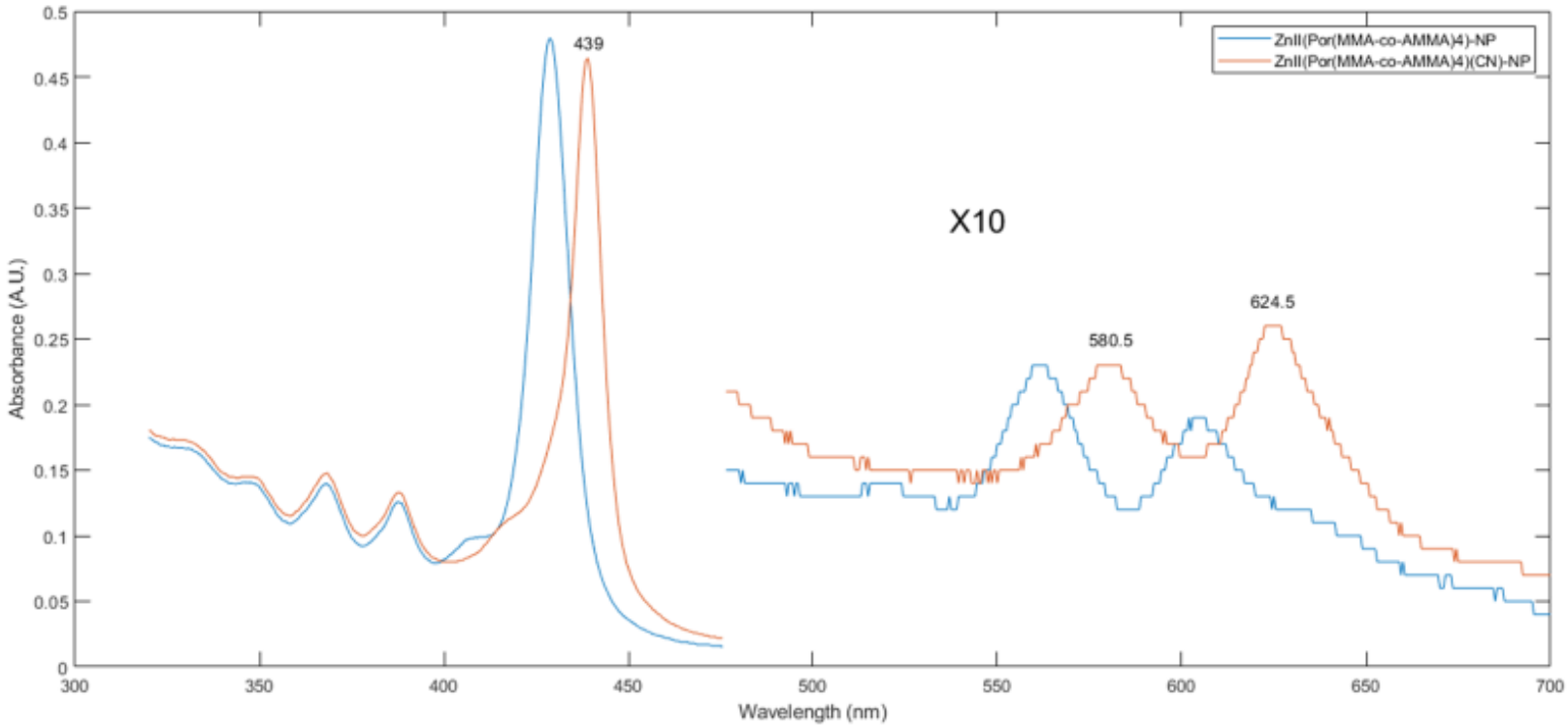

Figure A135: Comparison of UV-Vis absorbance spectra for Zn^{II}(Por(MMA-co-AMMA)$_4$)-NP (blue) and Zn^{II}(Por(MMA-co-AMMA)$_4$)(CN)-NP (red) at ~2.9 µM in DMF. Absorbance from 475 to 700 nm magnified X 10

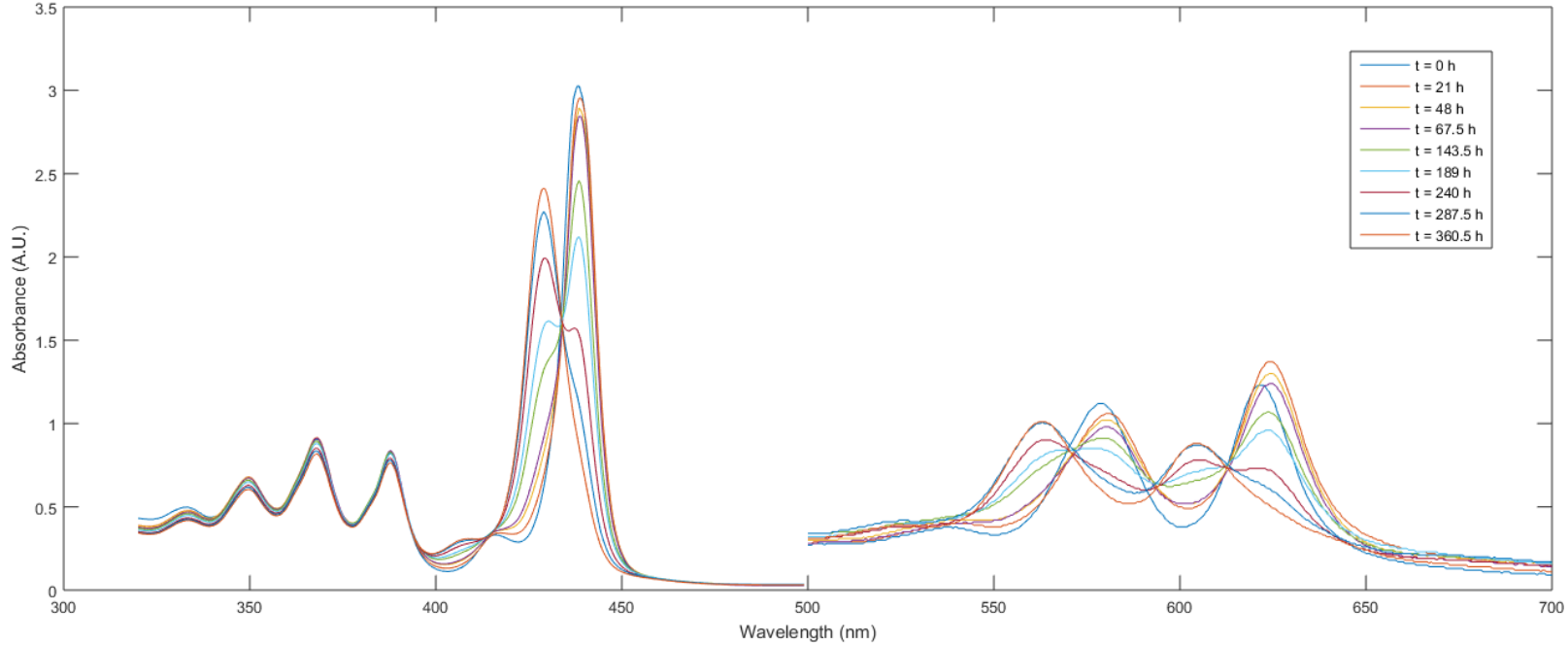

Figure A136: UV-Vis absorbance spectra of the evolution of Zn^{II}(Por(MMA-co-AMMA)$_4$)-NP at 0.1 mg/ml and 0.5 mM in DMF over time after cyanide addition. Solutions exposed to ambient air when transferring between scintillation vial to cuvette at each time interval. Absorbance from 500 to 700 nm magnified X 10

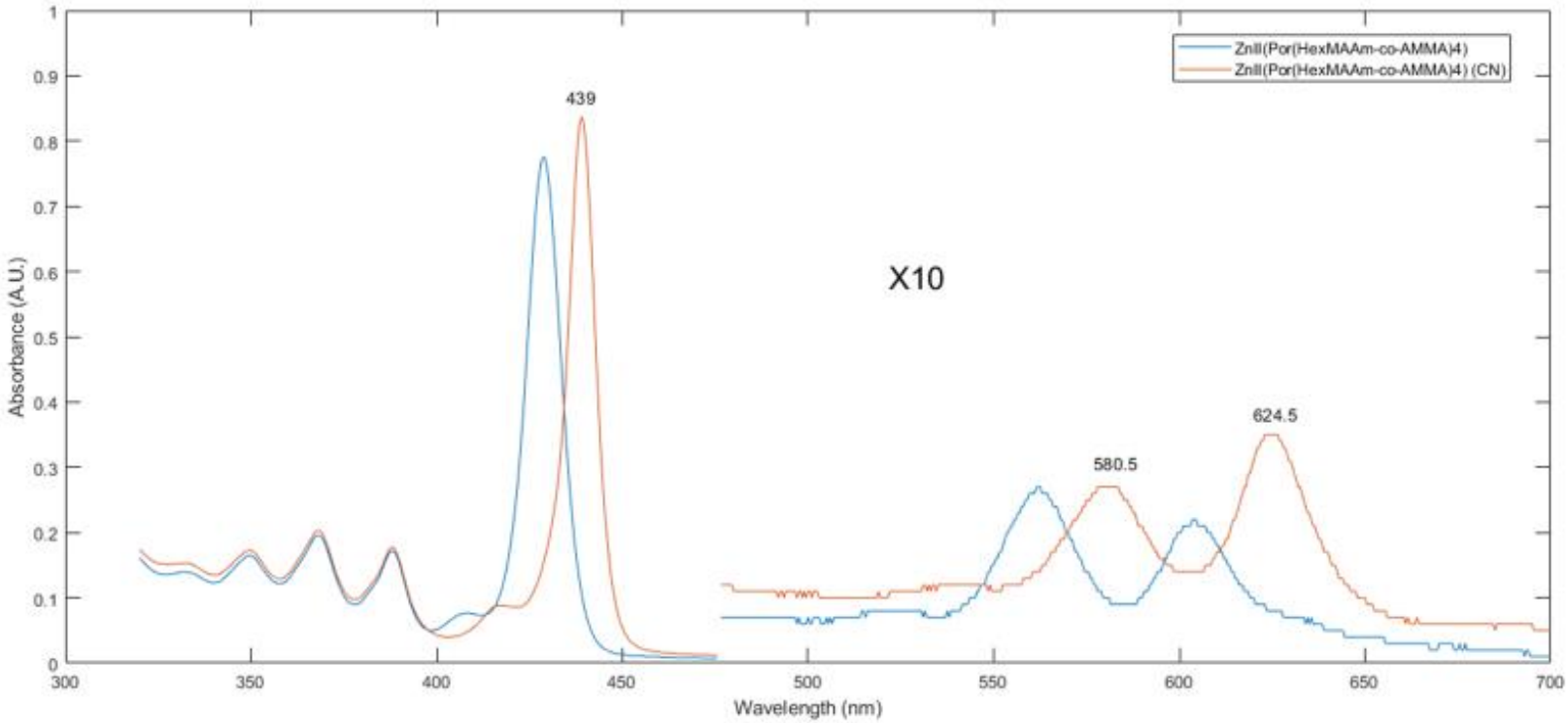

Figure A137: Comparison of UV-Vis absorbance spectra for Zn^{II}(Por(HexMAAm-co-AMMA)$_4$) (blue) and Zn^{II}(Por(HexMAAm -co-AMMA)$_4$)(CN) (red) at ~2.9 µM in DMF. Absorbance from 475 to 700 nm magnified X 10

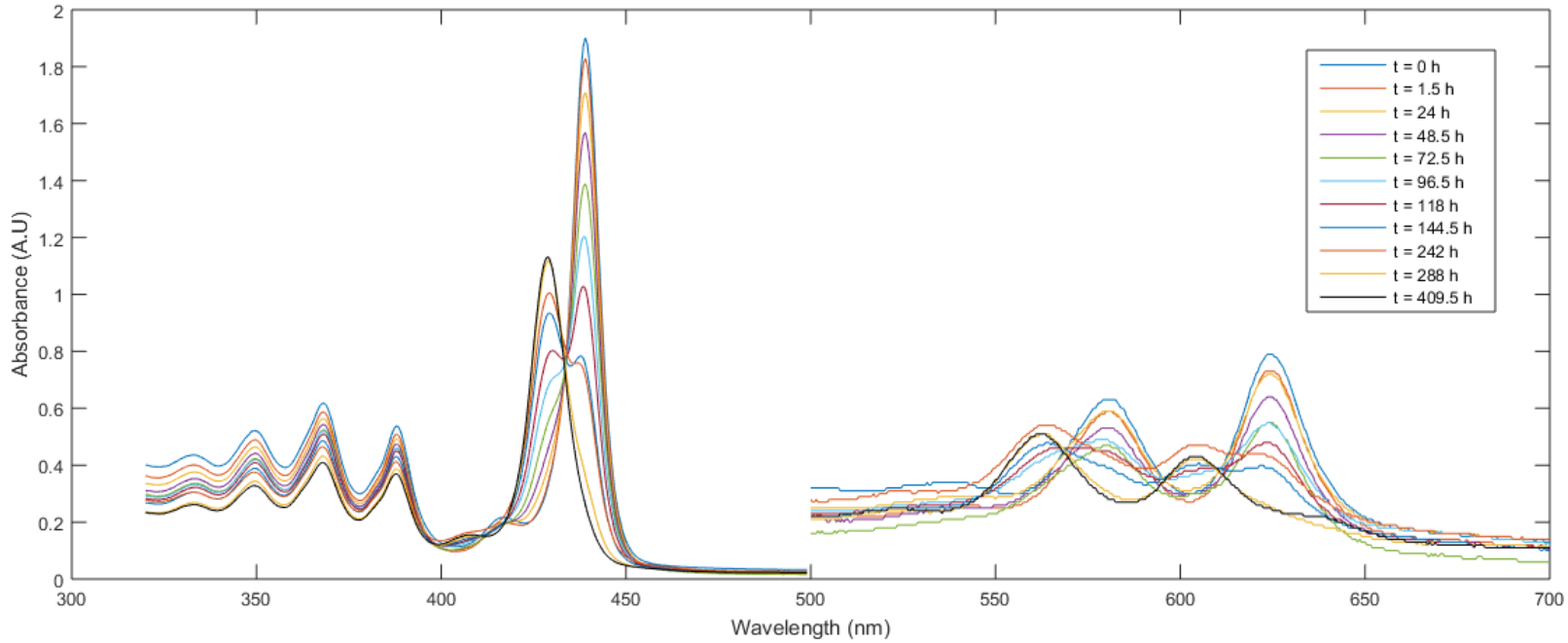

Figure A138: UV-Vis absorbance spectra of the evolution of Zn^{II}(Por(HexMAAm-co-AMMA)$_4$) at 0.1 mg/ml and 0.5 mM in DMF over time after cyanide addition. Solutions exposed to ambient air when transferring between scintillation vial to cuvette at each time interval. Absorbance from 500 to 700 nm magnified X 10

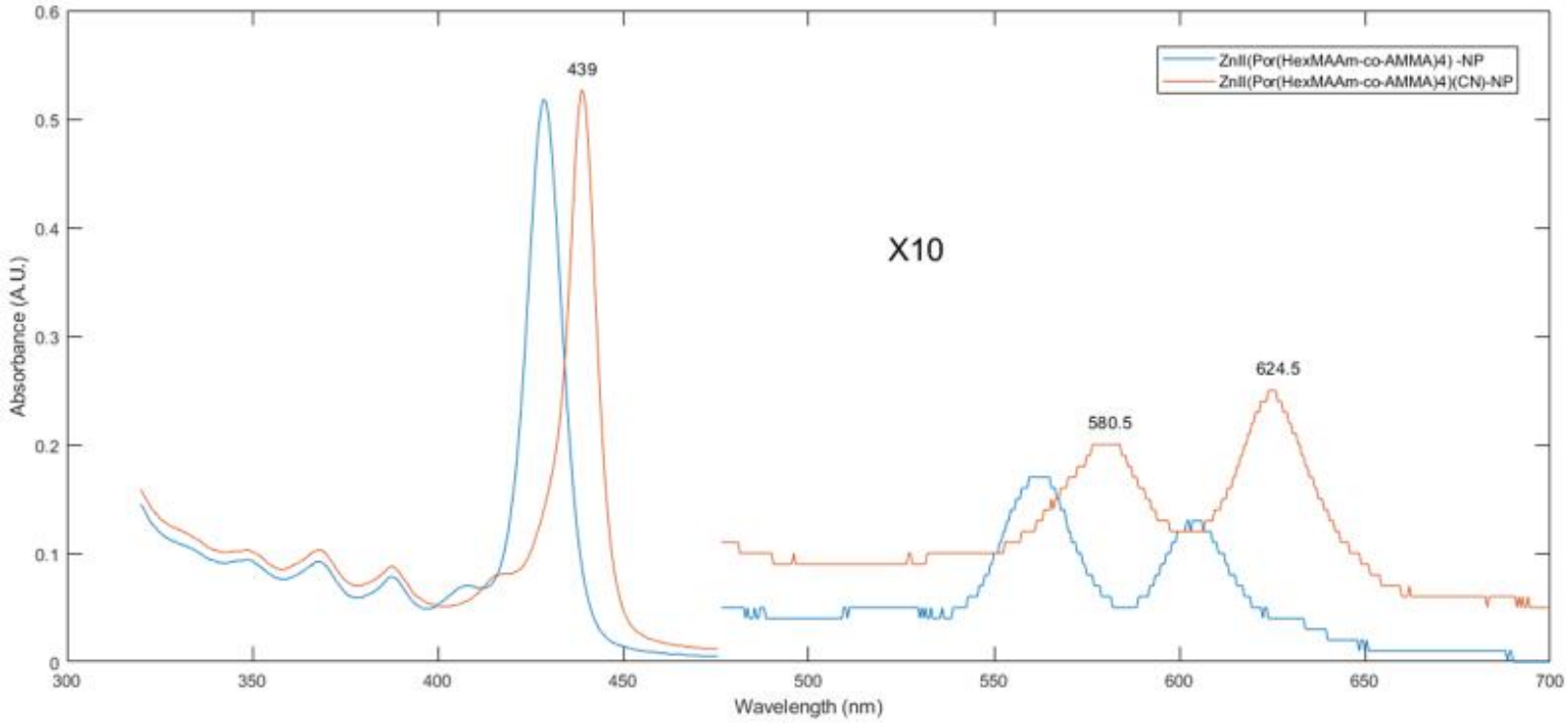

Figure A139: Comparison of UV-Vis absorbance spectra for Zn^{II}(Por(HexMAAm-co-AMMA)$_4$)-NP (blue) and Zn^{II}(Por(HexMAAm -co-AMMA)$_4$)(CN)-NP (red) at ~2.9 µM in DMF. Absorbance from 475 to 700 nm magnified X 10

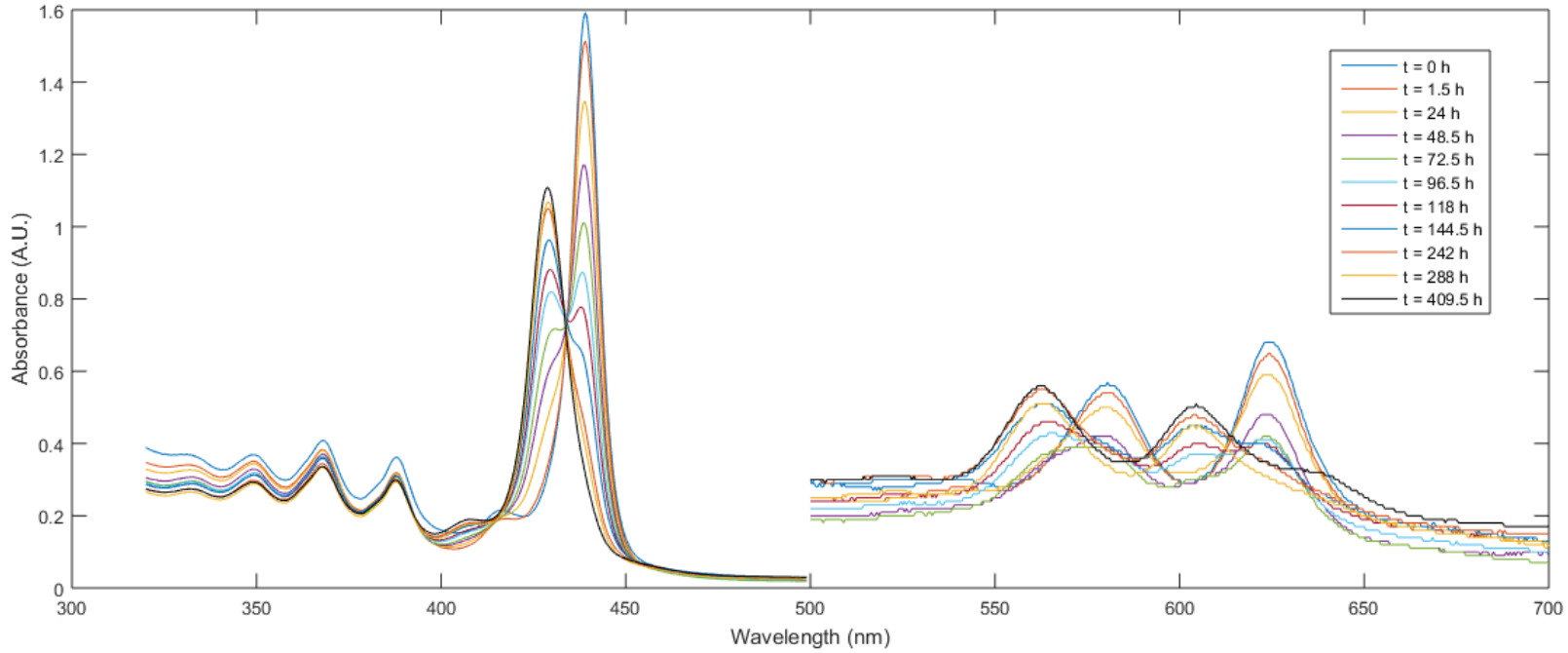

Figure A140: UV-Vis spectrums of the evolution of Zn^{II}(Por(HexMAAm-co-AMMA)$_4$)-NP at 0.1 mg/ml and 0.5 mM in DMF over time after cyanide addition. Solutions exposed to ambient air when transferring between scintillation vial to cuvette at each time interval. Absorbance from 500 to 700 nm magnified X 10

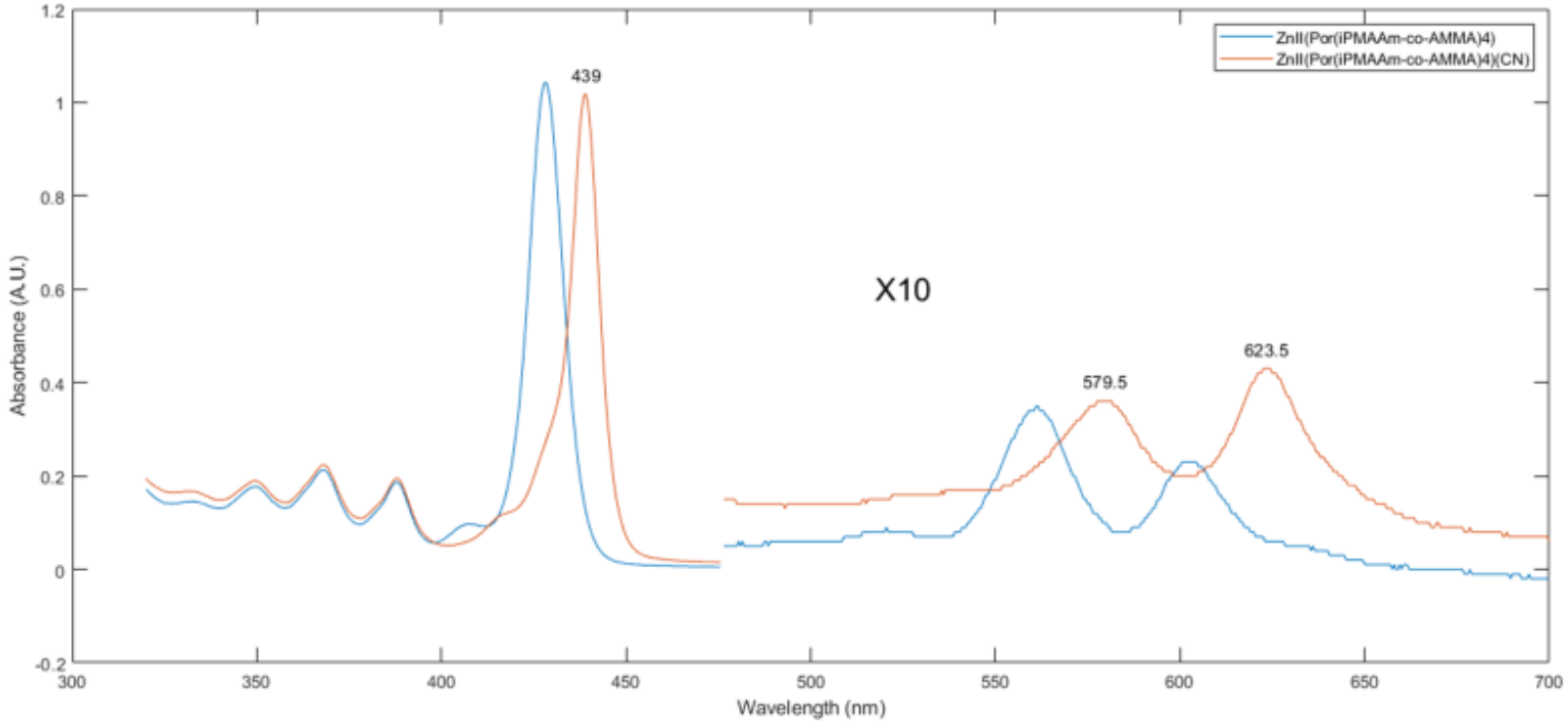

Figure A141: Comparison of UV-Vis absorbance spectra for Zn^{II}(Por(iPMAAm-co-AMMA)$_4$) (blue) and Zn^{II}(Por(iPMAAm -co-AMMA)$_4$)(CN) (red) at ~2.9 µM in DMF. Absorbance from 475 to 700 nm magnified X 10

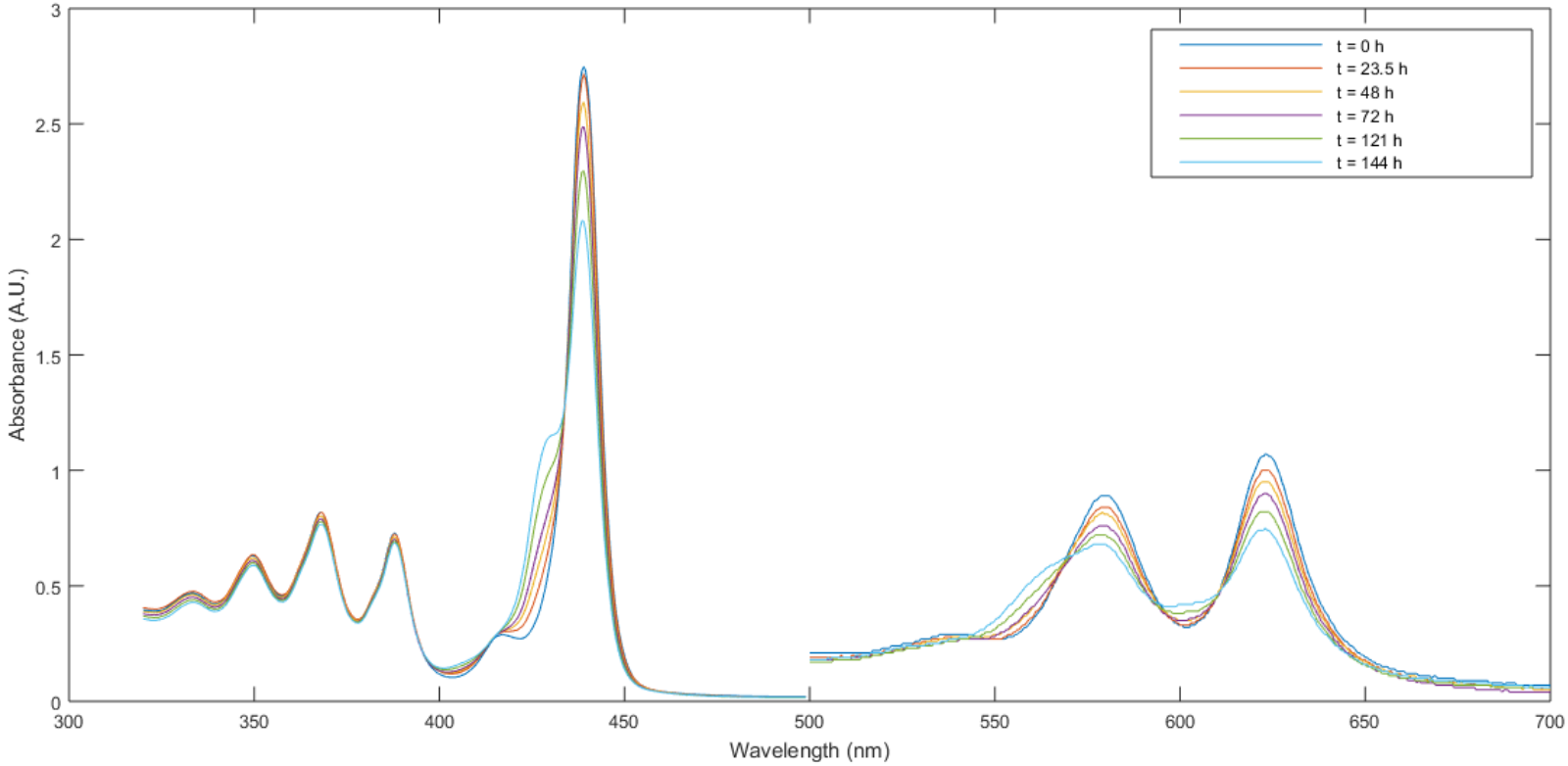

Figure A142: UV-Vis absorbance spectra of the evolution of Zn^{II}(Por(iPMAAm-co-AMMA)$_4$) at 0.1 mg/ml and 0.5 mM in DMF over time after cyanide addition. Solutions exposed to ambient air when transferring between scintillation vial to cuvette at each time interval. Absorbance from 500 to 700 nm magnified X 10

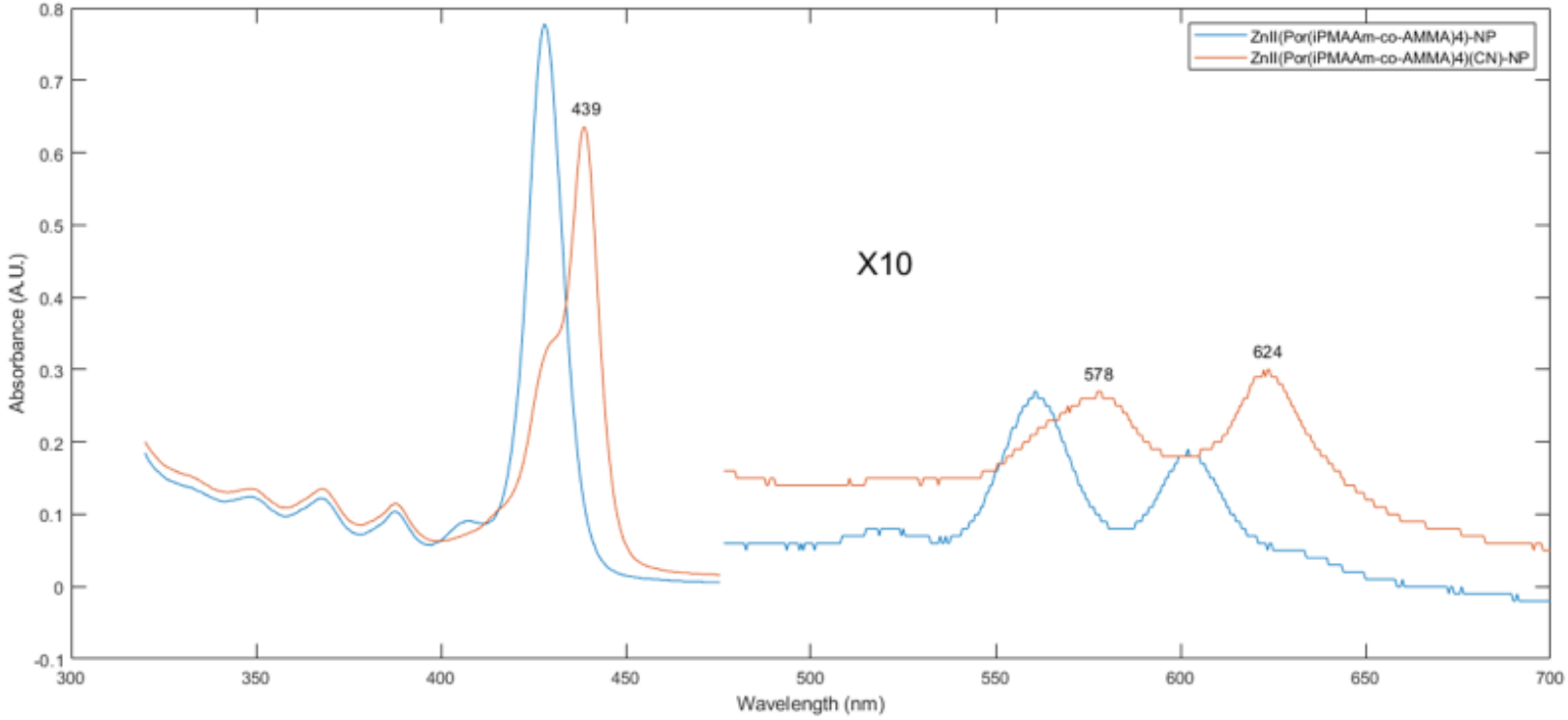

Figure A143: Comparison of UV-Vis absorbance spectra for Zn^{II}(Por(iPMAAm-co-AMMA)$_4$)-NP (blue) and Zn^{II}(Por(iPMAAm -co-AMMA)$_4$)(CN)-NP (red) at ~2.9 µM in DMF. Absorbance from 475 to 700 nm magnified X 10

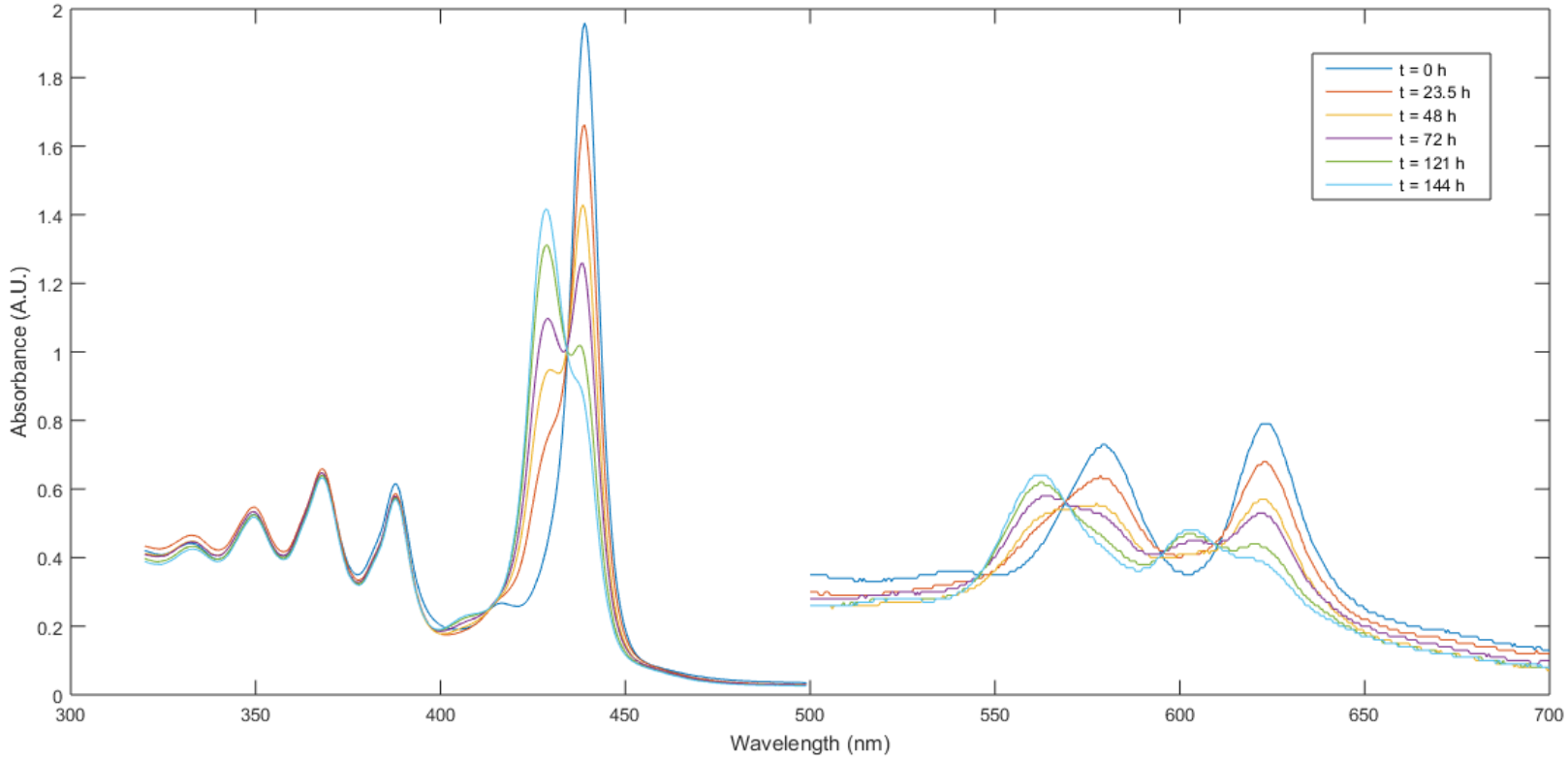

Figure A144: UV-Vis absorbance spectra of the evolution of Zn^{II}(Por(iPMAAm-co-AMMA)$_4$)-NP at 0.1 mg/ml and 0.5 mM in DMF over time after cyanide addition. Solutions exposed to ambient air when transferring between scintillation vial to cuvette at each time interval. Absorbance from 500 to 700 nm magnified X 10

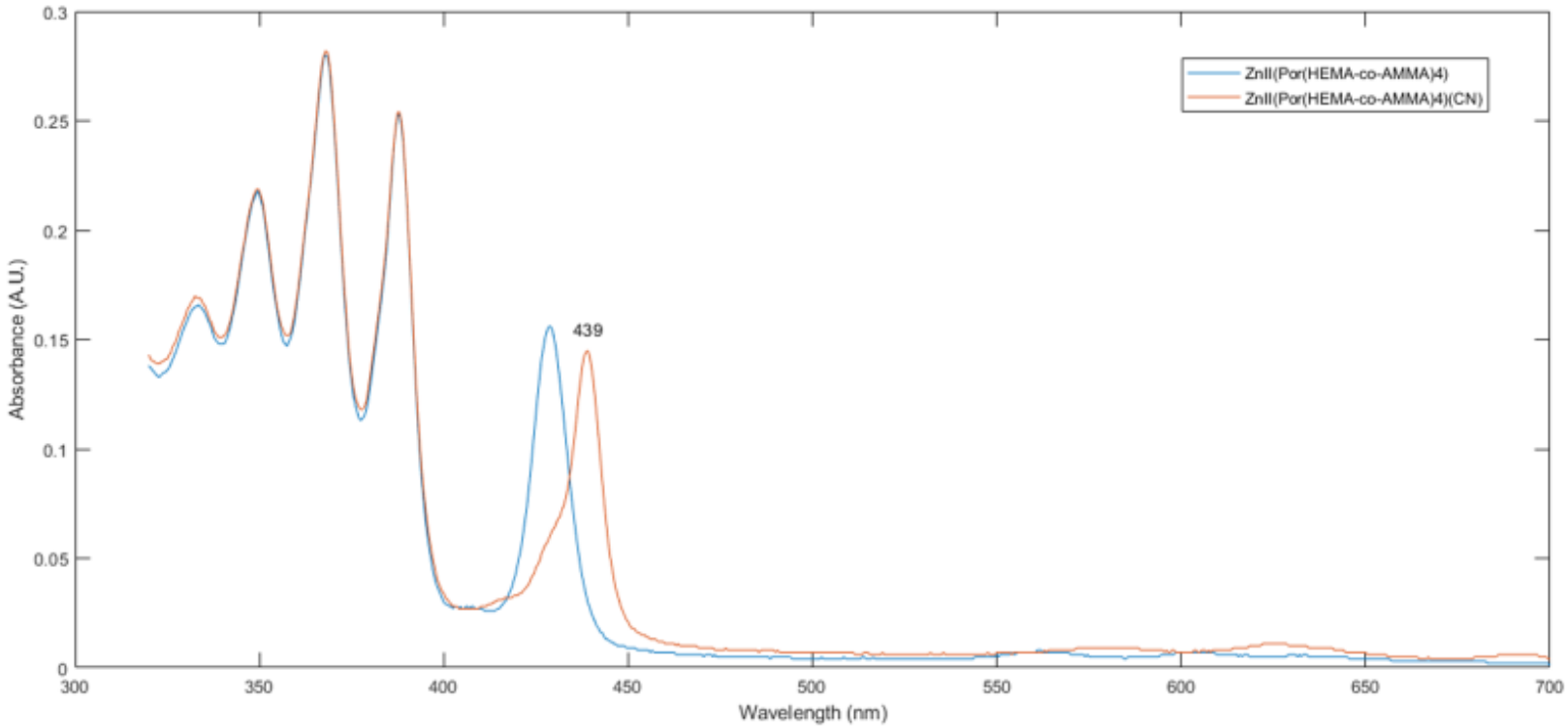

Figure A145: Comparison of UV-Vis absorbance spectra for Zn^{II}(Por(HEMA-co-AMMA)$_4$) (blue) and Zn^{II}(Por(HEMA-co-AMMA)$_4$)(CN) (red) at ~2.9 µM in DMF. Absorbance from 475 to 700 nm magnified X 10

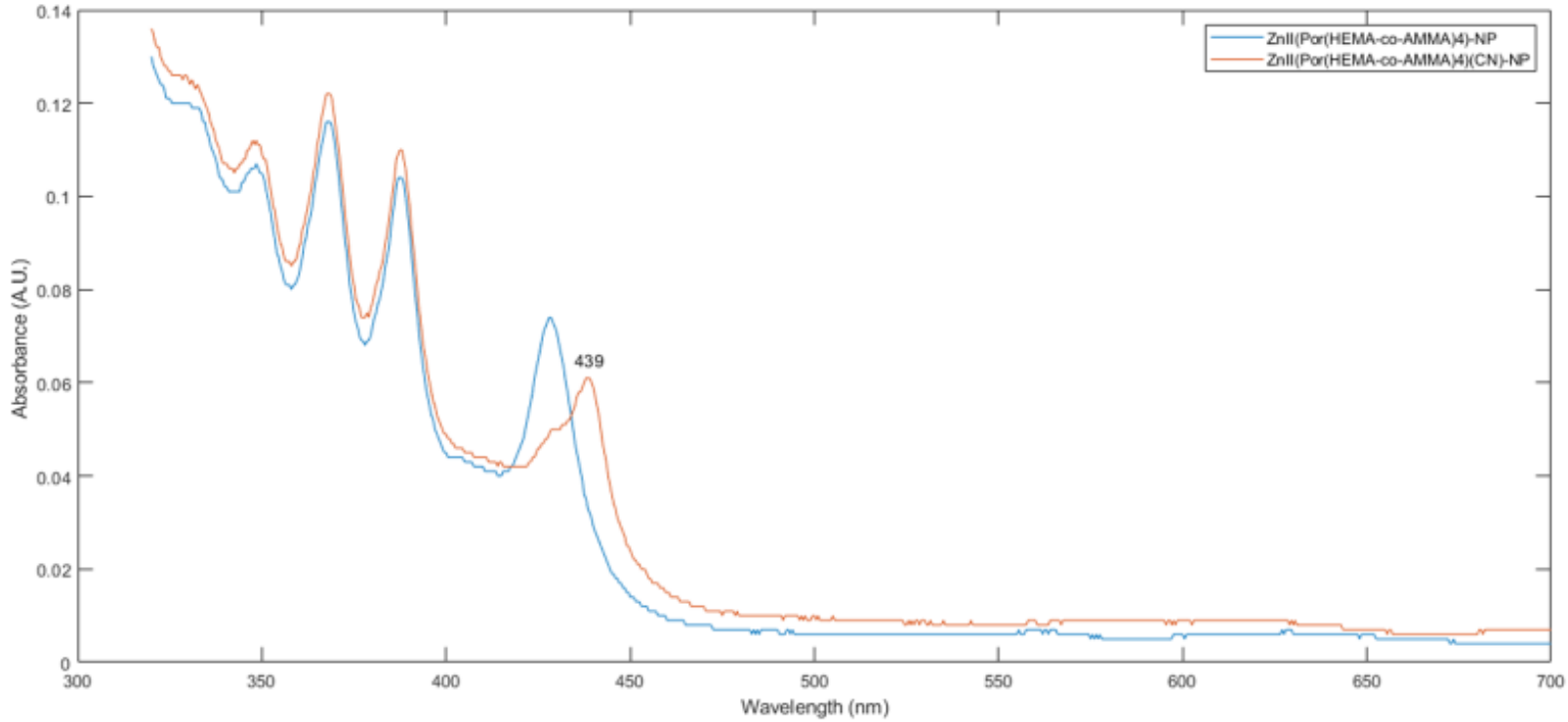

Figure A146: Comparison of UV-Vis absorbance spectra for Zn^{II}(Por(HEMA-co-AMMA)$_4$)-NP (blue) and Zn^{II}(Por(HEMA-co-AMMA)$_4$)(CN)-NP (red) at ~2.9 µM in DMF. Absorbance from 475 to 700 nm magnified X 10

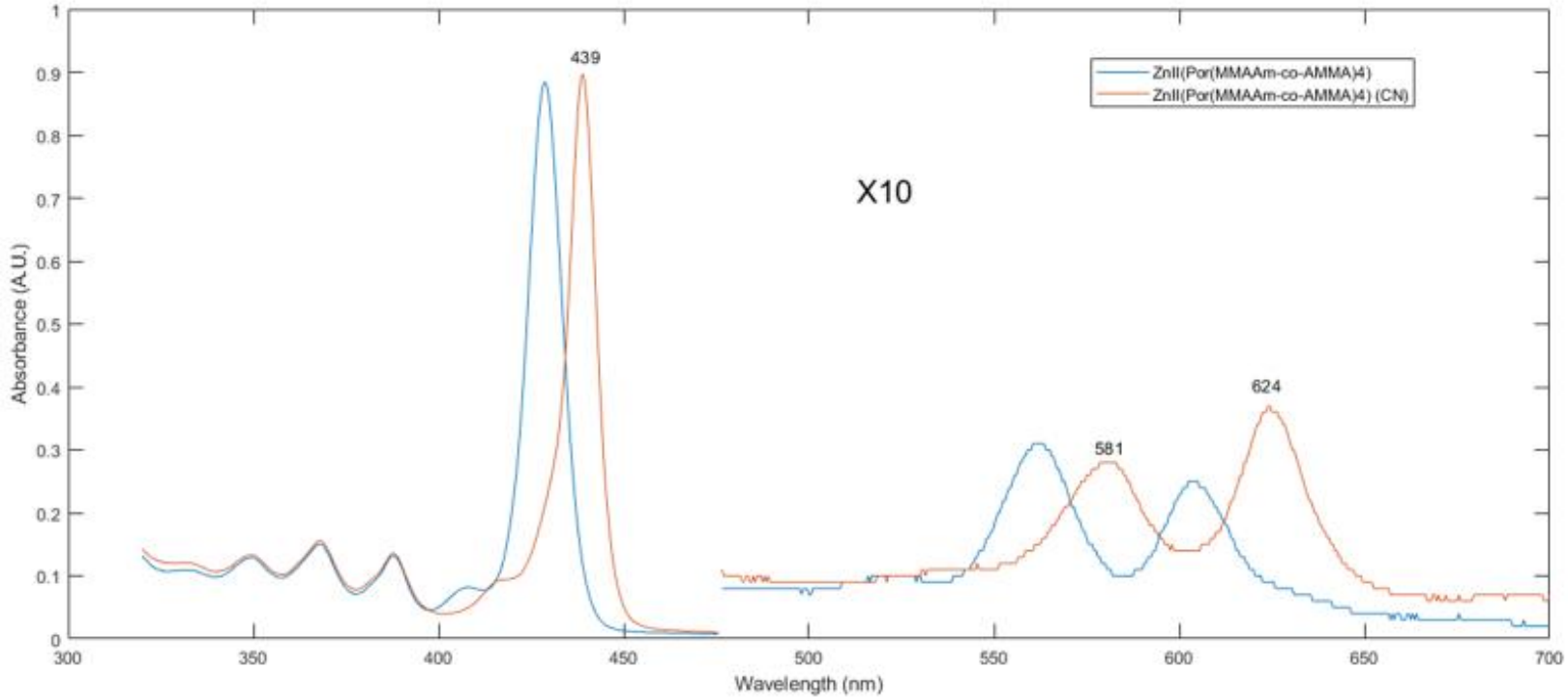

Figure A147: Comparison of UV-Vis absorbance spectra for Zn^{II}(Por(MMAAm-co-AMMA)$_4$) (blue) and Zn^{II}(Por(MMAAm-co-AMMA)$_4$)(CN) (red) at ~2.9 µM in DMF. Absorbance from 475 to 700 nm magnified X 10

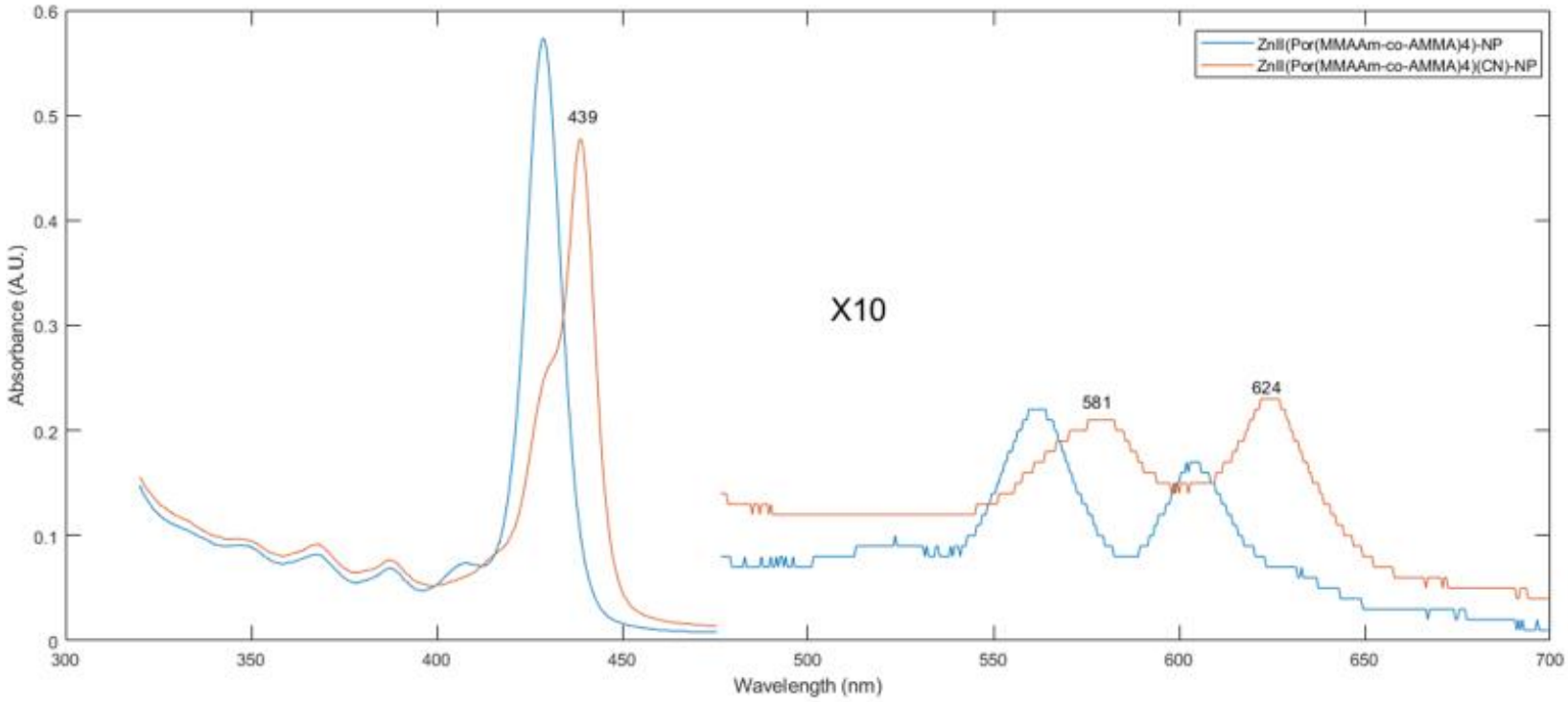

Figure A148: Comparison of UV-Vis absorbance spectra for Zn^{II}(Por(MMAAm-co-AMMA)$_4$)-NP (blue) and Zn^{II}(Por(MMAAm-co-AMMA)$_4$)(CN)-NP (red) at ~2.9 µM in DMF. Absorbance from 475 to 700 nm magnified X 10

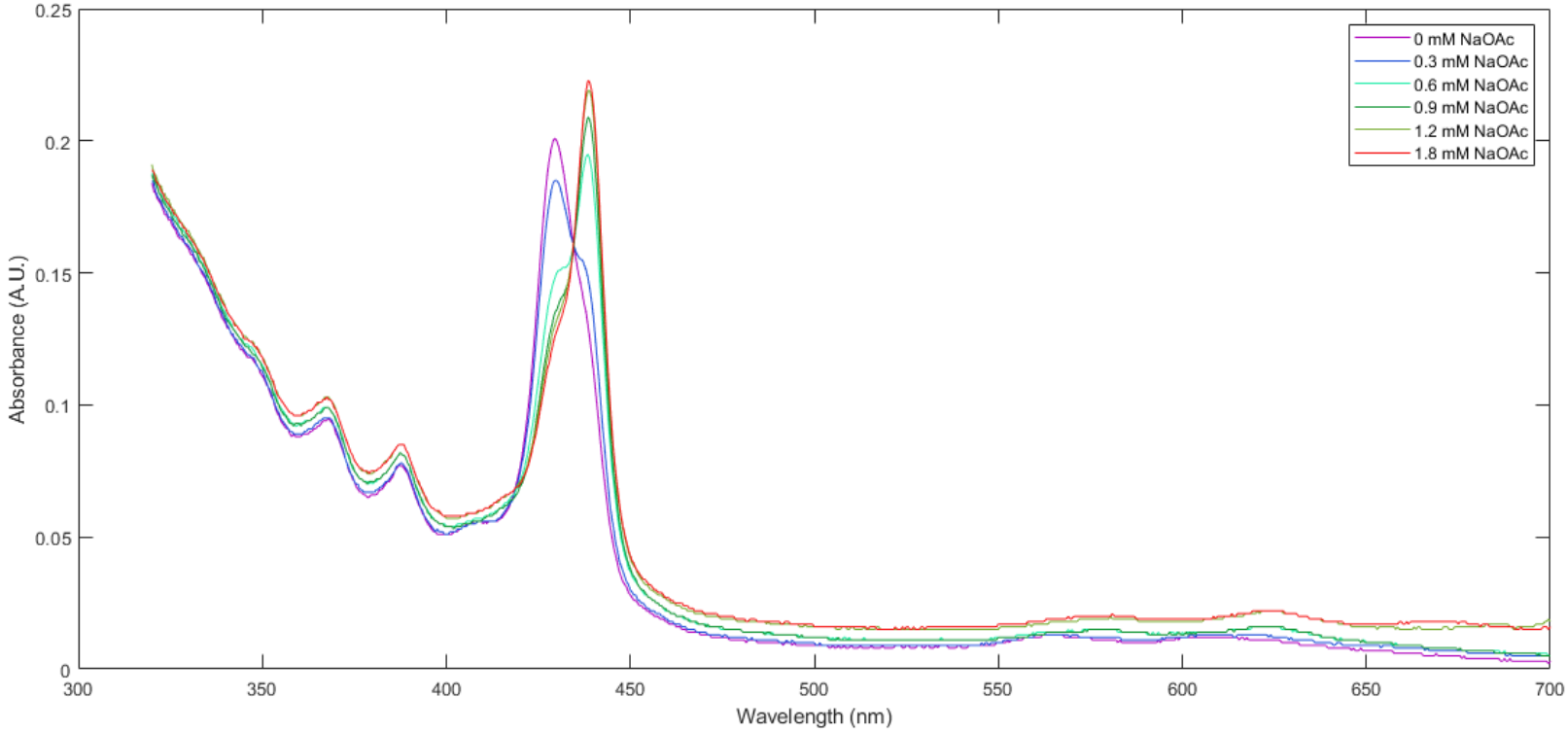

Figure A149: UV-Vis spectrums of Zn^{II}(Por(HexMAAm -co-AMMA)$_4$) at ~2.9 µM and 0.5 mM in DMF titrated with sodium acetate two weeks after cyanide addition.

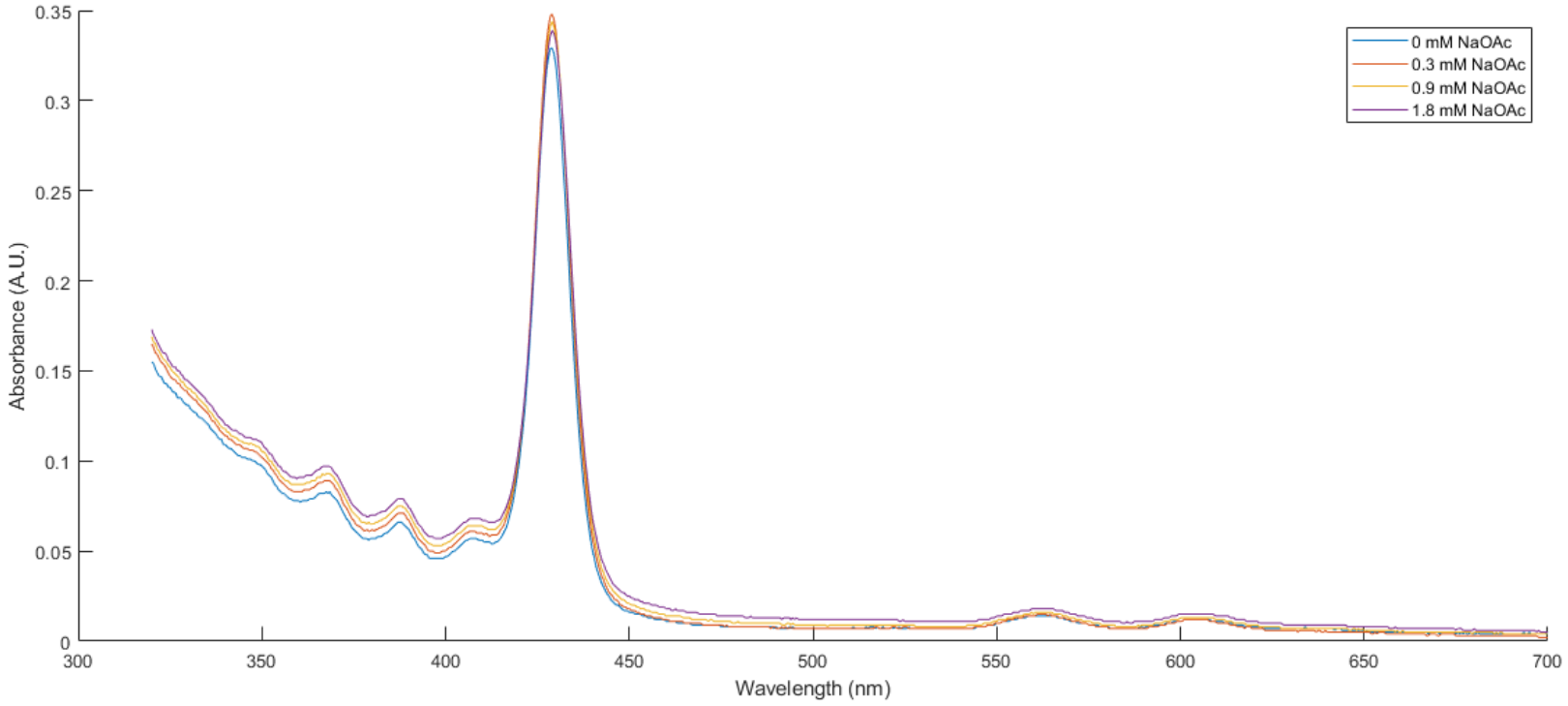

Figure A150: UV-Vis spectrums of fresh Zn^{II}(Por(HexMAAm -co-AMMA)$_4$) at ~2.9 µM in DMF solution titrated with sodium acetate.